Comparison of Non-reactive Solute Transport Models for the Evaluation of Fluid Flow in Leaching Beds

Michael Dumisane Odidi

A thesis presented for the degree of

Doctor of Philosophy

Centre for Bioprocess Engineering Research
Department of Chemical Engineering
Faculty of Engineering & the Built Environment
University of Cape Town

May, 2023

Under the supervision of:

Prof Susan T. L. Harrison

Dr Marijke Fagan-Endres

Declaration

I know that plagiarism is wrong. Plagiarism is to use another's work and pretend it is one's own. I declare that this thesis is my own unaided work. Any assistance or support that was received has been explicitly acknowledged and any contributions from the work of other people has been attributed, cited and referenced. This thesis has not been submitted to any other university for any degree or other qualifications.

I confirm that I have been granted permission by the University of Cape Town's Doctoral Degrees Board to include the following publications in my PhD thesis, and where co-authorships are involved, my co-authors have agreed that I may include the publications:

1. **Odidi M D**, Fagan-Endres M A, Harrison S T L, "Moisture absorption rates via capillary suction within packed beds – The effect of material and fluid properties with implications for heap leaching operations", *Hydrometallurgy*. 2023 Jan Vol. 215, 105975, doi:10.1016/j.hydromet.2022.105975.
2. Fagan-Endres M A, **Odidi M D**, Harrison S T L, "An accurate residence time distribution measurement method for low volumetric flowrate systems, with application to heap leaching columns", *Chemical Engineering Communications*. 2023 Jan, p1-7, doi:10.1080/00986445.2023.2169679.
3. **Odidi M D**, Fagan-Endres M A, Harrison S T L, "Residence time distribution analysis of drip irrigated beds – the effect of material and fluid properties with implications for heap leaching practice", *Minerals*, 2023 Feb, 13, 267, doi:10.3390/min13020267.
4. **Odidi M D**, Fagan-Endres M A, Harrison S T L, "Comparison of non-reactive solute transport models for the evaluation of fluid flow in packed beds with implications for heap leaching practice", (Submitted, in review).

Signature: Signed by candidate Date: May 31, 2023

Name: Michael Dumisane Odidi Student no: ODDMIC002

Abstract

Heap leaching is a hydrometallurgical process used for the extraction of minerals within complex and typically low grade ores. An important factor in the mineral dissolution process is the contact efficiency between the irrigation fluid (lixiviant) and the targeted mineral, which is influenced by both the solid and fluid properties of the system. One of the principal challenges related to the contact efficiency is preferential flow, cited to result in low extraction rates and in extreme cases, heap failure. Preferential flow reveals itself on two scales in drip irrigated heaps, referred to as the bed and solution scale. The bed scale takes a macro view of the heap and deals with uneven wetting profiles characterized by the presence of wet and dry sections. Linked to this is capillary suction effects which play an important role in the establishment of fluid flow profiles within the heap. The solution scale focuses on preferential flow behaviour in the wetted sections of the heap characterized by variations in the residence times of fluid elements. Such variations produce fast flowing, slow flowing and stagnant solution pools. Therefore, ideal solution flow behaviour in a heap results in uniform wetting at the bed scale and plug flow behaviour with similar fluid residence times at the solution scale. Though bed scale preferential flow can be visually observed, diagnosing symptoms at the solution scale typically requires the generation, analysis and modelling of residence time distribution (RTD) curves.

The main objectives of this study were to firstly explore the effects that important material and fluid properties have on the steady state fluid flow profiles in drip irrigated beds characteristic of those used in laboratory scale column leaching studies and quantified using step tracer tests. This is based on the underlying principle that the movement of inert tracer molecules within an irrigated bed at steady state is identical to the solution flow path within the bed. The second objective was to test the ability of nine empirical and semi-empirical solute transport models to adequately fit the generated flow profiles or RTD curves. The third was to compare the magnitudes of the quantified model parameters to ascertain the level of solution scale preferential flow in the different beds and determine the adequate level

of model complexity needed to describe their flow profiles which facilitates identifying the controlling variables within the system.

Properties of the loading material that were identified as potentially most impactful with respect to heap operations were: porosity, wettability, particle shape and size distribution. Therefore, four different materials with unique inherent characteristics were selected for this study: glass beads (GB - spherical and non-porous), glass shards (GS - irregularly shaped and non-porous), greywacke (GW - irregularly shaped, porous and highly wettable) and malachite ore (MO - irregularly shaped, highly porous, low wettability and non-uniform composition). In terms of fluid properties, current models have already established a correlation between the concentration of dissolved chemical species within a fluid and its viscosity. This was relevant due to the variety of lixiviant compositions used in previous heap hydrology studies and the fact that the composition also varies with time within a reactive heap. To study the effects of this parameter on the establishment of flow profiles, glycerol was used as a viscosity modifier to formulate solutions with viscosities ranging from 0.8 to 2.2 cP, representative of the range experienced in heap leaching systems due to varying SO_4^{2-} concentrations.

The packed beds were characterized using their bulk densities, voidage, total liquid hold-ups, total bed saturations, 24-hour drain-down moisture percentages, solution and tracer breakthrough times. Beds containing both narrow and mixed particle size fractions were tested. The nine solute transport models used for RTD modelling included three compartmental model configurations (CM-1, CM-2, CM-3) and the tanks-in-series (TIS) model, all empirical in nature. The five semi-empirical models selected were the advection-dispersion (AD), piston exchange (PE), piston exchange-diffusion variant (PE-D) and piston dispersion and exchange (PDE) models. A novel model formulation called the piston dispersion and exchange-diffusion variant (PDE-D) model was also coded and tested, which incorporated both the longitudinal dispersion coefficient as well as a diffusional flux mass transfer mechanism.

The CM-2, AD and TIS were mono porosity models assuming all solution volumes within the beds were actively flowing which limited their ability to account for solution scale preferential flow. The CM-1, CM-3, PE, PE-D, PDE, PDE-D models were dual porous, accounting for

the presence of either dead or stagnant solution volumes. The model parameters used to account for preferential flow in the RTD profiles included: the fraction of dead to total solution volume, dynamic to total saturation fraction, number of TIS, ratio of parallel continuously stirred tank volumes, longitudinal dispersion coefficient, overall mass transfer coefficient and maximum diffusional pore length.

The cumulative RTD responses for the bed systems composed of narrow size fractions were noticeably impacted by particle size. These systems displayed symptoms of increased solution channelling behaviour at steady state, based on their relatively short tracer breakthrough times, as the average particle size was increased from $\sim$1 to 15 mm. The incorporation of $<$0.5 mm particles in agglomerated, mixed size beds with a particle top size of 8 mm, led to a high degree of similarity in the RTD responses regardless of the different material properties. This suggested that particle size distribution in such systems was the dominant factor affecting the RTD profiles. Similar to highly porous beds, beds with fines ($<$1 mm particles) present were also characterised by longer solution and tracer breakthrough times with relatively higher liquid hold-up and saturation levels indicative of a more uniform wetting profile (reduction in bed scale preferential flow). Increased capillary suction effects for the porous and fines inclusive systems, prior to the establishment of steady state fluid flux, were postulated to be responsible for the observed trends. Higher levels of particle wettability resulted in shorter solution and tracer breakthrough times with greater drain-down moisture percentages.

The solute transport modelling of the steady state RTD profiles revealed that the presence of fines in agglomerated mixed size beds led to reductions in dispersive effects, decreased formations of dead volumes and increased mass transfer rates between the dynamic and stagnant volumes present. All these point towards greater uniformity in fluid residence times (reduction in solution scale preferential flow). Similar results were obtained for the beds of narrow size fractions when the average particle size was reduced. It should be noted that the presence of ultra-fines ($<$0.1 mm) was found to increase the stagnant liquid hold-up in the columns. This was attributed to high magnitudes of capillary forces limiting the fraction of freely flowing liquids in such beds.

Raising the irrigation solution's viscosity from 0.8 to 2.2 cP led to minor increases in the mixing and dispersive effects of the RTD profiles but had no substantial impact on most of the other bed characteristics. Modelling results suggested that these non-ideal flow patterns were brought about by reductions in the dynamic saturation of the systems. All compartmental model configurations chosen were unable to adequately fit the RTD data from beds irrigated with 1.2 to 2.2 cP viscosity solutions. The RTD profiles were more suited to the dual porosity semi-empirical models which could account for stagnant volumes.

The main comparative modelling results across all systems studied showed that the PDE and PDE-D models were the top performers, based on a model fit analysis. This was due to their dual porous nature and relatively higher levels of complexity. The mono porosity models (CM-2, TIS and AD) performed the worst due to their inability to account for isolated and immobile liquid volumes. However when <2 mm particles were incorporated into the size distribution, even the mono porosity models were able to produce relatively good fits to the generated data. This was due to the increased liquid hold-up limiting bed scale preferential flow. The modelling parameter that was least applicable was the dual permeability concept which was a feature of the CM-2 and CM-3 models. Therefore, rather than having two separate dynamic liquid volumes with different solution flow rates (dual permeability), the bed systems tested were better described by the presence of dynamic and stagnant volumes with varying degrees of mass transfer (dual porosity).

Based on these results, the incorporation of <1 mm particles in agglomerates during heap formation, will bring about a more even distribution of solution, limiting preferential flow symptoms. In cases where ultra-fines (<0.1 mm particles) are present, increasing the fraction of particles with sizes >10 mm during agglomeration will aid in increasing the fraction of mobile (actively flowing) liquid within the heap due to the increased presence of macro voids. High levels of particle porosities (>2.5 m^2/g) will also aid in this aspect. This is proposed to be due to greater void network connectivity with an increase in porosity facilitating better mass transfer.

These insights were obtained through the analysis of experimentally generated data and model simulations. They have provided a better understanding of the movement of fluid

molecules within drip irrigated beds, which is essential for improved leaching performance. Building on this, the next step is to consider the effects of scale up and reactive systems on both empirical and simulated data.

Acknowledgements

I will firstly like to thank my various colleagues at Mintek, who recognized my potential and encouraged me to pursue a post-graduate degree. Dr Petrus van Staden and Ms Mariekie Gericke especially, have been a source of great help and motivation. I am deeply grateful for the financial support that Mintek offered me during the course of my research, without which, I would not have been able to begin this wild journey.

I will like to thank my two supervisors, Prof Sue Harrison and Dr Marijke Fagan-Endres, who have inspired growth in different facets of my life. Their guidance through all the various stages of my PhD journey was invaluable. I am truly grateful to have had supervisors that offered me the space and opportunity to learn and grow whilst providing direction whenever I felt lost, constantly motivating me to step outside my comfort zone. I consider my self fortunate to have been taken under their wings and only hope to make them proud with what I accomplish from here on out. Though he was not my supervisor, I am also incredibly grateful to Dr Thanos Kotsiopoulos for all his much needed help with my modelling and data analysis.

Thanks are due to all my colleagues at the Centre for Bioprocess Engineering Research (CeBER), both past and present. I will like to express my deep gratitude to Mr Emmanuel Ngoma, who was like a big brother to me, for all the help that he offered me with my experiments. It was truly a joy to work with him and learn from his vast expanse of technical skill and knowledge. Mr Tich Samkange was not only a great source of help, due to his resourcefulness, but also of constant joy and laughter. He made coming into the labs fun and exciting. Asking for help was a pleasurable experience as my interactions with him always left me feeling better. Tolbert Golela was an invaluable asset towards the completion of my research. He was approachable and always willing to help. I am grateful to have made such a loyal friend. I will also like to thank Ms Sharon Rademeyer who kept our labs organized and running like clockwork. Your level of professionalism has left a lasting impression on me. Also, to all the MSc and PhD students I had the pleasure of interacting

with, thank you. Hearing your stories and sharing mine really kept me motivated and allowed me to see the value in my work. Ms Annah Moyo was one such student who was always there to hear my problems and offer help at crucial moments in my journey. Thank you.

Special thanks are due to the lab managers and lab assistants at the various labs I had the pleasure of working in. I am grateful to Ms Shireen Govender, Mr Kenneth Maseko and Mr Monde Bekaphi at the Centre for Minerals Research (CMR) for all the help they offered me during my solid characterisation work. I will like to thank Associate Professor, Dr Belinda McFadzean and Mr Gary Groenmeyer for all their help with my wettability tests. I am also in the debt of all those who worked at the UCT Chemical Engineering analytical lab, for their meticulous and efficient analysis of all my samples. The guys at the UCT civil engineering laboratory also deserve my thanks for sourcing some of the materials I needed for my work.

I will like to acknowledge the team at the UCT High Performance Computing Centre, especially Mr Andrew Lewis who was always quick to offer me guidance in making use of the cluster. His help was really vital in allowing me to achieve the objectives my thesis.

To my friends who stood by me and supported me through the ups and downs of this journey, I will like to say thanks. To all my fellow Toasties at the UCT Toastmasters, I am thankful to have had such a supportive network of friends who allowed me to develop in ways I never thought possible. I will also like to express my gratitude to the late Professor Dee Bradshaw, the orignal founder of UCT Toastmasters Club, who was also my number one fan. Her memory and values live on within each fortunate soul she touched.

To my family, my mom, dad, Jaze, Emma and Glory, I will like to say thank you. Having such a solid foundation was what enabled me to leap for the stars. I am truly fortunate to have loved ones who always knew what to say to reignite my passion and get me back on my feet whenever I stumbled. I am truly proud of what we have accomplished together.

Lastly, without my faith, I would not have been able to complete this journey. I dedicate this PhD to my Heavenly Father, Jesus Christ, who despite all I am, has soo loved and cherished me.

Contents

Thesis Data: DOI Links

Table 1: DOI links to image files presented in thesis

Chapter	Item	DOI
Chapter 1	Images	10.25375/uct.15067521
Chapter 2	Images	10.25375/uct.15067653
Chapter 4	Images (2D Shape Descriptors)	10.25375/uct.15067761
Chapter 4	Images (Other Figures)	10.25375/uct.15067779
Chapter 4	Images (Analyzed Particle Images)	10.25375/uct.15067824
Chapter 5	Images	10.25375/uct.15067935
Chapter 6	Images (Flow Visualizations)	10.25375/uct.15067947
Chapter 6	Images (Model Algorithms)	10.25375/uct.15068112
Chapter 6	Images (Compartmental Model Configurations)	10.25375/uct.15068544
Chapter 6	Images (Model Response Analysis - AD)	10.25375/uct.15068820
Chapter 6	Images (Model Response Analysis - PDE)	10.25375/uct.15069249
Chapter 6	Images (Model Response Analysis - PDE-D)	10.25375/uct.15069420
Chapter 6	Images (Model Response Analysis - PE)	10.25375/uct.15069738
Chapter 6	Images (Model Response Analysis - PE-D)	10.25375/uct.15069825
Chapter 6	Images (Model Response Analysis - TIS)	10.25375/uct.15069828
Chapter 7	Images (Experimental Apparatus)	10.25375/uct.15069966
Chapter 7	Images (Measurement Cell Testing)	10.25375/uct.15069984
Chapter 9	Images (Model Fit Residuals - Glass beads)	10.25375/uct.15070002
Chapter 9	Images (Model Fit Residuals - Glass shards)	10.25375/uct.15070011
Chapter 9	Images (Model Fit Residuals - Greywacke)	10.25375/uct.15070032
Chapter 9	Images (Model Fit Residuals - Malachite ore)	10.25375/uct.15070035

Table 2: DOI links to data and code files presented in thesis

Chapter	Item	DOI
Chapter 4	Data (Excel Workbooks)	10.25375/uct.15070044
Chapter 4	Data (BET Analysis)	10.25375/uct.15070089
Chapter 5	Data (Excel Workbooks)	10.25375/uct.15070098
Chapter 6	Data (Excel Workbook - Core Model Codes)	10.25375/uct.15070107
Chapter 6	Data (Model Codes Python)	10.25375/uct.15070143
Chapter 7	Data (Excel Workbooks)	10.25375/uct.15070212
Chapter 7	Data (Scilab Code)	10.25375/uct.15070218
Chapter 8-9	Data (Excel Workbook)	10.25375/uct.15082407
Chapter 9	Data (Excel Workbooks)	10.25375/uct.15070224
Chapter 9	Data (Python Codes)	10.25375/uct.15070257

Nomenclature

The next set of lists describe several acronyms, symbols, super- and subscripts that will be used within the body of this document. SI units are given for the symbols but data may be presented in alternate units within the text. In such cases the units will be explicitly stated.

Acronyms

AD	Advection Dispersion model
BLS	Barren Leach Solution
CAPEX	Capital Expenditure
CFD	Computational Fluid Dynamics
CM	Compartmental Model
CSF	Continuum Surface Force
CSTR	Continuous Stirred Tank Reactor
DNS	Direct Numerical Simulations
GB	Glass Beads
GS	Glass Shards
GW	Greywacke
HPC	High Performance Computing
IUPAC	International Union of Pure and Applied Chemistry
MO	Malachite Ore
MSPD	Mixed Side-Pore Diffusion model
PCBs	Printed Circuit Boards
PDE	Piston Dispersion Exchange model
PEPT	Positron Emission Particle Tracking
PFR	Plug Flow Reactor
PLS	Pregnant Leach Solution
PNM	Pore Network Modelling

PSPD	Profile Side-Pore Diffusion model
QEMSCAN	Quantitative Evaluation of Minerals by Scanning Electron Microscopy
ROM	Run Of Mine
RTD	Residence Time Distribution
SPH	Smooth Particle Hydrodynamics
TIS	Tanks-in-Series model
UCT	University of Cape Town
VOF	Volume Of Fluids
XCT	X-ray Computed Tomography

Mineral Chemical Formulae

Biotite	$K(Mg,Fe)_3(AlSi_3O_{10})(OH,F)_2$
Bornite	Cu_5FeS_4
Chlorite	ClO_2
Chrysocolla	$Cu_{2-x}Al_x(H_{2-x}Si_2O_5)(OH)$
Ilmenite	$FeTiO_3$
Malachite	$Cu_2CO_3(OH)_2$
Musovite	$KAl_2(Si_3Al)O_{10}(OH,F)_2$
Quartz	SiO_2

Greek Symbols

β	Saturation	m^3liquid/m^3void
δ	Fluid mass transfer rate	m^3fluid/m^3s
ϵ	Electrical resistivity	$\Omega \cdot m$
Γ	Diffusion mechanism constant	[-]
γ	Surface Tension	N/m
μ	Viscosity	$Pa \cdot s$
ω	Empirical correction factor for diffusion coefficient	[-]
ϕ	Liquid hold-up	m^3liquid/m^3bed

ρ	Density	kg/m^3
τ	Residence time	s
θ	Contact angle	$^\circ$
υ	Electrical conductivity	S/cm
ε	Bed voidage	m^3void/m^3bed
ϑ	Volumetric liquid content	m^3liquid/m^3

Roman Symbols

A	Area	m^2
C	Concentration	mol/m^3
C_p	Packing constant - Intrinsic permeability	[-]
Cn	Washburn's packing constant	m^5
Cv	Manufacturer's viscometer constant	m^2/s^2
D	Fick's coefficient	m^2/s
d	Diameter or distance	m
g	Gravitational acceleration	m/s^2
H	Dimensional height	m
h	Fluid height or pressure head	m
I	Electrical current	A
J	Molar Flux	$mol/(m^2s)$
K	Hydraulic conductivity	m/s
k	Intrinsic permeability	m^2
K_ma	Overall mass transfer coefficient	s^{-1}
M	Mass	kg
n	Number of tanks: TIS model	[-]
P	Total pressure	N/m^2
r	Radius	m
S	Source term	m^3liquid/m^3s

t	Time	s
V	Volume or voltage	m^3 or V
v, U	Superficial velocity or volumetric flux	m/s
X	Maximum pore length	m
x	Spatial domain	m
z	Spatial domain	m

Subscripts

a	Air
ad	Advective
al	Air-liquid
b	Bed
c	Capillary
d	Dynamic
df	Diffusion
ds	Dispersion
e	External
f	Fast flowing fluid volume
i	Internal or represents spatial domain in numerical discretization
l	Liquid
p	Particle
r	Residual
s	Static/stagnant
sa	Solid-air
sl	Slow flowing fluid volume
sl	Solid-liquid
v	Voids

Other Symbols

$\bar{K}$	Cell constant	m^{-1}
$\bar{r}$	Ratio of flow volumes to system volume	[-]
$\bar{v}$	Kinematic viscosity	m^2/s
D^*	Effective diffusion coefficient	m^2/s
R_F	Cumulative fraction of particles	[-]

Chapter 1

Introduction

Mining involves the extraction of metals and minerals from ore bodies located around the globe with a simplified overview given in Figure 1.1 (Zanbak, 2012).

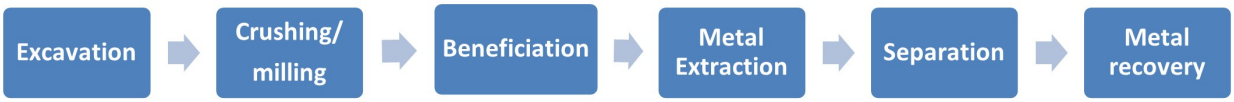

Figure 1.1: Simplified flow sheet of a typical mining operation, based on Zanbak (2012).

The excavation stage typically generates waste rock that is initially separated from the ore and stock piled. The valuable metals and minerals in the ore can be further concentrated through comminution and beneficiation processes such as crushing, grinding and flotation, the choice of which is dependent on the subsequent metal extraction process. The product rich stream is then sent for further processing involving the separation and recovery of the targeted species from the reagents used in the extraction process (Balasubramanian, 2016; Dwyer et al., 2012).

The are two main metal extraction pathways: pyrometallurgy and hydrometallurgy. Pyrometallurgical processes normally occur in furnaces at temperatures exceeding 1500°C and include the smelting, roasting and refining of ores. Hydrometallurgy falls under the broad older term of solution mining and involves the use of aqueous solution in the selective leaching (dissolution) of metal species from ore bodies and takes place at significantly lower temperatures (usually below 100°C) (Bartlett, 1992; Habashi, 2018). The choice of route to follow depends on the type of ore, its grade, environmental regulations as well as available finances. In most cases, hydrometallurgy is the preferred choice for the treatment of low grade ores and

can be used for small to large scale operations with relatively lower initial capital investment (Habashi, 2018). The focus of this thesis is on the leaching sub-process in hydrometallurgy.

Leaching is a physio-chemical process in which the metal species of interest undergo anion/cation exchange to form metal salts in the presence of an aqueous solution. The salts are then transported due to hydrological forces. Leaching has been observed to occur naturally in cases where rainwater seeps into soil, dissolves and transports soluble salts. There are different types of metal extraction operations that mimic this natural process. Examples include in-situ, dump, tank and heap leaching. The focus of this thesis is on heap leaching.

Heap leaching is ideal for the treatment of low grade ores. It has been applied in the extraction of a variety of base, precious and heavy metals such as copper, uranium, silver and gold. At first it was mainly utilized in the treatment of easy to leach oxide ores, but with the advent of heap bioleaching, its application has extended to sulphidic ores as well (Watling, 2006). In 2009, approximately 15% of the world's gold and copper were produced using this process. It was estimated that in 2013, there were over 300 heap leaching operations at different stages of development globally (Sinha and Smith, 2015). This number of operations is expected to rise as high grade ore resources become depleted.

Key challenges with heap leaching include high operational costs and lower than predicted metal extraction rates leading to low recoveries (Ghorbani et al., 2011). To alleviate these issues, more understanding of the sub-processes within heap leaching is being sought. These sub-processes include the chemistry, microbiology, air dynamics and hydrodynamics of a heap (Watling, 2006). With respect to heap hydrodynamics, the non-uniform flow and distribution of drip irrigated solution, commonly referred to as preferential, non-ideal or channelling flow, is a significant deleterious factor (Wu et al., 2007). This is because the success of many heap leaching operations is dependent on the efficient contact between reagent molecules, in the lixiviant solution, and the mineral grains within the ore as well as the subsequent transportation of dissolved species out of the heap (Ghadiri, 2019; Harrison, 2016). Therefore, understanding the factors influencing the establishment of solution flow profiles within heaps is vital in addressing some of the challenges associated with its hydrodynamics.

Preferential flow reveals itself on two scales (Figure 1.2). Upon drip irrigation of a dry heap,

bed scale preferential flow results in non-uniform wetting evidenced by the presence of both dry and wet sections. Moisture absorption via capillary suction plays a key role in this initial wetting process and is related to the physical properties of the ore (O'Kane et al., 1999). In the wetted sections of a heap, preferential flow results in a variation in fluid flow velocities at the solution scale, with actively flowing channels, stagnant and slow moving solution pools. There are relatively few studies dealing with solution scale symptoms of preferential flow in heaps and as such, this is the prime focus of this study though certain aspects relating to the bed scale phenomenon are discussed.

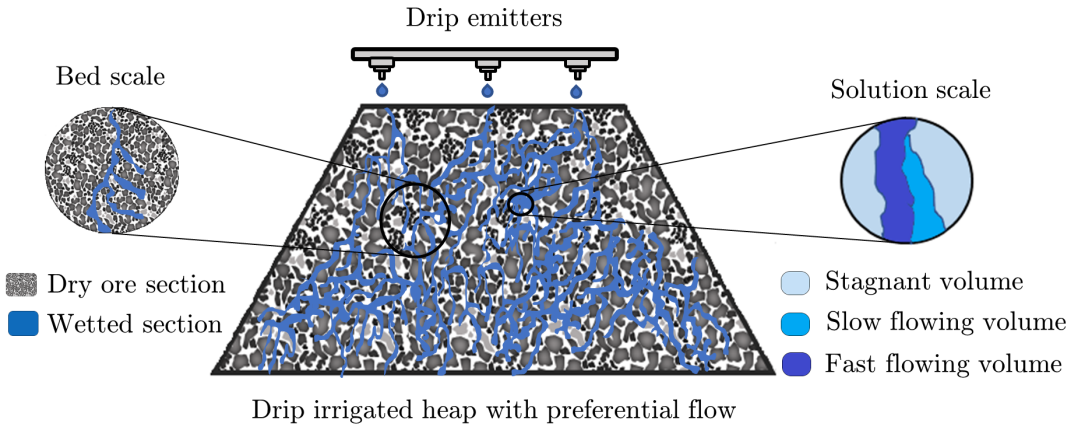

Figure 1.2: Preferential flow depiction on both the bed and solution scale in a drip irrigated heap (Odidi et al., 2022).

Tracer tests are typically used in the diagnosis of solution scale preferential flow behaviour. This is done via the generation of residence time distribution (RTD) curves which are subsequently modelled to quantify different solute transport parameters. In non-reactive systems irrigated with carefully selected tracer solutions, these solute transport parameters are descriptive of the fluid flow characteristics prevalent in the packed beds (Simunek and van Genuchten, 2006). The generated empirical and modelled data is used to address the concerns of a lack of fundamental research on hydrodynamic parameters specific to leaching test columns and the factors influencing these parameters (John, 2011; van Zyl et al., 1988).

Previous studies have touched on: the modelling of solute transport processes for the evaluation of flow profiles (Bouffard and Dixon, 2001; Bouffard and West-Sells, 2009; de Andrade

Lima, 2006; Dixon and Afewu, 2011; Ilankoon et al., 2013; Liu et al., 2015; van Staden and Petersen, 2018a); the effect of material properties on fluid flow (Fernando et al., 2019; Ilankoon and Neethling, 2013, 2016; Stevens et al., 2009); link between capillary suction and fluid flow (Ilankoon and Neethling, 2014, 2016; O'Kane et al., 1999; Wu et al., 2007; Yin et al., 2016) and the effect of solution viscosity in leaching systems (Ghadiri, 2019; Watling et al., 2014). However, some of these factors have been studied independently from any modelling work, hence there is limited information on the relationship between material properties, irrigation fluid properties, capillary suction and the modelling of RTD profiles for the diagnosis of solution scale preferential flow in packed beds. Additionally, there is little research to guide the choice of which solute transport models to use in the characterisation of RTD data from drip irrigated beds due to a lack of detailed comparative studies between the fitting abilities of the different models.

1.1 Objectives of this Thesis

The first objective of this thesis is to identify minimally researched bed and fluid properties that are likely to affect the solution scale preferential flow behaviour of drip irrigated beds and ascertain the current state of the art in the solute transport modelling of RTD profiles through a detailed literature review.

The second objective of this thesis is to test the effect that the identified properties have on moisture absorption rates and capacity via capillary action in packed beds.

The third objective is to assess the impact of the identified properties on bed characteristics and RTD profiles obtained via tracer tests on drip irrigated packed beds under steady state fluid flux.

The fourth objective is to perform a model response analysis on commonly used non-reactive solute transport models as well as develop a novel model formulation by combining the beneficial attributes of already existing models.

The fifth objective is to quantify the effect of the identified properties on solution scale preferential flow behaviour in packed beds utilizing model parameters fitted to RTD curves. This

allows for model comparisons in order to establish the appropriate level of model complexity needed to simulate RTD profiles of leaching beds.

The fundamental knowledge gained through this research will not only aid in the development of more comprehensive heap leaching models but also shed light on how certain operational variables can be altered to help combat preferential flow in heaps. However, due to the complex nature of leaching systems with the multitude of factors affecting their performance, certain aspects such as the effect of chemical reactions, particle segregation and aeration are beyond the scope of this study. Though allusions to the impact of the transient (wetting) stage on bed hydrodynamics will be made in this thesis, the main focus will be on the analysis of RTD profiles generated under steady state fluid flux to elucidate the symptoms of solution scale preferential flow. Therefore, transient fluid flow modelling is also beyond the scope of this study.

1.2 Outline of Thesis Chapters

Chapter 2: interrogates the key studies pertinent to heap leaching, its challenges, and the development of potential research areas.

Chapter 3: provides a detailed list of the experimental objectives with associated key questions that are pertinent to this study. The novel aspects of this study are also highlighted.

Chapter 4: presents the methodology used and results obtained for the characterisation of the irrigation fluids and packing materials utilized in this study.

Chapter 5: discusses the methodology used and results obtained for both moisture retention and capillary suction tests conducted on packed bed systems composed of the selected materials.

Chapter 6: introduces the nine solute transport models utilized in this study. The conceptualization, assumptions, limitations, equations, parameter descriptions, coding and response analysis for each of the selected models are presented and discussed. The stability analysis and solving algorithms are found in the appendices.

Chapter 7: gives a detailed account of the different apparatus, experimental set-up and methodology used to conduct salt tracer tests in packed bed systems. A special focus is given to the design, testing and implementation of a conductivity measurement cell used for online conductivity measurements.

Chapter 8: presents the experimental conditions, bed characterisation results and cumulative RTD profiles.

Chapter 9: presents the model fit results and parameter analysis along with an in depth discussion on the relevance of these two aspects to the tested bed systems.

Chapter 10: summarizes the main aspects of this work and gives recommendations on possible future research.

Chapter 2

Literature Review

This chapter reviews the heap leaching process, its difficulties, laboratory tests to identify solutions, fundamental principles and factors affecting fluid flow in leaching beds and the non-reactive solute transport modelling of fluid flow profiles in beds under steady state irrigation.

2.1 A Brief History of Heap (Bio)Leaching

Percolation leaching was documented for copper extraction in the Hartz Mountains area in Germany in the mid 16^{th} century (Ghorbani et al., 2016; John, 2011). Around the same time, Georgius Agricola illustrated what is arguably a heap leaching plant in De Re Metalllica (Kappes et al., 2002). However, the clearest reference to heap leaching dates back to 1752 with the first mention of a large scale operation for the extraction of copper from oxide and sulphide ores at Rio Tinto (John, 2011).

Though heap leaching has been practiced for centuries, sources, predominantly from the Western world, seem to agree that current heap leaching history began in the 20^{th} century with the establishment of the United State's Bureau of Mines. The prime focus was on the leaching of precious metals inspired by the increase in worldwide application of the cyanidation process for gold leaching after its conception in 1887 by J. S. MacArthur in England (Ghorbani et al., 2016; Zanbak, 2012). The commencement of the Cortex gold and silver heap leach project in 1969 can be used as an example of this (Kappes et al., 2002). This is also the time period in which microbial species, such as *Acidithiobacillus ferrooxidans*, capable of facilitating the metal dissolution process from sulphide minerals, were identified, ushering in the era of the heap bioleaching process (John, 2011). A recent study in 2013

placed the number of heap leaching operations above 300 with more to come as high grade ore reserves become depleted (Sinha and Smith, 2015).

2.2 An Overview of the Heap Leaching Process

A typical heap leaching block flow diagram is shown in Figure 2.1. It begins with the run-of-mine (ROM) ore which is crushed and/or agglomerated and then stacked upon an impermeable pad to form a heap. The heap is irrigated at the top with a lixiviant solution that percolates through the heap under the influence of gravity, dissolving the metal species of interest (extraction) and is collected in a PLS pond. The solution from this pond is sent to a metal's recovery unit in which the targeted metal is stripped, producing a barren leach solution (BLS) which is a regenerate of the lixiviant.

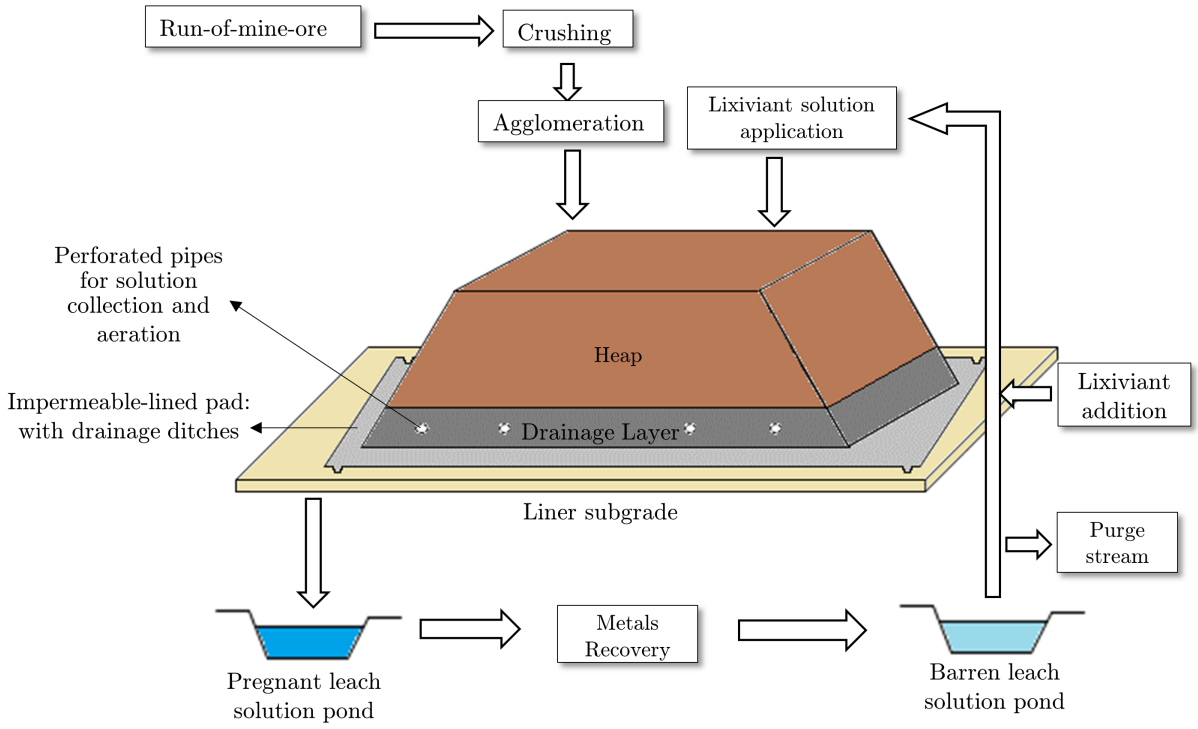

Figure 2.1: An overview of a typical heap leach flow sheet, based on Zanbak (2012).

Most of the solution from the BLS pond is then recycled back to the top of the heap together

with the addition of fresh lixiviant while a small portion is bled to reduce the build-up of impurities (John, 2011; Kappes et al., 2002; Zanbak, 2012). However, not all operations require a physical pond with some opting to transport the PLS directly to the processing plant using high capacity pumps. Total leach time can vary from months to years to decades depending on a variety of factors such as ore type, heap structure, irrigation rate, permeability, mineral liberation etc., (Kappes et al., 2002). The various components are now discussed in more detail.

2.2.1 Ore preparation

One of the defining features that separates heap leaching from dump leaching is the ore preparation stage prior to its stacking. It is important to highlight that not all the steps that will be mentioned here are mandatory and each may be applied with varying degrees of rigour in an actual heap leaching plant. The main purpose of ore preparation is to optimize particle size distribution for both mineral liberation and better heap permeability which lead to enhanced extraction rates (Ghorbani et al., 2016).

Ore blending is the first possible preparation step and is accomplished by mixing ores from different stockpiles to attain a more even distribution of minerals (Bartlett, 1992). The second preparation step is comminution, during which the size of ROM ore gets reduced. Communition uses multiple stages of jaw and cone crushers (Bartlett, 1992). The main aim is to enhance mineral liberation which reduces leaching time. However, crushing adds to the plant's operating costs meaning that the degree of liberation must be balanced with what is financially feasible (Ghorbani et al., 2016). There is no consensus in literature regarding a heap leaching top size. Some authors have proposed a range between 10 and 40 mm (Ghorbani et al., 2016), some have extended the maximum to 50 mm (Miller et al., 2003) and others to 75 mm (van Zyl et al., 1988) while Bartlett (1992) states that a reduction in top size to about -20 mm or -25 mm would be a good compromise.

Heaps are known to contain a wide range of particle sizes and one of the major issues that arises during heap construction is segregation which was proposed to lead to variations in permeability and non-uniform percolation (Bartlett, 1992). However, results from simulated

segregation studies on an oxide copper ore sample by van Staden and Petersen (2018) showed that though mimicking heap construction methodologies resulted in particle size distribution and bulk density variations in different sections of the constructed bed, there was no significant impact on leaching kinetics when compared to the unsegregated ore bed. In fact, a follow up study by the same authors (van Staden and Petersen, 2019), indicated that vertical stratification aided in the spread of irrigated solution. However, this did not result in any significant improvements to leach kinetics over the non-stratified bed. The authors mention that the results obtained could be dependent on the material tested, hence, segregation could still be potentially deleterious to leaching performance.

One of the main proposed solutions to segregation in heaps is agglomeration. It is defined as the consolidation of fine and coarse particles into larger shapes through the means of agitation (Bouffard, 2005). The major mechanism by which it reduces the effect of segregation is by the elimination of isolated fines. Agglomeration raises the bottom size fraction of heaps from close to 0 to approximately 2 mm (Miller et al., 2003). In their review of the agglomeration process, Bouffard (2005) states that authors have found that the proportion of fines less than 50 - 74 microns play a significant role in determining the need for agglomeration while van Zyl et al. (1988) mentioned that agglomeration is necessary whenever it is required that the feed be crushed to 19 mm or finer.

There are a variety of methods with which agglomeration can be achieved. One of three common ways that will be discussed is belt agglomeration in which ore that is being transported on conveyor belts is sprayed with agglomeration solution. Mixing of the different ore particles occurs at transfer points between conveyors. This is commonly done for ores containing less than 15% of -104 micron particles. The second is disc agglomeration in which ore is loaded onto a rotating disc and sprayed with solution. The aim is normally to produce pellets of uniform size. The third way is drum agglomeration in which ore is loaded into a cylindrical inclined drum that rotates to agitate and facilitate the binding of particles (Bouffard, 2005).

Another important issue to consider during the agglomeration process is the choice of agglomeration fluid. In many cases, agglomeration is carried out with the same fluid that will

be used during irrigation. However, the surface tension and van der Waals forces that hold particles together when using such solutions may not always be sufficient, necessitating the use of binders to impart added strength to the agglomerates (Bartlett, 1992; Bouffard, 2005). Binders can be either liquid or solid and work by forming a bridge, film or matrix around the agglomerates. It is also possible for binders to cause chemical reaction as is the case during the curing process in which a hydration reaction between calcium silicates and water occurs to form calcium hydroxide and calcium silicate hydrate. The formation of these compounds help to strengthen agglomerates and maintain the structural integrity of heaps. The effect of agglomeration on column hydrodynamics and solute transport is covered in sub-section 2.6.3.

2.2.2 Heap Structure

Selecting a leach pad site is crucial in designing a heap leaching plant. This poses an optimisation problem between haulage distance, environmental suitability and the amount of preparatory work that will need to be done on the selected site (Bartlett, 1992). Chosen sites usually have a large surface area and require a ground that is nearly flat but slightly tilted with a 1 to 3% slope to channel solution away from the heap and into collection systems (Ghorbani et al., 2016). Depending on the site, pad regrading may need to be done to achieve the desired slope (Ulrich et al., 2003). Once this is accomplished, a liner subgrade, which can take the form of a compacted bedding soil layer, is created to boost the performance of the geomembrane layer placed on top of it.

The geomembrane layer forms the primary liner underneath the heap (Ulrich et al., 2003). It has three main purposes: offer support to the heap by providing an adequate interface friction angle; collect and channel the solution from the drainage layer to the drainage pipes or collection dams; and most importantly, from an environmental perspective, prevent any penetration of solution into the ground (Bartlett, 1992). The membranes are commonly manufactured from polyethylene, with low density polyethylene (LDPE) used directly beneath heaps for its flexibility and high density polyethylene (HDPE) on the sides of the heap exposed to ultraviolet radiation. Both these materials are suitable for containing acidic and

alkaline solutions (Ghorbani et al., 2016; Ulrich et al., 2003).

Above the geomembrane is a drainage layer. This layer typically consists of natural gravel, mine rock or leached ore tailings. It is designed to provide a liquid disengagement zone and protect the geomembrane sheet from excessive fluid pressure by reducing the hydraulic head to zero (Kappes et al., 2002). This is accomplished through the incorporation of perforated drainage pipes, constructed of corrugated polyethylene tubing or HDPE, which transport the solution to storage ponds or processing facilities. The drainage layer should prevent clogging of the pipes and be significantly more permeable than the ore bed resting on top of it (Ulrich et al., 2003). In the case of heap bioleaching, it has become standard practice to lay aeration pipes underneath the heap with aeration rates varying from 0.2 to 2 $m^3/(m^2.h)$. This is to provide the oxygen needed for the microbial facilitated reactions (Petersen and Dixon, 2007b). Once the drainage layer is in place, stacking of the ore can commence.

It is common practice to have a successive sequence of ore layers or lifts stacked on top of each other during the life span of a heap leaching operation. These lifts can be constructed together prior to irrigation, or temporally staggered allowing for the sequential leaching of new lifts. In the latter, liners may be placed on the surface of the old lift, diverting solution away from it, if permeability issues arise. The main factor considered is the optimal use of available space and liner material. Currently, there are two main stacking methods: truck dumping and conveyor stacking. In the prior method, the ore is transported to the heap site in large haul trucks, which then off-load the ore using either an over end (dumping over the heap's edge) or plug-dumping (off-loading at the front face of the heap) method.

An important issue with truck dumping is the compaction of the top layers of the heap upon which the trucks drive. This can lead to severe loss in permeability and have a significant impact on the hydrodynamic characteristics of the heap. To prevent this, track vehicles or bulldozers with low ground pressure and ripper shanks can be used to level and rip the surface of the heap after construction or prior to the addition of a new lift. In the second method, conveyor stacking, ore is transported from the preparation plant to the heap using one or more overland conveyors that can reach up to 150 meters long. A system of conveyors then transports the ore across the active heap area and feed a radial stacker. The stacker

ranges between 25 to 50 meters long and rotates slowly, discharging ore at all points as it moves. Its movement and angle of discharge are motorized and controlled by an operator as the heap is constructed (Bartlett, 1992; Kappes et al., 2002). It is important to note that both of these methods can cause segregation as coarse particles roll faster to the bottom the heap and fines remain in the top layers (Ghorbani et al., 2016).

Irrigation systems used in heap leaching have the primary purpose of transporting and distributing solution across the heap. These systems consist of a network of pumps, pipes, tubing, valves and irrigations drips or sprinklers (Ulrich et al., 2003). The pipes and final distribution components are commonly constructed from either poly-vinyl chloride (PVC) or HDPE due to their cost-effective and structural properties. Metals tend to be avoided as materials of construction due to the highly corrosive heap leaching environment (Bartlett, 1992).

The choice of either sprinklers or drip emitters as the final distribution component comes with pros and cons regardless of selection. Sprinklers produce fine droplets which are shot in a high trajectory designed to offer uniform coverage over a set circular area. They tend to have solution application fluxes ranging from approximately 7 - 11 L/(m^2.h) without much flexibility. Though the uniform coverage is beneficial, heaps irrigated by sprinklers tend to suffer from high evaporation loses of up to 35% in hot climates (Bartlett, 1992). The main alternative, drip emitters, discharge singular droplets that fall vertically onto the surface of a heap. The rate of formation of droplets or flow rate depends on the line pressure which is usually lower than that of sprinklers. Due to this mechanism, drip emitters are able to significantly reduce evaporation loses. However, they do not offer uniform coverage and therefore require relatively closer spacing in a grid like pattern arrangement. In the past, it was common practice to allow each emitter to cover one square meter of surface area (Bartlett, 1992), however, more recent literature suggests that emitter spacings typically range from 0.03 - 0.1 m depending on the ore type being treated (Petersen and Dixon, 2007b). Another advantage of the emitter system is its flexibility regarding the range of solution application rates, allowing for major changes in flow rate to be made during a single leach cycle (Bartlett, 1992). Irrigation fluxes typically range from 5 - 20 L/(m^2.h) and will

again depend on the ore type and prior testing (Petersen and Dixon, 2007b).

The final major components of heap leaching plants are the ponds or solution storage facilities. These ponds are used to contain the PLS and BLS (optional) of the heap leaching operation. They are lined with impermeable material to prevent solution penetration into the ground and need to be of adequate size to receive excessive run-off in the case of flooding events or changing seasons such as the melting of snow in spring. If present, both ponds are typically located down slope from the heap, and in certain cases the BLS pond is at a slightly lower elevation of the two ponds. This is to receive and contain any overflows from the PLS pond (Bartlett, 1992).

2.2.3 Challenges With Heap Leaching

A lot of competition exists for mining technology with the efficiency of each metallurgical process being placed under scrutiny and heap leaching is no exception (Brierley, 2010). John (2011) mentions that based on his experience from 1990s to 2010s, 25% of heap leach operations around the world failed to produce a return on capital expenditure. The major reasons cited for these failures include bad heap design; a lack of representative samples for test work or a failure in scale up of laboratory data.

Poor heap design can sometimes go hand in hand with poor heap management. It encompasses factors such as the inadequate design of flow containment facilities leading to the over-flow of solution ponds; improper construction of the heap resulting in heap instability; compaction during stacking leading to the formation of impermeable layers on the surface of a heap; puncturing of the geomembrane layer leading to a lack of containment and seepage of leach solution into the environment (Ghorbani et al., 2016; John, 2011; Reichardt, 2008). Though most of these can be avoided with more rigorous planning and maintenance, in certain cases even well designed heaps still suffer from low recoveries.

As stated in Chapter 1 (Figure 1.2), preferential flow is a dominant factor responsible for low recoveries in heaps (Wu et al., 2007). An alternative definition of preferential flow at the solution scale, is flow in which different fluid components experience significantly different

fluid residence times (Trinchero et al., 2011). This is either in the form of stagnant volumes (no flow) or dual permeability (fast and slow flow volumes). This uneven distribution of flow velocities can result from an easily observable phenomenon such as the migration of fines to the bottom of heaps during irrigation resulting in reduced percolation and increased hydraulic head at the bottom (John, 2011). A possible solution to this is agglomeration which significantly decreases the mobility of fines. Preferential flow can also result from the presence of clay minerals. These minerals increase clogging of heaps over time as they swell and decrepitate which, if left unchecked, can instigate a heap collapse due to its saturated weight (Bartlett, 1992; Ghorbani et al., 2016). As a precaution, it is common practice to conduct ore characterisation in order to identify ores with clay minerals. If the concentration of such minerals are extensive, alternatives to heap leaching is then sought for such ores. However, even with agglomeration and proper ore characterisation, the preferential flow problem still persists. Researchers have attributed this to a number of factors including high levels of profile heterogeneity in the ore bed matrix, the presence of macro-pores that channel gravity dominated flow and some have cited the non-uniform surface coverage by drip emitters as another possible reason (Ilankoon and Neethling, 2016; Miller et al., 2003; Trinchero et al., 2011; Wu et al., 2007). To better understand how these different factors affect fluid flow, a wide array of laboratory tests and solute modelling exercises specific to heap leaching are carried out.

2.3 Laboratory Test Work for Heap Leach Design

Heap leaching laboratory test work allows researchers to ascertain the metallurgical and hydrodynamic response of an ore bed to aid in the prevention of potential heap failures.

The starting point is to obtain mineralogical information on the ore body and associated gangue minerals. This is an important step as some gangue minerals may be acid consuming or contain significant amounts of clay constituents as previously mentioned (van Staden et al., 2009). The characterisation process can be done through an Inductively Coupled Plasma Atomic Emission Spectroscopy (ICP-AES) analysis, X-ray Diffraction (XRD) or through

scanning electron microscopy techniques such as QEMSCAN (Kumar, 2016).

In reactive systems, the second step is to obtain data on the maximum possible extraction of the targeted mineral from the ore. Roll bottle tests are a common method for this particular data acquisition especially in mine and R&D environments. Parameters obtained from these tests include maximum total metal extraction, reagent requirements, optimum leaching temperature and the potential need for maintaining oxidizing conditions (van Staden et al., 2009; van Zyl et al., 1988). Though the data obtained from roll bottle tests is useful, quantitative kinetic information for the design of heap leach plants cannot be acquired from these tests. This necessitates a second testing phase typically conducted using columns.

Column tests involve loading a known amount of material into a column which is conventionally cylindrical in shape though square and rectangular shaped columns have also been utilized. The columns are fed with leach solution of known composition from the top. The solution percolates through the packed bed and is collected at the bottom, simulating a cylindrical slice of the heap. Factors of interest during these tests include the packing material used, particle size distribution, packing arrangement, lixiviant composition, solution application rate, bed size, microbial growth and attachment, heat generation, microbially facilitated reactions, chemical dissolution and precipitation reactions, evaporation etc.

To reduce the errors associated with the scaling up process of laboratory data, demonstration heaps or cribs can be constructed and used to run a variety of tests. These systems are typically designed to match the height of the anticipated heap lifts and can contain 1000 to 100 000 tons of ore. The typical magnitude of their physical dimensions impose a requirement for a significant amount of space, testing material, operating equipment, and operational expertise. Hence, they are only implemented if the value of the information gained from them outweighs the costs associated with their construction and testing. Researchers claim that the main advantage of these systems is their ability to more closely mimic the metallurgical and hydrodynamic behaviour of full scale heaps (Bartlett, 1992; Bouffard and West-Sells, 2009; Murr et al., 1981; Murr, 1979).

Generating a fundamental understanding of how different factors affect a process requires that they be studied in isolation. Therefore, due to the myriad of factors with the potential

to influence the hydrodynamics in leaching systems (e.g. microbial colonisation, chemical reactions, temperature fluctuations), it was important to limit the number of those investigated in this study for practical reasons. As such, only factors related to the physical intrinsic and extrinsic bed properties and lixiviant solution characteristics will be reviewed.

2.4 Hydrodynamic Modelling of Leaching Test Columns

The hydrodynamic modelling of irrigated packed beds involves the quantification of relevant hydrodynamic parameters used in analysing preferential flow behaviour. The prime focus of this section is on non-reactive solute transport models as these are the most commonly used in lab scale, steady state RTD studies. Heap leaching models dealing with chemical reactions, heat and mass transfer processes are not discussed in substantial detail. However, due to the intrinsic link between transient and steady state fluid flow, the aforementioned factor will also be given some exposition.

There are three main modelling approaches used in most scientific disciplines: phenomenological, empirical and semi-phenomenological/empirical. Phenomenological models are based on the physical laws governing the system and are advantageous in that they give accurate predictions about how a specific system will behave under different conditions. However, these models often involve the solving of differential equations making them highly complex and simplifying assumptions are typically needed. Alternatively, empirical models involve the fitting of an equation or curve to experimental data. These are useful for comparing systems run under similar conditions but do not have predictive capabilities. A combination of the two approaches exists in which some of the model parameters are based on physical laws but are optimized or calibrated based on experimental data (Mellado et al., 2011). Purely phenomenological heap leaching models are seldom found in literature due to the vast amount of parameters required to describe such an heterogeneous system. Therefore empirical and semi-phenomenological models constitute the main bulk of heap leaching models.

2.4.1 Fundamental Concepts

It is important to establish concepts and model parameter definitions related to solution flow behaviour in leaching beds.

2.4.1.1 Wettability and Capillarity

A key issue is the effect of the physical properties of packing material on capillary suction and how this affects fluid flow profiles in packed beds. The aim of this section is to communicate the fundamental knowledge regarding the concepts of wettability and capillarity.

There are typically three different phases present in unsaturated heaps. One solid phase (ore) and two fluid phases (leach solution and air). At the pore scale, one of the fluid phases is preferentially attracted to the surface of the solid phase. This is known as the wetting fluid (leach solution). Since both air and water (most leach solutions are aqueous solutions) are largely immiscible, they are separated by a well defined interface. This interface possesses surface energy or tension due to the difference in cohesive strengths of molecules in both fluids. A consequence of this is the pressure drop (ΔP) which is the difference in equilibrium pressure between the air (P_a) and liquid (P_l). When the solid phase is present, the shape of the interface, characterised by the contact angle (θ), is dependent on the magnitude of the surface tensions between the three phases.

$$\cos\theta = \frac{\gamma_{sa} - \gamma_{sl}}{\gamma_{al}} \tag{2.1}$$

Where γ_{sa}, γ_{sl} and γ_{al} are the surface tensions of the solid-air, solid-liquid and air-liquid interfaces, respectively. Equation (2.1), the Young equation, illustrates that a perfectly wetting fluid, one that spreads evenly over the whole solid surface, will have a θ equal to 0°, while a completely non wetting fluid will form a spherical droplet on the solid surface with a θ of 180°(refer to Figure 2.2a) (Stevens et al., 2009; Szymkiewicz, 2012).

Figure 2.2b illustrates the capillary rise phenomenon in a tube of constant diameter. The wetting fluid is attracted to the walls of the tube and therefore rises upwards. This upward mobility is counteracted by the effect of gravity and air pressure causing the column of liq-

uid to attain a finite height once equilibrium is achieved. The pressure difference (refer to Equation (2.2)), called capillary pressure (P_c), is proportional to the product of the surface tension of the air-liquid interface and the cosine of the contact angle, but inversely proportional to the tube/capillary radius (r_c). The capillary pressure can also be approximated by the product of the fluid height (h), fluid density (ρ_l) and gravitational acceleration (g).

$$\Delta P = P_c = P_a - P_l = \frac{2\gamma_{al}\cos\theta}{r_c} = h\Delta\rho_l g \tag{2.2}$$

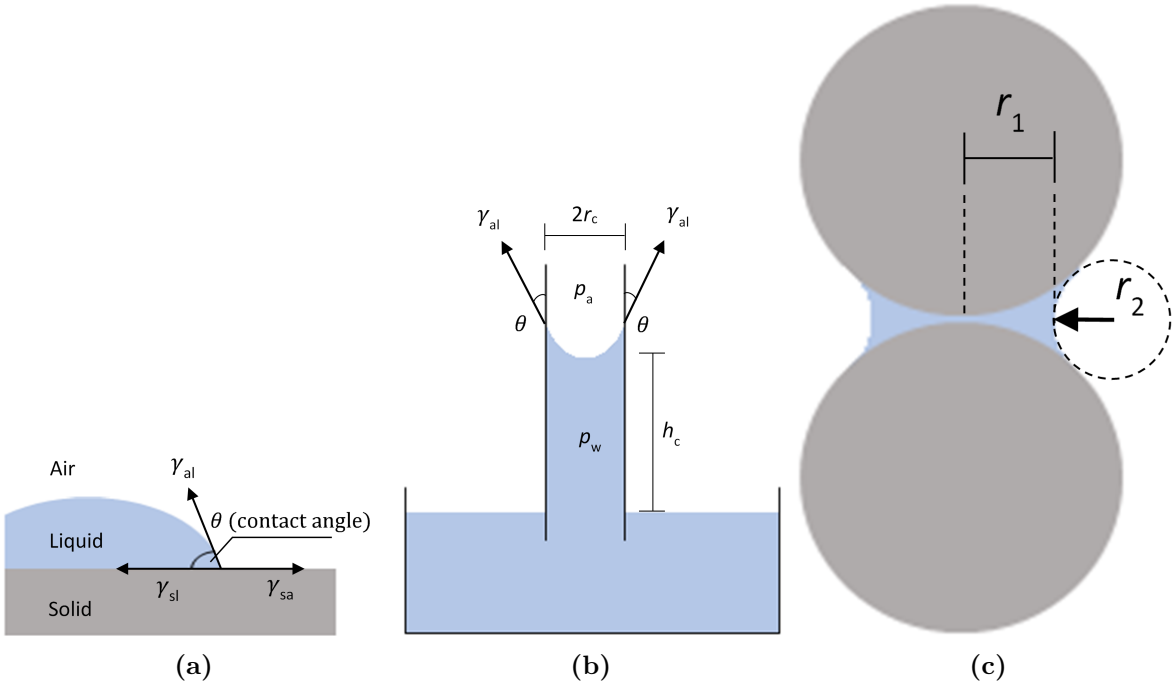

Figure 2.2: Ilustration of surface tension effects: (a) Fluid droplet on solid surface, (b) Capillary rise in a tube of constant diameter, (c) Liquid held between two spherical solid particles as a pendular ring (Based on Szymkiewicz (2012))

Another form in which capillary pressure expresses its effect is in the retention of fluid between two particles as shown in Figure 2.2c. For this configuration, the pressure difference is calculated from the Laplace equation shown in Equation (2.3). Again, the pressure drop is indirectly proportional to the main curvature radii of the interface (r_1 and r_2) with γ_{al} as the constant of proportionality (Szymkiewicz, 2012).

$$\Delta P = P_a - P_l = \gamma_{al}\left(\frac{1}{r_1} + \frac{1}{r_2}\right) \tag{2.3}$$

The three images shown in Figure 2.2 all deal with various isolated ideal components: perfectly flat solid surface (a), constant tube radius (b), spherical non-porous particles (c). However, in a heap all three of these mechanisms occur to different extents at different scales. This makes wettability and capillary suction measurements complicated in a heap leaching context. To illustrate this point, we see from Figure 2.3 that, in a particle cluster, the wetting fluid may be retained on the surface of particles (hygroscopic moisture), suctioned into particle pores or held at contact points between the particles (capillary moisture). All these fluid retention zones or capillary spaces will have different effective capillary pore sizes and different magnitudes of capillary forces. This leads to the creation of both mobile and immobile solution within the pore network with gravitational induced flow possible in macro-pores (Bartlett, 1992; Liu and Hashemzadeh, 2017).

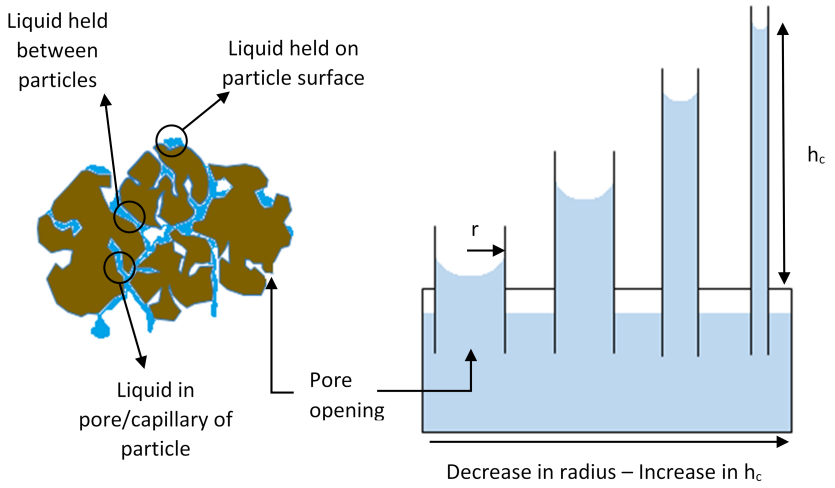

Figure 2.3: Moisture retention mechanisms in a particle cluster with variable pore sizes

It is possible to directly measure changes in capillary pressure at specific points in a packed bed using a tensiometer attached to a transducer (Dixon and Afewu, 2010). However, the number and location of the measuring units affects the representativeness of the data set. The design of these instruments must also not interfere with fluid movement within the beds.

An alternative method to quantifying capillary effects is to create a packed bed consisting of a large number of similar particles with intrinsic capillary properties (Stevens et al., 2009). The bed is formed by loading material into a column with a porous or water permeable base.

It is then lightly immersed in a fluid which, depending on the strength of capillary forces, is suctioned upwards. This continues until either complete saturation of the bed is reached or equilibrium is attained at a specific height. Similar to the constant diameter capillary tubes, the height is proportional to the capillary forces but in this case can prove difficult to accurately measure. Therefore, the increase in weight of the bed as it absorbs the liquid is measured with time and can also be used to calculate the wettability of the particles based on Washburn's equation, Equation (2.4) (Galet et al., 2010).

$$M_l^2 = \frac{Cn\rho_l^2\gamma_{al}\cos\theta}{\mu_l}t \tag{2.4}$$

Where M_l is the mass of fluid at time t, μ_l is the liquid viscosity (Pa.s) and Cn is a packing constant that depends only on the packing characteristic of the bed. It is common practice during these measurements to begin with a completely wetting fluid, i.e. a fluid with a θ of 0°, that has known properties (density, surface tension and viscosity) in order to obtain the packing constant. Care must be taken to maintain consistency in the way the columns are packed to ensure reproducibility of the results (Galet et al., 2010). Though capillary rise in a heap leaching context is still relatively under-researched, a few studies have employed this method as a measure of capillary suction forces (Bartlett, 1992; Yin et al., 2016).

2.4.1.2 Hydraulic Conductivity and Permeability

Bear (2013) defines hydraulic conductivity as the ability of a porous medium to conduct water under hydraulic gradients. It is based on the properties of the medium and the fluid. This implies that hydraulic conductivity is related to permeability which is an intrinsic property of the solid medium linked to aspects such as the size and structure of its pore network (Yang et al., 2008). Beds that conduct relatively large volumes of liquids within specific time frames are highly permeable or conductive. The hydraulic conductivity of an ore bed is also dependent on its level of saturation. The presence of air decreases the permeability of the bed, meaning that at 100% saturation, permeability and the now saturated hydraulic conductivity are at their maximum. A general equation for hydraulic conductivity (K_l - m/s) and its relation to the intrinsic permeability (k - m^2), density (kg/m^3) and viscosity of

the wetting fluid is shown in Equation (2.5).

$$K_l = \frac{k\rho g}{\mu_l} \tag{2.5}$$

2.4.1.3 Liquid Hold-up and Saturation

Liquid hold-up (ϕ_l) is an important hydraulic parameter in packed beds and is a measure of bed scale preferential flow (de Andrade Lima, 2006). Liquid accumulates during bed irrigation and reaches a constant volume at steady state. ϕ_l (m^3 liquid/m^3 bed) is defined as the fraction of liquid volume (V_l) to bed volume (V_b), as shown in Equation (2.6). A higher liquid hold-up typically results in a more uniformly wetted bed (reduction in bed scale preferential flow) but does not impact solution scale preferential flow. A similar parameter is total bed saturation (β_T), which is the fraction of void volume (V_v) occupied with liquid within the bed (refer to Equation (2.7)). β_T (m^3 liquid/m^3 void) is related to liquid hold-up via bed voidage (ε) which is simply the fraction of void volume to total bed volume (refer to Equation (2.8)). Liquid hold-up is divided into two main categories: internal ($\phi_{l,i}$) and external ($\phi_{l,e}$). Internal liquid hold-up refers to the liquid contained within the pores of porous particles in an ore bed. The external liquid hold-up therefore, is the remainder of the fluid located outside the particles' pores. It is taken as the sum of the dynamic ($\phi_{l,d}$) and residual ($\phi_{l,r}$) liquid hold-up as shown in Equation (2.9). Dynamic liquid hold-up refers to the free draining or mobile liquid within the bed while residual liquid hold-up is the moisture that remains in an ore bed after it is wetted and drained. This means that after drainage, two different liquid hold-ups are present in beds composed of porous particles: residual and internal liquid hold-up. Both of these combine to form the static liquid hold-up ($\phi_{l,s}$) shown in Equation (2.10). Utilizing the same principle, it is also possible to sub-divide total saturation into dynamic (β_d) and stagnant/static saturation (β_s) as shown in Equation (2.11) (Klerk, 2003). The presence of stagnant solution volumes is one of the indicators of solution scale preferential flow. Bouffard and Dixon (2001) study assumed dynamic liquid hold-up to be the volume of solution drained from the bed in a 24-hour period after irrigation was stopped. The authors recognized that even after 24 hours, small amounts of liquid were still

exiting the bed which is similar to the drainage behaviour of the system tested in Ilankoon and Neethling (2013). This highlights the difficulty in measuring dynamic liquid hold-up in beds composed of porous particles as drainage times could go well beyond 24 hours depending on the particle size fraction and bed volume.

$$\phi_l = \frac{V_l}{V_b} \tag{2.6}$$

$$\beta_T = \frac{V_l}{V_v} \tag{2.7}$$

$$\varepsilon = \frac{V_v}{V_b} \tag{2.8}$$

$$\phi_{l,e} = \phi_{l,d} + \phi_{l,r} \tag{2.9}$$

$$\phi_{l,s} = \phi_{l,r} + \phi_{l,i} \tag{2.10}$$

$$\beta_T = \beta_d + \beta_s \tag{2.11}$$

2.4.1.4 Solute Transport Processes - Advection

Advection refers to the transportation of solute molecules by the bulk movement of fluid. In heap leaching, gravity is considered the main driver of active solution flow in the vertical direction. Due to advection, non-reactive solutes are transported at the average linear velocity of the fluid. In a highly permeable bed, advection is the most dominant transport mechanism (Freeze and Cherry, 1979).

$$J_{ad} = v_l C \tag{2.12}$$

The advective flux (J_{ad} - mol/m^2.s) can be obtained from the product of the average linear liquid velocity (v_l - m/s) and and solute concentration (C - mol/m^3) (refer to Equation (2.12)).

2.4.1.5 Solute Transport Processes - Diffusion

Diffusion refers to the random movement of solute molecules due to their kinetic energy and results in their overall transportation down a concentration gradient (Freeze and Cherry, 1979). Diffusion is masked by any bulk hydraulic movement of solution and under such circumstances is considered negligible. Fick's two laws are widely used to describe the process of diffusion.

The first law states that the flux of a solute (J_{df}), with identical units as advective flux, is directly proportional to its concentration gradient ($\partial C/\partial x$ - - mol/m^3.m) with the diffusion coefficient (D_{df} - m^2/s) as the constant of proportionality, Equation (2.13).

$$J_{df} = -D_{df}\frac{\partial C}{\partial x} \tag{2.13}$$

The diffusion coefficients of electrolytes in aqueous solutions has been well studied with values in the range of 10^{-9} m^2/s (Miller, 1982; Sarraute et al., 2008). It has been proposed that the apparent diffusion coefficients of these ions in packed beds are smaller than in water due to longer diffusion paths created by the porous network of solid particles. It has been suggested that an empirical correction factor (ω) less than 1 be used to take this reduction from D to D^* into account, as shown in Equation (2.14) (Freeze and Cherry, 1979). However, there are no readily available values for the diffusion coefficient of electrolytes in packed beds and as such the empirical correction factor is also not known.

$$D^* = \omega D_{df} \tag{2.14}$$

Fick's first law of diffusion and the continuity equation is used to derive a relationship between the temporal rate of change of the concentration of a solute ($\partial C/\partial t$ - mol/m^3.s) to the variation in its spatial concentration ($\partial^2 C/\partial x^2$ - mol/m^3.m^2), also known as Fick's second law of diffusion, Equation (2.15).

$$\frac{\partial C}{\partial t} = \frac{\partial J_{df}}{\partial x} = D_d\frac{\partial^2 C}{\partial x^2} \tag{2.15}$$

2.4.1.6 Solute Transport Processes - Mechanical Dispersion

Mechanical dispersion is a microscopic process caused by three main mechanisms discussed below (Freeze and Cherry, 1979).

- Variation in drag force exerted on fluid molecules by the pore walls present within a channel leading to a velocity gradient.
- Differences in pore sizes of the flowing paths leading to further variation in flow velocities of fluid elements.
- Tortuosity of flow paths which leads to variation in the displacement of different fluid volumes at particular time intervals.

All three of these micro-processes lead to the spreading or mixing of solute particles beyond the threshold that is typical of just advective transport. Dispersion is linked to an increased presence of solution scale preferential or non-ideal flow. This spreading phenomena can either be parallel (longitudinal dispersion) or perpendicular to bulk flow (transverse dispersion). Furthermore, dispersion is considered to be anisotropic, meaning that the ratio of its magnitudes in the different directions is different for different systems. This attribute implies that adequate dimensionality of solute transport models may be dependent on the system (Dixon and Afewu, 2010). The macroscopic effect of dispersion can be described by Fick's law in a way analogous to that of diffusion as shown in Equation (2.16).

$$J_{ds} = -D_{ds}\frac{\partial C}{\partial x} \tag{2.16}$$

Where J_{ds} is the solute flux due to dispersion, D_{ds} is the hydrodynamic dispersion coefficient and the spatial concentration gradient is again represented by $(\partial C/\partial x)$. The relationship between the temporal and spatial variation of concentration due to diffusion is identical to the relationship caused by dispersion as shown in Equation (2.17).

$$\frac{\partial C}{\partial t} = \frac{\partial J_{ds}}{\partial x} = D_{ds}\frac{\partial^2 C}{\partial x^2} \tag{2.17}$$

Dispersion is relatively difficult to measure experimentally. Ilankoon et al. (2013) used neutrally buoyant tracer particles to measure dispersion in a packed bed via positron emission particle tracking (PEPT). Though this experiment was overall successful, it needed significantly high flow rates in order to produce large enough rivulets to transport the particles through the column. Another obvious constraint to this method is the availability of the highly sophisticated PEPT technology as well as the limitations it imposes on the bed geometries that can be studied. An alternative route that can be used to quantify the dispersion coefficient is through the fitting of a dispersion model to breakthrough curves obtained from tracer tests conducted on packed beds (Simunek and van Genuchten, 2006).

2.4.2 Transient Solution Flow Models

The pivotal transient solution flow models encountered in heap leaching are formulated based mostly on physical laws governing fluid flow in a medium. They deal with non-steady state fluid fluxes and hence require certain simplifications or assumptions to be solved. However, as mentioned previously, transient flow models or non-steady state behaviour are not the focus of this thesis, but due to their effect on steady state flow profiles, a general understanding of their structure is required.

2.4.2.1 Transient Uniform Flow Models

Uniform flow models assume homogeneity in the porous bed. They fall under the broader category of mono porosity models and describe the wetting of all the particles in the bed by a solution flowing at uniform velocity. These flow models make use of the continuity equation for fluid flow shown in Equation (2.18), which expresses the relationship between the volumetric fluid content (ϑ - m^3 liquid/m^3) and volumetric liquid flux or superficial liquid velocity (v_l - m/s) when a source/sink term (S - s^{-1}) is present. In most applications, fluid flow in heaps is assumed to be unidirectional and only the vertical spatial flux gradient is taken into consideration ($\partial v_l/\partial z$), as per Equation (2.19). However, multi-directional flow models have been developed, examples of which are found in literature (Cross et al., 2006;

Dixon and Afewu, 2010; Sheikhzadeh et al., 2005).

$$\frac{\partial \vartheta}{\partial t} = -\nabla v_l - S \tag{2.18}$$

$$\frac{\partial \vartheta}{\partial t} = -\frac{\partial v_l}{\partial z} - S \tag{2.19}$$

Darcy's law (Equation (2.20)), which expresses a directly proportional relationship between volumetric liquid flux and pressure gradient head ($\partial h/\partial z$) with the hydraulic conductivity as the constant of proportionality, is combined with Equation (2.19) to form the Richard's equation (Equation (2.21)).

$$v_l = K_l \frac{\partial h}{\partial z} \tag{2.20}$$

$$\frac{\partial \vartheta(h)}{\partial t} = -\frac{\partial}{\partial z}\left[K_l \frac{\partial h}{\partial z}\right] - S \tag{2.21}$$

2.4.2.2 Transient Preferential Flow Models

Due to the highly heterogeneous nature of heaps, preferential flow behaviour has been observed to occur (Wu et al., 2007). Therefore, preferential flow models which simulate the formation of non-ideal profiles with time may be more applicable to heaps. Currently, the most relevant of these are the dual porosity and dual permeability models (Simunek and van Genuchten, 2006), though mono porosity models with dispersion can be considered a type of preferential flow model (Iliuta et al., 1999).

Dual Porosity Flow Models

Transient dual porosity flow models simulate the temporal formation of two main liquid volumes: the dynamic (ϑ_d) and stagnant (ϑ_s). The proportion of stagnant to dynamic volume is proportional to the degree of solution scale preferential flow. Adding the volumetric water content of the two regions will give the total water content in the packed bed (Equation (2.22)). Mass balance calculations on the dynamic (Equation (2.23)) and stagnant zones (Equation (2.24)) are used to formulate these models. δ_l represents the mass transfer rate between the two regions. Both Equations (2.23) and (2.24) are solved simultaneously.

$$\vartheta = \vartheta_d + \vartheta_s \tag{2.22}$$

$$\frac{\partial \vartheta_d(h_d)}{\partial t} = -\frac{\partial}{\partial z}(v_l) - S_d - \delta_l \tag{2.23}$$

$$\frac{\partial \vartheta_s(h_s)}{\partial t} = -S_s - \delta_l \tag{2.24}$$

Dual Permeability

Transient dual permeability models simulate the temporal formation of two main fluid flow velocities arbitrarily named fast and slow solution volumes. Therefore, it is possible to have two different dispersion coefficients associated with each flow velocity, further adding to the complexity. Mass balance equations can be developed for the fast (Equation (2.25)) and slow (Equation (2.26)) flowing regions, respectively, where $\bar{r}$ is the ratio of the flow volumes to system volumes. Again, both zones are solved simultaneously (Simunek and van Genuchten, 2006).

$$\frac{\partial \vartheta_f(h_f)}{\partial t} = -\frac{\partial}{\partial z}(v_{l,f}) - S_f - \frac{\delta_l}{\bar{r}} \tag{2.25}$$

$$\frac{\partial \vartheta_{sl}(h_{sl})}{\partial t} = -\frac{\partial}{\partial z}(v_{l,sl}) - S_{sl} - \frac{\delta_l}{(1-\bar{r})} \tag{2.26}$$

The flow models presented here deal with time dependent fluxes and are capable of simulating bed scale preferential flow if preferential wetting parameters are included in their structure. Though they can offer temporal descriptions of the hydrodynamic behaviour of heaps, they are complex to implement especially in the case of dual porosity and dual permeability models. Due to this, most of the flow models encountered in literature take a macroscopic modelling approach, making use of uniform flow models but incorporate parametric equations relating the hydraulic conductivity and capillary head to the effective saturation of the bed. This allows for Equation (2.21) to be reformulated based on effective saturation, thereby accounting for the unsaturated flow characteristic within the bed (Dixon and Afewu, 2010).

A successful implementation of the dual porosity flow model can be found in work by Sheikhzadeh et al. (2005). In this case, the model was able to simulate transient liquid fluxes across a uniform, homogeneous, isotropic bed composed of spherical porous particles.

The macroscopic approach described above was used for the dynamic region, while a radial diffusion mechanism was used to account for fluid diffusing into the pores of the spherical particles. The assumption of uniformity and sphericity of the particles is a limitation to the applicability of the model to heap leaching systems but was necessary as variations in permeability and particle size were difficult to introduce into the model. This is one of the main reasons why dual permeability transient flow models are not widely used in heap leaching studies.

2.4.2.3 Developments in Fluid Flow Modelling

A few studies have applied computational fluid dynamics (CFD) technologies to study fluid flow in heaps. Examples include work by Mousavi et al. (2006) who performed direct numerical simulations (DNS) using the volume of fluid (VOF) method to study liquid flow through a granular, cylindrical bed containing monosized, spherical particles. Bennett et al. (2012) presented a comprehensive copper heap leach model using a CFD code. The model was able to take liquid and gas phase transport, as well as process chemistry into account. Barker et al. (2012) made use of Smoothed Particle Hydrodynamics (SPH) and incorporated surface tension effects using a continuum surface force (CSF) model to simulate unsaturated, multiphase flows in heap leaching. The study was able to simulate liquid flow over both SPH generated spherical particles as well as experimentally generated geometries of loose packing of rocks based on X-ray Computed Tomography (XCT) scans. McBride et al. (2017) studied preferential flow behaviour in unsaturated packed beds using an in-house multi-physics CFD framework. The authors were able to account for local preferential flow paths using the model and obtained results comparable to experimentally obtained data from a pseudo two dimensional column packed with ore. A 3D dual pore-system fluid flow model was proposed by Miao et al. (2017) in which the pore network was divided into macro- and micro-pores. The results were compared to a uniform and single pore scale model and suggests that dual pore-systems are needed for the accurate simulation of preferential flow paths.

A study by Fernando et al. (2020) investigated the use of Pore Network Modelling (PNM) in describing fluid flow in heap leaching systems. A main motivation behind PNM is the

reduction in computational intensity normally associated with DNS techniques. PNM requires the identification and extraction of the void structure of the porous medium using an imaging technique such as XCT. Only through this pore structure, which can be visualized as a pore-throat network, is flow then simulated. The removal of the solid matrix makes the simulation less computationally intensive. Though this technology has the potential to be used for specific heap leaching applications, it still needs to be optimized to take liquid hold-up, flow rate and channelling effects into account.

These models are highly phenomenological and capable of simulating flow in three dimensions, hence they are computationally intensive. This is one of the main reasons why in previous years, they have not been widely applied to heap leaching systems. Another reason is the difficulties experienced during DNS simulations in introducing a solid matrix to represent the ore particles present in heaps. In many cases simplified shapes are utilized with empirical data needed for the introduction of more complex shapes or packing.

An alternate approach has been to impose steady state flow profiles on the bed systems and calibrate these parameters using empirical data such as RTDs or quantified visual information. For instance, in the HeapSim model used in Petersen and Dixon (2007a), a dual porosity steady state solution profile was imposed on the simulated bed systems. Though actual heaps seldom reach complete steady state which could be a limitation to this approach, the duration of most heap leaching operations are relatively long which could see the heap attain pseudo steady state, especially in terms of hydrodynamics. Therefore, this methodology is beneficial and cost effective.

2.4.3 Solute Transport Models For Fluid Flow Analysis

Solute transport models aim to describe the movement of solute molecules within a specific medium. In reactive leaching systems, this process involves the transportation of reagents in the irrigation fluid to the mineral surface, bringing about the dissolution of the targeted minerals which are then transported away from the ore matrix and out of the heap. In non-reactive packed beds, which are used for fundamental studies on hydrodynamic behaviour, the movement of certain solute molecules, called tracers, mimic the fluid flow pat-

terns present. Hence the solute transport modelling of these tracers, can be used to diagnose the flow characteristics of packed beds. This is typically done through tracer tests resulting in the generation of RTD profiles. When these profiles are obtained under steady state fluid flux, their modelling can be used to identify symptoms of solution scale preferential flow based on the quantification of relevant hydrodynamic parameters (Bouffard and West-Sells, 2009; Simunek and van Genuchten, 2006). Therefore, unlike transient flow models, time dependent fluid fluxes are not simulated, rather the steady state distribution of flow volumes within an irrigated packed bed are characterized.

Tracer tests are performed by feeding a detectable, inert chemical (tracer) into a chosen system and then measuring its concentration at a specific position in the system as a function of time. There are two main types of tracer tests: pulse and step tests. In the pulse experiments, the tracer is introduced into the system in a quick dose over a short time interval, hence the name pulse. Accurate tracer mass balance is needed for this form of tracer test to ensure all the introduced tracer was eluted from the system. In step experiments, a tracer solution is continuously fed into the system and monitored until its concentration within the system reaches a constant value. A tracer balance is therefore not needed for this form of tracer input. These tests can be conducted on packed beds in either steady or unsteady state to characterize fluid flow under established or transient flux profiles, respectively (Govender-Opitz et al., 2017). This thesis focuses on systems under steady state.

The next sub-section will focus on the different kinds of solute transport models used for RTD characterisations in leaching studies.

2.4.3.1 Empirical Solute Transport Models

Compartmental Models

Compartmental models (CM) were developed from concepts presented by Levenspiel to model a packed bed as a combination of different flow volumes (Levenspiel, 2011). Ideal liquid volumes are represented as plug flow reactors (V_P), liquid volumes with non-ideal mixing effects as continuous stirred tank reactors (V_C) or isolated volumes completely cut off from active solute transport are represented as dead volumes (V_D). The volumes (V_C

and V_D) are indicative of solution scale preferential flow. The basis for these models are the different tracer responses an ideal plug flow reactor (PFR), refer to Figure 2.4, and continuously stirred tank reactor (CSTR), refer to Figure 2.5, will have when subjected to a tracer test (Fogler, 2006).

The equations used to derive these responses are given by Equation (2.27) for a PFR and Equation (2.28) for a CSTR, where C refers to the tracer concentration. It is possible to have different configurations consisting of multiple ideal units which make compartmental models very flexible.

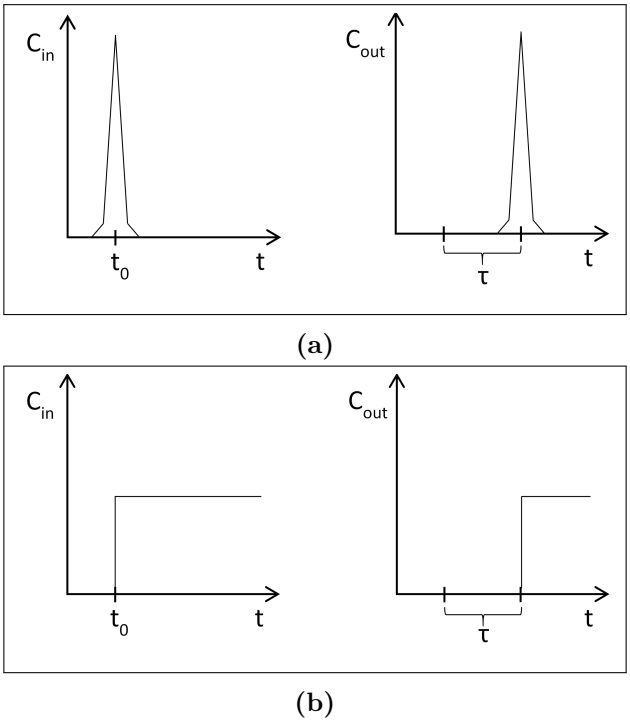

Figure 2.4: Response of an ideal PFR to: (a) Pulse input and (b) Step input tracer tests where τ is the time delay. Based on Fogler (2006).

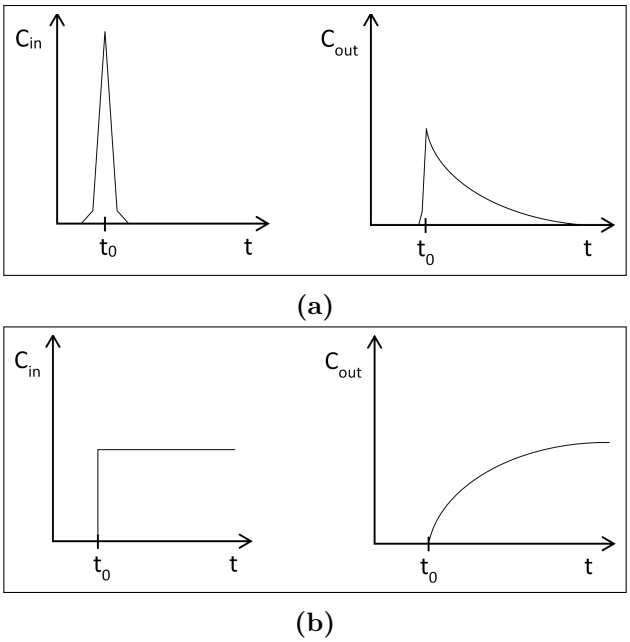

Figure 2.5: Response of an ideal CSTR to: (a) Pulse input and (b) Step input tracer tests. Based on Fogler (2006).

$$C_{out} = C_{in}[\text{with time delay of } \tau] \tag{2.27}$$

$$C_{out} = C_{in} e^{\frac{-t}{\tau}} \tag{2.28}$$

Tanks in Series Model

Another empirical model similar to CM but based around the concept of fully active flow (mono porosity), is the tanks-in-series (TIS) model. It is established on the ability of consecutive CSTRs in series to simulate plug flow behaviour. The TIS model has one parameter known as the number of tanks (n) in series. The greater the number of tanks predicted, the higher the degree of plug or ideal flow behaviour (lower degree of solution scale preferential flow). For a step input tracer test, the produced normalised concentration profile (F) can be calculated from Equation (2.29), where τ (s^{-1}) is the average residence time per tank and all other parameters have been previously defined (Fogler, 2006).

$$F(t) = \int_0^t \frac{t^{n-1}}{(n-1)!\,\tau^n} e^{-\frac{t}{\tau}} \tag{2.29}$$

2.4.3.2 Semi-phenomenological Solute Transport Models

Mono Porosity Model: AD

The advection-dispersion (AD) model is often used in the description of flow in non-ideal tubular reactors. The model makes use of both advective and dispersive fluxes with an inherent assumption of active solution volumes (mono porosity). The axial dispersion coefficient is incorporated to account for the spreading of molecules beyond the advective flow boundary and its magnitude is used to indicate the severity of non-ideal/preferential flow. A study by Ilankoon et al. (2013) used both empirical and modelling approaches with the AD model to quantify the dispersion coefficient in a packed bed of spherical beads. However, due to the simplicity of its model structure, the AD model can only account for minor deviations from ideality and its applicability to different packed bed systems remains to be tested. The differential Equation (2.30) is used to describe the temporal change in concentration ($\partial C/\partial t$) of a solute at a particular point (z) in the system.

$$\frac{\partial C}{\partial t} = D_{ds}\frac{\partial^2 C}{\partial z^2} - v_{ad}\frac{\partial C}{\partial z} \tag{2.30}$$

Dual Porosity Models: MSPD and PSPD

Unlike the mono porosity AD model, the mixed side-pore diffusion (MSPD) and profile side-pore diffusion (PSPD) models, originally proposed by Bouffard and Dixon (2001), are dual porosity solute transport models. They are based on the transport of solutes within steady state dual porosity flow profiles: a dynamic zone with active advective flow and a stagnant zone with no significant bulk movement of fluid. Therefore, these models best describe solute transport in beds under severe solution scale preferential flow. Mass transfer of solutes occurs between the two regions. For the MSPD model, this mass transfer can be described by an overall mass transfer coefficient ($K_m a$) shown in Equations (2.31) and (2.32) which represent the dynamic and stagnant zones, respectively.

MSPD

$$\textit{Dynamic: } \varepsilon_d\frac{\partial C_d}{\partial t} = -v\frac{\partial C_d}{\partial z} - K_m a(C_d - C_s) \tag{2.31}$$

$$\textit{Stagnant: } \frac{\partial C_s}{\partial t} = \frac{1}{\varepsilon_s} K_m a (C_d - C_s) \tag{2.32}$$

For the PSPD, three different diffusional mechanisms can be used to describe the diffusion of solutes into the stagnant zone: a linear mechanism ($\Gamma = 0$); cylindrical mechanism ($\Gamma = 1$); and a spherical mechanism ($\Gamma = 2$). Although the spherical diffusion mechanism was best at fitting RTD data generated in the above mentioned study, the other two mechanisms performed suitably.

PSPD

$$\textit{Dynamic: } \varepsilon_d \frac{\partial C_d}{\partial t} = -v \frac{\partial C_d}{\partial z} - \frac{D_{df}(\Gamma + 1)}{X} \frac{\partial C_s}{\partial x}\bigg|_{x=X} \tag{2.33}$$

$$\textit{Stagnant: } \varepsilon_s \frac{\partial C_s}{\partial t} = D_{df} \left[\frac{\partial^2 C_s}{\partial x^2} + \frac{\Gamma}{x} \frac{\partial C_s}{\partial x} \right] \tag{2.34}$$

Both the MSPD and PSPD assume plug flow behaviour in the dynamic region with mass transfer into solution filled pores oriented perpendicularly to the advection path. It should be noted that a modified version of the PSPD model, called the PSPD variable pore length model, was also proposed by Bouffard and Dixon (2001) and performed significantly well. However, due to the highly arbitrary nature in which the pore length distribution function was chosen, it can be argued that the added parameter in this model variation may provide an over-fit to the data without a clear empirical basis.

Dual porosity model: PDE

The piston dispersion and exchange (PDE) model has been used in the modelling of flow in fixed bed and trickle flow reactors (Iliuta et al., 1998; Saber et al., 2012). de Andrade Lima (2006) argued that dispersion, a symptom of solution scale preferential flow, was a phenomenon that could not be ignored when modelling solute transport in packed beds. Therefore, though it is also based on the dual porosity concept, it differentiates itself from the MSPD and PSPD models by incorporating a dispersion coefficient parameter in its dynamic formulation shown in Equation (2.35). It then uses an overall mass transfer coefficient to describe the exchange of solutes between the dynamic and stagnant zones, identical to the MSPD model (Equation (2.36)).

$$\textit{Dynamic: } \frac{\partial C_d}{\partial t} = D_{ds}\frac{\partial^2 C_d}{\partial z^2} - v_d\frac{\partial C_d}{\partial z} - \frac{K_m a}{\beta_d}(C_d - C_s) \tag{2.35}$$

$$\textit{Stagnant: } \frac{\partial C_s}{\partial t} = -\frac{K_m a}{\beta_s}(C_s - C_d) \tag{2.36}$$

Where subscript d and s refer to the dynamic and stagnant regions, respectively. Other parameters keep their previous definitions.

2.5 Solute Transport Modelling Review

This section presents a summary and comparison of the pivotal work done using solute transport models to characterise fluid flow in leaching beds. Bouffard and West-Sells (2009) used a compartmental model to model RTD data from three systems: cylindrical columns, cribs and a demonstration heap. The model consisted of four different volumes: plug flow, by-passing flow, well-mixed and dead volumes. Though the model struggled to fit the column data, it did perform better with data generated from both the crib and heap, predicting a significantly greater proportion of mixed and dead volumes (i.e. greater levels of solution scale preferential flow/channelling) for these two systems. The study also found that the proportion of dead to total volume was significantly greater for cribs packed with non-agglomerated ore compared to those filled with agglomerated packing. No 'goodness of fit' coefficient or residual analysis was presented which made comparisons of model fits difficult.

The Bouffard and Dixon (2001) study presented the MSPD and 4 variations of the PSPD models. Some of the modelling results of this study have already been discussed under sub-section 2.4.3. A summary of the main results are firstly that the diffusional flux mechanism used in describing the mass transfer between the dynamic and stagnant phases allowed the PSPD to outperform the MSPD in terms of model fit. Secondly, though increasing particle size and agglomeration brought about reductions in the stagnant liquid hold-up, a symptom of solution scale preferential flow, they also brought about reductions in the mass transfer rate between the dynamic and stagnant regions which resulted in longer asymptotes in the RTD profiles. The authors attributed this to the longer diffusional paths in larger particles. It is important to highlight that a uniform distribution solution delivery mechanism was

utilized in the study, along with the assumption of plug flow behaviour in the dynamic region, which could potentially reduce the applicability of the results to bed systems under drip irrigation.

van Staden and Petersen (2018a) compared the MSPD, PSPD (spherical diffusion) and HeapSim solute transport models to alternative models developed using the *PhreeqC* open-source platform. The alternative models were dual porous and were formulated with both an overall mass transfer coefficient and spherical diffusional flux mechanism. The main difference was that *PhreeqC* models used a 'tank-in-series' description for the dynamic volume rather than the plug-flow approach used in the others. The authors tested the *PhreeqC* and HeapSim models on a subset of Bouffard and Dixon (2001) experimental RTD. Of interest in this study are the hydrology results which showed that the *PhreeqC* and HeapSim models performed on par with the MSPD and PSPD models. There were no significant differences in the coefficient of determination across the different models within each model class. However the models formulated with the diffusional mechanism performed better than those utilizing an overall mass transfer coefficient, indicating that diffusional path lengths is an important solute transport parameter.

The lack of a significant difference in model fit analysis between the assumption of plug-flow and that of mixing behaviour in the dynamic phase of the different solute transport models in the van Staden and Petersen (2018a) study is an interesting point. The view has always been held that one of the main advantages of the PDE model, is its incorporation of the dispersion coefficient, but these results suggest that this may not be necessary in leaching beds, contrary to the views of de Andrade Lima (2006). One of the drawbacks of the van Staden and Petersen (2018a) study is the limited RTD data used when comparing the different models, hence the question of which model parameters are crucial and which are optional still remains. This point can be extended to the dual porosity concept. Though its importance in the modelling of solute transport behaviour has been shown by Ilankoon et al. (2013), this was done to a limited extent as only one type of packing (glass beads) and one particle size (18 mm) was used. Most other studies that attempt to quantify the benefits of the dual porosity approach, and consequently, the limitations of the mono porosity

assumption, have been conducted on trickle bed reactors whose flow rates, flow pattern and packing differ significantly from leaching beds.

2.6 Factors Affecting Heap Hydrodynamics

Factors that affect the steady state flow profiles of irrigated beds include: the packing material, particle size distribution, packing arrangement, irrigation system, irrigation rate, irrigation fluid and bed size. Some have been studied without any modelling and little is known about their effect on solution scale preferential flow behaviour. This section presents a discussion of these factors and identifies those requiring further modelling research.

2.6.1 Effect of Intrinsic Properties of Packing Material

Hydraulic conductivity is dependent on the intrinsic permeability of a packed bed. Permeability relates to properties such as particle porosity, shape, hydrophilicity and texture of the packing material used. As can be seen from Table 2.1, most empirical studies have focused on just one type of packing material, typically ore. Though ores are the most representative packing, their main disadvantage is their complexity. This makes it very difficult to decouple the effect of certain factors on preferential flow.

Ilankoon and Neethling (2013, 2014) made use of non-porous spherical glass beads and porous copper ore in narrow size ranges. In the first study, they showed that residual liquid hold-up and solution breakthrough time, decreased with an increase in particle size for both systems. However, both the solution breakthrough time and liquid hold-up for the ore system were relatively larger than for the beads. These were attributed to the ore's porosity and smaller inter-particle voids which led to greater capillary suction with a decrease in the proportion of gravitational flow. In the second study the authors were concerned with the modelling of transient liquid hold-ups and drainage velocity variations. The ore bed drained substantially more liquid in a longer time period compared to the beads. Fluid flow in the bead system was gravity dominated and acted as a front indicating ideal plug flow behaviour while the flow

Table 2.1: Summary of various empirical studies utilizing different packing materials, size fractions (S.F.), agglomerated (A) or non-agglomerated (NA) packings, bed geometries (B.G.), bed length to bed height ratios ($\frac{B_L}{B_H}$), bed length to maximum non-agglomerated particle diameter ratios ($\frac{B_L}{d_p}$), irrigation solutions (I.S.), irrigation modes (I.M.), irrigation fluxes (I.F.) and models in heap leaching literature with a focus on hydrology. [Key: N.M. - Not Mentioned, N/A - Not Applicable, Leach sol. - Leach solution, Emp. - Empirical, Sol.T. - Solute Transport]

Authors	Material	S.F. (mm)	A/NA	B.G.	$\frac{B_L}{B_H}$	$\frac{B_L}{d_p}$	I.S.	I.M.	I.F. ($L/m^2.h$)	Modelling
Bouffard and Dixon (2001)	Gold ore	< 19	Both	Cylindrical	2.05-6.45	13.3-26.7	$NaNO_3$ - Tracer	Uniform	4.75-10.2	MSPD & PSPD
Bouffard and West-Sells (2009)	Gold ore	<0.074->19	A	Cylindrical	20.4-24.4	13.2	Leach sol. & water	Uniform	3	CM
	Gold ore	<0.074-ROM	Both	Crib	2.28-2.63	126	Leach sol. & water	Point source	3-6	
	Gold ore	<0.074->19	A	Heap	0.04-0.06	N/A	Leach sol. & water	Point source	3	
de Andrade Lima (2006)	Quartz	2-2.36	NA	Cylindrical	14.6	24.2	Distilled water	Uniform	69.4-222	PDE
Dixon and Afewu (2010)	Copper ore	∼<0.09-25	A	Cylindrical	4-12	4-40	KCl - Tracer	Point source	3-30	Flow & Sol.T.
	Copper ore	∼<0.09-25	A	Rectangular	1.-5.7	4-22	Acidic solution	Point source	5-10	
Fagan et al. (2014)	Copper ore	<0.5-25	A	Cylindrical	0.34	Horizontal	Doped deionized water	Point source	1	None
	Copper ore	<0.1-18	A	Rectangular	2-12	∼ 5.6-33.3	Leach sol.	Point source	6	
Fernando et al. (2019)	Ore	16-20	NA	Rectangular	0.75-6	5-40	Deionized water	Point source	52.5	None
	Ore & PCBs	16-50	NG	Rectangular	0.75-6	2-16	Deionized water	Point source	52.5	
Fernando et al. (2020)	Ore	2.36-25	NA	Rectangular	0.83-2.20	4-10.6	Fluorescent dye	Point source	75.2-157.9	PNM
	Glass beads	8-16	NA	Rectangular	0.83-2.20	6.3-16.6	Fluorescent dye	Point source	75.2-157.9	
Govender et al. (2015)	Ore	<0.25->16	A	Cylindrical	2.7-4	∼ 5	Acidic solution	uniform	2	CM
Yang et al. (2008)	Mixed ore	<0.2-10	NA	Cylindrical	10	5	Leach sol.	N.M.	600	None
Ilankoon and Neethling (2012)	Glass beads	2-18	NA	Cylindrical	1.2-2.1	13.5-121.5	Deionized water	Uniform	27.2-435	Liq. Hold-up
Ilankoon and Neethling (2013)	Copper ore	2-45	NA	Cylindrical	1.2-2.1	5.4-60.8	Deionized water	Uniform	27-436	Liq. Hold-up
	Glass beads	2-18	NA	Cylindrical	1.2-2.1	13.5-121.5	Deionized water	Uniform	27-436	
Ilankoon et al. (2013)	Glass beads	18	NA	Cylindrical	1.2	13.5	Deionized water	Uniform	27-432	AD & PDE
Ilankoon and Neethling (2014)	Copper ore	8-11.2	NA	Cylindrical	1.2-3.3	21.7-30.4	Deionized water	Uniform	27-436	Liq. Hold-up
	Glass beads	10-14	NA	Cylindrical	1.2-3.3	17.4-24.3	Deionized water	Uniform	27-436	
Ilankoon and Neethling (2016)	Copper ore	2-26.5	NA	Rectangular	0.8-6	3.77-30.2	Deionized water	Point source	52.5	None
Ilankoon and Neethling (2019)	Ore	2-26.5	NA	Rectangular	0.75-6	3.8-30.2	Fluorescent dye	Point source	52.5	None
O'Kane et al. (1999)	Inert material	<0.075-20	NA	Column	N.M.	N.M.	Water	Uniform	3.4-34.2	None
Spurr (2008)	Chalcopyrite ore	<1-50	A	Cylindrical	1.34	6.4	Leach sol.	Point source	1.12	None
Trinchero et al. (2011)	Mine rock	<1000	NA	Pile	0.63	N/A	Water	Uniform	rainfall	Fluid flow
Wu et al. (2007)	Copper ore	<0.2-20	NA	Column	N.M.	N.M.	Water	Uniform	2880-90000	None
Wu et al. (2009)	Copper ore	<0.1-20	NA	Cylindrical	7.7	∼ 6.84	Leach sol.	Uniform	30	None
Yusuf (1984)	Rock particles	<2->15	NA	Cylindrical	3.2-11.7	∼6.27	NaCl - Tracer	Uniform	1.7-10.4	Emp. Sol. T

through the ore bed was non ideal with evidence of mixing/dispersion. This again was related to differences in capillary effects caused by porosity and corroborated the results found in the initial study. However, though shape was implicitly acknowledged as an important factor, the two materials used could not decouple the effect of both shape and porosity.

Fernando et al. (2019) studied the effect that incorporated thin sheets of printed circuit boards (PCBs) had on the liquid distribution of a rectangular ore bed. Different combinations and packing methodologies were used, ranging from an ore only packing (particle size: 16 - 20 mm), to a PCBs only packing (25 by 25 mm^2 and 50 by 50 mm^2), and finally to different mixtures of ore and PCB units. The ore only system saw a quick establishment of flow profiles and a slow but present lateral spread due to capillarity. Though the addition of the larger PCBs led to an increase in lateral liquid distribution there was a reduction in saturation. The authors postulated that the prior effect was due to the relatively higher surface area of the incorporated PCBs which led to alterations in horizontal flow profiles. A reduction in capillary held liquids due to the low porosity of the PCBs was deemed responsible for the latter effect. This was further illustrated with data showing that though the PCB only beds had significantly less channelling effects, they also experienced significantly smaller liquid hold-up values compared with the ore system.

The next study by Fernando et al. (2020) aimed to model fluid flow in different rectangular packed beds composed of glass beads and ore particles using a PNM approach (refer to Table 2.1 for more details). Similar to results by Ilankoon and Neethling (2013), data from the study showed that the ore system exhibited significantly higher liquid-hold up and degree of lateral spread. Again, the ore's porosity and a larger number of particle contact points within its system were cited as the dominant cause of this. The latter postulation is linked to the differences in shape of the two materials as this affects the number of contact points possible between them, but yet again this could not be decoupled from the effect of particle porosity.

The above mentioned studies have shown the importance of the role that particle shape, size, surface area and particle porosity play in the wetting and hold-up behaviour of packed beds. However, due to the relatively few number of studies, and the fact that they have typically

chosen two different extremes when it comes to packing properties (e.g. non-porous with sphericity, porous with irregularity or slightly porous thin sheets), the information obtained is limited.

Particle sphericity has been assumed for many heap leaching reaction and simulated flow models, such as the shrinking core model (Barker et al., 2012; Roman et al., 1974). However, questions of the impact that such an assumption has on the flow profiles and solute transport behaviour in heap leaching bed systems requires more understanding. There have been allusions made to the impact that angularity of particles have on capillary suction, yet the quantification of such particle shape descriptors is more prevalent in the study of soil mechanics than in heaps. Gibb et al. (1984) mention that spherical shape leads to a reduction in total porosity as particles tend to pack closer, yet solute transport modelling work surrounding this issue is scarce.

Another issue is the quantification of the degree of wettability of the different materials used. This has been shown to be an important characteristic in the dynamic to stagnant distribution of liquid in packed beds (van Swaaij et al., 1969) and, as shown in Equation (2.2), is directly related to capillary suction. In their modelling work, Ilankoon and Neethling (2013) mention that differences in contact angles of the materials could lead to different flow mechanisms across the particles (film or rivulet flow). The importance of wettability is further highlighted by the modification of the effective diffusivity term in the shrinking core model by Sánchez-Chacón and Lapidus (1997) to account for wettability of the ore bed. Though most heap leaching flow models incorporate saturation into their parameters, the effect of wettability on solute transport is still an area that requires further research due to the limited type of packings previously used.

Generating a fundamental understanding of the relationship between the physical properties of an ore bed and its fluid flow profile, requires that these properties must be studied in isolation or decoupled. This necessitates the use of non-ore materials with varying levels of complexity.

2.6.2 Effect of Particle Size Distribution

The size distribution of particles (or agglomerates) affects the permeability of an ore bed. Wickland et al. (2010) found that beds composed of higher ratios of waste rock (larger particles) to tailings had higher hydraulic conductivities and greater resistance to compressive forces or slumping. It has been suggested in literature that the intrinsic permeability is proportional to the square of the particle diameter (d_p) as shown in Equation (2.37), where C_p is a constant dependent on packing properties (Wu et al., 2007).

$$k = C_p d_p^2 \tag{2.37}$$

Particle size distribution is also an important factor in the leaching of an ore due to its effect on mineral liberation which affects recoveries. Beds composed of smaller particles have larger surface areas which could potentially provide more reactive surfaces, increasing reaction kinetics and leaching rates (Ghorbani et al., 2011; Mellado et al., 2011).

Ilankoon and Neethling (2016) tested lateral flow patterns in rectangular beds composed of both a narrow sized (20 - 26.5 mm) and a more realistic distribution of ore particles (2 - 26.5 mm). This experiment was later redone in the study Ilankoon and Neethling (2019), but with more sophisticated UV technology for flow visualisation. Results from both these studies showed that the more realistic size distribution exhibited higher degrees of lateral wetting by capillary action, but this wetting behaviour did not translate to active flow channels. The results agreed with those obtained by Fernando et al. (2020) who ran very similar tests with similar columns. Though capillary suction leads to greater contact efficiency between the packing and irrigation fluid, most of these contact zones are comprised of either stagnant (Dixon and Afewu, 2010) or slow flowing (Govender-Opitz et al., 2017) solution volumes. This suggests that capillary induced flow occurs mostly during the initial stages of irrigation and active movement substantially reduces once the capillaries are saturated. The effect of this was postulated to lead to a higher dependency on the diffusion transport mechanisms within the irrigated bed (Fernando et al., 2020).

Though capillary suction has been linked to the presence of fine materials in packed beds, few studies have quantified the extent of this linkage. The study by Yin et al. (2016) found

that the higher the mass fraction of fines in a graded copper ore bed, the greater the capillary rise. The study was however limited to just one type of packing material with no tracer test or solute transport modelling done.

Another critical point of discussion that relates to particle size distribution is the presence/absence of wall effects. This refers to an increase in the voidage near the walls of a packed bed and can have a significant impact on its flow characteristics and mass transfer. Suzuki et al. (2008) and Benenati and Brosilow (1962) found that the voidage was greatest next to the walls of a bed of glass beads and decreased in an oscillating fashion towards the centre. Klerk (2003) claimed that wall effects could be neglected when the bed to particle diameter ratio was above 13. This ratio was obtained by observing changes in bed voidage with different column diameters. However only glass beads of 3 mm were used in the experiment. Though work by Ribeiro et al. (2010) corroborated the ratio put forward by Klerk (2003), other values have been suggested. Yin et al. (2016) suggests a value of 6, Yusuf (1984) suggests 8, Bartlett (1992) states that a value above 10 is sufficient while Gibb et al. (1984) argued that a value above 30 is required. From Table 2.1, it can be seen that there is a significant variation in the bed length to particle diameter ratios (B_L/d_p) used in literature with some of the lowest values belonging to authors who made use of rectangular column geometries. B_L refers to column diameter in cylindrical columns and column width in rectangular columns. In these particular cases, the authors aimed to look at flow in purely 2-D and as such, limited the thickness of the rectangular boxes used. This proved to be a bit of an oversight in certain cases as wall effects were subsequently induced. Two such studies that reported a degree of flow along column walls were Ilankoon and Neethling (2019) and Fernando et al. (2020) which both had ratios of less than or equal to 4 (based on thickness). It should be noted that to assess wall flow features in detail in such pseudo 2D systems, a modified parameter, different to that employed for cylindrical columns, is required.

2.6.3 Effect of Loading Arrangement

Another important factor considered during the solute transport modelling of a particle bed is the way in which the bed is packed. As mentioned in sub-section 2.2.1, segregation is an

important factor in heap leaching operations. In the study by O'Kane et al. (1999), segregation was intentionally introduced during the loading of a column through the horizontal separation of fine and coarse textured material. The column was then irrigated with water across its entire surface. The study showed that due to segregation, different flow mechanisms are induced based on the magnitude of the applied liquid flux. When this flux is less than the saturated permeability of the fine material, preferential flow occurs in the fine section of the column, and when it is above the said value, the preferential flow switches to the coarse section as shown in Figure 2.6. The overall impact this has on heap leaching operations is the creation of 'blind' zones, as the authors call them, that receive little active flow which negatively affects extraction rates. However in van Staden and Petersen (2018b), it was found that though segregation had a negative impact on bulk density and hydraulic conductivity, no statistically significant difference was observed during leaching tests on the different beds.

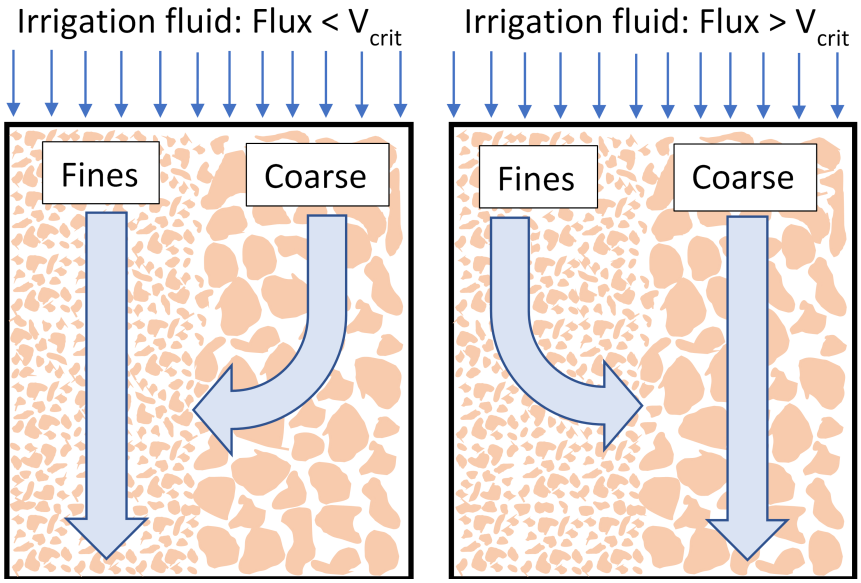

Figure 2.6: Illustration of the effect of liquid flux on preferential flow in a segregated column (Based on O'Kane et al. (1999)).

Segregation can be avoided with particle agglomeration (refer to sub-section 2.2.1). From Table 2.1, it can be seen that most studies choose to agglomerate when working with material less than 1 mm. Bouffard and Dixon (2001) studied the effect that agglomeration had on

the solute transport modelling of a packed bed composed of gold ore. The results showed that agglomeration tended to reduce both the experimental and model estimated stagnant liquid hold-up values in the bed whilst the experimental flowing liquid hold-up was not significantly affected. Also, the authors found that the ore particle size distribution prior to agglomeration had the most significant effect on pore held liquid, with beds composed of lower size fractions retaining significantly higher amounts of solution.

Bouffard and Dixon (2001) found more slumping in beds containing agglomerated ore than non-agglomerated ore because the agglomerated ore was naturally more porous. Segregation of fine and coarse material can exacerbate this effect as sections of the bed experience differing degrees of compaction leading to a greater variation in bulk densities and increased risk of preferential flow. However, agglomeration does not always result in greater slumping based on results presented by Bouffard and West-Sells (2009). In this particular study, a crib (big concrete box) loaded with agglomerated ore performed significantly better with respect to overall mineral extraction, compared to similar cribs containing non-agglomerated ore. Authors cited agglomeration as the reason for better fluid flow and air transport due to a higher resistivity to slumping. Based on this, it would seem that the overall effect of agglomeration may be dependent on the characteristics of the system tested.

2.6.4 Effect of Irrigation Mode and Solution Composition

Irrigation rate is the most studied factor because it is easily controlled after heap construction. Klerk (2003) found that increasing the liquid flux in a column packed with glass beads led to an increase in the dynamic liquid hold-up. These results are similar to those of de Andrade Lima (2006) who also found that the static liquid hold-up was not significantly affected. The opposite effect was observed by Ilankoon and Neethling (2012) who studied a packed bed of glass beads. The most apparent reason for this contrast in behaviours is the difference in packing materials. It should also be noted, that the fluxes used to obtain such behaviour in the different studies were significantly above the norm used in heap leaching operations. For this particular aspect, Klerk (2003) used a range of 360 - 1260 L/(m^2.h), de Andrade Lima (2006) used a range of 69.4 - 222 L/(m^2.h) and Ilankoon and Neethling

(2012) made use of fluxes in the range of 27.2 - 435 L/(m^2.h). Yusuf (1984) found that increasing the flow rates from 2 - 10 L/(m^2.h) did in fact lead to slight increases in overall liquid hold-up with this effect being more pronounced in beds composed of smaller sized rock particles (refer to Table 2.1).

The study by de Andrade Lima (2006) also reported on the effect of irrigation rate on liquid dispersion. The author made use of both Bodenstein (Equation (2.38)) and Peclet numbers (Equation (2.39)) and found that the axial dispersion coefficient decreased slightly as flow rate increased. This is in slight contradiction to equations proposed in a modelling study by Dixon and Afewu (2010) which indicated a proportional relationship between the longitudinal volumetric flux and longitudinal dispersion coefficient. Dixon and Afewu (2010) also predicted that increasing the irrigation rate will lead to an increase in the radial dispersion coefficient. It should be noted that in the de Andrade Lima (2006) study, the feed liquid was evenly distributed in the column, masking any radial dispersion effects. This raises another important issue in heap leaching literature, the choice of uniform distribution or point source irrigation.

$$Bo = \frac{v_l d_p}{D_{ds}} \tag{2.38}$$

$$Pe = \frac{v_l H_b}{D_{ds}} \tag{2.39}$$

In a laboratory setting, sprinklers and drip emmiters can be emulated using a uniform distributor or point source mechanism. In the prior mechanism, liquid is uniformly distributed over the surface of the packing while in the latter, liquid is emitted in a single stream or droplets at particular points. It is possible to have multiple distribution axes whilst using the point source mechanism. From Table 2.1 it can be seen that overall, there is an almost even split in the choice between the two delivery systems. However, most of the modelling work done on solute transport have utilized uniform distributors which force all advective flow to occur in the vertical direction. As such, flow in these systems have been adequately described using 1D semi-phenomenological solute transport models. However, extrapolation of these 1D models to beds with consistent lateral flow may be erroneous. Such lateral flow has been observed to occur in rectangular beds or cribs under point source irrigation (Fagan

et al., 2014; Fernando et al., 2020; Ilankoon and Neethling, 2016), and is also present in drip irrigated cylindrical beds which are typically used in the generation of reaction kinetic data (Spurr, 2008). Therefore, it is important to quantify the extent to which the presence of lateral flow, in drip irrigated laboratory scale cylindrical beds, affects the applicability of 1D solute transport models used for the evaluation of steady state fluid flow in such systems.

In sub-section 2.6.3, the work by O'Kane et al. (1999) regarding the effect of irrigation rate on preferential flow in a segregated column was discussed. The results of this study were corroborated by Wu et al. (2007) who also found that increasing the flow rate past a certain threshold led to preferential flow in the coarse section of a similarly segregated bed composed of copper ore. It should be noted that in order to observe this switch in preferential flow paths, the author had to exceed an irrigation flux of 64 200 L/(m^2.h), which is relatively very high compared to O'Kane et al. (1999) who were able to observe this switch over a range of 3.42 - 34.2 L/(m^2.h). The different packing materials utilized in both studies could be a possible reason for the significant contrast between the fluxes. Another reason could be differences in column geometries but this is difficult to pin point as Wu et al. (2007) did not provide the dimensions of the columns used in their study.

Another effect that an irrigation scheme can have, is in the creation of additional flow paths within a bed. Spurr (2008) worked with chalcopyrite ore in a cylindrical bed with multiple outlets. The results indicated that a decrease in liquid flux from 15.5 L/(m^2.h) to 5.5 L/(m^2.h) led to a slight increase in lateral or horizontal spreading for a mixed sized system. Fernando et al. (2020) found that by increasing the point source flow rate in a non-reactive rectangular bed from 75 - 158 L/(m^2.h), additional flow paths were created. This effect was also achieved by Ilankoon and Neethling (2016), who worked with a similar system. The difference though, is that the latter study achieved this through intermittent irrigation and not through flow rate manipulation. Another study by Fagan et al. (2014) found that when irrigation was stopped and then restarted, there was a more even distribution of flow in the wetted zone of a rectangular column packed with low grade copper ore. This was, however, postulated to be caused by changes in the structure of the agglomerates due to prior leaching. In the modelling study by Sheikhzadeh et al. (2005), utilizing periodic infiltration resulted in

quasi-steady state in which the degree of bed saturation varied between two limiting values. It was found that the fluctuations were dependent on not just the irrigation period, but also on the intrinsic permeability and height of the bed.

Table 2.1 shows a variety of irrigation fluids. In most acidic leach solutions, sulphuric acid (H_2SO_4) is normally used to obtain the desired pH making the SO_4^{2-} ion an important component in the solution chemistry of leaching fluids. This ion is also a product of the oxidation reaction of specific minerals, such as pyrite, and can build up in bio-leach solutions. A study conducted on the effect of SO_4^{2-} ions utilized solutions with concentrations over 100 g/L (Basson et al., 2013). Based on theoretical and experimental viscosity models, increasing the concentration of SO_4^{2-} ions, increases the viscosity of the solution (Pereira et al., 2001; Rhodes and Barbour, 1923), which according to Equation (2.5), should lead to a reduction in the bed's hydraulic conductivity. However, no studies were found of the effect of viscosity on heap performance. Watling et al. (2014) mentioned that an increase in viscosity could result in increased operational cost for solution management due to the added energy requirements needed by the pumping circuit. These illustrate that viscosity could be an important parameter in the characterisation of heap leaching irrigation fluids.

2.6.5 Effect of Scale

Heaps tend to under-perform in terms of rate of leaching and total metal extraction when compared to laboratory data (de Andrade Lima, 2006; Ghorbani et al., 2011; John, 2011). A postulated reason for this is the lack of fundamental research on hydrodynamic parameters specific to leaching test columns. In previous years, this has led to the formulation and application of 'rule of thumb' design criteria. Recently, substantial efforts have been made to model the different aspects of heap leaching and develop more sophisticated ways of scaling up.

The study by Bouffard and West-Sells (2009) showed that as scale was increased, the flow characteristics present within the beds deviated further from ideality. There are studies on the effect of scale on fluid flow in a horizontal direction (Dixon and Afewu, 2011; Fagan et al., 2014; Fernando et al., 2020; Ilankoon and Neethling, 2016; Spurr, 2008). The main results

from most of these studies have already been discussed, but one important factor to highlight is the effect of irrigation spacing. Ilankoon and Neethling (2016) found that increasing the number of drip emitters in their rectangular system and subsequently decreasing the horizontal scale of the bed, led to slightly more uniform flow profiles but did not completely eliminate channelling or preferential flow. This finding lends credence to the argument that even at smaller scales, preferential flow is still an observable phenomenon. When considering the vertical dimension, one of the proposed reasons for deviations from ideal flow is a decrease in the ratio of dynamic to stagnant liquid hold-up with an increase in column height as found in Bouffard and Dixon (2001). Such factors may be the reason for the inverse relationship experienced by Wu et al. (2009) between the percentage of extraction of the targeted metal species and the height of the heap. Increasing bed height is a convenient and effective way of not only testing the impact of scale, but also the predictive capabilities of semi-phenomenological models as bed height is an easily altered parameter in these models.

2.7 Literature Review Summary

In summary, the literature review presented here gave an overview of the heap leaching process: from site selection, to ore preparation, stacking and irrigation. Even when heaps are properly constructed and managed, the heap leaching process has been plagued with long extraction times, leading to low recoveries and in certain cases high operational costs. One of the major reasons cited for this is preferential flow, which manifests itself on both the bed and solution scale. At the bed scale, preferential flow results in the uneven wetting of the irrigated bed. At the solution scale, preferential flow results in varied residence times for different fluid elements. As the intrinsic link between solute transport and fluid flow was discussed in non-reactive bed systems under steady state fluid flux, it was then put forward that tracer tests are a robust way of obtaining valuable flow distribution information and diagnosing solution scale preferential flow symptoms.

The review showed that regarding test work, cylindrical column tests are the most common method by which kinetic data is obtained and factors of interests in these tests include

the packing material, particle size distribution, packing arrangement, lixiviant composition, solution application rate and scale. Solute transport models, such as the CM, AD, MSPD, PSPD, and PDE have been used to characterise flow profiles in such columns.

The review highlighted the following gaps in present literature. Firstly, regarding the intrinsic properties of packing material, studies have typically chosen different extremes when it comes to material properties: non-porous with sphericity, porous with irregularity and slightly porous thin sheets. There has been no published attempt at decoupling the effect of particle shape and particle porosity on the hydrodynamics and solute transport characteristics of leaching test columns.

A second gap area is the effect of packing wettability on capillary suction and its effect on the steady state flow profiles in a packed bed.

The third gap deals with solution viscosity. Theoretically, hydraulic conductivity is indirectly proportional to solution viscosity. Leach solutions typically contain ions, such as SO_4^{2-} which, based on viscosity models, can increase the viscosity of solutions depending on its concentration. However, most of these studies do not account for viscosity and some do not mention conducting tests in a temperature controlled environment. This raises the question as to the effect that an increase in solution viscosity has on the hydrodynamic behaviour of packed beds.

Fourthly, limitations of currently used solute transport models in the analysis of RTD profiles are not clear. Aspects such as the required level of model complexity and relevancy of model parameters have not been systematically studied especially in cylindrical beds under steady state drip irrigation.

There is a need to account for the effect of material properties (shape, size, porosity, wettability) and irrigation fluid viscosity on solution scale preferential flow in steady state, single drip point irrigated beds using different solute transport models. The comparisons of these different models under identical conditions will shed light on the critical model parameters needed to accurately describe the steady state fluid profiles and offer possible insights as to how preferential flow effects can be minimized in a heap.

Chapter 3

Objectives

Preferential flow has been cited as a dominant reason for the long extraction times during heap leaching. At the bed scale, it is characterised by uneven wetting, while at the solution scale, it results in the presence of dual permeable and dual porous solution volumes. Though the solution scale is the prime focus of this study and is commonly analysed under steady state fluid flux in laboratory column tests, the bed scale phenomena is also discussed. A fundamental understanding of these aspects requires that they be studied independently and due to their numerous nature, some have been identified as beyond the scope of this study. These include the effect of aeration, chemical reactions, particle segregation and temperature fluctuations. Previous works have touched on the importance of material and irrigation fluid properties (Fernando et al., 2019; Ilankoon and Neethling, 2013; Watling et al., 2014; Zhang and Yuan, 2019) as well as the modelling approach used in the quantification of relevant hydrodynamic parameters (Bouffard and West-Sells, 2009; Simunek and van Genuchten, 2006; van Staden and Petersen, 2018a). Areas of interest in this thesis were identified in section 2.7 and can be summarized as follows: decoupling the effect of particle shape from particle porosity, effect of packing wettability, impact of fluid viscosity, limitations of 1D solute transport models in the fitting of RTD curves and the relevance of commonly encountered hydrodynamic parameters in the quantification of solution scale preferential flow in heaps. This chapter will provide a more detailed list of the various experimental objectives and key research questions.

3.1 Key Objectives and Research Questions

The first objective of this study involves the selection and characterisation of packing materials and irrigation fluids, which are characteristic of the range used in model development work and typical of heap leaching operations.

Key research questions include:

1. What material properties affect the flow profiles in drip irrigated heaps?
2. Is it possible to decouple the effect of relevant material properties through appropriate material selection and characterisation?
3. How do higher concentrations of common ionic species (e.g. SO_4^{2-} ions) present in leaching solutions increase their viscosities and densities?

The second objective explores the effect of relevant material and fluid properties on the moisture absorption and retention capacities of the selected materials.

Key research questions include:

1. How do changes in particle size, shape, wettability and porosity affect the specific amount of moisture retained by the materials upon saturation and drainage?
2. How do changes in particle size, size distribution, shape, porosity and the degree of wettability affect the rate and amount of moisture absorbed/suctioned into packed beds of the selected materials by capillary forces?
3. How does solution viscosity affect the rate and amount of moisture suctioned into a packed bed by capillary forces?

The third objective explores the effect that material and bed properties have on bed characterisation parameters and the steady state solution flow (RTD) profiles of non-reactive, single point, drip irrigated beds.

Key research questions include:

1. How do material properties such as particle shape, porosity and wettability affect bed characterisation parameters such as bulk density, bed voidage, total liquid hold-up, total bed saturation and drain-down volumes?

2. How do bed properties such as particle size fraction, particle size distribution, top and bottom particle size limits affect bed characterisation parameters such as bulk density, bed voidage, total liquid hold-up, total bed saturation and drain-down volumes?

3. How do material properties such as particle shape, porosity and degree of wettability affect the steady state cumulative RTD curves of non-reactive, single point, drip irrigated packed beds?

4. How do bed properties such as particle size fraction, particle size distribution, top and bottom particle size limits affect the steady state cumulative RTD curves of non-reactive, single point, drip irrigated packed beds?

5. How does solution viscosity affect the steady state cumulative RTD curves generated from non-reactive packed beds under single point, drip irrigation?

The fourth objective deals with the appropriate level of model complexity needed by non-reactive solute transport models to adequately describe the steady state fluid flow or RTD profiles of non-reactive, single point, drip irrigated packed beds.

Key research questions include:

1. Do models with shared parameters but differing levels of complexity produce similar responses when such parameters are varied?

2. Are there differences in the capabilities of 1D and pseudo 2D solute transport models to adequately simulate the steady state RTD profiles generated from cylindrical packed beds under single point, drip irrigation?

3. Are semi-phenomenological solute transport models better than purely empirical models at simulating steady state RTD profiles of non-reactive, single point, drip irrigated packed beds?

4. Are dual porosity solute transport models better than mono porosity models at simulating steady state RTD profiles of non-reactive, single point, drip irrigated packed beds?

5. What are the essential modelling parameters needed to sufficiently describe the steady state RTD profiles of non-reactive packed bed systems under single point, drip irrigation?

The final objective explores the effect of material and bed properties on quantified hydrodynamic and solute transport parameters in relation to solution scale preferential flow diagnostics in steady state, drip irrigated, non-reactive packed beds.

1. How do different model parameters account for solution scale preferential flow in packed beds?

2. How do material and fluid properties such as particle shape, porosity, wettability and solution viscosity affect the magnitude of model parameters such as dead to total volume fraction, mixed to total volume fraction, longitudinal dispersion coefficient, dynamic to total saturation fraction, overall mass transfer coefficient and diffusional pore length?

3. How do bed properties such as particle size fraction, size distribution, top and bottom particle size limits affect the magnitude of model parameters such as dead to total volume fraction, mixed to total volume fraction, longitudinal dispersion coefficient, dynamic to total saturation fraction, overall mass transfer coefficient and diffusional pore length?

3.2 Novelty

The novelty of this research lies in the following points:

- The use of materials with different properties enabling the decoupling of particle shape

and porosity as well as accounting for particle wettability on the moisture absorption rates of packed beds via capillary suction.

- The effect, if any, that solution viscosity has on the moisture absorption characteristics of packed beds via capillary action, within a range applicable to heap leaching systems.
- The effect that particle shape, porosity, wettability, size fraction, bottom and top particle size limits and solution viscosity have on the steady state flow (RTD) profiles of single point, drip irrigated, non-reactive packed beds with regards to solution scale preferential flow diagnostics.
- A comprehensive study of the fitting capabilities of existing solute transport models as well as a new model formulation, to steady state flow (RTD) profiles of single point, drip irrigated, non-reactive packed beds.

This study will help inform heap practitioners on the fundamental factors affecting solution scale preferential flow behaviour in drip irrigated heaps, offer suggestions on how such behaviour can be effectively modelled as well as possible solutions to alleviate its presence.

Chapter 4

Material Selection and Characterisation

This chapter characterises the irrigation fluids and packing materials used. The first part focuses on viscosity and density measurements on both copper sulphate and glycerol solutions. The second part focuses on the mineralogical characterisation data, surface area analysis, contact angle measurements and particle shape analysis of the selected materials.

4.1 Liquid Characterisation

Liquid characterisation has not been a prime focus of past studies. From Equation (2.5), the hydraulic conductivity of an irrigated particle bed is directly proportional to the density and inversely proportional to the viscosity of the fluid. This makes both viscosity and density important parameters. Three different types of solutions were formulated and characterised. These were acidified solutions with dissolved metal and sulphate ions, non-reactive glycerol solutions and tracer solutions with dissolved potassium chloride (KCl).

Copper sulphide ores containing minerals such as chalcocite, covellite and chalcopyrite are typically leached in heaps. The dissolution of these minerals typically takes place in acidic solutions with both Cu^{2+} and $SO_4{}^{2-}$ ions present in solution. The concentrations of these ions typically increase during the leaching process. Basson et al. (2013) used over 100 g/L sulphate solutions to reflect bioheap leaching practice in South America. The impact of their concentration on the leaching solution properties is presented. Also, a proxy liquid was needed to study the isolated effect of viscosity on fluid flow. Glycerol was used for this.

In this section a short description of glycerol with its various uses is highlighted. Then the experimental methodology and apparatus used in the formulation and testing of the different solutions is elaborated on. Finally, the results from the various tests is presented and discussed. A background on viscosity theory and its measurement is found in Appendix A.

4.1.1 Glycerol as a Viscosity Modifier

To test the effects of viscosity without the chemical reactions that occur in leaching beds irrigated with acidic solutions, a pseudo fluid with neutral pH was required. Glycerol was selected for this purpose based on its characteristics. Refer to Figure 4.1 for its chemical structure.

Glycerol is hygroscopic and this attribute would need to be taken into account when evaluating drain down moisture in packed bed systems. It is water soluble due to the affinity of its polyol groups to form hydrogen bonds in water. It has a specific gravity of 1.26 which is higher than that of water, but its high solubility ensures that mixtures form aqueous solutions when mildly agitated. It has a relatively high viscosity at room temperature (∼875 cP), which allows it to act as a viscosity modifier for aqueous solutions (BD Editors, 2017; National Center for Biotechnology Information, 2021).

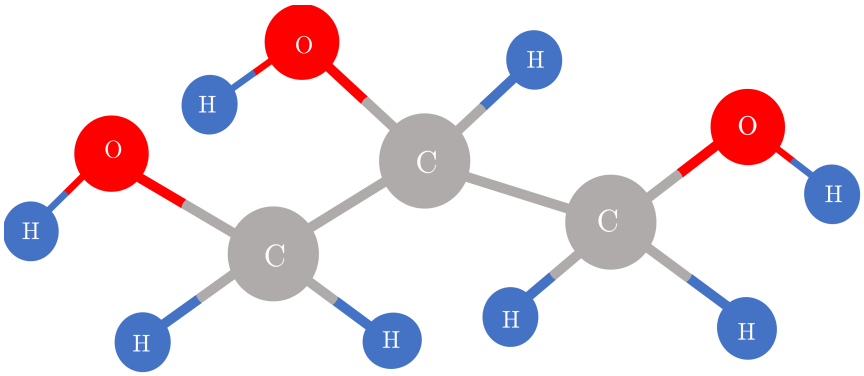

Figure 4.1: Chemical structure depiction of glycerol, C - Carbon, O - Oxygen, H - Hydrogen, based on National Center for Biotechnology Information (2021).

4.1.2 Experimental Apparatus and Methodology

4.1.2.1 Solution Formulation

Three main solutions were analysed for their viscosity and density: copper sulphate ($CuSO_4$), glycerol solutions, and glycerol solutions with KCl.

$CuSO_4$ Solutions

Acidified water with a pH of 1.15 was formulated by adding 95 - 99% sulphuric acid (H_2SO_4) to deionized water. Copper sulphate pentahydrate ($CuSO_4 \cdot 5H_2O$) salt was weighed and added to a beaker. A specific volume of acidified water was added to the beaker to dissolve the salt. The pH of the mixture was readjusted to 1.15 through the addition of small amounts of concentrated H_2SO_4. Five solutions (0, 36, 77.5, 119 and 161 g/L $CuSO_4$) with 0, 25, 50, 75 and 100 g/L SO_4 were prepared in triplicates.

Glycerol Solutions

Glycerol solutions of 0 to 35 wt% were prepared using pure glycerol (> 99% purity) mixed with deionized water in a volumetric flask. 0.7 and 7.5 g/L KCl was added to selected concentrations of glycerol solutions to explore the effect of the tracer. The viscosity of the formulated solutions were measured.

4.1.2.2 Viscosity

Equipment

The Cannon-Fenske Glass Capillary viscometer, shown in Figure 4.2a, was cleaned with an alkaline detergent, rinsed multiple times with water and acetone before being air dried. A water bath (L), was filled with deionised water and set to 30°C using a temperature controller box (K), with a water heating and circulation mechanism using a pump. The viscometer was immersed to point A using a clamp (J), ensuring bulb B was completely immersed. Between 7 and 10 mL of the liquid sample was poured into the viscometer via tube I and it was given 10-15 minutes to equilibrate to 30°C. This temperature was chosen as its is close to most heap leaching hydrology tests that are conducted at ambient temperature and also

laboratory bio-leaching studies that typically occur at 37°C. A suction bulb was attached to tube A of the viscometer and used to suction the liquid from bulb H, past the U-tube (G) and into bulb D. The liquid was suctioned to a point approximately 1 cm above mark C. The suction bulb was removed and the time taken for the liquid to fall from mark C to mark E was recorded. Tests were run in triplicate. The manufacturer's viscometer constant (Cv) was used to convert the time (t) measured into kinematic viscosity ($\bar{v}$), as shown in Equation (4.1). Equation (A.4) was used to convert kinematic viscosity to dynamic viscosity. The viscometer was then removed from the water bath, emptied, cleaned, dried and the process was repeated for the next sample.

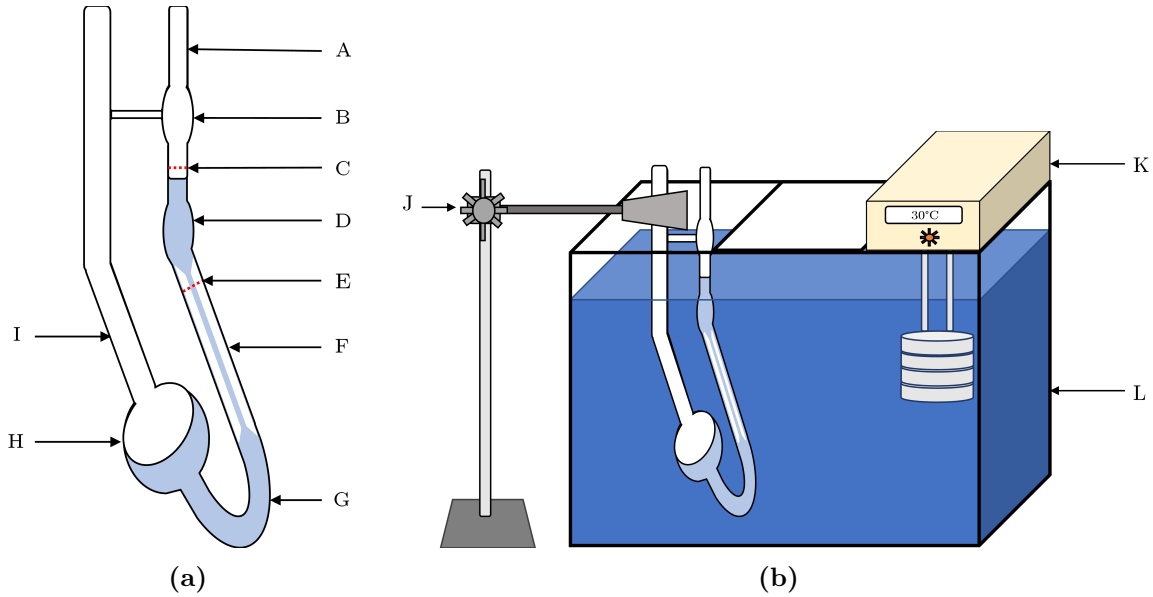

Figure 4.2: Experimental set up used in viscosity measurement tests, (a) Cannon-Fenske Glass Capillary viscometer, (b) Viscometer held by clamp in water bath maintained at constant temperature. Alphabetical labels are referred to in the text.

$$\bar{v} = Cv \times t \tag{4.1}$$

4.1.2.3 Density

Equipment

The water bath in Figure 4.2b was filled with deionized water and maintained at 30°C. Liquid

samples were poured into falcon tubes, sealed off and submerged in the water bath for 20 - 30 minutes to equilibrate to the water bath's temperature. A 10 mL measuring cylinder was tared. The falcon tubes were removed from the water bath and their contents were poured into the measuring cylinder. The volume and weight of the liquid were recorded. Measurements were done in triplicate.

4.1.3 Results and Discussion

4.1.3.1 Impact of SO_4^{2-} Ions on Viscosity and Density of Aqueous Solutions

From Figures 4.3a and 4.3b, an increase in sulphate ion concentration from 0 to 100 g/L led to a 80% increase in viscosity from 0.80 to 1.45 cP. Density was similarly affected with a 16% increase from 0.99 to 1.15 g/mL. These solutions are Newtonian. All data were obtained at 30°C.

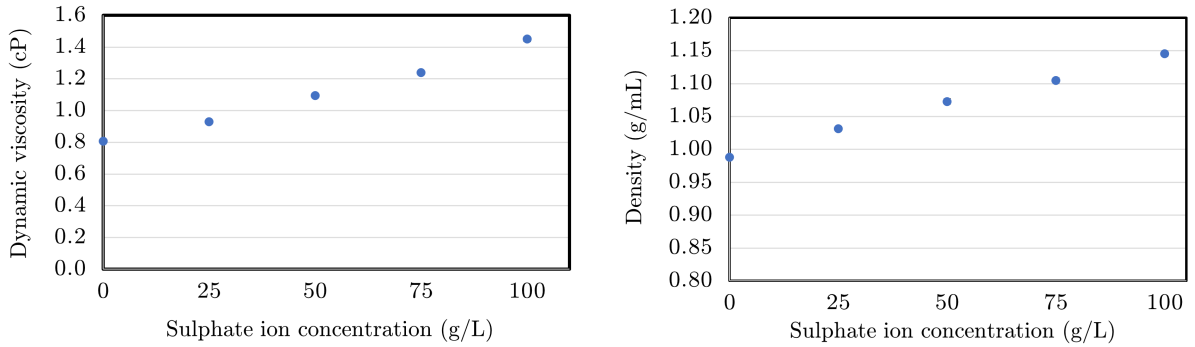

Figure 4.3: Average viscosity (a) and density (b) values (with error bars) for different concentrations of copper sulphate solutions measured at 30°C.

4.1.3.2 Newtonian Behaviour of Glycerol Solutions

To determine the suitability of glycerol as a proxy test fluid, the Newtonian behaviour of different glycerol solutions were ascertained using viscometers with different capillary sizes. Different size capillaries impart differing shear stresses on the solutions flowing through them and as highlighted in Appendix A, under laminar flow, Newtonian fluids maintain constant

viscosity regardless of the magnitude of shear stress applied.

Figure 4.4a shows that the different glycerol solutions exhibit Newtonian behaviour based on the consistency in viscosity values obtained using the different size viscometers. The measured values also agree well with those of Miner and Dalton (1953). An increase in glycerol concentration from 5 to 35 wt% led to an increase in viscosity from 0.91 to 2.17 cP. The glycerol concentration range applicable to the sulphate solutions is approximately 0 to 21 wt%. Figure 4.4b shows an 8% increase in density as the glycerol concentration was increased over the prior range mentioned. This is very similar to the results for the copper sulphate solutions.

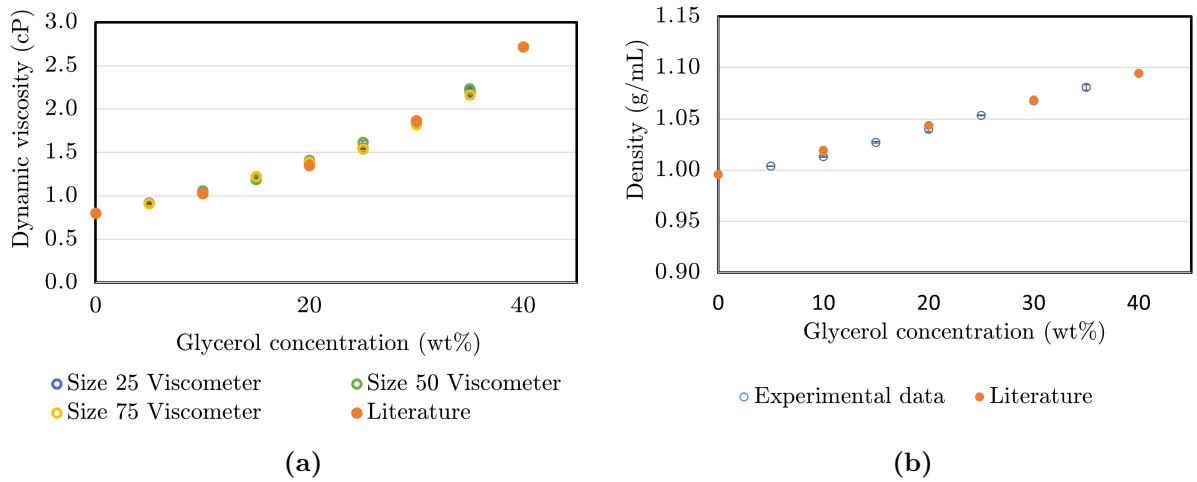

Figure 4.4: Average viscosity (a) and density values (b), (with error bars) for different concentrations of glycerol solutions measured at 30°C. Three viscometers with different capillary sizes were used for the viscosity measurements. Literature values were obtained from Miner and Dalton (1953).

4.1.3.3 Effect of KCl on Viscosity of Glycerol Solutions

KCl was identified as a possible tracer for RTD generation and therefore, should have a negligible impact on the liquid properties. Its effect on the viscosity of glycerol solutions was studied (refer to 4.5a).

KCl did not have a substantial effect on the viscosity or density of glycerol solutions over the selected range (Figure 4.5). The slight increase in density was expected due to the greater

amount of dissolved solutes present in the 7.5 g/L KCl solutions. Based on these results, it was decided that KCl would be an adequate salt tracer.

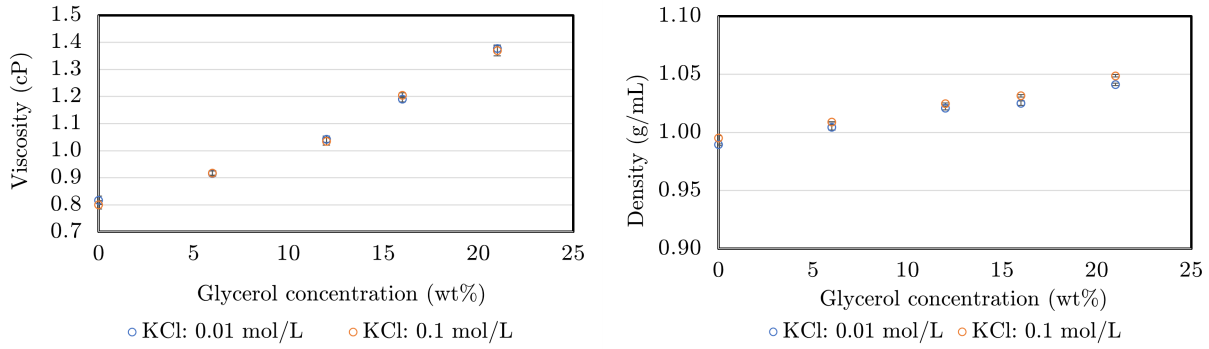

(a) **(b)**

Figure 4.5: Average viscosity, graph (a), and density values, graph (b), (with error bars) for different concentrations of glycerol solutions with KCl measured at 30°C.

4.2 Solid Characterisation

In order to decouple the effects of material properties on fluid flow and solute transport in packed bed systems, four different packing materials were chosen. These were glass beads (GB), glass shards (GS), greywacke (GW) and malachite ore (MO). GB were selected due to their sphericity and non-porosity (Figure 4.6a) . GS were irregular in shape and non-porous (Figure 4.6b). GW were porous and irregularly shaped (Figure 4.6c) and lastly, MO were porous, irregularly shaped and the most realistic leaching material (Figure 4.6d).

The glass beads were purchased from Sigma Aldrich and Lasec, respectively. Spherical glass marbles from a toy store were used as 15 mm beads. The shards were sourced from waste piles of broken shatter proof glass at a PG Glass centre located in Cape Town, South Africa. Once they were obtained they were screened into different size fractions. Greywacke stones were purchased from an Afrisam plant, a supplier of construction materials, also located in Cape Town. It is a sedimentary rock consisting mainly of quartz and feldspar (Hudson Institute of Mineralogy, 2021). The stones were crushed at UCT using a jaw crusher and sieved into different size fractions. Bags containing crushed, split and sieved samples of

malachite ore were provided by Mintek. Upon arrival, the ore was further sieved into more defined size fractions prior to their analysis and use.

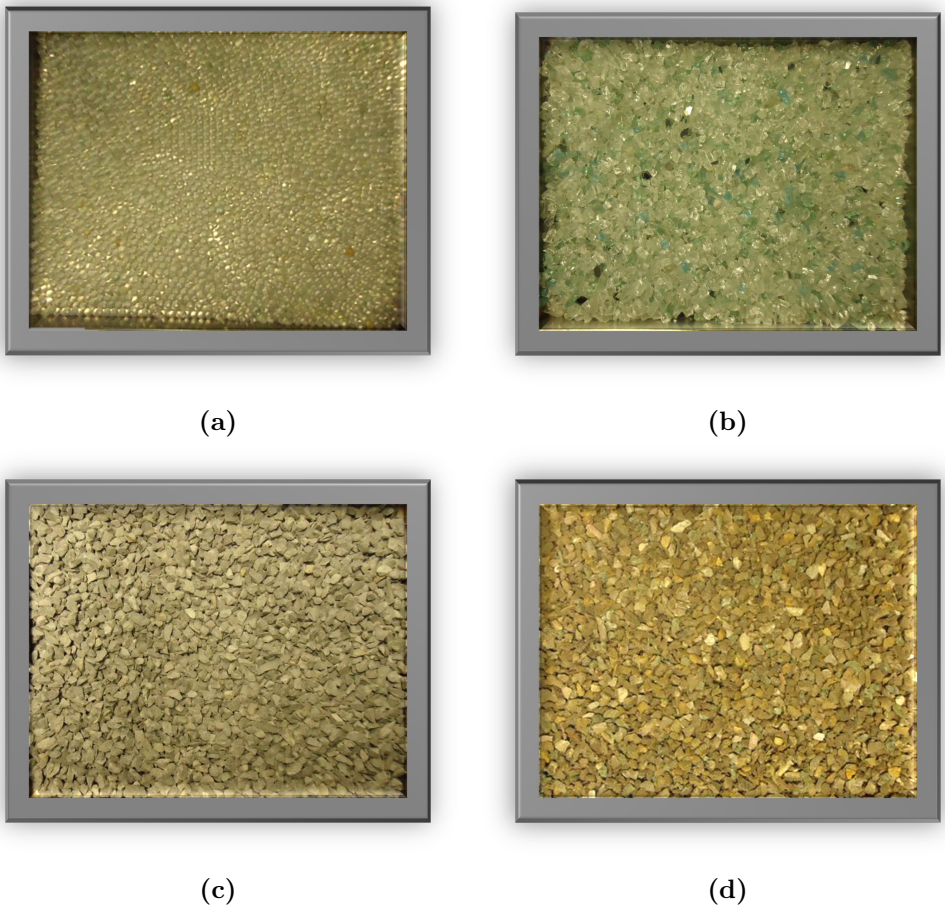

Figure 4.6: Different packing materials utilized in this study, (a) Glass beads (2 mm), (b) Glass shards (4.8 - 5.6 mm), (c) Greywacke (4.8 - 5.6 mm), (d) Malachite ore (4.8 - 5.6 mm).

4.2.1 Mineralogical Characterisation

The mineralogical characterisation of the malachite ore, the only reactive solid, was carried out by Ghadiri (2019). The ore was sieved into six size fractions: <0.25 mm, 0.25 - 1 mm, 1 - 2 mm, 2 - 5.6 mm, 5.6 - 8 mm and 8 - 16 mm. A portion of each fraction was combined and pulverised to <75 μm, the resulting representative powder was analyzed.

Based on the analysis by Ghadiri (2019) the ore consisted of 77% quartz (SiO_2) with copper

(Cu) in the form of malachite ($Cu_2CO_3(OH)_2$ - 7%) and Bornite (Cu_5FeS_4 - 2%) as well as iron (Fe) in the form of Bornite and ilmenite ($FeTiO_3$) - 5%). Other minerals such as muscovite (4%), biotite (1%), chlorite (0.4%) and chrysocolla (0.1%) were also present.

4.2.2 Surface Area and Pore Size Distribution

The Brunauer-Emmett-Teller (BET) method was used to estimate the surface area and pore size distribution of samples of the GW and MO materials. It works on the basic principle of gas, or in this case, nitrogen adsorption. The assumptions made during the analysis include ideal behaviour of gas molecules, no gas-gas interaction, homogeneous surface, formation of a mono layer and that all surface sites have the same adsorption energy for the adsorbate. The surface area of a material is therefore proportional to the amount of gas adsorbed onto its surface based on the transformation of the physisorption isotherm into a "BET plot" and derivation of the BET mono layer capacity.

The method typically involves two stages. In the first, Equation (4.2) is used to relate the relative gas pressure (p/p^o) and amount adsorbed (n_B) to the mono layer capacity (n_m), where parameter C_B is directly linked to the energy of mono layer adsorption. The second stage involves the calculation of the BET surface area (BET S.A.) from the mono layer capacity, specific molecular surface area ($\frac{\sigma_m}{M_m}$) and Avogadro's constant (L_{Av}) as shown in Equation (4.3) (Thommes et al., 2015).

$$\frac{p/p^o}{n_B\,(1-p/p^o)} = \frac{1}{n_m C_B} + \frac{C_B - 1}{n_m C}\,(p/p^o) \tag{4.2}$$

$$\text{BET S.A.} = n_m \cdot L_{Av} \cdot \frac{\sigma_m}{M_m} \tag{4.3}$$

The analysis was done at the UCT Chemical Engineering Analytical Laboratory. Samples weighing approximately one gram from two size fractions (0.1 - 0.5 mm and 0.5 - 1 mm) based on size limitations of the sample holders, were analysed. The samples were measured, placed in transparent sample tubes and degassed overnight in a Micromeritics, VacPrep 061 Sample Degas System at a maximum temperature of 200°C. Analysis was done using the Micromeritics TriStar II 3020 Surface Area and Porosity instrument at a bath temperature

of -195.8°C with nitrogen as the adsorptive. Data analysis and calculations were done on a desktop computer loaded with the TriStar II 3020 version 2.00 software package.

From Table 4.1, a reduction in size from 0.5 - 1 mm to 0.1 - 0.5 mm led to a 66% and 128% increase in the BET surface area for the GW and MO, respectively. MO had a specific surface area that was on average three times larger than that of GW, indicating a significantly higher porosity. The pore size data for MO was more sensitive to hysterisis with adsorption values being approximately 1.2 times larger than the desorption values. GW was more sensitive to size fraction with a 18 to 26% reduction in pore size as size fraction was increased. The significance of such deviations is difficult to analyse as these are average pore size values of relatively small magnitudes. The MO pore volume was significantly greater (2.7 - 3.8 times) than that of GW across the two size fractions shown. This corroborates the specific surface area data and lends further credence that MO was more porous than the GW. Both materials also experienced a reduction in pore volume with an increase in particle size fraction which again corresponds to the reduction in specific surface area.

Table 4.1: BET analysis results for both GW and MO. [Key: BET S.A. - BET surface area, Ad. - Adsorption, Ds. - Desorption, Pore vol. - Pore volume]

Material	**Size fraction (mm)**	**BET S.A. (m^2/g)**	**Pore size Ad. (Å)**	**Pore size Ds. (Å)**	**Pore vol. Ad. (cm^3/g)**	**Pore vol. Ds. (cm^3/g)**
Greywacke	0.1-0.5	1.68 ± 0.01	138	141	0.005	0.006
	0.5-1.0	1.01 ± 0.01	112	106	0.003	0.003
Malachite ore	0.1-0.5	5.88 ± 0.05	136	108	0.019	0.023
	0.5-1.0	2.58 ± 0.02	135	116	0.008	0.010

4.2.3 Wettability and Contact Angle Measurements

Wettability and contact angle measurements give an indication of the hydrophilicity of a material. Tests were carried out using the capillary suction method described in sub-section 2.4.1.1 and Washburn's Equation (2.4). GS, GW and MO were analysed. Due to their size, the GB did not possess any suction capabilities and hence, wettability of the beads was assumed to be similar to those of the glass shards.

A Krüss force tensiometer (K12/MK4 from Advanced Laboratory Solutions) was used to

carry out the measurements. The materials were pulverised and sieved to 38 - 53 μm. 10 g of material was loaded into a 1 cm I.D. cylindrical glass column up to a 3 cm height. A cut concentric piece of Genuine Whatman Filter Paper (No. 54) with a pore size of 22 μm was secured to the bottom of the column. The loaded column was placed inside the tensiometer and secured to a load cell. N-hexane with a purity $\geq$ 97.0% from Sigma-Aldrich was used as the completely wetting fluid to determine the packing constant prior to tests with the formulated solutions. The test liquid was poured into a 4.5 cm I.D. glass reservoir till a height of 3 cm. The reservoir was placed in a jacketed holder inside the tensiometer, maintained at 30°C using pumped water from a water bath. The liquid was given approximately 15 minutes to equilibrate to 30°C and an internal temperature probe was used to confirm the temperature.

The Krüss Laboratory Desktop software, version 3.2 was used to control the instrument, store and analyse the data. The column was lowered until it made contact with the liquid and the change in mass of the column at specific time intervals was recorded by the software. A plot of squared Mass vs. Time was generated and a straight line was fitted to the early portion of the graph. Washburn's equation was used to derive the packing constant and contact angles. Tests were conducted a minimum of three times to ensure reproducibility. Table 4.2 shows that the order of materials from most hydrophilic to least hydrophilic was GW, GS and MO. The relatively low wettability of MO is similar to the results by Lourenço et al. (2015) who made use of the sessile drop and Wilhelmy plate method. Carr (1948) obtained contact angles ranging from 40 - 90°C for a malachite ore sample using a variety of fluids and a specialized apparatus for visual measurements.

The results on the effect of glycerol concentration on wettability measurement shows that it did not have a significant impact with only a 1.1 - 2.4% deviation over the range studied. From Washburn's equation, though cos θ is proportional to viscosity, it is inversely proportional to density. As glycerol increased both the viscosity and density of water, these two effects seem to have counteracted each other during the quantification of cos θ.

Table 4.2: Average and standard deviation (SD) values from contact angle experiments conducted on the glass shards, greywacke and malachite ore materials using different solutions.

Material	Liquid	Contact angle
Glass shards	Water	50 ± 3.3
Greywacke	Water	40 ± 2.9
Malachite ore	Water	63 ± 3.4
	15 Wt% Glycerol	64 ± 0.9
	25 Wt% Glycerol	63 ± 0.5
	30 Wt% Glycerol	63 ± 0.5
	35 Wt% Glycerol	64 ± 0.5

4.2.4 Shape Analysis

In heap leaching, particle shape is heavily influenced by the excavation, crushing and milling methods employed. Though shape characterisation has not been giving much attention in a heap leaching context due to a heap's highly heterogeneous nature, laboratory scale studies have made use of packings with different shape characteristics with inference to the hydrodynamic behaviour of heaps. As particle shape is known to influence the way particles orient themselves in a packed bed, it is expected to affect the fluid flow profiles in irrigated beds. One of the main aims of this study is the decoupling of particle porosity and shape effects through the selection of appropriate materials.

Shape quantification can be done in either 2D or 3D with each choice possessing both pros and cons. 3D shape quantification will give the most accurate representation of an analysed particle. This is typically achieved using XCT or a 3D laser scanner. However the main disadvantages with this approach is the need for sophisticated machinery, complex and intricate image analysis software and an adequate repository for the significantly large amounts of data generated (Rodriguez, 2013). In many cases, physical and temporal constraints impose a limit on the number of particles that can be analysed using a 3D approach. 2D shape quantification methods deal with 2D projections of 3D objects, meaning that the accuracy of such methods depends on the choice of which direction observations are made. This could potentially lead to non-unique shape descriptors of particles. However, based on the relative

abundance of different 2D shape descriptors, the ability to analyse a large number of particles as well as the fast and low cost nature of its methodology, 2D shape quantification was chosen for this study.

In order to perform 2D shape analysis of the different particles, five factors were considered: particle arrangement, illumination, image capture, image post-processing and image analysis. These factors will now be discussed in more detail.

4.2.4.1 Particle Arrangement

It was important to generate clear particle outlines and hence prevent contact between different particles for accurate 2D shape quantification. This was achieved through the individual arrangement of 100 particles in a 10 by 10 grid with sufficient spacing provided. This spacing requirement and arrangement methodology imposed a 1 mm lower size fraction limit on what could be feasibly and accurately examined. All four materials were characterised but only a limited number of spherical beads (ten per size class) were analysed due to their uniformity in shape. A total of three hundred particles per size class (maximum of 11 size classes) were analysed for the other three materials.

The effect of particle orientation on the quantification of different shape descriptors was also examined. For this, 100 particles were arranged in the same 10 by 10 grid pattern. Once pictures were taken, each individual particle was rotated on one set of its axis in a particular direction. Pictures were taken and the particles were again rotated on a different set of axis to provide a different 2-D shape projection. Due to the fact that not all particles could be independently balanced on 3 different axes, some particle orientations were left unaltered in certain cases. This test was done on the largest size fraction common to GS, GW and MO because the effect of rotation is more prominent with large particles.

4.2.4.2 Particle Illumination

Illumination was an important aspect to ensure maximum contrast between the particles and their background. A rectangular light box with fluorescent bulbs located at the bottom

was used (refer to Figure 4.7). A thin sheet of white paper was placed over the box and covered with a thin pane of transparent glass (refer to Figure 4.7c). This provided an illuminated white background for the particles. The opaque particles, such as the greywacke and malachite ore, were able to generate clear outlines when placed on the bright surface, but the transparency of the shards and beads presented a challenge. To deal with this, both the shard and bead particles were spray coated with matte black paint.

Though the spray painting proved successful, the paint added a thin layer of thickness. Though care was taken to ensure uniformity, minor differences in coverage could not be totally eliminated. However, the relatively large number of particles analysed prevented these differences from significantly skewing the data.

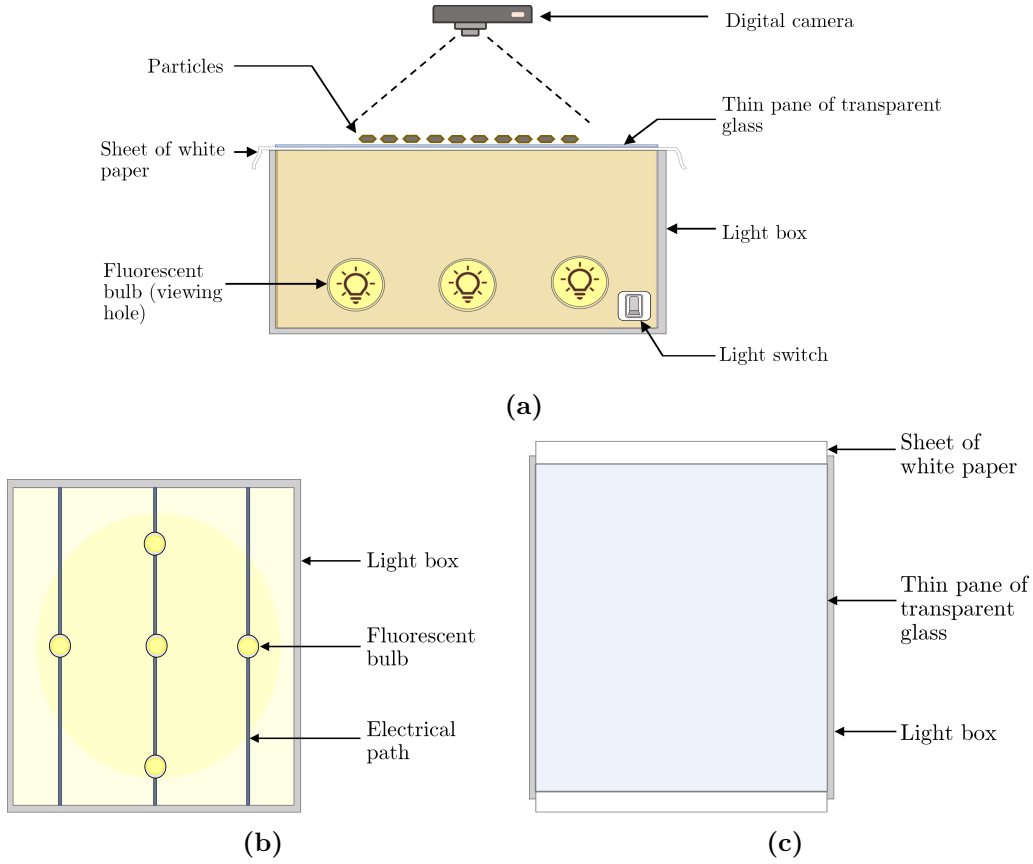

Figure 4.7: Different illustrations of the light box used for particle shape characterisation, (a) Side view, (b) Top view: Open, (c) Top view: Covered with paper and glass.

4.2.4.3 Image Capture

A Sony Cyber-shot DSC-W530, 14.1 mega-pixel digital camera with Carl Zeiss Vario-tessar 4X wide-angle optical zoom lens and 2.7 inch LCD display was used to capture images of the different particles. The camera was located at a sufficient height directly above the particles to limit shape distortions (refer to Figure 4.7a).

4.2.4.4 Image Post-processing

Captured images were uploaded to ImageJ computer software package for both image post-processing and analysis (refer to raw images shown in the left of Figures 4.8 and 4.9). The post-processing comprised of the calibration and cleaning of images to filter out the background and other non-particle elements. Calibration was done based on a measured scale that was captured along with the particles. When necessary, image filtering was achieved through the use of the bandpass filter option that only allowed captured objects within a specified pixel range to be retained for further analysis.

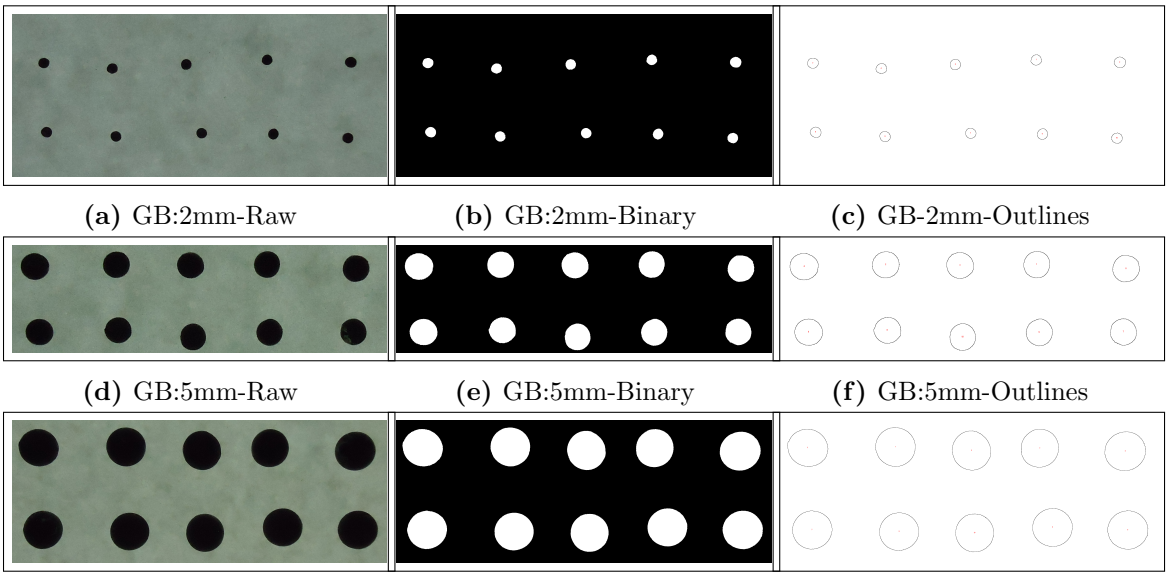

(a) GB:2mm-Raw **(b)** GB:2mm-Binary **(c)** GB-2mm-Outlines

(d) GB:5mm-Raw **(e)** GB:5mm-Binary **(f)** GB:5mm-Outlines

(g) GB:15mm-Raw **(h)** GB:15mm-Binary **(i)** GB-15mm-Outlines

Figure 4.8: Captured and processed images of spray painted 2, 5 and 15 mm GB.

Raw or filtered images were converted to 8-bit binary image files and a threshold was enabled

to maximise the distinction between particles and their background (refer to binary images shown in the middle of Figures 4.8 and 4.9). The product of the threshold routine was used for image analysis that generated the particle outlines (refer to particle outlines shown on the right in Figures 4.8 and 4.9). Both binary images and outlines were used during the quantification of the different 2D shape descriptors.

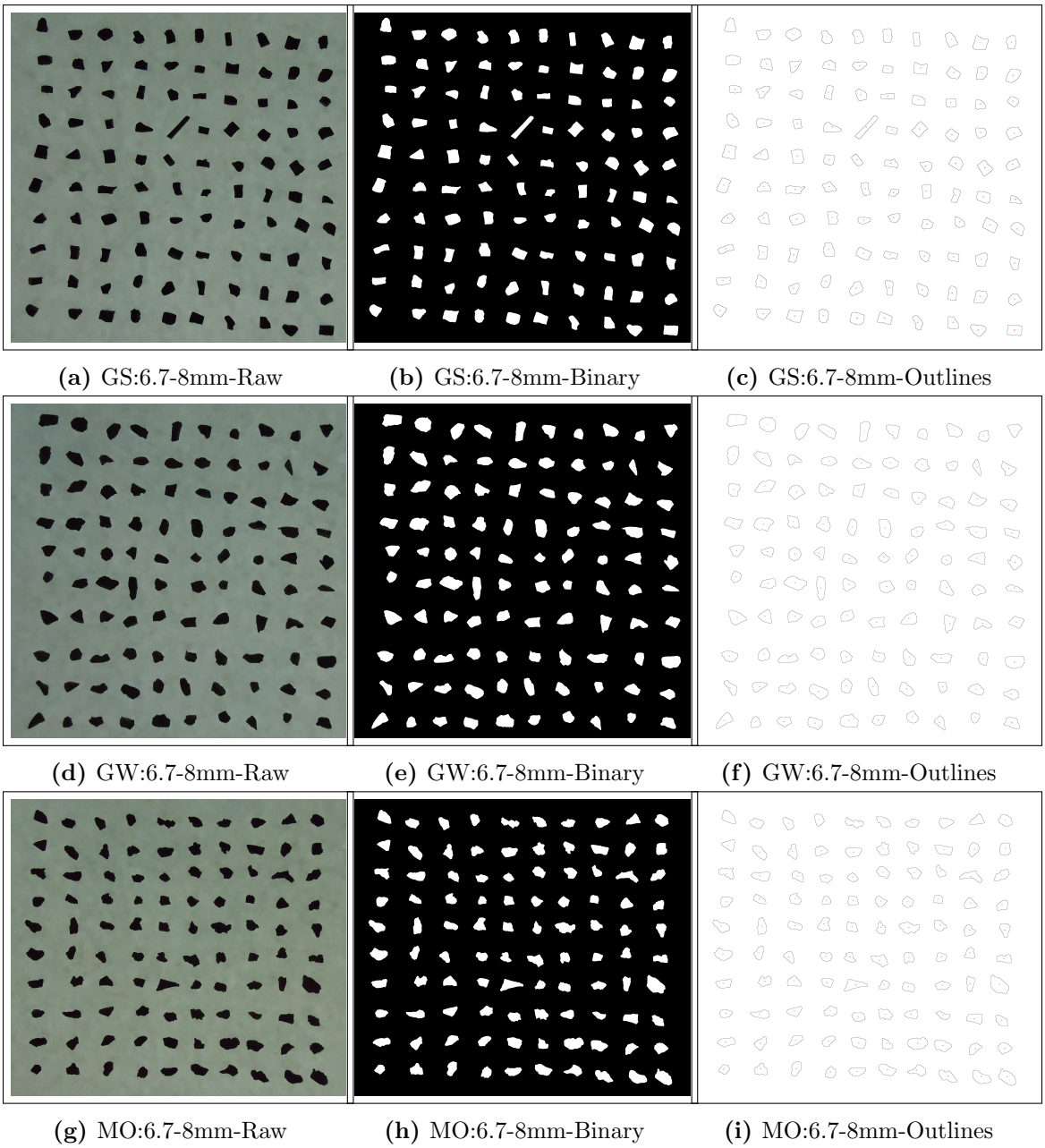

(a) GS:6.7-8mm-Raw **(b)** GS:6.7-8mm-Binary **(c)** GS:6.7-8mm-Outlines

(d) GW:6.7-8mm-Raw **(e)** GW:6.7-8mm-Binary **(f)** GW:6.7-8mm-Outlines

(g) MO:6.7-8mm-Raw **(h)** MO:6.7-8mm-Binary **(i)** MO:6.7-8mm-Outlines

Figure 4.9: Captured and processed images of 100 particles of spray painted GS, GW and MO with a size fraction of 6.7 - 8 mm.

4.2.4.5 Image Analysis

Image analysis was done using the BioVoxxel Toolbox plugin for ImageJ created by Jan Brocher. This toolbox came with an extended particle analyser that allowed for the quantification of a variety of 2-D shape descriptors (Brocher, 2014). The different descriptors and methodologies used in their quantifications are shown in Table 4.3.

Table 4.3: Illustrating the different 2-D shape descriptors (SD) used and how they were quantified.

2-D SD	Description	How it was obtained	
Area	Total area occupied by particle	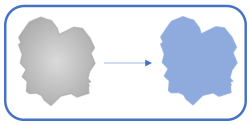	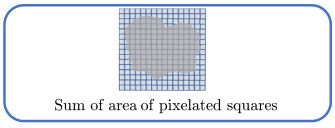
Aspect ratio	Ratio of maximum to minimum length	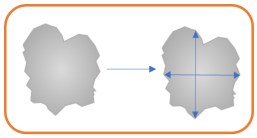	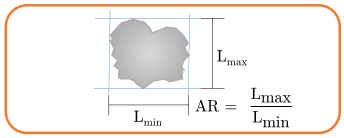
Circularity	How shape compares to a circle	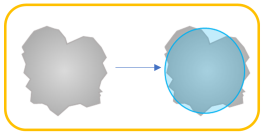	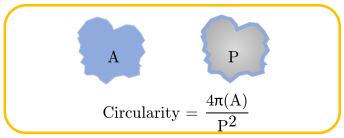
Compactness	Alternate measure of circularity	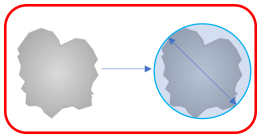	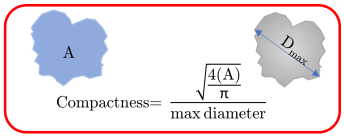
Extent	Degree of particle's rectangularity	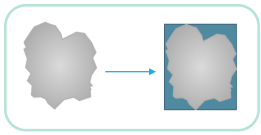	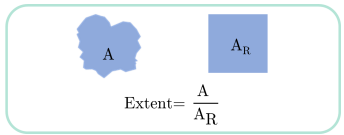
Perimeter	Distance around shape	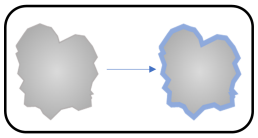	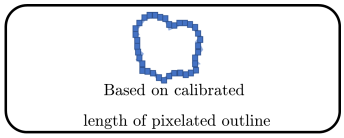
Solidity	Measure of convexity	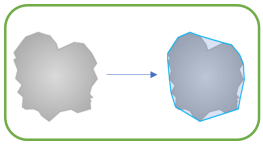	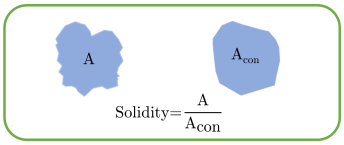

4.2.4.6 Results and Discussion

Experimental tags were formulated for the different materials and size fractions used in this work. Descriptions of the tags that apply to this section are found in Table 4.4.

Table 4.4: Experimental tags used in data representation.

Size fraction (mm)	Experimental tag Materials			
	Glass beads	**Glass shards**	**Greywacke**	**Malachite ore**
2	GB-1	(-)	(-)	(-)
5	GB-2	(-)	(-)	(-)
15	GB-3	(-)	(-)	(-)
1.0-2.0	(-)	GS-6	GW-6	MO-6
2.0-2.8	(-)	GS-8	GW-8	MO-8
2.8-4.0	(-)	GS-9	GW-9	MO-9
4.0-4.75	(-)	GS-11	GW-11	MO-11
4.75-5.6	(-)	GS-12	GW-12	MO-12
5.6-6.7	(-)	GS-14	GW-14	MO-14
6.7-8.0	(-)	GS-15	GW-15	MO-15
8.0-9.6	(-)	(-)	GW-16	MO-16
9.6-11.2	(-)	(-)	GW-17	MO-17
11.2-13.2	(-)	(-)	GW-18	MO-18
13.2-16.0	(-)	(-)	GW-19	MO-19

The quantified shape descriptors for the materials can be found in Appendices B, Figure B.1 through to Figure B.12. A comparison of the average descriptor values between the materials and a perfect sphere across the 1 to 8 mm size range can be found in Table 4.5.

A perfectly spherical particle will have an aspect ratio, circularity, compactness and solidity equal to 1 with an extent equal to approximately 0.785. The average aspect ratio for the materials was greater than 1 while their average compactness, solidity and circularity values were less than 1. The extent values for the materials were less than those of a perfect sphere. Across the materials, the GB were the closes to that of a perfect sphere, showing between 3 to 12% deviation. The other three materials (GS, GW and MO) had average aspect ratios ranging between 1.55 and 1.62 which indicates a degree of particle elongation along

a particular dimension, leading to deviations from sphericity. The total average circularity values for the three materials ranged between 26 to 28% less than those of a sphere. The compactness values were also less by approximately 19%. However in terms of solidity, all the materials showed high levels of convexity, indicating that most of the particles analysed did not possess any deep kinks or highly irregular, jagged boundaries.

There were no major statistical differences in shape between the GS, GW and MO. Porosity, which is linked to surface texture, as well as wettability are expected to play a more significant role in the flow profiles obtained from the beds. This means that these factors could be effectively decoupled from shape to some degree.

Table 4.5: Average and standard deviation of five shape descriptor values acquired over a 1 - 8 mm size fraction range for GB, GS, GW, MO.

Shape descriptor	**Calc. value**	**Average values**			
	PS	GB	GS	GW	MO
Aspect ratio	1.00	1.05 ± 0.01	1.55 ± 0.44	1.62 ± 0.45	1.58 ± 0.41
Circularity	1.00	0.88 ± 0.00	0.74 ± 0.08	0.73 ± 0.08	0.72 ± 0.08
Compactness	1.00	0.98 ± 0.01	0.82 ± 0.09	0.81 ± 0.09	0.81 ± 0.09
Extent	0.79	0.77 ± 0.01	0.68 ± 0.09	0.67 ± 0.07	0.67 ± 0.07
Solidity	1.00	0.97 ± 0.01	0.94 ± 0.03	0.93 ± 0.03	0.92 ± 0.03

Effect of Particle Orientation on 2D Shape Descriptor Values

To further explore the extent to which 2D shape descriptors could represent 3D particles, a test was carried out on the 6.7 - 8 mm particles. One hundred particles were analysed in three different orientations (refer to sub-section 4.2.4.1). Figures B.13, B.14 and B.15 in Appendix B show the results of the effect that particle orientation had on quantified shape descriptor values.

Standard deviations across the three orientations were calculated and expressed as a percentage of the average (refer to Table 4.6). All three materials recorded their highest deviations for area and aspect ratio which indicates that these are the most sensitive to particle orientation. Solidity values were the most consistent across all three orientations and can be considered the least sensitive descriptor. As expected, increases in aspect ratios was coupled

with reductions in circularity and compactness (refer to c, d and e of Figures B.13, B.14 and B.15).

The GS showed the most variation in shape descriptor values with particle orientation based on the standard deviation (%). This is partly because the shards were the most easy to balance on their three different axes to provide different 2D projections. With the GW and MO, it was more difficult to fully rotate all 100 particles. A second reason is due to the limitation imposed on the shards' thickness by the glass manufacturing process. This meant that whilst the other two dimensions could vary unbounded in size, the third dimension, the shard's thickness, had an upper limit between 6 - 10 mm. Hence, certain orientations led to noticeable differences in particle outlines. As mentioned previously, only shards passing through a sieve size of 8 mm were utilized in this work, to prevent significant bias in particle shape due to this reason.

Table 4.6: Standard deviations of average shape descriptor values across three orientations, expressed as a percentage of the mean for the GS, GW and MO materials.

Shape Descriptor	**Standard deviation (%)**		
	GS	**GW**	**MO**
Area (mm^2)	14.65	6.25	8.31
Perimeter (mm)	6.93	1.96	3.48
Aspect ratio (-)	12.19	7.64	8.09
Circularity (-)	3.17	2.43	1.55
Compactness (-)	5.75	2.95	3.30
Extent (-)	4.93	1.29	1.46
Solidity (-)	0.45	0.34	0.06

To summarize, differences due to particle orientation were not significant as there was substantial variation in descriptor values for each orientation. Therefore, in the analysis of 300 randomly placed particles, variations due to particle orientation can offset each other and therefore not have a significant impact on the average descriptor values.

4.2.5 Solid Characterisation Summary

A summary table of the different physical properties of the selected material can be found in Table 4.7. Mineralogical data was presented for MO and showed that the ore consisted mainly of quartz and malachite. BET analysis was conducted on samples of both the GW and MO, and it was found that on average the MO sample had a surface area three times larger than the GW sample. A similar relationship existed for pore volume. Contact angle measurements results showed that GW was the most hydrophilic, followed by GS and MO. The effect of glycerol concentration on wettability was also studied and revealed that within the chosen concentration range, glycerol had no significant effect.

Table 4.7: Summary of the physical properties of selected materials.

Property	**Packing Material**			
	Glass beads	**Glass shards**	**Greywacke**	**Malachite ore**
Compostion	Uniform	Uniform	Non-uniform	Non-uniform
Porosity	Non-porous	Non-porous	Porous	Highly porous
Shape	Spherical	Irregular	Irregular	Irregular
Packing orientation	Ordered	Random	Random	Random
Wettability	Moderate	Moderate	High	Low

The results of the 2D shape characterisation showed that though minor differences existed between the irregularly shaped materials (GS, GW and MO), it was not statistically significant. This led to the conclusion that shape could be effectively decoupled from porosity and wettability. The properties of the four selected materials allowed for the effect of particle shape (GB vs. GS), particle porosity (GS vs. GW vs. MO) and, to an extent, particle wettability (GW vs. GS vs. MO) to be studied. The limitation in the incomplete decoupling of particle porosity from wettability was noted.

Chapter 5

Effect of Material and Fluid Properties on Moisture Absorption and Retention

This chapter presents the methodology and results for moisture retention and capillary suction tests conducted on the four chosen materials.

5.1 Moisture Retention

In order to ascertain the effect of particle shape, porosity and wettability on the ability of the chosen materials to retain moisture after having been completely saturated, a testing procedure was devised and implemented.

5.1.1 Experimental Apparatus and Methodology

An illustration of the procedure used to conduct the moisture retention tests is found in Figure 5.1. A 1-L conical flask was cleaned, weighed and left to dry overnight (A). Approximately 50 g of solid material was then added to the flask (B). 500 mL of deionized water was also added and the flask was re-weighed. The flask was then sealed using aluminium foil and left for a period of time at room temperature (C). In the case of the non-porous beads, the minimum time was approximately 3 hours, while for the GS, GW and MO, the minimum time was 24 hours. Afterwards, the flasks were unsealed and re-weighed. A 100-mesh screen was attached to the top of the flask (D). The flasks were then inverted and the water was

allowed to drain out through the mesh. The contents were shaken with care to avoid the loss of solid particles but also allow for the drainage of excessive moisture (E). The flasks were placed upright, the mesh screen was removed and the flasks were weighed again (F). Tests were done in triplicate for the different materials and size fractions.

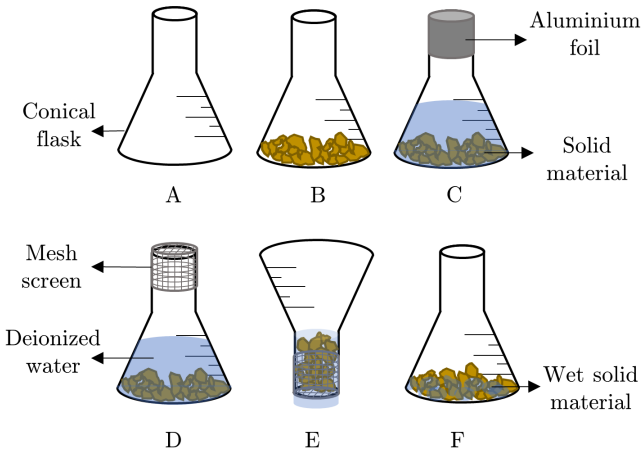

Figure 5.1: Illustration of methodology used for the moisture retention tests carried out on the four chosen materials. Alphabetical labels represent temporal sequence of events and are discussed in text.

With respect to the irregularly shaped materials, size fractions ranging from 1 to 8 mm were tested for all the materials, with an additional size fraction (13.2 - 16 mm), tested for the GW and MO particles. A bottom size limit of 1 mm was imposed as below this size, the loss of solid material during the drainage process was an issue, requiring the need of more sophisticated drainage equipment.

Prior to the tests, the average moisture retained in 12 empty flasks, after they were filled with water and drained, was measured. The value was subtracted from the mass of moisture retained by the different materials during the tests. This was done to account for the droplets of moisture left behind on the surface of the flasks not associated with its material content. The adjusted mass of water retained was then divided by the total mass of material placed in the flask to obtain the specific moisture retained (mass of liquid per mass of material). The specific moisture retained is therefore defined as the mass of water left after drainage per mass of material.

5.1.2 Results and Discussion

Figure 5.2 shows that the specific moisture retained by the GB was dependent on their size. The 2 mm beads retained approximately 4 and 8 times as much moisture per gram of packing as the 5 and 15 mm beads, respectively. As the beads are non-porous, this finding is attributed to the higher surface area available for moisture adsorption a the 2 mm size. The 2 mm beads were also observed to have small amounts of capillary held moisture between the particles, even after the agitation employed during the drainage process. This was not observed in the case of the 5 and 15 mm beads. A reduction in bead size increased the number of particle to particle contact points which resulted in a greater amount of capillary held liquid. Only in the case of the 2 mm beads, were the pore radii at the connection points small enough to generate capillary forces capable of withstanding the agitation of the beads during drainage.

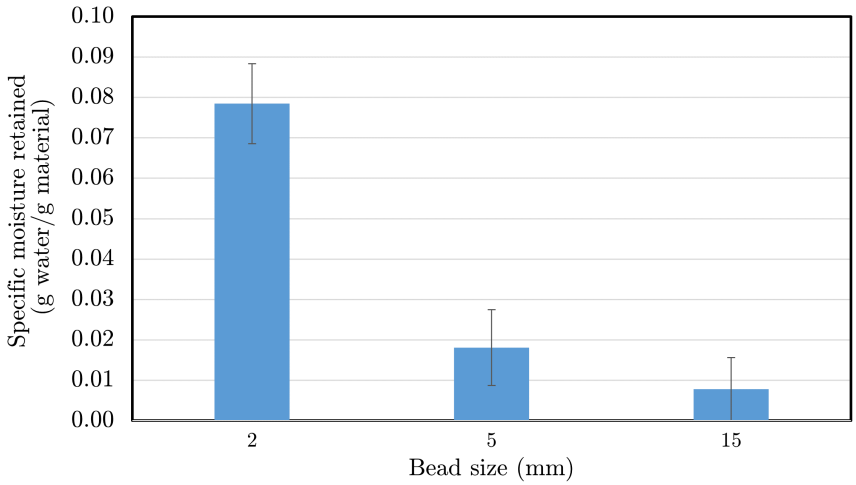

Figure 5.2: Specific moisture retained by glass beads of different sizes.

Like the beads, the specific moisture retained by the irregularly shaped materials is inversely related to the particle size (Figure 5.3). When comparing the 1 - 2 mm and 6.7 - 8 mm size fractions, the GS, GW and MO particles experienced a 86%, 88% and 74% reduction, respectively, in the specific moisture retained by the larger particles. This behaviour was explained by a reduction in surface area when size fraction was increased. However an increase in the GS size fraction from 4 to 8 mm did not have a substantial effect on the

specific moisture retained. This indicates three things. Firstly, the increase in specific moisture retention by materials with lower size fractions is likely due to an increase in capillary held liquid. Secondly, for non-porous materials, the liquid is held at particle-particle contact points as these points form voids with sufficiently small radii capable of generating strong capillary forces. Thirdly, above a certain size threshold (4 - 5 mm), liquid retained by capillary forces at particle-particle contact points are weakly held and can easily be drained when these contact points are broken by agitation, leaving behind surface adsorbed moisture.

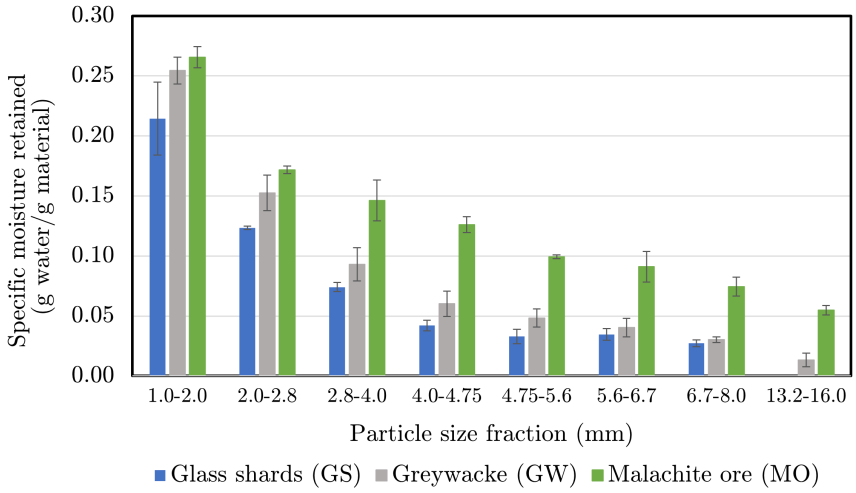

Figure 5.3: Results from moisture retention tests conducted on different size fractions of glass shards, greywacke and malachite ore particles using water.

For the GW and MO, more moisture was retained when compared with the GS particles due to particle porosity. For example, at the 1 - 2 mm size fraction, the GW and MO particles held on to 19% and 24% more moisture, respectively, than the GS. The MO particles, which possessed the highest levels of porosity (refer to Chapter 3, sub-section 4.2.2), retained the most moisture. In fact, as size fraction increased, the difference in proportion of specific moisture retained by the MO particles compared to the other materials increased indicating a stronger dependence on porosity for moisture retention by larger particles (> 4 mm).

The GS across the 1 to 2.8 mm size fractions were able to retain between 57 - 173% more moisture than the 2 mm GB. This trend was also observed when comparing the 4.75 - 5.6 mm GS particles to the 5 mm GB, as they were able to retain approximately 81% more moisture. Both of these materials are non-porous and similar in composition, therefore

the differences observed in their values for the specific moisture retained can be mainly attributed to the difference in their shapes and how this influenced the number of particle-particle contact points and surface area available for adsorption. Compared to the shards, the spherical 2 mm beads had a lower number of contact points and hence smaller amounts of moisture that could be held by capillary forces. At the 4.75 - 5.6 mm size fraction, surface area availability could be the main reason behind the differences observed between the two materials. The more compact spherical beads possessed a relatively smaller specific surface area available for liquid adsorption.

Capillary forces due to particle porosities resulted in higher moisture retentions, with particle wettability seemingly not having a substantial effect. This may have resulted from the fact that all of the particles were completely saturated prior to drainage, thereby masking or interfering with the influence of a particle's affinity for the wetting fluid. Therefore, though these results offer insights into the different factors affecting moisture retention, the information gained is limited as the initial wetting behaviour of the materials is overlooked. This initial behaviour is important in a heap leaching context as beds are typically dry prior to irrigation.

5.2 Moisture Absorption

A key aspects of this work, is the effect that the physical properties of different packing materials and solution viscosity have on capillary suction within a packed bed. It can be that capillary effects play a role in the establishment of fluid flow profiles in irrigated beds. In this section, the experimental apparatus, methodology and results from moisture absorption tests via capillary action is presented and discussed.

From the fundamental principles governing the strength of capillary forces (refer to section 2.4.1.1) and the findings from previous studies in this area, capillary strength is mainly influenced by the presence of micro-pores within a packed bed (Bartlett, 1992; Stevens et al., 2009; Wu et al., 2007; Yin et al., 2016). Excluding the contribution of particle porosity, a characteristic property present at all particle sizes, these micro-pores are more likely to form

in sections of the bed populated by the smaller sized particles. It is possible, therefore, to study factors influencing capillary strength using small scale bed systems composed of particles with relatively small size fractions. These systems will allow for replicate tests to be run without the excessive consumption of limited packing material, hence allowing for more statistically significant trends in the data to be captured and analysed.

5.2.1 Experimental Apparatus and Methodology

The experimental set-up used for the bed characterisation and capillary suction tests is shown in Figure 5.4. The characterisation involved the quantification of bulk densities and voidages to account for the effect of these variables on the different beds' capacity for moisture absorption. A summary of the size fractions, experimental tags, solutions used in the tests with their associated viscosity and density values can be found in Tables 5.1 and 5.2.

The column loading procedures were identical for both the characterisation and capillary suction tests, with the only difference being the material used to seal the column base. An AWS SR-1 digital hanging scale with a sensitivity of approximately 1 g was attached to an elevated clamp. Between 90 and 100 g of material was loaded into a 2.5 cm inner diameter glass column without compaction and attached to the load cell. For the test using the mixed size fraction (0.1 – 2.8 mm), 25 g from each of the four narrow size fractions were combined and shaken in a small plastic bag to ensure adequate mixing before being loaded. Segregation of particles sizes was minimized as best as possible.

For the bed characterisation tests, the bottom of the column was sealed with a waterproof cap. The packing height and bed diameter were used to calculate the bed volume. This, together with the mass of loaded material, was used to calculate the bulk density of the bed. To find the voidage, the beds were slowly saturated with water at room temperature through the incremental addition of 1 mL of liquid using a pipette. The addition stopped once the solution began to pool on the top surface of the packed bed. The voidage was calculated from the volume of solution fed into the column and the total measured volume of the packed bed. Tests were conducted in triplicate. The degree of bed saturation (β_T) during subsequent tests could then be calculated using Equation (2.7) as the ratio of liquid

volume to void volume.

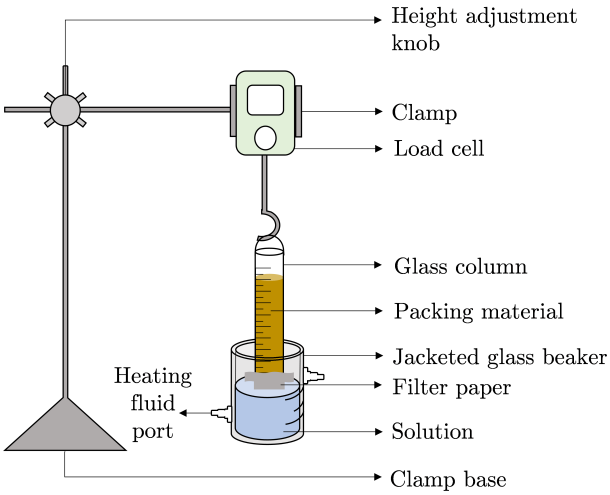

Figure 5.4: Illustration of the experimental set-up used to conduct capillary suction tests on the chosen packing materials.

Table 5.1: Experimental tags for the particle size fractions used in the capillary suction tests.

Size fraction (mm)	Experimental tag Materials			
	GB	**GS**	**GW**	**MO**
2	GB-1	(-)	(-)	(-)
0.1-0.5	(-)	GS-1	GW-1	MO-1
0.5-1.0	(-)	GS-4	GW-4	MO-4
1.0-2.0	(-)	GS-6	GW-6	MO-6
2.0-2.8	(-)	GS-8	GW-8	MO-8
0.1-2.8	(-)	GS-Mix	GW-Mix	MO-Mix

Table 5.2: The characteristics of the five test solutions used in capillary suction tests measured at 30°C.

Test solutions		
Glycerol (wt%)	**μ (cP)**	**ρ (g/mL)**
0	0.8	1.00
15	1.2	1.03
25	1.6	1.05
30	1.9	1.07
35	2.2	1.08

For the capillary suction tests, genuine Whatman Filter Paper No. 54 with a pore size of 22 μm was weighed and secured to the bottom of the glass column. 100 mL of testing fluid was poured into a jacketed glass beaker located below the packed column and maintained at 30°C. The packed column was gently lowered until the bottom of the column (covered with filter paper) contacted the fluid in the beaker, as shown in Figure 5.4. This allowed the fluid to suction upwards into the packed bed. The mass of the column was recorded over time. The height of fluid in the beaker was maintained through the addition of small volumes of testing fluid using a 1 mL pipette when required. The fluid additions were done slowly and spaced out to ensure that they did not cause any surface disturbances and had no substantial impact on the temperature of the bulk fluid, which was also monitored. Testing was concluded when no significant change in the column's mass was measured over an extended time period. Tests were performed in triplicate for all of the five formulated test solutions (refer to Table 5.2)

5.2.2 Empirical Modelling of Liquid Absorption Data

Yin et al. (2016) recognized that liquid absorption data derived from upward infiltration capillary suction tests on packed beds could be described, to a reasonable extent, by the empirical relationship shown in Equation 5.1.

$$M = at^b \tag{5.1}$$

In this case, M is the total mass of fluid absorbed at time t. Empirical constants a and b are fitting constants, exerting different effects on the absorption curves produced as shown in Figure 5.5. Parameter a is mostly responsible for the initial rate of absorption in the early portions of the graph, governing the height of the absorption curve. An increase in parameter a increases the initial absorption rate and amount. Parameter b is mostly responsible for the latter section, governing the 'tail' end of the curve. Increasing the magnitude of b leads to an increase in the latter rate and amount of absorption, thereby increasing the time required for equilibrium to be achieved.

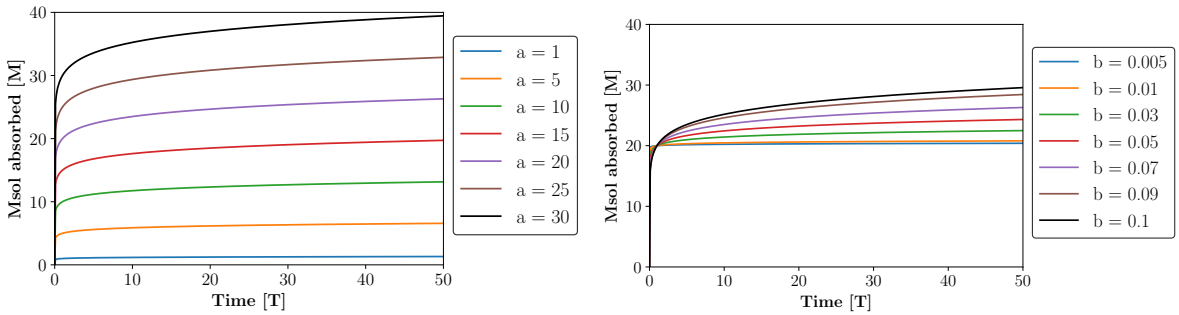

(a) **(b)**

Figure 5.5: (a) Effect of parameter 'a' on the output of the empirical absorption model while 'b' is held at 0.07; (b) Effect of parameter 'b' on the output of the empirical absorption model while 'a' is held at 20.

The base-line values of parameters a and b kept constant during the response analysis were 20 and 0.07, respectively. As this is a purely empirical model, both parameters are not directly related to any physical property of the systems but are implicitly affected by them.

The empirical model was coded using the Python programming language and the Scientific Python Development Environment (*Spyder*) version 4.1.5. The model was optimized using the differential evolution algorithm (*diffev2*) from the *mystic* package. The error function shown in Equation (5.2) was minimised by the solver. The regression correlation coefficient (R^2) was used during data analysis.

$$F = \sqrt{\sum_{n=1}^{N} \left(C_{Model} - C_{Experiment}\right)^2} \tag{5.2}$$

5.2.3 Results and Discussion

Of the different materials tested (refer to Table 5.1), the 2 mm beads did not exhibit any capillary suction effects and therefore only data for the remaining three materials are presented and discussed.

5.2.3.1 Bulk Density and Bed Voidage

The results of the bulk density and bed voidage tests are presented in Figures 5.6a and 5.6b, respectively. The beds composed of MO particles consistently had average bulk densities between 6 – 16% lower and bed voidages around 6 – 28% greater than the GS and GW systems. This can be attributed to the larger particle porosities of the MO particles which correlates to the higher specific surface area within the same size fraction reported in Table 4.1. Differences in bulk density and voidage between the GS and GW beds were minor. The higher bulk densities (evident for GS and MO) and low bed voidages (evident across GS, GW and MO) of the mixed particle size fraction (0.1 – 2.8 mm) beds can be attributed to the smaller particles residing in the voids created by the larger particles, resulting in a more compact arrangement. This is consistent with theoretical analysis of bed packings and results by previous researchers (Yin et al., 2016).

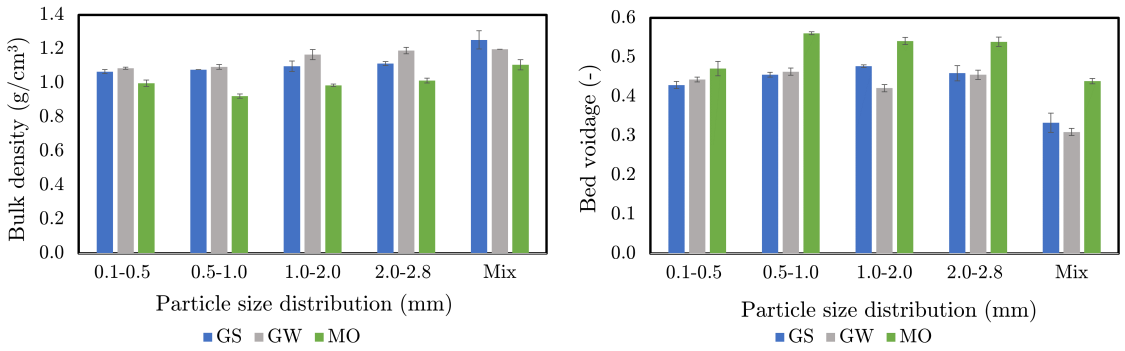

(a) **(b)**

Figure 5.6: Bulk density (a) and porosity (b) results from packed beds composed of different size fractions of GS, GW and MO particles.

The beds experienced a decrease in bed voidage with an increase in bulk density. There are some deviations from this which could be attributed to particle heterogeneities present within each material that led to fluctuations in their intrinsic density values. Minor experimental error due to the subjectivity in the qualitative determination of when a bed is completely saturated could also have played a part. However, the data was reasonably precise as the highest standard deviation in the calculated bed voidage values across all the tests was 0.025 for the GS-Mix (0.1 -2.8 mm) system, which was only 7% of the average voidage.

5.2.3.2 Effect of Particle Size Fraction on Capillary Suction

The experimental and modelling results from the water capillary suction tests on the beds composed of narrow and mixed size fractions of the selected materials can be found in Figure 5.7. The optimized values for model parameters a and b can be found in Figure 5.8 with a summary of the goodness of fit and total saturation data found in Table 5.3.

All three materials experienced a reduction in the total mass of solution absorbed and maximum level of saturation reached as the size fraction increased from 0.1 – 0.5 mm (size class 1) to 2.0 – 2.8 mm (size class 8). This was more pronounced for the GS system which experienced a 99% reduction, while the GW and MO particle beds showed an 85% and 84% reduction, respectively. The same trend is evident for model parameter a. Across the three materials, there was a 75% to 99% reduction in the value of this parameter indicating a substantial decrease in both the initial solution absorption rate and the extent of absorption as the size fraction was raised. This significant decrease in capillary action indicates its crucial dependence on particle size and hence the size of the pores within a packed bed. This is based on the understanding that beds composed of finer particles form pore networks consisting of pores with relatively smaller diameters due to increased contact surface areas. The results agree with those by Yin et al. (2016), who also observed a reduction in the capillary rise height with an increase in particle size fraction.

The results from the mixed size fraction (0.1 – 2.8 mm) present an interesting case. Comparing these results (Figure 5.7e) to size class 4 (Figure 5.7b), it is observed that even though the mixed particle beds were able to absorb 18 – 25% more solution than the beds composed of 0.5 – 1.0 mm particles, the optimized values for parameter a showed a 4 – 9% reduction in magnitude when comparing the two size systems (refer to Figure 5.8a). This illustrates that the initial rate of solution absorption, proportional to the magnitude of parameter a, was negatively impacted by the increase in particle top size from 1.0 mm to 2.8 mm.

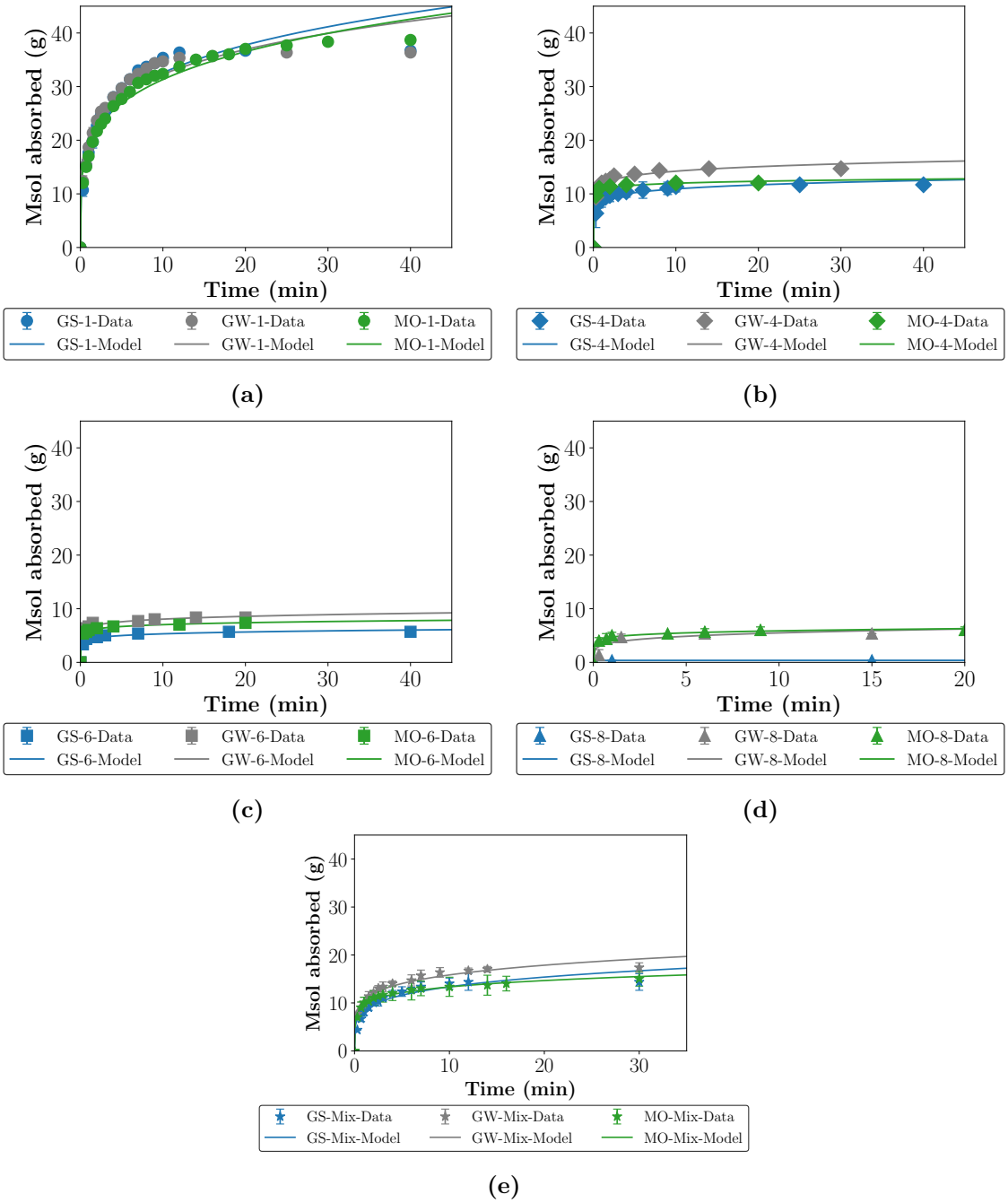

Figure 5.7: Experimental and model predicted values for the mass of solution (M_{SOL}) absorbed during water capillary suction tests by packed beds composed of different materials and size fractions.

However, the mixed size beds had a parameter b value approximately 2 – 3 times larger than those of the size class 4 systems. This illustrates that on average, the mixed sized beds took

longer to achieve steady state and were able to keep absorbing solution, albeit at a relatively slow rate, for a longer duration of time. It could be that it was the presence of the finer material (< 0.5 mm) increasing the proportion of small to larger diameter pores and hence capillary pressure, that allowed for this continuous absorption ultimately leading to greater masses of solution absorbed. It is worthwhile noting that the amount absorbed by the mixed size bed (top size: 2.8 mm) was 52 – 61% less than that of size class 1 (top size: 0.5 mm) for the three materials, with an initial rate of absorption that was 48 – 58% less. Therefore the increase in particle top size also had a negative impact on strength of capillary suction forces within packed beds.

Table 5.3: Optimized model parameter values, goodness of fit data and maximum saturation levels reached for various bed systems.

Packing material	**E-tag**	**Model Parameter and goodness of fit data**				**Max. Sat.**
		a	b	R^2	**Error**	$[\beta_T]$
Glass shards	GS-1	19.943	0.213	0.924	11.702	0.92
	GS-4	8.748	0.097	0.970	1.882	0.28
	GS-6	4.325	0.090	0.979	0.731	0.01
	GS-8	0.364	0.001	1.000	0.001	0.01
	GS-Mix	8.387	0.203	0.933	3.946	0.48
Greywacke	GW-1	20.698	0.193	0.935	10.577	0.90
	GW-4	11.749	0.083	0.981	1.813	0.35
	GW-6	6.554	0.090	0.988	0.821	0.23
	GW-8	3.656	0.178	0.830	2.097	0.14
	GW-Mix	10.621	0.174	0.974	2.785	0.68
Malachite ore	MO-1	18.814	0.221	0.977	6.954	0.82
	MO-4	10.811	0.044	0.994	0.804	0.20
	MO-6	5.949	0.073	0.998	0.244	0.14
	MO-8	4.716	0.096	0.990	0.533	0.11
	MO-Mix	9.730	0.137	0.986	1.610	0.38

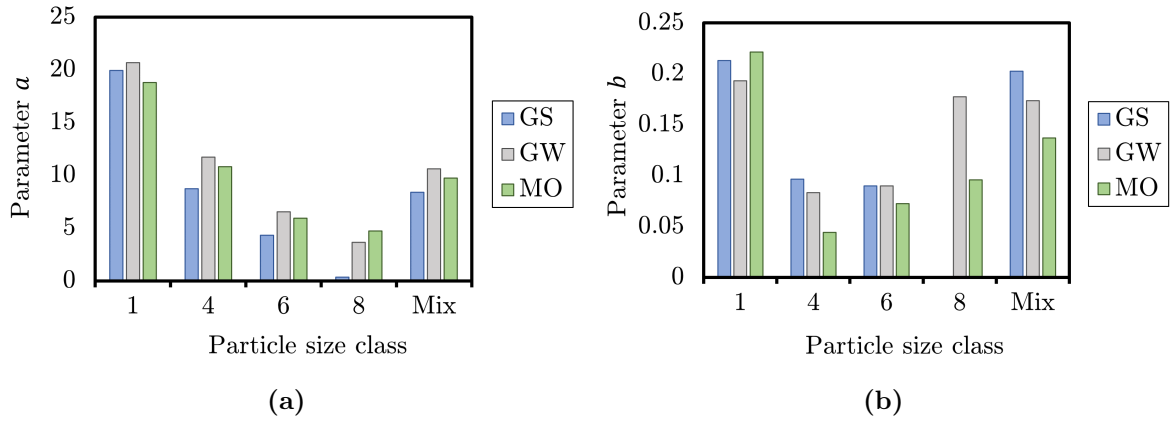

Figure 5.8: Optimized model parameter values for (a) parameter 'a' and (b) parameter 'b' based on the fitting of experimental data from capillary suction tests on the different material beds using water as the test fluid.

5.2.3.3 Effect of Particle Porosity and Wettability on Capillary Suction

From Figure 5.7a, it is evident that the absorption curves for the GS-1, GW-1 and MO-1 systems are all nearly identical although these materials had varying levels of particle porosities, bed voidages and water affinities. This indicates the primacy of the effect that particle size fraction has on capillary forces within a packed bed. The impacts of the other material properties are only noticeable at larger size fractions. This suggests that a sufficient capillary force in beds composed of the smaller particle sizes does not benefit from interaction with other contributors to capillary force; however, at larger particle sizes the interaction is seen.

The absorption curves in Figure 5.7b show that the GW-4 system was able to absorb between 22% to 26% more solution than the GS-4 and MO-4 beds. The fact that the GW particles were the most hydrophilic suggests that particle wettability, alongside particle size, were the leading factors influencing the strength of capillary forces at the 0.5 – 1.0 mm size range. Similar trends were also observed for size class 6 (1.0 – 2.0 mm) beds. The effects of particle size were still apparent as both the non-porous GS-4 and highly porous MO-4 systems behaved similarly with respect to the total amount of solution absorbed. However, the fact that the MO systems had a 20 – 27% higher value for parameter a compared to

the GS beds, suggests that the presence of particle porosities allowed for greater initial fluid absorption rates.

In Figure 5.7d, the highly porous MO-8 (2.0 - 2.8 mm) bed was able to absorb the most solution, though the amount absorbed was not vastly different than that for the GW-8 system. This is not the case when comparing both systems to the non-porous GS-8 bed, which showed negligible capillary suction capabilities. The beds of non-porous shards were only able to absorb approximately 0.4 g of solution, which was 13 – 15 times less than the porous systems. It can therefore be argued that particle porosity played an increasingly important role in the strength of capillary forces as particle size was increased.

Previous studies have already established the importance of capillary suction in the lateral spread of drip irrigated solution in particle beds (refer to section 2.6.2). The pertinent implications of the results from this study on heap leaching systems, is the necessity of the inclusion of fine materials, <1 mm, for the generation of capillary forces. The data from section 5.2.3.2 suggests that the higher the top particle size, the lower the combined strength of capillary forces within the bed which may ultimately lead to increased chances of preferential wetting. However, the presence of particle porosities in a heap would allow for capillary action even in cases where the top particle size is relatively large, evidenced by comparisons between the porous and non-porous mixed beds (Figure 5.7e). This is because in beds composed of larger particles, intra-particle pores are more likely to be smaller in size than inter-particle voids, leading to greater capillary strength. The data also suggests that higher degrees of particle wettability aids in the initial spreading of irrigated solution by capillary action within a bed. This is based on the relatively faster initial absorption rates of the highly wettable GW system, reflected in the higher parameter a values (Figure 5.8a). This is proposed to reduce the formation of bed scale preferential flow channels.

5.2.3.4 Effect of Solution Viscosity on Capillary Suction

The capillary moisture absorption curves obtained with solutions of different viscosity are shown in Figure 5.9. The optimized model parameter values can be found in Figure 5.10, while the model fit parameters and maximum total saturation values can be found in Table

5.4.

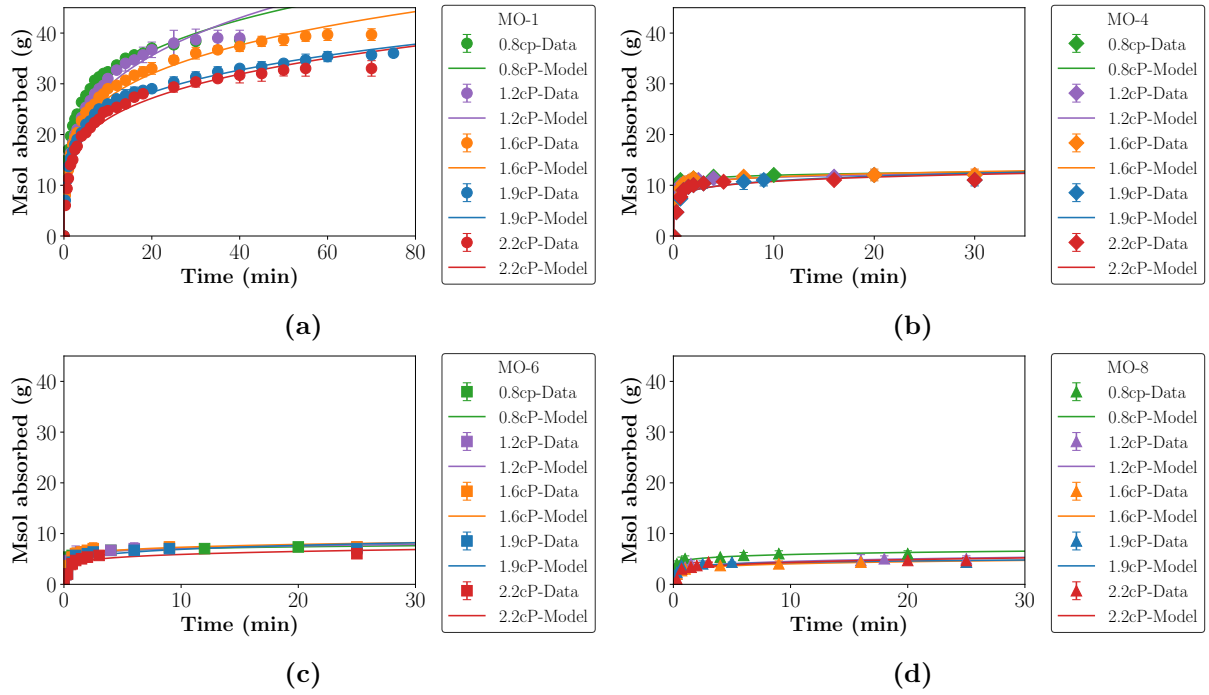

Figure 5.9: The effect of fluid viscosity on the experimental and model predicted values for the mass of solution (M_{SOL}) absorbed during capillary suction tests on MO beds with different particle sizes of (a) 0.1 - 0.5 mm, (b) 0.5 - 1.0 mm, (c) 1.0 - 2.0 mm and (d) 2.0 - 2.8 mm.

The effect of solution viscosity is most clearly apparent in the results for the lowest particle size tested, 0.1 – 0.5 mm (Figure 5.9a). In this case, though the final amount of solution absorbed was relatively unaffected by the increase in viscosity from 0.8 to 1.6 cP, which is equivalent to comparing a 0 g/L SO_4^{2-} solution to >100 g/L SO_4^{2-} solution in terms of viscosity, there is a 16% reduction in the initial rate of absorption, which is reflected in the optimized a values. Further increases in viscosity led to further reductions, not just in the rate but also in the final amount of solution absorbed and maximum levels of saturation reached. These findings can be explained by the increased resistance to flow for higher viscosity solutions when shear rate is kept constant. Therefore, even under similar capillary pressures, higher viscosity fluids took longer to meander their way through the pore networks present within the bed by capillary action. The increase in density also meant that similar masses of fluids occupied smaller volumes, hence the reduction in saturation levels.

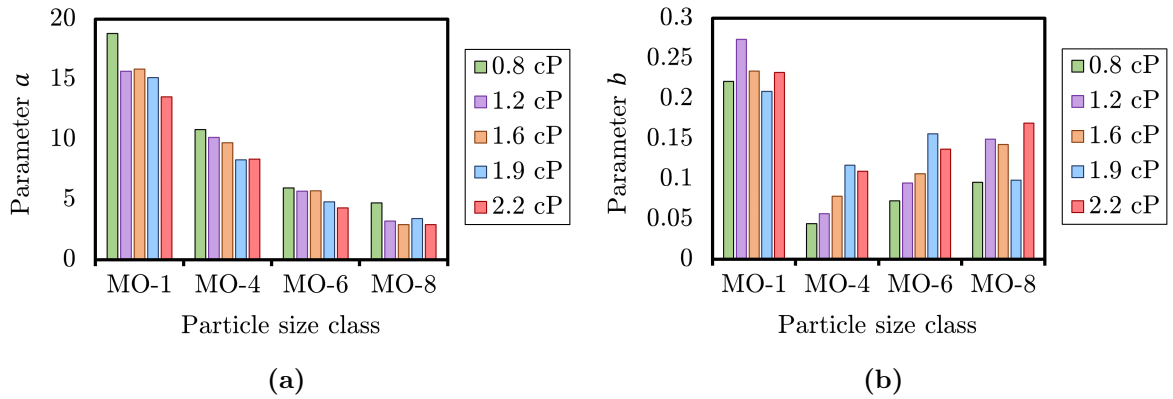

Figure 5.10: Optimized model parameter values for (a) parameter 'a' and (b) parameter 'b' based on the fitting of experimental data from capillary suction tests on MO beds using different viscosity fluids.

The reduction in the initial rate of absorption with an increase in solution viscosity, reflected by the values of parameter a, is a trend that occurs across all the 4 size classes (refer to Figure 5.10a). In the case of parameter b, the overall trend is reversed. For example, for the MO-4 system, there was a more than 70% increase in the value of parameter b as viscosity was raised from 0.8 cP to 2.2 cP (refer to Figure 5.10b). This suggests that the beds exposed to higher viscosity solutions took longer to reach steady state and carried on absorbing solution at relatively slow rates.

The implication of this for heap leaching operations is that leaching reactions which lead to the increased concentration of dissolved ions can impact the propensity for lateral movement and spread by capillary action as well as solution flow rates. Therefore, heaps with high concentrations of ions such as SO_4^{2-} within their leach solutions, are potentially at a higher risk of the formation of preferential flow channels. This is because such fluids may be more susceptible to channelling by gravitational forces due to increased resistance to lateral movement. This channelling effect is likely to be more apparent within macro-pores as these will have the weakest capillary forces. The micro-pores are expected to not only experience increased resistance to lateral movement but to flow in general. However, the results here will need to be corroborated with fluid flow profile data from beds irrigated with varying viscosity solutions before any major conclusions can be drawn. This is done in Chapter 8.

Table 5.4: Optimized model parameter values, goodness of fit data and maximum saturation (β_T) levels reached for MO bed systems subjected to capillary suction tests with different viscosity fluids (Liq. visc.)

Packing material	**E-tag**	**Liq. visc. (cP)**	**Model Parameter and goodness of fit data**				**Max. Sat.**
			a	b	R^2	Error	$[\beta_T]$
Malachite ore	MO-1	0.8	18.8	0.22	0.977	6.954	0.82
		1.2	15.7	0.27	0.975	8.161	0.81
		1.6	15.9	0.23	0.976	8.594	0.80
		1.9	15.1	0.21	0.973	8.217	0.76
		2.2	13.5	0.23	0.967	8.143	0.67
	MO-4	0.8	10.8	0.04	0.994	0.804	0.20
		1.2	10.2	0.06	0.990	1.065	0.21
		1.6	9.7	0.08	0.950	2.452	0.21
		1.9	8.3	0.12	0.894	3.468	0.19
		2.2	8.4	0.11	0.892	3.482	0.19
	MO-6	0.8	5.9	0.07	0.998	0.244	0.14
		1.2	5.7	0.09	0.976	0.967	0.14
		1.6	5.7	0.11	0.926	1.835	0.13
		1.9	4.8	0.16	0.861	2.604	0.12
		2.2	4.3	0.14	0.857	2.080	0.11
	MO-8	0.8	4.7	0.10	0.990	0.533	0.11
		1.2	3.2	0.15	0.958	0.944	0.10
		1.6	2.9	0.14	0.977	0.600	0.08
		1.9	3.4	0.10	0.936	0.964	0.08
		2.2	2.9	0.17	0.858	1.728	0.08

5.3 Chapter Summary

The first aim of the work presented in this chapter was to ascertain the effect of particle shape, size, particle porosity and wettability on the ability of the chosen materials to retain moisture. Similar amounts of GB, GS, GW and MO particles belonging to different size fractions were tested. The results showed that the specific mass of moisture retained was inversely related to particle size. Though surface adsorption played an important role, it was proposed that the leading mechanism behind moisture retention, especially for the lower size fractions, was capillary suction. This was based on the observation of capillary held liquid

at particle-particle contact points. Above a size fraction of approximately 5 mm, the contact points were easily broken and the liquid was easily drained. In the case of the non-porous particles, this left behind only the surface adsorbed moisture. For the porous materials, it was possible for liquid to be held by capillary forces within particle pores. It was argued that this additional holding site was the reason the highly porous MO particles were able to retain significantly more moisture than both the GW and GS particles across all the size fractions.

Particle shape was found to play two main roles during the moisture retention tests. Firstly, it influenced the number of particle-particle contact points and secondly, it influenced the specific surface area available for moisture adsorption. Hence, the GB, which were the most compact due to their high degree of sphericity held on to the least amount of moisture after drainage when compared to the other materials of similar sizes.

The second section of this chapter aimed to quantify the effect that particle size and particle size distribution, associated bed voidage, particle porosity and wettability, as well as solution viscosity, have on capillary forces within a packed bed. This was done through the empirical modelling of moisture absorption data from upward infiltration capillary tests on different packed bed systems, with material properties representative of those encountered in heap leaching studies.

Reduction in particle size was shown to be the main factor influencing the strength of capillary forces, though higher levels of particle wettability and particle porosities also led to increased capillary action. Smaller pore size diameters which exist for lower size fractions and at high particle porosities were deemed responsible for the dominant effects observed. Higher water affinities leading to the preferential wetting of the hydrophilic material was proposed to be responsible for the wettability effects observed. Where inter-particle pores were larger, limiting capillary forces, interaction was observed between particle size effects, wettability and particle porosity. Increases in fluid viscosity, which correlate with increasing concentrations of dissolved ions typical in heap leaching processes, were found to result in slower moisture absorption rates and longer absorption times due to the increased resistance to fluid flow.

Chapter 6

Models Development and Response Analysis

The solute transport modelling of tracer generated RTD curves from drip irrigated packed beds under steady state fluid flux allows for the quantification of solution scale preferential flow characteristics. Two main modelling approaches were employed in this study: empirical and semi-empirical/phenomenological (refer to section 2.4.3).

The fully empirical models comprised of three compartmental model configurations (CM-1, CM-2 and CM-3) and the tanks-in-series (TIS) model. The selected semi-phenomenological models were: the advection dispersion (AD) model, the piston exchange (PE) model, the piston exchange diffusion variant (PE-D) model, the piston dispersion and exchange (PDE) model and the piston dispersion and exchange - diffusion variant (PDE-D) model. Eight of the nine models were chosen due to their use in prior studies, whilst the PDE-D model was developed through the combination of some of the other model's characteristics. Each of the models have unique elements which affect their individual abilities to fit experimentally generated RTD profiles. By comparing the quality of their fit and the quantified values of their parameters, solution scale preferential flow behaviour can be diagnosed.

The content of this chapter is as follows: model conceptualization, assumptions, limitations, equations, parameter descriptions and response analysis is presented and discussed. The discretization of the model equations, stability analysis and simplified model fitting algorithms can be found in Appendices C, D and E, respectively.

6.1 Compartmental Models

The main idea behind compartmental models (CM) is to simulate solute transport in a packed bed using different flow volumes. The three main volumes are the CSTR (V_C), PFR (V_P) and dead (V_D) volumes.

Figures 6.1, 6.2 and 6.3 illustrate the transport of tracer/solute molecules at different time points, injected into an ideal PFR, CSTR, as well as a flow volume with dead spaces, respectively. In an ideal PFR, these molecules will move with an average uniform velocity through the volume simulating sections with no axial mixing.

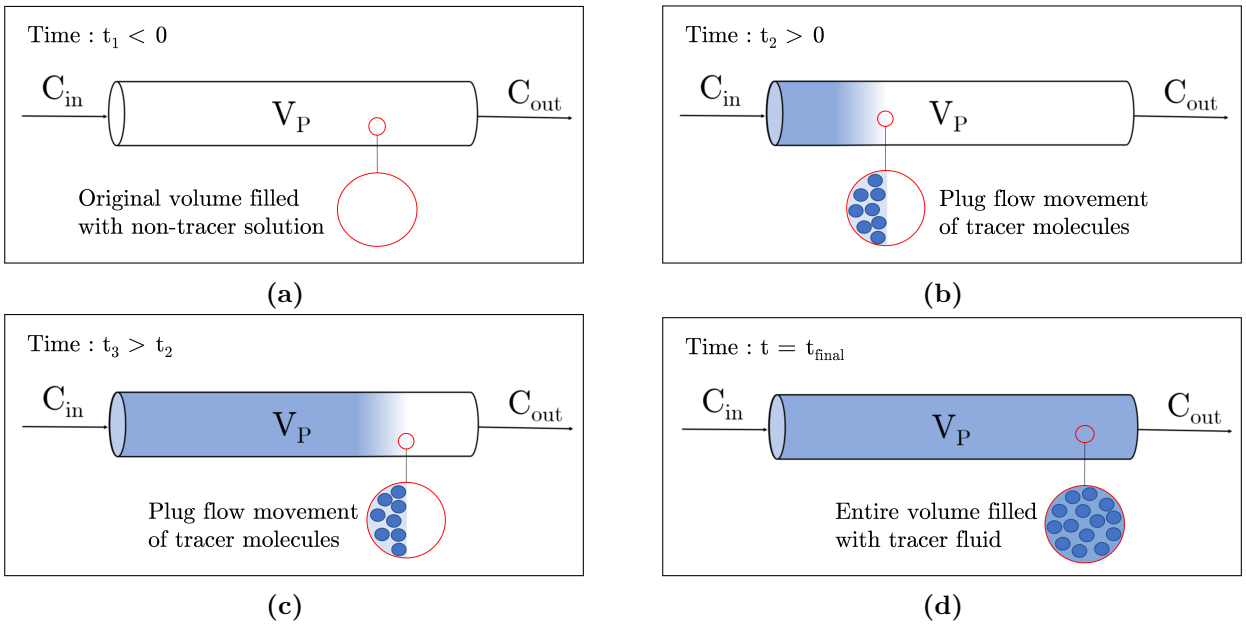

Figure 6.1: Solute transport of tracer molecules continuously injected, at t = 0, into a PFR under steady state flow. Tracer concentration represented by C.

In an ideal CSTR, the tracer concentration of the stream exiting the volume is equal to its concentration within the volume due to the assumption of perfect mixing. Hence, the CSTR volume is used to simulate the mixing effect caused by the mechanical dispersion of solute molecules within a packed bed.

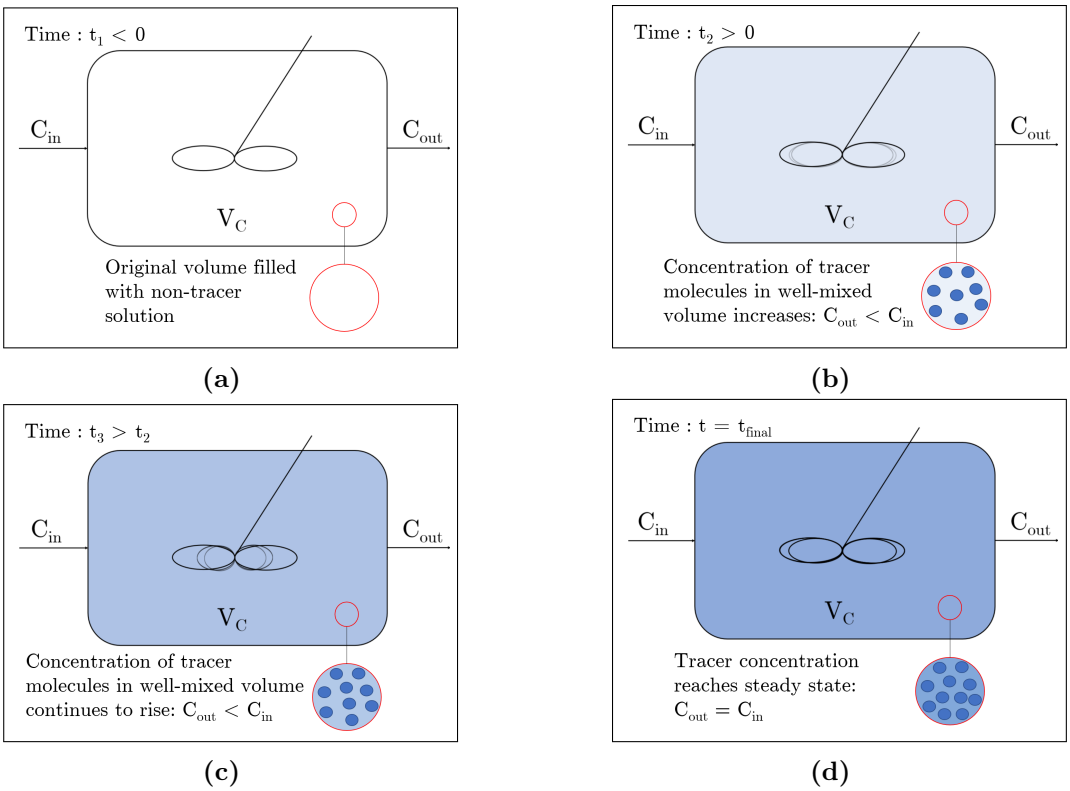

Figure 6.2: Solute transport of tracer molecules continuously injected, at t = 0, into a CSTR under steady state flow. Tracer concentration represented by C.

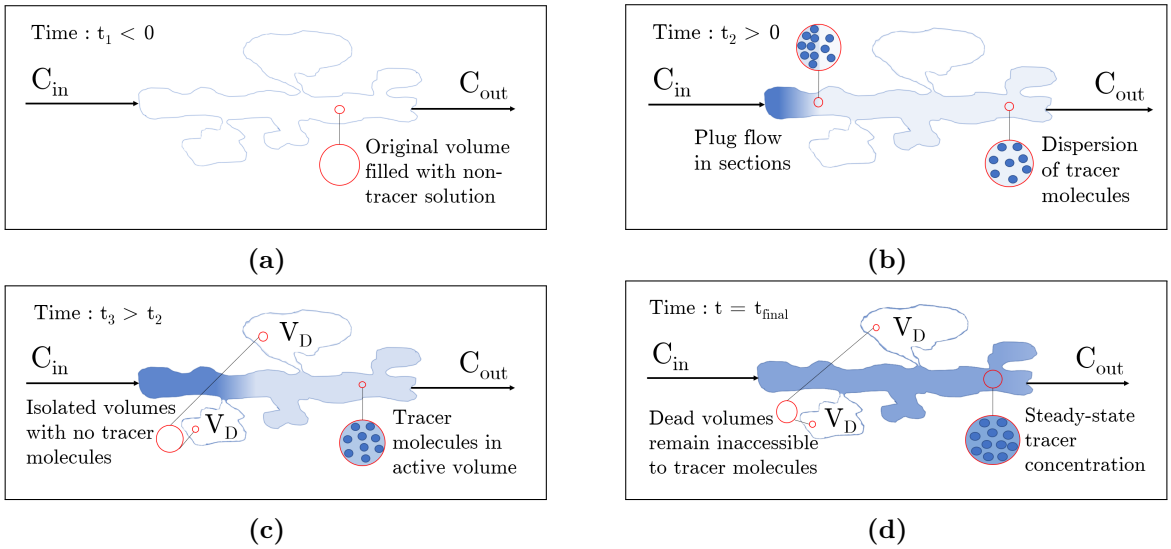

Figure 6.3: Solute transport of tracer molecules continuously injected, at t = 0, into a flow volume with associated dead regions. Tracer concentration represented by C.

Dead volumes form during the wetting phase of a bed but become isolated from the bulk fluid volume during steady state. They refer to immobile volumes of solution that are inaccessible to solutes, not even by diffusion.

6.1.1 Model Characteristics, Assumptions and Limitations

The main characteristics, assumptions and limitations of the CM models are as follows:

- They are highly empirical (non-physically representative fitting parameters) and therefore lack predictive capabilities
- Used in the modelling of non-ideal RTD profiles.
- Utilized as an analytical tool for diagnosing and comparing different bed systems under similar conditions.
- The unlimited number and variety of configurations possible can make the selection of a particular configuration arbitrary (multiple configurations can have similar fits).
- Does not account directly for unsaturated flow parameters in packed beds such as porosity and saturation.
- Lacks dimensionality but is able to simulate different flow paths (e.g parallel CSTRs) that do not have any particular physical orientation to the main advective flow path.

6.1.2 Model Configurations

The three compartmental configurations chosen for this study are shown in Figure 6.4. The first configuration (CM-1) consists of a PFR and CSTR in series with a dead volume. This is the simplest of the three configurations. The second arrangement (CM-2), has a PFR in series with two parallel CSTRs with equal volumetric flow rates but different residence times. In this case, rather than a dead volume, the parallel CSTRs simulate dual permeable flow (fast and slow flowing regions) within a packed bed. The third configuration (CM-3) incorporates both a dead volume and parallel CSTRs, making it the most complex. The presence of dual permeable flow, mixing and dead volumes are all symptoms of solution scale preferential flow.

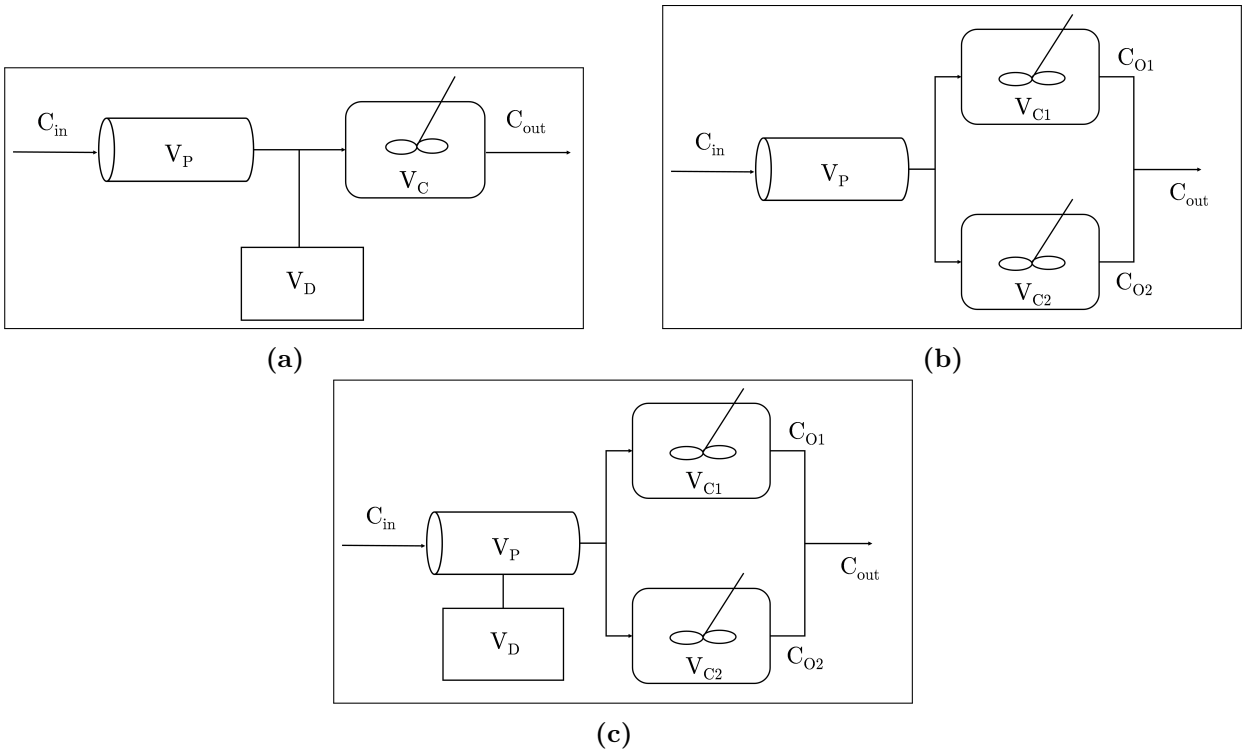

Figure 6.4: Different compartmental configurations used in this study, (a) CM-1 , (b) CM-2 and (c) CM-3.

6.1.3 Model Equations

The modelling equations for the three compartmental models, CM-1, CM-2 and CM-3 are discussed below. These equations are used to simulate RTD curves from flow through systems.

6.1.3.1 PFR Compartment

The residence time of a PFR volume (τ_P), described by Equation (6.1), represents the tracer breakthrough time. It is calculated by the taken the quotient of the PFR volume (V_P) and total volumetric flow rate (Q_T). The output response of a PFR is identical to its input with the a lag time represented by the residence time (refer to Equation (2.27) and Figure 2.4b in Chapter 2).

$$\tau_P = \frac{V_P}{Q_T} \tag{6.1}$$

6.1.3.2 CSTR Compartment

A mass balance on the tracer molecules entering into a CSTR volume is shown in Equation (6.2). At steady state, accumulation is equal to zero and Equation (6.3), showing the temporal rate of change of tracer concentration (dC/dt), is derived.

$$\text{Accumulation} = \text{In - Out} \tag{6.2}$$

$$V_C \frac{dC}{dt} = Q_{in} C_{in} - Q_{Out} C \tag{6.3}$$

With the assumption of a constant volumetric flow rate (Q) and separation of variables:

$$\int_{C_{in}}^{C_{out}} \frac{1}{(C_{in} - C)} dC = \int_0^t \frac{Q}{V_C} dt \tag{6.4}$$

Integrating leads to:

$$ln\left(\frac{(C_{in} - C_{out})}{C_{in}}\right) = -\frac{Q}{V_C} t \tag{6.5}$$

Rearranging to find C_{out}

$$C_{out} = C_{in}\left(1 - e^{-\frac{t}{\tau_C}}\right) \text{ where } \tau_C = \frac{V_C}{Q} \tag{6.6}$$

Equation (6.6) is the equation used to calculate the outlet tracer concentration at time t for CM-1. In the case of CM-2 and CM-3, where there are two CSTRs in parallel and C_{in} is equal to 1, Equation 6.7 is derived.

$$C_{out} = \frac{Q_1}{Q_T}\left(1 - e^{-\frac{t}{\tau_1}}\right) + \frac{Q_2}{Q_T}\left(1 - e^{-\frac{t}{\tau_2}}\right) \tag{6.7}$$

A summary of the model symbols, the parameters they represent and how they were obtained can be found in Table 6.1.

Table 6.1: Summary of model parameters used in the compartmental models and how they were obtained.

Symbol	Model parameter	How it is obtained
Controlled parameters		
C_{in}	Normalised inlet solute concentration (-)	Controlled variable
Q_T	Total volumetric flow rate (mL/min)	Controlled variable
t	Time (min)	Controlled variable
Experimentally obtained or calculated parameters		
$Q_{1,2}$	Compartmental volumetric flow rate (mL/min)	Calculated
V_T	Total flow volume (mL)	Measured
V_P	Plug flow volume (mL)	Calculated (experimental data)
τ_P	PFR residence time (min)	Calculated (experimental data)
τ_C	CSTR residence time (min)	Calculated (model results)
Fitted and output parameters		
C_{out}	Normalised outlet solute concentration (-)	Main model output
V_C	Continuous stirred tank volumes (mL)	Fitted variable
V_D	Dead volume (mL)	Fitted variable

6.1.4 Model Coding and Fitting

The models were fitted using the *Solver* function in Microsoft® Excel® software from Microsoft 365 MSO. The solving method chosen was the Generalized Reduced Gradient (GRG) Non-linear algorithm. This is a local solver that requires an initial guess in the vicinity of the solution in order to converge. The *MultiStart* option, which causes the GRG Non-linear method to run repeatedly using various starting points, was used in the fitting of the selected parameters for the three configurations. This option simulates a global solver algorithm. The error function shown in Equation (5.2) was the objective function chosen to be minimized in the solving process. Equations (6.8), (6.9) and (6.10) represent the various constraints used.

$$V_C \geq 0 \tag{6.8}$$

$$V_D \geq 0 \tag{6.9}$$

$$V_P + V_C + V_D == V_T \tag{6.10}$$

6.2 Tanks-In-Series Model

The tanks-in-series (TIS) model is very similar in concept to the compartmental models. It consists of consecutive CSTR tanks in series. The tanks all have identical volumes, possess one inlet and outlet stream and are arranged in series (refer to Figure 6.5). The number of tanks determines the type of flow profile simulated. A lower number is used to simulate RTD curves with a relatively high degree of dispersion (preferential flow). A higher number is used to simulate curves that possess plug (ideal) flow profile features.

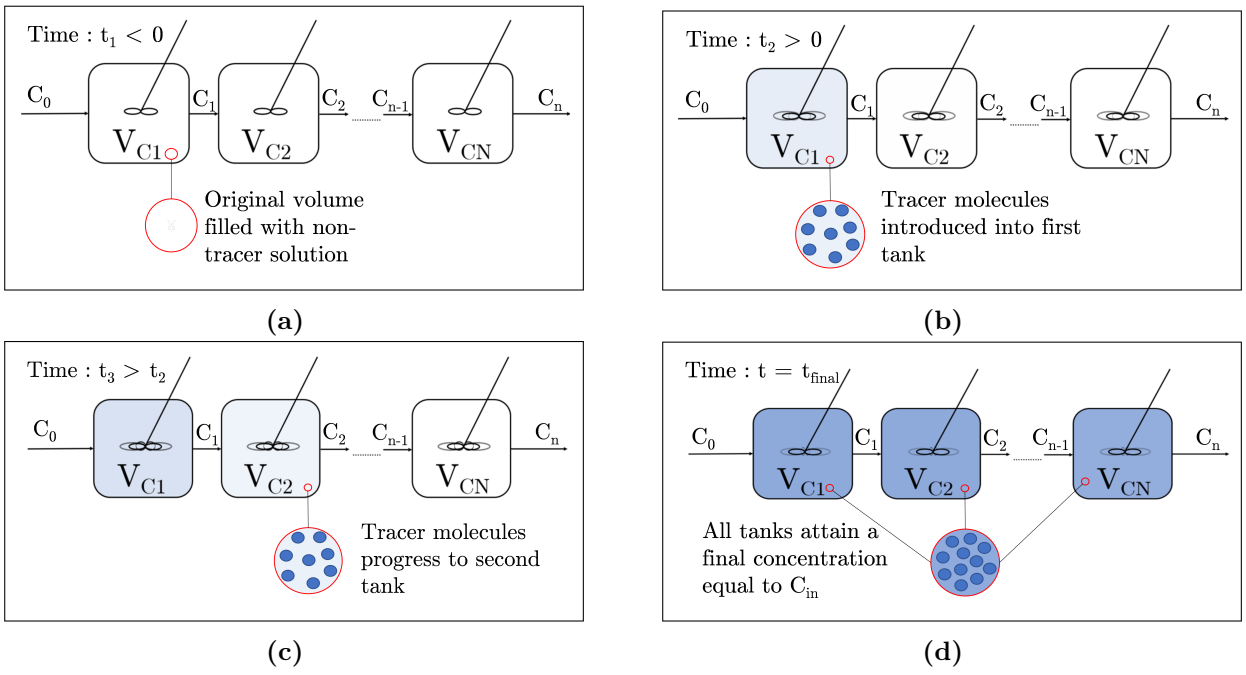

Figure 6.5: Solute transport of tracer molecules continuously injected, at t = 0, into multiple CSTRs in series, continuously injected into V_{C1} at t = 0, with concentration represented by C.

6.2.1 Model Assumptions and Limitations

The main assumptions and limitations of the TIS model are as follows:

- Utilized as an analytical tool for diagnosing and comparing different RTD profiles under similar conditions

- Relatively inflexible as it has only one adjustable parameter
- Highly empirical and therefore lacks predictive capabilities
- Does not account for unsaturated flow parameters
- A mono porosity model without physical dimensionality

6.2.2 Model Equations

The derivation of the descriptive equation for the TIS model is discussed below. Equations (6.3) through to (6.6) are applicable in the description of the concentration profile for a single CSTR tank. When adding a second tank-in-series (V_{C2} in Figure 6.5), Equation (6.11) can be derived (refer to Table 6.2 for a description of the different parameters used).

$$V_{C2}\frac{dC_2}{dt} = Q_1C_1 - Q_2C_2 \tag{6.11}$$

Equation (6.11) can be extended for N number of tanks in series:

$$V_{CN}\frac{dC_n}{dt} = Q_{n-1}C_{n-1} - Q_nC_n \tag{6.12}$$

With the assumption of identical volumes ($V_{Cn-1} = V_{Cn}$) and constant volumetric flow rate ($Q_{n-1} = Q_n$), Equation (6.12) can be written as:

$$\frac{dC_n}{dt} + \frac{N}{\tau}C_{n-1} = \frac{N}{\tau}C_n \tag{6.13}$$

It should be noted here that $\tau = V_T/Q$. Equation (6.13) can be solved using an integrating factor, which in this case is $e^{\left(\frac{Nt}{\tau}\right)}$. Multiplying Equation (6.13) with the integrating factor yields:

$$e^{\left(\frac{Nt}{\tau}\right)}\frac{dC_n}{dt} + e^{\left(\frac{Nt}{\tau}\right)}\frac{N}{\tau}C_n = e^{\left(\frac{Nt}{\tau}\right)}\frac{N}{\tau}C_{n-1} \tag{6.14}$$

When integrating both sides of Equation (6.14) with respect to time, the left side of the equation can be further simplified, based on the product rule, and rearranged to:

$$C_n = \frac{N}{\tau}e^{\left(-\frac{Nt}{\tau}\right)}\int_0^t C_{n-1}e^{\left(\frac{Nt}{\tau}\right)}dt \tag{6.15}$$

Equation (6.15) is analagous to Equation (2.29). It can be solved for N number of tanks in

series to produce Equation (6.16):

$$\frac{C_n}{C_0} = 1 - e^{\left(-\frac{Nt}{\tau}\right)} \left[1 + \frac{Nt}{\tau} + \frac{1}{2!}\left(\frac{Nt}{\tau}\right)^2 + ... + \frac{1}{(N-1)!}\left(\frac{Nt}{\tau}\right)^{N-1}\right] \tag{6.16}$$

Table 6.2: Summary of model parameters used in the TIS model and how they were obtained.

Symbol	Model parameter	How it is obtained
Controlled parameters		
C_0	Normalised inlet solute concentration (-)	Controlled variable
Q_n	Volumetric flow rate (mL/min)	Controlled variable
t	Time (min)	Controlled variable
Experimentally obtained or calculated parameters		
V_C	Volume of each CSTR (mL)	Calculated (model results)
V_T	Total flow volume (mL)	Measured
τ	Mean residence time (min)	Calculated (experimental data)
Fitted and output parameters		
C_n	Outlet solute concentration (-)	Main model output
N	Number of CSTR tanks (-)	Fitted variable

6.2.3 Model Coding and Fitting

The TIS model was coded using the Python programming language on the Jupyter Notebook version 5.5.0. Due to the fact that the model contained only one adjustable parameter, the number of tanks (N), that takes on discrete integer values, the fitting process was done manually. The error function (Equation (5.2)) was monitored as the number of tanks was increased from a starting value of one. Once this function reached a minimum value, the fitting process was terminated.

6.2.4 Model Response Analysis

Figure 6.6 shows the model's response to increasing N from 1 to 100. The higher the number of tanks, the more the concentration profile resembles that of a PFR.

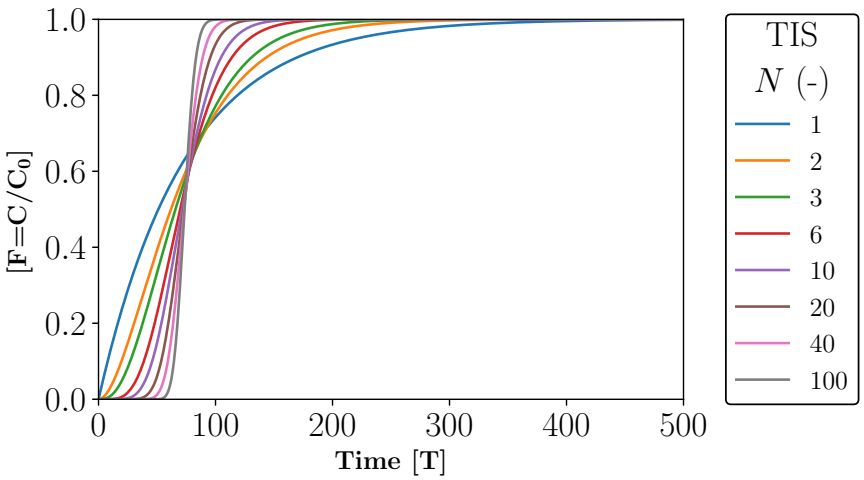

Figure 6.6: TIS model's response to varying number of tanks (N). [F - Normalised solute concentration, Time - Dimensional time units]. The value of the parameters kept constant during the analysis are (with dimensional units: [L] - length unit, [M] - mass unit, [T] - time unit): $Q = 0.678$ [L^3/T] and $V_T = 50$ [L^3].

6.3 Advection Dispersion Model

The advection dispersion (AD) model is a semi-phenomenological solute transport model which, as the name suggests, combines advective and dispersive forms of solute transport. It is one of the simplest solute transport models that accounts for non-ideal (preferential) flow through the inclusion of the dispersion parameter. It is a mono porosity solute transport model, assuming that all the liquid volume present within a system is actively flowing and capable of transporting solute molecules (refer to Figure 6.7). Similar to the TIS model, the AD model has one fitting parameter, the dispersion coefficient (D_{ds}). Its simple structure limits the extent to which the model can account for preferential flow profiles.

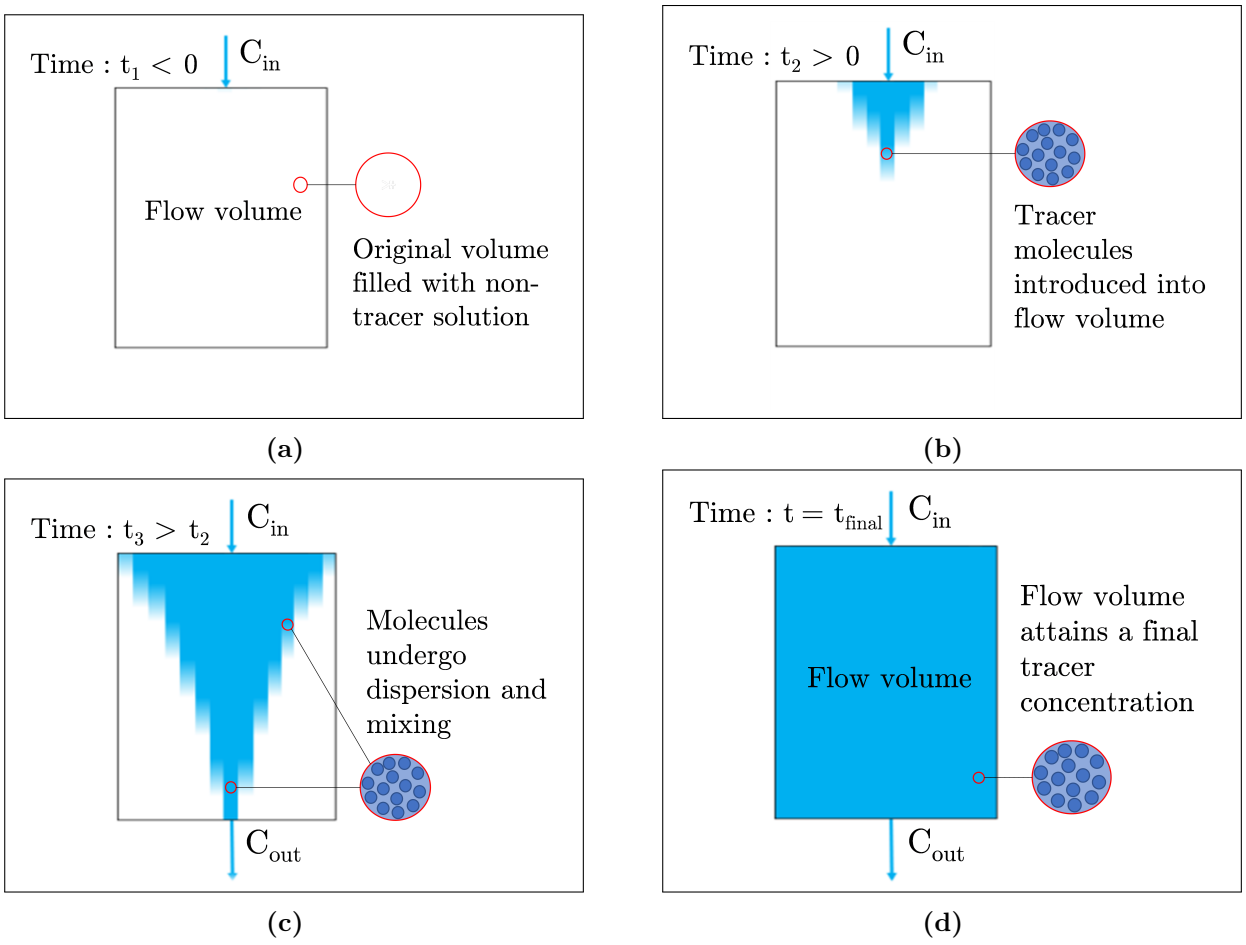

Figure 6.7: Solute transport of tracer molecules continuously injected into a flow volume at t = 0, as described by the AD model with tracer concentration represented by C.

6.3.1 Model Characteristics, Assumptions and Limitations

The main characteristics, assumptions and limitations of the AD model used in this study are as follows:

- 1D mono porosity solute transport model
- Solute molecules undergo dispersion as they flow through the volume
- All symptoms of non-ideal solute transport/flow can be attributed to the dispersion of molecules
- Advective velocity and dispersion coefficient are constant for a particular system

6.3.2 Model Equations

A mass balance on solute molecules around a control volume of interest yields:

$$\begin{aligned}&\text{Accumulation} = [\text{Rate}_{\text{in}} \text{ by advection} + \text{Rate}_{\text{in}} \text{ by dispersion}]\\&-[\text{Rate}_{\text{out}} \text{ by advection} + \text{Rate}_{\text{out}} \text{ by dispersion}]\end{aligned} \tag{6.17}$$

Assigning model specific parameters (refer to Table 6.3) to a system at steady state yields:

$$\varepsilon\beta_T \frac{\partial C}{\partial t} = \frac{D_{ds}}{L^2}\frac{\partial^2 C}{\partial z^2} - \frac{U}{L}\frac{\partial C}{\partial z} \tag{6.18}$$

Table 6.3: Summary of model parameters used in the AD model and how they were obtained.

Symbol	Model parameter	How it is obtained
Controlled parameters		
$C(0,t)$	Normalised inlet solute concentration (-)	Controlled variable
t	Time (min)	Controlled variable
z	Spatial dimension - normalized length (-)	Controlled variable
L	Packed bed length (m)	Controlled variable
Experimentally obtained or calculated parameters		
β_T	Total saturation (m^3 liquid/m^3 void)	Calculated (experimental data)
ε	Total bed voidage (m^3 void/m^3 bed)	Measured
U	Superficial velocity (m/min)	Calculated (experimental data)
Fitted and output parameters		
C	Normalized outlet solute concentration (-)	Main model output
D_{ds}	Dispersion coefficient (m^2/min)	Fitted variable

Initial (I.C.) and Boundary conditions (B.C.) needed for solving Equation (6.18) are giving in Equation (6.19)

$$\begin{aligned}&\text{I.C. } C(z,0) = 0\\&\text{B.C. } C(0,t) = 1\\&\text{B.C. } \left.\frac{\partial C}{\partial t}\right|_{z=L} = 0\end{aligned} \tag{6.19}$$

The discretization of the AD model equations can be found in Appendix C.1 with the stability analysis in Appendix D.1. A summary of its model parameters can be found in Table 6.3.

6.3.3 Model Coding and Fitting

The AD model was coded using the Python programming language on the Jupyter Notebook version 5.5.0 software run on the UCT High Performance Computing (HPC) cluster. To fit the model, the *mystic* package was imported and the differential evolution algorithm (*diffev2*) was chosen. The main ideas behind this method were developed by Kenneth Price and Rainer Storm in 1955. It is a population based stochastic optimization algorithm that utilizes mutation, crossover and selection operators to evolve individuals from the population and achieve convergence. It can optimize an objective function with the incorporation of constraints. Its three main advantages over other methods are its ability to (Laguna-Sanchez et al., 2016; Mishra and Shinde, 2017):

- Find the true global minimum regardless of initial parameter values
- Fast convergence
- Few control parameters

The objective function minimised by the algorithm is shown in Equation (5.2). A simplified optimisation algorithm used to obtain the final parameter values for the AD model is shown in Appendix E, Figure E.1. It should be noted that this does not represent the intricate algorithm employed in the *diffev2* minimisation method when fitting parameters.

6.3.4 Model Response Analysis

The AD model's dispersion coefficient (D_{ds}) was varied to ascertain its effect on the AD model's output (see Figure 6.8). Though it is common practice to introduce dimensionless variables into the modelling equations, parameters were kept dimensional during fitting to allow for model to model comparisons presented in Chapter 9.

A reduction in the magnitude of the dispersion coefficient brought about a reduction in degree of mixing and an increase in breakthrough time. As D_{ds} is decreased, the RTD profile takes on a more ideal, plug flow behaviour especially noticeable at $D = 10^{-7}$ [L^2/T].

This is an expected response as advection becomes the dominant form of solute transport at low magnitudes of D_{ds}.

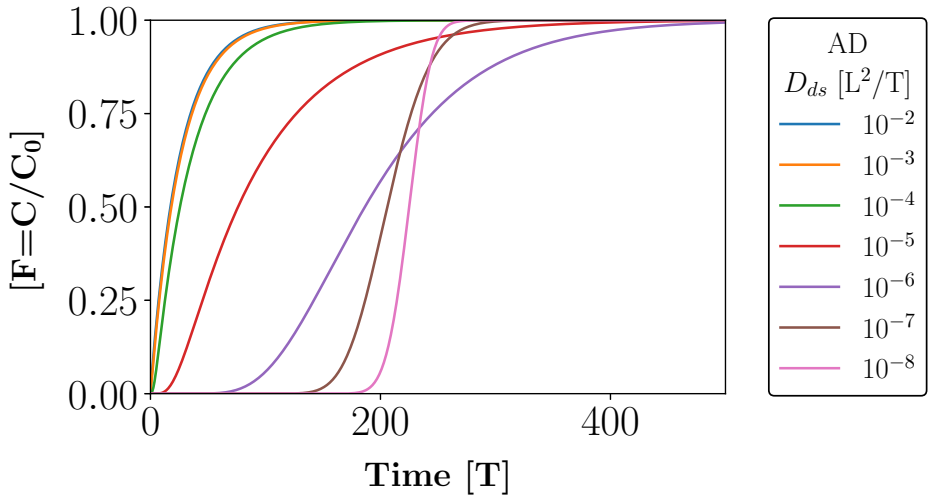

Figure 6.8: AD model's response to changes in the dispersion coefficient (D_{ds}) parameter. [F - Normalised solute concentration, Time - Dimensional time units]. The value of the parameters kept constant during the analysis are (with dimensional units: [L] - length unit, [M] - mass unit, [T] - time unit): $\varepsilon = 0.4$ [-], $U = 10^{-4}$ [L/T] and $L = 0.33$ [L].

6.4 Piston Exchange Model

The piston exchange (PE) model is similar to the MSPD model used by Bouffard and Dixon (2001). It is a dual porosity solute transport model based on the assumption of a more severe form of solution scale preferential flow profile (presence of stagnant volumes) and is therefore a natural progression from mono porosity models (refer to Figure 6.9).

In the dynamic volume, solute transport is mainly by advection and follows an ideal plug flow behaviour while in the stagnant, no flow occurs and hence no advective transport. However, there is mass transfer from the dynamic to the stagnant volume, governed by an overall mass transfer coefficient ($K_m a$). In an actual packed bed, the dynamic volume is thought to be comprised of the medium to large voids in the void network, where solution is free to flow without substantial resistance. The stagnant region, which is assumed to be well mixed with uniform concentration, is comprised of micro-pores/voids, where stagnant

pools of solutions exist due to capillary forces. This void network traverses both intra- and inter-particle spaces. The incorporation of the stagnant volume and associated overall mass transfer coefficient are the only means by which the PE model accounts for preferential flow.

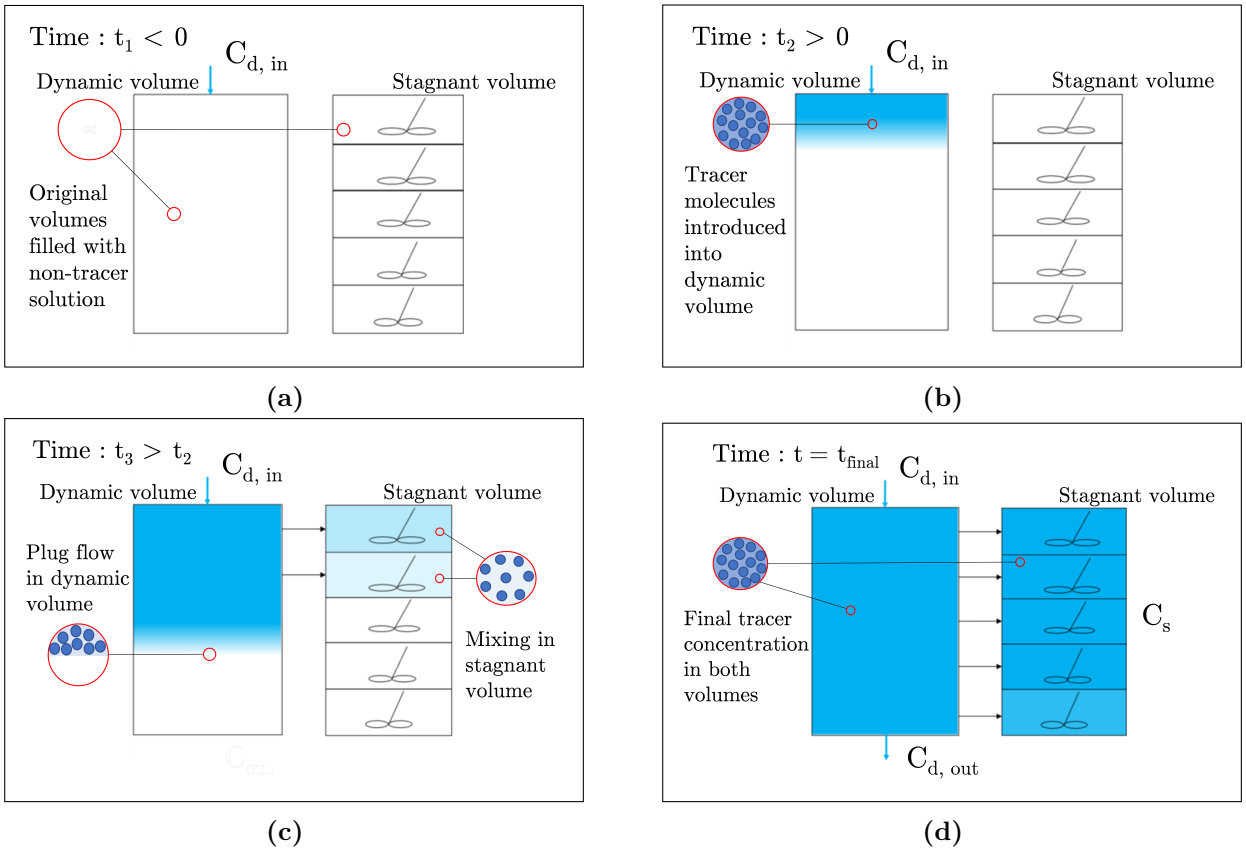

Figure 6.9: Solute transport, as described by the PE model, at different time frames, for a step input of tracer molecules injected into the dynamic flow volume at t = 0, with concentration represented by C.

6.4.1 Model Characteristics, Assumptions and Limitations

The main characteristics, assumptions and limitations of the PE model are as follows:

- 1D vertical advective flow with lateral diffusion of solute molecules
- Two distinct volumes: dynamic and stagnant
- Solute molecules are assumed to move as a front in the dynamic phase (no dispersion)
- Micro-pores constituting the stagnant phase are assumed to be of uniform length and

oriented normally to the advection channels

- Diffusion gradient between the flowing liquid and micro-pores is greater than the gradient between adjacent pores, hence no cross transfer between pores
- Uniform concentration within stagnant phase. It is assumed that individual pores possess relatively small volumes.
- Constant overall mass transfer coefficient

6.4.2 Model Equations

Solute mass balance in dynamic volume

$$\begin{aligned}&\text{Accumulation} = [\text{Rate}_{\text{in}} \text{ by advection}] - [\text{Rate}_{\text{out}} \text{ by advection }] \\ &- [\text{Rate}_{\text{out}} \text{ by mass transfer}]\end{aligned} \tag{6.20}$$

Assigning model specific parameters (refer to Table 6.4) to a system at steady state yields:

$$\frac{\partial C_d}{\partial t} = -\frac{U}{L\varepsilon\beta_d}\frac{\partial C_d}{\partial z} - \frac{K_m a}{\varepsilon\beta_d}(C_d - C_s) \tag{6.21}$$

Solute mass balance in stagnant volume

$$\text{Accumulation} = [\text{Rate}_{\text{in}} \text{ by mass transfer}] \tag{6.22}$$

Assigning model specific parameters to a system at steady state yields Equation (6.23):

$$\frac{\partial C_s}{\partial t} = \frac{K_m a}{\varepsilon(\beta_T - \beta_d)}(C_d - C_s) \tag{6.23}$$

Initial (I.C.) and Boundary conditions (B.C.) needed for solving Equation (6.21) and Equation (6.23) are giving in Equation (6.24)

$$\begin{aligned}&\text{I.C. } C_d(z,0) = 0 \\ &\text{I.C. } C_s(z,0) = 0 \\ &\text{B.C. } C_d(0,t) = 1 \\ &\text{B.C. } \left.\frac{\partial C_d}{\partial t}\right|_{z=L} = 0\end{aligned} \tag{6.24}$$

The discretization of the PE model equations can be found in Appendix C.2 with the stability

analysis in Appendix D.2. A summary of its model parameters can be found in Table 6.4.

Table 6.4: Summary of model parameters used in the PE model and how they were obtained.

Symbol	Model parameter	How it is obtained
Controlled parameters		
$C_d(0,t)$	Inlet solute concentration (-)	Controlled variable
t	Time (min)	Controlled variable
z	Spatial dimension - normalized length (-)	Controlled variable
L	Packed bed length (m)	Controlled variable
Experimentally obtained or calculated parameters		
β_T	Total saturation (m^3 liquid/m^3 void)	Calculated (experimental data)
ε	Total bed voidage (m^3 void/m^3 bed)	Measured
U	Superficial velocity (m/min)	Calculated (experimental data)
Fitted and output parameters		
β_d	Dynamic saturation (m^3 liquid/m^3 void)	Fitted variable
C_d	Normalized outlet solute concentration (-)	Main model output
C_s	Normalized solute concentration (stagnant volume)(-)	Model output
$K_m a$	Overall mass transfer coefficient (min^{-1})	Fitted variable

6.4.3 Model Coding and Fitting

The PE model was coded and fitted using the same coding language, software and package as the AD model (refer to section 6.3.3). A simplified optimisation algorithm used to obtain the final parameter values for the PE model is shown in Appendix E, Figure E.2.

6.4.4 Model Response Analysis

The fitting parameters in the PE model equation were varied to ascertain the effect each had on the model output for both the dynamic and stagnant regions. The results of the analysis are shown in Figure 6.10.

It can be seen that when the $K_m a$ values are greater than U ($10^{-1} - 10^{-3}$ [T^{-1}]), the concentration profiles in the stagnant zone matches those in the dynamic zone (refer to Figures

6.10a and 6.10b). This is because mass transfer is no longer a limitation and the solutes move freely into the stagnant volumes. As $K_m a$ decreases, breakthrough time in the dynamic zone reduces until $K_m a$ reaches a magnitude of 10^{-6} [T^{-1}], after which further reductions no longer have a substantial effect on the RTD profile. This is a logical model response as less mass transfer means an increase in the solute concentration of the dynamic volume which results in shorter exit times. At low $K_m a$ values, U becomes the principal driving force in the advective transport of solute molecules and the the dynamic zone experiences plug flow like behaviour.

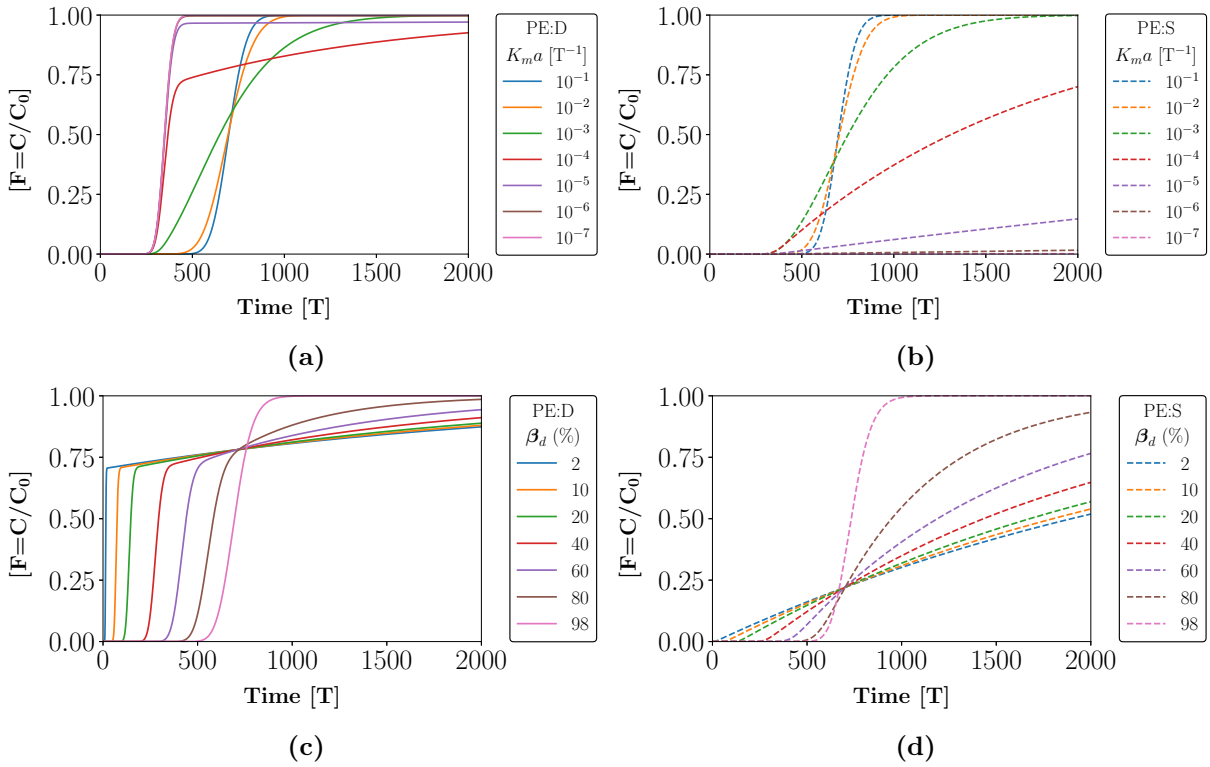

Figure 6.10: Showing the response of the final dynamic (PE:D) and stagnant (PE:S) volume nodes of the PE model to changes in the overall mass transfer coefficient ($K_m a$) and dynamic saturation (β_d). [F - Normalised solute concentration, Time - Dimensional time units]. The value of the parameters kept constant during the analysis are (with dimensional units: [L] - length unit, [M] - mass unit, [T] - time unit): $\varepsilon = 0.4$ [-], $U = 10^{-4}$ [L/T], $\beta_T = 0.5$ [-], $L = 0.35$ [L], $\beta_d = 0.25$ [-] (a) and (b), $K_m a = 10^{-6}$ T^{-1} (c) and (d)

The dynamic saturation parameter (Figures 6.10c and 6.10d) is directly proportional to the breakthrough time of solute molecules. At very high dynamic saturations, the relatively

small stagnant volumes attain equilibrium concentrations rapidly and their RTD profiles mirror the dynamic phase. At low dynamic saturations, solute molecules are able to make their way through the bed and out at the bottom in relatively short time periods. During this time, the effect of solute transfer from the dynamic to stagnant volume is masked by the rapid movement of solute molecules in the dynamic region. This results in the first half of the curves exhibiting channelling behaviour. Once the solute concentration in the dynamic phase reaches a certain value (approximately 0.70 in this simulation), the transfer process, governed by the overall mass transfer coefficient becomes an important factor. This results in the second half of the curves possessing very long tails, indicative of large stagnant volumes.

The sharp kinks in some of the curves in Figure 6.10c, are largely due to the assumption of a perfectly mixed stagnant volume cell. This means that the concentration gradient at the interface between the dynamic and stagnant volumes is maintained at a significantly high level for long durations of time. This is because the solute molecules transferred are assumed to immediately disperse into the entirety of the stagnant volume, reducing their impact on the solute concentration at the interface. This effect is exacerbated in the case where these volumes are significantly larger than their dynamic counterparts. During these instances, the solute transfer rate becomes approximately constant for long durations due to the slow decrease in the magnitude of the concentration at the interface. Hence, the latter part of the curves approximate straight lines at lower dynamic saturations.

6.5 Piston Exchange - Diffusion Variant Model

The piston exchange - diffusion variant (PE-D) model is similar to the profile side pore diffusion (PSPD) model used by Bouffard and Dixon (2001). It is a progression from the PE model with the main difference being the inclusion of a diffusional mass transfer mechanism within the stagnant zones of the packed bed (refer to Figure 6.11).

The PE-D model is based on the dual porosity concept of dynamic and stagnant volumes (solution scale preferential flow). The model has two fitted parameters to account for preferential flow: dynamic saturation (β_d) and maximum pore length (X). Advection is the

only form of solute transport in the dynamic phase, hence the assumption of perfect plug flow behaviour. Mass transfer, using a diffusion mechanism, occurs from the dynamic to the stagnant region. The rate of transfer is governed by the diffusion coefficient (D_{df}) of solute molecules. This means that the assumption of an evenly mixed pore space is excluded from this model.

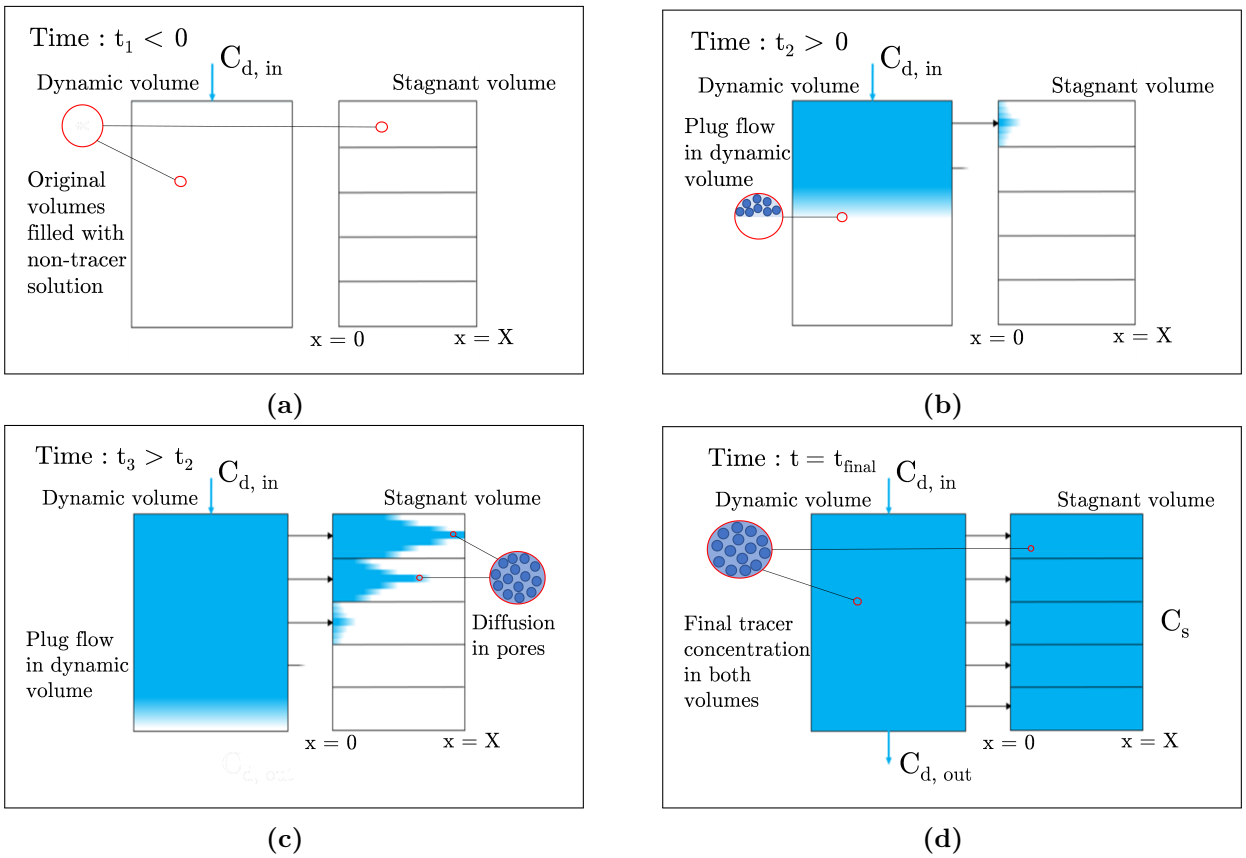

Figure 6.11: Solute transport visualisation as described by the PE-D model, at different time frames, for a step input of tracer molecules injected into a dynamic flow volume at t = 0, with concentration represented by C.

6.5.1 Model Characteristics, Assumptions and Limitations

The main characteristics, assumptions and limitations of the PE-D model are as follows:

- 1D vertical advective flow with lateral diffusion
- Two distinct volumes: dynamic and stagnant

- Solute molecules are assumed to move as a front in the dynamic volume
- Micro-pores constituting the stagnant volume are assumed to be of uniform length and oriented normally to the advection channels
- A linear diffusion mechanism governs transport within pores, therefore transfer is governed by concentration gradient at the pore liquid and bulk solution interface
- Diffusion gradient between the flowing liquid and pores is greater than the gradient between adjacent pores, hence, no cross transfer between pores

6.5.2 Model Equations

Solute mass balance in dynamic volume

$$\begin{aligned}&\text{Accumulation} = [\text{Rate}_{\text{in}} \text{ by advection}] - [\text{Rate}_{\text{out}} \text{ by advection }] \\ &- [\text{Rate}_{\text{out}} \text{ by diffusional mass transfer}]\end{aligned} \tag{6.25}$$

Assigning model specific parameters (refer to Table 6.5) to a system at steady state yields:

$$\frac{\partial C_d}{\partial t} = -\frac{U}{L\varepsilon\beta_d}\frac{\partial C_d}{\partial z} - \frac{D}{\varepsilon\beta_d X^2}\frac{\partial C_s}{\partial x}\bigg|_{x=0} \tag{6.26}$$

Solute mass balance in stagnant zone

$$\text{Accumulation} = [\text{Rate}_{\text{in}} \text{ by linear diffusional mass transfer}] \tag{6.27}$$

$$\frac{\partial C_s}{\partial t} = \frac{D}{\varepsilon(\beta_T - \beta_d)X^2}\frac{\partial^2 C_s}{\partial x^2} \tag{6.28}$$

Initial (I.C.) and Boundary conditions (B.C.) needed for solving Equation (6.26) and Equation (6.28) are giving in Equation (6.29). The discretization of the PE-D model equations can be found in Appendix C.3 with the stability analysis in Appendix D.3. A summary of its model parameters can be found in Table 6.5.

$$
\begin{aligned}
&\text{I.C. } C_d(z,0) = 0 \\
&\text{I.C. } C_s(x,0) = 0 \\
&\text{B.C. } C_d(0,t) = 1 \\
&\text{B.C. } C_s(0,t) = C_d|_{x=0} \\
&\text{B.C. } \left.\frac{\partial C_s}{\partial t}\right|_{x=X} = 0 \\
&\text{B.C. } \left.\frac{\partial C_d}{\partial t}\right|_{z=L} = 0
\end{aligned}
\tag{6.29}
$$

Table 6.5: Summary of model parameters used in the PE-D model and how they were obtained.

Symbol	Model parameter	How it is obtained
	Controlled parameters	
$C_d(0,t)$	Inlet solute concentration (-)	Controlled variable
L	Packed bed length (m)	Controlled variable
t	Time (min)	Controlled variable
z	Spatial dimension - normalized length (-)	Controlled variable
x	Spatial dimension - normalized length (-)	Controlled variable
	Obtained or calculated parameters	
β_T	Total saturation (m^3 liquid/m^3 void)	Calculated (experimental data)
D	Diffusion coefficient (m^2/min)	Obtained from literature
ε	Total bed voidage (m^3 void/m^3 bed)	Measured
U	Superficial velocity (m/min)	Calculated (experimental data)
	Fitted and output parameters	
β_d	Dynamic saturation (m^3 liquid/m^3 void)	Fitted variable
C_d	Normalized outlet solute concentration (-)	Main model output
C_s	Normalized solute concentration (stagnant volume)(-)	Model output
X	Pore length (m)	Fitted variable

6.5.3 Model Coding and Fitting

The PE-D model was coded and fitted using the same coding language, software and package as the AD model (refer to sub-section 6.3.3). A simplified optimisation algorithm used to obtain the final parameter values for the PE-D model is shown in Appendix E, Figure E.3.

6.5.4 Model Response Analysis

The results of the effect of dynamic saturation (β_d), maximum pore length (X) and diffusion coefficient (D_{df}) on the RTD profiles for both the dynamic and stagnant volumes of the model will be discussed separately.

6.5.4.1 Dynamic Volume

In Figure 6.12a an increase in β_d, equivalent to a decrease in β_s, results in a more ideal RTD profile that approximates plug flow behaviour. A point to note is the absence of the sharp kinks that were present in the PE curves when the same parameter was varied at low β_d values (refer to Figure 6.10c). For the PE-D model, a more gradual change in curvature is acquired. This is due to the diffusional mechanism governing the mass transfer in the stagnant region. Instead of the maintenance of a large concentration gradient at the dynamic-stagnant interface due to the assumption of perfect mixing, the linear diffusion of solutes in the stagnant phase acts as a buffer, preventing the magnitude of this gradient from remaining excessively high.

The response of the model to varying magnitudes of the diffusion coefficient can be found in Figure 6.12b. At high values of D_{df} (around 10^{-3} [L^2/T] in this simulation), the mass transfer rate of solute molecules in the stagnant region is relatively fast. This allows for the concentration gradient at the interface between the dynamic and stagnant volumes to be maintained at a relatively higher magnitude. Hence, there is increased solute transport between both volumes, leading to longer breakthrough times in the dynamic region. As D_{df} decreases, there is a gradual increase in the degree of ideal plug flow behaviour which is typical of what one would expect when the fraction of solute molecules remaining in the dynamic region increases. The interval between 10^{-4} and 10^{-5} [L^2/T] is a region of heightened sensitivity which is based on the interrelationship between the velocity and diffusion parameter, as the velocity was kept constant at $U = 10^{-4}$ [L/T].

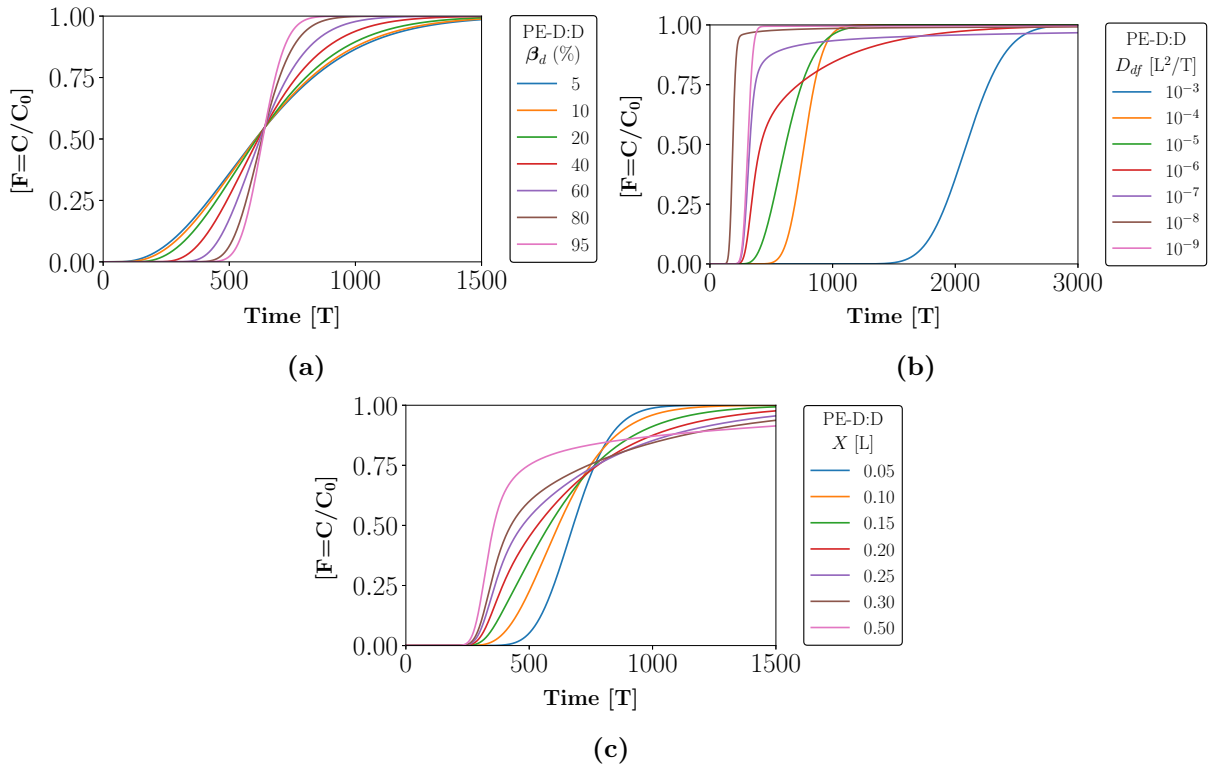

Figure 6.12: Response of the final dynamic volume node of the PE-D model to changes in the dynamic saturation (β_d), diffusion coefficient (D_{df}) and maximum pore length (X). [F - Normalised solute concentration, Time - Dimensional time units]. The value of the parameters (with dimensional units: [L] - length unit, [M] - mass unit, [T] - time unit) kept constant during the analysis are: $\varepsilon = 0.4$ [-], $U = 10^{-4}$ [L/T], $\beta_T = 0.5$ [-], $L = 0.31$ [L], $\beta_d = 0.25$ [-] (b) and (c), $X = 0.1$ [L] (a) and (b), $D_{df} = 10^{-5}$ [L^2/T] (a) and (c).

The effect of increasing the maximum pore length (X) on the PE-D model's response is shown in Figure 6.12c. X is a complex variable as its magnitude has multiple simultaneous effects. Firstly, it is one of the factors governing the mass transfer rate of solute molecules from the dynamic to stagnant regions, as shown by Equation (6.26) and (6.28). At low pore length values ($X = 0.05$ to 0.15), the mass transfer rate of solute molecules from the dynamic volume is significantly high, leading to longer breakthrough times. However, shorter pores mean that the solute concentration within them reaches equilibrium faster. This in turn causes the dynamic region to also attain a final solute concentration in a shorter time period. As pore length increases, diffusional mass transfer rate is reduced and more solute molecules are able to remain in the dynamic region, experiencing shorter breakthrough times. However,

longer pores take longer to attain the equilibrium solute concentration which increases the duration of mass transfer between both regions. Hence, the RTD profiles of the dynamic region have longer asymptotes.

6.5.4.2 Stagnant Volume

Figure 6.13 illustrates the effect of the dynamic saturation on the concentration profiles within the stagnant pores. As dynamic saturation increases from 30% to 90%, there is a corresponding decrease in stagnant saturation from 70% to 10%. A smaller stagnant volume means a reduction in the time taken for the solute concentration in the pores to achieve the same concentration as that in the dynamic zone. Hence, the RTD profiles within the pores begin to collapse on each other (refer to Figures 6.13a, 6.13c and 6.13e). This is confirmed by the spatial concentration profiles within the pores attaining the maximum concentration value across the length of the pores in shorter time periods (refer to Figures 6.13b, 6.13d and 6.13f).

It is observed from Figure 6.14 that D_{df} has a significant impact on the concentration profiles within the stagnant volume/pores. At a $D_{df} = 10^{-3}$ [L^2/T], the concentration profile within the pores is identical to those within the dynamic region (refer to Figure 6.14a). This is because at such a high diffusion coefficient, mass transfer is no longer a limitation and the pores immediately attain the equilibrium solute concentration. As D_{df} decreases from 10^{-3} to 10^{-7} [L^2/T], differences in the RTD curves between the dynamic and stagnant regions emerge and become more pronounced. Mass transfer becomes a significant limiting factor and the solutes have difficulty diffusing through the entire length of the pores (refer to Figure 6.14f).

The maximum pore length (X) not only affects the diffusion path, but also the diffusion rate. From Figure 6.15, it is evident that increasing X, causes a similar effect as decreasing D_{df}, when it comes to the spatial concentration profiles within the pores (refer to Figures 6.15b, 6.15d and 6.15f).

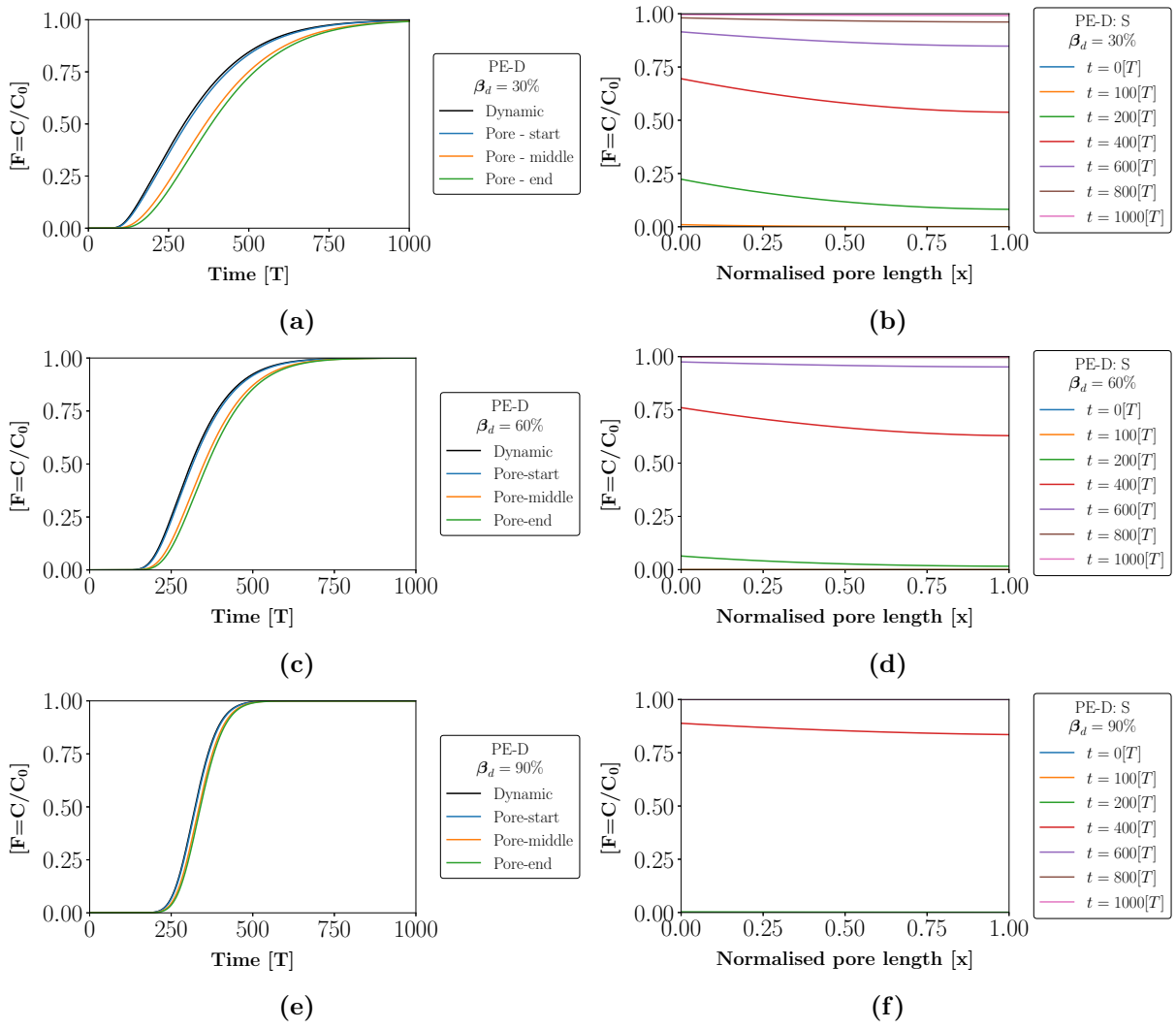

Figure 6.13: Response of the PE-D model to changes in the dynamic saturation (β_d). Temporal change in concentration of the dynamic region and associated stagnant pore at three different locations are shown on the left. Spatial change in concentration profiles for the pore at different time points are shown on the right. [F - Normalised solute concentration, Time - Dimensional time units]. The value of the parameters kept constant during the analysis are (with dimensional units: [L] - length unit, [M] - mass unit, [T] - time unit): $\varepsilon = 0.4$ [-], $U = 10^{-4}$ [L/T], $\beta_T = 0.5$ [-], $L = 0.31$ [L], $X = 0.1$ [L] and $D_{df} = 10^{-5}$ [L^2/T].

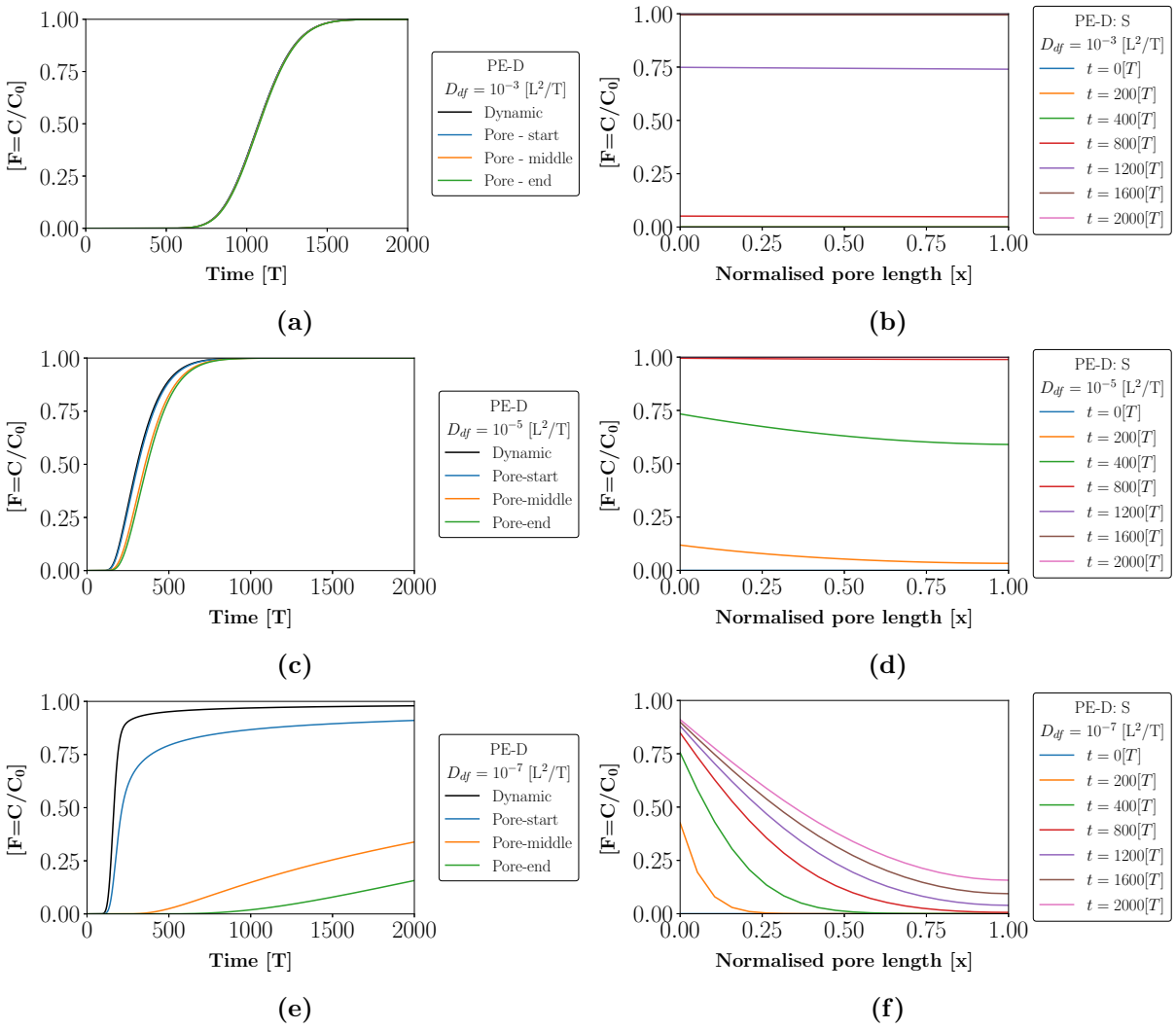

Figure 6.14: Response of the PE-D model to changes in the diffusion coefficient (D_{df}). Temporal change in concentration of the dynamic region and associated stagnant pore at three different locations are shown on the left. Spatial change in concentration profiles for the pore at different time points are shown on the right. [F - Normalised solute concentration, Time - Dimensional time units]. The value of the parameters kept constant during the analysis are (with dimensional units: [L] - length unit, [M] - mass unit, [T] - time unit): $\varepsilon = 0.4$ [-], $U = 10^{-4}$ [L/T], $\beta_T = 0.5$ [-], $L = 0.31$ [L], $\beta_d = 0.25$ [-] and $X = 0.1$.

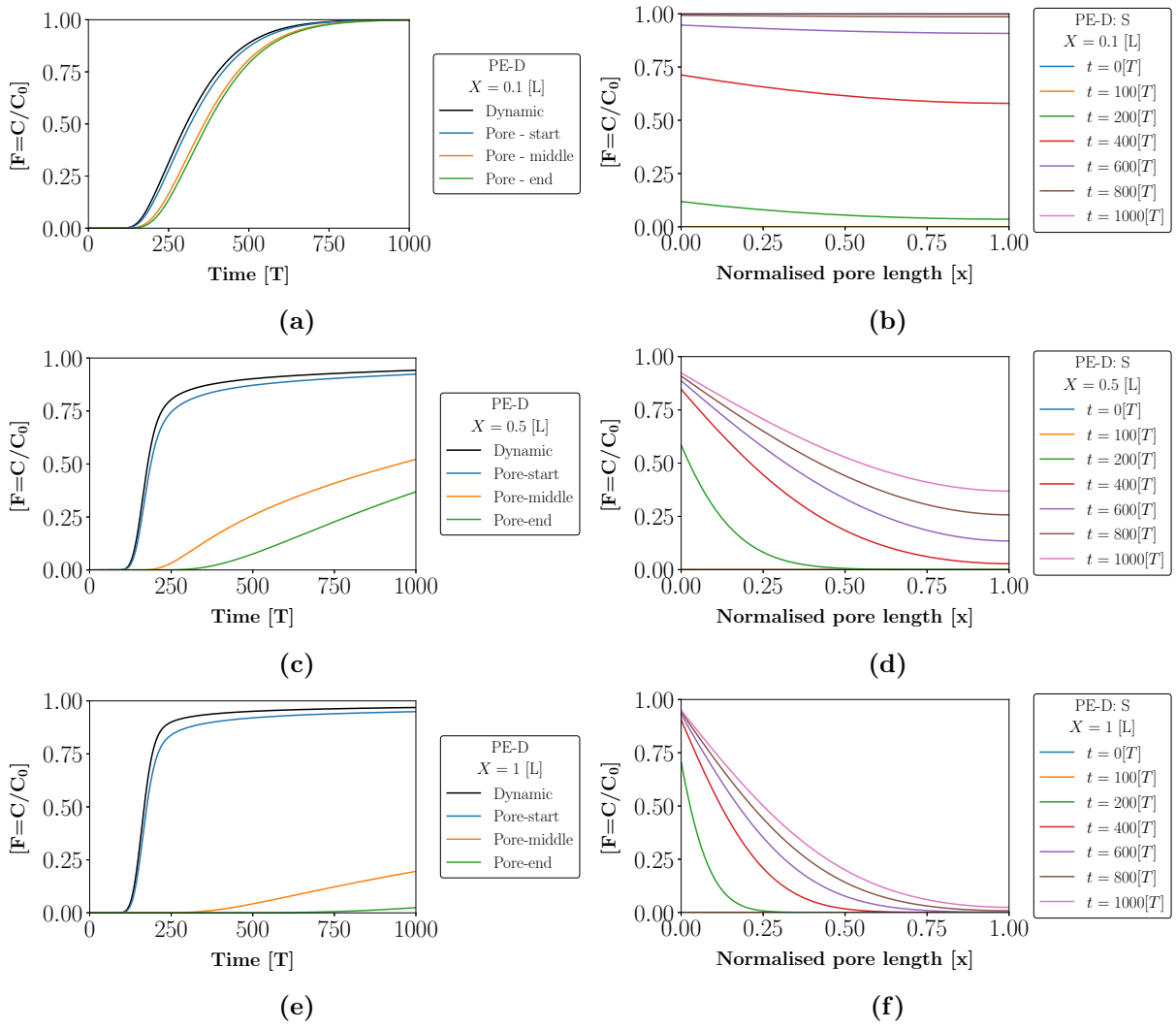

Figure 6.15: Response of the PE-D model to changes in the pore length (X). Temporal change in concentration of the dynamic region and associated stagnant pore at three different locations are shown on the left. Spatial change in concentration profiles for the pore at different time points are shown on the right. [F - Normalised solute concentration, Time - Dimensional time units]. The value of the parameters kept constant during the analysis are (with dimensional units: [L] - length unit, [M] - mass unit, [T] - time unit): $\varepsilon = 0.4$ [-], $U = 10^{-4}$ [L/T], $\beta_T = 0.5$ [-], $L = 0.31$ [L], $\beta_d = 0.25$ [-] and $D_{df} = 10^{-5}$ [L^2/T].

6.6 Piston Dispersion Exchange Model

The piston dispersion exchange (PDE) model is a dual porosity solute transport model that combines elements of the AD and PE models (refer to Figure 6.16). It was used in the

work by de Andrade Lima (2006) and incorporates both D_{ds} and $K_m a$ into its formulation. Therefore, it is considered more complex than the PE and PE-D models. The PDE model divides the flow volume into a dynamic and stagnant phase . In the dynamic phase, solute molecules undergo dispersion and mixing, similar to the AD model. There is solute transport from the dynamic to the stagnant volume, governed by an overall mass transfer coefficient, similar to the PE model. The stagnant phase is assumed to be well mixed with uniform concentration. The physical representations of both these volumes in an actual packed bed was discussed in section 6.4. This means that the PDE model has three fitting parameters to account for non-ideal/preferential flow: the dispersion coefficient, fraction of dynamic to stagnant saturation and their associated mass transfer coefficient.

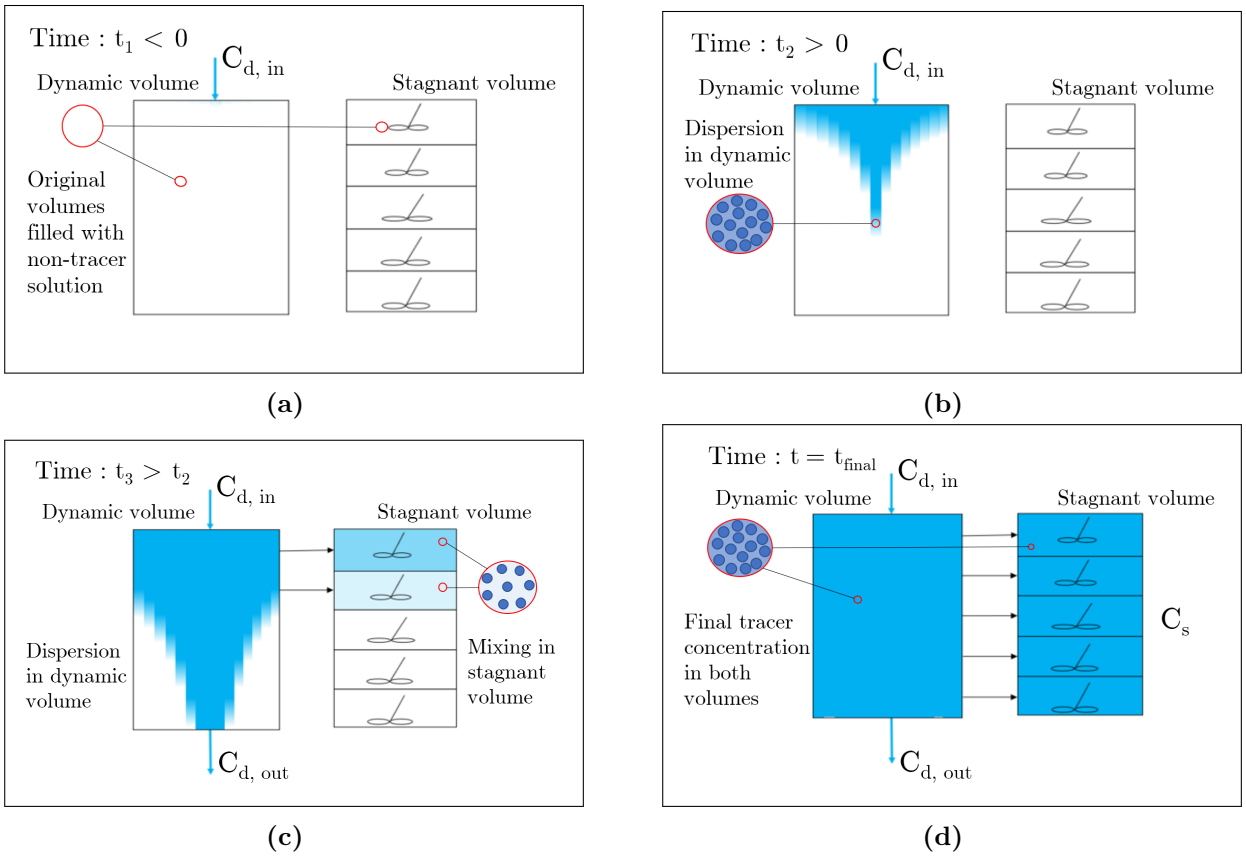

Figure 6.16: Solute transport visualisation as described by the PDE model, at different time frames, of tracer molecules injected into a dynamic flow volume at t = 0, with concentration represented by C.

6.6.1 Model Characteristics, Assumptions and Limitations

The main characteristics, assumptions and limitations of the PDE model are as follows:

- 1D vertical flow with dispersion and lateral solute transport
- Two distinct volumes: dynamic and stagnant
- Micro-pores constituting the stagnant phase are assumed to be of uniform length and oriented normally to the advection-dispersion channels
- Uniform concentration within pores
- Concentration gradients between the flowing liquid and pores is greater than gradient between adjacent pores, hence no cross transfer between pores
- Constant dispersion and mass transfer coefficients

6.6.2 Model Equations

Solute mass balance in dynamic volume

$$\begin{aligned}&\text{Accumulation} = [\text{Rate}_{\text{in}} \text{ by advection} + \text{Rate}_{\text{in}} \text{ by dispersion}] \\ &-[\text{Rate}_{\text{out}} \text{ by advection} + \text{Rate}_{\text{out}} \text{ by dispersion}]\text{- } [\text{Rate}_{\text{out}} \text{ by mass transfer}]\end{aligned} \tag{6.30}$$

Assigning model specific parameters (refer to Table 6.6) to a system at steady state yielded:

$$\frac{\partial C_d}{\partial t} = \frac{D_{ds}}{L^2 \varepsilon \beta_d}\frac{\partial^2 C_d}{\partial z^2} - \frac{U}{L\varepsilon\beta_d}\frac{\partial C_d}{\partial z} - \frac{K_m a}{\varepsilon\beta_d}(C_d - C_s) \tag{6.31}$$

Solute mass balance in stagnant volume

$$\text{Accumulation} = [\text{Rate}_{\text{in}} \text{ by mass transfer}] \tag{6.32}$$

Assigning model specific parameters to a system at steady state yielded the same equation as Equation (6.23). Initial (I.C.) and Boundary conditions (B.C.) needed for solving Equation (6.31) and Equation (6.23) are identical to those shown in Equation (6.24).

The discretization of the PDE model equations can be found in Appendix C.4 with the stability analysis in Appendix D.4. A summary of its model parameters is found in Table 6.6.

Table 6.6: Summary of model parameters used in the PDE model and how they were obtained.

Symbol	Model parameter	How it is obtained
Controlled parameters		
$C_d(0,t)$	Inlet solute concentration (-)	Controlled variable
t	Time (min)	Controlled variable
z	Spatial dimension - normalized length (-)	Controlled variable
L	Packed bed length (m)	Controlled variable
Experimentally obtained or calculated parameters		
β_T	Total saturation (m^3 liquid/m^3 void)	Calculated (experimental data)
ε	Total bed voidage (m^3 void/m^3 bed)	Measured
U	Superficial velocity (m/min)	Calculated (experimental data)
Fitted and output parameters		
β_d	Dynamic saturation (m^3 liquid/m^3 void)	Fitted variable
C_d	Normalized outlet solute concentration (-)	Main model output
C_s	Normalized solute concentration (stagnant volume)(-)	Model output
D_{ds}	Dispersion coefficient (m^2/min)	Fitted variable
$K_m a$	Overall mass transfer coefficient (min^{-1})	Fitted variable

6.6.3 Model Coding and Fitting

The PDE model was coded and fitted using the same coding language, software and package as the AD model (refer to sub-section 6.3.3). A simplified fitting algorithm used to obtain the final parameter values for the PDE model is shown in Appendix E, Figure E.4.

6.6.4 Model Response Analysis

The PDE model's response to the variation of the dynamic saturation coefficient is very similar to that of the PE model (refer to Figures 6.10c and 6.17a). However, incorporation of D_{ds} results in smoother profiles. This is because, even without mass transfer, D_{ds} still introduces non-ideal flow characteristics in the dynamic region. Hence, as β_d decreases, the dispersion of molecules in the dynamic region causes a less instantaneous transition into a

mass transfer dominated section of the RTD profile.

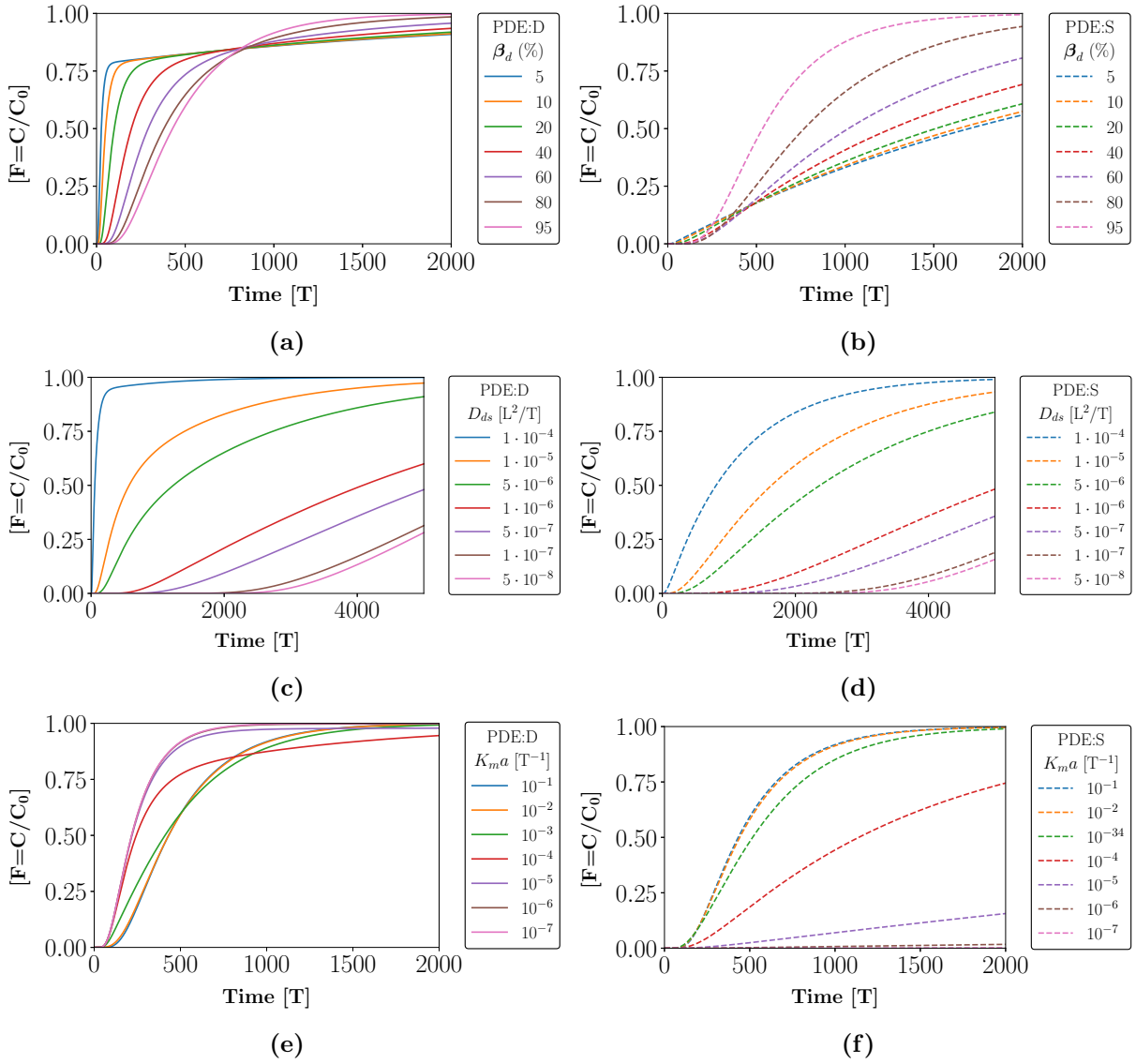

Figure 6.17: Response of the final dynamic and stagnant volume node of the PDE model to changes in the dynamic saturation (β_d), dispersion coefficient (D_{ds}) and overall mass transfer coefficient ($K_m a$). [F - Normalised solute concentration, Time - Dimensional time units]. The value of the parameters kept constant during the analysis are (with dimensional units: [L] - length unit, [M] - mass unit, [T] - time unit): $\varepsilon = 0.4$ [-], $U = 10^{-4}$ [L/T], $\beta_T = 0.5$ [-] , $L = 0.31$ [L], $\beta_d = 0.25$ [-] [excluding (a) and (b)], $D_{ds} = 10^{-5}$ [L^2/T] [excluding (c) and (d)], $K_m a = 10^{-4}$ [T^{-1}] [excluding (e) and (f)].

D_{ds} in the PDE model exerts a similar effect on the model's RTD output profile as that of the AD model (refer to Figures 6.17c and 6.8). High magnitudes lead to faster solute exit times

from the dynamic region due to the rapid mixing and spreading of molecules. It is important to note that the increase in plug flow behaviour as the magnitude of D_{ds} decreases, is not as noticeable as it was for the AD model. This is due to the dual porosity nature of the PDE model. The presence of β_d introduces non-ideal flow characteristics to the model's output, depending on its magnitude. This means that even at low dispersion rates, the generated RTD profiles can still possess high degrees of non-ideal flow characteristics. In terms of the stagnant region (refer to Figure 6.17d), it can be seen that there is no substantial difference between the dynamic and stagnant regions when varying D_{ds}.

The PDE model has a similar response to the PE model when $K_m a$ is varied (refer to Figures 6.10a and 6.17e). Increasing its value leads to slightly longer breakthrough times in the dynamic region due to an increase in the transfer of solute molecules to the stagnant region as seen in Figure 6.17f. The RTD of solute molecules in the stagnant region directly mirrors those in the dynamic region for higher overall mass transfer coefficient values (10^{-1} and 10^{-2} [T^{-1}]). At such values, the resistance to mass transfer is minimal and is no longer the dominant factor affecting the RTD profiles. Decreasing $K_m a$ decreases the final solute concentrations of the stagnant region which is an expected model response.

6.7 Piston Dispersion Exchange - Diffusion Variant Model

The piston dispersion exchange - diffusion variant (PDE-D) model combines elements of the PE-D and PDE models. It divides the flow volume into the dynamic and stagnant regions (Figure 6.18). It is a progression from the PE-D model because of the incorporation of D_{ds}, and also a progression from the PDE model through the utilization of X instead of $K_m a$. This means that the assumption of an evenly mixed pore space is excluded from this model. Therefore, the PDE-D model has three means of accounting for non-ideal/preferential flow: D_{ds}, β_d/β_T and X. There are currently no solute transport studies, in a heap leaching context, utilizing this exact model formulation.

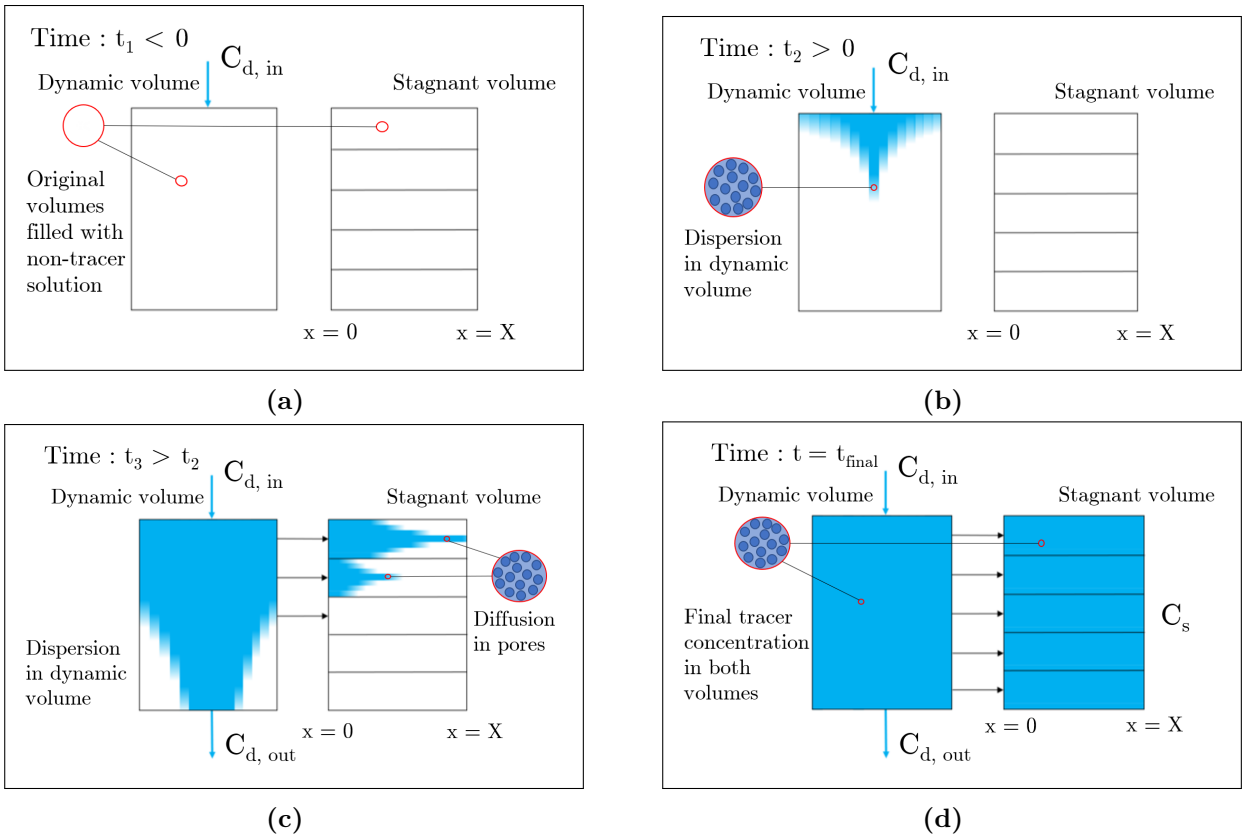

Figure 6.18: Solute transport visualisation at different time frames, as described by the PDE-D model, of tracer molecules injected into a dynamic flow volume at t = 0, with concentration represented by C.

6.7.1 Model Characteristics, Assumptions and Limitations

The main characteristics, assumptions and limitations of the PDE-D model are as follows:

- 1D vertical flow with dispersion and lateral solute transport
- Two distinct volumes: dynamic and stagnant
- Micro-pores constituting the stagnant volume are assumed to be of uniform length and oriented normally to the advection channels
- Diffusion mechanism governs transport within pores using the concentration gradient at the pore liquid and bulk solution interface
- Diffusion gradient between the flowing liquid and pores is greater than the gradient between adjacent pores, hence, no cross transfer between pores

- Constant pore length, dispersion and diffusion coefficient

6.7.2 Model Equations

Assigning model specific parameters (refer to Table 6.7) to Equation (6.33) yields Equation (6.34).

Solute mass balance in dynamic volume

$$\begin{aligned} &\text{Accumulation} = [\text{Rate}_{\text{in}} \text{ by advection} + \text{Rate}_{\text{in}} \text{ by dispersion}] \\ &- [\text{Rate}_{\text{out}} \text{ by advection} + \text{Rate}_{\text{out}} \text{ by dispersion}] \\ &- [\text{Rate}_{\text{out}} \text{ by diffusional mass transfer}] \end{aligned} \tag{6.33}$$

Table 6.7: Summary of model parameters used in the PDE-D model and how they were obtained.

Symbol	Model parameter	How it is obtained
Controlled parameters		
$C_d(0,t)$	Inlet solute concentration (-)	Controlled variable
L	Packed bed length (m)	Controlled variable
t	Time (min)	Controlled variable
z	Spatial dimension - normalized length (-)	Controlled variable
x	Spatial dimension - normalized length (-)	Controlled variable
Experimentally obtained or calculated parameters		
β_T	Total saturation (m^3 liquid/m^3 void)	Calculated (experimental data)
D	Diffusion coefficient (m^2/min)	Obtained from literature
ε	Total bed voidage (m^3 void/m^3 bed)	Measured
U	Superficial velocity (m/min)	Calculated (experimental data)
Fitted and output parameters		
β_d	Dynamic saturation (m^3 liquid/m^3 void)	Fitted variable
C_d	Normalized outlet solute concentration (-)	Main model output
C_s	Normalized solute concentration (stagnant volume)(-)	Model output
D_{ds}	Dispersion coefficient (m^2/min)	Fitted variable
X	Pore length (m)	Fitted variable

$$\frac{\partial C_d}{\partial t} = \frac{D_{ds}}{L^2 \varepsilon \beta_d} \frac{\partial^2 C_d}{\partial z^2} - \frac{U}{L \varepsilon \beta_d} \frac{\partial C_d}{\partial z} - \frac{D}{\varepsilon \beta_d X^2} \frac{\partial C_s}{\partial x}\bigg|_{x=0} \tag{6.34}$$

Solute mass balance in stagnant volume

Solute transport in the stagnant region is identical to that shown for the PE-D model (Equation (6.28)) with the same boundary conditions shown in Equation (6.29).

The discretization of the PDE-D model equations can be found in Appendix C.5 with the stability analysis in Appendix D.5. A summary of its model parameters is found in Table 6.7.

6.7.3 Model Coding and Fitting

The PDE-D model was coded and fitted using the same coding language, software and package as the AD model (refer to sub-section 6.3.3). A simplified optimisation algorithm used to obtain the final parameter values for the PDE-D model is shown in Appendix E, Figure E.5.

6.7.4 Model Response Analysis

The PDE-D model has three fitting parameters β_d, D_{ds} and X that were varied during the parameter response analysis. As with the PE-D model, the results of the effect of these parameters on the RTD profiles for both the dynamic and stagnant volumes of the model will be discussed separately.

6.7.4.1 Dynamic Volume

Figure 6.19a shows the effect of dynamic saturation on the RTD profile for the dynamic region of the PDE-D model. A reduction in breakthrough time but increase in asymptotic behaviour is noticeable as β_d decreases. The observed trend is very similar to those for the PE and PDE models with the points discussed previously applying here as well (refer to sub-sections 6.4.4 and 6.6.4).

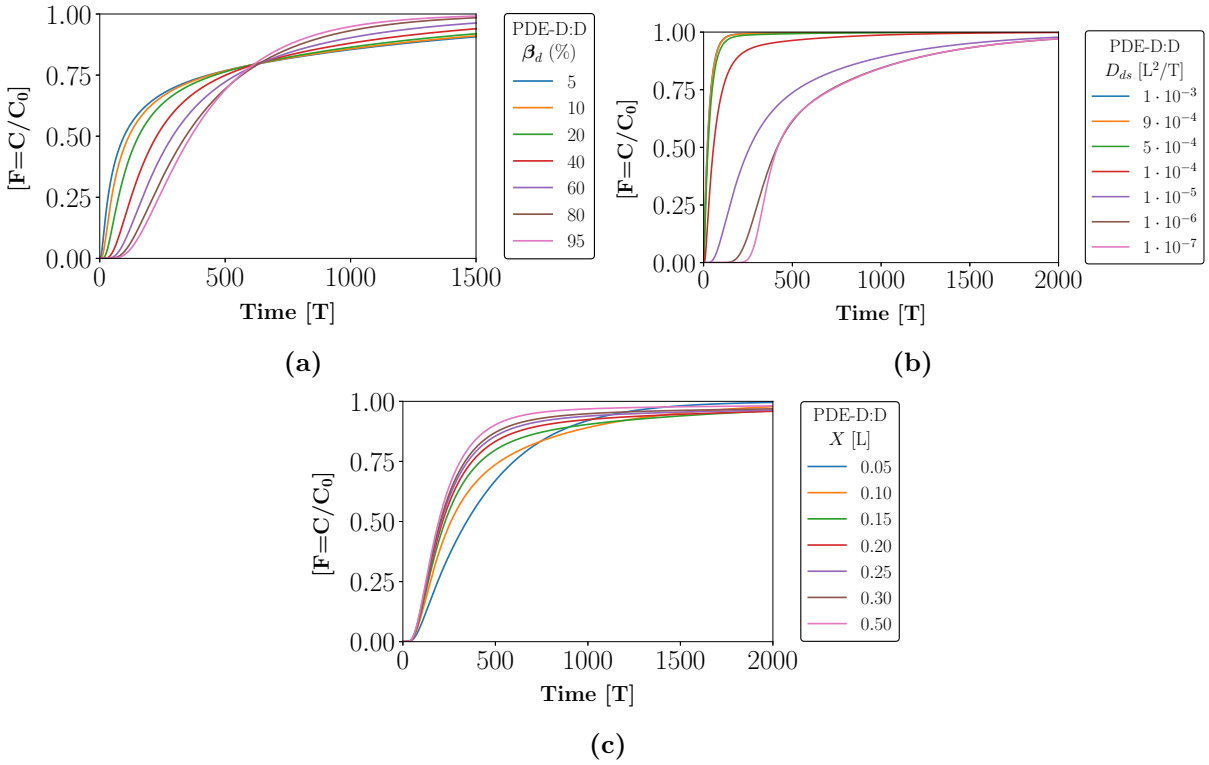

Figure 6.19: Response of the final dynamic volume node of the PDE-D model to changes in the dynamic saturation (β_d), dispersion coefficient (D_{ds}) and maximum pore length (X). [F - Normalised solute concentration, Time - Dimensional time units]. The value of the parameters kept constant during the analysis are (with dimensional units: [L] - length unit, [M] - mass unit, [T] - time unit): $\varepsilon = 0.4$ [-], $U = 10^{-4}$ [L/T], $\beta_T = 0.5$ [-] , $L = 0.31$ [L], $D_{df} = 10^{-6}$ [L^2/T], $\beta_d = 0.25$ [-] (b) and (c), $D_{ds} = 10^{-5}$ [L^2/T] (a) and (c), $X = 0.1$ [L] (a) and (b).

The effect of D_{ds} is shown in Figure 6.19b. At high values of D_{ds}, there is an almost instantaneous elution of tracer molecules from the packed bed. Lower magnitudes of D_{ds} lead to longer breakthrough times. Similar to the PDE model, the PDE-D model does not show a notable increase in plug flow behaviour as D_{ds} decreases, with the reasons mentioned previously applying in this case as well (refer to sub-section 6.6.4).

Figure 6.19c shows that at relatively low values of X, there is a lower initial rate of solute molecules exiting the dynamic region. However, the concentration within this region reaches its maximum value relatively quicker. As the value of X becomes greater, the rate of solute molecules exiting the dynamic volume also rises initially but the curves then transition into

a slower rate with relatively longer asymptotes. The reasons for this behaviour are similar to those given for the PE-D model, which were discussed in sub-section 6.5.4. It should be noted that the presence of D_{ds} has somewhat limited the model's sensitivity to parameter X. This is noticeable when comparing Figures 6.12c to 6.19c. The reason for this is simply that the presence of D_{ds} offers the model an additional non-ideal flow parameter, making it less sensitive to changes in the others.

6.7.4.2 Stagnant Volume

Figure 6.20 illustrates the effect of the dynamic saturation on the concentration profiles within the stagnant pores. As β_d increases, the time taken for C_s to match C_d is reduced. This is also evident in the results for the temporal concentration profiles, which begin to merge with each other (refer to Figures 6.20a, 6.20c and 6.20e).

From Figures 6.21a, 6.21c and 6.21e, as D_{ds} decreases, breakthrough time in the dynamic region increases and this has a knock down effect on the concentration profiles at the start of the pores. However, once the molecules are within the pores, the magnitude of D_{ds} has no influence on their transport. It has previously been shown in the results for the PE-D model (refer to sub-section 6.5.4), that the diffusion coefficient (D_{df}) is the dominant parameter affecting the concentration of solute molecules within the stagnant pores.

The effect that the value of X has on the PDE-D model output, is very similar to what was observed for the PE-D model. From Figure 6.22, it is evident that increasing X, increases the diffusion distance that solute molecules travel within the stagnant region. Hence, it takes longer for a uniform concentration profile to be established within the pores.

The reduced sensitivity of the dynamic region to parameter X is observed in the nearly identical dynamic curves when comparing Figures 6.22c and 6.22e. This meant that beyond a certain threshold, which is dependent on the magnitudes of the other parameters, further increases in X had no effect on the the dynamic region. This has was attributed to the presence of D_{ds}, decreasing the model's reliance on X to produce certain profile changes.

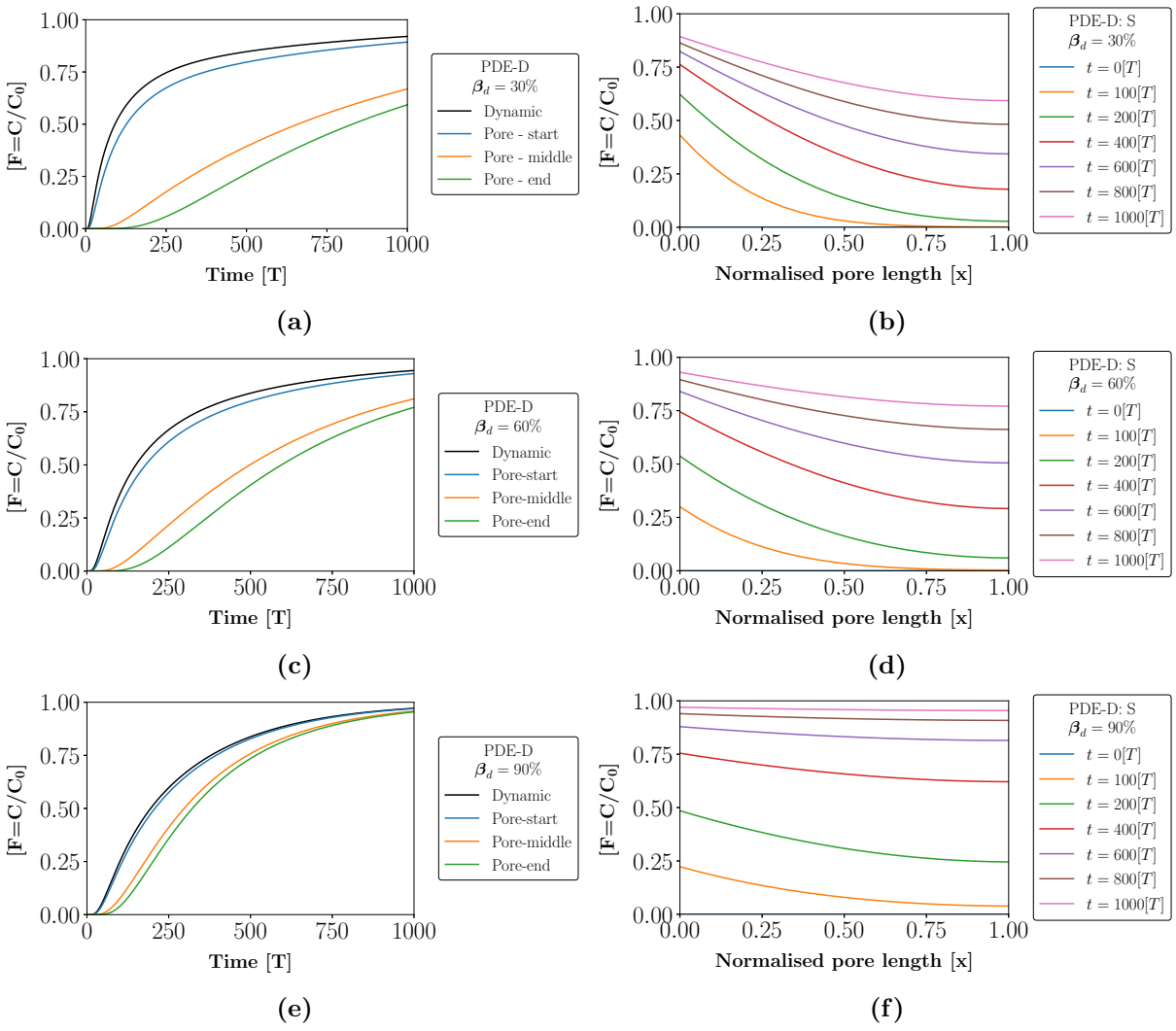

Figure 6.20: Response of the PDE-D model to changes in the dynamic saturation (β_d). Temporal change in concentration of the dynamic region and associated stagnant pore at three different locations are shown on the left. Spatial change in concentration profiles for the pore at different time points are shown on the right. [F - Normalised solute concentration, Time - Dimensional time units]. The value of the parameters kept constant during the analysis are (with dimensional units: [L] - length unit, [M] - mass unit, [T] - time unit): $\varepsilon = 0.4$ [-], $U = 10^{-4}$ [L/T], $\beta_T = 0.5$ [-] , $L = 0.31$ [L], $D_{df} = 10^{-6}$ [L^2/T], $D_{ds} = 10^{-5}$ [L^2/T] and $X = 0.1$ [L].

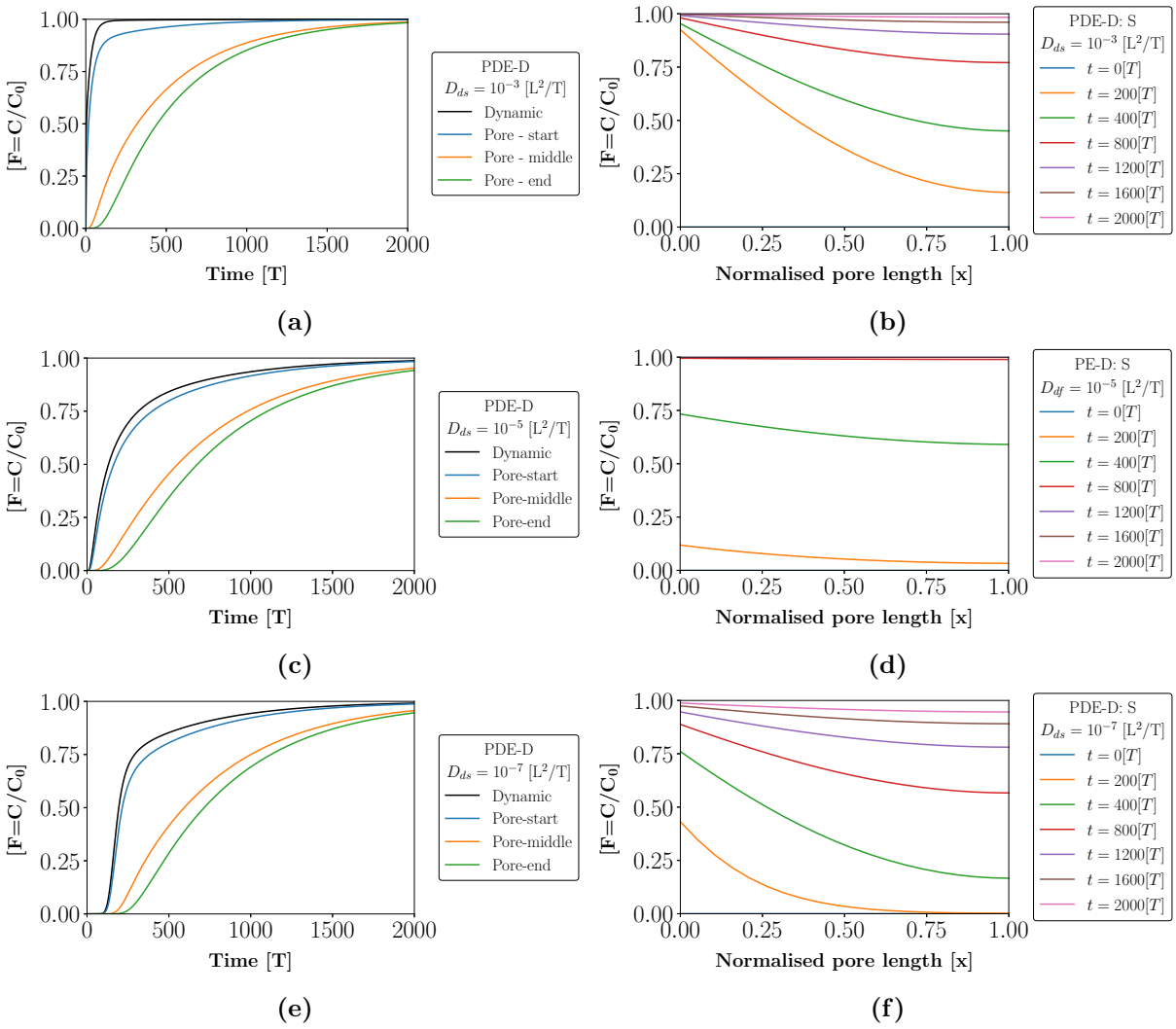

Figure 6.21: Response of the PDE-D model to changes in the dispersion coefficient (D_{ds}). Temporal change in concentration of the dynamic region and associated stagnant pore at three different locations are shown on the left. Spatial change in concentration profiles for the pore at different time points are shown on the right. [F - Normalised solute concentration, Time - Dimensional time units]. The value of the parameters kept constant during the analysis are (with dimensional units: [L] - length unit, [M] - mass unit, [T] - time unit): $\varepsilon = 0.4$ [-], $U = 10^{-4}$ [L/T], $\beta_T = 0.5$ [-] , $L = 0.31$ [L], $D_{df} = 10^{-6}$ [L^2/T], $\beta_d = 0.25$ [-], $X = 0.1$ [L].

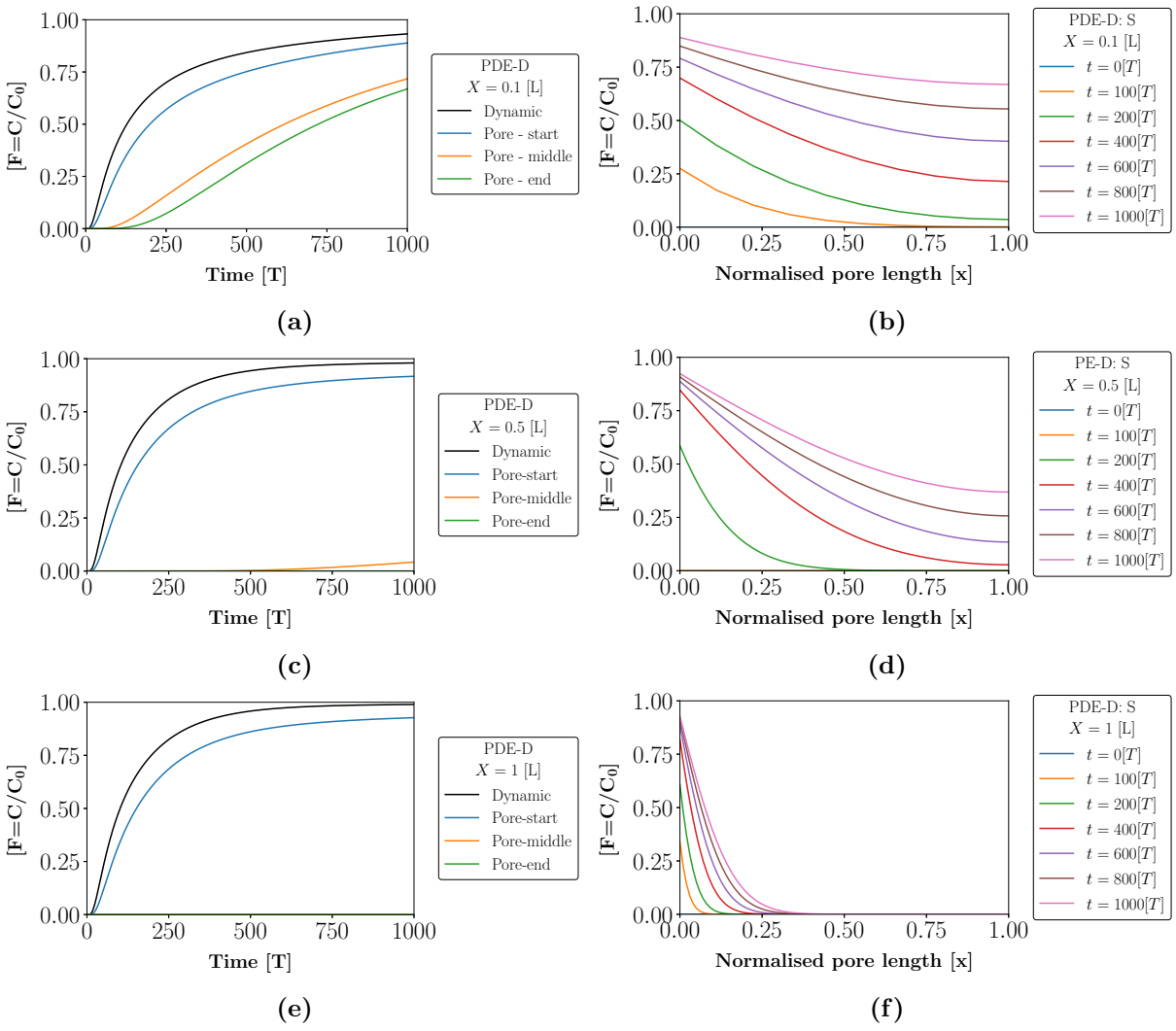

Figure 6.22: Response of the PDE-D model to changes in the pore length (X). Temporal change in concentration of the dynamic region and associated stagnant pore at three different locations are shown on the left. Spatial change in concentration profiles for the pore at different time points are shown on the right. [F - Normalised solute concentration, Time - Dimensional time units]. The value of the parameters kept constant during the analysis are (with dimensional units: [L] - length unit, [M] - mass unit, [T] - time unit): $\varepsilon = 0.4$ [-], $U = 10^{-4}$ [L/T], $\beta_T = 0.5$ [-] , $L = 0.31$ [L], $D_{df} = 10^{-6}$ [L^2/T], $\beta_d = 0.25$ [-] and $D_{ds} = 10^{-5}$ [L^2/T].

6.8 Chapter Summary

This chapter presented the model conceptualization, assumptions, equations, fitting algorithm and model response analysis of the nine different solute transport models chosen for this study. The chosen models comprised of four empirical models: three compartmental model configurations (CM-1, CM-2 and CM-3) and the tanks-in-series (TIS) model. Five semi-phenomenological models were also selected: the advection dispersion (AD) model, the piston exchange (PE) model, piston exchange diffusion variant (PE-D) model, the piston dispersion and exchange (PDE) model and the piston dispersion and exchange - diffusion variant (PDE-D) model. A summary of the controlled, experimentally obtained, calculated, fitted and output parameters for the selected models is shown in Table 6.8.

A model response analysis was conducted on the TIS, AD, PE, PE-D, PDE and PDE-D models to ascertain the effect of varying the different fitting parameters. The analysis was not done on the compartmental models due to their highly empirical nature. Increasing the number of tanks in series (N) of the TIS model brought about the expected increase in plug flow behaviour. Reductions in the dynamic saturation (β_d) of the PE, PE-D, PDE and PDE-D models brought about longer asymptotes in the RTD curves, indicative of the increased presence of stagnant volumes and non-ideal flow characteristics. Increasing the magnitude of the dispersion coefficient (D_{ds}) for the AD, PDE and PDE-D models brought about high degrees of solution channelling behaviour. The extent of this effect was found to be dependent on model formulation. Varying the overall mass transfer coefficient ($K_m a$) in the PE and PDE models led to increases in tracer breakthrough times at high magnitudes and the opposite effect at low magnitudes. However, these results were not as discernible when mass transfer was not the dominant factor.

The impact of varying the diffusional pore length (X) in the PE-D and PDE-D models revealed a complex interaction which showed that at high values of X, a more plug flow like profile is obtained in the dynamic region but this was coupled with long asymptotes in the latter part of the RTD curves. Decreasing its value led to a more dispersed profile but faster achievements of equilibrium concentrations. The results from the models showed that they gave practical responses to the varied parameters leading to the conclusion that they could

all be further tested through the analysis of RTD profiles generated from packed beds.

Table 6.8: Summary of model parameters for the selected models and how they were obtained.

Symbol	Model parameter	How it is obtained	Associated models
Controlled parameters			
C_0	Inlet solute concentration (-)	Controlled variable	CM-1, CM-2, CM-3, TIS
$C_d(0,t)$	Inlet solute concentration (-)	Controlled variable	AD, PE, PE-D, PDE, PDE-D
L	Packed bed length (m)	Controlled variable	AD, PE, PE-D, PDE, PDE-D
Q_T	Total volumetric flow rate (mL/min)	Controlled variable	CM-1, CM-2, CM-3, TIS
t	Time (min)	Controlled variable	All models
x	Spatial dimension - normalized length (-)	Controlled variable	PE-D, PDE-D
z	Spatial dimension - normalized length (-)	Controlled variable	AD, PE, PE-D, PDE, PDE-D
Experimentally, Literature obtained or calculated parameters			
β_T	Total saturation (m^3 liquid/m^3 void)	Calculated (experimental data)	PE, PE-D, PDE, PDE-D
D	Diffusion coefficient (m^2/min)	Obtained from literature	PE-D, PDE-D
ε	Total bed voidage (m^3 void/m^3 bed)	Measured	AD, PE, PE-D, PDE, PDE-D
τ	Mean residence time (min)	Calculated (experimental data)	TIS
τ_P	PFR residence time (min)	Calculated (experimental data)	CM-1, CM-2, CM-3
τ_C	CSTR residence time (min)	Calculated (model results)	CM-1, CM-2, CM-3
U	Superficial liquid velocity (m/min)	Calculated (experimental data)	AD, PE, PE-D, PDE, PDE-D
V_C	Volume of each CSTR (mL)	Calculated (model results)	CM-1, CM-2, CM-3, TIS
V_T	Total flow volume (mL)	Measured	CM-1, CM-2, CM-3, TIS
V_P	Plug flow volume (mL)	Calculated (experimental data)	CM-1, CM-2, CM-3
Fitted and output parameters			
β_d	Dynamic saturation (m^3 liquid/m^3 void)	Fitted variable	PE, PE-D, PDE, PDE-D
C_d	Normalized outlet solute concentration (-)	Main model output	AD, PE, PE-D, PDE, PDE-D
C_s	Normalized solute concentration (stagnant volume)(-)	Model output	PE, PE-D, PDE, PDE-D
D_{ds}	Dispersion coefficient (m^2/min)	Fitted variable	AD, PDE, PDE-D
$K_m a$	Overall mass transfer coefficient (min^{-1})	Fitted variable	PE, PDE
N	Number of CSTR tanks (-)	Fitted variable	TIS
V_C	Continuous stirred tank volume (mL)	Fitted variable	CM-1, CM-2, CM-3
V_D	Dead volume (mL)	Fitted variable	CM-1, CM-3
X	Pore length (m)	Fitted variable	PE-D, PDE-D

Chapter 7

RTD Experimental Design and Set-up

The design and set-up of the experimental rig for tracer tests form an integral part of the RTD data generation process. Important factors include the shape and physical dimensions of the bed, the construction material of its containment vessel, the state of its material prior to loading, the agglomeration procedure utilized for size mixtures, the loading methodology, the choice of irrigation fluid, mode of irrigation and data capturing components.

Since glycerol solutions with dissolved KCl were selected as tracer fluids, conductivity measurements will provide an efficient way of monitoring the concentration of KCl. Therefore, in terms of the data capturing components needed, it was necessary to design and test a conductivity measurement cell with a fitted conductivity probe in order to establish its response to various inputs. This response is decoupled from that of the packed beds.

This chapter begins with a brief background on tracer test with conductivity theory and its measurement found in Appendix F. The experimental design and methodology used during the set-up and testing of the different packed bed systems is highlighted. Different bed characterisation parameters are elucidated with a focus on how they are obtained. Lastly, details on the conductivity measurement cell's design, its mixing behaviour analysis and how this behaviour is accounted for during the processing of raw conductivity data is discussed.

7.1 Background: Salt Tracer Tests

Tracer tests are typically performed to elucidate symptoms of non-ideal or preferential flow in a packed bed through the analysis and modelling of the obtained RTD curve (Bouffard and Dixon, 2001; Bouffard and West-Sells, 2009; Zhang and Yuan, 2019). The main principle behind the test is that the movement of the tracer molecules mimic the fluid flow patterns

present within the bed system, hence the generated RTD curves can be considered flow profiles.

KCl was used a salt tracer due to its inert nature and its minimal impact on the solution's viscosity within the concentration range chosen (refer to section 4.1). Its concentration in the different solutions was obtained by measuring their conductivities. The step input form of tracer delivery was utilized in this study.

7.2 Experimental Apparatus and Methodology: Tracer Tests

This section provides an overview of the experimental rig used while conducting salt tracer tests, the design, packing and irrigation of the packed beds, the bed characterisation methodology and the design of a conductivity measurement cell.

7.2.1 Design, Packing and Irrigation of Test Column

The overview of the experimental rig is shown in Figure 7.1 while the important design elements of the PVC column used in the tests can be found in Figure 7.2. The column had an inner diameter of 100 mm and a total height of 500 mm. A standard bed height of 160 mm was used for a majority of the tests. A concentric drainage plate consisting of ± 3 mm apertures was placed approximately 60 mm from the base of the column to provide a liquid disengagement area. The column was wrapped with heating coils and insulated with aluminium foil. A temperature probe to measure the temperature within the column was inserted in the temperature probe port. The information obtained from this probe was relayed to the temperature control box which maintained the column's temperature at the user defined set temperature, which in this case was 30°C.

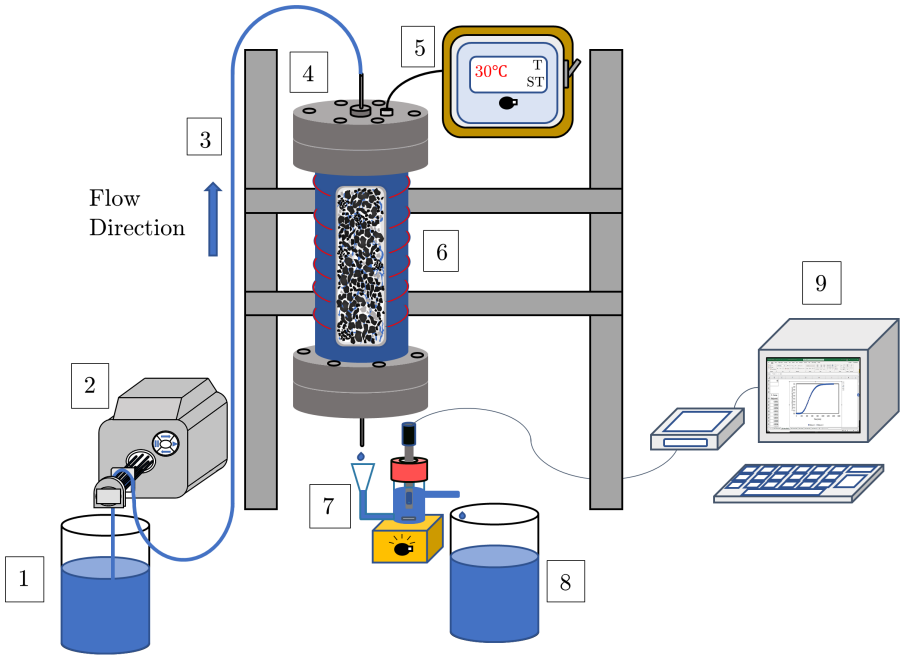

Figure 7.1: Illustration of the experimental set-up used to conduct tracer tests on the packing materials. It consisted of a (1) 20 L feed tank, (2) peristaltic pump, (3) pump plastic tubing, (4) cylindrical test column, (5) temperature control box, (6) heating coils, (7) conductivity measurement cell, (8) 20 L effluent tank and (9) desktop computer with data logging software (Graphical Analysis 4).

Before packing the column, a drainage layer, approximately 35 mm in height, consisting of two layers of 24 mm glass marbles was inserted at the base of the column. This was to prevent the elution of fines and the clogging of the drainage (refer to Figure 7.3).

For non-agglomerated packing, dry material was loaded into the column in small incremental masses using a scoop. No attempt was made to compact the bed, meaning the packing methodology was dry, random and non-compacted. For the agglomerated case, the desired mass of material was loaded into a cylindrical plastic bucket with an inner diameter of 32 cm and a total height of 40 cm. A measured volume of agglomeration solution, identical in composition to the irrigation solution but without KCl, was then poured onto the surface of the material in the bucket. The bucket was then rotated manually, alternating between a clockwise and anti-clockwise direction. This was done until the adhesion of a majority of the fine material to coarser particles was visually observed. Upon completion, the total amount of agglomeration moisture used was recorded and the agglomerated material was loaded into

the column using the same methodology as with the dry material. In this case however, the packing methodology can be classified as moist, random and non-compacted.

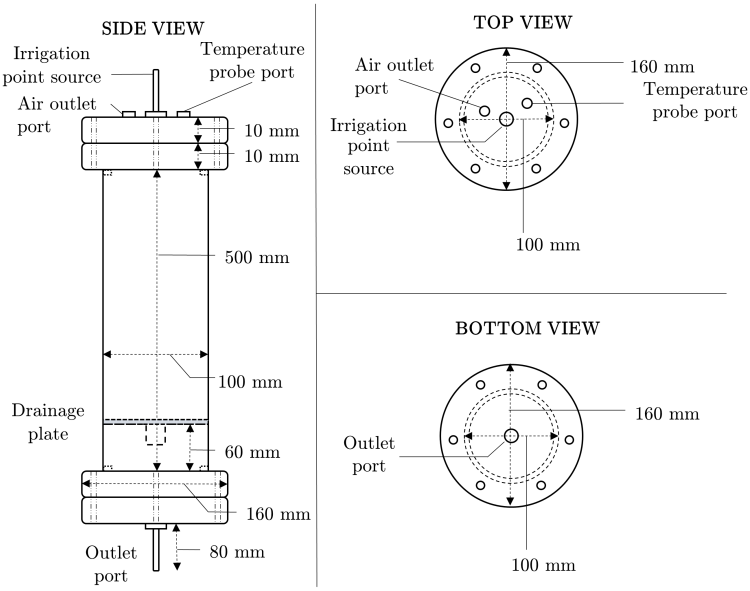

Figure 7.2: PVC cylindrical column dimensions used in tracer tests (Odidi et al., 2020).

Packed beds consisting of both narrow and mixed particle size fractions were tested. For the size mixtures, the Gates-Gaudin-Schumann (GGS) distribution function, shown in Equation (7.1), was used to ensure consistency in the amount of material added per size fraction. The cumulative fraction (R_F) of particles with a diameter less than or equal to d_p was calculated by raising the quotient of the selected and maximum particle diameter ($d_{p,max}$) present in the distribution to the power of m. The parameter m gives the measure of spread of particle sizes within the system. The GGS distribution function has been used in various other studies as a means of characterising the size distributions of different particle aggregates (Bouffard and Dixon, 2001; Macías-García et al., 2004; Vitez and Trávníček, 2011). For this study, m was chosen to equal 0.4 to mimic size distributions of leaching beds and the resulting size distribution for the various mixtures is presented in Figure 7.4. This value was kept constant across the different size mixtures in order to provide a good basis for future comparisons of other extrinsic bed parameters.

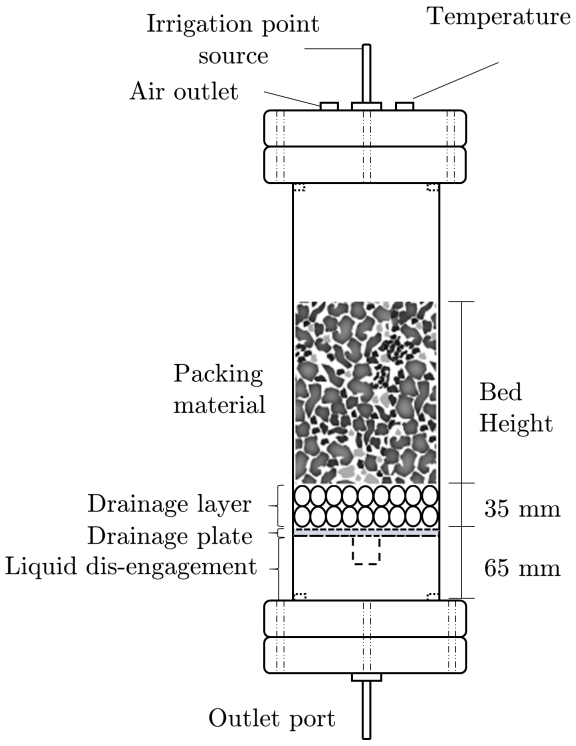

Figure 7.3: Illustration of how the packed beds were constructed (Odidi et al., 2020).

$$R_F(d_p) = \left(\frac{d_p}{d_{p,max}}\right)^m \tag{7.1}$$

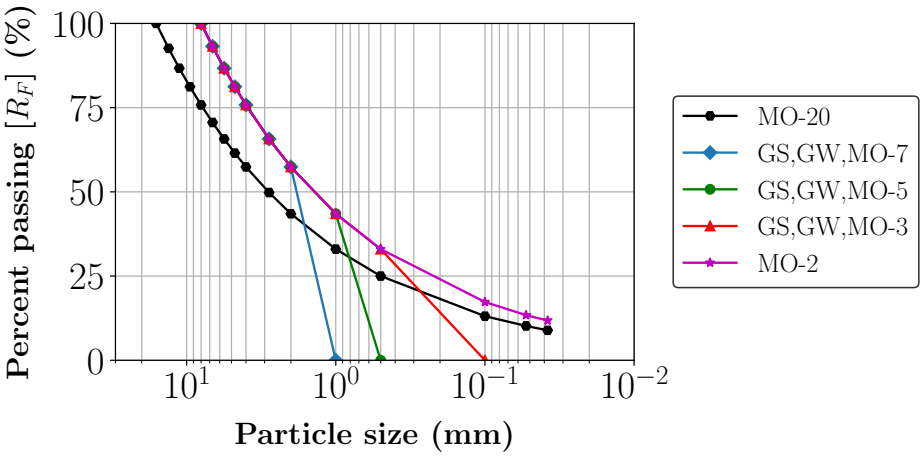

Figure 7.4: Particle size distributions of the various size mixtures formulated with the GGS distribution function that were used in the composition of different packed bed systems. R_F represents the mass percentage of particles with diameters passing specific sieve sizes.

The overall top particle size used in the tests was 16 mm. As the bed diameter was kept constant at 10 cm, the minimum bed to particle diameter ratio was 6.25. This was within the range, suggested by Yin et al. (2016), that alleviated wall effects.

How Tracer Tests were Conducted

1. The packed column was irrigated with a 0.7 g/L feed solution at an average flux of 5 L/(m^2.h) from the singular point source (Figure 7.1) using a peristaltic pump. U was calculated by dividing the volumetric flow rate (m^3/h) by the bed diameter (m^2).

2. The effluent from the packed bed was collected and measured until the volumetric flow rate of solution fed into it equalled the flow rate out of it (steady state).

3. The time required for steady state to be achieved varied from 10 minutes to more than 24 hours, depending on the packing.

4. The tracer test was then commenced by replacing the feed to the column with a KCl solution of higher concentration (e.g 3.7 and 7.5 g/L KCl - tracer solutions)

5. The conductivity of the solution exiting the column was logged using the conductivity measurement cell and Graphical analysis 4 software from the start of the tracer test.

6. Once the conductivity of the effluent solution stabilized, the test was concluded.

7. The conductivity data was plotted against time to obtain the cumulative RTD profiles. These were later normalised.

8. Two step-up tracer tests were done sequentially to ensure reproducibility of RTD profiles for all the bed systems.

9. The irrigation to the column was switched off and drain-down moisture was collected for 24 hours.

10. After the 24-hour drain-down period, the columns were flooded to obtain the liquid accessible bed voidage.

7.2.2 Bed Characterisation Methodology

The packed bed systems were characterised using seven different experimental parameters: bulk density, bed voidage, solution breakthrough time, tracer breakthrough time, total liquid hold-up, total saturation and 24-hour drain-down moisture.

The bulk densities were calculated by dividing the total mass of the dry packed bed's contents by its volume. This parameter gives an indication as to how densely the particle beds were packed. As none of the beds were compacted, the bulk densities were mostly influenced by the intrinsic properties of the different materials such as density, particle shape and porosity. In cases were slumping was visually observed to have occurred, approximate slump height was measured and commented on.

Bed voidage (ε) was defined as the ratio of the void volume (empty space) present within the bed to its total volume. It was obtained by gradually filling the bed's pore spaces with irrigation solution pumped upwards at a rate of approximately 9 mL/min. This was done upon the completion of a tracer test. The volume of solution fed plus the volume of moisture already contained within the bed made up the void volume. Therefore the total bed voidage values obtained using this method can be classified as the total liquid accessible bed voidage. Bouffard and Dixon (2001) utilized a similar methodology during their tracer experiments on a refractory gold ore bed. The drawbacks of this method included the slight level of subjectivity involved in determining the exact moment the void spaces at the top of the bed were adequately saturated, the possibility of trapped air bubbles leading to an underestimation of the voidage value as well as the need for an accurate balance on the amount of solution that was present within the bed. Compaction of the bed during flooding was not an issue as the original bed height was marked prior to saturation.

The solution breakthrough time has been previously defined as the time difference between irrigation commencement and the emergence of the first fluid droplets at the bottom of a packed bed. It gives an indication as to the intrinsic permeability of the bed. A highly permeable bed will rapidly conduct solution through it whilst a bed with low permeability will offer a greater resistance to fluid flow. It can also be used to identify symptoms of channelling behaviour as very quick breakthrough times (solution and tracer) along with low

levels of liquid hold-up could indicate a lack of uniform wetting, especially in drip irrigated beds.

The steady state tracer breakthrough time is similar to the solution breakthrough time parameter. In the case of a step-up tracer test, it refers to the time difference between the commencement of the tracer feed irrigation and the time at which the first distinctive rise in tracer concentration in the bed's effluent is measured. It is obtained through the analysis of the generated cumulative RTD curves and gives an indication as to the degree of plug flow behaviour as well as the relative amount of mobile liquid volume present within the bed at steady state.

The total liquid hold-up (ϕ_l) is the ratio of liquid volume to total bed volume in an irrigated packed bed, as shown by Equation (2.6). Only minor levels of slumping were observed in a few of the tests and it did not have a substantial impact on the total bed volume, which was measured prior to irrigation. The total liquid volume is the accumulated solution volume within the packed bed in the time period between the start of irrigation and the establishment of steady state. It is similar to the total liquid saturation (β_T) parameter, which is the total liquid volume divided by void volume. The total liquid hold-up comprises of both dynamic and stagnant solution. In this thesis, the term stagnant solution refers to immobile volumes that are still accessible to solute molecules at steady state, mainly by diffusion. While the term isolated/dead volumes is used to refer to immobile solution that is completely sealed off from bulk fluid movement and is not accessible to tracer molecules at steady state, not even by diffusion. Stagnant solutions are believed to form through capillary suction effects during the wetting phase of a bed whilst isolated solution volumes are believed to form through the mechanical dispersion of fluid droplets by the solid packing leading to their random displacement within the bed.

The 24-hour drain-down moisture values were obtained from the studied packed bed systems after tracer tests were completed. The feeds to the individual bed systems were stopped and the moisture exiting each bed was collected and measured for a period of 24 hours. This methodology has been used by authors such as Bouffard and Dixon (2001) and Ilankoon and Neethling (2013) to obtain the dynamic liquid hold-up within a packed bed. However, as

discussed in sub-section 2.6.3, for certain bed systems, the 24-hour period proved insufficient to obtain an accurate estimate of the total amount of mobile solution. Hence, in this study, the measured 24-hour drain-down moisture was expressed as a percentage of total liquid hold-up and taken as a rough indication of a bed's dynamic solution volume.

7.2.3 Conductivity Measurement Cell Design

The design of the conductivity measurement cell was optimized to meet three requirements:

1. It needed to accommodate the fitting of a conductivity probe.
2. The measurement cell needed to contain a sufficient amount of solution to fully immerse the electrodes of the fitted probes.
3. The design needed to limit any excess volume to ensure that the measurement cell remained as sensitive as possible to changes in its inlet concentration

The chosen design consisted of the following components (refer to Figure 7.5) :

- Plastic funnel
- Rubber tubes
- Cylindrical glass vessel with two ports

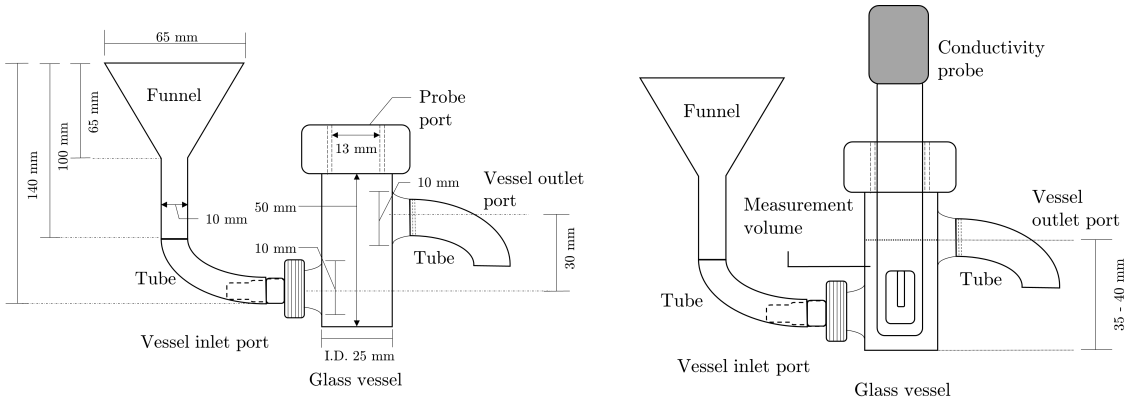

Figure 7.5: Conductivity measurement cell design (a) without conductivity probe and (b) with conductivity probe inserted

The funnel was used to direct the effluent solution from the column into the glass vessel, which contained the conductivity probe. The vessel's inlet was located near its base therefore, the collected solution flowed upwards and exited at the outlet port located near the vessel's top. The vessel had a working volume of approximately 17 mL with the Vernier conductivity probe inserted (Figure 7.5b). It was placed on a stirrer platform and a small magnetic stirrer was used to agitate its contents and ensure uniformity in its concentration, eliminating the presence of dead volumes.

7.2.3.1 Measurement Cell Diagnostics

In order to ascertain the mixing profile of the conductivity measurement cell for a step change in tracer concentration, a few diagnostic tests were run. The first step was to calibrate the conductivity probes used in the measurement cell. The second step was to test the cell's response to a single step change in its feed concentration of KCl. The third step was to tests its response to multiple step changes in its feed concentration of KCl.

7.2.3.2 Conductivity Probe Calibration

Calibration of the Vernier Conductivity Probe consisted of preparing 50 mL of aqueous glycerol solutions of varying concentrations of KCl ranging from 0 to ∼11 g/L. The equation used to relate the conductivity readings in millisiemens (mS) to concentration in grams per litre (g/L) is the straight line equation given by Equation (7.2). The linear trend lines fitted to the raw data are shown in Figure 7.6. The relevant properties of the solutions and the values of the fitted parameters (m and c) can be found in Table 7.1. The results show that the concentration of KCl was proportional to the conductivity of all the solutions over the concentration range measured (refer to Figure 7.6).

$$y = mx + c \tag{7.2}$$

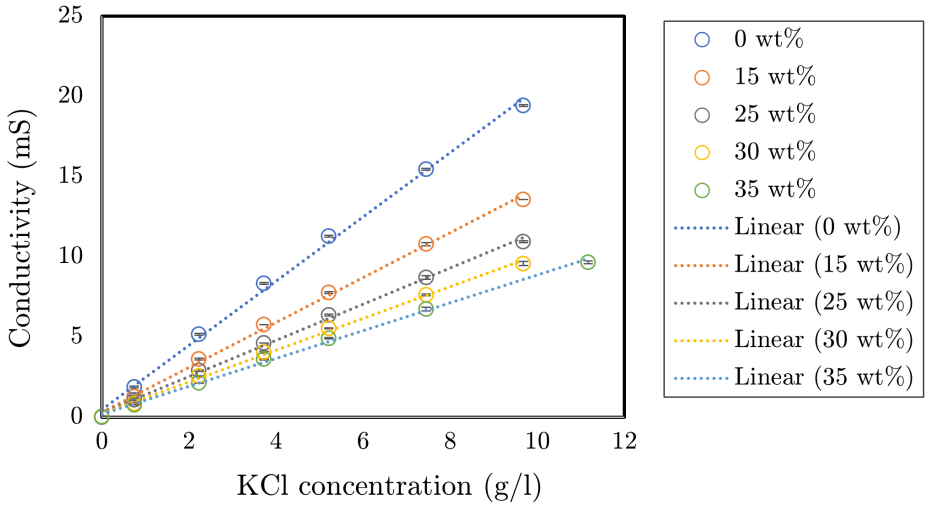

Figure 7.6: Calibration curves obtained for aqueous glycerol solutions (concentration represented as wt%) with dissolved KCl.

Table 7.1: Values of gradient (m), y-intercept (c) and regression coefficient (R^2) obtained from the linear trend lines used to fit the calibration data for different viscous solutions with dissolved KCl.

Glycerol (wt%)	μ (cP)	m	c	R^2
0	0.8	2.00	0.48	0.9975
15	1.2	1.40	0.31	0.9979
25	1.6	1.13	0.27	0.9978
30	1.9	0.99	0.21	0.9977
35	2.2	0.87	0.19	0.9976

7.2.3.3 Mixing Behaviour in Measurement Cells - Methodology

The design of the measurement cell required that its contents be agitated in order to ensure uniformity in its solute concentration. It was therefore necessary to obtain its cumulative RTD profile as a means of quantifying its mixing behaviour. This would enable the decoupling of the mixing effects present in the measurement cell from that of the packed bed system during subsequent tracer tests. The cumulative RTD profiles were obtained by conducting single and multiple-step tracer tests on an individual conductivity measurement cell with a fitted conductivity probe.

Single Step Tracer Test - Effect of Tracer Concentration

The effect of tracer concentration on the cumulative RTD profiles for the measurement cells was ascertained using a singular feed and three different concentrations of tracer solutions. The solutions were formulated by adding specific amounts of KCl salt to volumetric flasks which was then dissolved in deionized water. The feed solution had a 0.7 g/L concentration of KCl while the three tracer solutions possessed concentrations of 2.2 g/L, 5.2 g/L and 7.5 g/L KCl, respectively.

Before the start of the step up tracer tests, the cell was then filled with the feed solution and its contents were stirred using a magnetic stirrer. At time = 0, the chosen tracer solution was pumped into the funnel at a rate of approximately 0.7 mL/min (refer to Figure 7.7). The conductivity of the solution within the measurement cell was automatically logged using the Graphical Analysis 4 software loaded on a desktop computer. The tests were terminated once the conductivity readings within the cell stabilised. Tests were done in triplicates.

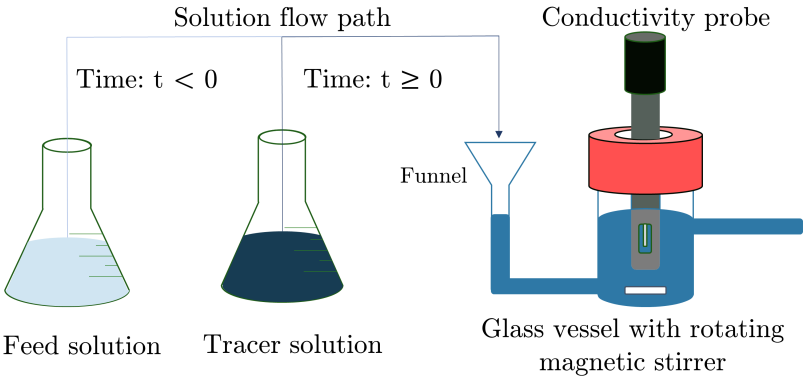

Figure 7.7: Illustration of how the single step tracer tests were carried out on the conductivity measurement cell.

Single Step Tracer Test - Effect of Solution Viscosity

The effect of solution viscosity on the mixing profile of the measurement cell was tested using five glycerol solutions. For the feed solutions, 0.7 g/L of KCl was added to each of the

glycerol solutions. For the 0 to 30 wt% glycerol solutions, 7.4 g/L KCl was added to make up the tracer solutions. In the case of the 35 wt% glycerol solution, 9.7 g/L KCl was added to counteract the dampening effect an increase in viscosity had on conductivity as shown in Figure 7.6. The tracer tests were conducted as just described (Figure 7.7).

Multiple Step Tracer Test

For an actual tracer test on a packed bed system, the KCl concentration of the feed to the measurement cells would be constantly changing. Based on this scenario, it was necessary to test the effect that multiple step inputs of tracer solutions with increasing KCl concentrations, had on the mixing profile within the measurement cell. Figure 7.8 illustrates how these tests were carried out.

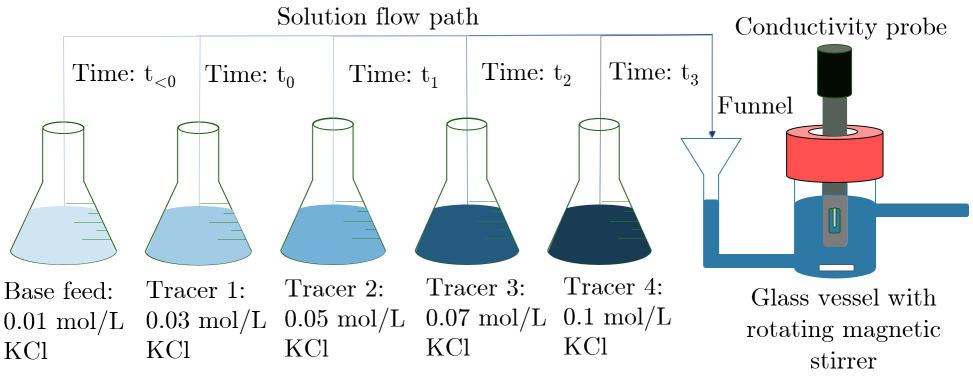

Figure 7.8: Illustration of how the multiple step tracer tests were carried out on the conductivity measurement cell.

Five solutions were formulated through the dissolution of specific amounts of KCl in deionized water: a base feed solution (0.7 g/L KCl) and four tracer solutions (2.2 g/L, 3.7 g/L, 5.2 g/L and 7.5 g/L KCl). Tests were conducted similarly to the single step tracer test with the feed solution to the cell changed at specific times. Tests 1 to 4 used 10, 15, 20 and 30 minute intervals, respectively, between concentration changes.

7.2.3.4 Mixing Behaviour in Measurement Cells - Results and Discussion

Single Step Tracer Test - Effect of Tracer Concentration

Figure 7.9b shows that the normalised F-curves for the different tracer solutions are all almost identical. This indicates that the normalised cumulative RTD profile for the measurement cell is independent of the tracer concentration used over the range tested. This is a crucial finding as it forms the basis for the subsequent modelling work done to account for the mixing in the measurement cells.

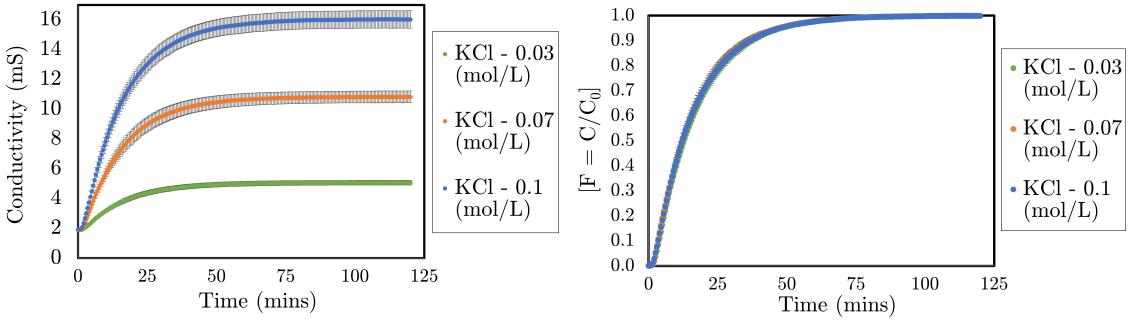

(a) **(b)**

Figure 7.9: Average conductivity (a) and average normalised cumulative RTD (b) profiles for the single step tracer tests conducted on the conductivity measurement cell with 2.2, 5.2 and 7.5 g/L KCl aqueous tracer solutions

Single Step Tracer Test - Effect of Solution Viscosity

Figure 7.10a shows the reduction in conductivity measurements with an increase in solution viscosity. The curve for the 35 wt% glycerol solution reaches a higher maximum conductivity value than that for the 30 wt% glycerol solution due to the higher concentration of KCl used in its case. Despite differences in absolute conductivity readings, the normalised F-curves shown in Figure 7.10b are all nearly identical. This indicates that similar to tracer concentration, viscosity did not have an impact on the mixing behaviour of the measurement cell over the viscosity range tested. Hence, the effect of solution viscosity, within this range, could be ignored when accounting for the cell's mixing behaviour.

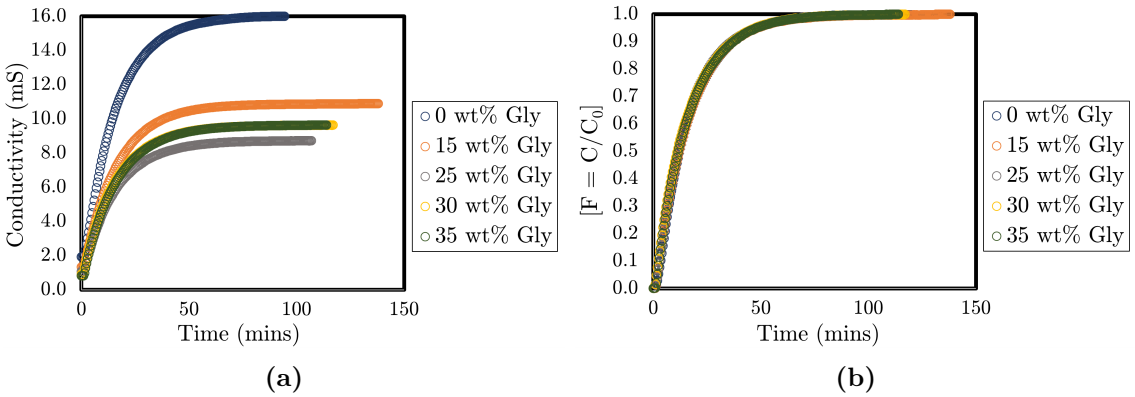

Figure 7.10: Average conductivity (a) and average normalised cumulative RTD (b) profiles for the single step tracer tests conducted on the measurement cell with 0, 15, 25, 30 and 35 wt% glycerol solutions with dissolved KCl as the tracer.

Multiple Step Tracer Test

Figure 7.11 shows the normalised output concentration profiles from the measurement cell when subjected to multiple step increases in inlet tracer concentrations. Increasing the time interval between each change in step input resulted in a more staggered response from the measurement cell. This is evident when comparing Figures 7.11a and 7.11d.

However, the important fact to note is that the mixing profile remains constant and is independent of concentration across equal time intervals. This can be visually observed in Figure 7.12 which divides the graph in Figure 7.11d into three sections to illustrate the identical nature of the mixing profiles. The last section was omitted as its time interval was greater than the previous three, hence it possessed a long asymptote.

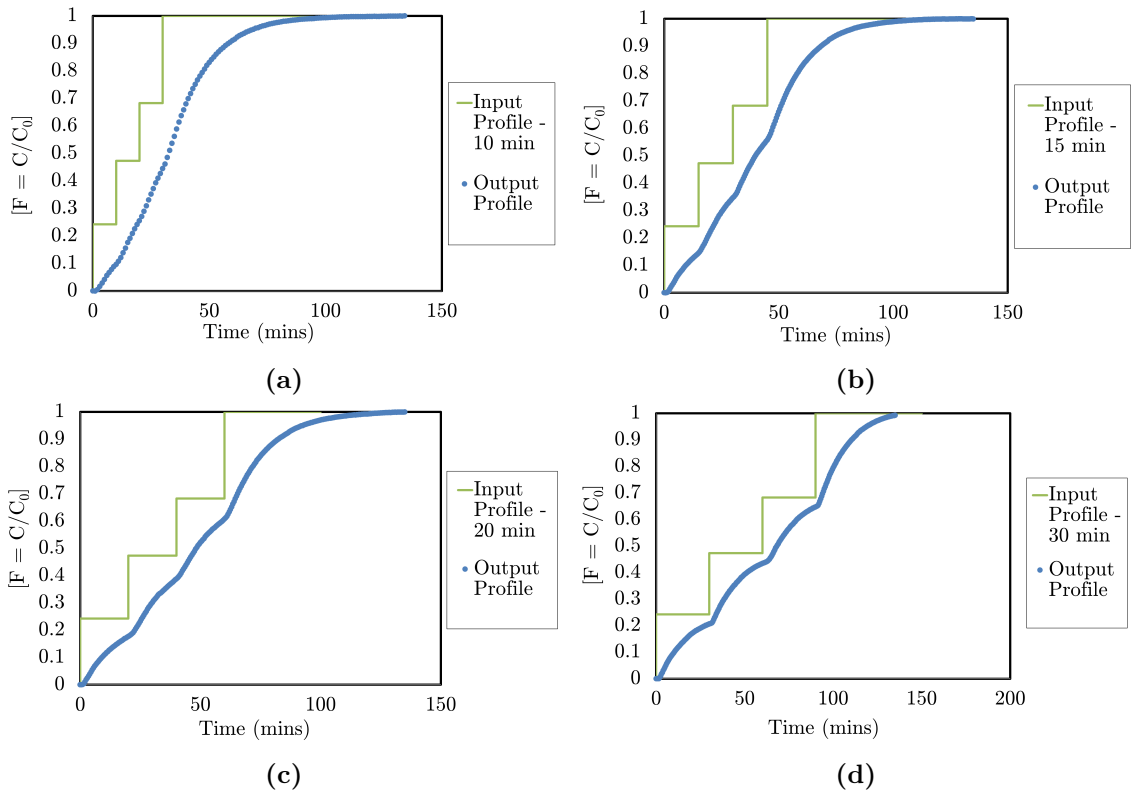

Figure 7.11: Normalised concentration profiles obtained from the multiple step tracer tests carried out on the measurement cell using time intervals of (a) 10 minutes, (b) 15 minutes , (c) 20 minutes and (d) 30 minutes between each change in input.

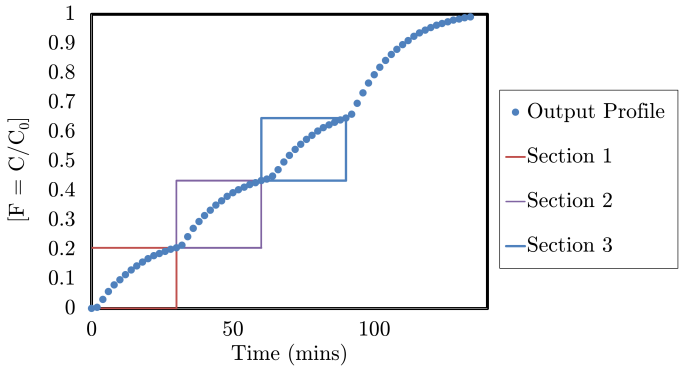

Figure 7.12: Illustration of the identical nature of the mixing profiles at each interval, prior to the last, for the multiple step tracer tests (Time interval = 30 minutes)

7.2.4 Accounting for Mixing In Measurement Cell

One of the common ways to take the mixing effects in a measurement cell into account is to assume that the cell is a well mixed system and can be described by the characteristic equation for a CSTR. Though this method is useful, it has a few draw backs that necessitated its modification. The original approximation method and its modified form will now be discussed.

7.2.4.1 CSTR Approximation Method

Assuming that the measurement cell can be approximated as a CSTR, the characteristic equation of its mixing profile without any reactions was given by Equation (6.3). Writing this equation in integral form and rearranging to find C_{in} resulted in:

$$\int_0^t C_{in}dt = C_{out}(t)\tau_r + \int_0^t C_{out}dt \tag{7.3}$$

Using the classic definition of an integral shown in Equation (7.4) for a function $f(x)$ that is continuous in the interval $[a, b]$ and is divided into n subintervals of equal width, Δx, with a point from the subinterval (x_i^*) being chosen, Equation (7.3) could be approximated as Equation (7.5).

$$\int_a^b f(x)dx = \lim_{n\to\infty} \sum_{i=0}^{n} f(x_i^*)\Delta x \tag{7.4}$$

$$\sum_{i=0}^{n} C_{in,i}\Delta t \approx C_{out,n}\tau_r + \sum_{i=0}^{n} C_{out,i}\Delta t \tag{7.5}$$

Equation (7.5) could be simplified to obtain the inlet concentration entering the measurement cell as shown in Equation (7.6):

$$C_{in,n} \approx \frac{C_{out,n}\tau_r}{\Delta t} + \sum_{i=0}^{n} C_{out,i} - \sum_{i=0}^{n-1} C_{in,i} \tag{7.6}$$

One of the major assumptions in the derivation of Equation (7.6) was that there existed a time interval, Δt, during which the inlet concentration to the measurement cell remained constant. The validity of this assumption was dependent on the length of this time interval

as well as the response time of the measurement cell for the particular system being studied. Shorter time intervals are to be used for systems with quick response times and *vice versa*. One of the main draw backs with this method was that a single Δt must be be chosen at the start and maintained during the course of the calculation for stability reasons. This was alluded to in the preamble to Equation (7.4). In certain cases however, having a single Δt resulted in fluctuations and a lack of adequate discernible trends. The former caused by sections of the original curve with a cramming of data points and the latter by sections with a sparse distribution of points. In such cases being able to change the value of Δt for different sections of the curve would allow for a smooth approximated profile to be generated.

7.2.4.2 Compartmental Model Approximation Method

A modified version of the CSTR approximation method was developed to allow for more flexibility with regards to the time intervals used during calculations of C_{in}. The method had two stages. The first was the fitting of a compartmental model configuration consisting of a PFR and CSTR in series (refer to Figure 7.12) to the normalised mixing profile shown in Figure 7.9b. The second step was to use the fitted equation to calculate the tracer concentration of the inlet solution to the measurement cell.

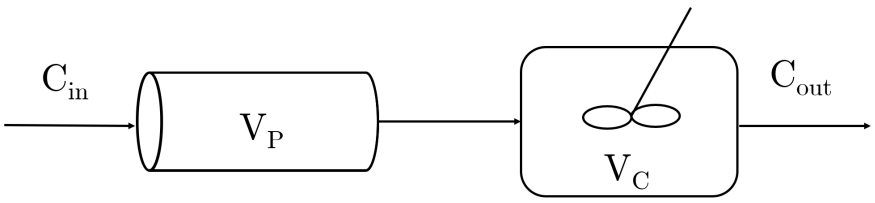

Figure 7.13: Compartmental model configuration used in characterising the mixing profile in the conductivity measurement cell, where C_{in} is the concentration of the feed to the cell.

7.2.4.3 Fitting of Compartmental Model to Measurement Cell

The compartmental model configuration was chosen based on a qualitative analysis of the mixing profile from the measurement cell (refer to Figure 7.9b). The profile showed a relatively small lag period followed by the typical S-shape curve associated with the cumulative

RTDs from CSTRs. The PFR component was used to simulate the lag period. The model equation (Equation (7.7)) is a slight modification to the CM-1 model equation. In this case, the time is adjusted for the lag period caused by the PFR component.

$$C_{out} = 1 - e^{-\frac{t-\tau_P}{\tau_C}} \tag{7.7}$$

Equation (7.7) was fitted to the normalised output concentration profile from the measurement cells using the *Solver* function on Microsoft® Excel® software from Microsoft 365 MSO. The regression coefficient (R^2) was optimized to its max value by varying the CSTR residence time. The results are shown in Figure 7.14. The optimized model parameter values can be found in Table 7.2.

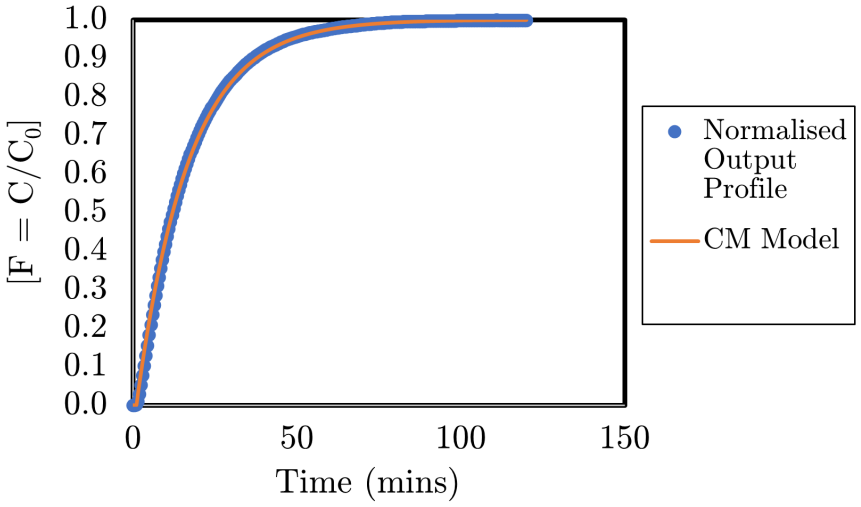

Figure 7.14: Fitting of the compartmental model to the normalised mixing profile for the conductivity measurement cells.

Table 7.2: Regression coefficient (R^2) and optimized compartmental model parameter values obtained for the fitted model curve.

Model parameters	Optimized value	Units
Q	0.7	mL/min
τ_P	1	min
τ_C	15.9	min
R^2	1.000	(-)

The results show the compartmental model configuration was able to accurately describe the normalised mixing profile of the measurement cell. This is based on a qualitative analysis of the model fit as well as the significantly high R^2 value of 1.000 obtained. This made it possible to calculate the normalised concentration at any time chosen within the tested range.

7.2.4.4 Modelling Out Of Mixing Effects Using CM Model

The methodology used in accounting for the mixing effects present in the measurement cell can be explained with the aid of an annotated diagram shown in Figure 7.15. This diagram represents a hypothetical inlet and outlet concentration profile for the measurement cell. A time interval, represented by Δt in the figure, during which the concentration of tracer molecules entering the measurement cell is assumed to be constant, is again utilized. This assumption carries the same limitations as mentioned previously in sub-section 7.2.4.1.

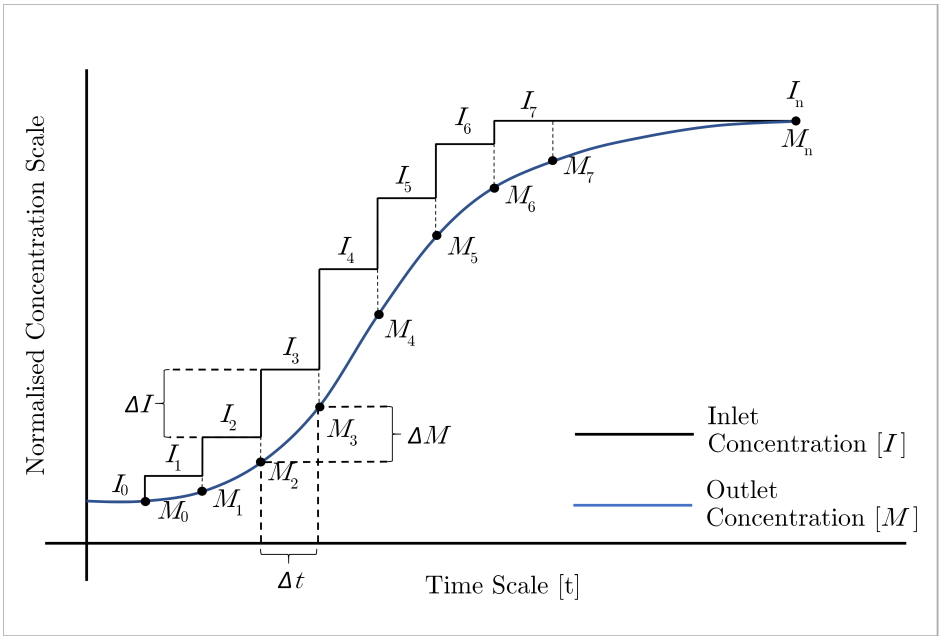

Figure 7.15: An annotated diagram depicting a step-wise increase in inlet tracer concentration of the measurement cell and the resulting outlet concentration profile. Used in the development of the compartmental model approximation method.

In this scenario, at the beginning of each time interval, the tracer concentration at the inlet

to the measurement cell increases by a variable ΔI. This causes a corresponding increase in the outlet concentration denoted by another variable, ΔM, during the same interval. As the conductivity probes are located inside the measurement cell, it is the M data points (outlet tracer concentration) that would be experimentally obtained. Therefore, the goal of this methodology is to be able to calculate the I data points (inlet concentration) using the M points. To do this, both Figures 7.14 and 7.15 are utilized.

In Figure 7.15, $I_0 = M_0$ as both points represent the concentration of the feed solution to the cell prior to any influx of tracer molecules. The initial lag period in both Figures 7.14 and 7.15 can be ignored at the start. A variable, F_t, is assigned to represent the normalised concentration value calculated at a time equal to Δt for just the CSTR component of the fitted compartmental model in Figure 7.14. This is done using Equation (7.8) with the optimised compartmental model parameters. The lag in response time, represented by the plug flow volume is taken into consideration during the final step of the approximation as it only needs to be accounted for once.

$$C_{out} = 1 - e^{-\frac{t}{\tau_C}} \tag{7.8}$$

A sample calculation of F_t for a Δt of 10 minutes is shown below:

$$\begin{aligned} F_t &= 1 - e^{\frac{-t}{\tau_C}} \\ &= 1 - e^{\frac{-10}{15.91}} \\ &= 0.467 \end{aligned} \tag{7.9}$$

This F_t value is then used in Equation (7.10) to calculate the inlet concentration at the point representing the onset of tracer molecules entering the well mixed portion of the measurement cell.

$$\begin{aligned} M_1 &= F_{t1}(I_1 - I_0) \\ \therefore I_1 &= \frac{M_1}{F_{t1}} + I_0 \end{aligned} \tag{7.10}$$

To explain in words what Equation (7.10) represents: it states that for a time interval of Δt, the tracer concentration in the liquid in the measurement cell will only manage to reach

a fraction of the inlet concentration. This fraction is represented by F_t, which takes on values ranging from 0 to 1. Therefore, in 10 minutes, an increase in the inlet concentration of $(I_1 - I_0)$ [M/L^3] will translate into a 0.467 $\times$ $(I_1 - I_0$) [M/L^3] increase in the outlet concentration.

It is important to note that the accuracy of this method is dependent on the assumption that the mixing behaviour of the measurement cell is constant, which was confirmed by the previous results within the range tested. This imposed a requirement that the flow rate to the cell be kept within the range of 0.7 mL/min.

In order to calculate the inlet concentration at the next time point, the concentration deficit from the previous time step must be added to the new change in inlet concentration whilst also taking into account the new base concentration level, M_1. This is shown in Equation (7.11).

$$\begin{aligned} M_2 =& F_{t2}(I_2 - M_1) + M_1 \\ \therefore I_2 =& \frac{M_2 - M_1}{F_{t2}} + M_1 \end{aligned} \tag{7.11}$$

The trend shown in Equation (7.11) carries on until the final point and can be rewritten in a more general format shown in Equation (7.12). As each point along the I staggered curve is calculated individually, different values of Δt can be used.

$$\begin{aligned} M_n =& F_{tn}(I_n - M_{n-1}) + M_{n-1} \\ \therefore I_n =& \frac{M_n - M_{n-1}}{F_{tn}} + M_{n-1} \end{aligned} \tag{7.12}$$

After adjusting for the CSTR component of the measurement cell, the next step is to account for the lag phase. This is simply done by subtracting the lag time or shifting the approximated RTD curve to the left by a time equal to τ_P.

The main advantage this method had over the previous CSTR approximation method, was its ability to utilize different Δt and F_t values at different points whist still maintaining stability. Small Δt values could be used for sections of the concentration curve experiencing rapid changes in concentration values and large Δt values could be used for sections with more gradual changes.

7.2.4.5 Testing of the Compartmental Model Approximation Method

The accuracy of the compartmental model approximation method in accounting for the mixing effects within the measurement cell was tested in two different ways.

The first test involved simulating a tracer test on two CSTRs individually and also in series based on their characteristic equations. In this simulation, the first CSTR represented a packed bed and the second represented the measurement cell. The mixing in the second CSTR was modelled out of the cumulative RTD profile for the two CSTRs in series using the compartmental model approximation method. The result was then compared to the analytical solution for the cumulative RTD of the first individual CSTR. ‘

The second test involved taking the data from the multi-step tracer tests conducted on the measurement cell, shown in Figure 7.11, and modelling out its mixing effects using the same method. The resultant curve was then compared to the input profiles fed to the measurement cell.

CSTRs in Series Test

All simulations for this test were done using SciLab version 6.0.1 open source software. The two CSTRs shown in Figure 7.16 were simulated using the analytical equation for a CSTR (Equation (7.8)). For the simulation of the tanks in series, the SciLab *ode* function was used to integrate Equation (7.13). The parameter values used in all the simulations are shown in Table 7.3. The results are shown in Figure 7.17.

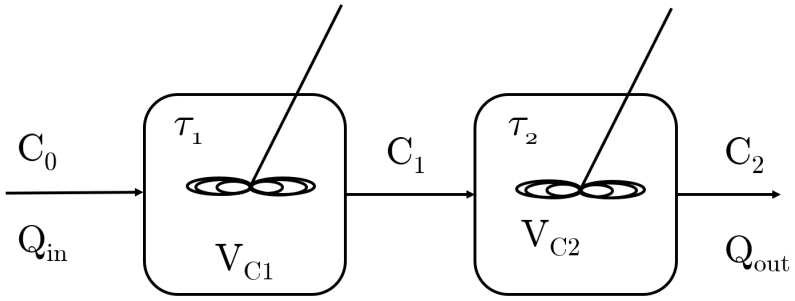

Figure 7.16: Illustration of the two CSTRs in series simulated during the testing of the compartmental model approximation method.

$$\frac{dC_2}{dt} = \left(\frac{1}{\tau_2}\right)\left(C_0 - C_0 e^{\left(\frac{-t}{\tau_1}\right)} - C_2\right) \tag{7.13}$$

Table 7.3: Values of the different parameters used during the simulation of two CSTRs.

Model parameters	Values	Dimensional units
C_0 [at t $\geq$ 0]	1	(-)
C_2 [at t = 0]	0	(-)
Q_{in}	0.7	[L^3/T]
Q_{out}	0.7	[L^3/T]
τ_1	28.6	[T]
τ_2	21.4	[T]
Δt	1	[T]
V_{C1}	20	[L^3]
V_{C2}	15	[L^3]

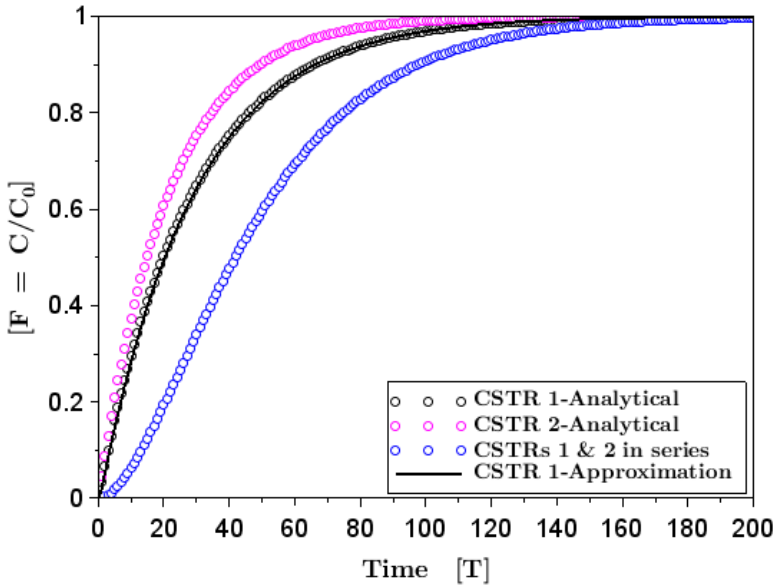

Figure 7.17: Simulated outlet concentration profiles for two CSTRs, both individually and in series. The approximate profile for CSTR 1 was derived from the two CSTRs in series' profile using the compartmental model approximation method.

The results during the simulation of the two CSTRs, show that the analytical and approximated outlet concentration profiles for CSTR 1 are nearly identical, with an R^2 coefficient

of 0.9999 when comparing the fit of the approximated to the analytical. Based on this, the compartmental model approximation method was successful in modelling out the mixing effects produced by CSTR 2 from the tanks in series profile.

Multiple Step Tracer Test

The next test of the compartmental approximation method involved taking the results shown in Figure 7.11 and re-deriving the input profile of the tracer concentration fed to the measurement cells as shown in Figure 7.18.

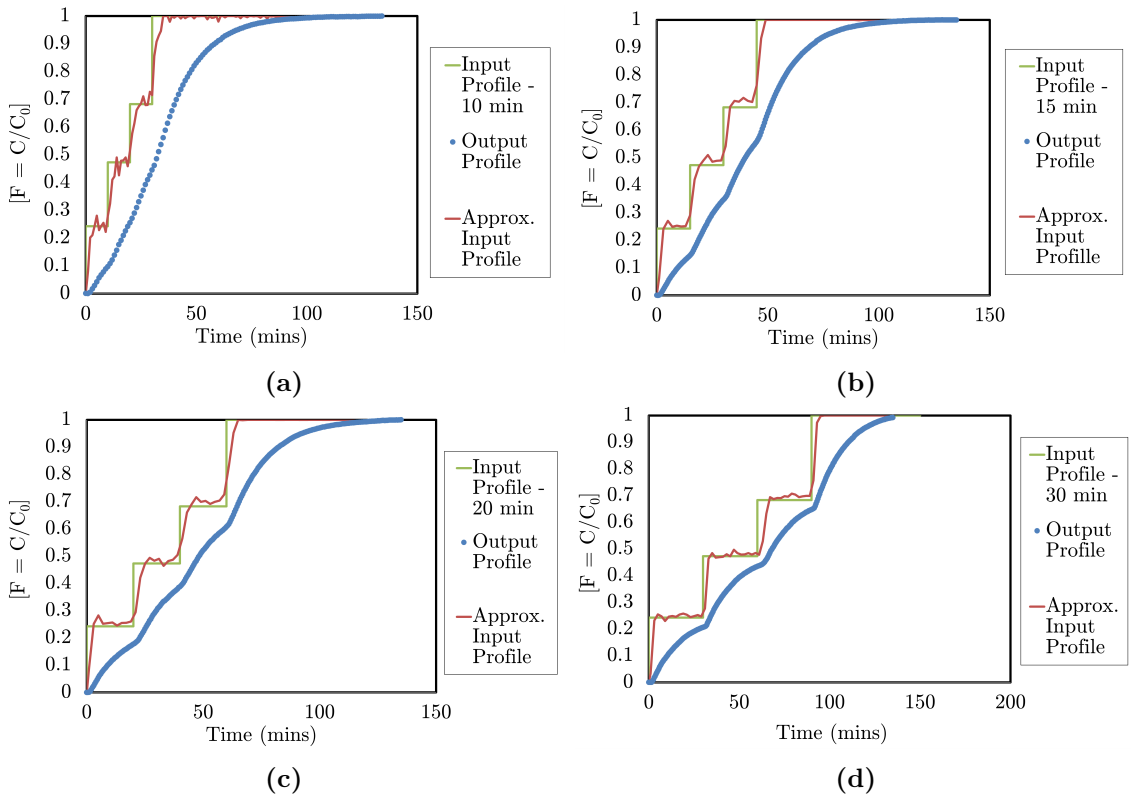

Figure 7.18: Actual and approximated input concentration profiles used during the multiple step tracer tests carried out on the measurement cell using time intervals of (a) 10 minutes, (b) 15 minutes , (c) 20 minutes and (d) 30 minutes between each change in input. The approximated input profiles were calculated using the compartmental model approximation method to account for the mixing effect in the measurement cells.

It can be seen that the approximation method was able to reproduce the major aspects of the input concentration profiles. The minor fluctuations were due to the inherent variations in the measured outlet concentration data and not introduced by the method itself. This

claim is supported by the smooth approximated concentration profile obtained during the two CSTRs in series simulations (refer to Figure 7.17). Therefore, minor fluctuations in the output data are expected to be caused by more pronounced fluctuations in the input data as the mixing in the measurement cell dampens their effect. The fluctuations are less pronounced for the longer time intervals ($\Delta t = 20$ and 30 mins) as the inlet concentration profiles were kept constant for longer, leading to greater stability in the outlet profiles. Overall, the method was able to model out the mixing effects present in the measurement cell to a sufficient degree.

7.3 Chapter Summary

This chapter presented the details on the experimental set-up for conducting salt tracer tests on different packed bed systems. The main components of the set-up consisted of an insulated cylindrical PVC column and a conductivity measurement cell. The packing methodology employed was dry/moist, random and non-compacted. A step tracer delivery method was chosen. The packed columns were irrigated from a central port located at the vessel's top. Solution would then exit the column from its outlet port, located at the bottom. The eluted solution was fed into a conductivity measurement cell consisting of a funnel, glass vessel and conductivity probe. This allowed for the online monitoring of KCl concentration in the collected solution.

The compartmental model approximation method was developed and found to be a viable way for accounting for the mixing effects in the measurement cell. This allowed for the cumulative RTD profile of the packed bed to be decoupled from that of the measurement cell and could be used in subsequent tracer tests.

Seven bed characterisation parameters were chosen, which were: the bulk density, bed voidage, solution breakthrough time, tracer breakthrough time, total liquid hold-up, total saturation and 24-hour drain-down moisture. The methodologies used to obtain this parameters were discussed along with their relevancy in diagnosing preferential flow behaviour.

Chapter 8

RTD Studies on Selected Packed Bed Systems

A key objective of this research was to ascertain the effect that particle shape (GB vs. GS), particle porosity (GS vs. GW vs. MO), wettability (GW vs. GS vs. MO), size fraction and size distribution as well as irrigation fluid viscosity, have on the steady state fluid flow profiles in drip irrigated laboratory scale packed beds characteristic of heaps.

This chapter discusses the experimental conditions, bed characterisation results and an initial qualitative assessment of the cumulative RTD profiles obtained using the methodologies set out in Chapter 7. A more focused discussion on the modelling of the cumulative RTD curves is presented in Chapter 9.

8.1 Experimental Conditions

The experimental tags (E-tag) and the experimental conditions under which the tracer tests were conducted are shown in Table 8.1. Three tracer experiments were conducted for the GB; nine for GS, ten for GW and nineteen for MO. A bed height of 16 cm was used for a majority of the tests. Though this is relatively small compared to actual heaps, it proved sufficient in generating the type and amount of data required to meet the objectives of this study.

Table 8.1: Experimental conditions used during various tracer tests. [Key: size fractions (S.F.), bed height (B.H.), irrigation solution (I.S.), max [KCl] in feed (F) and tracer (T), irrigation flux (I.F.) and agglomerated/non-agglomerated (A/NA)].

Material	E-tag	S.F. (mm)	B.H. (m)	Temp (°C)	I.S.	I.S. [μ] (cP)	[[KCl]$_F$ (g/L)	[[KCl]$_T$ (g/L)	I.F. (L/m^2.h)	A/NA
Glass beads	GB-1	2	0.16	30	Water	0.8	0.7	7.5	5.2	NA
	GB-2	5	0.16	30	Water	0.8	0.7	7.5	5.2	NA
	GB-3	15	0.16	30	Water	0.8	0.7	7.5	5.2	NA
Glass shards	GS-3	0.1 - 8.0	0.16	30	Water	0.8	0.7	7.5	5.0	A
	GS-5	0.5 - 8.0	0.16	30	Water	0.8	0.7	7.5	5.0	A
	GS-6	1.0 - 2.0	0.16	30	Water	0.8	0.7	7.5	5.2	NA
	GS-7	1.0 - 8.0	0.16	30	Water	0.8	0.7	7.5	4.9	A
	GS-8	2.0 - 2.8	0.16	30	Water	0.8	0.7	7.5	5.2	NA
	GS-10	2.8 - 4.8	0.16	30	Water	0.8	0.7	7.5	5.1	NA
	GS-12	4.8 - 5.6	0.16	30	Water	0.8	0.7	7.5	5.2	NA
	GS-13	4.8 - 6.7	0.16	30	Water	0.8	0.7	7.5	5.1	NA
	GS-15	6.7 - 8.0	0.16	30	Water	0.8	0.7	7.5	5.1	NA
Greywacke	GW-3	0.1 - 8.0	0.16	30	Water	0.8	0.7	7.5	5.0	A
	GW-5	0.5 - 8.0	0.16	30	Water	0.8	0.7	7.5	5.0	A
	GW-6	1.0 - 2.0	0.16	30	Water	0.8	0.7	7.5	5.2	NA
	GW-7	1.0 - 8.0	0.16	30	Water	0.8	0.7	7.5	4.9	A
	GW-8	2.0 - 2.8	0.16	30	Water	0.8	0.7	7.5	5.2	NA
	GW-10	2.8 - 4.8	0.16	30	Water	0.8	0.7	7.5	5.1	NA
	GW-12	4.8 - 5.6	0.16	30	Water	0.8	0.7	7.5	5.2	NA
	GW-13	4.8 - 6.7	0.16	30	Water	0.8	0.7	7.5	5.1	NA
	GW-15	6.7 - 8.0	0.16	30	Water	0.8	0.7	7.5	5.1	NA
	GW-19	13.2 - 16.0	0.16	30	Water	0.8	0.7	7.5	5.2	NA
Malachite ore	MO-2	0 - 8.0	0.16	30	Water	0.8	0.7	7.5	5.0	A
	MO-2-1.5H	0 - 8.0	0.24	30	Water	0.8	0.7	7.5	5.0	A
	MO-2-2H	0 - 8.0	0.31	30	Water	0.8	0.7	7.5	5.1	A
	MO-2-NA	0 - 8.0	0.13	30	Water	0.8	0.7	7.5	5.0	NA
	MO-2-15G	0 - 8.0	0.16	30	15 wt% Gly	1.2	0.7	7.5	5.0	A
	MO-2-25G	0 - 8.0	0.16	30	25 wt% Gly	1.6	0.7	7.5	5.1	A
	MO-2-30G	0 - 8.0	0.16	30	30 wt% Gly	1.9	0.7	7.5	5.4	A
	MO-2-35G	0 - 8.0	0.16	30	35 wt% Gly	2.2	0.7	9.7	5.0	A
	MO-3	0.1 - 8.0	0.16	30	Water	0.8	0.7	7.5	5.0	A
	MO-5	0.5 - 8.0	0.16	30	Water	0.8	0.7	7.5	5.0	A
	MO-6	1.0 - 2.0	0.16	30	Water	0.8	0.7	7.5	5.2	NA
	MO-7	1.0 - 8.0	0.16	30	Water	0.8	0.7	7.5	4.9	A
	MO-8	2.0 - 2.8	0.16	30	Water	0.8	0.7	7.5	5.2	NA
	MO-10	2.8 - 4.8	0.16	30	Water	0.8	0.7	7.5	5.1	NA
	MO-12	4.8 - 5.6	0.16	30	Water	0.8	0.7	7.5	5.2	NA
	MO-13	4.8 - 6.7	0.16	30	Water	0.8	0.7	7.5	5.1	NA
	MO-15	6.7 - 8.0	0.16	30	Water	0.8	0.7	7.5	5.1	NA
	MO-19	13.2 - 16.0	0.16	30	Water	0.8	0.7	7.5	5.2	NA
	MO-20	0 - 16.0	0.16	30	Water	0.8	0.7	7.5	5.3	A

8.2 Cumulative RTD and Bed Characterisation Results and Discussion

The definitions of the bed characterisation parameters, how they were obtained and their potential impact on the fluid flow profiles within packed bed systems were discussed in sub-section 7.2.2.

8.2.1 Effect of Particle shape

The effect of particle shape on both the cumulative RTD and bed characterisation parameters for the GB and GS packed beds is shown in Figures 8.1 and 8.2. Both these systems were non-porous with similar compositions, meaning that particle shape was the main difference.

The results presented here suggest that particle shape exerts more of an influence on the cumulative RTD profiles at the smaller size range (1 - 3 mm). Though both the GB and GS systems exhibited symptoms of steady state solution channelling with quick solution and tracer breakthrough times (Figures 8.1a and 8.2a), this channelling behaviour was slightly more prevalent in the GB-1 system with a solution breakthrough time of approximately 16 minutes compared with the GS-6 ($\sim$35 minutes) and GS-8 packed beds ($\sim$22 minutes).

The fact that all three systems in the 1 - 3 mm size range attained similar total liquid hold-up values, which were relatively low and averaged around 0.02, yet the GB-1 RTD profile still displayed enhanced channelling effects points towards the presence of isolated solution volumes within the bed. Based on Ilankoon and Neethling (2013), the liquid rivulets flowing across the irregularly shaped shards are likely to have greater tortuosity which could result in increased connectivity compared to the beads. This is supported by the 24-hour drain-down moisture data, which was significantly lower for the GB-1 system (3.1%) than for the shards (17 - 47%). Additionally, the spherical nature of the 2 mm beads resulted in a denser packing arrangement (refer to Figure 8.1b), typical of the trend found in literature (Fernando et al., 2020). Therefore the similar liquid hold-up values at the 1 - 3 mm size range also meant that the absolute mass of fluid retained in the GB-1 bed was lower.

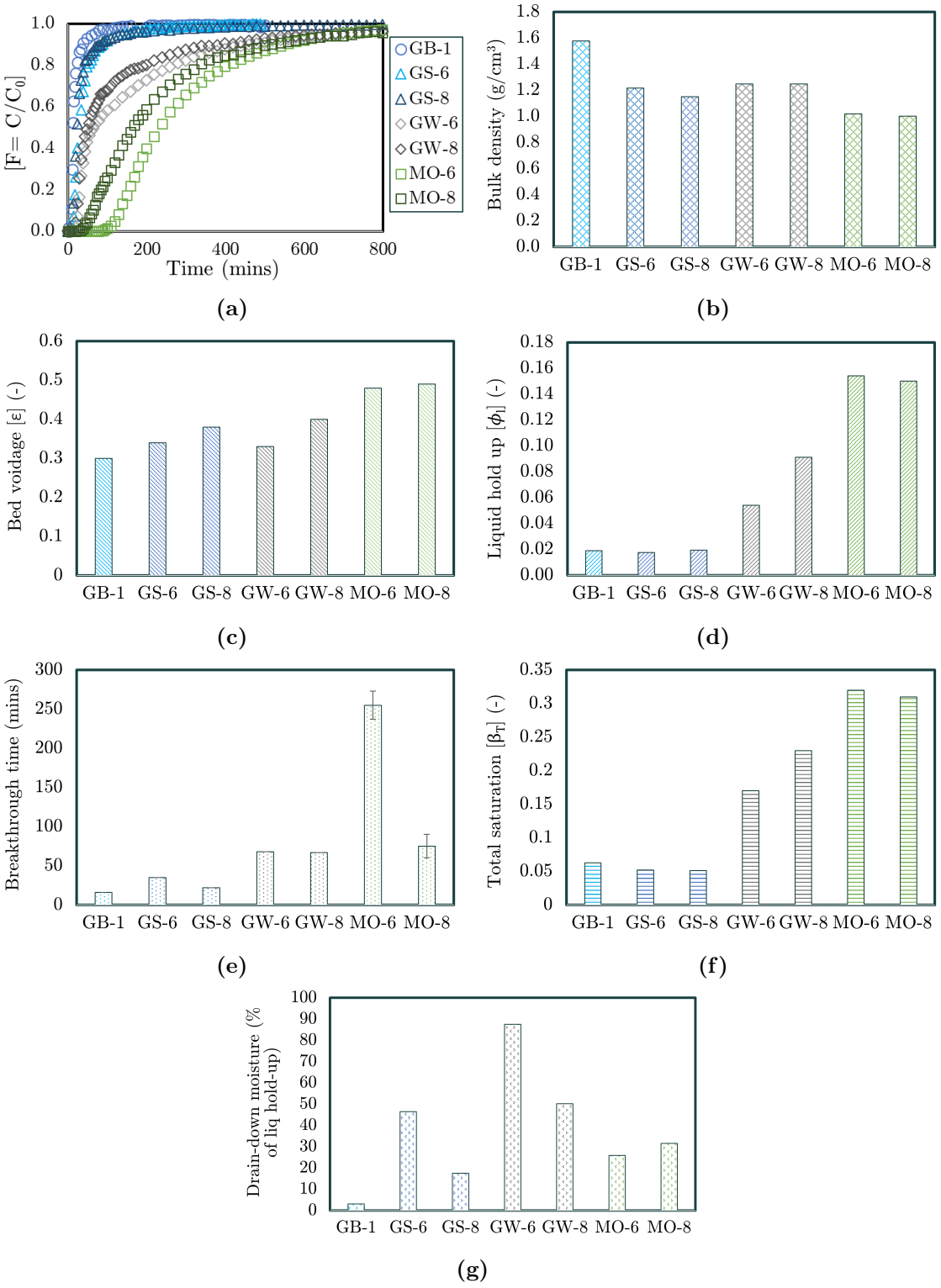

Figure 8.1: (a) Cumulative RTD, (b) Bulk density, (c) Bed voidage, (d) Total liquid hold-up, (e) Solution breakthrough time, (f) Total saturation and (g) 24-hour drain-down moisture for GB, GS, GW and MO particles with size fractions ranging from 1 to 3 mm.

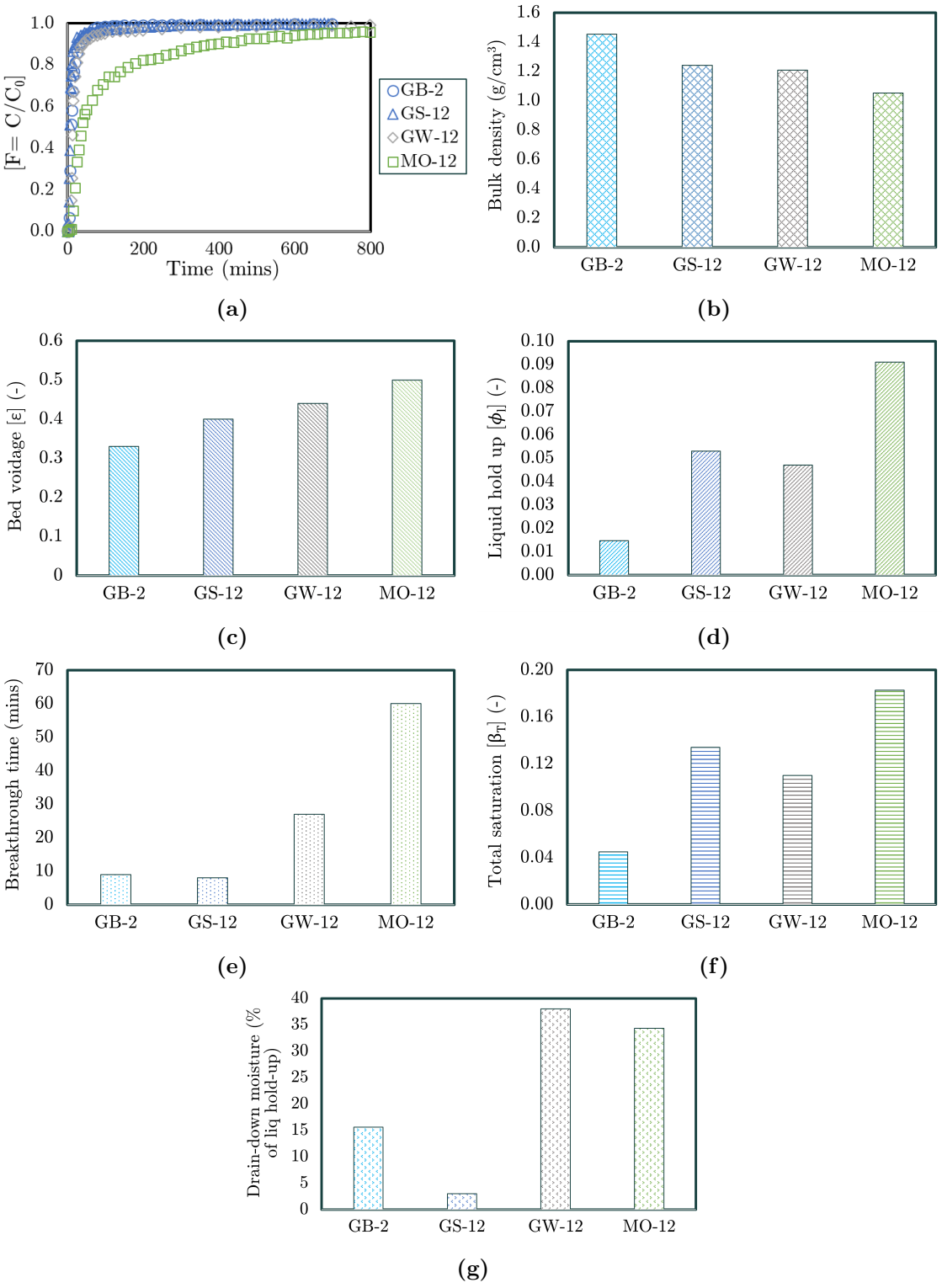

Figure 8.2: (a) Cumulative RTD, (b) Bulk density, (c) Bed voidage, (d) Total liquid hold-up, (e) Solution breakthrough time, (f) Total saturation and (g) 24-hour drain-down moisture for packed beds composed of GB, GS, GW and MO particles with size fractions ranging from 4.8 to 5.6 mm.

At the 5 mm size range, the GB and GS systems behaved similarly concerning their RTD profiles (Figure 8.2a) and bed characterization parameters. The main difference being the shorter solution breakthrough time and lower liquid hold-up for the GB-2 bed. Based on the liquid retainment results discussed in sub-section 5.1.2, variation in capillary suction effects between both beds are not the likely cause of such differences at such particle sizes. It is likely that the unique shape characteristics of the two materials led to variations in the degree of mechanical dispersion and lateral spreading of fluid droplets. This probably occurred during the transient, initial wetting stages of the beds as their steady state RTD profiles are near identical. The GS particles, being flatter and in certain cases longer, had a higher probability of redirecting the flow of fluid droplets away from the central-vertical axis of the column. However, unlike the enhanced connectivity that is proposed to have occurred at the 1 - 3 mm size range in the GS beds due to their irregular shapes, the longer particle length scales at the 5 mm size fraction likely resulted in the formation of radially dispersed isolated fluid pockets and increased total liquid hold-up. The lateral movement or mechanical dispersion of fluid droplets could become more prominent as the ratio of particle to liquid droplet size increases. This is in line with the observations made by Fernando et al. (2019), in which an increase in the lateral spreading of solution was detected when flat PCBs were incorporated into an irrigated ore bed. Table 8.2 gives a summary of the effect of particle shape on the various bed characterisation parameters.

Table 8.2: Summary of the comparative effect of particle shape on the various bed characterisation parameters.

Parameter	**Spherical (GB)**	**Irregularly shaped (GS)**
Bulk density	Higher	Lower
Bed voidage	Lower	Higher
Total liquid hold-up	Lower	Higher
Total saturation	Lower	Higher
Solution breakthrough time	Shorter	Longer
Tracer breakthrough time	Similar	Similar
Drain-down moisture percentage	Similar	Similar

8.2.2 Effect of Particle Porosity and Wettability

The impact of particle porosity and wettability on both the cumulative RTD profiles and bed characterisation parameters can be observed in Figures 8.1 to 8.9.

8.2.2.1 Particle Size Range: 1 - 3 mm

Beginning with the results for the 1 - 3 mm size fraction range shown in Figure 8.1, the MO bed systems exhibited the lowest bulk densities, highest voidage, highest liquid hold-up and saturation as well as the longest solution and tracer breakthrough times. As the MO particles were significantly more porous than the other three materials (refer to sub-section 4.2.2), enhanced capillary effects in smaller sized pores contributed to greater fluid retention likely due to improved lateral spreading as observed by Fernando et al. (2019).

The GW beds had the second highest liquid hold-up, total saturation values and liquid breakthrough times at this size fraction. The GW RTD curves are quite peculiar in that they display both channelling effects and the presence of stagnant solution volumes. The channelling effects, based on the quick tracer breakthrough times, are likely a result of enhanced wettability whilst the moderate levels of porosities brought about the presence of capillary induced stagnant solution pools. Higher levels of wettability also contributed to higher drain-down moisture percentages likely due to lower solution flow resistance. The porous nature of the GW particles was not noticeably reflected in the bed voidage data as the values for the GW (0.33 - 0.40) and the non-porous GS (0.34 - 0.38) systems are very similar. This highlights the importance of void size distributions and material properties as certain beds may possess identical voidage, but have contrasting RTD profiles.

With regards to the drain-down moisture, the GB, GS, GW and MO systems had average percentages of 3, 32, 69 and 29%, respectively. These values are thought to be a rough reflection of the dynamic liquid hold-up within the beds. The non-porous systems with little moisture retainment capacities drained substantially less moisture, especially the spherical beads. In the case of the MO beds, it was visually observed that droplets of liquid were still exiting even after the 24-hour period. Hence, it is expected that if the period of time was

increased, the MO beds would have achieved higher percentage values.

8.2.2.2 Particle Size Range: 2.8 - 4.8 mm

The results for the GS-10, GW-10 and MO-10 systems at the 2.8 - 4.8 mm size fraction range can be seen in Figure 8.3. The cumulative RTD profile for the GS-10 system indicates high levels of solution channelling with very little mixing. This point is supported by liquid hold-up values that were 78% and 84% less than those of the GW and MO systems, respectively. A similar trend was observed for the total saturation parameter. The 24-hour drain-down moisture as a percentage of the total liquid hold-up for the GS system was ∼11% which was 3 to 4 times smaller than those of the GW and MO systems. Its non-porous nature is the most likely reason for the observed trends.

8.2.2.3 Particle Size Range: 4.8 - 6.7 mm

Data shown in Figure 8.2 for the 4.8 - 5.6 mm size range, further illustrate the effect of particle porosity with greater levels of capillary induced stagnant solution volumes based on the relatively longer asymptote and higher liquid hold-up displayed by the MO-12 system. All three profiles displayed channelling behaviour (quick tracer breakthrough times) with no noticeable asymptotes for the GS-12 and GW-12 beds.

The trend evident in Figure 8.4 is an increase in the liquid hold-up, total saturation, solution breakthrough times and drain-down moisture values as the degree of particle porosity increased. The results also suggests that particle wettability influenced the fraction of mobile liquid present within the bed as the GW-13 (Figure 8.4g) and other GW systems consistently drained higher fractions of their total liquid hold-up. However, it is still unclear if the 24-hour drain-down moisture percentages are a true reflection of the dynamic liquid hold-up within a bed. Also, the cumulative RTD curves for the MO-12 and MO-13 beds are nearly identical which indicates that its steady state flow profile was not substantially influenced by the increase in particle top size from 5.6 to 6.7 mm. This resilience to the effects caused by changes in its particle top size can be attributed to its higher levels of porosity and will be a discussion point in subsequent sections.

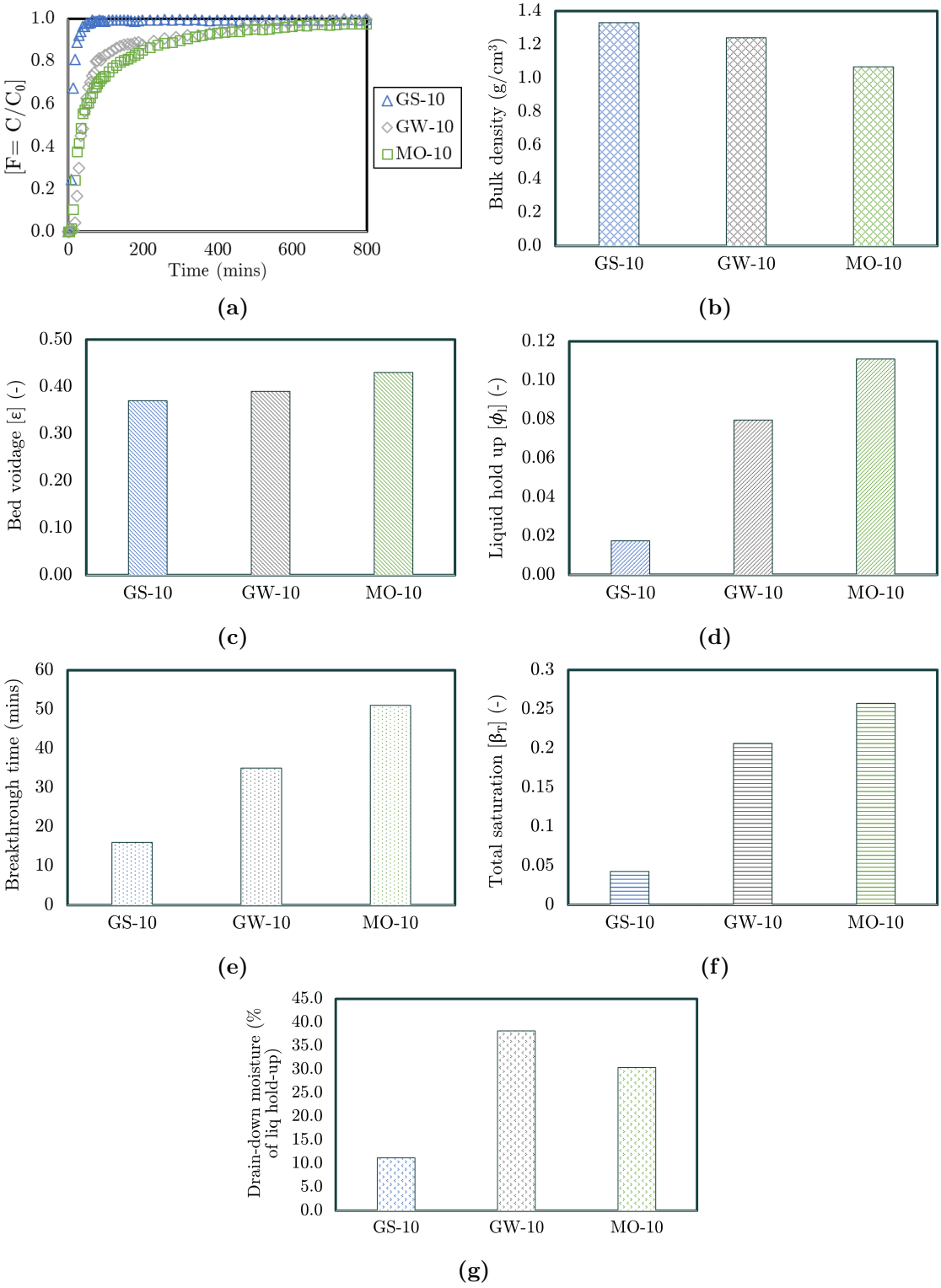

Figure 8.3: (a) Cumulative RTD, (b) Bulk density, (c) Bed voidage, (d) Total liquid hold-up, (e) Solution breakthrough time, (f) Total saturation and (g) 24-hour drain-down moisture for packed beds composed of GS, GW and MO particles with size fractions ranging from 2.8 to 4.8 mm.

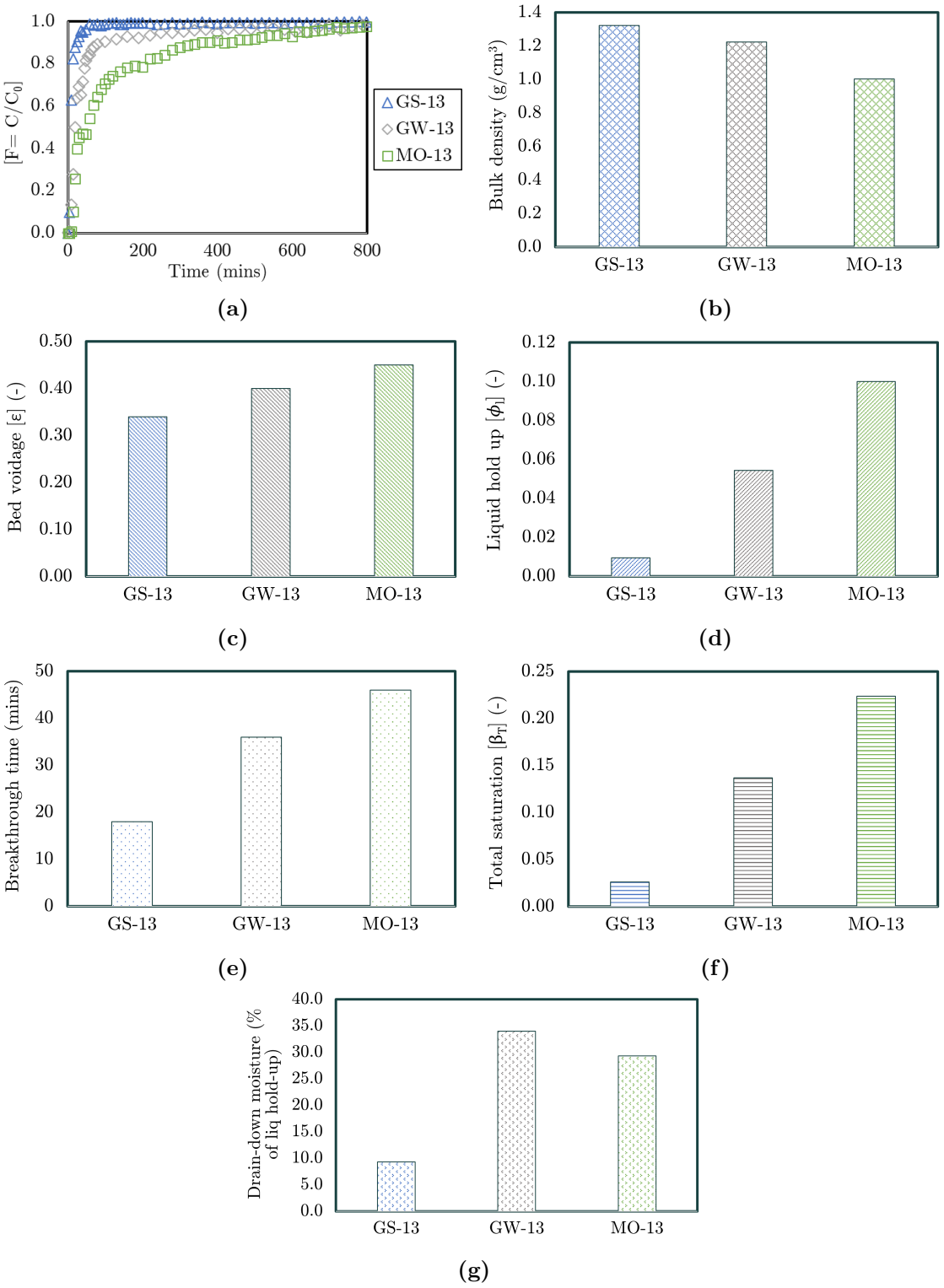

Figure 8.4: (a) Cumulative RTD, (b) Bulk density, (c) Bed voidage, (d) Total liquid hold-up, (e) Solution breakthrough time, (f) Total saturation and (g) 24-hour drain-down moisture for packed beds composed of GS, GW and MO particles with size fractions ranging from 4.8 to 6.7 mm.

8.2.2.4 Particle Size Range: 6.7 - 8 mm

The cumulative RTD profiles for all three systems shown in Figure 8.5 point towards solution channelling behaviour at steady state. This is more evident in the GS-15 bed which had a solution breakthrough time that was between 62 - 65% less than those of the porous systems with a drain-down moisture of only 2% of its liquid hold-up. The porous GW-15 and MO-15 systems had slightly longer asymptotes in their RTD profiles compared to the GS-15 bed. This suggests they had higher volumes of stagnant solution caused by stronger capillary forces. This is supported by the liquid hold-up value for the MO-15 bed, which was approximately 2 to 4 times greater than those of GW-15 and GS-15 systems, respectively.

The $\sim$14 percent higher drain-down moisture percentage of the GW-15 system compared to the MO-15 system is consistent with previous results and can be attributed to its higher wettability allowing for a higher fraction of freely draining liquid. In this case, additional droplets were not observed emerging from the columns after the 24-hour period. This means that the difference in their liquid hold-up values were most likely due to lower fractions of dynamic solution volumes within the MO-15 bed.

8.2.2.5 Particle Size Range: 13.2 - 16 mm

The cumulative RTD profiles for the GB-3, GW-19 and MO-19 systems show steady state channelling behaviour (Figure 8.6). The wide pore spaces created by the arrangement of the large particles within the beds ensured little resistance to fluid movement resulting in short tracer breakthrough times. The effect of porosity is more evident in the bed characterisation parameters and RTD asymptotes of the MO-19 system. It had a 2 to 4 times longer solution breakthrough time, a 2 times greater liquid hold-up and 3 times greater total saturation value compared to the other beds. Also, MO-19 likely possessed a substantial fraction of isolated solution volumes based on its higher liquid hold-up but similar RTD response to the other beds. This suggests that in porous systems composed of large particles, the pore network within each particle exists more independently of the others due to fewer particle-particle contact points, increasing the probability of isolated solution volumes.

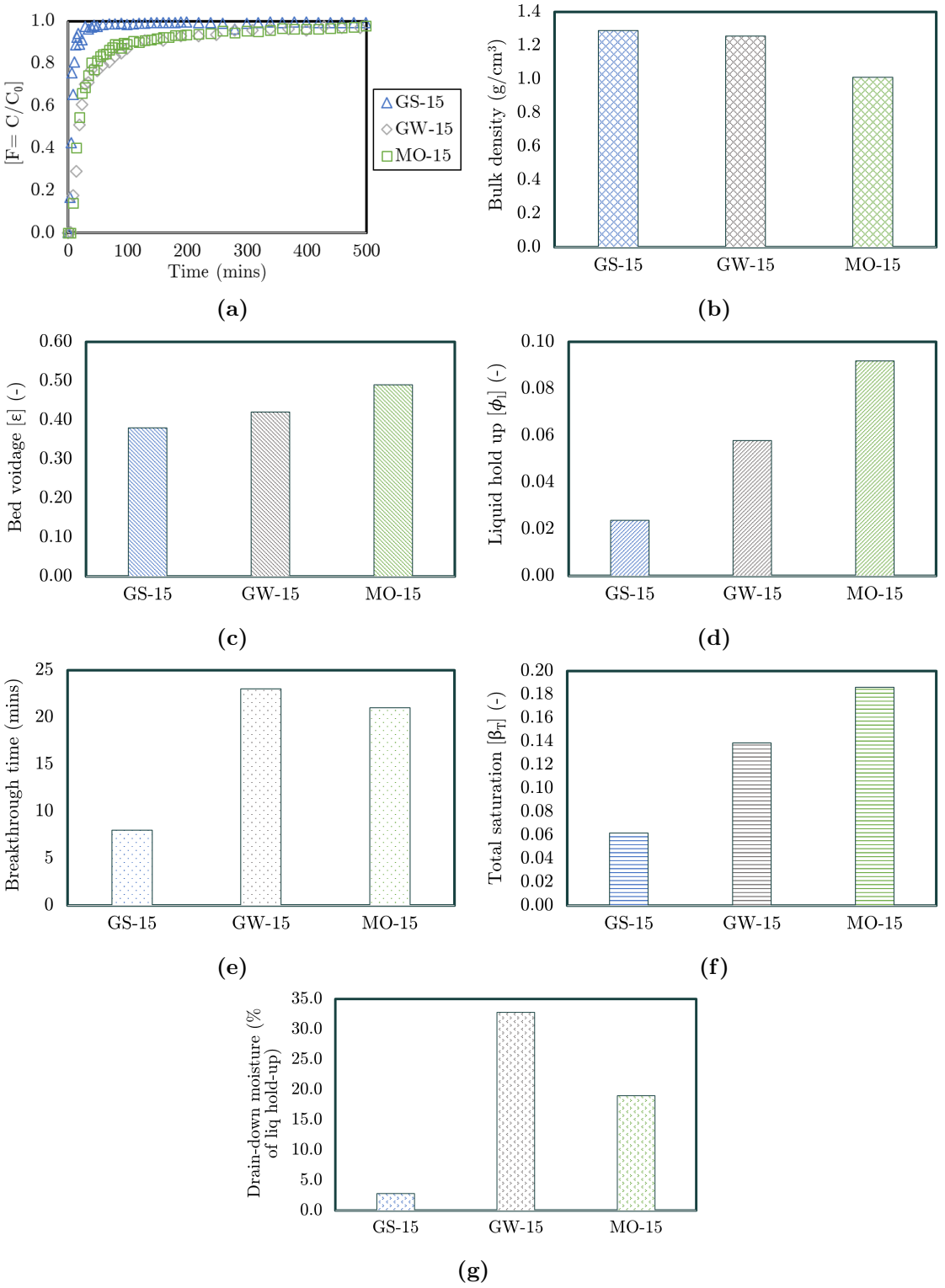

Figure 8.5: (a) Cumulative RTD, (b) Bulk density, (c) Bed voidage, (d) Total liquid hold-up, (e) Solution breakthrough time, (f) Total saturation and (g) 24-hour drain-down moisture for packed beds composed of GS, GW and MO particles with size fractions ranging from 6.7 to 8 mm.

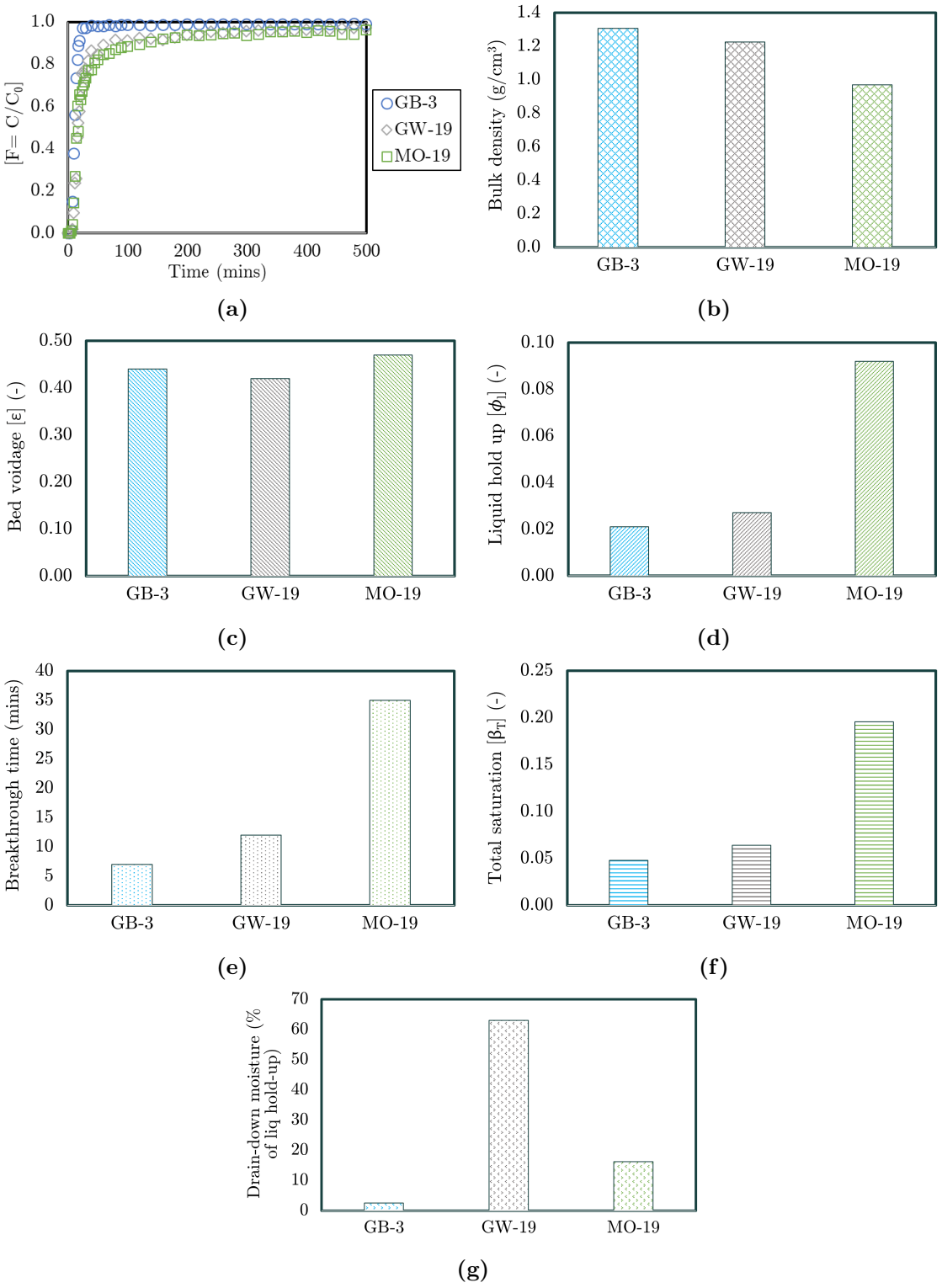

Figure 8.6: (a) Cumulative RTD, (b) Bulk density, (c) Bed voidage, (d) Total liquid hold-up, (e) Solution breakthrough time, (f) Total saturation and (g) 24-hour drain-down moisture for packed beds composed of GB, GW and MO particles with size fractions ranging from 13.2 to 16 mm.

8.2.2.6 Particle Size distribution: 0.1 - 8 mm

From the results shown in Figure 8.7, the near identical nature of all three profiles suggests that particle size distribution, or more specifically, the inclusion of fines, was the dominant factor influencing the shape of the curves at the 0.1 - 8 mm size range. This level of similarity extends to the bulk densities and solution breakthrough times data which show a 2% and 9% highest percentage difference, respectively, across the three systems. However, the total liquid hold-up for the MO-3 system was approximately 29% greater than those of the GS and GW systems. This suggests stronger capillary forces were still present in the MO bed. Higher wettability in the GW bed led to a slightly shorter tracer breakthrough time which is in line with previous results. It should be noted that trapped air bubbles during the flooding process used to determine total voidage are proposed to be responsible for the discrepancy between bulk density and voidage values for the different systems. A similar issue was encountered during capillary tests as discussed in sub-section 5.2.3.1.

8.2.2.7 Particle Size distribution: 0.5 - 8 mm

At a size distribution of 0.5 - 8.0 mm (Figure 8.8), the MO-5 bed's tracer breakthrough time was between 3 and 4 times longer than that of the GS-5 and GW-5 systems. This corresponds to a 2 times greater solution breakthrough time, 1.5 times greater total liquid hold-up and 35 - 40% higher total saturation level for the MO-5 bed. This is in line with previous results indicating enhanced lateral spread of drip irrigated solution, facilitated by the higher levels of porosity and capillary effects, during the initial wetting stages. The higher wettability and moderate porosity of the GW-5 bed could be responsible for its shorter breakthrough time and better drainage behaviour, compared to MO-5.

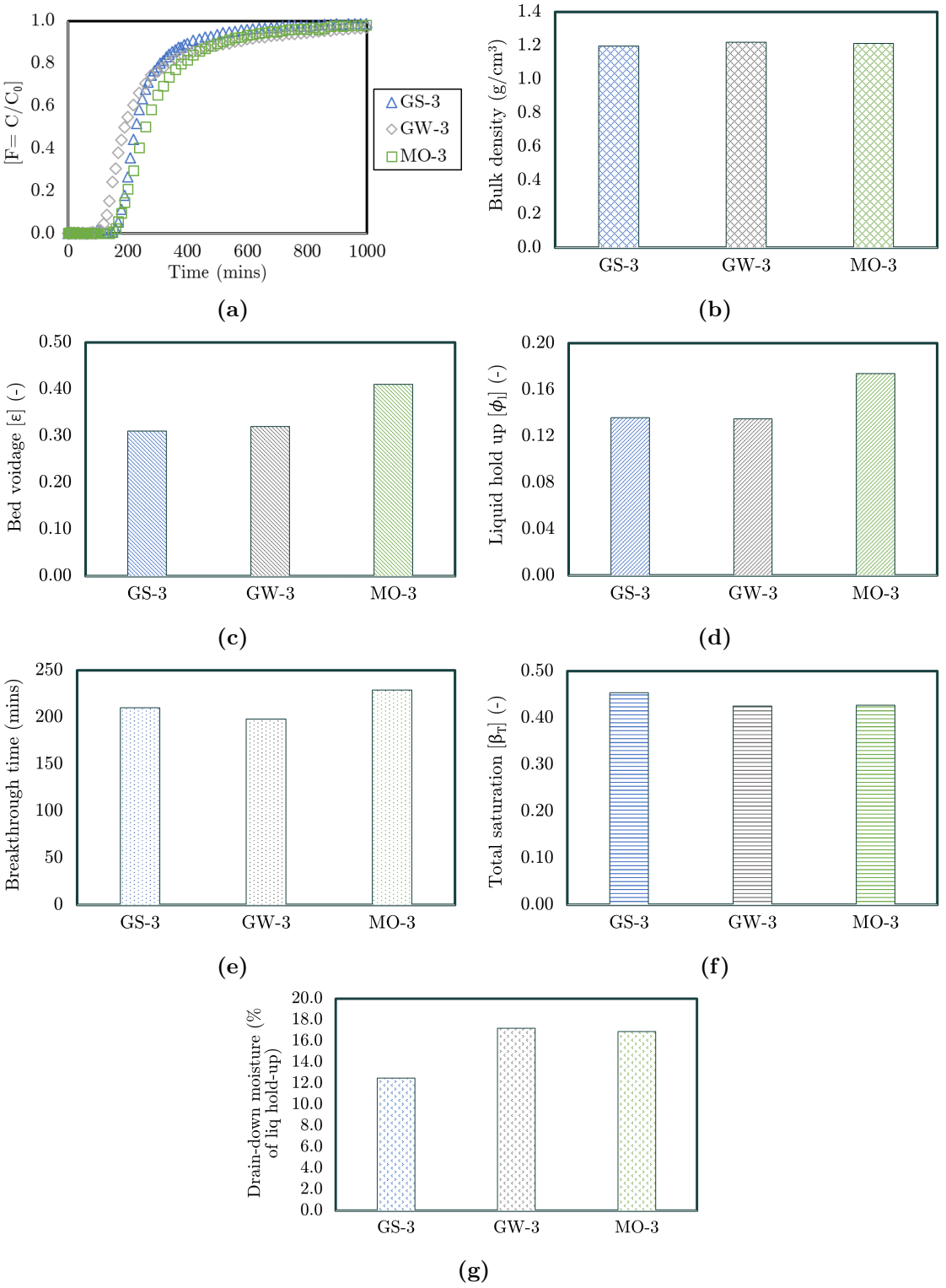

Figure 8.7: (a) Cumulative RTD, (b) Bulk density, (c) Bed voidage, (d) Total liquid hold-up, (e) Solution breakthrough time, (f) Total saturation and (g) 24-hour drain-down moisture for packed beds composed of GS, GW and MO particles with size fractions ranging from 0.1 to 8 mm.

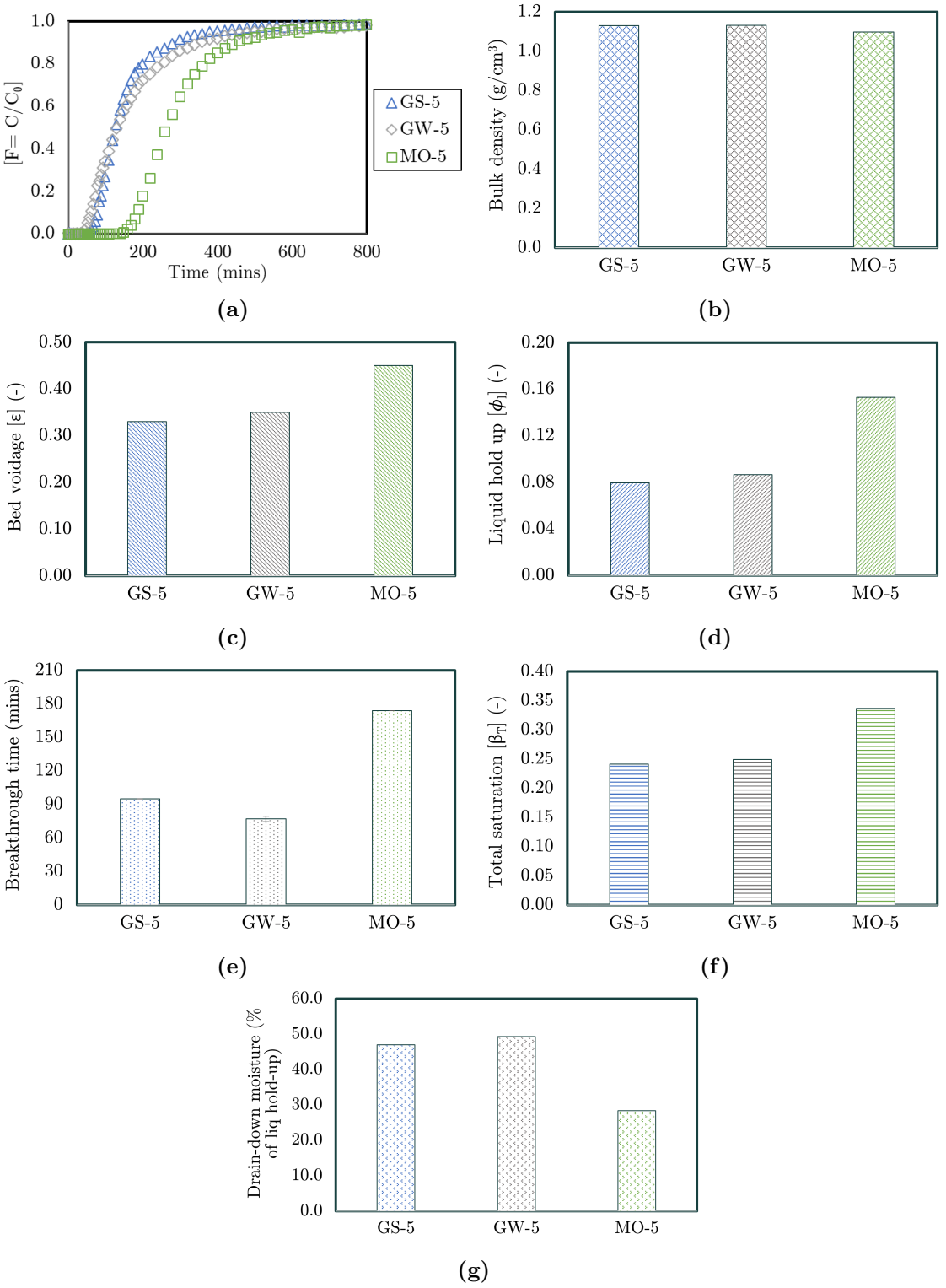

Figure 8.8: (a) Cumulative RTD, (b) Bulk density, (c) Bed voidage, (d) Total liquid hold-up, (e) Solution breakthrough time, (f) Total saturation and (g) 24-hour drain-down moisture for packed beds composed of GS, GW and MO particles with size fractions ranging from 0.5 to 8 mm.

8.2.2.8 Particle Size distribution: 1 - 8 mm

The cumulative RTD profiles in Figure 8.9 show that the MO-7 system displayed a significantly longer steady state tracer breakthrough time (∼1 hour) compared to the GS-7 and GW-7 beds. The solution breakthrough times, total liquid hold-up and saturation values show a similar trend. Both the GS-7 and GW-7 profiles exhibit solution channelling behaviour with very quick steady state tracer breakthrough times ranging between 9 - 14 minutes with indications of stagnant solution volumes. The effect of particle porosity and wettability when comparing these two systems is slightly noticeable in their RTD profiles but more apparent when considering the greater total liquid hold-up and solution breakthrough times measured for the GW-7 bed.

It is proposed that though particle wettability exerted more of an influence on the initial wetting behaviour (prior to steady state) of the beds, its effect is still noticeable at steady state with shorter tracer breakthrough times indicating lower resistance to solution flow.

8.2.2.9 Summary on the Effect of Particle Porosity and Wettability

Overall, higher particle porosities were associated with lower bulk densities, higher voidage, greater 24-hour drain-down moisture volumes, more liquid hold-up and total bed saturations as well as longer solution breakthrough times. It could be that the increased capillary suction effects present in beds composed of porous particles played a crucial role in their moisture absorption and retention properties. These results are consistent with the results by Ilankoon and Neethling (2013), however the current work goes beyond this through the decoupling of particle shape and porosity.

Though porosity and wettability had minimal effects on the RTD profiles for the mixed sized 0.1 - 8 mm beds, total liquid hold-up and drainage behaviour showed positive correlations to the degree of porosity. Differences between the systems became more apparent as the bottom particle size was raised from 0.1 mm to 1 mm, suggesting that particles within this size range are a strong determining factor of steady state flow profiles.

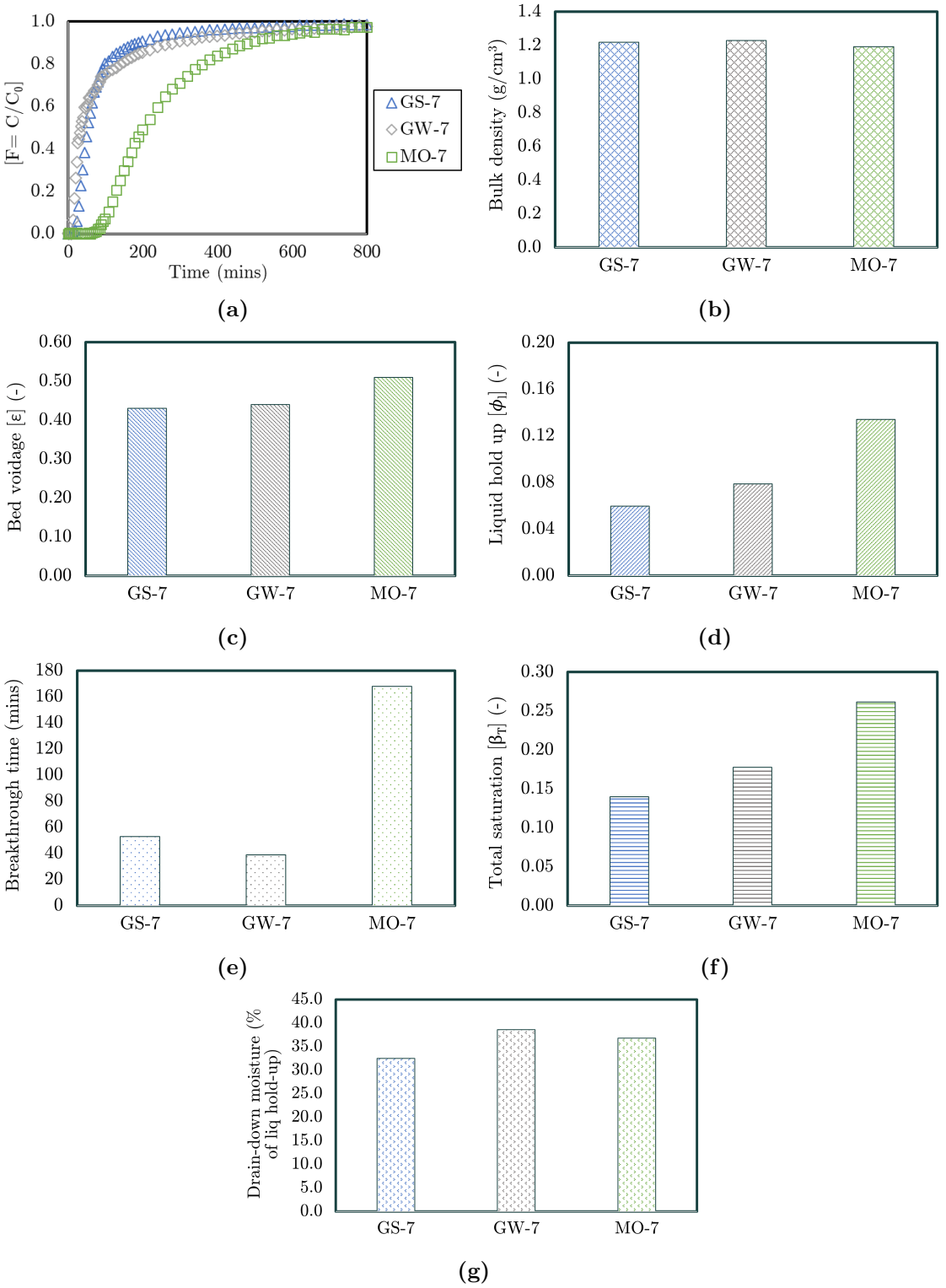

Figure 8.9: (a) Cumulative RTD, (b) Bulk density, (c) Bed voidage, (d) Total liquid hold-up, (e) Solution breakthrough time, (f) Total saturation and (g) 24-hour drain-down moisture for packed beds composed of GS, GW and MO particles with size fractions ranging from 1 to 8 mm.

The highly porous MO system had substantially longer tracer and solution breakthrough times, as well as higher liquid hold-up and drain-down moisture values at the 0.5 and 1 mm bottom particle size beds. It is proposed that the higher degree of void network connectivity resulted in a higher number of possible fluid flow paths. This could have led to a greater lateral spread of irrigated solution in the MO system which contributed to its total liquid hold-up.

The GW mixed sized beds, composed of the relatively more hydrophilic GW particles, tended to have relatively shorter solution and, in certain cases tracer breakthrough times and consistently higher drain-down moisture percentages compared to the other systems. This occurred even in cases where it had similar or larger total liquid hold-ups. This implied that the GW beds provided less resistance to fluid flow both during the wetting and steady state phases, which resulted in quicker breakthrough times (solution and tracer) and higher drain-down volumes. Table 8.3 gives a summary of the effect of particle porosity and wettability on the various bed characterisation parameters.

Table 8.3: Summary of the effect of increases in particle porosity and wettability on the various bed characterisation parameters. Key: "↑" represents an increase in magnitude of the parameter while "↓" represents a decrease; (-) means no evident trend.

Parameter	**↑ Particle porosity**	**↑ Wettability**
Bulk density	↓	(-)
Bed voidage	↑	(-)
Total liquid hold-up	↑	(-)
Total saturation	↑	(-)
Solution breakthrough time	↑	↓
Tracer breakthrough time	↑	↓
Drain-down moisture percentage	↑	↑

8.2.3 Effect of Particle Size Fraction in Narrow Sized Beds

This section discusses the effect of particle size on the cumulative RTD profiles and bed characterisation parameters for the beds composed of narrow size fractions . A summary of the bed characterisation parameters for each packed bed system analysed can be found in

Table 8.4.

8.2.3.1 GB Systems

For the GB, increasing the bead size from 2 to 15 mm led to a 17% decrease in bulk density from 1.6 to 1.3 g/cm^3 . This corresponds to a 47% increase in the measured bed voidage values from 0.30 to 0.44. This could be due to the reduction in particle to particle contact points, due to a decrease in surface area to volume ratio with an increase in the diameter of spherical particles. The total liquid hold-up varied between 0.015 and 0.021 while drain-down moisture values varied between 0.5 (15.6% of liquid hold-up) and 0.72 mL (3.1% of liquid hold-up) without a definite trend in both these parameters. However, there was a significant decrease of 24% in total bed saturation and 56% in solution breakthrough time comparing the 2 to 15 mm beads. The cumulative RTD profiles of all three systems displayed channelling behaviour with particle size not having a substantial impact on the shape of the curves.

8.2.3.2 GS Systems

The narrow particle size ranges tested for the non-porous, irregularly shaped GS systems were: 1 - 2 mm (GS-6), 2 - 2.8 mm (GS-8), 2.8 - 4.8 mm (GS-10), 4.8 - 5.6 mm (GS-12), 4.8 - 6.7 mm (GS-13) and 6.7 - 8.0 mm (GS-15).

Particle size did not have a discernible impact on the bulk density, total liquid hold-up and total saturation values for the different beds. Though bulk density showed little variation, the average total liquid hold-up (0.02) and bed saturation (0.06) values displayed significant variability with standard deviation values of 0.01 and 0.03, respectively.

There was a 77% decrease in solution breakthrough time and 80% reduction in drain-down moisture percentage when comparing the GS-6 to GS-15 beds. These can be due to increases in the diameter of void spaces formed in beds composed of larger particles, facilitating the channelling of solution along the central-vertical irrigation axis.

With regards to the cumulative RTD profiles for the narrow size GS systems (refer to Figures

8.1a through to 8.5a), there is a noticeable reduction in the length of the asymptotes of the RTD curves as the size fraction increased over the discussed range. This, together with the reduction in tracer breakthrough times and relatively small total liquid hold-ups, reinforces the notion of an increase in liquid channelling behaviour as particle size increased.

Table 8.4: Bed characterization parameters for different packed bed systems defined by their experimental tags (E-tags).[Key: size fraction (S.F.), Bulk density [B.D.], Bed volume [B.V.], Total liquid hold-up [L.H.], Total bed saturation [T.S.], Breakthrough time [B.T.], 24-hour drain-down moisture [D.M.] and approximate time at which F-curve reaches 0.99 [T:F =0.99 (min)]]

E-tag	**S.F. (mm)**	**B.D. (g/cm^3)**	**B.V.** [ε]	**L.H.** [ϕ_l]	**T.S.** [β_T]	**B.T. (min)**	**D.M. (mL)**	**T:F =0.99 (min)**
GB-1	2	1.58	0.30	0.02	0.06	16	0.7	210
GB-2	5	1.45	0.33	0.01	0.04	9	0.5	130
GB-3	15	1.31	0.44	0.02	0.05	7	0.6	240
GS-3	0.1-8.0	1.20	0.31	0.14	0.45	210	21.6	1059
GS-5	0.5-8.0	1.13	0.33	0.08	0.24	95	45.5	819
GS-6	1.0-2.0	1.22	0.34	0.02	0.05	35	10.0	300
GS-7	1.0-8.0	1.22	0.43	0.06	0.14	53	23.6	899
GS-8	2.0-2.8	1.15	0.38	0.02	0.05	22	4.1	520
GS-10	2.8-4.8	1.33	0.37	0.02	0.04	16	2.4	84
GS-12	4.8-5.6	1.24	0.40	0.05	0.13	8	1.8	300
GS-13	4.8-6.7	1.32	0.34	0.01	0.03	18	1.0	109
GS-15	6.7-8.0	1.29	0.38	0.02	0.06	8	0.8	89
GW-3	0.1-8.0	1.22	0.32	0.14	0.43	198	28.2	1279
GW-5	0.5-8.0	1.13	0.35	0.09	0.25	77	52.0	1039
GW-6	1.0-2.0	1.25	0.33	0.05	0.17	68	57.5	1150
GW-7	1.0-8.0	1.23	0.44	0.08	0.18	39	37.0	1039
GW-8	2.0-2.8	1.25	0.40	0.09	0.23	67	55.7	1120
GW-10	2.8-4.8	1.24	0.39	0.08	0.21	35	37.0	859
GW-12	4.8-5.6	1.21	0.44	0.05	0.11	27	21.5	800
GW-13	4.8-6.7	1.22	0.40	0.05	0.14	36	22.5	999
GW-15	6.7-8.0	1.26	0.42	0.06	0.14	23	23.1	939
GW-19	13.2-16.0	1.22	0.42	0.03	0.06	12	20.8	960
MO-2	0-8.0	1.19	0.44	0.26	0.58	302	31.9	1479
MO-2-1.5H	0-8.0	1.19	0.44	0.21	0.48	319	37.8	1940
MO-2-2H	0-8.0	1.16	0.42	0.21	0.51	446	52.5	1819
MO-2-NA	0-8.0	1.47	0.39	0.36	0.92	447	29.4	1439
MO-2-15G	0-8.0	1.20	0.44	0.24	0.55	296	39.6	1239
MO-2-25G	0-8.0	1.17	0.47	0.27	0.56	334	49.9	1079
MO-2-30G	0-8.0	1.18	0.51	0.32	0.63	255	46.6	1099
MO-2-35G	0-8.0	1.19	0.46	0.23	0.51	245	48.2	1145
MO-3	0.1-8.0	1.21	0.41	0.17	0.43	229	35.8	1219
MO-5	0.5-8.0	1.10	0.45	0.15	0.34	174	53.0	919
MO-6	1.0-2.0	1.02	0.48	0.15	0.32	255	48.4	960
MO-7	1.0-8.0	1.19	0.51	0.13	0.26	168	60.0	979
MO-8	2.0-2.8	1.00	0.49	0.15	0.31	75	57.7	1079
MO-10	2.8-4.8	1.07	0.43	0.11	0.26	51	41.0	1059
MO-12	4.8-5.6	1.05	0.50	0.09	0.18	60	46.2	1100
MO-13	4.8-6.7	1.00	0.45	0.10	0.22	46	35.8	939
MO-15	6.7-8.0	1.01	0.49	0.09	0.19	21	21.2	939
MO-19	13.2-16.0	0.97	0.47	0.09	0.20	35	18.2	1080
MO-20	0-16.0	1.22	0.47	0.26	0.55	259	21.4	1199

8.2.3.3 GW Systems

For the GW system, the narrow particle size fractions tested were: 1 - 2 mm (GW-6), 2 - 2.8 mm (GW-8), 2.8 - 4.8 mm (GW-10), 4.8 - 5.6 mm (GW-12), 4.8 - 6.7 mm (GW-13), 6.7 - 8.0 mm (GW-15) and 13.2 - 16.0 mm (GW-19).

From the data shown in Table 8.4, there was no observable relationship between bulk density and particle size. Liquid accessible bed voidage values were, for the most part, positively correlated with particle size fraction. However, the presence of an observable trend in bed voidage values and lack of one in bulk density values are possibly due to trapped air bubbles during flooding.

There were no definite trends between total liquid hold-up and particle size fraction which had an average value of 0.06 with a standard deviation of 0.02, indicating significant variability. However, similar to the GB systems, bed saturation values decreased as the particle size fraction increased. When comparing the GW-6 to the GW-19 system, there was a 62% reduction in bed saturation. This is due to the higher liquid accessible bed voidage values at the larger size fractions.

There was an 82% decrease in solution breakthrough time from 68 to 12 minutes and a 64% reduction in the volume of the drain-down solution from 58 to 21 mL (refer to Table 8.4) when comparing the GW-6 and GW-19 bed systems. The reasons given during the discussion of the GS systems' results are proposed to be applicable to this case as well.

The cumulative RTD profiles show a reduction in the length of the asymptotes as size fraction was increased (refer to Figures 8.1a through to 8.6a). A decrease in lateral movement of solution and increase in solution channelling behaviour at steady state could be the cause. It is very likely that the increase in size fraction led to greater ratios of isolated solution volumes during the initial wetting stages, prior to the establishment of steady state fluid flux.

8.2.3.4 MO Systems

For the MO beds, the narrow size fractions tested were: 1 - 2 mm (MO-6), 2 - 2.8 mm (MO-8), 2.8 - 4.8 mm (MO-10), 4.8 - 5.6 mm (MO-12), 4.8 - 6.7 mm (MO-13), 6.7 - 8.0 mm (MO-15) and 13.2 - 16.0 mm (MO-19).

There were no definite trends between particle size fraction, bulk density and bed voidage values for the MO systems (refer to Table 8.4). There was a 40% decrease in total liquid hold-up and total bed saturation as size fraction was increased from 1 - 2 mm to 13.2 - 16.0 mm. Based on the moisture retainment (refer to sub-section 5.1.2) and capillary suction results (refer to sub-sections 5.2.3.3), it is likely that the highly porous MO beds relied relatively more on capillary suction for their high liquid hold-up values.

Similar to the GW packed beds, the MO system experienced a 86% and 38% reduction in solution breakthrough time and drain-down moisture percentage, respectively, as particle size fraction was increased from 1 - 2 mm to 13.2 - 16.0 mm. Increased presence of macro-voids leading to solution channelling down the central-vertical axis at larger size fractions is again proposed to be responsible for the trend observed.

The effect of particle size fraction on the cumulative RTD profiles of the MO packed beds is similar to those observed for the GW and GS systems (refer to Figures 8.1a through to 8.6a). There was an increase in channelling behaviour due to reasons discussed previously.

8.2.3.5 Summary on the Effects of Particle Size Fraction in Narrow Sized Beds

Overall, the results acquired for the narrow size fraction systems composed of irregularly shaped materials, showed that bulk density was not substantially influenced by particle size, except in the case of the GB due to their spherical nature which allowed for highly regularized and uniform packing.

Total liquid hold-up was not consistently affected by particle size fraction for a majority of the systems. It was only the highly porous MO packed beds that showed a negative correlation between particle size and total liquid hold-up. Also, the MO system, along with the GB and GW packed beds displayed decreasing bed saturation with increasing particle

size fractions. This was due to one of two reasons, either an increase in bed voidage (GB and GW) or reduction in total liquid hold-up as particle size increased (MO).

All the different material beds displayed reductions in solutions breakthrough times and 24-hour drain-down moisture volumes as particle size fraction increased. This could be due to higher levels of solution channelling, both during the wetting stage and at steady state due to the presence of macro-voids in the beds composed of larger size fractions. Table 8.5 gives a summary on the effects of particle size fraction on bed characterisation parameters in narrow particle size beds.

Table 8.5: Summary of the effect of increases in particle size fraction on bed characterisation parameters in beds composed of narrow size fractions [1 - 2 mm to 6.7 - 8 mm (GS) to 13.2 - 16 mm (GB, GW, MO)]. GB - spherical, non-porous; GS - irregularly shaped, non-porous; GW - irregularly shaped, porous, highly hydrophilic; MO - irregularly shaped, highly porous. Key: "↑" means an increase in magnitude of parameter while "↓" means a decrease; (-) means no evident trend.

Parameter	**↑ Narrow size fraction**			
	GB	**GS**	**GW**	**MO**
Bulk density	↓	(-)	(-)	(-)
Bed voidage	↑	↑	↑	(-)
Total liquid hold-up	(-)	(-)	(-)	↓
Total saturation	(-)	↓	↓	↓
Solution breakthrough time	↓	↓	↓	↓
Tracer breakthrough time	↓	↓	↓	↓
Drain-down moisture percentage	(-)	↓	↓	↓

8.2.4 Effect of Particle Size Limits in Mixed Sized Beds

The impact of upper and lower particle size limits on the cumulative RTD profile and bed characterisation parameters is shown from Figure 8.7 through to Figure 8.10. A summary of the bed characterisation parameters for the different bed systems can be found in Table 8.4.

8.2.4.1 GS Systems

When comparing the GS-3 (0.1 - 8 mm), GS-5 (0.5 - 8 mm) and GS-7 (1 - 8 mm) bed systems, the main effect of raising the bottom size from 0.1 to 0.5 to 1 mm was a steady reduction in the tracer breakthrough time which went from 89 to 49 to 4 minutes. The solution breakthrough times were similarly affected with a reduction from 210 to 95 to 42 minutes. These results correspond with a steady decrease in liquid hold-up as the bottom size fraction was increased (0.14, 0.07 and 0.06). Reduced capillary forces, which were shown to be more dominant at the 0.1 to 0.5 mm size range (refer to sub-section 5.2.3.2), are proposed to be responsible for the trend observed.

Though there was no observable trend in the bulk density data, there was a 6% increase when comparing the bed voidage of the GS-3 to GS-5 system and a 30% increase when comparing the GS-5 to GS-7 system. These results suggest that the GS-3 and GS-5 packed beds possessed substantially higher volumes of liquid inaccessible void spaces. The 24-hour drain-down moisture percentage increased as the bottom particle size was increased. Decreased levels of capillary suction forces allowing for less resistance to fluid flow is deemed responsible for the observed effects.

Minor levels of bed slumping, between 0.5 - 1.5 cm were observed for the GS-3 and GS-5 systems. It was unclear as to whether this happened prior to steady state or more gradually over the course of the tests. However, due to the thickness of the beds' drainage layers, which were approximately 3.5 cm in length (refer to Figure 7.3), the impact of the slumping behaviour was minimized.

8.2.4.2 GW Systems

The trend in the cumulative RTD profiles of the GW beds is very similar to that for the GS packed beds. The step increase in particle bottom size from 0.1 to 1 mm reduced the steady state tracer breakthrough times from 99 to 5 minutes. A similar trend existed for the solution breakthrough times which showed an 80% drop when comparing the GW-3 to GW-7 packed beds.

The mixing behaviours for the three GW mixed sized beds appear consistent (refer to Figures 8.7a, 8.8a and 8.9a) but similarly to the GS systems, the GW-7 profile exhibits a slightly longer asymptote which points towards the increased presence of stagnant volumes. This is based on the almost identical amount of time (1039 minutes) both the GW-5 and GW-7 profiles took to reach a value of 0.99 even though the GW-7 curve had a shorter tracer breakthrough time. The modelling results for the different RTD curves are discussed in the subsequent chapter.

The points made during the discussion of the bed voidage and bulk density values for the GS system are proposed to be applicable here as well. Also, there were substantial reductions in both total liquid hold-up and bed saturation as the bottom particle size was increased. Minor levels of slumping between 0.5 and 1.5 cm were measured for the GW-3 and GW-5 systems but the effects are unlikely to have caused any major compaction issues due to the presence of the drainage layer.

8.2.4.3 MO Systems

Two additional bed systems were tested along with the MO-3, MO-5 and MO-7 systems: 0 - 8 mm (MO-2) and 0 - 16 mm (MO-20). The compiled results are shown in Figure 8.10 and the data can be found in Table 8.4.

An increase in the bottom size from 0 to 1 mm, whilst keeping the top size constant at 8 mm, brought about a reduction in the steady state tracer breakthrough time from 189 to 69 minutes. The striking difference between the tracer concentration profile for the MO-2 and the other four systems, is its longer tracer breakthrough time and asymptote. This implies that there were greater volumes of stagnant solution within the MO-2 bed. Due to the fact that it contained the highest mass fraction of fine particles, it is likely that the capillary suction forces present within it were relatively strong. Therefore, once liquid volumes were suctioned in, they were held practically stagnant.

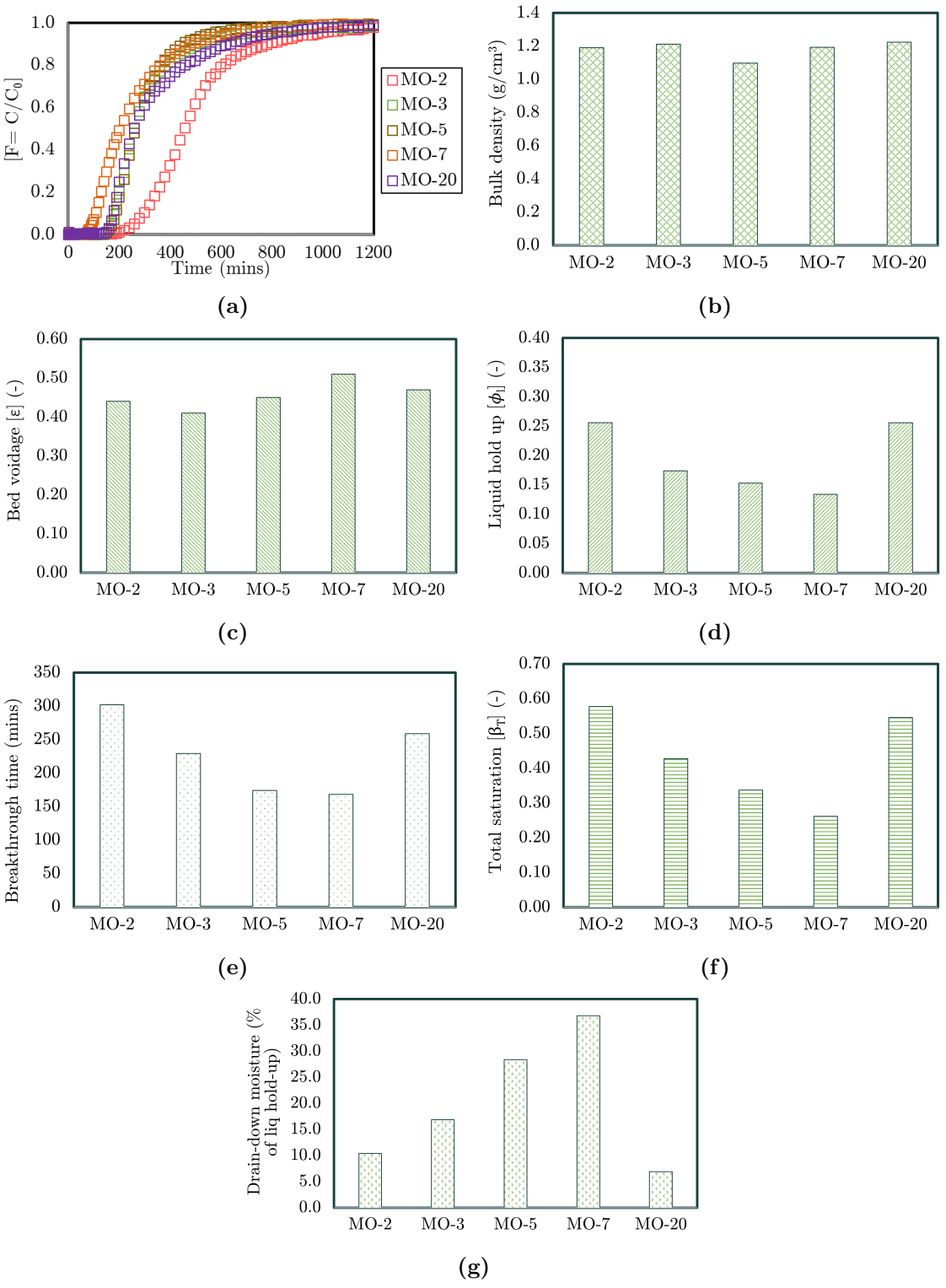

Figure 8.10: (a) Cumulative RTD, (b) Bulk density, (c) Bed voidage, (d) Total liquid hold-up, (e) Solution breakthrough time, (f) Total saturation and (g) 24-hour drain-down moisture for beds composed of MO particles with size fractions ranging from 0 to 16 mm.

Based on the enhanced mixing effects seen in the GS-7, GW-7 and MO-7 beds, the increase in bottom size limit could have led to reduced levels of uniformity within the void networks present within the beds. Finer particles tend to fill up crevices and spaces between larger particles especially during agglomeration, facilitating the formation of more uniform void sizes within agglomerates. Their exclusion contributed towards the mixing effects seen.

Total liquid hold-up, saturation and breakthrough time all decreased as the bed's bottom particle sizes were increased. There was a 72% increase in the drain-down moisture percentage however, as said previously, it is not clear as to whether the 24-hour measurement period is sufficient to be indicative of the dynamic liquid hold-up within the systems.

Raising the top size from 8 mm (MO-2) to 16 mm (MO-20) whilst keeping the bottom size constant at 0 mm initially resulted in a more ideal RTD profile. However, the latter section of the MO-20 curve exhibits a longer asymptote indicating the presence of stagnant solution volumes. This could be due to a reduction in the inter-connectedness of the void network as the top size within the bed was raised. This point is further discussed in Chapter 9, section 9.3.2.1.

8.2.4.4 Summary on the Effect of Particle Size Limits in Mixed Sized Beds

Overall, raising the bottom particle size limits (i.e. removing the finer particles) led to reductions in both the solution breakthrough times and total liquid hold-up values but an increase in drain-down moisture percentages. This suggests an increase in the hydraulic conductivities/permeabilities of the beds and could be due to decreased capillary forces which limited the lateral movement of solution and reduced saturation levels.

The major impacts of bottom particle size limits on the cumulative RTD profiles generated were primarily, a reduction in the tracer breakthrough time as the bottom limit was raised. The mixing behaviours were minimally affected but displayed signs of increased dispersive effects at the largest bottom size limit. This led to the postulation of an increase in the pore size variability within agglomerates when fine particles are excluded from the size distribution.

Increasing the top size limit of the MO systems led to reductions in the drain-down volumes and percentages. The fact that the MO-2 and MO-20 beds had similar liquid hold-up levels yet the MO-20 bed's RTD profile had a longer asymptote points towards an increased presence of stagnant solution volumes in the MO-20 system.

Though minor levels of slumping were observed for the GS and GW beds with lower bottom particle size limits, it is proposed that bed compaction was minimized due to the presence and thickness of a highly porous drainage layer (refer to sub-section 7.2.1). Table 8.6 gives a summary on the effect of particle size limits on the various bed characterisation parameters.

Table 8.6: Summary of the effect of increases in bottom size limits (B.S.L.) [0 to 1 mm] and top size limits (T.S.L.) [8 to 16 mm] on bed characterisation parameters in beds composed of mixed size fractions. GB - spherical, non-porous; GS - irregularly shaped, non-porous; GW - irregularly shaped, porous, highly hydrophilic; MO - irregularly shaped, highly porous. Key: "↑" means an increase in magnitude of parameter while "↓" means a decrease; (-) means no evident trend.

Parameter	**↑ B.S.L**			**↑ T.S.L**
	GB	**GS**	**GW**	**MO**
Bulk density	(-)	(-)	(-)	(-)
Bed voidage	↑	↑	(-)	(-)
Total liquid hold-up	↓	↓	↓	(-)
Total saturation	↓	↓	↓	(-)
Solution breakthrough time	↓	↓	↓	↓
Tracer breakthrough time	↓	↓	↓	↓
Drain-down moisture percentage	(-)	(-)	↑	↑

8.2.5 Effect of Packing Height and Non-Agglomeration

The effect of packing height and state of agglomeration on the cumulative RTD and bed characterisation results for the MO system are shown in Figure 8.11. The three bed heights tested were 0.16 m (MO-2), 0.24 m (MO-2-1.5H) and 0.31 m (MO-2-2H). The GGS particle size distribution, ranging from 0 - 8 mm, was kept constant across all three tests.

The cumulative RTD profiles in Figure 8.11a show that increasing the packing height led to increases in the steady state tracer breakthrough times. There was an 83% increase when

the height was raised from 0.16 m to 0.24 m and a 68% increase when the height was further raised to 0.31 m. The same trend was observed in the solution breakthrough times which had a 48% increase across the total height range. These results were expected as when other parameters are kept constant, a longer bed has a higher moisture holding capacity which increases the average residence times of solute molecules. Minor differences in the shapes of the RTD profiles can be seen, especially in the case of the 0.24 m bed height system. These differences allude to slightly higher degrees of mixing or dispersive effects for the MO-2-1.5H bed.

There was a reduction of approximately 18% in total liquid hold-up and bed saturation as the height was increased from 0.16 to 0.24 m. Further increases in packing height had no noticeable impact on these parameters. Therefore, these results may not be indicative of a trend but due to random variations in bed properties during testing. This is in line with the simulation results by Sheikhzadeh et al. (2005), that found bed height to mostly affect the time required for steady state to be reached without it having a substantial impact on other intrinsic bed characterisation parameters.

The cumulative RTD profile for the non-agglomerated bed (MO-2-NA) shows a 77% longer steady state tracer breakthrough time compared with the MO-2 system. It also has a more constant rate of increase in outlet tracer concentration right until the F-curve approached its maximum value. Such a profile could be due to a stratified bed, with mixing effects present in each layer. The non-agglomerated bed had a bulk density value 23% greater and a bed voidage value 11% percent less than the agglomerated system. This is similar to what was observed by Bouffard and West-Sells (2009), in which cribs packed with agglomerated ore exhibited higher bed voidage values compared to non-agglomerated crib systems. This can be attributed to the shape and size of agglomerates as they tend to be more spherical as well as more uniform in size and therefore pack less densely than non-agglomerated material, resulting in higher bed voidage values.

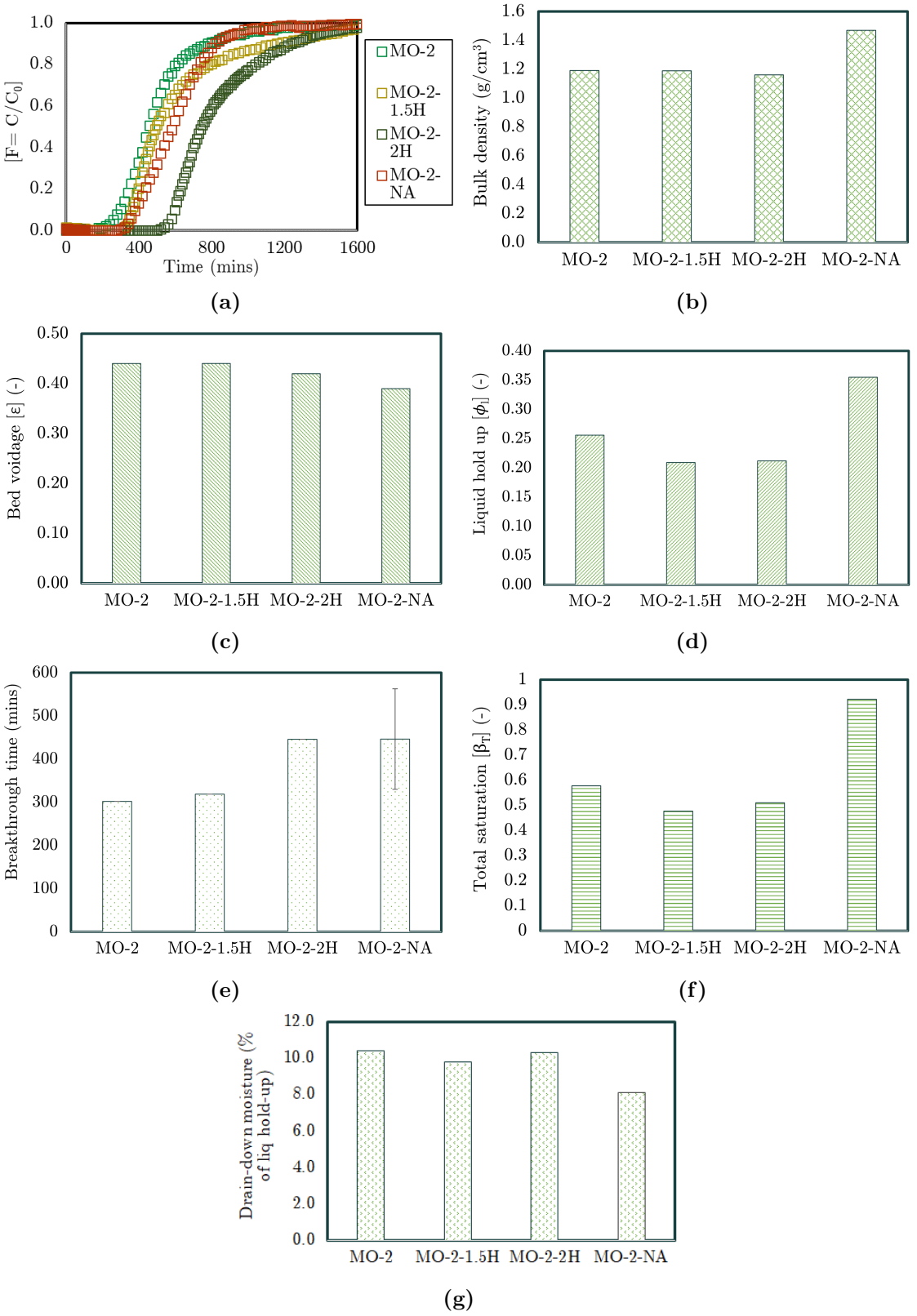

Figure 8.11: (a) Cumulative RTD, (b) Bulk density, (c) Bed voidage, (d) Total liquid hold-up, (e) Solution breakthrough time, (f) Total saturation and (g) 24-hour drain-down moisture for different MO packed bed systems (particle size: 0 - 8 mm).

The non-agglomerated bed achieved a 39% greater total liquid hold-up than the agglomerated system, which translated to a 92% total bed saturation level. This meant that the non-agglomerated bed was very close to complete saturation and flooding. Following on from this, the ∼8% drain-down moisture suggests that most of the extra moisture within the non-agglomerated bed was immobile. These results are very similar to those by Bouffard and Dixon (2001) in which non-agglomerated packed beds of gold ore particles achieved greater levels of bed saturation due to their substantially higher degree of stagnant liquid hold-ups compared to their agglomerated counter parts.

A summary table on the effects of bed height and non-agglomeration on the various bed characterisation parameters can be found at the end of sub-section 8.2.6 in Table 8.7.

8.2.6 Effect of Irrigation Fluid Viscosity

The effect of the irrigation fluid's viscosity on the cumulative RTD and bed characterisation parameters is shown in Figure 8.12. Beds composed of MO particles in the 0 - 8 mm size range were utilized for these tests. The five fluid viscosities used were 0.8 cP (MO-2), 1.2 cP (MO-2-15G), 1.6 cP (MO-2-25G), 1.9 cP (MO-2-30G) and 2.2 cP (MO-2-35G).

From the cumulative RTD results, there were few differences in the shape of the different profiles. For instance, the increase in viscosity from 0.8 to 2.2 cP brought about 19% and 63% reductions in solution and steady state tracer breakthrough times, respectively. Mixing or dispersive effects were also moderately increased along with the 24-hour drain-down moisture percentage. These results, combined with the similar levels of liquid hold-up (0.25 ± 0.01) obtained by the various systems, suggests that raising the viscosity increases a solution's resistance to flow in micro and meso-voids, whilst the increase in density makes it more susceptible to channelling by gravitational forces in macro-voids. This results in a greater spread of solute residence times.

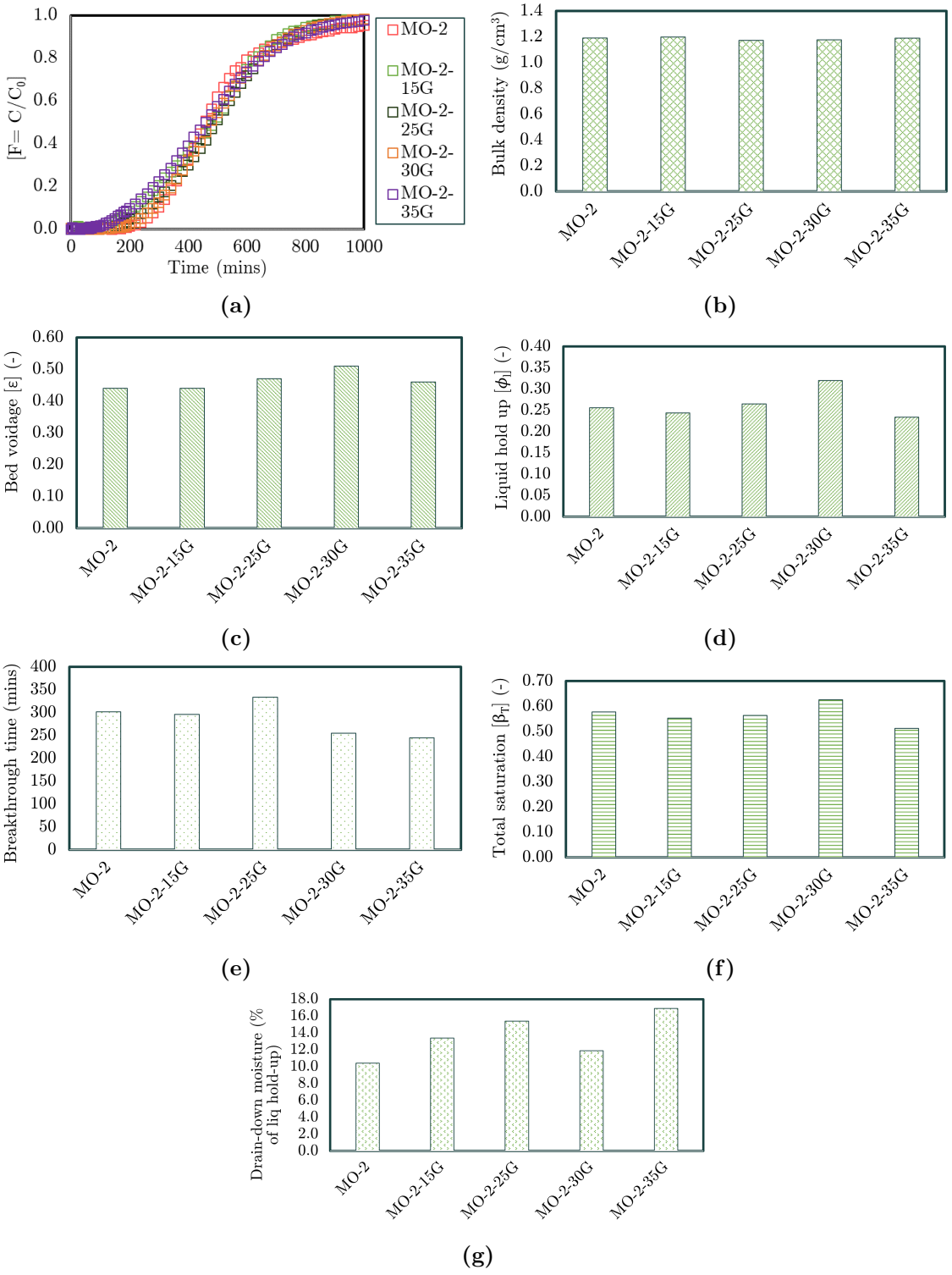

Figure 8.12: (a) Cumulative RTD, (b) Bulk density, (c) Bed voidage, (d) Total liquid hold-up, (e) Solution breakthrough time, (f) Total saturation and (g) 24-hour drain-down moisture for MO packed bed systems irrigated with different viscosity solution (particle size: 0 - 8 mm).

In the case of the MO-2-30G packed bed, the irrigation flux measured (5.35 L/m^2.h) was slightly higher than the average flux (5.04 L/m^2.h) for the other four systems (refer to Table 8.1). Based on results by de Andrade Lima (2006) and Klerk (2003), this played a role in its larger total liquid hold-up and bed saturation values. Table 8.7 gives a summary on the effects of irrigation fluid viscosity on the various bed characterisation parameters.

Table 8.7: Summary of the effect of increases in bed height (B.H.) [0.16 to 0.24 to 0.31 m], non-agglomeration (N.A.) and increases in liquid viscosity (L.V.) [0.8 to 2.2 cP] on the malachite ore (MO - irregularly shaped and highly porous) bed characterisation parameters. Key: "↑" means an increase in magnitude of parameter while "↓" means a decrease; (-) means no evident trend.

Parameter	**↑ B.H.**	**N.A.**	**↑ L.V.**
Bulk density	(-)	↑	(-)
Bed voidage	(-)	↓	(-)
Total liquid hold-up	↓	↑	(-)
Total saturation	↓	↑	(-)
Solution breakthrough time	↑	↑	↓
Tracer breakthrough time	↑	↑	↓
Drain-down moisture percentage	(-)	↓	↑

Chapter 9

Model Fit and Parameter Analysis

A key objective of this thesis was to utilize the nine solute transport models presented in Chapter 6 to quantify hydrodynamic parameters based on the steady state RTD curves presented in Chapter 8.

In this chapter, simulated steady state cumulative RTDs and model parameter values are analysed. Model residual curves are found Appendix G.

9.1 Summary of Selected Models

Table 9.1 summarizes the defining features of the nine models.

Table 9.1: Defining features of the nine selected solute transport models used in the simulation of RTD data

Model	Type	Defining feature
CM-1	Empirical	PFR and CSTR in series with dead volume
CM-2	Empirical	PFR in series with two parallel CSTRs
CM-3	Empirical	PFR in series with two parallel CSTRs and dead volume
TIS	Empirical	CSTRs in series
AD	Semi-phenomenological	Uniform flow, mono-porosity with dispersion coefficient
PE	Semi-phenomenological	Preferential flow, dual-porosity with overall mass transfer coefficient
PE-D	Semi-phenomenological	Preferential flow, dual-porosity with diffusion controlled mass transfer
PDE	Semi-phenomenological	Preferential flow, dual-porosity with dispersion coefficient and overall mass transfer coefficient
PDE-D	Semi-phenomenological	Preferential flow, dual-porosity with dispersion coeficient and diffusion controlled mass transfer

9.2 Simulated RTD and Model Residual Analysis

9.2.1 GB Systems

The fitted RTD and residual analysis curves for the GB can be found in Figure 9.1 and Appendix G (Figure G.1), respectively. The residuals represent the difference between the experimental and model values at each time point.

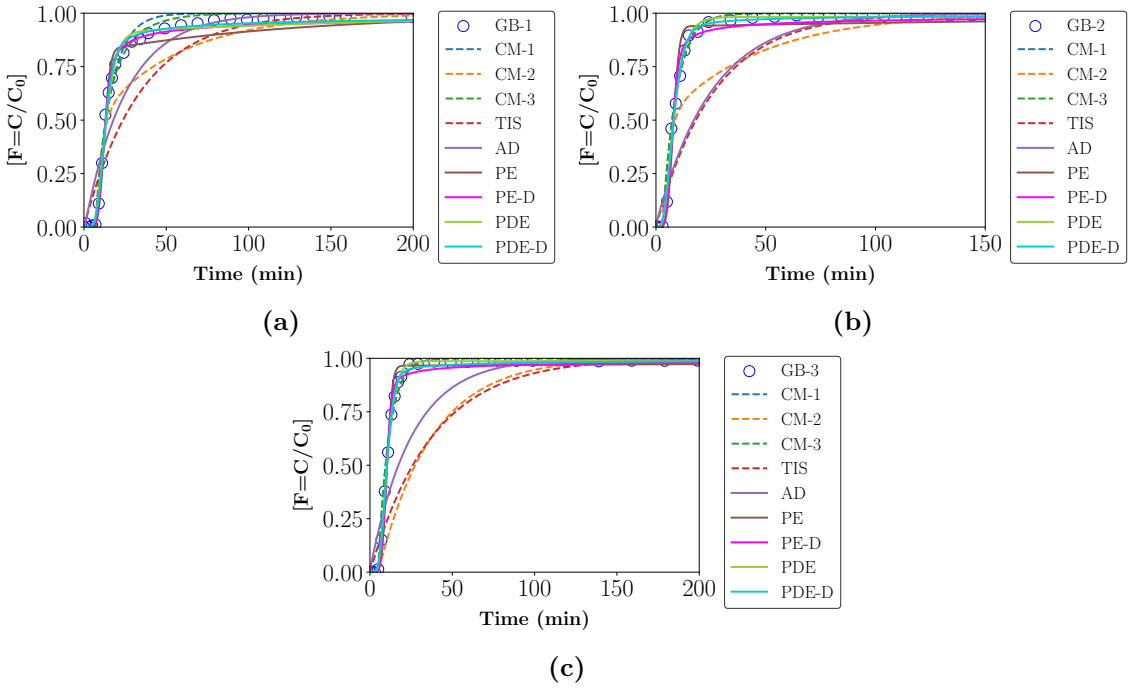

Figure 9.1: Fitted RTD data for packed beds filled with GB: (a) GB-1 (2 mm), (b) GB-2 (5 mm), (c) GB-3 (15 mm).

Based on the results, most of the models were able to fit the RTD data generated from all three GB systems. However, the mono porosity models (TIS, CM-2 and AD) struggled to recreate the steady state channelling effects (quick tracer breakthrough times with no asymptotes) present in the data sets. This led to negative residual values with magnitudes as high as 0.5 in certain cases. The top performing models were the PDE and PDE-D models.

9.2.2 GS Systems

The fitted results for the GS systems are shown in Figures 9.2 and 9.3 while the residual analysis can be found in Figures G.2 and G.3. The models provided a good fit to most of the data but for the GS-10, GS-12 and GS-15 systems, the mono porosity models (CM-2, TIS and AD) struggled to fit the beginning portions of the curve. It is likely that these systems contained substantial amounts of isolated solution volumes which the mono porosity models are unable to account for.

Overall, based on a qualitative analysis, the PDE and PDE-D were the best performing models. Also, the PE-D model had instances were it recorded relatively high residual values, indicating that its model structure was not totally suited to some of the GS data.

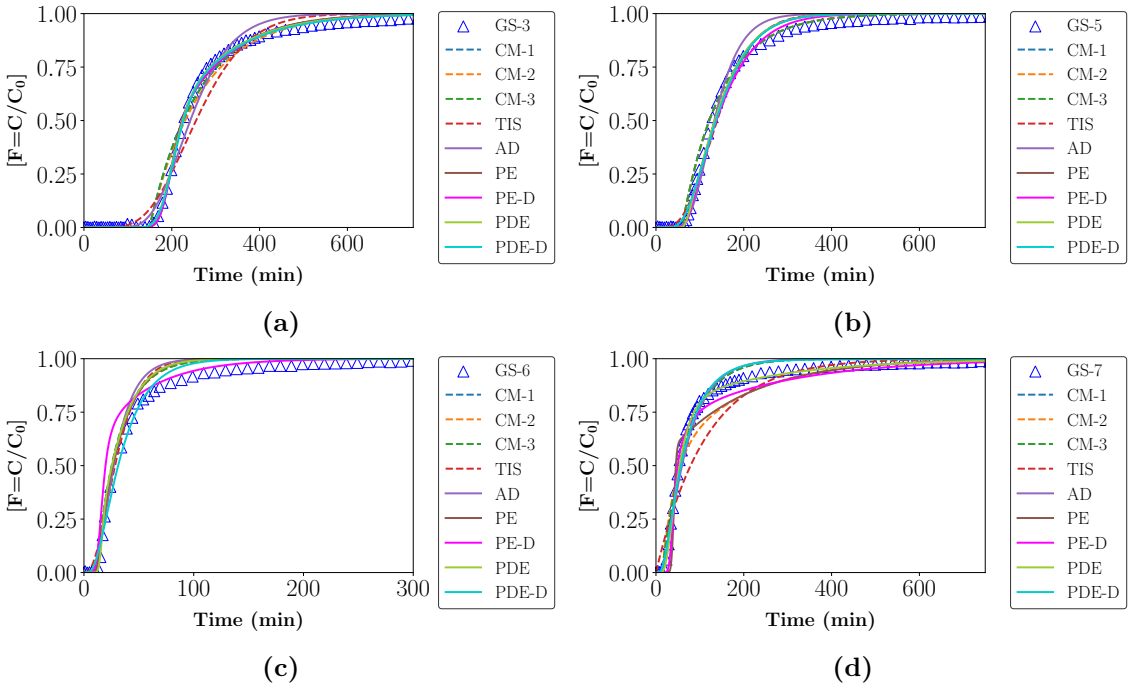

Figure 9.2: Fitted RTD data for packed columns filled with GS: (a) GS-3 (0.1 - 8 mm), (b) GS-5 (0.5 - 8 mm), (c) GS-6 (1 - 2 mm) and (d) GS-7 (1 - 8 mm).

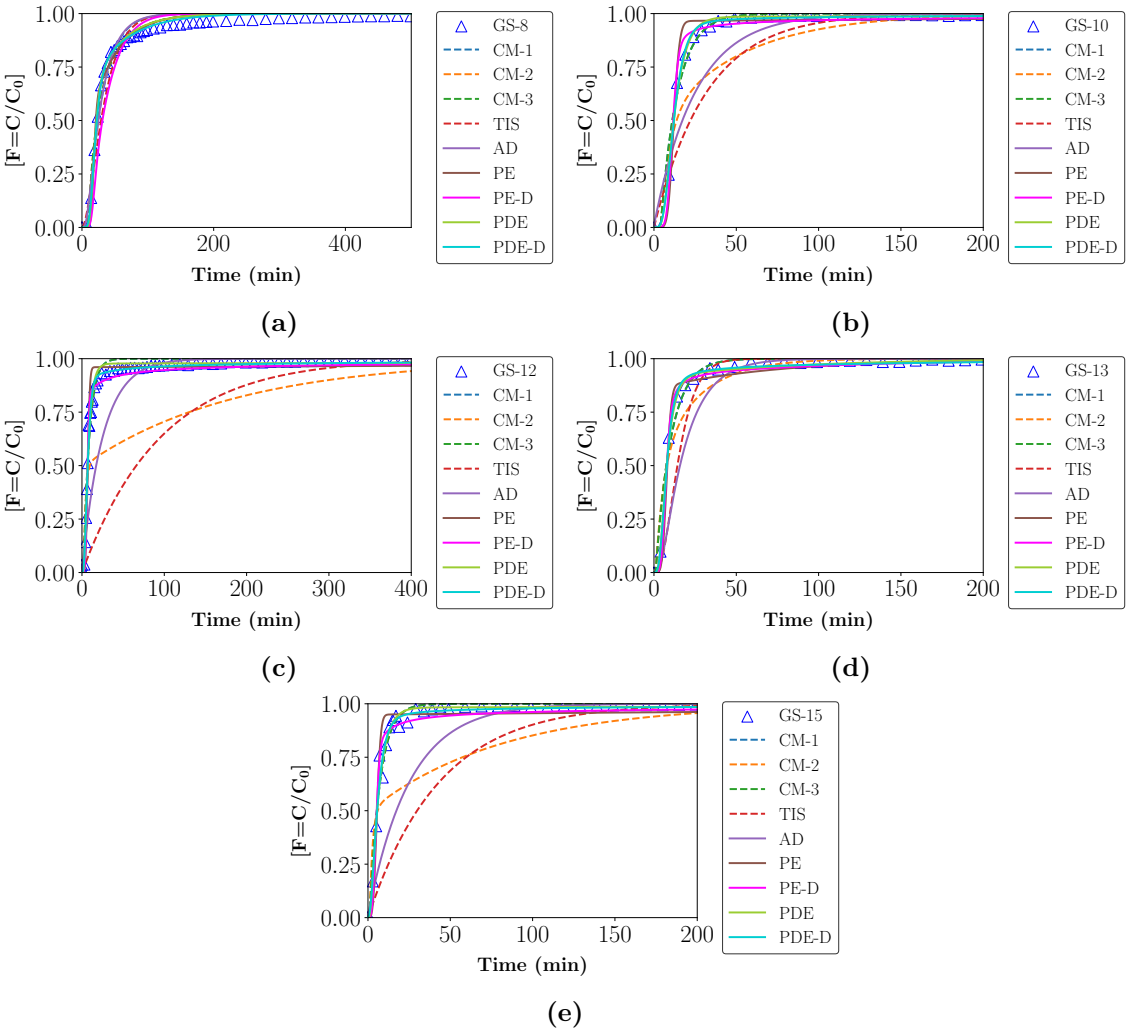

Figure 9.3: Fitted RTD data for packed columns filled with GS: (a) GS-8 (2.0 - 2.8 mm), (b) GS-10 (2.8 - 4.8 mm), (c) GS-12 (4.8 - 5.6 mm), (d) GS-13 (4.8 - 6.7 mm) and (e) GS-15 (6.7 - 8 mm).

9.2.3 GW Systems

The fitted RTDs are found in Figures 9.4 and 9.5, while the residual curves are found in Figures G.4 and G.5. CM-1 and AD models prioritized fitting the beginning portions of the cumulative RTD curves and deviated from the main trend in the latter sections (Figures 9.4d, 9.4e, 9.4f and G.4h). The TIS, CM-2 and PE models fit the latter portions of the RTD data better than the beginning sections.

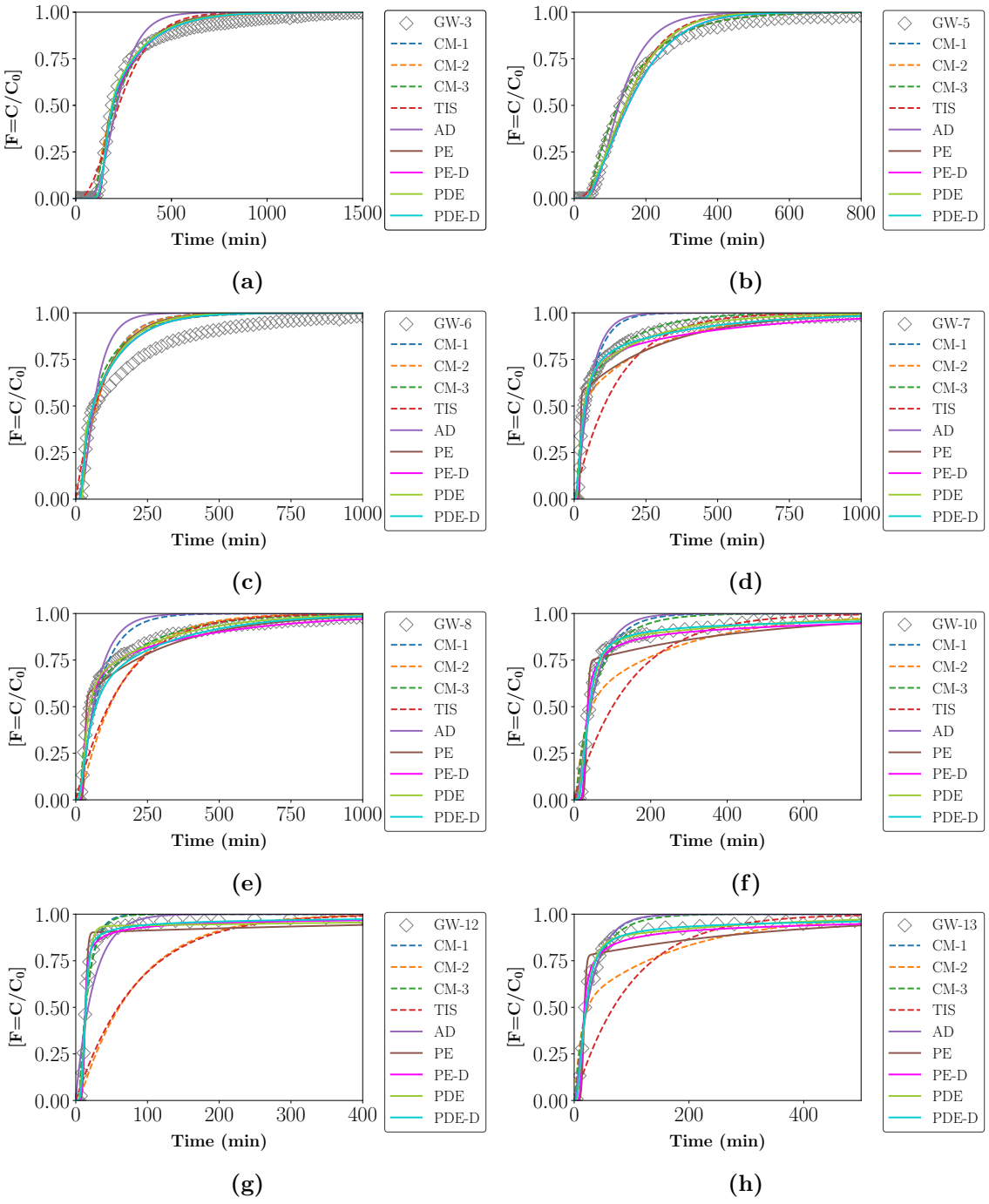

Figure 9.4: Fitted RTD data for packed columns filled with GW: (a) GW-3 (0.1 - 8 mm), (b) GW-5 (0.5 - 8 mm), (c) GW-6 (1 - 2 mm), (d) GW-7 (1 - 8 mm), (e) GW-8 (2.0 - 2.8 mm), (f) GW-10 (2.8 - 4.8 mm), (g) GW-12 (4.8 - 5.6 mm) and (h) GW-13 (4.8 - 6.7 mm).

This indicates that the GW beds with smaller particles had two distinct solute transport rates. The initial rate is likely influenced by enhanced wettability leading to channelling

effects in the early portion of the curves. The second rate is likely influenced by capillary induced stagnant zones leading to longer asymptotes in the RTD profiles. For the mid-sized to large particle beds, only the channelling effects are present and most models cope better with this singular factor. Overall, the PDE and PDE-D models performed the best followed by the PE-D model.

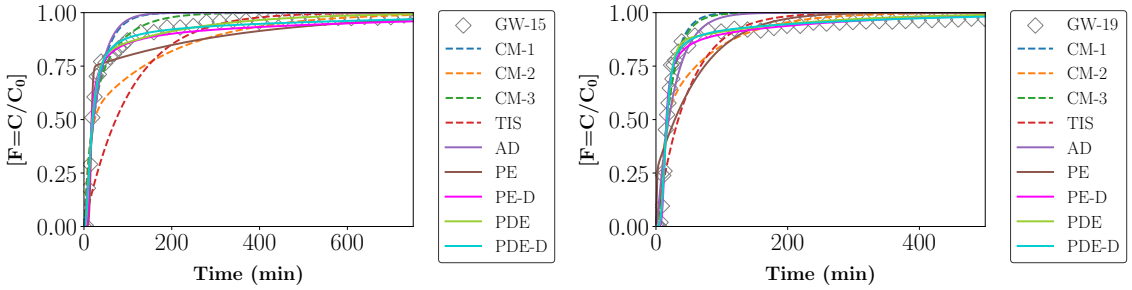

Figure 9.5: Fitted RTD data for packed columns filled with GW: (a) GW-15 (6.7 - 8 mm) and (b) GW-19 (13.2 - 16 mm).

9.2.4 MO Systems

Figures 9.6 to 9.10 show the fitted RTD results for the MO systems.

Particle Size Fraction and Distribution

For MO-2 to MO-8, most models adequately fitted the cumulative RTD profiles. However, for the MO-10 to MO-20 beds variations in model fits become more noticeable. The exclusion of <2 mm particles reduced the fits of the TIS, CM-1, CM-2, CM-3 and AD models. The PDE and PDE-D were the top performing models across the MO-2 to MO-20 systems.

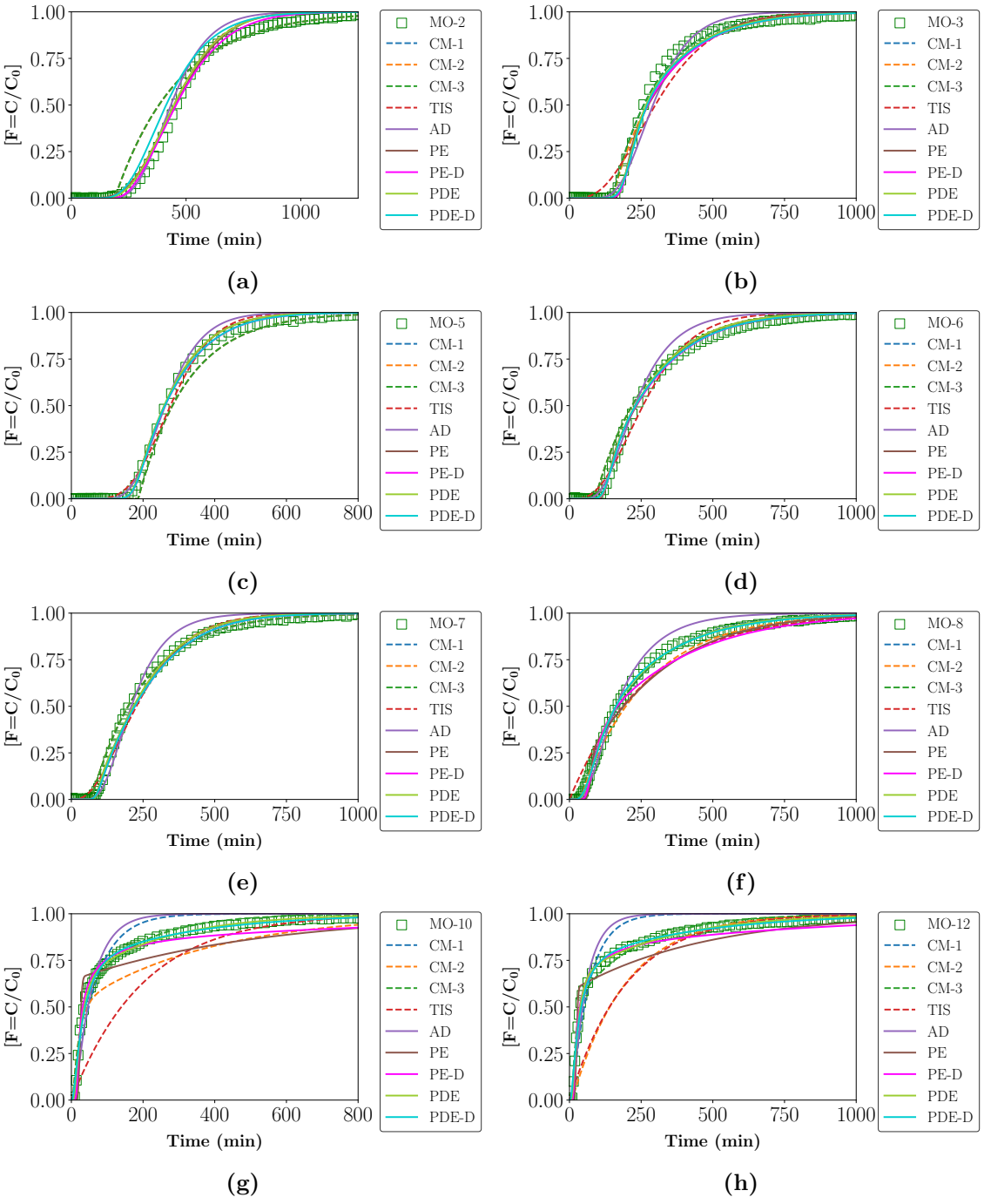

Figure 9.6: Fitted RTD data for packed columns filled with MO: (a) MO-2 (0 - 8 mm), (b) MO-3 (0.1 - 8 mm), (c) MO-5 (0.5 - 8 mm), (d) MO-6 (1 - 2 mm), (e) MO-7 (1 - 8 mm), (f) MO-8 (2.0 - 2.8 mm), (g) MO-10 (2.8 - 4.8 mm) and (h) MO-12 (4.8 - 5.6 mm).

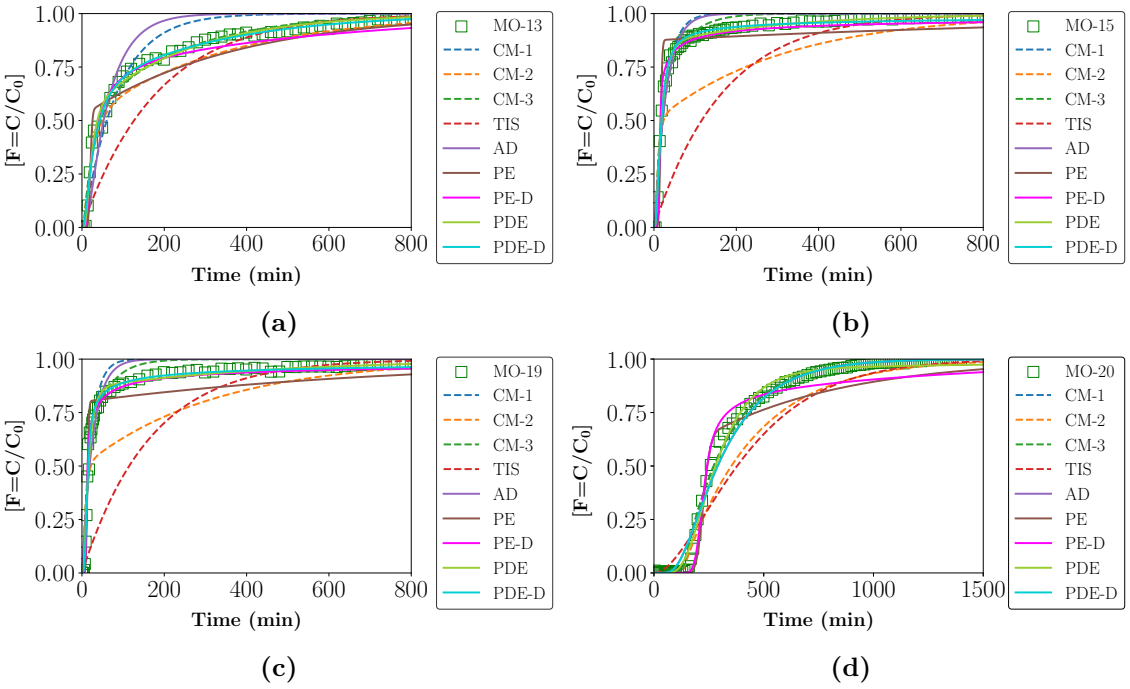

Figure 9.7: Fitted RTD data for packed columns filled with MO: (a) MO-13 (4.8 - 6.7 mm), (b) MO-15 (6.7 - 8.0 mm), (c) MO-19 (13.2 - 16.0 mm) and (d) MO-20 (0 - 16.0 mm) .

Packing Height

The effect of bed height is shown in Figures 9.8 and G.8, respectively. All the models were able to reproduce a majority of the experimental RTD data features but failed in certain aspects. For the 1.5 times normal bed height system,, the models overestimated the RTD values for the latter portion of the curve. This is more noticeable from the residual analysis (Figure G.8b).

At twice the normal bed height, the models provide a sufficient fit to the data but struggle to fit middle portions of the curve and asymptotes. These results indicate that bed size is an important parameter in the ability of the various models to fit the generated data set. Overall, the models with a diffusion controlled mass transfer mechanism between the the dynamic and stagnant regions (PE-D and PDE-D), were the most successful at fitting the data.

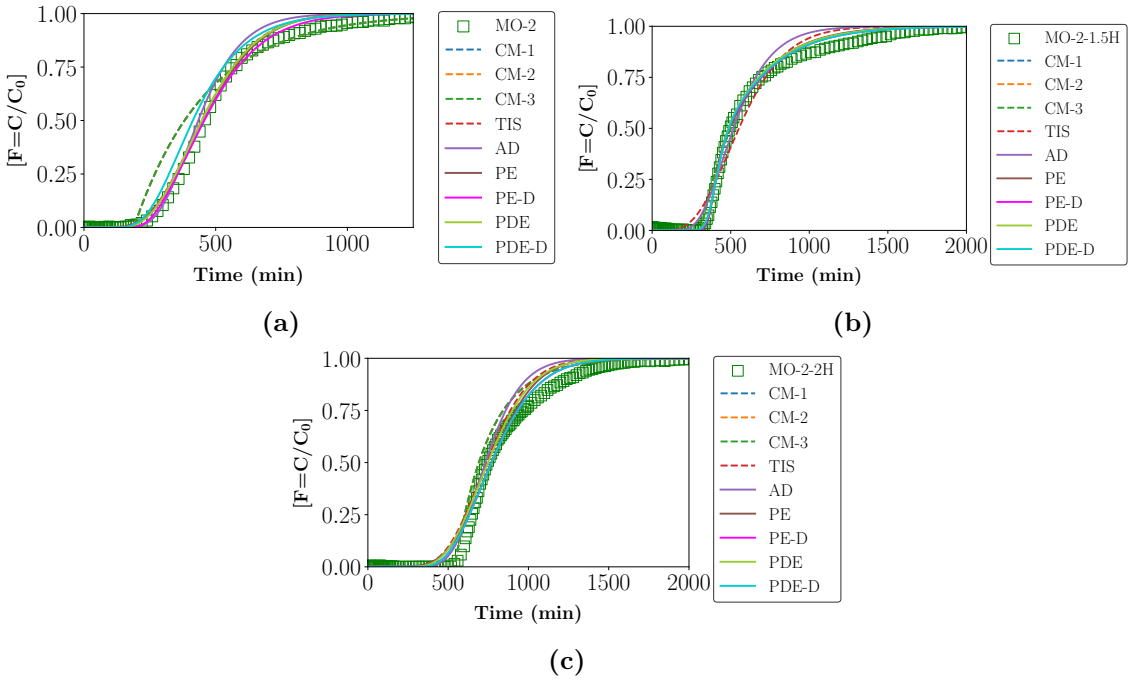

Figure 9.8: Fitted RTD data for packed columns filled with 0 - 8 mm MO particles with different bed heights: (a) MO-2 (normal bed heigth), (b) MO-2-1.5H (1.5 × normal bed height) and (c) MO-2-2H (2 × normal bed height).

State of Agglomeration

The results for the agglomerated and non-agglomerated beds (Figure 9.9), show that most of the models were able to fit the RTD profile for both systems.

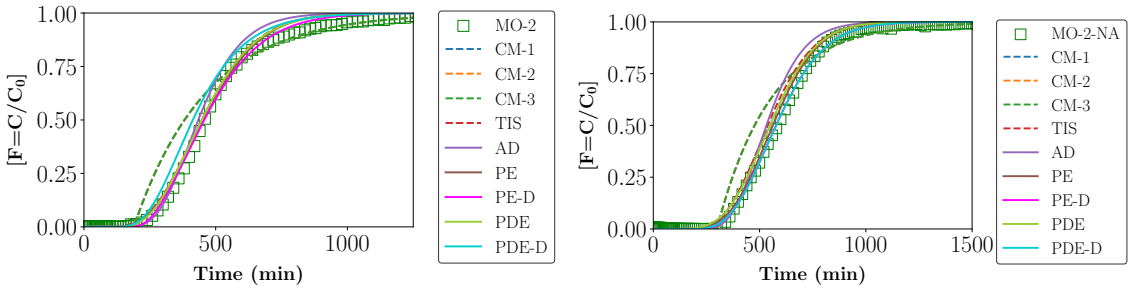

Figure 9.9: Fitted RTD data for packed columns filled with 0 - 8 mm MO particles: (a) agglomerated (MO-2) and (b) non-agglomerated (MO-2-NA).

However, all three compartmental models struggled with the non-agglomerated system,

showing significant deviations with maximum residual values greater than 0.2. Therefore the configuration chosen were not suited for the non-agglomerated bed. The AD and TIS models showed the next highest deviations with maximum residual values around 0.1. The best performing models were the PE-D and PDE-D models, which produced identical responses.

Solution Viscosity

The effect of irrigation solution viscosity on model fits is shown in Figures 9.10 and residual analysis in Figure G.10.

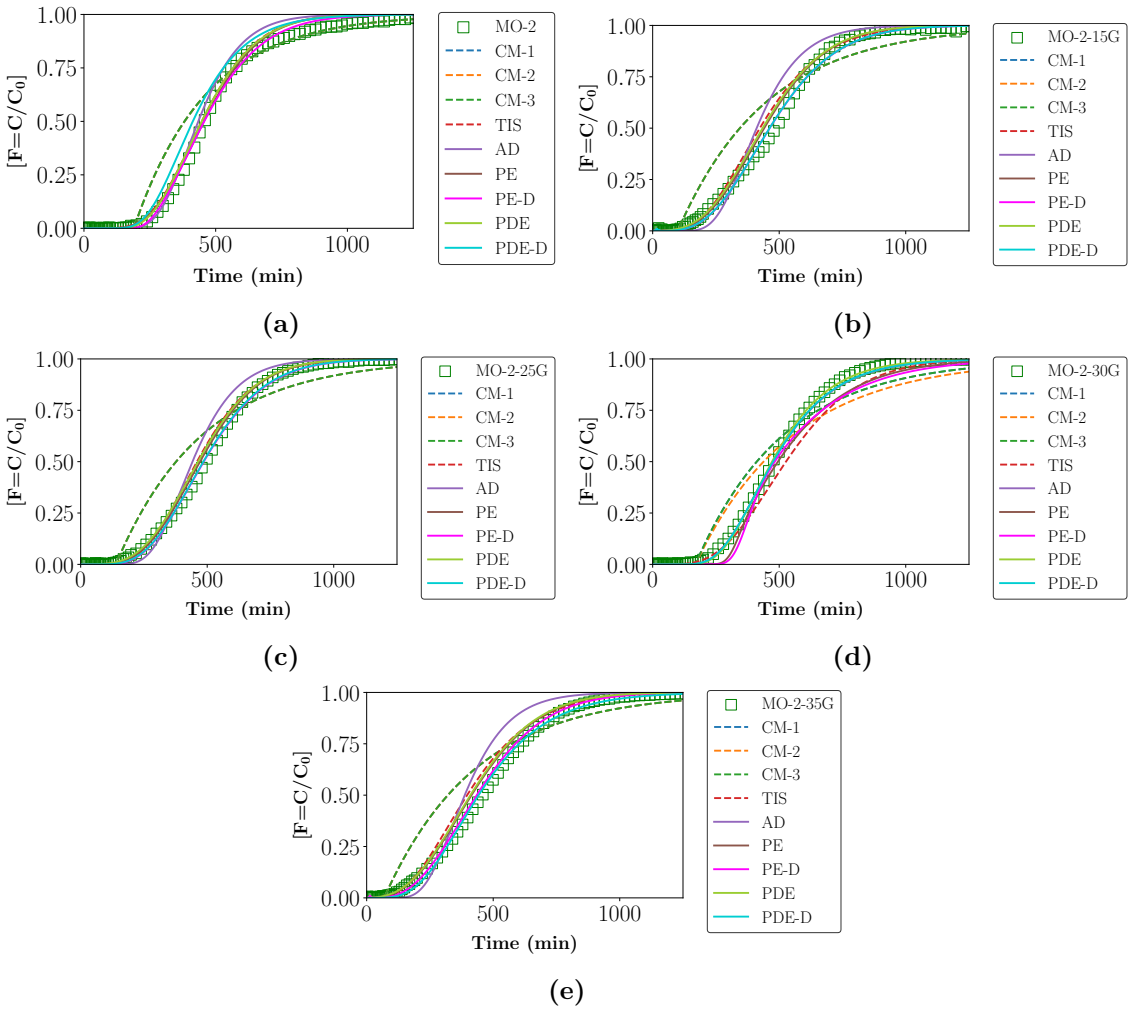

Figure 9.10: Fitted RTD data for packed columns filled with 0 - 8 mm MO particles and irrigated with solutions of different viscosities: (a) MO-2 (0.8 cP), (b) MO-2-15G (1.2 cP), (c) MO-2-25G (1.6 cP), (d) MO-2-30G (1.9 cP) and (e) MO-2-35G (2.2 cP).

It is evident that all three compartmental models struggled to reproduce the RTD data for the 1.2 cP (MO-2-15G) to 2.2 cP (MO-2-35G) beds. For the most part, each gave identical responses with relatively high maximum residual values of 0.2. The AD model also showed relatively high deviation with an average maximum residual value above 0.1 across all four systems. The TIS model outperformed the AD model for a majority of the data sets. Overall, the best performing models were the PDE-D and PE-D models, though other models like the PE and PDE also performed relatively well.

9.3 Model Parameter and Goodness of Fit Analysis

In this section, the fitted parameter values and goodness of fit data for the nine solute transport models based on their simulated RTD curves will be presented and analysed. An overall summary of the data can be found in Tables H.1 and H.2 in Appendix H.

9.3.1 Overall Least Squared Error and Regression Analysis

Model fit analysis focuses on the average least squared error and regression coefficient values for: beds composed of different packing materials, with and without fines and with narrow or mixed sized fractions.

9.3.1.1 Effect of Packing Material Properties

The least squared error and regression coefficient comparisons across the different packing materials can be found in Figure 9.11. In the case of the MO beds, values for the non-agglomerated system, as well as those beds irrigated with solutions other than water, were excluded from all the calculations.

Figures 9.11a and 9.11b show that the mono porosity models (CM-2, TIS and AD) had their largest average error (lowest R^2 values) for the GB systems and their lowest error for the MO beds. This is an interesting response as due to the isolated fluid pockets formed within the GB beds during their initial wetting stages, the mono porosity models struggled to account

for both the presence of these inactive volumes and the high degree of channelling observed. In the case of the MO system, though it recorded the highest total liquid hold-up values, a large fraction of these volumes were active (refer to section 8.2) which explains why the mono porosity models coped better with these profiles.

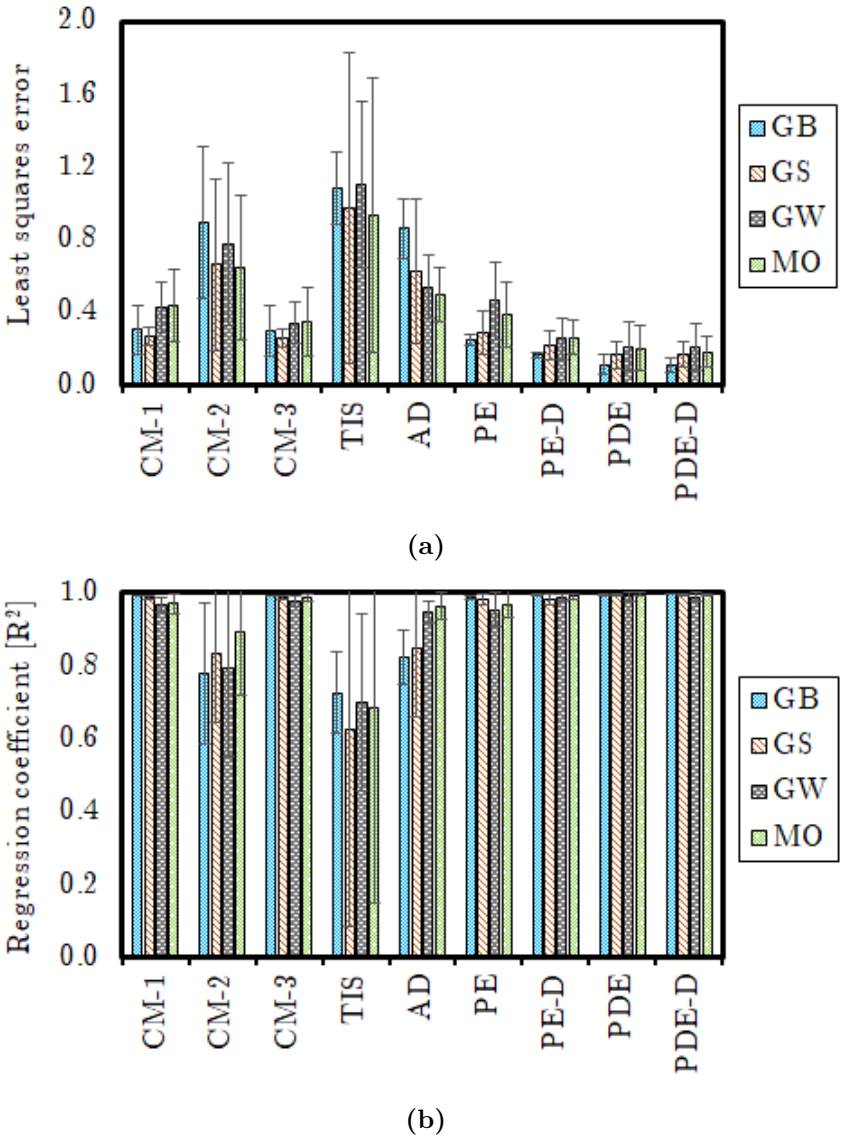

Figure 9.11: (a) Least squares error and (b) regression analysis model comparisons for the different packing materials.

The dual-porosity models (PE, PE-D, PDE and PDE-D) as well as the CM models with dead volumes (CM-1 and CM-3) all performed much better than the mono porosity models.

This is based on the average error and regression coefficients (refer to Figures 9.11a and 9.11b). For instance, when comparing the average fit across all the systems, the CM-1 model obtained an average error of 0.35 and regression coefficient of 0.98 while the CM-2 model obtained values of 0.74 and 0.83, respectively.

The CM-1, CM-3, PE, PE-D, PDE and PDE-D models were better at fitting RTD profiles from non-porous systems (GB and GS) than porous packed beds (GW and MO). This is quite evident in the values acquired for the PE model which showed an average error value of 0.27 across the non-porous systems and a value of 0.42 for the porous systems. Based on a qualitative analysis of the fitted curves shown in Figures 9.4 to 9.7, most of the deviation occurred at the asymptotes of the RTD curves which are associated with the presence of stagnant liquid zones (Yusuf, 1984). As capillary effects are more present in beds composed of porous particles, one could argue that they lead to the creation of stagnant zones within a bed. However, it is unclear in a drip irrigated system, as to whether these zones are truly stagnant or just located further away from the central irrigation axis, which could result in a greater spread of solute residence times, regardless of whether or not the solutions are actively moving. Still, the presence of capillary forces is an important factor in the modelling of packed beds.

9.3.1.2 Effect of Fines

For the data shown in Figures 9.12a and 9.12b, the goodness of fit values for the "<2 mm included" category, were calculated from average error and regression coefficient values for all the bed systems with particle bottom sizes less than 2 mm and vice versa for the "<2 mm excluded" category. These results were compiled to ascertain the effect that capillary suction, shown to be more prevalent in beds composed of finer particles, had on the the data fitting capabilities of the different models.

Mono porosity models were better able to fit data from beds with fines. With finer particles included, the TIS model obtained an average error value of 0.50 and a R^2 value of 0.98. Without the finer particles, it had an average error of 1.42 and a R^2 value of 0.42. Similar trends are evident for the AD and CM-2 models. This suggests that the presence of capillary

suction effects reduced the formation of completely isolated flow volumes within the various bed systems during the initial wetting stages, confirming the mono porosity assumption.

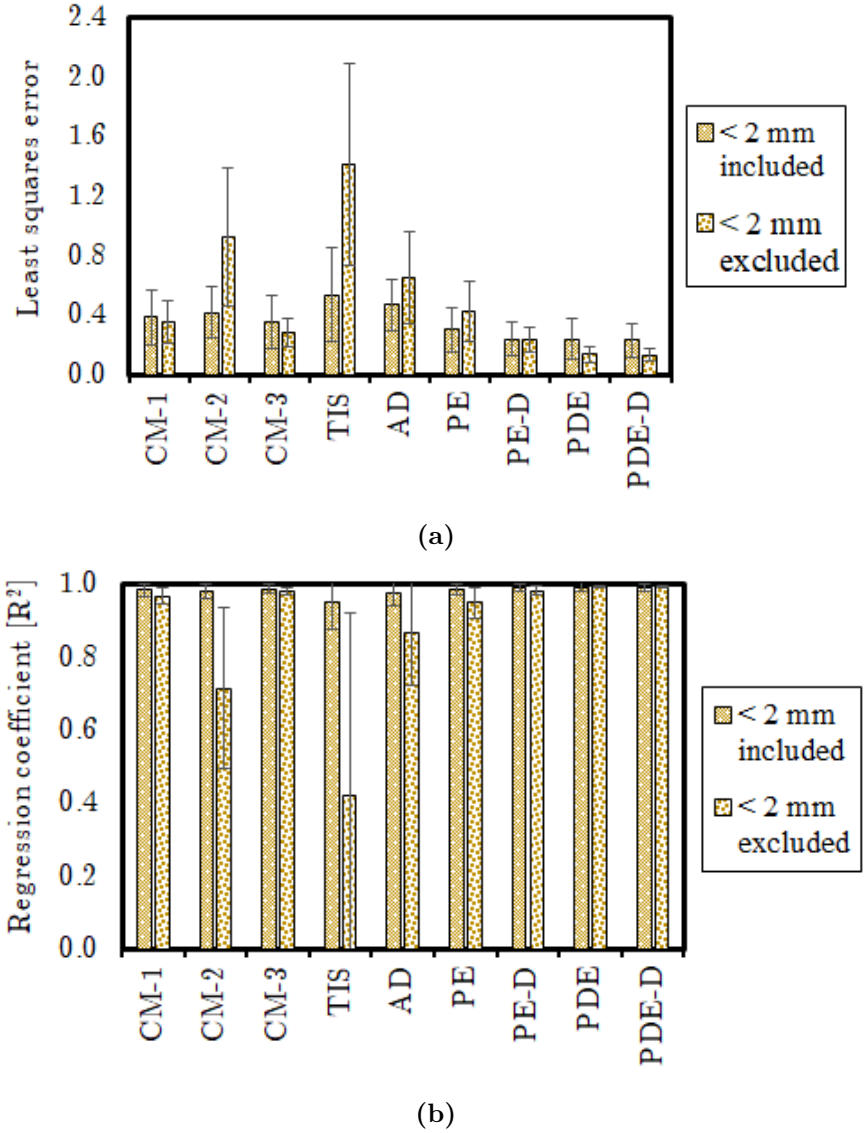

Figure 9.12: (a) Least squares error and (b) regression analysis model comparisons for packed bed systems in which particles with size < 2 mm were either included or excluded.

At first glance, the assertion that capillary effects lead to a reduction in the presence of isolated liquid volumes may seem to imply a reduction in stagnant liquid hold-up. However, based on the definitions given in section 7.2.2 there is a critical difference between stagnant liquid zones and isolated liquid volumes. Therefore, it is possible that though capillary suc-

tion reduces the occurrence of isolated volumes, they could aid in the formation of stagnant volumes. Stagnant volumes, can still be accounted for, in a limited sense, by mono porosity models, whilst isolated or dead volumes present more a challenge.

The effect of the presence of fines, on the dual porosity and compartmental models with included dead volumes, was varied. The PE model, similar to the mono porosity models coped better with beds in which fines were included. Data for the CM-1 and PE-D models suggests these models had no preference and gave similar responses regardless of whether fines were included or not. The CM-3, PDE and PDE-D models all displayed a slight preference for data generated from beds without fines. As these were the most complex models, their added level of complexity enabled them to handle isolated volumes better than the other models.

RTD profiles from beds without fines were more difficult to simulate, requiring greater levels of sophistication in model formulations. Therefore, based on the results, the inclusion of finer particles (<2 mm) into a packed bed increases the modelling options available for the simulation of RTD profiles, as even the mono porosity models performed relatively well in these cases.

9.3.1.3 Effect of Size Distribution

The data for the "Narrow size fractions" displayed in Figure 9.12 were calculated by taking the average error and regression coefficient values for the all the bed systems with a top and bottom size difference less than 3 mm. The "Mixed size fraction" data consisted of bed systems with a top and bottom size difference greater than 3 mm. The previously mentioned MO systems were again excluded from the calculations.

The results follow a similar trend to those for the <2 mm included and excluded categories. This is because, for permeability reasons, most of the narrow size fractions contained particles with sizes greater than 2 mm. Hence, the "Narrow size fractions" have fitting trends similar to the "<2 mm excluded" data sets and the "Mixed size fraction" to the "<2 mm included" group. This meant that the mono porosity models struggled the most to fit the data from the beds with narrow size fractions due to the lack of capillary effects. The TIS model

again showed the highest average error value of 1.25 and highest standard deviation of 0.69. The CM-2 and AD models also recorded significantly high error values of 0.85 and 0.64, respectively. The CM-1 and PE models performed slightly worse with the narrow size fractions when compared to the mixed fraction.

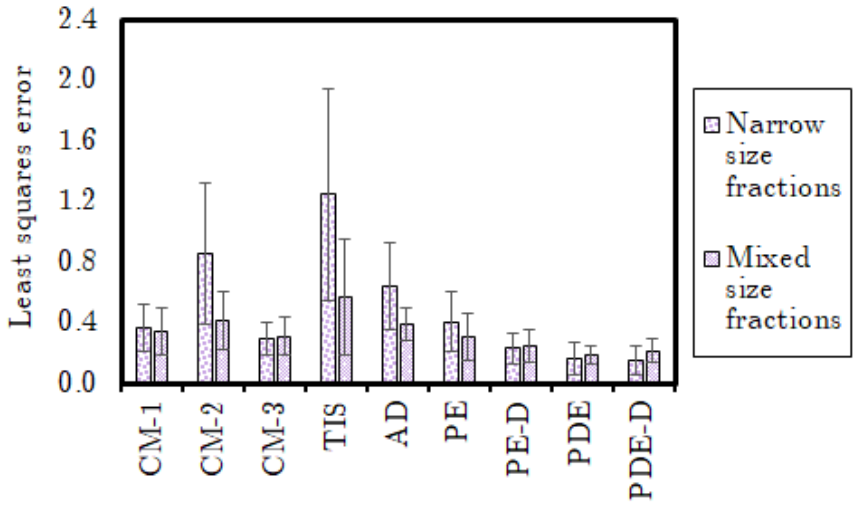

(a)

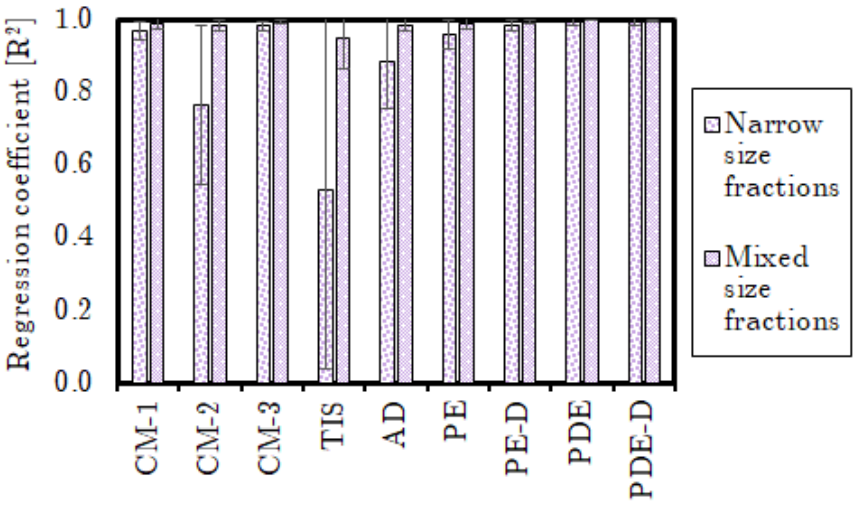

(b)

Figure 9.13: (a) Least squares error and (b) regression analysis model comparisons for packed systems composed of either narrow or mixed size fractions.

Though CM-3, PE-D, PDE and PDE-D models showed minor preferences for the narrow size fractions, they also performed relatively well at fitting the data generated from beds with the

mixed size fractions. Overall, the PDE and PDE-D models were the top performing models for reasons given in previous discussion about fines.

9.3.2 Model Parameter Analysis

This section discusses the optimized values for the main fitting parameters in each of the nine models. In order to limit computational times, lower and upper boundaries were set. These boundaries are described in Table 9.2. It should be noted that in CM model cases, additional constraints to ensure conservation of mass were applied. These were shown in Equations (6.8), (6.9) and (6.10).

Table 9.2: Lower and upper boundaries used during the optimization of the different model parameters.

Symbol	Model parameter	Lower Boundary	Upper boundary
CM Models			
V_C	Volume of each CSTR (mL)	$1 \cdot 10^{-5}$	$V_T - V_P$
V_D	Dead Volume (mL)	$1 \cdot 10^{-5}$	$V_T - V_P$
TIS Model			
N	Number of CSTR tanks (-)	1	None
AD, PDE and PDE-D Models			
D_{ds}	Dispersion coefficient (m^2/min)	$1 \cdot 10^{-9}$	None
PE, PE-D, PDE and PDE-D Models			
β_d	Dynamic saturation	$1 \cdot 10^{-5}$	β_T
PE and PDE Models			
$K_m a$	Overall mass transfer coefficient (min$^-$1)	$1 \cdot 10^{-9}$	None
PE-D and PDE-D Models			
X	Maximum pore length (m)	$1 \cdot 10^{-3}$	0.2

For the CM model volumes and dynamic saturation coefficient, the lower constraints ensured that the parameters were still able to be used for the model calculations but were of a small enough magnitude to render their effects insignificant. The upper constraints were based on the total volume or total saturation limits based on measured experimental data.

The N parameter in the TIS model was given a lower constraint of 1 to ensure that an output was generated, while no upper limit was utilized. Therefore, only when the error was

successfully minimized, did the manual optimization process stop.

The reasoning for the mass transfer and dispersion coefficient constraints was the irrigation fluid's superficial velocity which averaged around $8 \cdot 10^{-5}$ m/min. Therefore at the lower boundary of $1 \cdot 10^{-9}$, the effects of the dispersion and mass transfer coefficients would be negligible. A top boundary was not given for these parameters to give the optimiser more freedom to explore different values.

In the case of the maximum pore length (X), the limits chosen were related to the diameter of the beds which was kept constant at 0.1 m. The lower size limit of 0.001 m was chosen for computational stability. The upper limit (0.2 m) was arbitrarily chosen to be two fold longer than the bed diameter to account for tortuosity in the diffusional pore length.

9.3.2.1 Dead Volumes

Dead volumes are pockets of fluids completely isolated from the steady state flow path within packed bed systems. As these volumes do not aid solute transport, their presence is to be avoided in a heap leaching context. Therefore understanding how various factors affect their formation is an important step for the successful design of heap leaching operations.

Figure 9.14 shows an increase in the dead to total volume fraction (V_D/V_T) with particle size across all four narrow size fraction systems. The results support the argument for enhanced mechanical dispersion of liquid droplets in beds with larger particle length scales during the wetting stages. The random nature of this fluid displacement results in the formation of isolated volumes that are disconnected from the main flow path at steady state. The amount of fluid displaced increases with particle sphericity and decrease with porosity. This is based on the average V_D/V_T obtained by the two models for each packing, which were 0.61 for the GB system, 0.45 for the GS system, 0.51 for the GW system and 0.37 for the MO system.

The extra parallel CSTR component present in the CM-3 model allowed it to account for dual permeable flow which resulted in better fits compared to CM-1. This suggests that some of the liquid volumes in the beds, rather than being completely dead, flowed at relatively slower velocities.

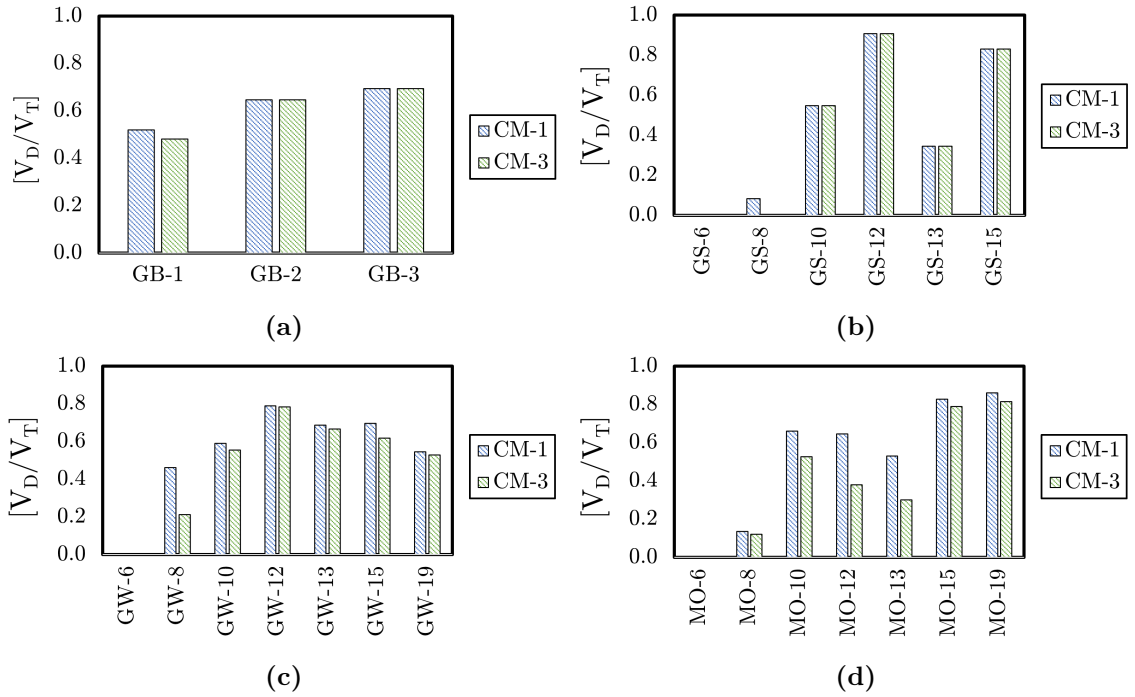

Figure 9.14: Fitted fractions of dead to total volume for beds with narrow size fractions: (a) GB, (b) GS, (c) GW and (d) MO.

Figure 9.15 shows that at a top size of 8 mm and bottom size less than 1 mm (e.g GW-3 and GW-5), little to no dead volumes were obtained by the models. Raising the particle bottom size to 1 mm (GS-7 and GW-7) and top size to 16 mm (MO-20) brought about a substantial increase in V_D/V_T. These results support the assertion made in section 8.2.2 regarding a reduction in dead volumes with an increase in void network connectivity aided by the presence of fines or porous particles.

Packing height and non-agglomeration did not seem to have any impact on V_D/V_T. The dead volumes for the MO-2, MO-2-1.5H, MO-2-2H and MO-2-NA systems were all equal to zero for both the CM-1 and CM-3 models (refer to Table H.1). It is again likely that the presence of fines (<2 mm particles) and porosity were the dominant factors responsible for the lack of dead volumes.

The data for the effect of irrigation fluid viscosity on the presence of dead volumes found no relationship between the two factors. However, it should be borne in mind that all the compartmental models had a relatively more difficult time fitting the RTD data from beds

irrigated with higher viscosity solutions. The average R^2 coefficient across the systems for the CM-1 and CM-3 models was 0.956.

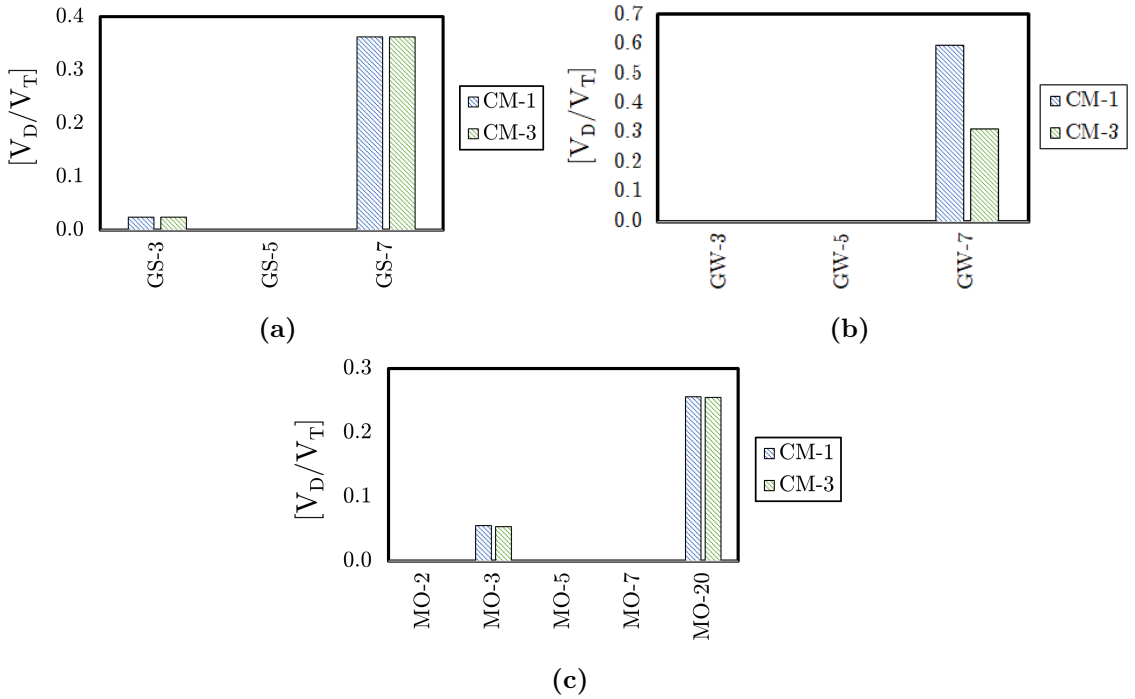

Figure 9.15: Fitted fractions of dead to total volume for beds with mixed size fractions and varying lower size limits: (a) GS, (b) GW and (c) MO [No data is shown when values equal 0].

9.3.2.2 Dual Permeability

Dual permeability is a form of preferential flow and refers to variations in the flow velocities of different fluid volumes within a packed bed. The presence of dual permeable zones can be elucidated using the CM-2 and CM-3 models. Both these model had two CSTRs in parallel. When the fitted CSTR volumes are equal, the calculated fraction of V_{Cmin}/V_{CT} will be 0.5, which indicate no dual permeable zones. The degree to which the calculated fraction deviates from this maximum value is proportional to the difference in the solute residence times between the two CSTR volumes.

From the results in Figure 9.16, there was an increase in the presence of dual permeable regions with higher levels of particle porosities pointing to the formation of more complex

flow patterns. This is understandable considering that the non-porous systems (GB and GS) displayed symptoms of channelling behaviour (refer to section 8.2.2), thereby confining flow to the central irrigation axis with little possibility of variation in fluid flow rates. The MO systems show a positive correlation between dual permeable regions and particle size fraction, likely due to the increased disparity between intra-particle pore and inter-particle void flow regions in beds composed of larger particles.

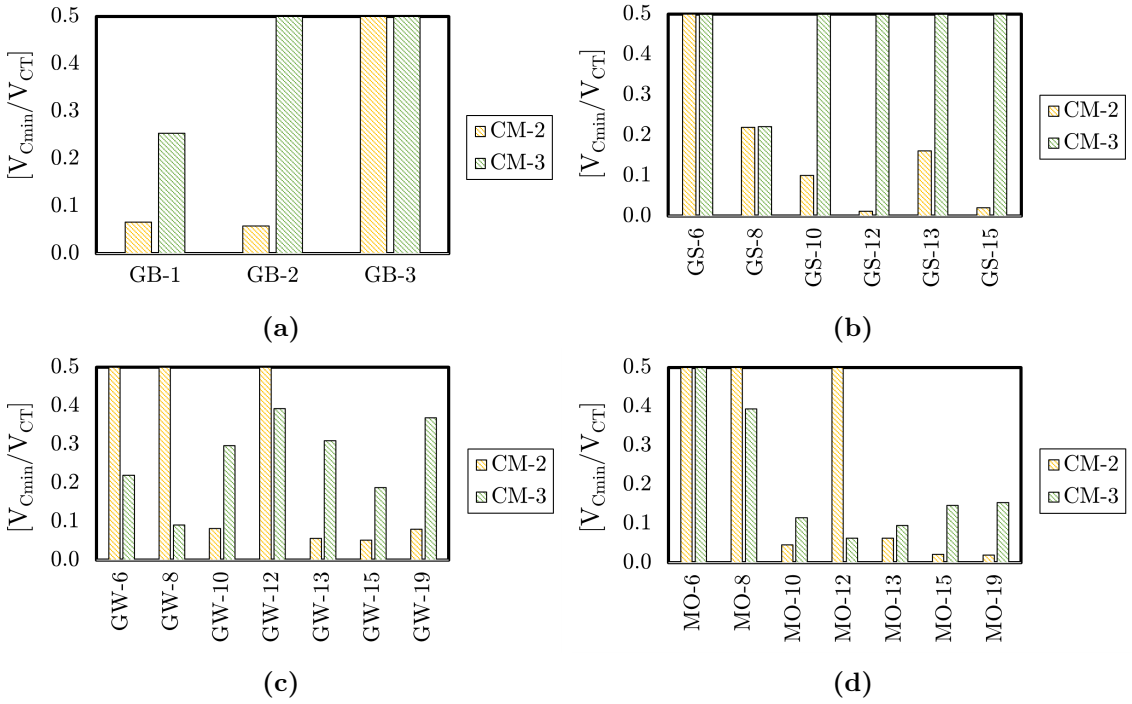

Figure 9.16: Fitted fractions of the minimum to total CSTR volumes for beds with narrow size fractions: (a) GB, (b) GS, (c) GW and (d) MO.

The fractions obtained by the CM-2 model are substantially different to those of CM-3. Based on their R^2 values, 0.763 (CM-2) and 0.983 (CM-3), the ability to account for dead volumes in these systems was an advantageous feature of the CM-3 model.

The results of the mixed sized beds in Figure 9.17 show little evidence of the presence of dual permeable regions. Therefore, agglomeration with fines reduced the occurrence of dual permeable flow within these beds. This beneficial effect is also apparent in the results for the MO bed systems of different packing heights, state of agglomeration (Figure 9.18a) and those irrigated with different viscosity solutions (Figure 9.18b). However, other preferential

flow characteristics could still be present within the beds.

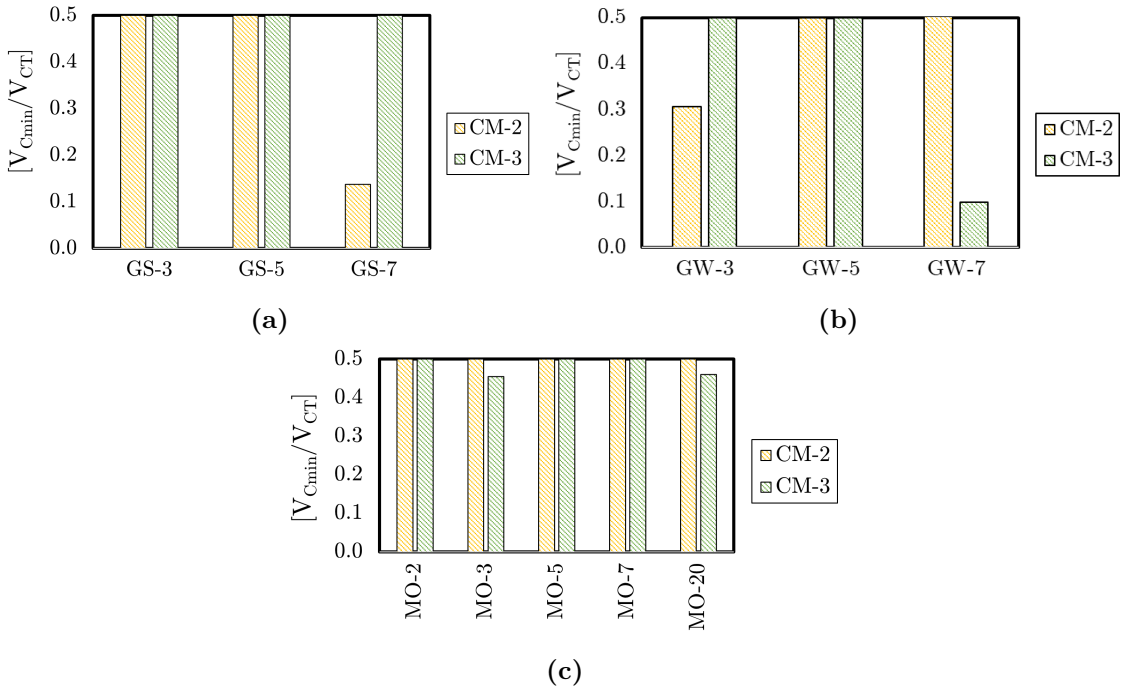

Figure 9.17: Fitted fractions of the minimum to total CSTR volumes for beds with mixed size distributions and varying lower size limits: (a) GS, (b) GW and (c) MO.

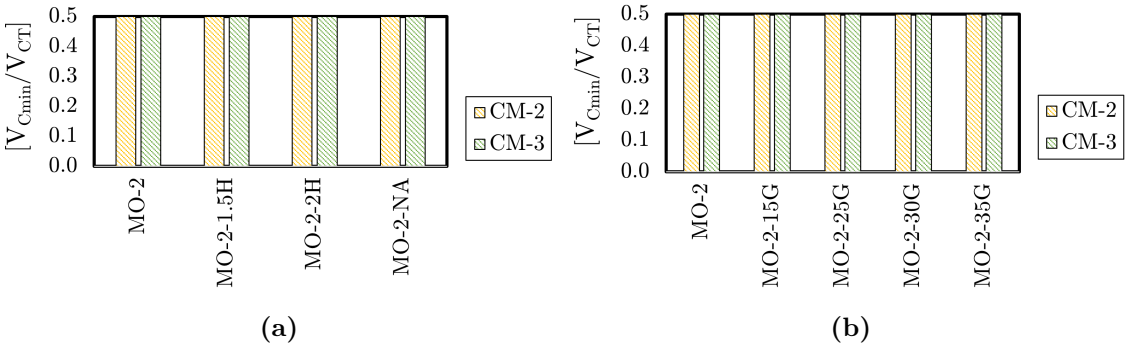

Figure 9.18: Fitted fractions of the minimum to total CSTR volumes for 0 - 8 mm MO beds with: (a) different packing heights and states of agglomeration, (b) irrigated with solutions of varying viscosities.

9.3.2.3 Plug flow vs. CSTR behaviour

The degree to which the cumulative RTDs of the beds resembled either CSTR or PFR flow profiles can be ascertained from parameter N of the TIS model. In certain cases, a higher degree of uniform plug flow behaviour may be beneficial in ensuring that all the reactants that are fed to a heap, spend a sufficient amount of time to fully react within the bed.

It should be noted that the TIS model performed the worst at fitting the experimental RTD data especially in the case for the narrow size fractions for which the model attained an R^2 value of 0.489 (refer to Figure 9.13). This explains why for the majority of the results in Figure 9.19, the model defaulted to a value of 1 CSTR tank as it could not cope with the RTD profiles generated. There is a slight decrease in the number of tanks predicted as particle size fraction increased for the GS data.

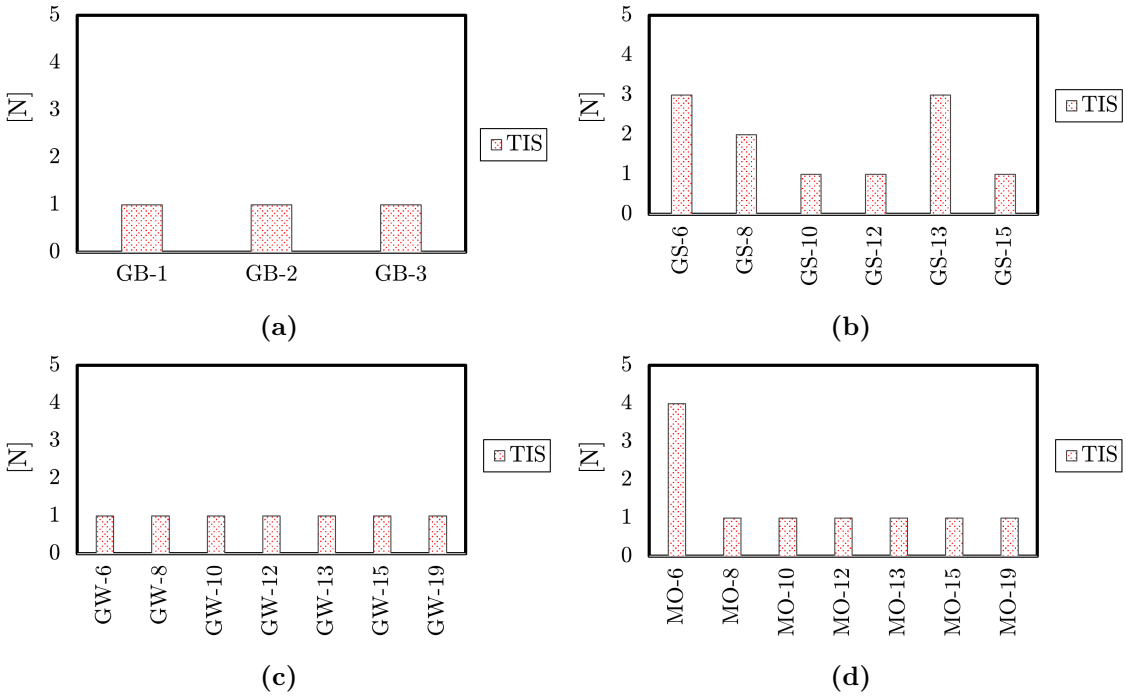

Figure 9.19: Fitted number of CSTRs in series for beds with narrow size fractions: (a) GB, (b) GS, (c) GW and (d) MO.

The TIS model attained a relatively high average R^2 value of 0.973 across all three bed types for the mixed size distributions. Figure 9.20 shows a decrease in the number of CSTR

tanks as either the bottom or top size was increased. For instance, raising the bottom size of the GS system from 0.1 (GS-3) to 1 mm (GS-7) resulted in a decrease in the optimized number of tanks from 8 to 1. For the MO system, raising the top size from 8 (MO-2) to 16 mm (MO-20) resulted in a similar reduction. These results also show a decrease in tracer breakthrough time (plug flow behaviour) with an increase in the top and bottom particle size, as shown in Table 8.6.

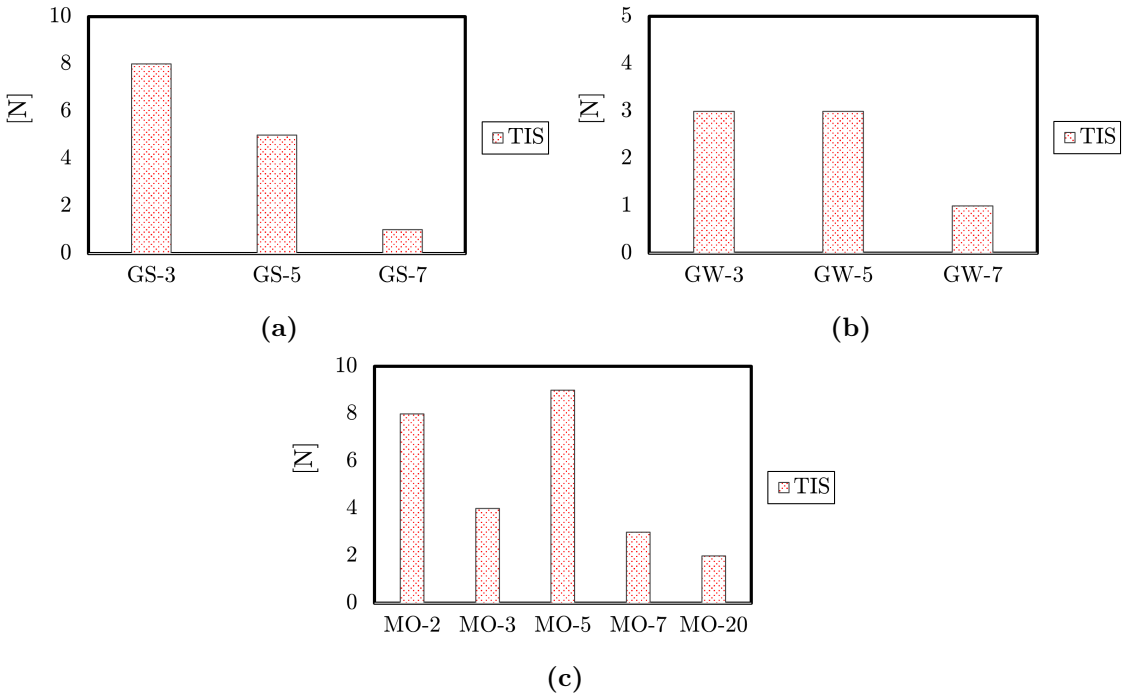

Figure 9.20: Fitted number of CSTRs in series for the TIS model for beds with mixed size distributions and varying lower size limits: (a) GB, (b) GS, (c) GW and (d) MO.

Figure 9.21 shows that though increasing the bed height did not have a consistent impact on N, there was still an increase as bed height was doubled. A similar result was obtained when comparing the agglomerated to the non-agglomerated system. This increase in plug flow behaviour was mainly reflected in the increase in the tracer breakthrough time. For the non-agglomerated bed, the TIS obtained an R^2 value of 0.994. This suggests that the TIS model does relatively well at fitting data generated from beds with relatively high total liquid hold-ups. Perhaps, this is because fluid volumes in such beds have a high probability of being continuous reducing the chances of isolated volumes. This verifies the mono porosity

assumption on which the TIS model is built.

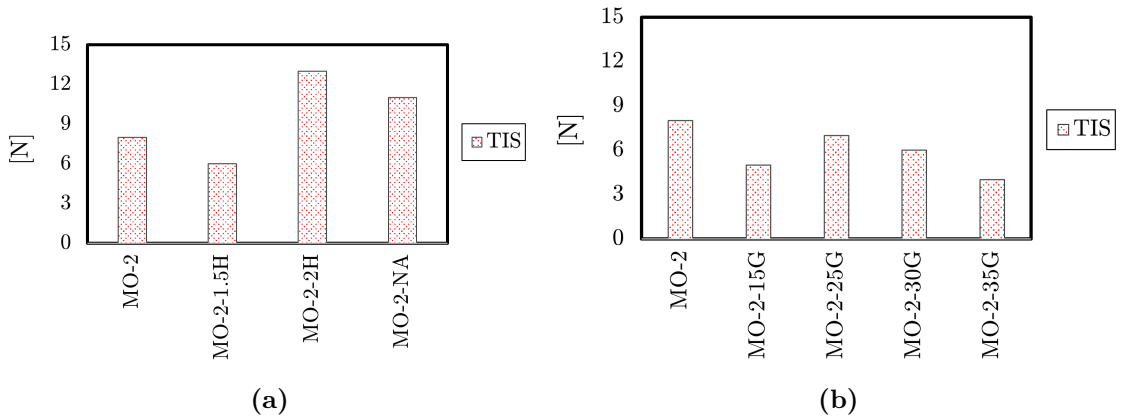

Figure 9.21: Fitted number of CSTRs in series for 0 - 8 mm MO bed systems with: (a) different packing heights and states of agglomeration, (b) irrigated with solutions of varying viscosities.

From Figure 9.21b, overall, the number of tanks predicted decreased as viscosity was increased. For example, there was a 50% reduction in the number of tanks when comparing the MO-2 (0.8 cP) to the MO-2-35G (2.2 cP) system, which is reflected in the increased mixing and dispersive effects in the RTD curves (refer to Figure 9.10). This may result from enhanced gravitational flow of higher density solutions in medium to large pores. For small to micro-pores, reductions in fluid flow velocities due to wall friction would be exacerbated at higher viscosities. Hence, the overall effect is a a greater spread in the RTD curve. In terms of model fit analysis, the TIS model performed significantly well for the higher viscosity bed systems which is again attributed to their high liquid hold-ups. It achieved an average R^2 value of 0.991 for the four systems irrigated with 1.2 - 2.2 cP solutions.

9.3.2.4 Fraction of Dynamic to Total Saturation

The fraction of dynamic to total saturation (β_d/β_T) gives an indication of the proportion of actively flowing liquid volume to the total liquid volume present in a packed bed system. This is an important parameter in a heap leaching context as it directly affects the solute residence times that can be expected and hence, extraction rates. The differences between stagnant volumes and isolated/dead volumes discussed in section 7.2.2 should be noted.

The dual porosity models in Figure 9.22 show a reduction in β_d/β_T with an increase in particle size fraction for the GB and MO systems. It was earlier proposed that the increased mechanical dispersion caused by larger particles resulted in an increased formation of dead volumes. Based on these results, it can also be argued that the volumes formed were not completely isolated but rather stagnant volumes with relatively slow rates of mass transfer (see discussion on mass transfer rates in sub-section 9.3.2.6). The results for the GS and GW systems do not portray any significant relationship between β_d/β_T and particle size fraction. The low β_d/β_T fractions for the GS-12 and GS-15 system, correspond to the high V_D/V_T predicted by the compartmental models.

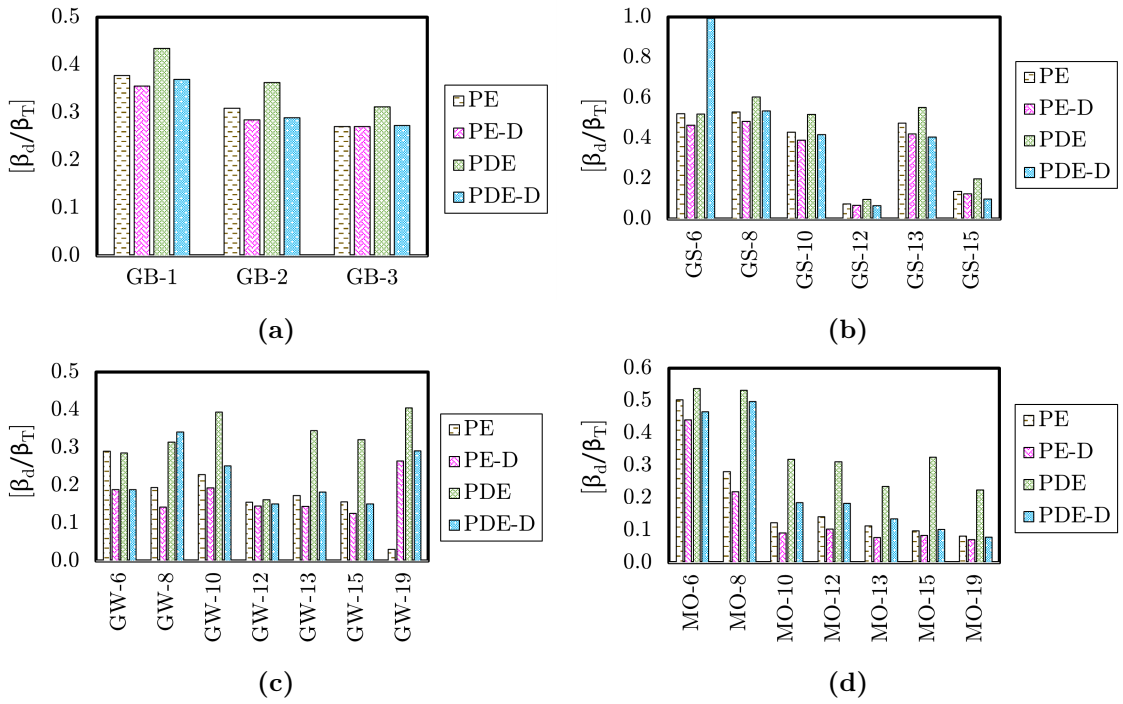

Figure 9.22: Fitted fractions of dynamic to total saturation for beds with narrow size fractions: (a) GB, (b) GS, (c) GW and (d) MO.

Though all four models performed relatively well at fitting the data (see Figure 9.13), their responses are dissimilar. Most notably, the PDE model consistently predicted higher β_d/β_T values than the other three models across all bed systems. This difference is most striking for the GW systems in which the average fraction value by the PDE model (0.32) across the various tests was 67% greater than average value (0.19) of the other three models combined.

This suggests that the presence of D_{ds} resulted in elevated predictions of the dynamic to total saturation. This is also the case for the PE-D and PDE-D models, as the latter obtained a 29% higher average β_d/β_T across all systems compared to the PE-D model.

For the PE, PE-D and PDE models, there was a decrease in β_d/β_T as the bottom particle size in mixed sized beds was increased (Figure 9.23). One of the exceptions to this was the MO system in which β_d/β_T increased as the particle bottom size limit was raised from 0 to 0.1 mm. This indicates that excessive capillary pressures resulting from the inclusion of <0.1 mm particles increases the formation of stagnant volumes instead of aiding dynamic flow.

The behaviour of the PDE-D model in certain cases is very different from the other models and even hits the set parameter boundaries indicating that its highly complex structure may have influenced its fitted parameter values. In this case, making them arbitrary and reducing their physical applicability. Therefore model over-complexity is an important factor in the RTD simulations of packed beds.

The effect of bed height on β_d/β_T for the PE, PE-D and PDE models is not consistent (refer to Figure 9.24). The lack of a discernible trend may have been due to random differences in the way the particles within both beds arranged themselves which affected the cumulative RTD profiles. In the case of the non-agglomerated bed β_d/β_T decreased for all four models when compared to the agglomerated bed. This indicates that non-agglomeration led to an increase in the stagnant liquid saturation, which agrees with the bed characterisation data (refer to sub-section 8.2.5) as well as the modelling results by Bouffard and Dixon (2001).

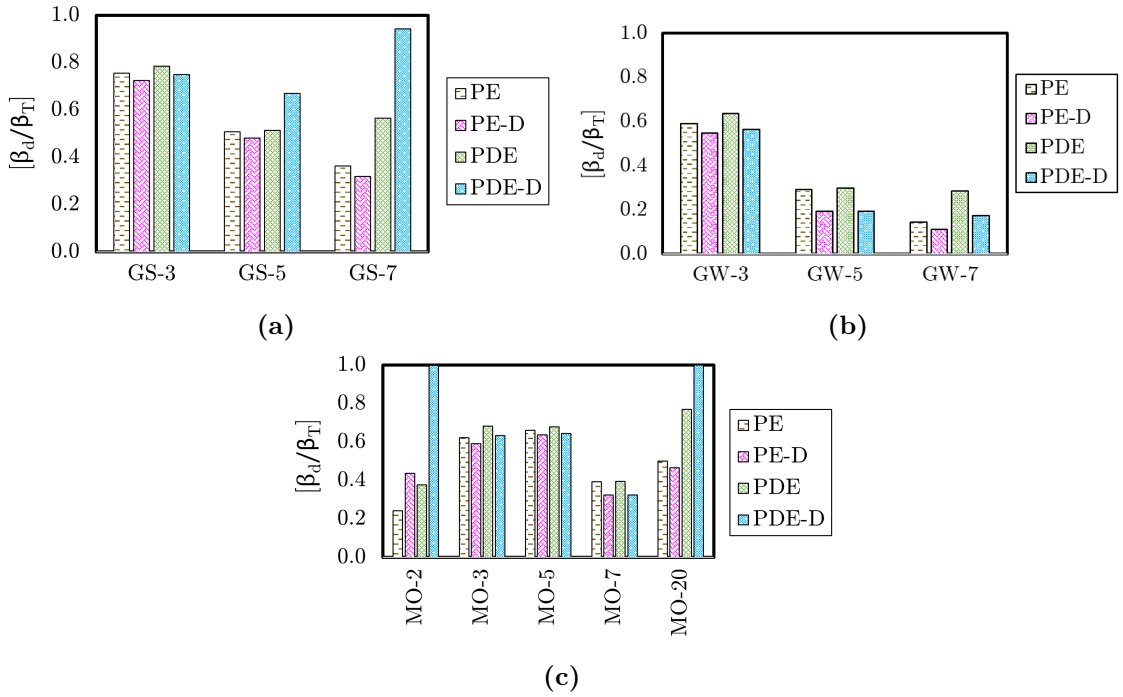

Figure 9.23: Fitted fractions of dynamic to total saturation for beds of mixed size distributions with varying lower size limits: (a) GB, (b) GS, (c) GW and (d) MO.

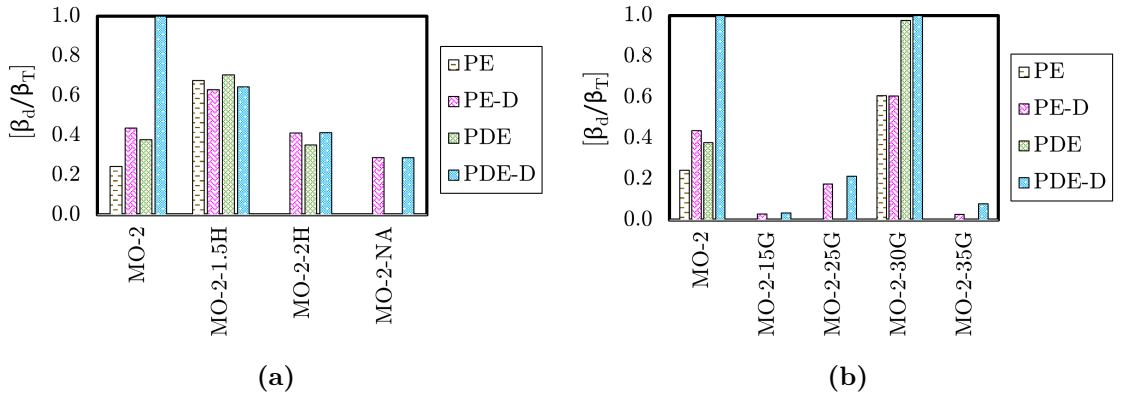

Figure 9.24: Fitted fractions of dynamic to total saturation for beds of 0 - 8 mm MO particles with: (a) different packing heights and states of agglomeration, (b) irrigated with solutions of varying viscosities. Note: models with bars that are not visible indicate a fraction value of 0

From Figure 9.24b, there is a significant drop in β_d/β_T as solution viscosity was increased. Similar to the effects of agglomeration state, the PE and PE-D models' values were close to zero for bed systems irrigated with 1.2 to 2.2 cP solutions. The two models obtained

slightly higher values but still attributed a majority of the liquid volume present in the higher viscosity systems to the stagnant region. This is different to what the 24-hour drain-down volumes data suggested (refer to sub-section 8.2.6), which implies that this parameter may not be a reliable indicator of the dynamic volume concept expressed in these models.

The most notable exception in all these cases is the MO-2-30G bed system which is clearly an outlier. The two factors that contributed to this are the slightly higher irrigational flux measured for this system (5.35 L/m^2.h vs 5.03 L/m^2.h) and the higher liquid hold-up value (0.32 vs 0.24) compared to the average of the other systems (refer to Figure 8.12).

9.3.2.5 Longitudinal Dispersion Coefficient

The longitudinal dispersion coefficient (D_{ds}) gives a measure on the extent of the axial mixing behaviour present in an irrigated packed bed system. Since the irrigational flux was kept constant at 5 L/m^2.h, comparisons of D_{ds} values are possible across the various systems without the need for a dimensionless variable such as Peclet's number. Though these values cannot be directly compared to those in literature, the main trends and conclusions are still placed into context with previous research. Also, the mono porosity AD model had an average R^2 coefficient value of 0.883 across all bed systems with narrow size fractions. This was significantly lower than those obtained by the PDE (0.993) and PDE-D (0.994) models.

From Figure 9.25 (note: y-axis was drawn in reverse logarithmic scale), though the AD model consistently showed an increase in D_{ds} with an increase in particle size fraction, its poor fit to the data is evinced by its tendency to obtain unrealistically high D_{ds} values for a majority of the non-porous systems. The PDE and PDE-D models display only mildly proportional relationships between D_{ds} and particle size fraction as well as slight increases in D_{ds} with porosity. Therefore, it can be argued that fluid molecules in beds composed of larger particles experience higher levels of longitudinal dispersion perhaps due to gravitational channelling in macro-pores. The PDE-D model tended to obtain lower D_{ds} values compared to the PDE model. This suggests that the added complexity of the diffusional mass transfer mechanism present in the PDE-D model made it less reliant on D_{ds} when accounting for non-ideal flow characteristics.

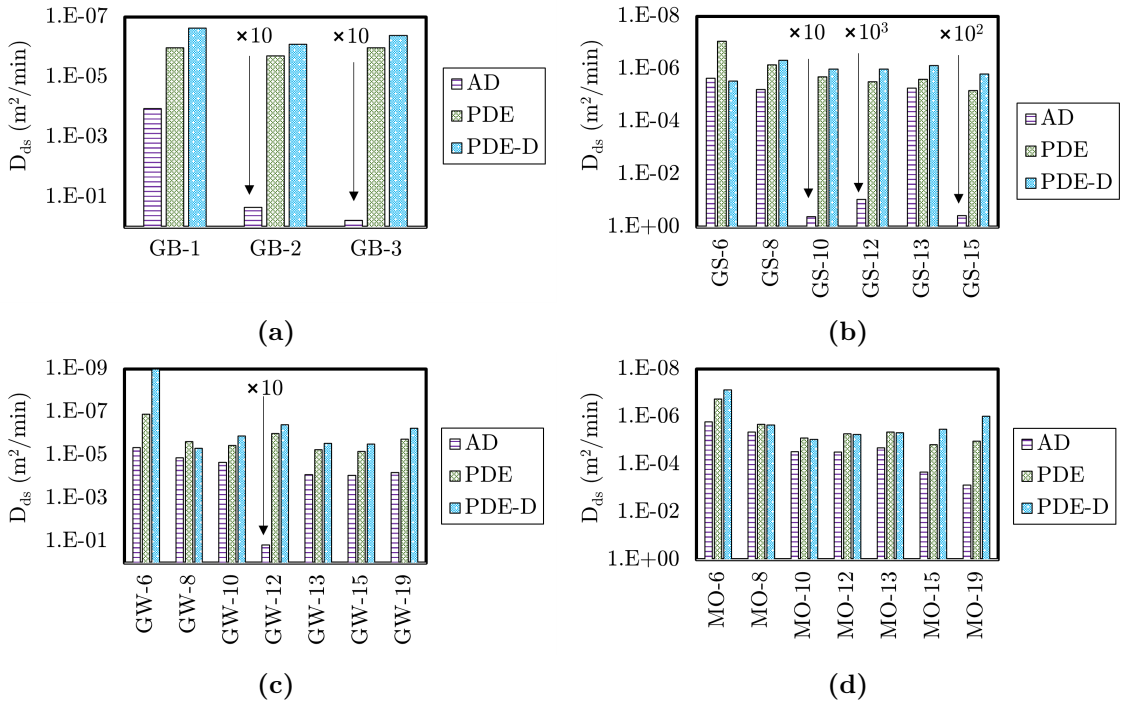

Figure 9.25: Fitted dispersion coefficients for bed systems composed of different packings with narrow size fractions: (a) GB, (b) GS, (c) GW and (d) MO [Note: y-axis is plotted in reverse logarithmic scale and certain values for the AD model need to be multiplied by powers of 10].

For the mixed sized GS system (refer to Figure 9.26), an increase in the particle bottom size from 0.1 to 1 mm did not have a significant impact on the AD model's D_{ds} but led to increases in those of the PDE and PDE-D models. For the GW systems, D_{ds} increased over the 0.1 to 1 mm bottom particle size range for the AD and PDE models. All three models gave different responses for the MO systems. The AD model's coefficient increased, the PDE model's remained at a specified range, while the most complex PDE-D model saw a decrease. Based on these results, it would seem that the value of D_{ds} was highly dependent on the model structure.

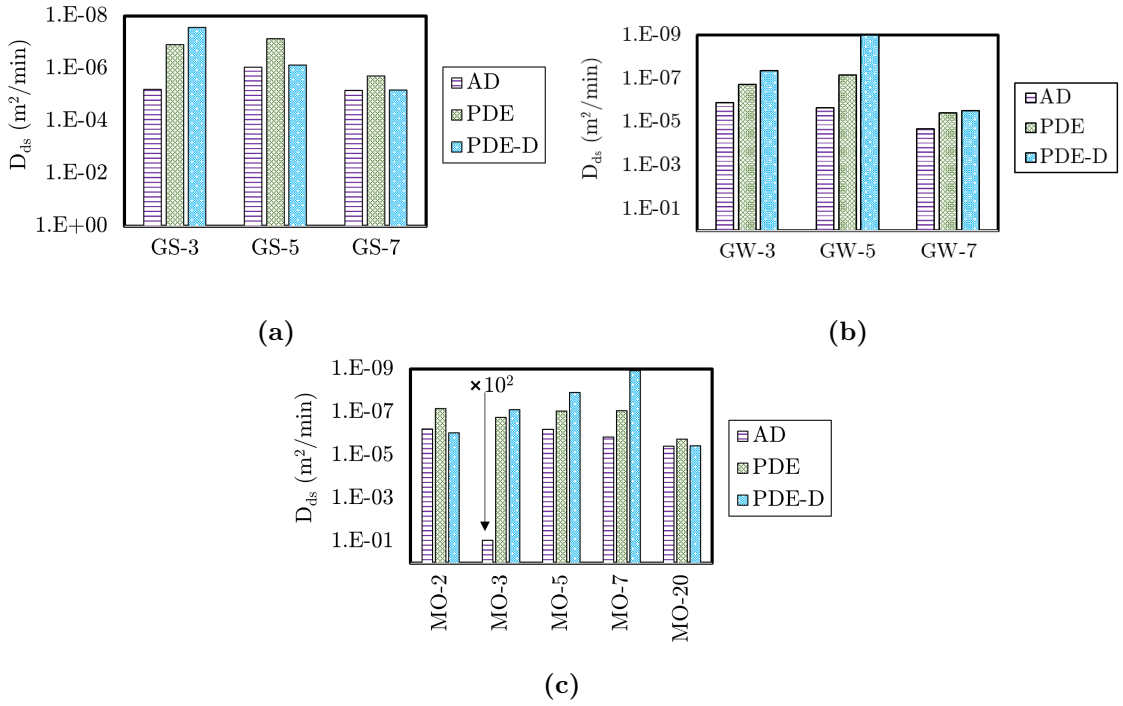

Figure 9.26: Fitted dispersion coefficient for beds of mixed size distributions and varying lower size limits: (a) GB, (b) GS, (c) GW and (d) MO [Note: y-axis is plotted in reverse logarithmic scale and certain values for the AD model need to be multiplied by powers of 10].

In the discussion of the RTD curves for the mixed sized systems presented in 8.2.4, the expected response was an increase in D_{ds} with an increase in the particle bottom size limit. Though each model struggled to give consistent responses across the different packed beds, the overall trend evident, especially for the AD and PDE models are in line with what was expected.

Increasing the particle top size for the MO system from 8 to 16 mm led to noticeable increases in D_{ds} for all three models. The most notable was from the PDE model which obtained a more than 100 fold increase across this range. This reinforces earlier postulations of the increase in gravitational channelling in macro pores with slower velocities in micro-pores resulting in greater dispersive effects in larger particle size porous beds.

Both the AD and PDE models do not show any substantial effect of bed height on their D_{ds} in Figure 9.27a. The PDE-D model however, shows a steady decline as bed height was

raised to two times the standard bed height. This was not an expected response as with all things kept more or less constant, the bed height should not have such a significant impact on D_{ds}. It would seem that PDE-D model is more prone to hitting the lower boundaries of the dispersion coefficient and reinforces the earlier point of model over-complexity for these particular beds.

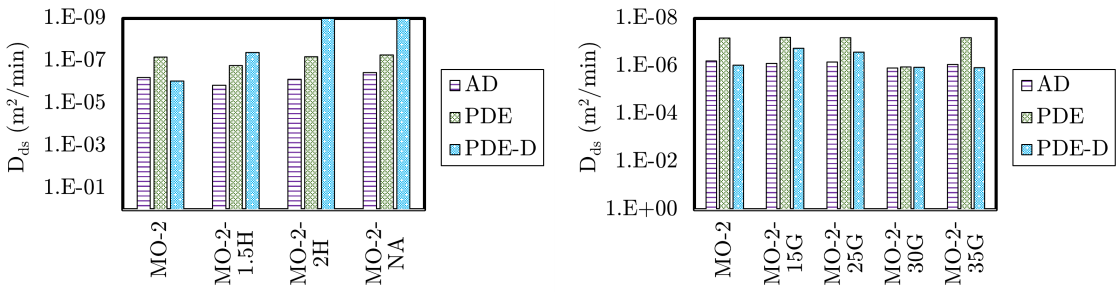

Figure 9.27: Fitted dispersion coefficients for beds of 0 - 8 mm MO particles with: (a) different packing heights and states of agglomeration, (b) irrigated with solutions of varying viscosities. [Note: y-axis is plotted in reverse logarithmic scale].

The results in Figure 9.27b show that the D_{ds} for the AD and PDE models were not substantially impacted by the change in fluid viscosity. The result for the MO-2-30G system displayed a bit of variation but the reasons behind this have been previously discussed in section 9.3.2.4. The PDE-D model did not show any consistent trends but had the most variation amongst the three models. Based on the discussion in 8.2.6, the expected response was an increase in D_{ds} as the solution's viscosity was increased. However, the models chose to rather reduce the value of the dynamic saturation parameter, which was also a viable way of accounting for the non-ideal flow characteristics present within the RTD profiles.

9.3.2.6 Overall Mass Transfer Coefficient

For the PE and PDE models, the transport of solutes from the dynamic to the stagnant regions was described by an overall mass transfer coefficient ($K_m a$). Understanding the factors influencing $K_m a$ is beneficial for future modelling applications and heap design. Similarly to D_{ds}, absolute values of $K_m a$ are presented and discussed here to facilitate comparisons

between the different model formulations, a key objective in this thesis.

Figure 9.28 shows a reduction in the value of $K_m a$ predicted by both the PE and PDE models as particle size fraction in narrowly sized beds was increased. For instance, the value for GB-2 was roughly 5 to 7 times greater than that for the GB-3 system. The GS experienced a reduction in its coefficient value in the order of 10^{-3} over the 1 to 5 mm size fraction range, the GW experienced a 10^{-2} fold reduction while the MO beds showed a less than 10^{-1} reduction over a similar size range.

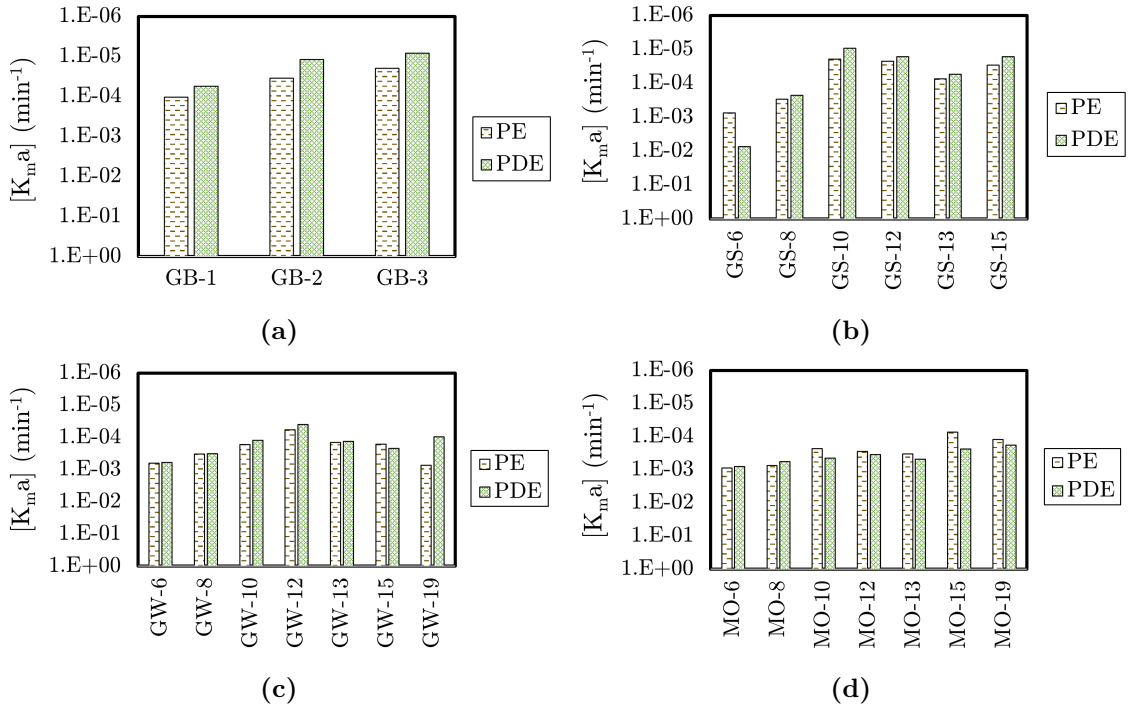

Figure 9.28: Fitted overall mass transfer coefficients for beds with narrow size fractions: (a) GB, (b) GS, (c) GW and (d) MO [Note: y-axis is plotted in reverse logarithmic scale].

These results indicate two things. Firstly, that an increase in the narrow particle size fraction reduces the exchange rate of material between the dynamic and the stagnant regions. Therefore, even though relatively high stagnant volumes were predicted by these models for beds composed of larger particles, the reduction in $K_m a$ means that these volumes acted more like dead volumes. This correlates with the rapid rise in dead to total volume fractions obtained by the compartmental models as particle size fraction was increased (refer to Figure 9.14). Therefore, discussion points raised concerning isolated fluid volumes are applicable

here. Secondly, the degree of particle porosity acted as a buffer against the rapid decline in $K_m a$ as particle size fraction was increased. This is likely due to a greater number of fluid flow paths, which increases the probability of connected fluid volumes. Additionally, the $K_m a$ values of the PE and PDE are in good agreement with each other though for the GB, GS and GW systems, the PE model obtained slightly higher values likely due to the presence of D_{ds} in the PDE model.

From Figure 9.29, there is no discernible trend in the optimized $K_m a$ values across all the packing materials. However, comparing the PDE model results for the MO-2 system with a bottom size of 0 to the MO-3 bed, its optimized $K_m a$ value was roughly 8 times greater. Similar values were obtained for the PE model. This significant increase in the value of $K_m a$ suggests that capillary effects, brought about through the incorporation of fine particles leading to greater liquid hold-ups and enhanced void network connectivity are beneficial to the mass transfer process. Raising the top size from 8 (MO-2) to 16 mm (MO-20) resulted in a 0.01 to 0.05 fold decrease in $K_m a$ for both models as shown in Figure 9.29c. This corresponds to the relatively high dead to total volume fraction obtained by the CM-1 and CM-3 models for the MO-20 bed (refer to Figure 9.15c).

From Figure 9.30, increasing the packed bed height did not have a consistent impact on the value of $K_m a$. Though the value for the MO-2-1.5H system was noticeably lower than the other two, it is likely that random variations in the packed bed structure were at play, resulting in the differences seen in the shape of the RTD curves (refer to Figure 8.11a).

With regards to the effect of non-agglomeration, the PE and PDE models experienced a 3 and 4 fold increase in their $K_m a$ values, respectively, when comparing the MO-2 and MO-2-NA packed beds. This can be attributed to the significantly higher bed saturation levels of 92% measured for the non-agglomerated system. This meant that a vast majority of the liquid volumes present within the bed were in contact with each other as previously stated, which aided in the mass transfer of the solute molecules.

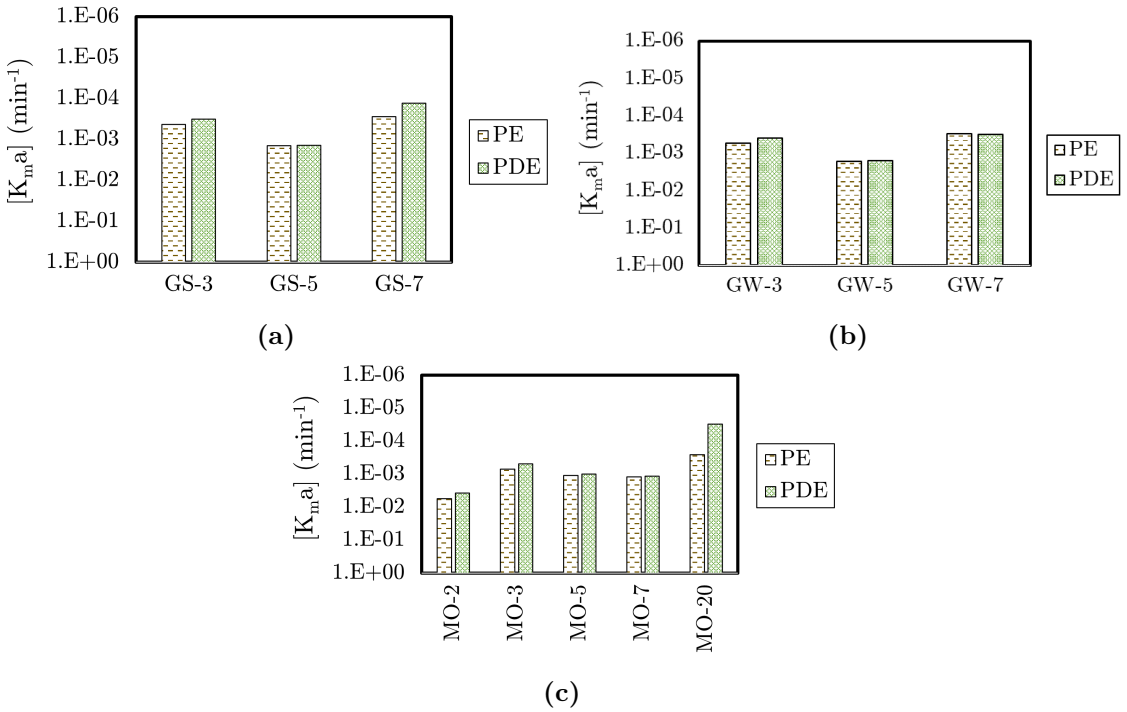

Figure 9.29: Fitted overall mass transfer coefficients for beds with mixed size distributions with varying lower size limits: (a) GB, (b) GS, (c) GW and (d) MO (MO) [Note: y-axis is plotted in reverse logarithmic scale].

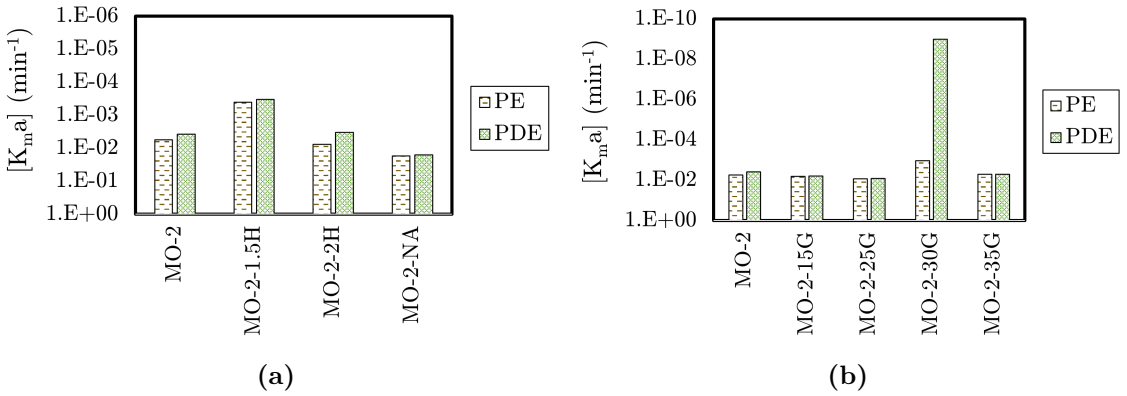

Figure 9.30: Fitted overall mass transfer coefficients for beds of 0 - 8 mm MO particles with: (a) different packing heights and states of agglomeration, (b) irrigated with solutions of varying viscosities. [Note: y-axis is plotted in reverse logarithmic scale].

From the results in Figure 9.30b, increasing the viscosity of the irrigation solution did not have a substantial effect on the fitted values of the overall mass transfer coefficients for both

models. The only exception was the MO-2-30G bed whose data has already been classified as an outlier when discussing the dynamic to total saturation fractions.

9.3.2.7 Maximum Pore Length

The PE-D and PDE-D models made use of a diffusional flux mechanism to describe the mass transfer of solute molecules between the dynamic and stagnant volumes. One of the critical parameters involved with this mechanism is the maximum pore length (X). Though the name of this parameter suggests that it is a physical and experimentally measurable quantity, this is not necessarily the case as was discussed in the study by Bouffard and Dixon (2001). This is an intricate parameter that not only affects the solute transfer rate but also the time needed for the tracer concentration within the stagnant volume to achieve equilibrium. As both the PE-D and PDE-D models performed relatively well at fitting the data, understanding how various factors impacted the value of this parameter will shed light on its physical representation and applicability in a heap leaching context.

Figure 9.31 shows an increase in X as particle size fraction was increased for both the PE-D and PDE-D models. In the case of the GB systems, the increase is consistent across the three bead sizes tested with X more than doubling in value for both models when comparing the GB-1 and GB-3 packed beds. For the irregularly shaped materials the value of X increases until it stabilizes at a particular size fraction. For the GS packed beds, the increase occurs within the 1 to 5 mm particle size range. For the GW systems, the range is extended to 6 mm and for the MO beds the range is extended until 8 mm. This suggests that an increase in particle size led to longer diffusion paths for solute molecules in the stagnant regions. This also meant slower mass transfer rates and follows a similar trend to the data for the dead to total volume fractions and the overall mass transfer coefficients.

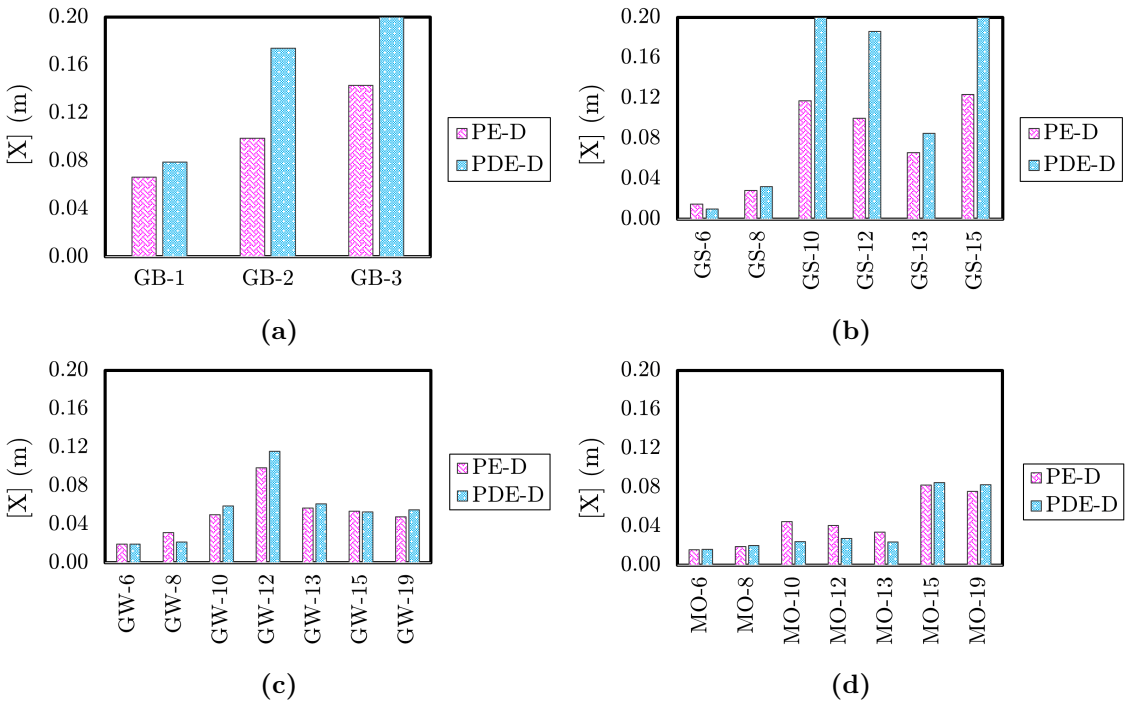

Figure 9.31: Fitted maximum pore lengths for beds with narrow size fractions: (a) GB, (b) GS, (c) GW and (d) MO.

The results in Figure 9.31 agree with the major findings from Bouffard and Dixon (2001) which showed an increase in the value of X, for the PSPD model (similar to the PE-D), as particle size was increased. Also, these results offer further evidence that the presence of particle porosity acts as a buffer against the decrease in mass transfer rates as particle size fraction within a narrow sized packed bed increases. This can again be attributed to better void network connectivity, reducing the diffusional length solute molecules have to travel in stagnant regions.

The results in Figure 9.32 show that at particle bottom sizes of 1 mm or less, the optimized values of X tended to be relatively low for beds composed of mixed size distributions. This was the case across all three systems for the PE-D model, with the prior discussion relating to increased void network connectivity could be applicable here as well. The PDE-D model, however, hit the top boundary for the X parameter at the 1 mm bottom size limit for the GS-7 and MO-20 beds. These high values for X correspond to the relatively high dispersion coefficients obtained by the PDE-D model (refer to Figure 9.26). This seems to be the

model's way of trying to reconcile the high degree of channelling behaviour exhibited in the early portions of the RTD curves for these systems, with their long asymptotes (refer to Figures 8.9a and 8.10a). Though the added complexity (inclusion of the dispersion coefficient) resulted in slightly better fits by the PDE-D model, it indicates that without the presence of fines or at large particle top sizes, the fitted X values were more a function of the model's structure than a true physical reflection of the pore lengths in the bed.

Raising the bed height, state of agglomeration and changes in irrigation fluid viscosity (refer to Figure 9.33) did not have a consistent impact on the value of X. The results for the non-agglomerated bed are different to those for $K_m a$. This indicates that the value of X was not as dependent on liquid hold-up as $K_m a$, meaning that the 58% saturation reached by the MO-2 system was sufficient in limiting the diffusional length of solute molecules in the stagnant region to a base value of around 0.005 m. Further increases in saturation did not have an effect on X.

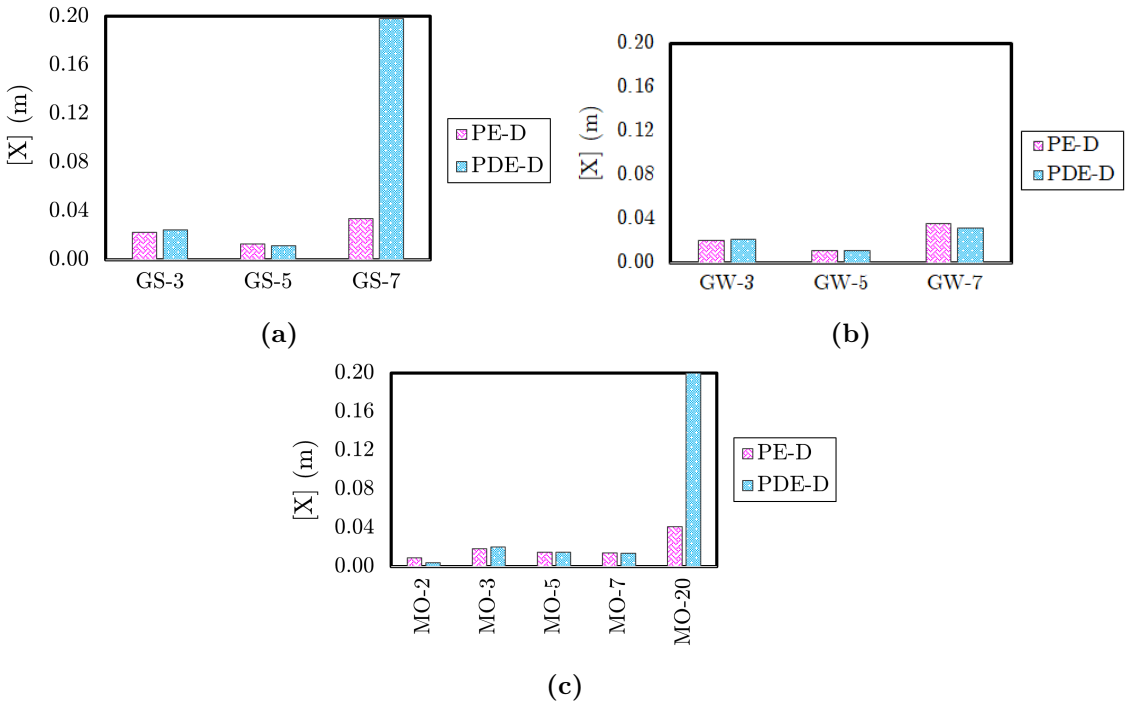

Figure 9.32: Fitted maximum pore lengths for beds with mixed size distributions and varying lower size limits: (a) GB, (b) GS, (c) GW and (d) MO

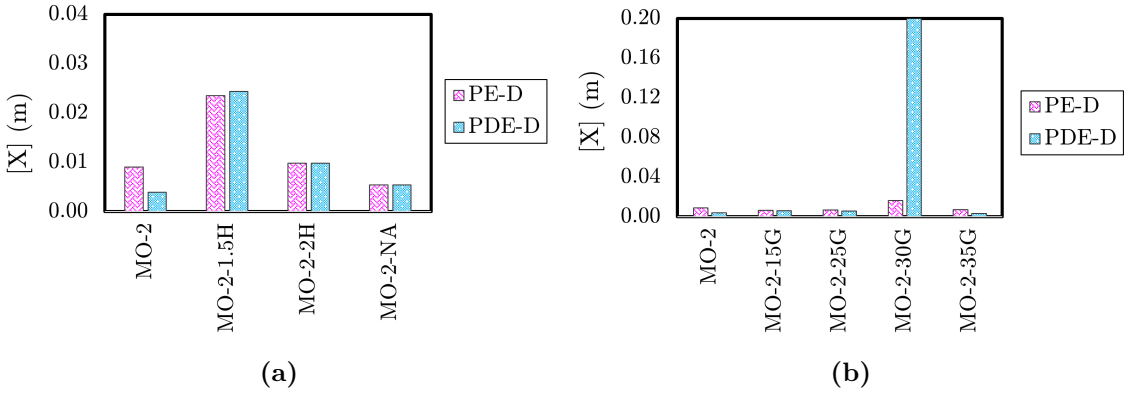

Figure 9.33: Fitted maximum pore lengths for beds of 0 - 8 mm MO particles with: (a) different packing heights and states of agglomeration, (b) irrigated with solutions of varying viscosities.

9.3.2.8 Relevance of Different Model Parameters

In order to establish the important model parameters that were needed for the accurate simulations of the cumulative RTD curves, a summary of the major trends from the results are shown in Table 9.3.

Table 9.3: Major trends displayed by model parameters [Key: Narrow size fraction (N.S.F.), Bottom particle size limit (B.P.S.), Top particle size limit (T.P.S), Packing height (P.H.), Agglomerated to non-agglomerated (A. to N.A.), "↑" means increase, "↓" mean decrease and "-" means no discernible trend.]

Parameter	**Model**	**Major trends**										
		N.S.F ↑				**B.P.S ↑**			**T.P.S ↑**	**P.H. ↑**	**A. to N.A.**	**Vicosity ↑**
		GB	GS	GW	MO	GS	GW	MO	MO	MO	MO	MO
Dead volume	CM-1	↑	↑	↑	↑	↑	↑	-	↑	-	-	-
$[V_D]$	CM-3	↑	↑	↑	↑	↑	↑	-	↑	-	-	-
Dual permeability	CM-2	↓	↑	↑	↑	↑	↓	-	-	-	-	-
	CM-3	↓	-	-	↑	-	↑	-	-	-	-	-
No. of tanks $[N]$	TIS	-	↓	-	-	↓	↓	-	↓	↑	↑	↓
Dynamic saturation $[\beta_d]$	PE	↓	↓	↓	↓	↓	↓	-	↑	-	↓	↓
	PE-D	↓	↓	-	↓	↓	↓	-	↑	-	↓	↓
	PDE	↓	-	-	↓	↓	-	-	↑	-	↓	↓
	PDE-D	↓	↓	-	↓	-	↓	↓	-	↓	↓	↓
Dispersion coeff. $[D_{ds}]$	AD	↑	↑	↑	↑	-	↑	↑	↑	-	-	-
	PDE	-	↑	-	↑	↑	↑	-	↑	-	-	-
	PDE-D	-	-	-	-	↑	-	↓	↑	↓	↓	-
Mass transfer coeff. $[K_m a]$	PE	↓	↓	-	↓	-	-	↓	↓	-	↑	-
	PDE	↓	↓	↓	↓	-	-	↓	↓	-	↑	-
Max pore length $[X]$	PE-D	↑	↑	↑	↑	-	-	-	↑	↑	-	-
	PDE-D	↑	↑	↑	↑	↑	-	-	↑	↑	-	-

For the CM-1 and CM-3 models, the ability to account for the presence dead volumes (V_D) proved vital in enabling them to outperform the CM-2 model in terms of the goodness of fit. From Table 9.3, it is evident that particle size was the dominant factor influencing the presence of these volumes. Increases in the particle size range, bottom particle size and top particle size limits all resulted in increases in the fractions of dead volumes by both models. In fact, whenever fines were incorporated into the size mixture, the acquired dead volume values from both models were close to zero. In the study by Bouffard and West-Sells (2009), it was found that there were no dead volumes present in laboratory beds composed of previously agglomerated crushed ore. Though the particle size distribution used in the study was not explicitly stated, the fact that the particles were previously agglomerated indicates that the original distribution contained fine material. Hence, the results of the study are in line with those from this current work.

Bouffard and West-Sells (2009) investigated the influence of scale and found that at the heap scale, compartmental models with dead volumes were needed to fit the RTD data. However, based on a mini-experiment, the study found that the volumes were not actually dead but rather stagnant as they still participated in the exchange of material. This is important because even though definite trends were observed for V_D/V_T in this work, dual porosity models with stagnant volumes were, in certain cases, better able to fit the RTD data. This suggests that completely dead volumes may not be applicable to leaching beds, but rather stagnant volumes with varying levels of mass transfer rates, which are able to simulate different degrees of "dead spaces", may be more appropriate.

Only a few beds displayed dual permeability flow based on the fitted values from the CM-2 model (refer to Table 9.3). As the fit of CM-2 was notably worse than the other CMs, the trends observed are not valid. Therefore, dual permeability was not a significant issue in a majority of the systems. A more sophisticated version of the dual permeability concept was applied by Gibson (2020) which attempted to use the RTD data from cylindrical packed bed columns composed of crushed synthetic ore to predict the column leaching data. The model made use of a number of parallel flow channels that consisted of multiple CSTRs in series. The results showed that the model struggled to fit the data which was attributed

to shortcomings in the assumptions used in the development of the model. Therefore, it is possible that the dual permeability modelling concept is not applicable to laboratory leaching systems but perhaps to taller beds.

The TIS was the worst performing model. Therefore, even though trends with N were observed, this parameter proved insufficient in fitting the RTD profiles. Other models were better at representing the concept of plug vs. mixed flow. Though it was expected that the TIS and AD models would behave similarly (Fogler, 2006), this was not the case. The main disadvantages of TIS is its highly empirical nature and restriction on the values for N to integers. This is unlike the AD model's D_{ds}. However, TIS was able to fit the flow profiles of beds with fine material due to their higher liquid hold-ups and smaller isolated liquid volumes.

The dynamic saturation parameter (β_d) displayed consistent trends across the different systems. It enabled the semi-empirical dual porosity models to outperform the mono porosity models. These results echo those from Ilankoon et al. (2013), which found that the dual porosity PDE model was better able to fit RTD data generated from a cylindrical bed composed of glass beads than the mono porosity AD model. The study by Yusuf (1984) also alluded to this outcome but was unable to test it due to limitations in computational technology at the time. However, the current work has been more rigorous in its comparisons of different model formulations and number of bed properties studied.

The presence of D_{ds} helped to improve the fit of the PDE and PDE-D models. de Andrade Lima (2006) argued for its inclusions when simulating flows in heap leaching systems. However, though the PDE-D was a top performing model, it showed relatively few trends in regards to this parameter. There were very few instances where both the PDE and PDE-D models displayed similar correlations between D_{ds} and the other factors shown in Table 9.3. Therefore, even though the inclusion of D_{ds} was necessary, the absolute values were not totally intrinsic to the properties of the systems being studied. Rather, they were also dependent on the model structure, both in terms of dimensionality and complexity though the data does indicate a mildly proportional relationship between D_{ds} and level of porosity.

AD had only D_{ds} as a fitting parameter, while the PDE and PDE-D were also able to account

for the transport of solute molecules away from the vertical dynamic flow path. As these models performed better than AD, the longitudinal dispersion coefficient is not sufficient when accounting for non-ideal flow in drip irrigated beds. The lateral movement of solution should also be taken into account. This is very similar to the views put forward by Dixon and Afewu (2010), which questioned the applicability of 1D models to systems in which lateral dispersion occurs.

$K_m a$ decreased as particle size range, bottom and top particle size limits were increased. Agglomeration led to reductions in $K_m a$ and the more porous systems obtained higher values. All these results indicate a positive correlation between $K_m a$ and total liquid hold-up and are in line with the modelling study by Sánchez-Chacón and Lapidus (1997), which proposed that an increase in the effective wettability and hence the liquid hold-up of particles leads to a decrease in the particle's resistance to internal mass transfer processes. This is a crucial factor in the applicability of the popular shrinking core kinetic reactive model which assumes evenly wetted particles for the transport of reactants into and dissolution of products out of mineral grains (Roman et al., 1974). Such an assumption may only be applicable to systems with high liquid hold-ups. There was very good agreement between the $K_m a$ values obtained by the PE and PDE models. This suggests that the trends were true reflections of the actual systems being studied and not dependent on model structure.

The PE-D and PDE-D models used of a maximum pore length (X) for diffusional mass transfer between the dynamic and stagnant phases. Table 9.3 shows an increase in X as particle size and packing height increased, corroborating the results by Bouffard and Dixon (2001) for their PSPD model. However, in their case, agglomeration led to an increase in the value of X while in this study, there was no significant difference between the agglomerated and non-agglomerated beds. Perhaps if more non-agglomerated systems were tested, an observable trend may have emerged. Nevertheless, the diffusional flux mechanism allowed the PE-D model to outperform the PE model, similar to results by Bouffard and Dixon (2001) and van Staden and Petersen (2018a). However, diffusion in the PDE-D model did not offer substantial benefits when compared to the results of the PDE model. This suggests that it was more important as a solute transport variable within the limitations of two

fitting parameters (i.e. PE vs. PE-D). With three fitting parameters, there were indications of model over-complexity and it is therefore proposed, that in some of the systems studied, only one parameter, between the D_{ds} or X, was required for the simulation of the RTD curves.

9.3.3 Summary of Model Parameter and Error Analysis

The models ability to fit the cumulative RTD data generated were more dependent on a bed's particle size distribution than on its porosity and wettability. Though the mono porosity models displayed slight preferences for the highly porous MO systems and struggled the most with the non-porous GB beds, they performed reasonably well with data generated from the mixed size beds regardless of material properties. This was especially true in cases where the beds possessed relatively high liquid hold-ups, a condition which was more prevalent when bottom particle sizes were less than 1 mm. This led to the postulation that an increase in liquid hold-up, mainly due to capillary suction effects in drip irrigated systems, reduced the probability of isolated or dead volumes which benefited the mono porosity models. This is due to increased probability of connected liquid volumes as liquid hold-up within a specified bed voidage increases. However, in beds with <0.1 mm particles, strong capillary forces led to higher fractions of stagnant to total saturations, limiting the applicability of the mono porosity assumption.

Similarly, the dual porosity models did not show any major preferences with regards to intrinsic material properties. They were better than mono porosity models at fitting data from beds with narrow particle size fractions and mixed size distributions due to their ability to account for the presence of stagnant and isolated solution volumes.

Increasing the irrigation fluid's viscosity negatively affected the ability of the compartmental models to adequately fit the RTD data. The AD model also struggled. However, the TIS model, which was the worst performing model, managed to do relatively well in this regard. This indicates that higher viscosity solutions tended to result in stratified layers of compartmentalised mixing zones which were well described by the tanks-in-series concept. The main model parameter affected by the increase in the irrigation fluid's viscosity was the

dynamic saturation parameter which decreased across all the models, suggesting that higher viscosity solutions tend to form higher fractions of stagnant volumes within a drip irrigated packed bed.

Of the dual porosity models, the PDE and PDE-D models did noticeably better. This suggests that their added complexity, which required the fitting of three parameters, was beneficial.

The presence of dead, dynamic and stagnant volumes were very important factors in the RTD simulations. D_{ds} allowed for enhanced model fits to a majority of the data sets but its magnitude was influenced by the model's structure. Kma in the PDE model was a viable and accurate way to describe the mass transfer process between the dynamic and stagnant solution volumes. However the diffusional flux mechanism led to better fits in a two fitting parameters structure, but led to redundancy and model over-complexity issues when D_{ds} was included. The dual permeability flow concept described by the CM-2 and CM-3 models was not relevant to the systems studied.

Overall, the PDE and PDE-D were the top performing models in describing the steady state fluid flow profiles of single point, drip irrigated, non-reactive beds. On further analysis, the PDE delivered a better balance between model complexity and parameter relevance. It remains to be tested whether the improved performance of the PDE model holds on scale up to larger leaching systems or whether the PDE-D will provide benefit here.

Chapter 10

Conclusions and Recommendations

This chapter summarizes the met objectives and main results. The applications of this study to industrial heaps is also presented and recommendations for future research are made.

10.1 Summary of Met Objectives and Main Results

10.1.1 Selection, Characterisation and Testing of Relevant Material and Fluid Properties

One of the objectives of this work was the selection and characterisation of intrinsic material and fluid properties that were relevant for the better understanding of factors influencing the steady state fluid flow profiles in packed columns and their potential to affect heap leaching operations.

Viscometric and gravimetric results showed that increasing the concentration of SO_4^{2-} ions from 0 to 100 g/L led to an increases in viscosity from 0.80 to 1.45 cP and in density from 0.99 to 1.15 g/mL. As leach solutions contain a variety of ionic species which impact solution viscosity, the effect of increases in solution viscosity on the moisture absorption, RTD responses and characterisation parameters of different ore bed systems were tested using inert glycerol solutions, which were found suitable as proxy test fluids. In addition, the concentration of potassium chloride, the chosen salt tracer, was confirmed to not have a substantial impact on the solutions' viscosities and densities.

Four different solid materials with unique characteristics were chosen and characterised for their shape, porosity, wettability and mineralogical composition. The results showed that

the glass beads (GB) were spherical, non-porous, uniform in composition and had moderate wettability. Glass shards (GS) were irregularly shaped, non-porous, uniform in composition and had moderate wettability. Greywacke (GW) particles were irregularly shaped, moderately porous, non-uniform in composition and had high wettability. Malachite ore (MO) particles were irregularly shaped, highly porous, non-uniform in composition and had low wettability. The properties of the four selected materials allowed for the effect of particle shape (GB vs. GS), particle porosity (GS vs. GW vs. MO) and, to an extent, particle wettability (GW vs. GS vs. MO) to be studied. The limitation in the incomplete decoupling of particle porosity from wettability was noted.

In terms of the moisture retention properties of the selected materials, the results showed that the porous materials (GW and MO) were able to retain substantially more moisture than the other solids. Also, the specific mass of moisture retained by the materials was inversely related to their particle size. Surface adsorption is believed to have played the dominant role in the moisture retention process for the non-porous GB and GS, especially at large sizes. However, at the lower size fractions and for the porous GW and MO, capillary suction is proposed to have been the dominant moisture retention mechanism. Particle shape (spherical vs. irregular) was postulated to have influenced the number of particle-particle contact points and also the specific surface area available for moisture adsorption, hence spherical GB held on to the least amount of moisture.

The upward fluid infiltration method was found to be efficient in the measurements of the relative strength of capillary forces within packed beds. The results indicated that particle size was the principal factor influencing absorption rates in these tests. Beds composed of smaller/finer particles absorbed more moisture and had higher saturation. This could have been due to smaller diameter pores present within their void networks. At the mid size range, particle wettability is proposed to have played an important role while at the largest size range, particle porosity is believed to be the main factor influencing capillary effects in the packed bed systems.

Increasing the wetting fluid's viscosity and density led to reductions in the mass and rate of solution absorbed. These effects were more apparent at smaller particle size ranges.

Increased susceptibility of denser fluid droplets to the downward pull of gravitational forces along with a higher resistance to flow of more viscous solutions was deemed responsible for the results.

10.1.2 RTD Studies on Different Packed Beds

A key aim of this research was to establish the effect of particle shape, size, size distribution, porosity, wettability as well as irrigation fluid viscosity on the bed characterisation parameters and cumulative, steady state RTD profiles of packed beds, with reference to heap leaching. Step tracer tests, using KCl solutions, on cylindrical packed bed systems were performed.

10.1.2.1 Effect of Particle Shape

At the 1 - 3 mm particle size, the beds composed of non-porous spherical beads showed evidence of higher proportions of isolated fluid volumes compared to those composed of the non-porous, irregularly shaped shards. Higher levels of tortuosity in the liquid rivulets flowing across the shards, leading to greater connectivity was deemed responsible for this. However at a particle size of approximately 5 mm, the behaviour was reversed, with the shards exhibiting more symptoms of isolated fluid volumes. This was attributed to increased mechanical dispersion of fluid droplets by the flatter and longer GS particles, resulting in the redirection of a larger portion of the flow away from the central-irrigation axis. The non-porous nature of the shards meant that this redirection resulted in the formation of relatively higher fractions of isolated fluid volumes that contributed to the total liquid hold-up but did not participate in the active flow at steady state. Though the steady state RTD profiles for both the GB and GS systems were nearly identical, the GB beds showed slightly higher levels of solution channelling. This should be borne in mind in future leaching hydrodynamic test work involving the use of spherical particles.

10.1.2.2 Effect of Particle Porosity and Wettability

Higher levels of particle porosities were associated with lower bulk densities, higher voidage, more drain-down moisture collected, greater liquid hold-up and higher bed saturation. Increased capillary suction effects and more flow path options were responsible for the observed differences.

There were instances in which the effects of particle porosity were secondary to that of particle size on the steady state RTD profiles. For example, in beds with average narrow particle sizes greater than 7 mm, the RTD profiles exhibited severe solution channelling with tracer breakthrough times that were <5 minutes. Though the porous GW and MO beds had more liquid hold-up, the results suggests that a substantial proportion of these were isolated. Similarly, particle porosity exerted only minor influences on the cumulative RTD profiles for mixed sized beds with lower size limits between 0.1 - 0.5 mm.

The effect of particle wettability on the steady state characteristics of the systems were secondary to those of particle size and porosity especially when <2 mm particles were included in the size distribution. However, mixed sized beds composed of the relatively hydrophilic GW particles tended to have shorter solution and tracer breakthrough times and higher drain down moisture percentages. This implies that higher levels of wettability resulted in channelling behaviour that was minor at the scale tested.

10.1.2.3 Effect of Particle Size Fraction in Narrow Sized Beds

Raising the particle size is proposed to increase the fraction of macro voids within packed beds. This was likely responsible for the increased fluid channelling behaviour evidenced by reductions in solution and tracer breakthrough times across the beds as the size fraction was increased from 1 - 2 mm to 13 - 16 mm. The MO beds showed a 40% reduction in total liquid hold-up with the increase in size fraction while the other systems did not display any consistent trends between the two parameters. This suggests that highly porous beds, are more dependent on capillary suction effects, which are stronger at small size fractions, for their liquid absorption and hence, total liquid hold-up values, which corroborates the

findings from the moisture absorption and retention tests.

10.1.2.4 Effect of Particle Size Limits

In the mixed sized beds, raising the top (8 to 16 mm) and bottom particle size limits (0 to 1 mm) is proposed to have resulted in weaker capillary forces leading to decreased lateral movement of irrigated solution away from the central-vertical axis. The end results for increasing bottoms size limits were 40 to 60% reductions in total liquid hold-ups and 55 to 70% reductions in overall bed saturation values. Tracer breakthrough times were also reduced by 50 to 95%, indicating increased channelling behaviour at steady state. There was evidence of slightly elevated levels of dispersive effects attributed to the decrease in void size uniformity as fines were excluded or larger particles were introduced.

10.1.2.5 Effect of Packing Height, Non-agglomeration and Fluid Viscosity

Increasing the bed height led to increases in both solution and tracer breakthrough times. Though slightly higher levels of mixing behaviour were evident in the cumulative RTD curves, the other characterisation parameters were not consistently affected.

When comparing agglomerated vs. non-agglomerated beds of 0 - 8 mm MO particles, non-agglomeration resulted in a bed that possessed a 23% higher bulk density, 11% lower bed voidage, 39% higher liquid hold-up and a 92% total bed saturation level. This meant that the non-agglomerated bed was close to flooding. The higher bulk densities in the non-agglomerated bed is proposed to have resulted in strong capillary pressures that aided the formation of stagnant solution volumes. This was especially the case for the lower sections of the bed where the fines tended to migrate both during the loading process and upon irrigation.

Changes in the irrigation fluid's viscosity had no discernible impact on most of the beds' characterisation parameters, but led to significant decreases of up to 97% in dynamic volume fractions based on modelling results. This was attributed to increased resistance to flow in micro-pores resulting in relatively longer residence.

10.1.3 Coding, Sensitivity and Stability Analysis on Selected Models

The implicit discretization scheme employed for the solving of the semi-phenomenological models was confirmed to be unconditionally stable for well posed problems based on the Von Neumann stability analysis.

A model response analysis was conducted on the TIS, AD, PE, PE-D, PDE and PDE-D models to ascertain the effect of varying their different fitting parameters. The analysis was not done on the compartmental models due to their highly empirical nature. Increasing the number of tanks in series (N) of the TIS model brought about the expected increase in plug flow behaviour. Reductions in the dynamic saturation (β_d) of the PE, PE-D, PDE and PDE-D models brought about longer asymptotes in the RTD curves, indicative of the increased presence of stagnant volumes and non-ideal flow characteristics. Increasing the magnitude of the dispersion coefficient (D_{ds}) for the AD, PDE and PDE-D models brought about high degrees of solution channelling behaviour. The extent of this effect was found to be dependent on model formulation. Varying the overall mass transfer coefficient ($K_m a$) in the PE and PDE models led to increases in tracer breakthrough times at high magnitudes and the opposite effect at low magnitudes. However, these results were not as discernible when mass transfer was not the dominant factor. The impact of varying the diffusional pore length (X) in the PE-D and PDE-D models revealed a complex interaction which showed that at high values of X, a more plug flow like profile is obtained in the dynamic region but this was coupled with long asymptotes in the latter part of the RTD curves. Decreasing its value led to a more dispersed profile but faster achievements of equilibrium concentrations. The results from the models showed that they gave practical responses to the varied parameters leading to the conclusion that they could all be further tested through the analysis of RTD profiles generated from packed beds.

10.1.4 Model Fit and Parameter Analysis

A key aim of this thesis was the quantification and comparisons of the different fitted parameters.

10.1.4.1 Model Fit Analysis

The model fit parameters were more influenced by the particle size distribution of the beds than on their intrinsic properties (i.e. porosity and wettability). The mono porosity models (CM-2, AD and TIS) obtained R^2 values as low as 0.4 for beds in which fines (<2 mm) were excluded, but obtained values greater than 0.9 when the bottom size limits were less than 1 mm. It is proposed that the increase in liquid hold-up, mainly due to capillary effects, of beds containing fines reduced isolated or dead volumes which contributed to improved fits by the mono porosity models. The dual porosity (CM-1, CM-3, PE, PE-D, PDE and PDE-D) models provided better fits overall (R^2 >0.95) due to their ability to account for the presence of dead or stagnant volumes.

Raising the packing height and the initial state of packing prior to loading (i.e. agglomerated vs. non-agglomerated) did not have a consistent impact on model fit though there were minor signs that dual porosity models with diffusion controlled mass transfer coped better with the height increase. However, increasing the irrigation fluid's viscosity negatively affected the abilities of the CM models as well as the AD model to simulate the RTD profiles. This was in contrast to the TIS model which performed relatively well and indicated that higher viscosity solutions tended to result in compartmentalised mixing zones within irrigated beds.

Of the dual porosity models, the PDE and PDE-D models performed better than the rest due to their three fitting parameters. However, in certain cases these resulted in only minor improvements to the data fit.

10.1.4.2 Model Parameter Analysis

One of the key questions this work aimed to address was the level of model complexity and parameters needed to adequately describe steady state fluid flow profiles within drip irrigated,

non-reactive beds. A summary of the model parameters and how they were obtained is found in Table 10.1. The results indicated that models with dynamic, stagnant and dead volumes performed better at fitting the RTD data from the packed beds. The dead volume parameter present in the CM models could also be simulated by the PE, PE-D, PDE and PDE models through reductions in the magnitude of their mass transfer rates to their stagnant volumes. Therefore, these models were also more flexible in describing regions not completely dead, but with very slow rates of mass transfer which provided more accurate descriptions of the RTD profiles in certain cases.

Though D_{ds} allowed the PDE and PDE-D models to outperform the other dual porosity models, its magnitude was influenced by the model structure. This combined with the relatively poor performance of the AD model suggests that in drip irrigated heap leach systems, D_{ds} alone is not sufficient when accounting for non-ideal flow characteristics. The lateral movement of solution also needs to be taken into account either through the incorporation of a lateral dispersion coefficient or some other technique describing the movement of fluid molecules away from the central-vertical axis. This was partly accomplished by the pseudo 2D PDE and PDE-D models using different mechanisms that resulted in disparities in their coefficient values.

The overall mass transfer coefficient ($K_m a$) adequately described tracer transport between the dynamic and stagnant volumes within the beds. Though the diffusional flux mechanism improved model fit when comparing the PE and PE-D, it led to redundancy and model over-complexity issues when comparing the PDE and PDE-D. The dual permeability model concept present in the CM-2 and CM-3 models was not applicable to the systems tested though an increase in scale could result in its relevance. In conclusion, though the PDE and PDE-D models were the best performers, the magnitudes of the fitted PDE parameters were more practical and physically representative.

Table 10.1: Summary of model parameters for the selected models and how they were obtained.

Symbol	Model parameter	How it is obtained	Associated models
Controlled parameters			
C_0	Inlet solute concentration (-)	Controlled variable	CM-1, CM-2, CM-3, TIS
$C_d(0,t)$	Inlet solute concentration (-)	Controlled variable	AD, PE, PE-D, PDE, PDE-D
L	Packed bed length (m)	Controlled variable	AD, PE, PE-D, PDE, PDE-D
Q_T	Total volumetric flow rate (mL/min)	Controlled variable	CM-1, CM-2, CM-3, TIS
t	Time (min)	Controlled variable	All models
x	Spatial dimension - normalized length (-)	Controlled variable	PE-D, PDE-D
z	Spatial dimension - normalized length (-)	Controlled variable	AD, PE, PE-D, PDE, PDE-D
Experimentally, Literature obtained or calculated parameters			
β_T	Total saturation (-)	Calculated (experimental data)	PE, PE-D, PDE, PDE-D
D	Diffusion coefficient (m^2/min)	Obtained from literature	PE-D, PDE-D
ε	Total bed voidage (-)	Measured	AD, PE, PE-D, PDE, PDE-D
τ	Mean residence time (min)	Calculated (experimental data)	TIS
τ_P	PFR residence time (min)	Calculated (experimental data)	CM-1, CM-2, CM-3
τ_C	CSTR residence time (min)	Calculated (model results)	CM-1, CM-2, CM-3
U	Superficial liquid velocity (m/min)	Calculated (experimental data)	AD, PE, PE-D, PDE, PDE-D
V_C	Volume of each CSTR (mL)	Calculated (model results)	CM-1, CM-2, CM-3, TIS
V_T	Total flow volume (mL)	Measured	CM-1, CM-2, CM-3, TIS
V_P	Plug flow volume (mL)	Calculated (experimental data)	CM-1, CM-2, CM-3
Fitted and output parameters			
β_d	Dynamic saturation (-)	Fitted variable	PE, PE-D, PDE, PDE-D
C_d	Normalized outlet solute concentration (-)	Main model output	AD, PE, PE-D, PDE, PDE-D
C_s	Normalized solute concentration (stagnant volume)(-)	Model output	PE, PE-D, PDE, PDE-D
D_{ds}	Dispersion coefficient (m^2/min)	Fitted variable	AD, PDE, PDE-D
$K_m a$	Overall mass transfer coefficient (min^{-1})	Fitted variable	PE, PDE
N	Number of CSTR tanks (-)	Fitted variable	TIS
V_C	Continuous stirred tank volume (mL)	Fitted variable	CM-1, CM-2, CM-3
V_D	Dead volume (mL)	Fitted variable	CM-1, CM-3
X	Pore length (m)	Fitted variable	PE-D, PDE-D

10.2 Applications of Findings to Industrial Heaps

This work aimed to enhance understanding of key parameters influencing solution-ore contacting in laboratory scale packed beds such that these can be exploited to address issues at heap scale in applications. A primary concern related to this is the uneven distribution of flow. This phenomenon is referred to as preferential flow and occurs both on a bed scale, which deals with the wetting and liquid hold-up behaviour of the entire bed, as well as on a

solution scale dealing with the variation in flow velocities of fluid volumes within the wetted sections of the bed. Though flow profiles at steady state were the primary focus of this study, the influence of the wetting stage was also discussed. Bed scale preferential flow was characterised by the solution breakthrough times along with liquid hold-up and saturation levels in drip irrigated beds. Under steady state flow, solution scale preferential flow was characterised by the solute transport modelling of RTD curves to quantify stagnant and/or isolated fluid volumes along with other relevant model parameters.

With regards to bed scale preferential flow, the inverse correlation found between total liquid hold-up and particle size limits necessitates the inclusion and agglomeration of fines with larger particles in drip irrigated heaps to aid in the uniform distribution of solution during the wetting stage. This initial wetting behaviour is facilitated by capillary forces which were shown to be stronger in beds with particles <1 mm. An increase in liquid hold-up will help to reduce the probability of completely dry sections in heaps which is the first step in addressing uneven flow distribution. The quick solution breakthrough times, indicative of channelling behaviour, experienced by narrow size beds with average particle sizes >7 mm and without the presence of fines also attest to this point. However, as particle porosity played a dominant role in liquid absorption and hold-up capacity when fines were excluded from the bed systems, heaps composed of highly porous particles (specific surface area >2.5 m^2/g) are more likely to be evenly wetted under drip irrigation.

Agglomeration was shown to be important as the >90% saturation levels in the non-agglomerated bed would result in heap failure at the larger scale due to stability issues. This reinforces the importance of agglomeration in heap leaching systems that contain fine material and are in line with the findings and conclusions put forward in Bouffard (2005) and Bouffard and West-Sells (2009).

Upon the establishment of steady state fluid flux, the modelling results showed that the probability of dead or isolated solution volumes was significantly reduced to less than 0.05 with the inclusion of <1 mm particles in mixed size, agglomerated beds. As these beds also displayed relatively high liquid hold-ups, it is proposed that an increase in liquid hold-up increases the probability of continuous liquid volumes. However, though beds with ultra-fine

particles (bottom size limit <0.1 mm), showed little to no dead volumes, they possessed relatively greater stagnant to dynamic liquid volume ratios. In such cases, the top particle size can be moderately increased to between 10 and 15 mm, depending on the mass fraction of fines, to promote the presence of less resistant flow paths and facilitate dynamic flow. Agglomeration is advised and binding agents can be used to prevent the mobilisation of fines during irrigation which would lead to the same issues encountered in the non-agglomerated bed.

The modelling results indicated that beds composed of larger particles tended to experience higher levels of dispersion at steady state, which in certain cases resulted in the channelling of a portion of the irrigated solution. It is therefore advised that the larger the top particle size, the greater the necessity for the inclusion of fines in mixed size heaps. Increasing the top particle size will facilitate dynamic flow through the creation of macro-voids as larger particles tend to have smaller surface areas resulting in fewer particle-particle contact points per given mass. Though dynamic flow is beneficial, agglomeration with fines is needed to regulate the size of these voids, increase uniformity and limit channelling routes. High levels of particle porosities will also help to increase total liquid hold-up via stronger capillary forces within pores which will limit bed scale preferential flow.

When stagnant volumes are present in reactive heaps, the rate of solute transport is a key parameter in ensuring that dissolved mineral species are able to diffuse out of the stagnant regions and into the main flow path. The results for the overall mass transfer coefficients indicate an increase in transport rates with a decrease in bottom particle size from 1 to 0.1 mm in mixed sized beds. Therefore, the presence of fines during the agglomeration of the beds is again beneficial in ensuring the efficient transport of molecules between the stagnant and dynamic regions. This is believed to be linked to greater liquid hold-up and levels of connectivity between both particle pores (where stagnant volumes are likely to reside) and inter-particle voids (where the dynamic volumes are likely to reside) when fines are included in agglomerates. This recommendation is supported by the reduction in the diffusional pore length parameter of the PE-D and PDE-D models with a reduction in bottom particle size.

During heap operations, the initial solution breakthrough time is often not as important as

the total liquid hold-up and bed saturation parameters. Therefore, as long as the ore is not predominantly hydrophobic, the effects of particle wettability would be secondary to those of particle size and porosity. However, during the final stages of heap operations, where it is desired to drain the heap and recover any residual dissolved mineral species, higher levels of ore wettability will be beneficial for improved drainage behaviour based on the higher rate and fractions of liquid hold-up drained by the hydrophilic particle beds.

The reduction in moisture absorption rates and amount via capillary suction within packed beds as fluid viscosity was increased, suggests that higher degrees of mineral dissolution in heaps that result in high sulphate concentrations in solution, could limit further solution absorption and liquid distribution. This combined with increases in the stagnant liquid hold-up of beds irrigated with higher viscosity solutions could reduce or slow mineral extraction rates in the overall heap. Periodic monitoring of the viscosity of both the lixiviant and PLS solutions will help inform changes to feed composition to address any potential issues. However, the major impact viscosity had was on the reduced ability of the CM models to fit the generated data. Therefore, more sophisticated semi-empirical models are needed to describe fluid flow and solute transport in heaps irrigated with >2 cP solutions.

The PDE and PDE-D models were the best performers and can be used in their current form for describing non-reactive, steady state, cumulative RTD profiles in packed beds characteristic of slices of a heap around single drip emitter points. Data on the effect of bed height on the ability of the models to fit the data show early indications that models with diffusion controlled mass transfer (PDE-D) will provide more accurate simulations on larger scale systems. However, the height parameter may be of more relevance in the modelling of reactive heap leaching systems, where top-down chemical reactions, following the flow path of the irrigation fluid, may result in vertical spatial heterogeneities as leach time progresses.

10.3 Recommendations For Future Work

The main recommendation of this work will be the impact of scale on the various factors studied. This can be accomplished using taller cylindrical columns than those used in this

study, as well as rectangular columns for lateral flow tests.

The impact of the systematic exclusion of fines on lateral flow profiles should be tested using rectangular columns with multiple outlets. This will provide empirical data on the relationship between capillary suction and lateral flow and help corroborate the findings made in this study.

The impact of agglomeration (with and without binders) on lateral flow using a rectangular column geometry will further elucidate the role agglomeration plays in preventing bed scale preferential flow. Experimenting with different column loading strategies such as alternating layers of fine and coarse particles and testing the effect this has on RTD profiles and liquid hold-up behaviour will help inform heap construction methodologies.

The impact of viscosity on solution flow should be studied in taller cylindrical columns to further elucidate its effect in heaps. Studying the effect of viscosity on lateral solution flow using rectangular columns is also recommended to generate empirical data on its effect on the initial wetting behaviour of a packed bed.

It will be interesting to see how the different models cope with larger scale packed beds, in terms of taller cylindrical columns and also in rectangular columns were lateral movement of solution is not restricted. This will elucidate issues regarding the appropriate level of model dimensionality and complexity needed to adequately simulate fluid flow in heaps.

An area of interest for a future modelling study, will be to incorporate different diffusional mechanisms (cylindrical and spherical) into the PDE-D model, similar to what was originally done for the PSPD (PE-D) model by Bouffard and Dixon (2001). This will provide additional information on differences in models' predictions regarding the effect that pore space geometry and dimensionality have on the RTDs of solute molecules within packed beds. It is advised that such model formulations be tested on larger scale systems which may avoid the issues of model over-complexity encountered for the PDE-D model in this work. The incorporation of reaction kinetics into these models for the modelling of reactive systems is another possible research area. These have potential to lead to the improvement of current scale up algorithms in heap leaching studies.

References

Balasubramanian, A. (2016). An overview Of mining methods. Technical report, University of Mysore. URL https://www.researchgate.net/publication/314502989_AN_OVERVIEW_OF_MINING_METHODS.

Barker, D. J., Parameswaran, G., and Neethling, S. J. (2012). SPH simulation of packed-beds and columns applied to heap-leaching. In *Ninth International Conference on CFD in the Minerals and Process Industries*, Melbourne, Australia. CSIRO, CSIRO Australia.

Bartlett, R. W. (1992). *Solution mining: Leaching and fluid recoveries of materials*. Gordon and Breach Science Publishers, 1st edition.

Basson, P., Gericke, M., Grewar, T., Dew, D., and Nicol, M. (2013). The effect of sulphate ions and temperature on the leaching of pyrite. III. Bioleaching. *Hydrometallurgy*, 133: 176–181. ISSN 0304-386X. doi: https://doi.org/10.1016/j.hydromet.2013.01.008. URL http://www.sciencedirect.com/science/article/pii/S0304386X1300011X.

BD Editors. (2017). Glycerol. Accessed: 2021-01-23. https://biologydictionary.net/glycerol/.

Bear, J. (2013). *Dynamics of Fluids in Porous Media*. Courier Corporation, reprint edition.

Benenati, R. F. and Brosilow, C. B. (1962). Void fraction distribution in beds of spheres. *A.I.Ch.E. Journal*, 8(3):359–361.

Bennett, C., McBride, D., Cross, M., and Gebhardt, J. (2012). A comprehensive model for copper sulphide heap leaching: Part 1 Basic formulation and validation through column test simulation. *Hydrometallurgy*, 127-128:150–161. ISSN 0304-386X. doi: https://doi.org/10.1016/j.hydromet.2012.08.004. URL http://www.sciencedirect.com/science/article/pii/S0304386X12001831.

Bouffard, S. (2005). Review of agglomeration practice and fundamentals in heap leaching. *Mineral Processing and Extractive Metallurgy Review - MINER PROCESS EXTR METALL REV*, 26:233–294. doi: 10.1080/08827500590944009.

Bouffard, S. and Dixon, D. (2001). Investigative study into the hydrodynamics of heap leaching processes. *Metallurgical and Materials Transactions B*, 32:763–776. doi: 10.1007/s11663-001-0063-1.

Bouffard, S. and West-Sells, P. (2009). Hydrodynamic behavior of heap leach piles: Influence of testing scale and material properties. *Hydrometallurgy*, 98:136–142. doi: 10.1016/j.hydromet.2009.04.012.

Brierley, C. (2010). Biohydrometallurgical prospects. *Hydrometallurgy*, 104(3):324–328. ISSN 0304-386X. doi: https://doi.org/10.1016/j.hydromet.2010.03.021. URL http://www.sciencedirect.com/science/article/pii/S0304386X10001398.

Brocher, J. (2014). BioVoxxel Toolbox. Accessed: 2021-01-03. https://imagej.net/BioVoxxel_Toolbox.

Carlos, F. (2006). ASEN 5519-006: Fluid-structure interaction - Spring 2004: Aerospace engineering eciences - University of Colorado at Boulder. Accessed: 2018-03-21. https://www.colorado.edu/engineering/CAS/courses.d/FSI.d/Home.html.

Carr, J. S. (1948). Studies of contact angles on oxidized copper minerals. Master's thesis, Missouri School of Mines and Metallurgy. https://core.ac.uk/download/pdf/229285314.pdf.

Cross, M., Bennett, C., Croft, T., McBride, D., and Gebhardt, J. (2006). Computational modeling of reactive multi-phase flows in porous media: Applications to metals extraction and environmental recovery processes. *Minerals Engineering*, 19(10): 1098–1108. ISSN 0892-6875. doi: https://doi.org/10.1016/j.mineng.2006.05.004. URL http://www.sciencedirect.com/science/article/pii/S0892687506001415. Selected papers from Computational Modelling '05, Cape Town, South Africa.

de Andrade Lima, L. (2006). Liquid axial dispersion and holdup in column leaching. *Minerals Engineering*, 19(1):37–47. ISSN 0892-6875. doi: https://doi.org/10.1016/j.mineng.2005.05.020. URL http://www.sciencedirect.com/science/article/pii/S089268750500172X.

Dixon, D. G. and Afewu, K. I. (2011). Mathematical modelling of heap leaching under drip irrigation. In *Percolation Leaching: The status globally and in Southern Africa 2011*, pages 255–283. The South African Institute of Mining and Metallurgy.

Dixon, D. G. and Afewu, K. (2010). AMIRA P768A - Module C (Heap Hydrology): Final Report - UBC Research Team. Technical report, UBC.

Dwyer, R., Bruckard, W., Rea, S., and Holmes, R. (2012). Bioflotation and bioflocculation review: Microorganisms relevant for mineral beneficiation. *Mineral Processing and Extractive Metallurgy*, 121:65–71. doi: 10.1179/1743285512Y.0000000005.

Fagan, M. A., Ngoma, I. E., Chiume, R. A., Minnaar, S., Sederman, A. J., Johns, M. L., and Harrison, S. T. (2014). MRI and gravimetric studies of hydrology in drip irrigated heaps and its effect on the propagation of bioleaching micro-organisms. *Hydrometallurgy*, 150: 210–221. ISSN 0304-386X. doi: https://doi.org/10.1016/j.hydromet.2014.04.022. URL http://www.sciencedirect.com/science/article/pii/S0304386X14001029.

Fernando, A., Ilankoon, I. M. S. K., Krishnan, S., and Chokshi, V. (2019). The effects of packing shape and structure on liquid distribution of heap leaching systems: Addition of PCBs as non-ore particles. *Hydrometallurgy*, 187. doi: 10.1016/j.hydromet.2019.05.010.

Fernando, W. A. M., Ilankoon, I., Rabbani, A., and Chong, M. N. (2020). Applicability of pore networks to evaluate the inter-particle flow in heap leaching. *Hydrometallurgy*, 197: 105451. ISSN 0304-386X. doi: https://doi.org/10.1016/j.hydromet.2020.105451. URL http://www.sciencedirect.com/science/article/pii/S0304386X20303315.

Fogler, H. S. (2006). *Elements of Chemical Reaction Engineering*, chapter 14: Models for Nonideal Reactors, pages 945–1007. Pearson Education.

Freeze, R. A. and Cherry, J. A. (1979). *Groundwater*, chapter 2 and 9. Prentice-Hall 1979, Englewood Cliffs, New Jersey, illustrated edition.

Galet, L., Patry, S., and Dodds, J. (2010). Determination of the wettability of powders by the Washburn capillary rise method with bed preparation by a centrifugal packing technique. *Journal of Colloid and Interface Science*, 346(2):470–475. ISSN 0021-9797. doi: https://doi.org/10.1016/j.jcis.2010.02.051. URL `http://www.sciencedirect.com/science/article/pii/S0021979710002547`.

Ghadiri, M. (2019). *Investigating variables affecting heap (bio)leaching through determining access to sub-surface mineral grains by micro-scale X-ray tomography.* PhD thesis, Department of Chemical Engineering, Faculty of Engineering and the Built Environment, University of Cape Town.

Ghorbani, Y., Becker, M., Mainza, A., and Franzidis, J.-P. (2011). Large particle effect in chemical/biochemical heap leach processes-A review. *Minerals Engineering*, 24:1172–1184. doi: 10.1016/j.mineng.2011.04.002.

Ghorbani, Y., Franzidis, J.-P., and Petersen, J. (2016). Heap leaching technology-Current state, innovations, and future directions: A review. *Mineral Processing and Extractive Metallurgy Review*, 37:73–119. doi: 10.1080/08827508.2015.1115990.

Gibb, J. P., Barcelona, M. J., Ritchey, J. D., and LeFaivre, M. H. (1984). Effective porosity of geologic materials - First annual report. Technical report, Illinois State Water Survey.

Gibson, B. A. K. K. (2020). Residence time investigation of artificial silver ores in heap leaching using cyanide lixiviant. Master's thesis, University of Cape Town. Department of Chemical Engineering.

Govender, E., Bryan, C. G., and Harrison, S. T. (2015). A novel experimental system for the study of microbial ecology and mineral leaching within a simulated agglomerate-scale heap bioleaching system. *Biochemical Engineering Journal*, 95:86–97. ISSN 1369-703X. doi: https://doi.org/10.1016/j.bej.2014.12.001. URL `https://www.sciencedirect.com/science/article/pii/S1369703X14003404`.

Govender-Opitz, E., Kotsiopoulos, A., Fagan-Endres, M., and Harrison, S. T. (2017). Insight into solute and microbial transport in heap (bio)leaching systems using residence time distribution. *Hydrometallurgy*, 168:1–6. ISSN 0304-386X. doi: https://doi.org/10.1016/j.hydromet.2016.10.002. URL `https://www.sciencedirect.com/science/article/pii/S0304386X16306958`. Hydrometallurgy Special Issue (SI): IBS 2015.

Habashi, F. (2018). Pyro- versus hydrometallurgy or dry versus wet methods. *JOJ Material Science*, 3(4). URL `https://juniperpublishers.com/jojms/pdf/JOJMS.MS.ID.555618.pdf`.

Harrison, S. T. L. (2016). *Acidophiles: Life in extremely acidic environments*, chapter 16, pages 265–284. Caister Academic Press, U.K. doi: https://doi.org/10.21775/9781910190333.16.

Hudson Institute of Mineralogy. (2021). Greywacke. Accessed: 2021-02-09. https://www.mindat.org/min-49126.html.

Ilankoon, I. M. S. K. and Neethling, S. (2013). The effect of particle porosity on liquid holdup in heap leaching. *Minerals Engineering*, 45:73–80. doi: 10.1016/j.mineng.2013.01.016.

Ilankoon, I. M. S. K. and Neethling, S. (2014). Transient liquid holdup and drainage variations in gravity dominated non-porous and porous packed beds. *Chemical Engineering Science*, 116:398–405. doi: 10.1016/j.ces.2014.05.017.

Ilankoon, I. M. S. K. and Neethling, S. (2016). Liquid spread mechanisms in packed beds and heaps. The separation of length and time scales due to particle porosity. *Minerals Engineering*, 86:130–139. doi: 10.1016/j.mineng.2015.12.010.

Ilankoon, I. M. S. K., Cole, K., and Neethling, S. (2013). Measuring hydrodynamic dispersion coefficients in unsaturated packed beds: Comparison of PEPT with conventional tracer tests. *Chemical Engineering Science*, 89:152–157. doi: 10.1016/j.ces.2012.11.013.

Ilankoon, I. and Neethling, S. (2012). Hysteresis in unsaturated flow in packed beds and heaps. *Minerals Engineering*, 35:1–8. ISSN 0892-6875. doi: https://doi.org/10.1016/j.mineng.2012.05.007. URL http://www.sciencedirect.com/science/article/pii/S0892687512001975.

Ilankoon, I. and Neethling, S. (2019). Inter-particle liquid spread pertaining to heap leaching using UV fluorescence based image analysis. *Hydrometallurgy*, 183:175–185. ISSN 0304-386X. doi: https://doi.org/10.1016/j.hydromet.2018.12.007. URL http://www.sciencedirect.com/science/article/pii/S0304386X18305644.

Iliuta, I., Thyrion, F., and Muntean, O. (1998). Axial Dispersion of Liquid in Gas-Liquid Cocurrent Downflow and Upflow Fixed-Bed Reactors with Porous Particles. *Chemical Engineering Research and Design*, 76(1):64–72. ISSN 0263-8762. doi: https://doi.org/10.1205/026387698524488. URL http://www.sciencedirect.com/science/article/pii/S026387629871620X. Materials Processing.

Iliuta, I., Larachi, F., and Grandjean, B. (1999). Residence time, mass transfer and back-mixing of the liquid in trickle flow reactors containing porous particles. *Chemical Engineering Science*, 54(18):4099–4109. ISSN 0009-2509. doi: https://doi.org/10.1016/S0009-2509(99)00120-7. URL http://www.sciencedirect.com/science/article/pii/S0009250999001207.

John, L. W. (2011). The art Of heap leaching - The fundamentals. In *Percolation Leaching: The status globally and in Southern Africa 2011*, pages 17–42. BIOMET Engineering, The Southern African Institute of Mining and Metallurgy.

Kappes, D. W., Barratt, D. J., Halbe, D. N., and Mular, A. L. (2002). Precious metal heap leach design and practice. In *Mineral Processing Plant Design, Practice, and Control: Proceedings*, pages 1606–1630. Society for Mining, Metallurgy, and Exploration. ISBN 0873352238. URL https://www.tib.eu/de/suchen/id/BLCP%3ACN048984368.

Klerk, A. (2003). Liquid holdup in packed beds at low mass flux. *AIChE Journal*, 49: 1597–1600. doi: 10.1002/aic.690490622.

Kumar, R. (2016). Characterisation of minerals and ores: On the complementary nature of select techniques and beyond. *Transactions of the Indian Institute of Metals*, 70(2): 253–277.

Laguna-Sanchez, G. A., Olguin-Carbajal, M., Cruz-Cortes, N., Barron-Fernandez, R., and Cadena-Martinez, R. (2016). A differential evolution algorithm parallel implementation in a GPU. *Journal of Theoretical and Applied Information Technology*, 86(2):184–195.

Leblanc, G. E., Secco, R. A., Kostic, M., and deBruyn, J. R. (1999). *The measurement, instrumentation and sensors handbook*, chapter 30: Viscosity Measurement, pages 1–23. CRC Press L.L.C. URL http://materias.df.uba.ar/l2aa2020c1/files/2012/07/Measurement-Instrumentation-Sensors.pdf.

Levenspiel, O. (2011). *Tracer technology: Modeling the flow of fluids*. Springer Science and Business Media, New York, illustrated edition.

Liu, J. Z., Wu, A. X., and Zhang, L. W. (2015). Numerical analysis on flow and solute transmission during heap leaching process. *Mathematical Problems in Engineering*, 2015: 1–5. doi: https://doi.org/10.1155/2015/982436. Article ID 982436.

Liu, W. and Hashemzadeh, M. (2017). Solution flow behavior in response to key operating parameters in heap leaching. *Hydrometallurgy*, 169:183–191. ISSN 0304-386X. doi: https://doi.org/10.1016/j.hydromet.2017.01.007. URL http://www.sciencedirect.com/science/article/pii/S0304386X16305436.

Lourenço, S., Woche, S., Bachmann, J., and Saulick, Y. (2015). Wettability of crushed air-dried minerals. *Géotechnique Letters*, 5:173–177. doi: 10.1680/geolett.15.00075.

Macías-García, A., Cuerda-Correa, E. M., and Díaz-Díez, M. (2004). Application of the Rosin–Rammler and Gates–Gaudin–Schuhmann models to the particle size distribution analysis of agglomerated cork. *Materials Characterization*, 52(2):159–164. ISSN 1044-5803. doi: https://doi.org/10.1016/j.matchar.2004.04.007. URL https://www.sciencedirect.com/science/article/pii/S1044580304000853.

McBride, D., Ilankoon, I., Neethling, S., Gebhardt, J., and Cross, M. (2017). Preferential flow behaviour in unsaturated packed beds and heaps: Incorporating into a CFD model. *Hydrometallurgy*, 171:402–411. ISSN 0304-386X. doi: https://doi.org/10.1016/j.hydromet.2017.06.008. URL http://www.sciencedirect.com/science/article/pii/S0304386X16305461.

Mellado, M. E., Casanova, M. P., Cisternas, L. A., and Gálvez, E. D. (2011). On scalable analytical models for heap leaching. *Computers & Chemical Engineering*, 35(2):220–225. ISSN 0098-1354. doi: https://doi.org/10.1016/j.compchemeng.2010.09.009. URL http://www.sciencedirect.com/science/article/pii/S0098135410003169.

Miao, X., Narsilio, G. A., Wu, A., and Yang, B. (2017). A 3d dual pore-system leaching model. part 1: Study on fluid flow. *Hydrometallurgy*, 167:173–182. ISSN 0304-386X. doi: https://doi.org/10.1016/j.hydromet.2016.11.015. URL https://www.sciencedirect.com/science/article/pii/S0304386X16309343.

Miller, D. G. (1982). Estimation of Tracer Diffusion Coefficients of Ions in Aqeous Solution. Technical report, University of California, Livermore, California.

Miller, G., Knight, S., and Parker, A. J. (2003). Ore geo-mechanical properties and effects on copper heap leach kinetics. In *ALTA Copper-8 2003*, pages 1–19, Australia. ALTA.

Miner, C. S. and Dalton, N. N. (1953). Physical properties Of glycerine and its solutions. Printed. Published and copyrighted by Reinhold Publishing Corp.

Mishra, D. K. and Shinde, V. (2017). A comparative study of differential evolution algorithm for global numerical optimization. *Indian Journal of Computer Science and Engineering*, 8(4):519–525.

Mousavi, S. M., Jafari, A., Yaghmaei, S., Vossoughi, M., and Sarkomaa, P. (2006). Computer simulation of fluid motion in a porous bed using a volume of fluid method: Application in heap leaching. *Minerals Engineering*, 19:1077–1083.

Murr, L. E., Schlitt, W. J., and Cathles, L. M. (1981). Experimental observations of solution flow in the leaching of copper-bearing waste. In *'SME-AIME Fall Meeting and Exhibit'*, pages 1–18, Denver, Colorado.

Murr, L. (1979). Observations of solution transport, permeability, and leaching reactions in large, controlled, copper-bearing waste bodies. *Hydrometallurgy*, 5(1):67–93. ISSN 0304-386X. doi: https://doi.org/10.1016/0304-386X(79)90028-8. URL https://www.sciencedirect.com/science/article/pii/0304386X79900288.

National Center for Biotechnology Information. (2021). PubChem compound summary for CID 753, Glycerol. Accessed: 2021-01-23. https://pubchem.ncbi.nlm.nih.gov/compound/Glycerol.

Nkonga, B. (2009). Numerical methods for PDE: finite differences and finite volumes. Accessed: 2021-03-20. https://math.unice.fr/~nkonga/Cours/FDFV/AdvDif.pdf.

Odidi, M., Harrison, S. T. L., Fagan-Endres, M., Ngoma, E., and Petersen, J. (2020). Equipment for studies on heap leaching test columns. University of Cape Town. Figure. https://doi.org/10.25375/uct.11907027.v2.

Odidi, M., Harrison, S. T. L., and Fagan-Endres, M. (2022). Preferential flow in drip irrigated heaps. University of Cape Town. Figure. https://doi.org/10.25375/uct.21435300.

O'Kane, M., L., B. S., and Haug, M. D. (1999). A Framework for improving the ability to understand and predict the performance of heap leach piles. In *Proceedings of the COPPER 99 - COBRE 99 International Conference*, volume 4, pages 409–419. The Minerals, Metals and Materials Society. URL `https://www.okc-sk.com/new/wp-content/uploads/2012/02/Heap-Leach-Research-Copper-1999-Confernce.pdf`.

Patankar, S. V. (1980). *Numerical heat transfer and fluid flow*, chapter Four: Heat Conduction, pages 41–74. CRC Press, 1st edition. eBook Published: 31 October 2018.

Pereira, G., Moreira, R., Vázquez, M. J., and Chenlo, F. (2001). Kinematic viscosity prediction for aqueous solutions with various solutes. *Chemical Engineering Journal*, 81 (1):35–40. ISSN 1385-8947. doi: https://doi.org/10.1016/S1385-8947(00)00203-5. URL `http://www.sciencedirect.com/science/article/pii/S1385894700002035`.

Petersen, J. and Dixon, D. (2007a). Modelling zinc heap bioleaching. *Hydrometallurgy*, 85 (2):127–143. ISSN 0304-386X. doi: https://doi.org/10.1016/j.hydromet.2006.09.001. URL `http://www.sciencedirect.com/science/article/pii/S0304386X06002283`.

Petersen, J. and Dixon, D. (2007b). Principles, Mechanisms And Dynamics of Chalcocite Heap Bioleaching. *Microbial Processing of Metal Sulfides*, pages 193–218. doi: 10.1007/1-4020-5589-7_10.

Radiometer Analytical SAS. (2004). Conductivity: Theory and practice. Printed, 72 rue d'Alsace, 69627 Villeurbanne Cedex, France. Web: `www.radiometer-analytical.com`.

Reichardt, C. (2008). Heap leaching and the water environment - Does low cost recovery come at a high environmental cost? In *Mine Water and the Environment*, pages 395–398. International Mine Water Association.

Rhodes, F. H. and Barbour, C. B. (1923). The viscosities of mixtures of sulfuric acid and water. *Industrial and Engineering Chemistry*, 15(8):850–852.

Ribeiro, A. M., Neto, P., and Pinho, C. (2010). Mean porosity and pressure drop measurements in packed beds of monosized spheres: Side wall effects. *International Review of Chemical Engineering*, 2(1):40–46.

Rodriguez, J. M. (2013). *Importance of the Particle Shape on Mechanical Properties of Soil Materials*. PhD thesis, Department of Civil, Environmental and Natural Resources Engineering, Division of Mining and Geotechnical Engineering Lulea University of Technology.

Roman, R. J., Benner, B. R., and Becker, G. W. (1974). Diffusion model for heap leaching and its application to scale-up. *Society of Mining Engineers*, 256:247–252.

Saber, M., Truong, T., Pham-Huu, C., and Edouard, D. (2012). Residence time distribution, axial liquid dispersion and dynamic–static liquid mass transfer in trickle flow reactor containing β-SiC open-cell foams. *Chemical Engineering Journal*, s 185–186:294–299. doi: 10.1016/j.cej.2012.01.045.

Sarraute, S., Gomes, M., and Pádua, A. (2008). Diffusion coefficients of ionic liquids in water: anion and cation size effect. URL https://www.researchgate.net/publication/281049225_Diffusion_coefficients_of_ionic_liquids_in_water_anion_and_cation_size_effect.

Sheikhzadeh, G., Mehrabian, M., Mansouri, S., and Sarrafi, A. (2005). Computational modelling of unsaturated flow of liquid in heap leaching - Using the results of column tests to calibrate the model. *International Journal of Heat and Mass Transfer*, 48:279–292. doi: 10.1016/j.ijheatmasstransfer.2004.08.007.

Simunek, J. and van Genuchten, M. T. (2006). *The Handbook of Groundwater Engineering*, chapter Contaminant Transport in the Unsaturated Zone Theory and Modelling, pages 22:1–46. Taylor & Francis Group, Boca Raton.

Sinha, K. P. and Smith, M. E. (2015). Cold climate heap leaching. In *Proceedings of the 3rd International Conference on Heap Leach Solutions, 2015*, pages 409–423, Reno, NV, USA. InfoMine.

Spurr, N. R. L. (2008). Interrelationship of hydrology, microbial colonisation and hydrometallurgy in a simulated chalcopyrite heap leach. Master's thesis, Department of Chemical Engineering, University of Cape Town.

Stevens, N., Ralston, J., and Sedev, R. (2009). The uniform capillary model for packed beds and particle wettability. *Journal of Colloid and Interface Science*, 337 (1):162–169. ISSN 0021-9797. doi: https://doi.org/10.1016/j.jcis.2009.04.086. URL http://www.sciencedirect.com/science/article/pii/S0021979709005621.

Suzuki, M., Shinmura, T., Iimura, K., and Hirota, M. (2008). Study of the wall effect on particle packing structure using X-ray Micro Computed Tomography. *Advanced Powder Technology*, 19(2):183–195. ISSN 0921-8831. doi: https://doi.org/10.1163/156855208X293817. URL http://www.sciencedirect.com/science/article/pii/S0921883108603477.

Szymkiewicz, A. (2012). *Modelling water flow in unsaturated porous media: Accounting for nonlinear permeability and material heterogeneity*. GeoPlanet: Earth and Planetary Sciences. Springer Berlin Heidelberg. ISBN 9783642235597. URL https://books.google.co.za/books?id=MoMkIy7ja-EC.

Sánchez-Chacón, A. and Lapidus, G. (1997). Model for heap leaching of gold ores by cyanidation. *Hydrometallurgy*, 44(1):1–20. ISSN 0304-386X. doi: https://doi.org/10.1016/S0304-386X(96)00052-7. URL http://www.sciencedirect.com/science/article/pii/S0304386X96000527.

Thommes, M., Kaneko, K., Neimark, A. V., Olivier, J. P., Rodriguez-Reinoso, F., Rouquerol, J., and Sing, K. S. W. (2015). Physisorption of gases, with special reference to the evaluation of surface area and pore size distribution (IUPAC Techincal Report). *Pure and Applied Chemistry*, 87(9-10):1051–1069.

Trefethen, L. N. (1996). Finite difference and spectral methods for ordinary and partial differential equations. Accessed: 2021-03-09. http://people.maths.ox.ac.uk/trefethen/pdetext.html.

Trinchero, P., Beckie, R., Sanchez-Vila, X., and Nichol, C. (2011). Assessing preferential flow through an unsaturated waste rock pile using spectral analysis. *Water Resources Research*, 47. doi: 10.1029/2010WR010163.

Ulrich, B., Andrade, H., and Gardner, T. (2003). Lessons learnt from heap leaching operations in South America - An update. *Journal- South African Institute of Mining and Metallurgy*, 103:23–28.

van Staden, P. J. and Petersen, J. (2018a). First-order exchange and spherical diffusion models of heap leaching in PhreeqC. *The Journal of th South African Institute of Mining and Metallurgy*, 118:681–694.

van Staden, P. J. and Petersen, J. (2018b). The effects of simulated stacking phenomena on the percolation leaching of crushed ore, Part 1: Segregation. *Minerals Engineering*, 128: 202–214. doi: 10.1016/j.mineng.2018.08.045.

van Staden, P., Robertson, S., Gericke, M., Neale, J., and Seyedbagheri, A. (2009). Maximising the value derived from laboratory testwork towards heap leaching design. In *Base Metals Conference 2009*, pages 185–200. doi: 10.13140/2.1.4231.1042.

van Staden, P. and Petersen, J. (2018). The effects of simulated stacking phenomena on the percolation leaching of crushed ore, part 1: Segregation. *Minerals Engineering*, 128:202–214. ISSN 0892-6875. doi: https://doi.org/10.1016/j.mineng.2018.08.045. URL https://www.sciencedirect.com/science/article/pii/S0892687518304059.

van Staden, P. and Petersen, J. (2019). The effects of simulated stacking phenomena on the percolation leaching of crushed ore, part 2: Stratification. *Minerals Engineering*, 131:216–229. ISSN 0892-6875. doi: https://doi.org/10.1016/j.mineng.2018.11.021. URL https://www.sciencedirect.com/science/article/pii/S0892687518305053.

van Swaaij, W. P. M., Charpentier, J. C., and Villermaux, J. (1969). Residence time distribution in the liquid phase of trickle flow in packed columns. *Chemical Engineering Science*, 24:1083–1095.

van Zyl, D. J. A., Hutchison, I. P. G., and Kiel, J. E., editors. (1988). *Introduction to evaluation, design and operation of precious metal heap leaching projects*, chapter 4: Testing of ore, pages 61–67. Society of Mining Engineers Inc.

Vitez, T. and Trávníček, P. (2011). Particle size distribution of a waste sand from a waste water treatment plant with use of rosin–rammler and gates–gaudin–schumann mathematical model. *Acta Universitatis Agriculturae et Silviculturae Mendelianae Brunensis*, 59: 197–201. doi: 10.11118/actaun201159030197.

Watling, H. (2006). The bioleaching of sulphide minerals with emphasis on copper sulphides — A review. *Hydrometallurgy*, 84(1):81–108. ISSN 0304-386X. doi: https://doi.org/10.1016/j.hydromet.2006.05.001. URL http://www.sciencedirect.com/science/article/pii/S0304386X06001125.

Watling, H., Shiers, D., Li, J., Chapman, N., and Douglas, G. (2014). Effect of water quality on the leaching of a low-grade copper sulfide ore. *Minerals Engineering*, 58:39–51. ISSN 0892-6875. doi: https://doi.org/10.1016/j.mineng.2014.01.005. URL http://www.sciencedirect.com/science/article/pii/S0892687514000065.

Webster, J. G., editor. (2004). *Electrical measurement, signal procesing, and displays*, chapter Electrical Conductivity and Resistivity, pages 7:1–14. CRC Press LLC, 1 edition.

Weller, H. (2016). Time-stepping, numerical stability, dispersion and conservation. Accessed: 2021-03-11. http://www.met.reading.ac.uk/~sws02hs/teaching/dcmip2016/Weller_2_lec.pdf.

Wickland, B. E., Wilson, G. W., and Wijewickreme, D. (2010). Hydraulic conductivity and consolidation response of mixtures of mine waste rock and tailings. *Canadian Geotechnical Journal*, 47:472–485.

Wilke, J., Kryk, H., Hartmann, J., and Wagner, D. (2007). Theory and praxis of capillary viscometry - an introduction. Printed, Germany.

Wu, A., Yin, S., Yang, B., Wang, J., and Qiu, G. (2007). Study on preferential flow in dump leaching of low-grade ores. *Hydrometallurgy*, 87(3):124–132. ISSN 0304-386X. doi: https://doi.org/10.1016/j.hydromet.2007.03.001. URL http://www.sciencedirect.com/science/article/pii/S0304386X07000643.

Wu, A., Yin, S., Qin, W., Liu, J., and Qiu, G. (2009). The effect of preferential flow on extraction and surface morphology of copper sulphides during heap leaching. *Hydrometallurgy*, 95:76–81. doi: 10.1016/j.hydromet.2008.04.017.

Yang, B., Wu, A., Jiang, H., and Chen, X. (2008). Evolvement of permeability of ore granular media during heap leaching based on image analysis. *Transactions of Nonferrous Metals Society of China*, 18(2):426–431. ISSN 1003-6326. doi: https://doi.org/10.1016/S1003-6326(08)60075-8. URL http://www.sciencedirect.com/science/article/pii/S1003632608600758.

Yin, S., Leiming, W., Chen, X., and Wu, A. (2016). Effect of ore size and heap porosity on capillary process inside leaching heap. *Transactions of Nonferrous Metals Society of China*, 26:835–841. doi: 10.1016/S1003-6326(16)64174-2.

Yusuf, R. (1984). Liquid flow characteristics in heap and dump leaching. Master's thesis, University of New South Wales, Sydney, Australia.

Zanbak, C. (2012). Heap leaching technique in mining within the context of Best Available Techniques (BAT). Technical report, Euromines - The

European Association of Mining Industries, Metal Ores and Industrial Minerals. URL http://www.euromines.org/files/mining-europe/mining-techniques/batforheapleaching-feb2013-c.zanbak-euromines.pdf.

Zhang, W. and Yuan, S. (2019). Characterizing preferential flow in landfilled municipal solid waste. *Waste Management*, 84:20–28. ISSN 0956-053X. doi: https://doi.org/10.1016/j.wasman.2018.11.023. URL http://www.sciencedirect.com/science/article/pii/S0956053X18306871.

Appendices

Appendix A

Viscosity Theory and Measurement

The application of shear stress to a fluid will cause it to undergo continuous deformation, referred to as "flow". The term viscosity is defined as the internal friction of a fluid and indicates its resistance to flow under the action of such shear forces. An illustration of this can be found in Figure A.1.

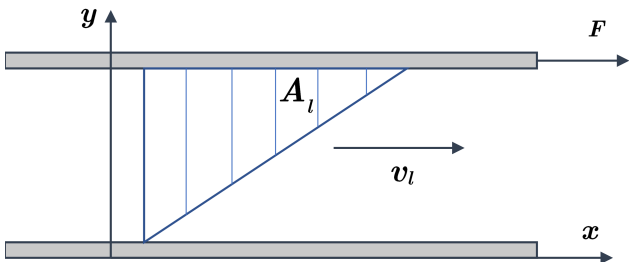

Figure A.1: Basic illustration showing a shearing force being applied to a fluid between two plates. A force (F) applied to top plate causes it to move and drag the the fluid in the direction of the force. The fluid velocity (v_l) of each layer diminishes until it reaches zero at the lower plate, also no known as no slip condition, based on Leblanc et al. (1999).

The shear stress of the fluid ($\dot{\tau}$), is defined as the quotient of the force applied to the plate (F), and the boundary surface (A_l) of the liquid, Equation (A.1). The shear strain rate ($\dot{\gamma}$) is taken as the differential of the liquid velocity (dv_l) with respect to the differential of the distance between the two plates (dy) also known as the velocity gradient, Equation (A.2).

$$\dot{\tau} = \frac{F}{A_l} \tag{A.1}$$

$$\dot{\gamma} = \frac{dv_l}{dy} \tag{A.2}$$

Based on Newton's law of viscosity, the shear strain is proportional to the shear rate, with the dynamic viscosity coefficient as the constant of proportionality, Equation (A.3).

$$\dot{\tau} = \mu\dot{\gamma} \tag{A.3}$$

The kinematic viscosity ($\bar{v}$) links dynamic viscosity to density and is shown in Equation (A.4).

$$\bar{v} = \frac{\mu}{\rho} \tag{A.4}$$

Newton's law of viscosity (Equation (A.3)) is only valid for laminar flow and only applicable to a class of fluids called Newtonian fluids. For these fluids, the viscosity is independent of strain rate, represented by the straight line in Figure A.2. Examples of such fluids are pure, unassociated gases, liquids and solutions of low molecular weight. Some materials may experience an increase in the viscosity coefficient as shear rate is increased. These materials are said to exhibit dilatancy, with an example being corn starch in water. Other materials experience a decrease in viscosity with an increase in shear rate, known as pseudo-plastic materials. An example of such a fluid/material is blood (refer to Figure A.2). In a heap leaching context, most leach solutions are aqueous solutions and flow through the heap is normally laminar due to the low flow rates typically employed (Bartlett, 1992). Hence, most of the fluids encountered are Newtonian fluids that obey Newton's law of viscosity.

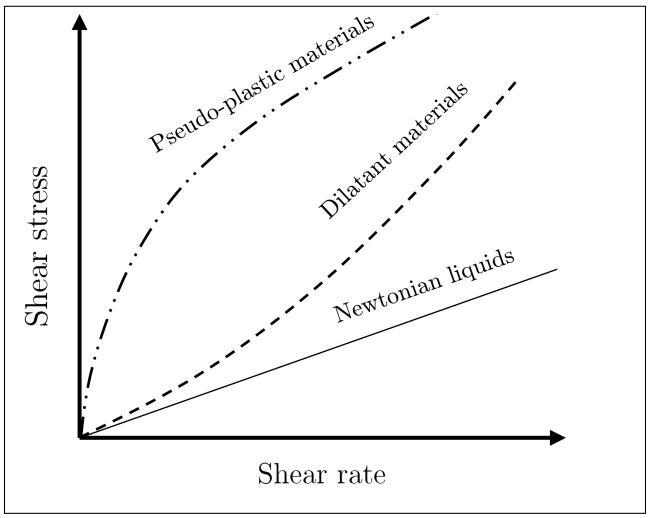

Figure A.2: Shear stress versus strain profiles for Newtonian and non-Newtonian fluids, based on Leblanc et al. (1999).

Different instruments for viscosity measurements are found in literature. Examples include the falling-ball, rotational and capillary viscometers. Of the three, the capillary viscometer was chosen for this study. The mechanism behind its viscosity measurements is the velocity drop experienced by fluids flowing through a capillary. This results in a laminar tube flow profile within the capillary (refer to Figure A.3). Viscosity measurements utilizing this method are said to occur under idealised conditions with the following assumptions:

- Laminar and isothermal flow
- Newtonian flow behaviour
- Negligible pressure effects
- Incompressibility of the fluid
- Negligible end effects (sufficiently long capillary required)

The Hagen-Poiseuille Law, shown in Equation (A.5) is used to describe the relationship between the volumetric flow rate (Q) and the viscosity of a fluid flowing through a capillary of defined radius (R) and length (L), (refer to Figure A.3). From Equation (A.5), it can be seen that the longer it takes for a fixed volume of fluid to flow through a capillary of fixed radius, the higher the fluid's viscosity. This is the concept behind viscosity tests using capillary viscometers.

$$\mu = \frac{\pi R^4 \Delta P}{8LQ} \tag{A.5}$$

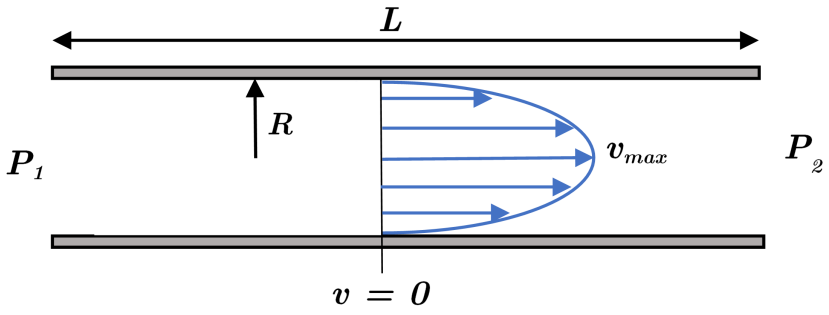

Figure A.3: Velocity profile of a fluid under laminar flow in a capillary, based on Wilke et al. (2007).

Appendix B

2-Dimensional Shape Descriptor Results

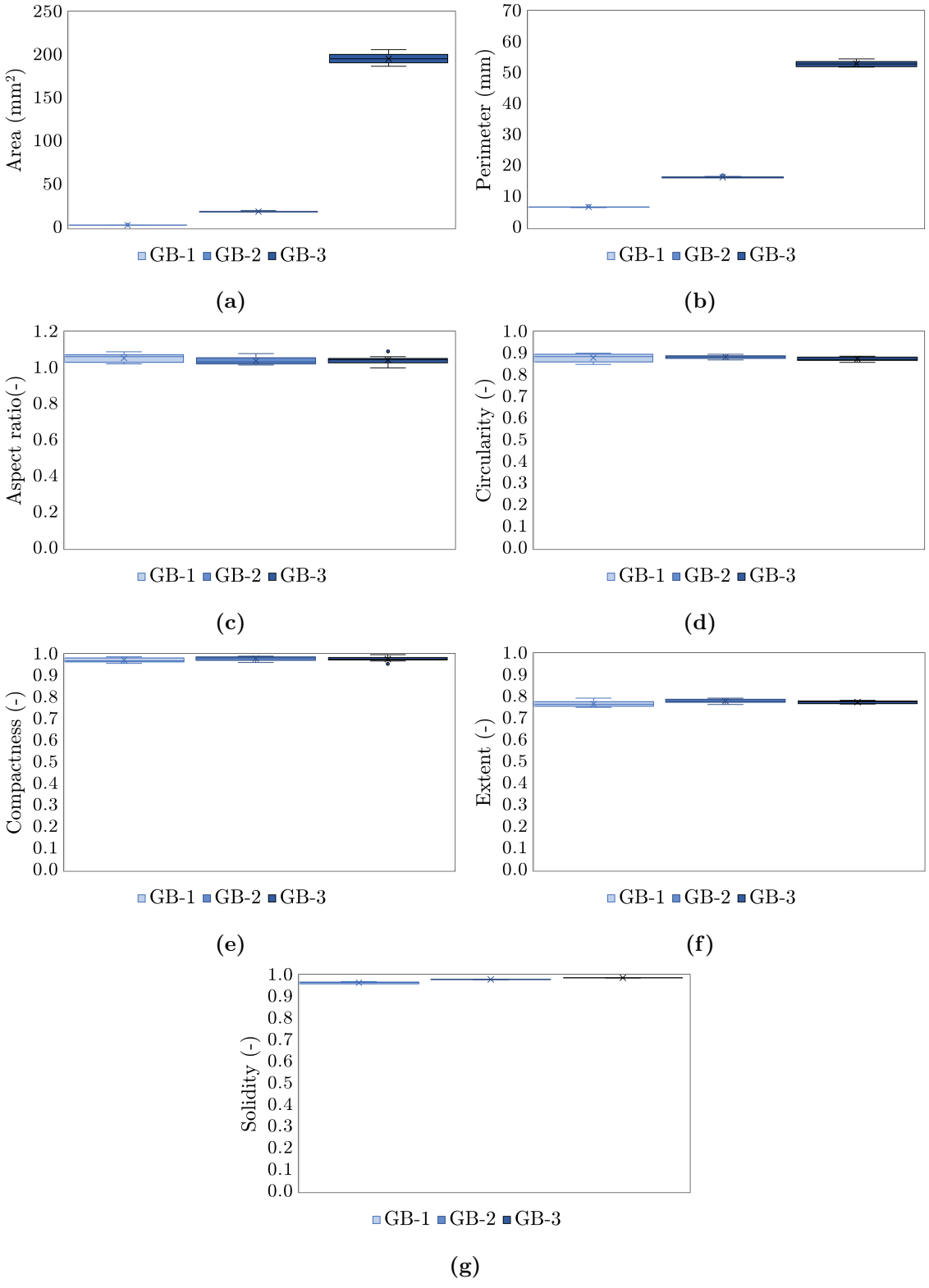

Figure B.1: Box and whisker plots depicting quantified values for various shape descriptors based on the 2-D shape analysis of a set of 10 glass beads with three different sizes (Dots - outliers, Inside main box: x - mean value, middle horizontal line - median).

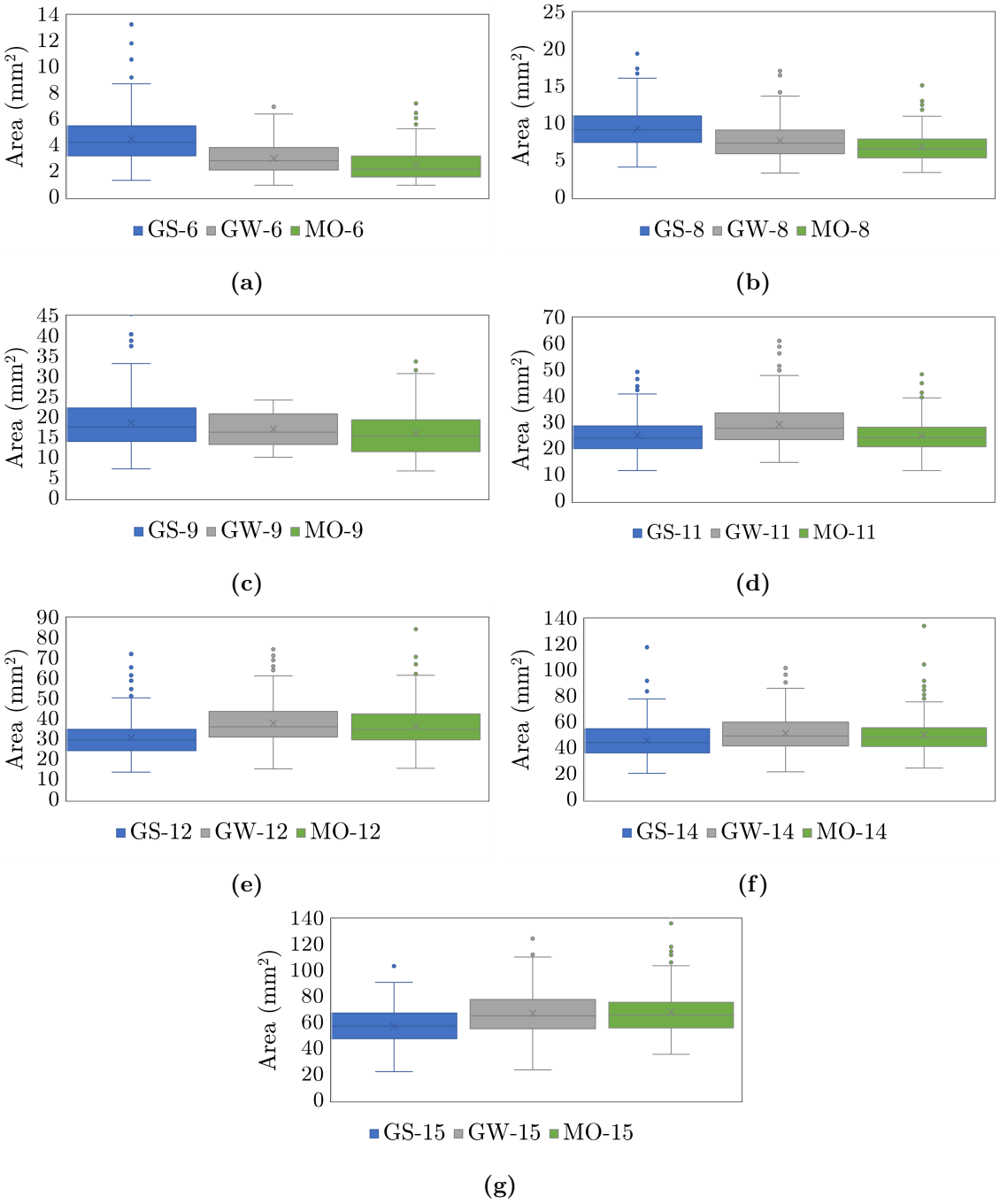

Figure B.2: Box and whisker plots depicting quantified values for area based on the 2-D shape analysis of 300 glass shard, greywacke and malachite ore particles belonging to different size fractions (Dots - outliers, Inside main box: x - mean value, middle horizontal line - median).

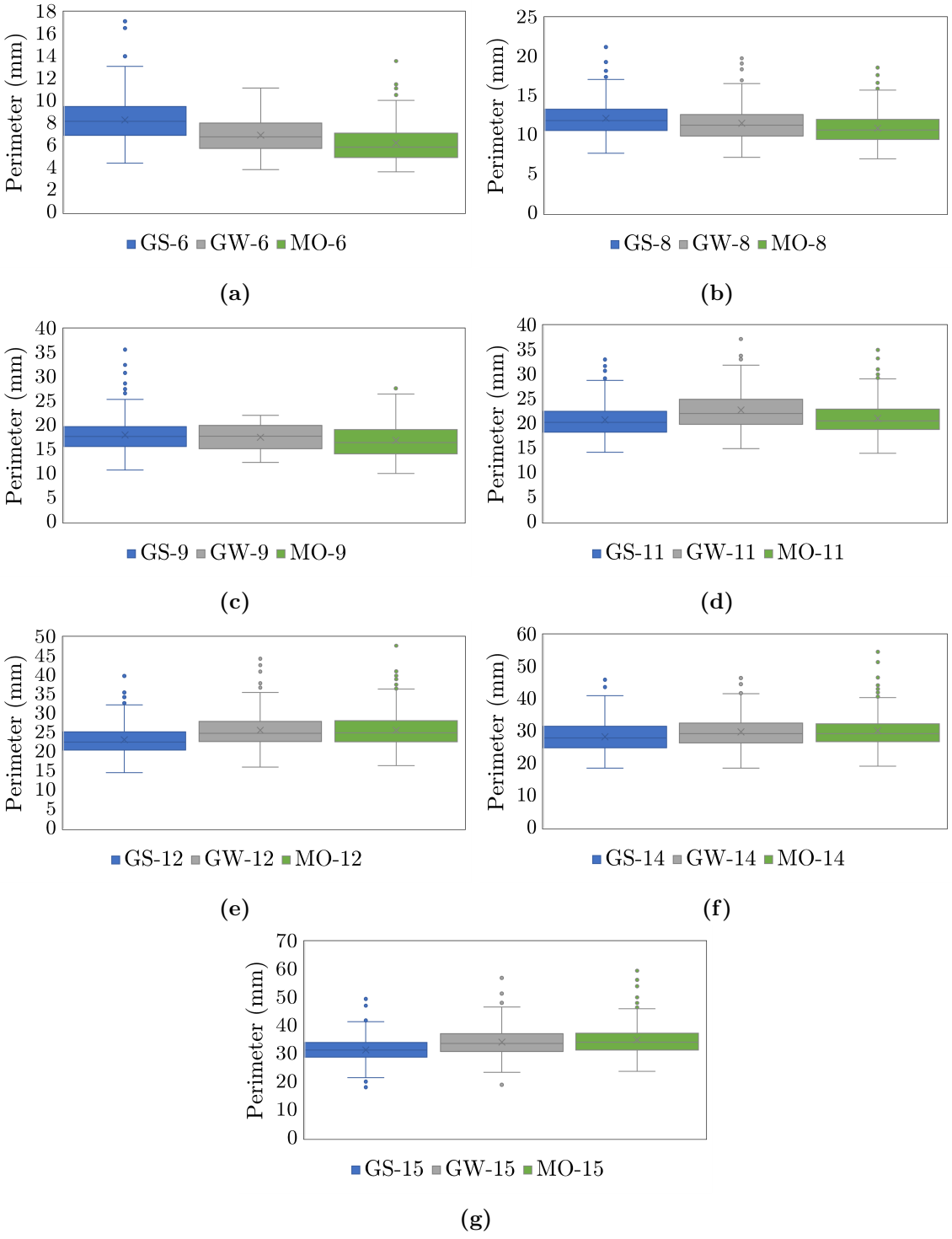

Figure B.3: Box and whisker plots depicting quantified values for perimeter based on the 2-D shape analysis of 300 glass shard, greywacke and malachite ore particles belonging to different size fractions (Dots - outliers, Inside main box: x - mean value, middle horizontal line - median).

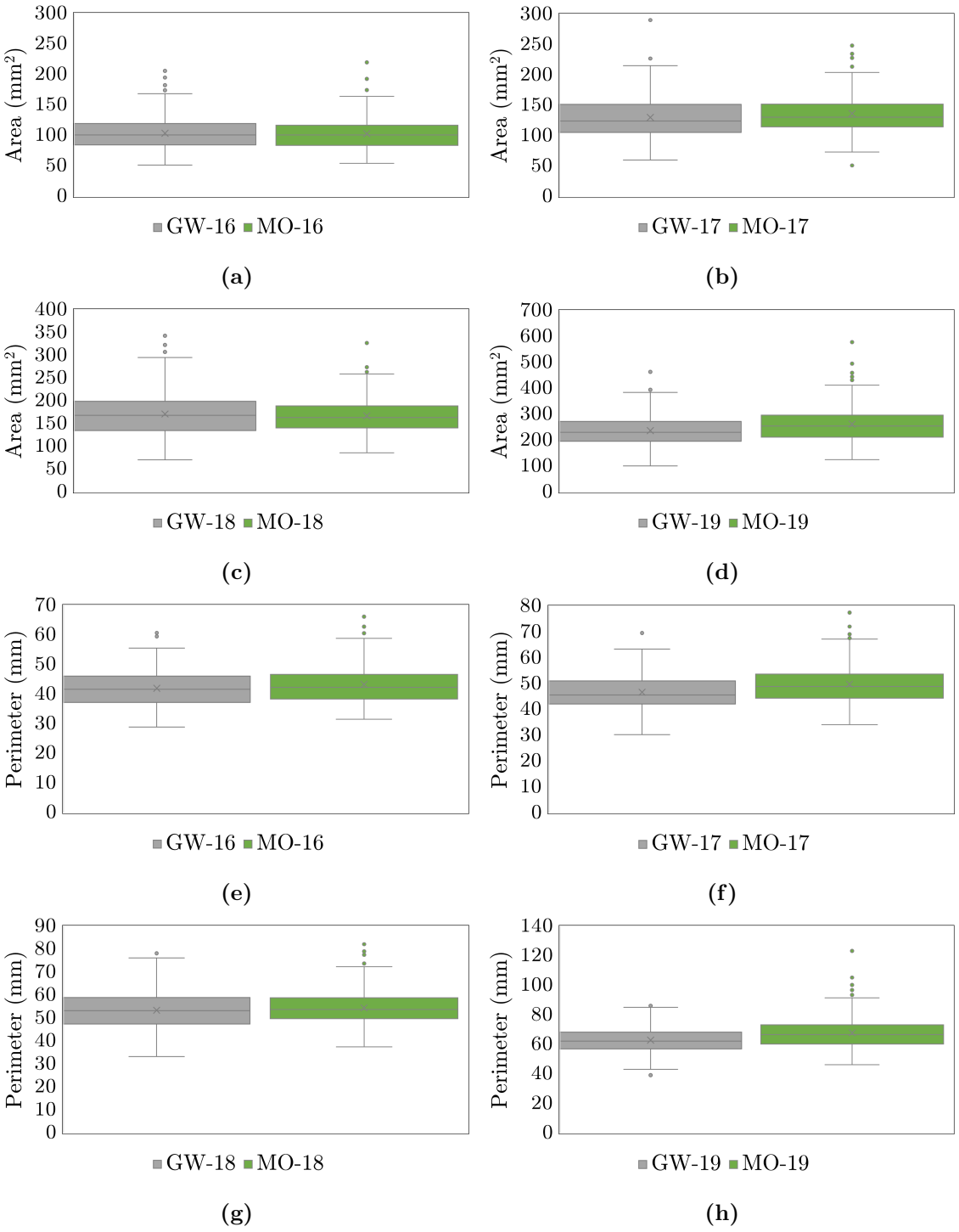

Figure B.4: Box and whisker plots depicting quantified values for area (a - d) and perimeter (e - h)based on the 2-D shape analysis of 300 greywacke and malachite ore particles belonging to different size fractions (Dots - outliers, Inside main box: x - mean value, middle horizontal line - median).

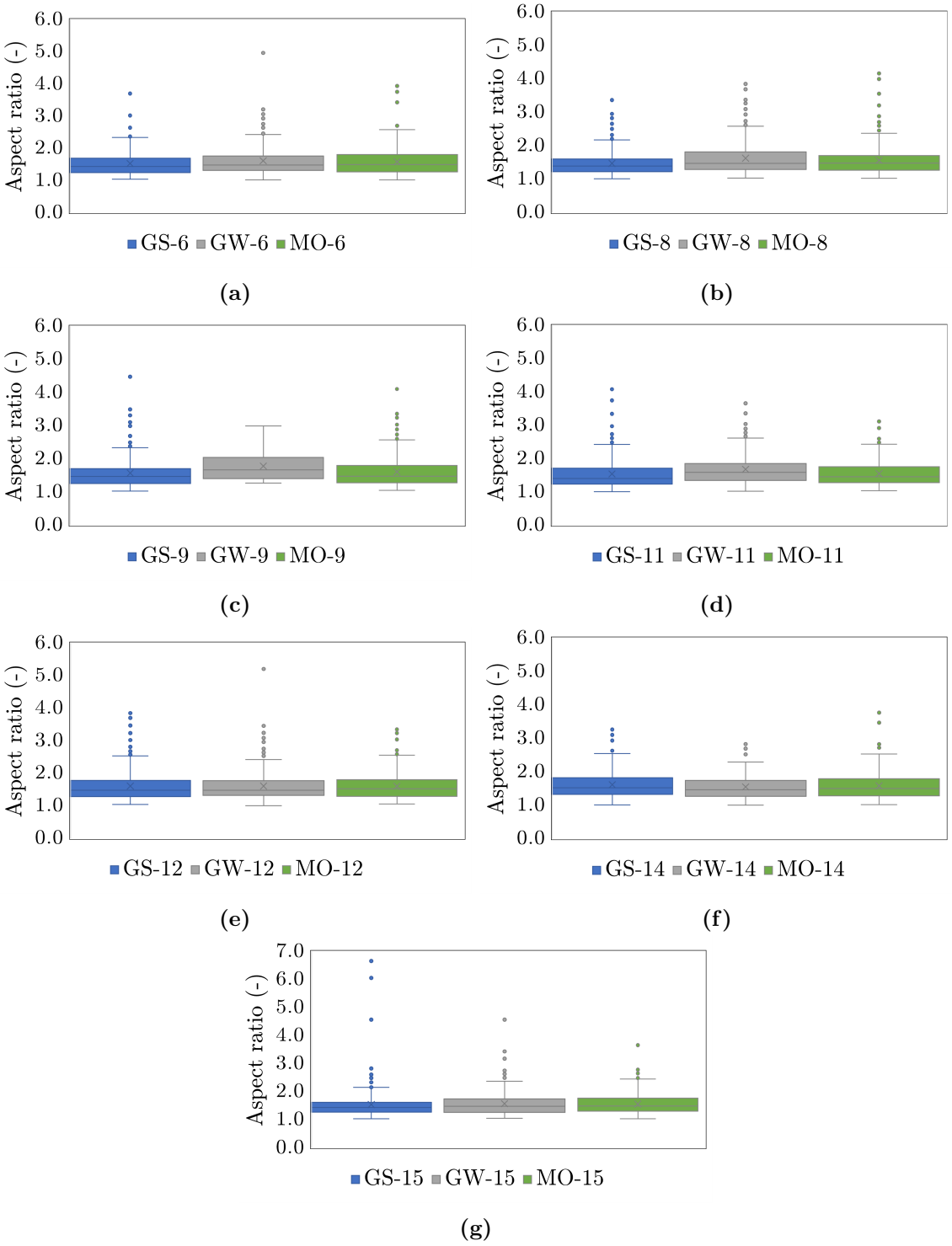

Figure B.5: Box and whisker plots depicting quantified values for aspect ratio based on the 2-D shape analysis of 300 glass shard, greywacke and malachite ore particles belonging to different size fractions (Dots - outliers, Inside main box: x - mean value, middle horizontal line - median).

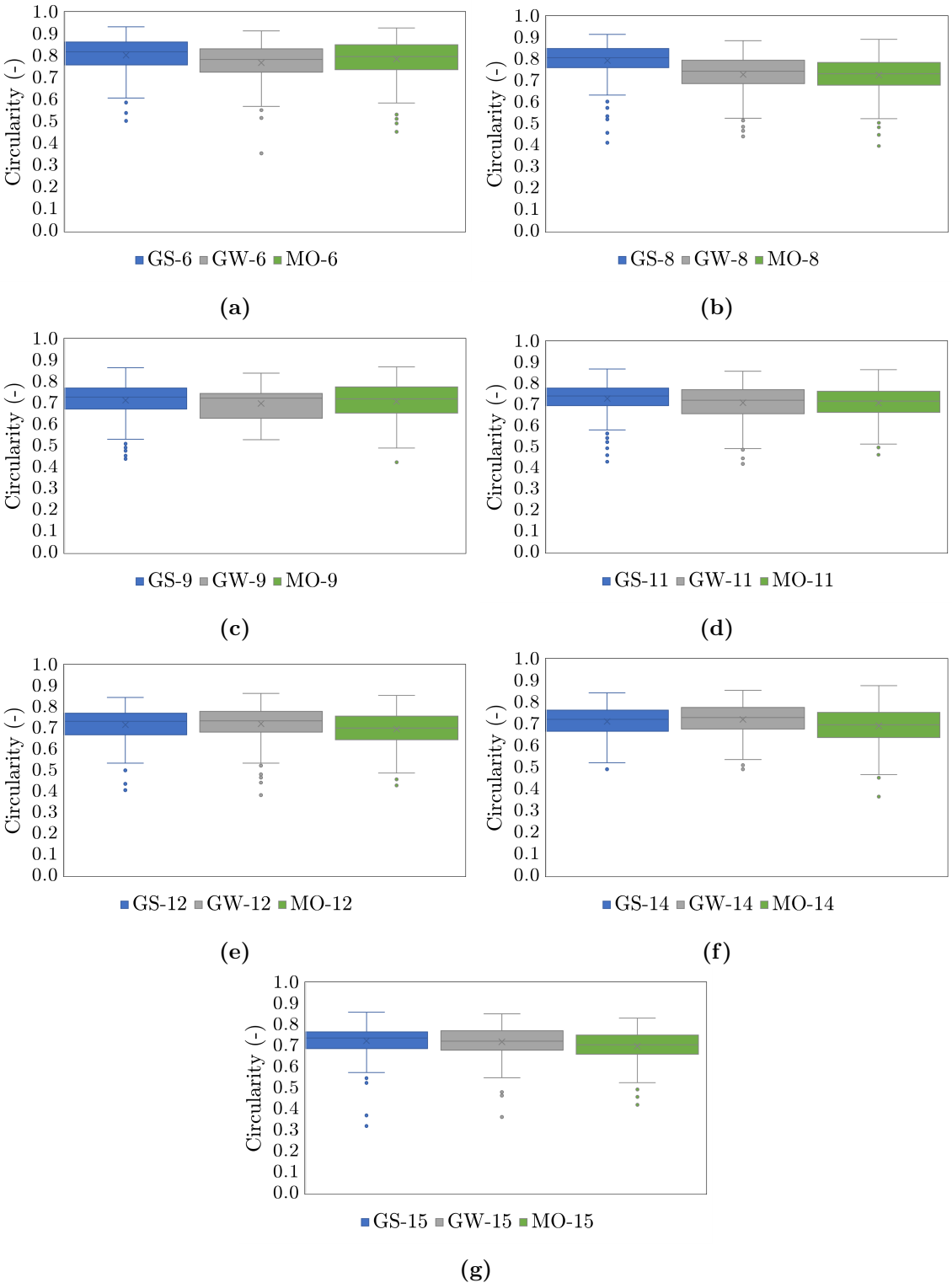

Figure B.6: Box and whisker plots depicting quantified values for circularity based on the 2-D shape analysis of 300 glass shard, greywacke and malachite ore particles belonging to different size fractions (Dots - outliers, Inside main box: x - mean value, middle horizontal line - median).

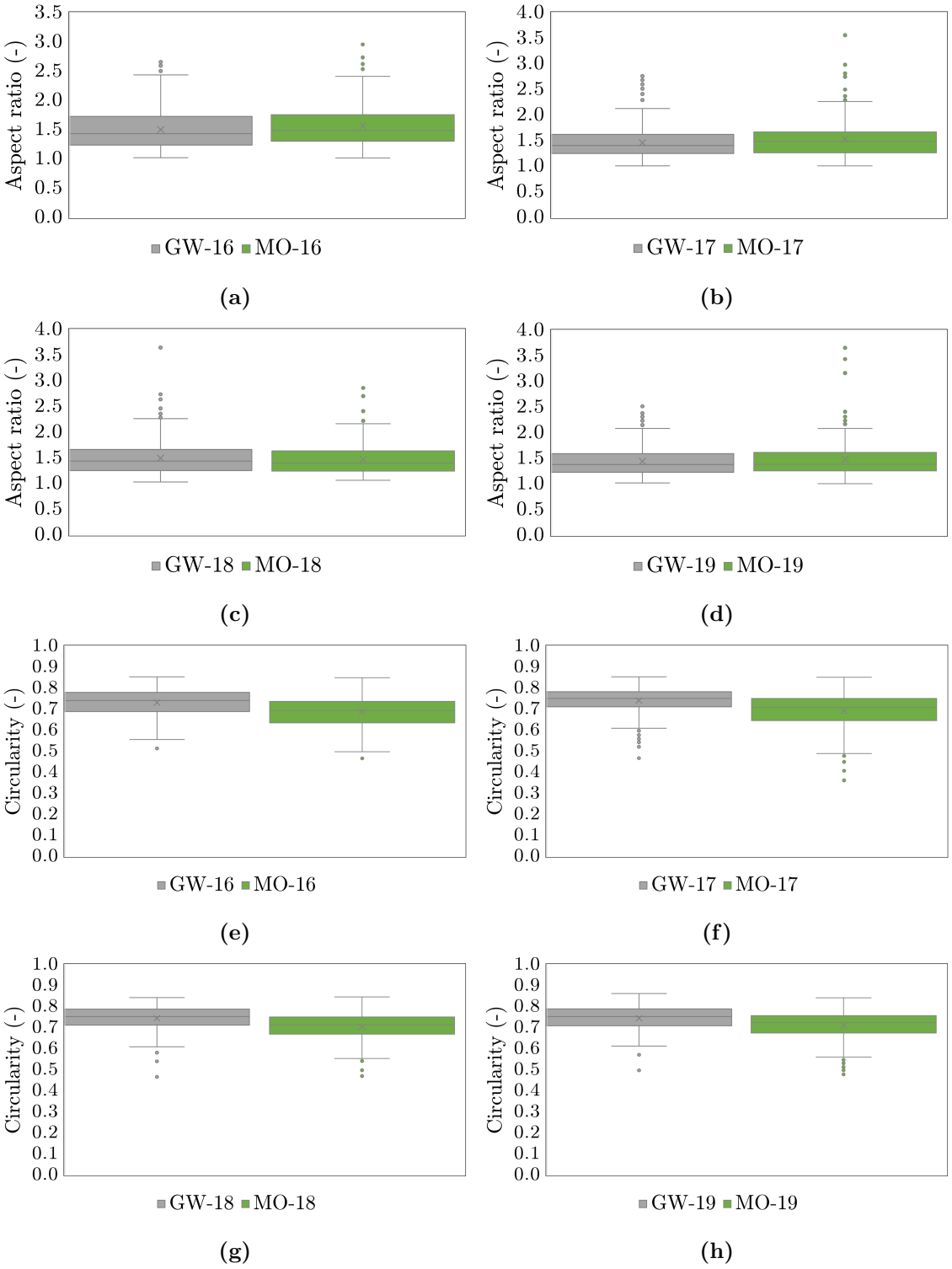

Figure B.7: Box and whisker plots depicting quantified values for aspect ratio (a - d) and circularity (e - h) based on the 2-D shape analysis of 300 greywacke and malachite ore particles belonging to different size fractions (Dots - outliers, Inside main box: x - mean value, middle horizontal line - median).

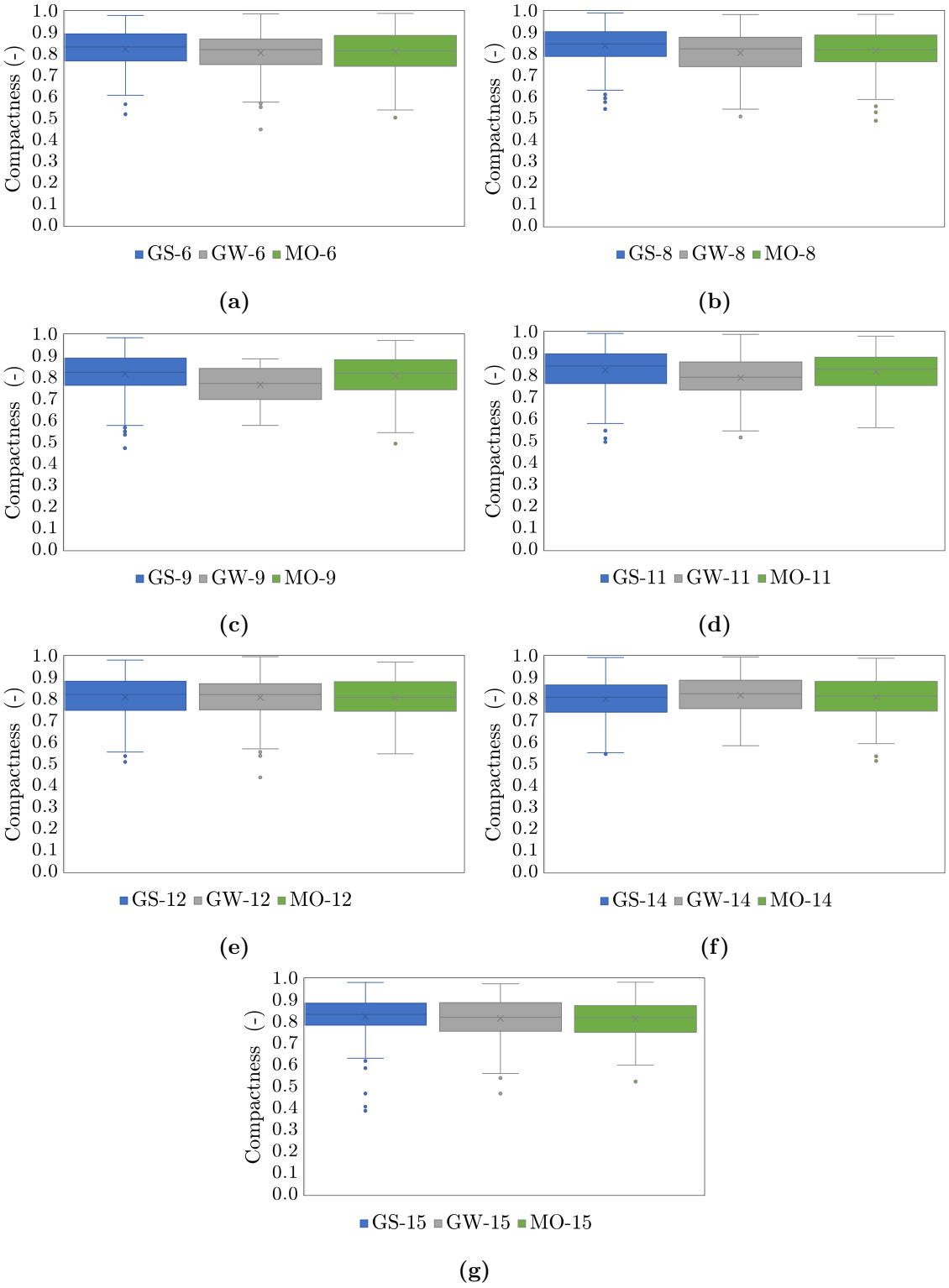

Figure B.8: Box and whisker plots depicting quantified values for compactness based on the 2-D shape analysis of 300 glass shard, greywacke and malachite ore particles belonging to different size fractions (Dots - outliers, Inside main box: x - mean value, middle horizontal line - median).

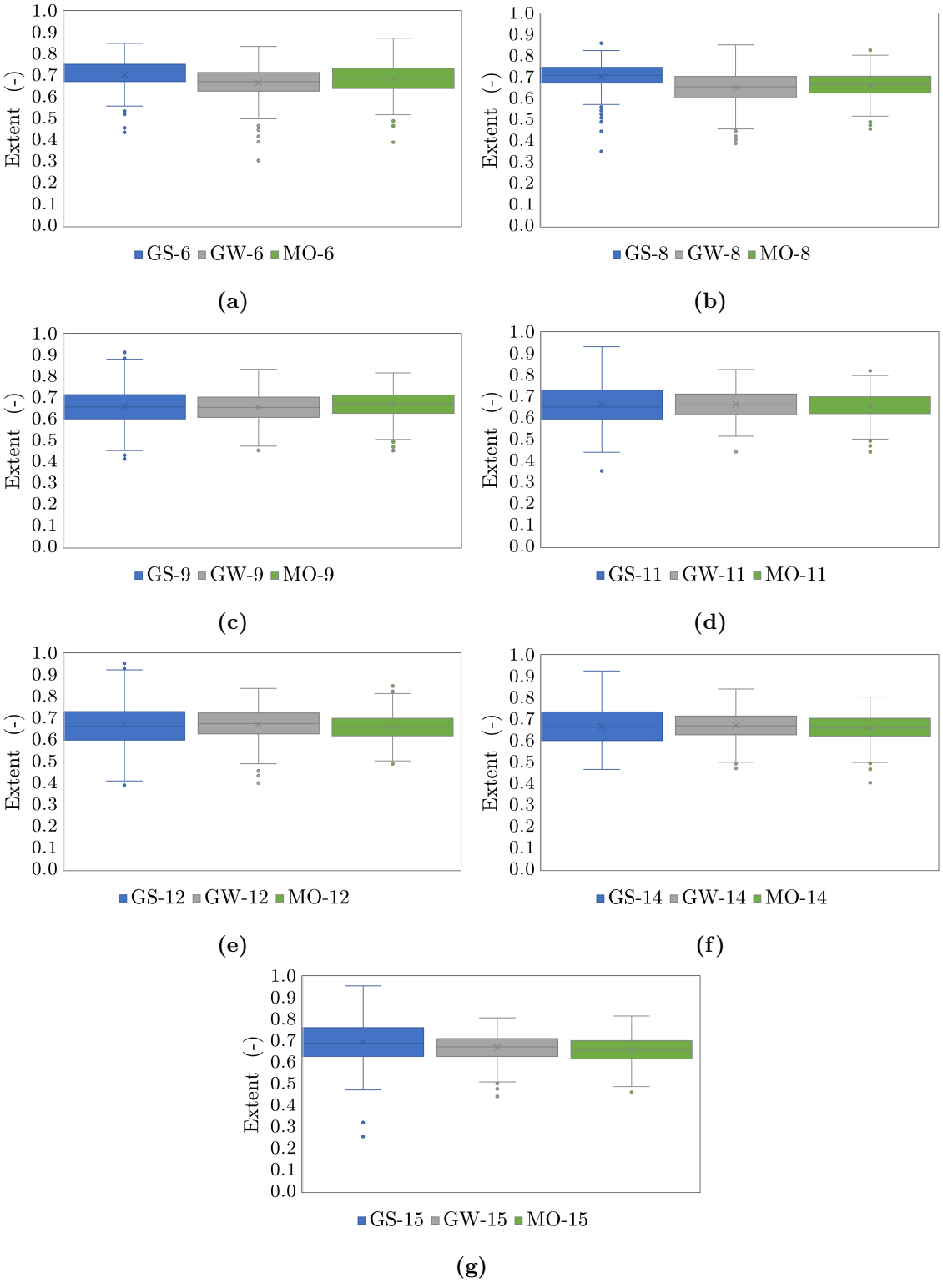

Figure B.9: Box and whisker plots depicting quantified values for extent based on the 2-D shape analysis of 300 glass shard, greywacke and malachite ore particles belonging to different size fractions (Dots - outliers, Inside main box: x - mean value, middle horizontal line - median).

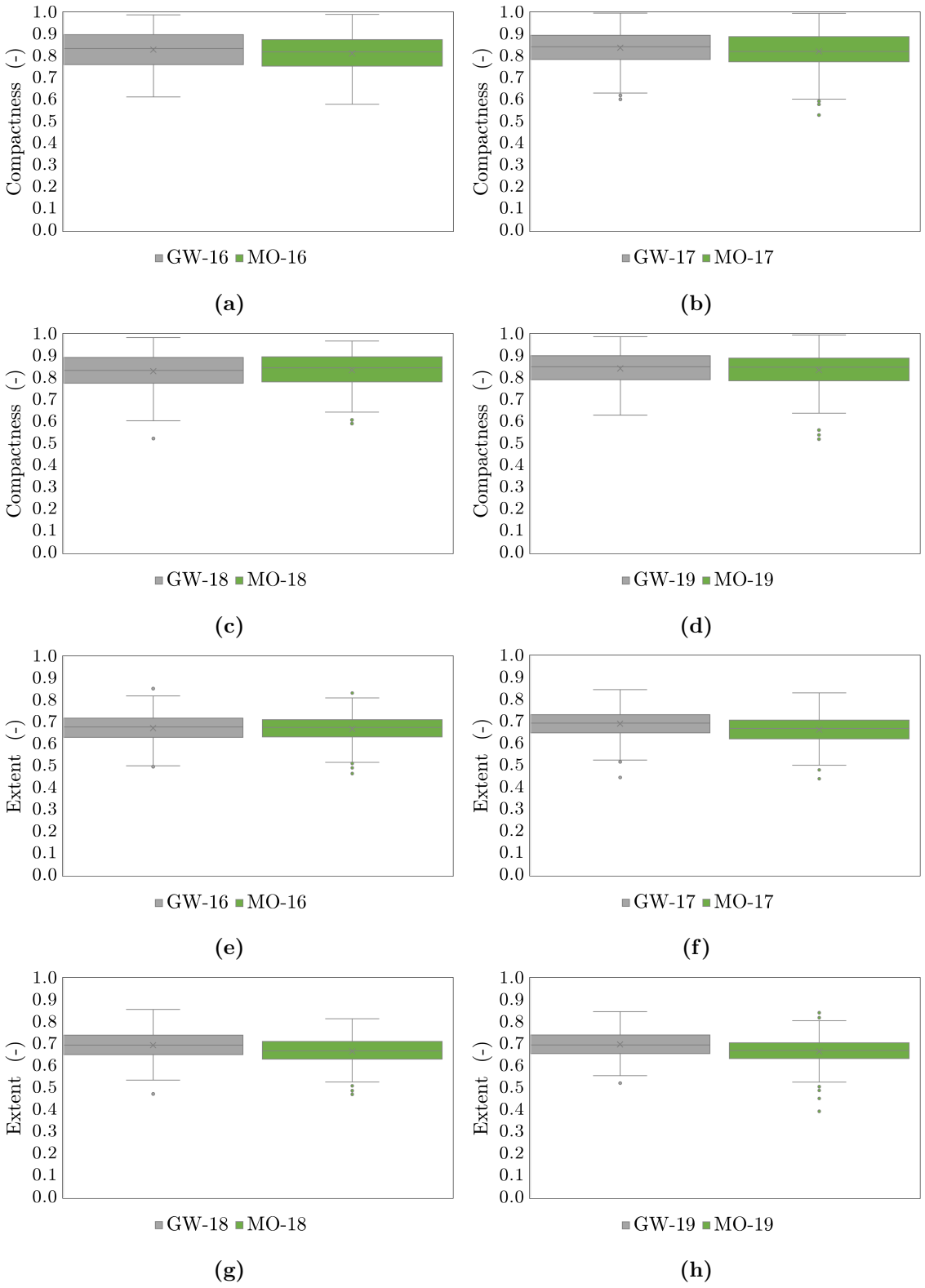

Figure B.10: Box and whisker plots depicting quantified values for compactness (a - d) and extent (e - h) based on the 2-D shape analysis of 300 greywacke and malachite ore particles belonging to different size fractions (Dots - outliers, Inside main box: x - mean value, middle horizontal line - median).

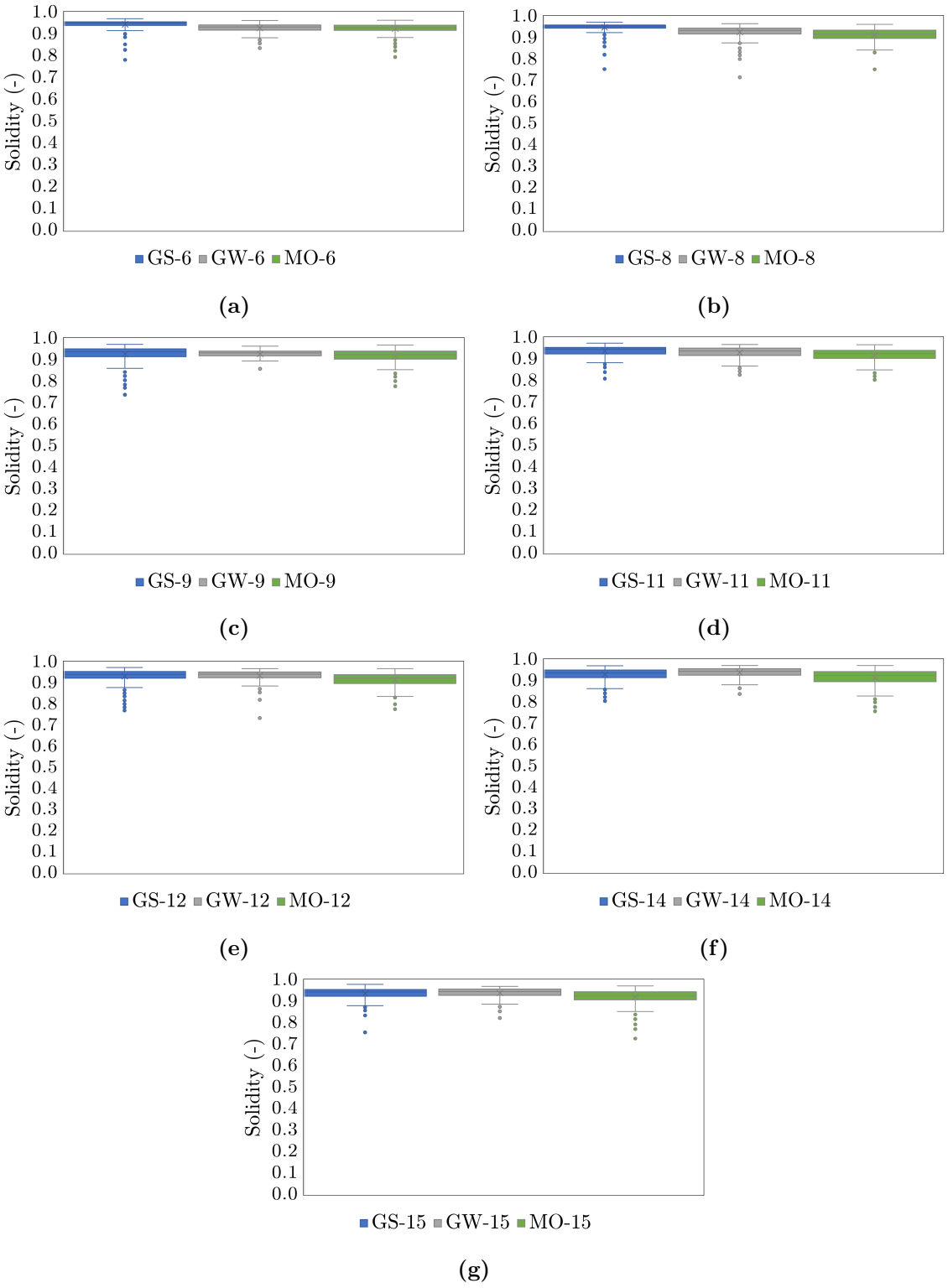

Figure B.11: Box and whisker plots depicting quantified values for solidity based on the 2-D shape analysis of 300 glass shard, greywacke and malachite ore particles belonging to different size fractions (Dots - outliers, Inside main box: x - mean value, middle horizontal line - median).

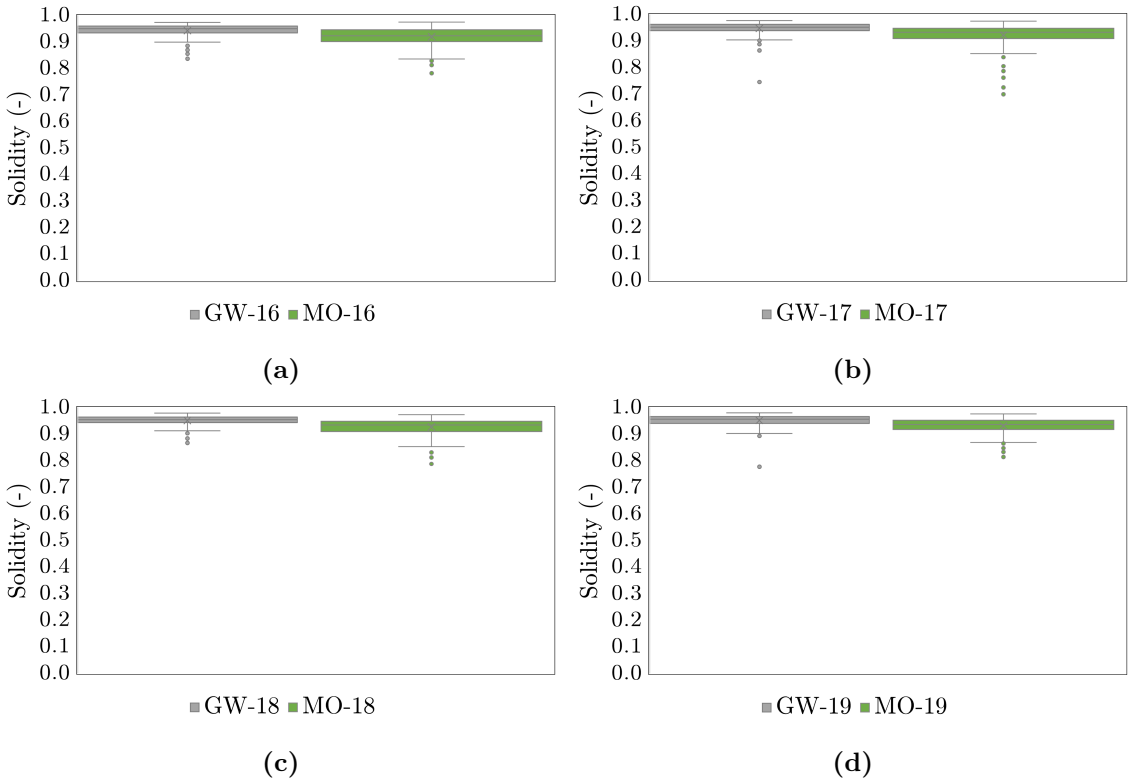

Figure B.12: Box and whisker plots depicting quantified values for solidity based on the 2-D shape analysis of 300 greywacke and malachite ore particles belonging to different size fractions (Dots - outliers, Inside main box: x - mean value, middle horizontal line - median).

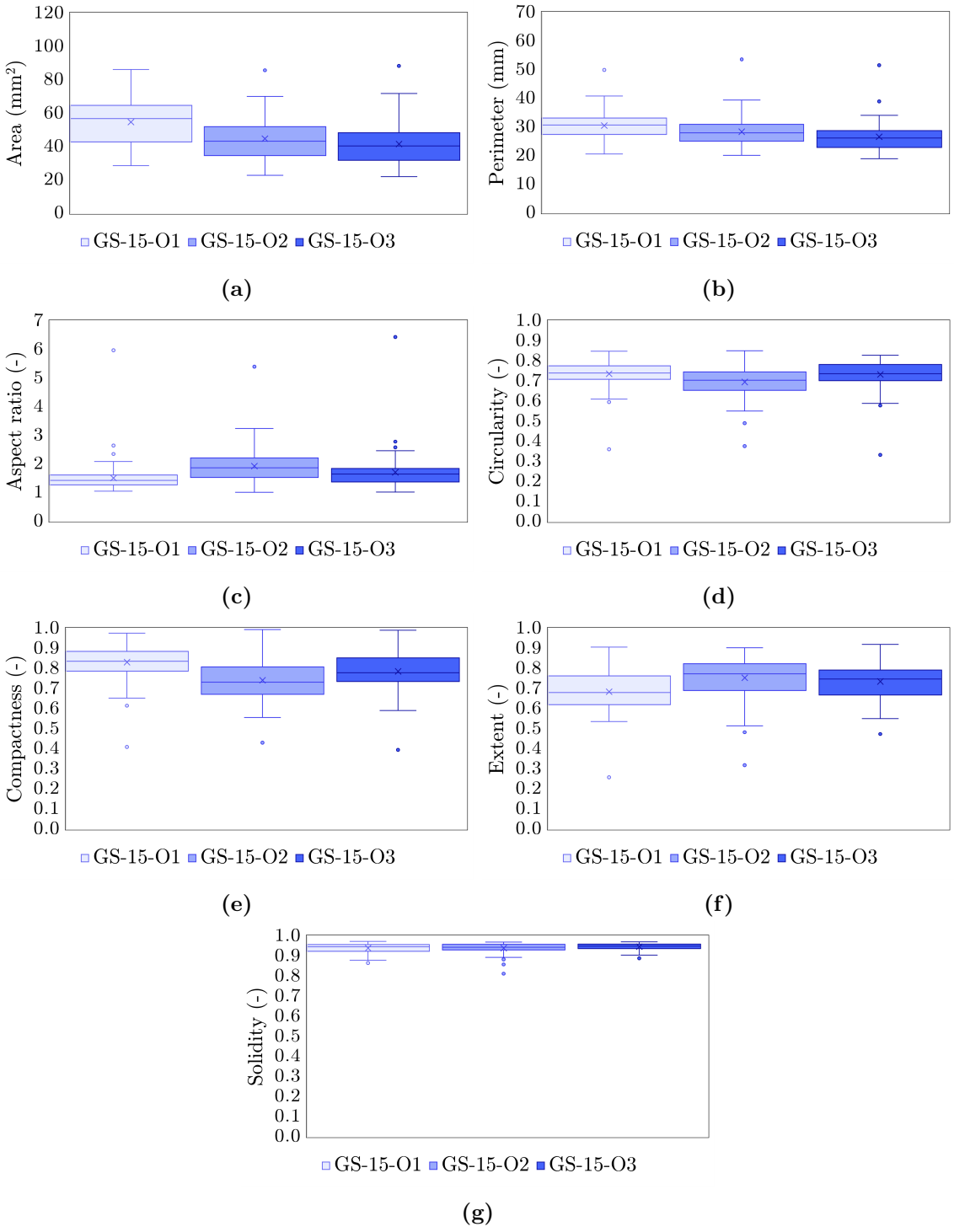

Figure B.13: Box and whisker plots depicting quantified values for various shape descriptors based on the 2-D shape analysis of 100 glass shard particles arranged in 3 different orientations: O1, O2 and O3.

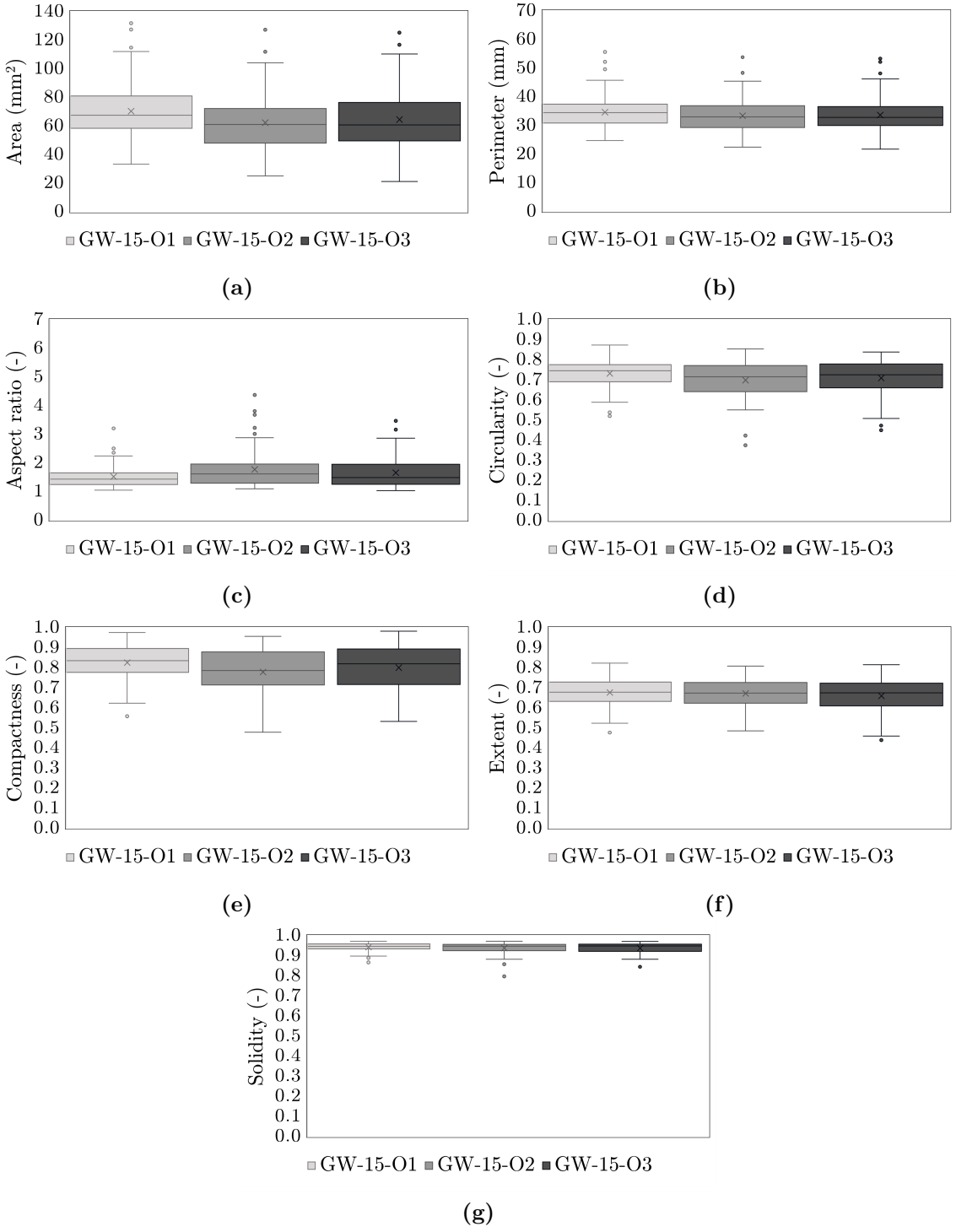

Figure B.14: Box and whisker plots depicting quantified values for various shape descriptors based on the 2-D shape analysis of 100 greywacke particles arranged in 3 different orientations: O1, O2 and O3.

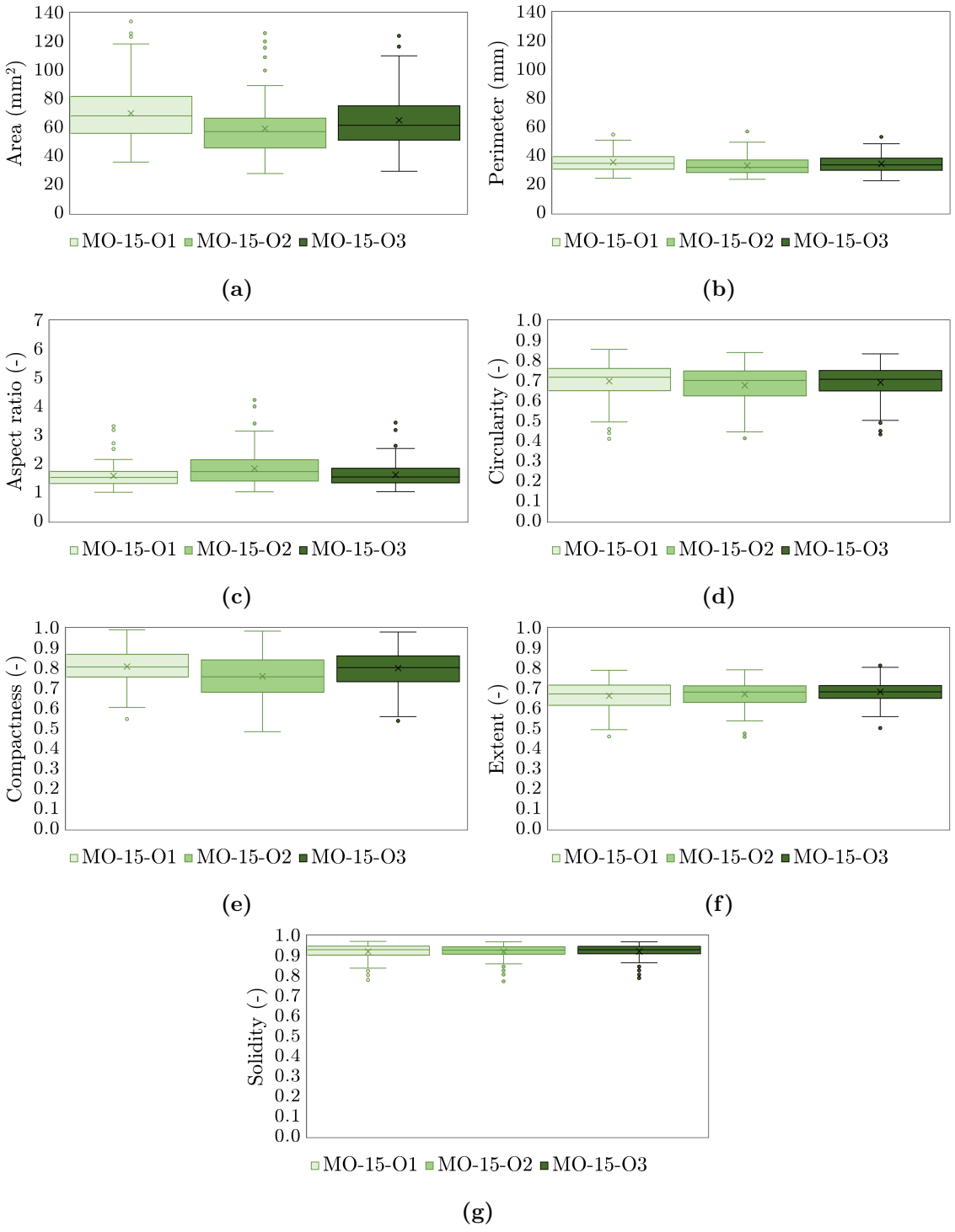

Figure B.15: Box and whisker plots depicting quantified values for various shape descriptors based on the 2-D shape analysis of 100 malachite ore particles arranged in 3 different orientations: O1, O2 and O3.

Appendix C

Discretization of the Semi-Phenomenological Models

C.1 Discretization of the AD Model

For the coding of the model equations, numerical discretization methods were employed. The symbol j is used for temporal discretization and the symbol i for spatial discretization ($1 \leq i \leq n$). The forward difference was used for the time derivative as shown in Equation (C.1).

$$\frac{\partial C}{\partial t} = \frac{C_i^{j+1} - C_i^j}{\Delta t} \tag{C.1}$$

The implicit central difference method, shown in Equation (C.2) and (C.3), was used for the spatial dimensions:

$$\frac{\partial^2 C}{\partial z^2} = \frac{C_{i+1}^{j+1} - 2C_i^{j+1} + C_{i-1}^{j+1}}{\Delta z^2} \tag{C.2}$$

$$\frac{\partial C}{\partial z} = \frac{C_{i+1}^{j+1} - C_{i-1}^{j+1}}{2\Delta z} \tag{C.3}$$

An implicit discretization scheme was chosen as it aids in numerical stability during the solving process (Nkonga, 2009). Combining the different discretized elements results in Equation (C.4).

$$\frac{C_i^{j+1} - C_i^j}{\Delta t} = \frac{D_{ds}}{\varepsilon \beta_T L^2} \left[\frac{C_{i+1}^{j+1} - 2C_i^{j+1} + C_{i-1}^{j+1}}{\Delta z^2} \right] - \frac{U}{\varepsilon \beta_T} \left[\frac{C_{i+1}^{j+1} - C_{i-1}^{j+1}}{2\Delta z} \right] \tag{C.4}$$

The following variables were defined for the simplification of the equations:

$$\begin{aligned} r &= \varepsilon \beta_T L^2 \Delta z^2 \\ p &= D_{ds} \Delta t \\ q &= U \Delta t L \Delta z \end{aligned} \tag{C.5}$$

Using the new variables and multiplying out Equation (C.4) produced Equation (C.6).

$$-2rC_i^j = (2p + q)C_{i-1}^{j+1} - (4p + 2r)C_i^{j+1} + (2p - q)C_{i+1}^{j+1} \tag{C.6}$$

A tri-diagonal matrix, with assigned variable name B, was formulated:

$$B = \begin{bmatrix} -(4p+2r) & (2p-q) & 0 & \dots & \dots & 0 \\ (2p+q) & -(4p+2r) & (2p-q) & 0 & \dots & 0 \\ 0 & \ddots & \ddots & \ddots & \ddots & \vdots \\ \vdots & \ddots & \ddots & (2p+q) & -(4p+2r) & (2p-q) \\ 0 & \dots & \dots & 0 & (2p+q) & -(4p+2r) \end{bmatrix}$$

Boundary conditions were given by the following column vectors:

$$\vec{b}_{j+1} = \begin{bmatrix} C_0 \\ 0 \\ \vdots \\ 0 \end{bmatrix} \qquad \vec{d}_{j+1} = \begin{bmatrix} 0 \\ 0 \\ \vdots \\ C_{n-1}^{j+1} \end{bmatrix}$$

The insulated boundary condition is accounted for by the term C_{n-1}^{j+1} which is based on the central difference discretization of the insulated boundary condition shown in Equation (C.7).

$$\left.\frac{\partial C}{\partial t}\right|_{z=L} = \frac{C_{n+1}^{j+1} - C_{n-1}^{j+1}}{2\Delta t} = 0 \qquad \therefore C_{n+1}^{j+1} = C_{n-1}^{j+1} \tag{C.7}$$

The concentrations were also written in vector notation:

$$\vec{C}_{j+1} = \begin{bmatrix} C_1^{j+1} \\ C_2^{j+1} \\ \vdots \\ C_n^{j+1} \end{bmatrix} \qquad \vec{C}_j = \begin{bmatrix} C_1^{j} \\ C_2^{j} \\ \vdots \\ C_n^{j} \end{bmatrix}$$

Where n is the last position in the spatial domain. This allows for the solving of the implicit equation, Equation (C.6), in order to obtain the concentration at the next time step. which can be written in vector notation as Equation (C.8).

$$\vec{C}_{j+1} = \vec{B}^{-1}\left[(-2r)\vec{C}_j - (2p+q)\vec{b}_{j+1} - (2p-q)\vec{d}_{j+1}\right] \tag{C.8}$$

C.2 Discretization of the PE Model

Numerical methods were used in the discretization of the PE model's equations. The forward difference numerical method was used for the time derivative as shown in Equation (C.1).

C.2.1 Dynamic Volume

In the dynamic volume, the implicit upwind (backward difference) method was used for the spatial dimension as shown in Equation C.9.

$$\frac{\partial C_d}{\partial z} = \frac{C_i^{j+1} - C_{i-1}^{j+1}}{\Delta z} \tag{C.9}$$

Substituting the discretized elements into Equation (6.21) resulted in:

$$\frac{C_i^{j+1} - C_i^j}{\Delta t} = -\frac{U}{L\varepsilon\beta_d}\left[\frac{C_i^{j+1} - C_{i-1}^{j+1}}{\Delta z}\right] - \frac{K_m a}{\varepsilon(\beta_d)}(C_i^{j+1} - C_{s,i}^j) \tag{C.10}$$

The following variables were defined for the simplification of Equation (C.10):

$$\begin{aligned} p &= \Delta t L \Delta z K_m a \\ q &= \varepsilon\beta_d L \Delta z \\ r &= U \Delta t U \end{aligned} \tag{C.11}$$

Substituting the simplified variables shown in Equation (C.11) into Equation (C.10) resulted in the following:

$$-qC_i^j = rC_{i-1}^{j+1} - (q + r + p)C_i^{j+1} + pC_{s,i}^j \tag{C.12}$$

This allowed for the formation of a bi-diagonal matrix assigned variable name B:

$$B = \begin{bmatrix} -(q+r+p) & 0 & 0 & \dots & \dots & 0 \\ r & -(q+r+p) & 0 & 0 & \dots & 0 \\ 0 & \ddots & \ddots & \ddots & \ddots & \vdots \\ \vdots & \ddots & \ddots & \ddots & \ddots & 0 \\ 0 & \dots & \dots & 0 & r & -(q+r+p) \end{bmatrix}$$

The boundary conditions were represented by column vectors identical to those used in the

AD model's discretization (refer to Appendix C.1). It should be noted that the insulated boundary condition still applies, however this term is not shown as it was be multiplied by 0 in the final equation.

The concentrations were also written in vector notation:

$$\vec{C}_{j+1} = \begin{bmatrix} C_1^{j+1} \\ C_2^{j+1} \\ \vdots \\ C_n^{j+1} \end{bmatrix} \qquad \vec{C}_j = \begin{bmatrix} C_1^{j} \\ C_2^{j} \\ \vdots \\ C_n^{j} \end{bmatrix} \qquad \vec{C}_{s,j} = \begin{bmatrix} C_{s,1}^{j} \\ C_{s,2}^{j} \\ \vdots \\ C_{s,n}^{j} \end{bmatrix}$$

Where n is the last position in the spatial domain. Writing Equation (C.12) in vector notation by substituting the relevant vectors and matrices produces Equation (C.13).

$$\vec{C}_{j+1} = \vec{B}^{-1}\left[(-q)\vec{C}_j - r\vec{b}_{j+1} - p\vec{C}_{s,j}\right] \tag{C.13}$$

C.2.2 Stagnant zone

The stagnant volume was discretized as follows:

$$\frac{C_{s,i}^{j+1} - C_{s,i}^{j}}{\Delta t} = \frac{K_m a}{\varepsilon(\beta_T - \beta_d)}(C_i^{j+1} - C_{s,i}^{j}) \tag{C.14}$$

$$w = \frac{K_m a \Delta t}{\varepsilon(\beta_T - \beta_d)} \tag{C.15}$$

Simplification of the stagnant zone by substituting Equation (C.15) into Equation (C.14) and writing in vector notation results in Equation (C.16). The initial condition was accounted for during the coding of the model.

$$\vec{C}_{s,j+1} = w\vec{C}_j + (1-w)\vec{C}_{s,j} \tag{C.16}$$

C.3 Discretization of the PE-D Model

Numerical methods were used in the discretization of the model equations. The forward difference scheme was used for the time derivative as shown in Equation (C.1). The im-

plicit upwind (backward difference) method was used for the spatial dimension involving the normalised bed length (z) as shown in Equation (C.9).

C.3.1 Dynamic Volume

In terms of the concentration gradient governing the mass transfer from the dynamic to the stagnant zone, the backward difference method was also utilized:

$$\left.\frac{\partial C_s}{\partial x}\right|_{x=0} = \frac{C^j_{s,0} - C^j_{s,1}}{\Delta x} \tag{C.17}$$

Substituting the discretized elements into Equation (6.26) resulted in:

$$\frac{C^{j+1}_i - C^j_i}{\Delta t} = -\frac{U}{L\varepsilon\beta_d}\left[\frac{C^{j+1}_i - C^{j+1}_{i-1}}{\Delta z}\right] - \frac{D}{\varepsilon\beta_d X^2}\frac{C^j_{s,0} - C^j_{s,1}}{\Delta x} \tag{C.18}$$

The following variables were defined for the simplification of Equation (C.18):

$$\begin{aligned} p &= \varepsilon\beta_d L\Delta z X^2 \Delta x \\ q &= U\Delta t \Delta x X^2 \\ w &= D\Delta t L \Delta z \end{aligned} \tag{C.19}$$

Substituting the simplified variables shown in Equation (C.19) into Equation (C.18) resulted in the following:

$$-pC^j_i = -(q+p)C^{j+1}_i + qC^{j+1}_{i-1} - w(C^j_{s,0} - C^j_{s,1}) \tag{C.20}$$

This allowed for the formation of a bi-diagonal matrix assigned variable name B:

$$B = \begin{bmatrix} -(q+p) & 0 & 0 & \dots & \dots & 0 \\ q & -(q+p) & 0 & 0 & \dots & 0 \\ 0 & \ddots & \ddots & \ddots & \ddots & \vdots \\ \vdots & \ddots & \ddots & \ddots & \ddots & 0 \\ 0 & \dots & \dots & 0 & q & -(q+p) \end{bmatrix}$$

The boundary conditions were represented by column vectors identical to those used in the AD model's discretization (refer to Appendix C.1). It should be noted that the insulated boundary condition still applies, however this term is not shown as it was be multiplied by

0 in the final equation.

The concentrations were also written in vector notation with structures identical to those used in the PE model's discretization (refer to sub-section C.2). Writing Equation (C.20) in vector notation by substituting the relevant vectors and matrices produces Equation (C.21), which is used to obtain the dynamic concentration at the next time step.

$$\vec{C}_{j+1} = \vec{B}^{-1}\left[(-P)\vec{C}_j - q\vec{b}_{j+1} + w(C^j_{s,0} - C^j_{s,1})\right] \tag{C.21}$$

C.3.2 Stagnant Volume

In the discretization of the stagnant volume, the forward finite difference scheme was used for the temporal rate of change as shown in Equation (C.1). The implicit central difference was used for the discretization of the spatial pore dimension, as seen in Equation (C.22).

$$\frac{\partial^2 C_s}{\partial x^2} = \frac{C^{j+1}_{s,i-1} - 2C^{j+1}_{s,i} + C^{j+1}_{s,i+1}}{\Delta x^2} \tag{C.22}$$

Substituting the discretized elements into Equation (6.28) resulted in:

$$\frac{C^{j+1}_{s,i} - C^j_{s,i}}{\Delta t} = \frac{D}{\varepsilon(\beta_T - \beta_d)X^2}\left[\frac{C^{j+1}_{s,i-1} - 2C^{j+1}_{s,i} + C^{j+1}_{s,i+1}}{\Delta x^2}\right] \tag{C.23}$$

New simplification variables were defined:

$$\begin{aligned} r &= \varepsilon(\beta_T - \beta_d)X^2\Delta x^2 \\ s &= D\Delta t \end{aligned} \tag{C.24}$$

Rearranging and substituting the new variables into Equation (C.23) resulted in:

$$-rC^j_{s,i} = sC^{j+1}_{s,i-1} - (r+2s)C^{j+1}_{s,i} + sC^{j+1}_{s,i+1} \tag{C.25}$$

A tridiagonal matrix V was defined:

$$V = \begin{bmatrix} -(r+2s) & s & 0 & \dots & \dots & 0 \\ s & -(r+2s) & s & 0 & \dots & 0 \\ 0 & \ddots & \ddots & \ddots & \ddots & \vdots \\ \vdots & \ddots & \ddots & \ddots & \ddots & s \\ 0 & \dots & \dots & 0 & s & -(r+2s) \end{bmatrix}$$

The boundary conditions for a single pore were represented by column vectors:

$$\vec{b}_{s,j+1} = \begin{bmatrix} C_{s,1}^{j+1} \\ 0 \\ \vdots \\ 0 \end{bmatrix} \qquad \vec{d}_{s,j+1} = \begin{bmatrix} 0 \\ 0 \\ \vdots \\ C_{s,n-1}^{j+1} \end{bmatrix}$$

The reason for the term $C_{s,n-1}^{j}$ is due to the insulated boundary condition shown in Equation (6.29) and discretized in the same way as shown in Equation (C.7). The concentrations are also written in vector notation for a single pore:

$$\vec{C}_{s,j+1} = \begin{bmatrix} C_{s,1}^{j+1} \\ C_{s,2}^{j+1} \\ \vdots \\ C_{s,n}^{j+1} \end{bmatrix} \qquad \vec{C}_{s,j} = \begin{bmatrix} C_{s,1}^{j} \\ C_{s,2}^{j} \\ \vdots \\ C_{s,n}^{j} \end{bmatrix}$$

It should be noted that each pore will have different values for their boundary conditions based on the propagation of the solute molecules in the dynamic zone. Rearranging, substituting the V matrix and writing Equation (C.25) in vector notation resulted in Equation (C.26):

$$\vec{C}_{s,j+1} = \vec{V}^{-1}\left[-r\vec{C}_{s,j} - s\vec{b}_{s,j+1} - s\vec{d}_{s,j+1}\right] \tag{C.26}$$

C.4 Discretization of the PDE Model

Numerical methods were used in the discretization of the model equations. The forward difference numerical scheme was used for the time derivative as shown in Equation (C.1).

The second order partial differential equation was discretized using Equation (C.2). The implicit central difference scheme was used for the spatial first order partial differential equation, as seen in Equation (C.27).

C.4.1 Dynamic Volume

$$\frac{\partial C_d}{\partial z} = \frac{C_{i+1}^{j+1} - C_{i-1}^{j+1}}{2\Delta z} \tag{C.27}$$

Substituting the discretized elements into Equation (6.31) resulted in Equation (C.28)

$$\frac{C_i^{j+1} - C_i^j}{\Delta t} = \frac{D_{ds}}{L^2 \varepsilon \beta_d}\left[\frac{C_{i+1}^{j+1} - 2C_i^{j+1} + C_{i-1}^{j+1}}{\Delta z^2}\right] - \frac{U}{L\varepsilon\beta_d}\left[\frac{C_{i+1}^{j+1} - C_{i-1}^{j+1}}{\Delta z}\right] - \frac{K_m a}{\varepsilon(\beta_d)}(C_i^{j+1} - C_{s,i}^j) \tag{C.28}$$

The following variables were defined for the simplification of Equation (C.28):

$$\begin{aligned} p &= \Delta z^2 L^2 \varepsilon \\ q &= D\Delta t \\ r &= U\Delta t \Delta z L \\ s &= \Delta t \Delta z^2 L^2 K_m a \end{aligned} \tag{C.29}$$

Substituting the simplified variables shown in Equation (C.29) into Equation (C.28) resulted in the following:

$$(-2p)C_i^j = (2q + r)C_{i-1}^{j+1} - (2p + 4q + 2s)C_i^{j+1} + (2q - r)C_{i+1}^{j+1} + 2sC_{s,i}^j \tag{C.30}$$

This allowed for the formation of a tridiagonal matrix assigned variable name B:

$$B = \begin{bmatrix} -(2p+4q+2s) & (2q-r) & 0 & \dots & \dots & 0 \\ (2q+r) & -(2p+4q+2s) & (2q-r) & 0 & \dots & 0 \\ 0 & \ddots & \ddots & \ddots & \ddots & \vdots \\ \vdots & \ddots & \ddots & \ddots & \ddots & \ddots \\ 0 & \dots & \dots & \dots & (2q+r) & -(2p+4q+2s) \end{bmatrix}$$

The boundary conditions were represented by column vectors identical to those used in the AD model's discretization (refer to Appendix C.1).

The concentrations were also represented as vectors identical to those used in the PE model's discretization (refer to sub-section C.2). Writing Equation (C.30) in vector notation by substituting the relevant vectors and matrices produces Equation (C.31).

$$\vec{C}_{j+1} = \vec{B}^{-1}\left[(-2p)\vec{C}_j - (2q+r)\vec{b}_{j+1} - (2q-r)\vec{d_{j+1}} - 2s\vec{C}_{s,j}\right] \tag{C.31}$$

C.4.2 Stagnant Volume

The stagnant volume was discretized in the same way as the PE model:

$$\frac{C_{s,i}^{j+1} - C_{s,i}^{j}}{\Delta t} = \frac{K_m a}{\varepsilon(\beta_T - \beta_d)}(C_i^{j+1} - C_{s,i}^{j}) \tag{C.32}$$

$$w = \frac{K_m a \Delta t}{\varepsilon(\beta_T - \beta_d)} \tag{C.33}$$

Simplification of the stagnant zone by substituting Equation (C.33) into Equation (C.32) and writing in vector notation resulted in Equation (C.34). The initial condition was accounted for during the coding of the model.

$$\vec{C}_{s,j+1} = w\vec{C}_{j+1} + (1-w)\vec{C}_{s,j} \tag{C.34}$$

C.5 Discretization of the PDE-D Model

C.5.1 Dynamic Volume

Numerical methods were used in the discretization of the model equations. The forward difference numerical scheme was chosen for the time derivative as shown in Equation (C.1). The implicit upwind (backward difference) method was used for the spatial dimension involving the normalised bed length, z, as shown in Equation (C.9). The second order partial differential equation involving z^2 was discretized using Equation (C.2).

Substituting the discretized elements into Equation (6.34) resulted in Equation (C.35).

$$\frac{C_i^{j+1} - C_i^j}{\Delta t} = \frac{D_{ds}}{L^2 \varepsilon \beta_d} \left[\frac{C_{i+1}^{j+1} - 2C_i^{j+1} + C_{i-1}^{j+1}}{\Delta z^2} \right] - \frac{U}{L \varepsilon \beta_d} \left[\frac{C_i^{j+1} - C_{i-1}^{j+1}}{\Delta z} \right] - \frac{D}{\varepsilon \beta_d X^2} \frac{C_{s,0}^j - C_{s,1}^j}{\Delta x} \tag{C.35}$$

The following variables were defined for the simplification of Equation (C.35):

$$\begin{aligned} p &= L^2 \varepsilon \beta_d X^2 \Delta x \Delta z^2 \\ q &= D_{ds} X^2 \Delta x \Delta t \\ r &= UL \Delta X^2 \Delta x \Delta t \\ s &= DL^2 \Delta z^2 \Delta t \end{aligned} \tag{C.36}$$

Substituting the simplified variables shown in Equation (C.36) into Equation (C.35) resulted in the following:

$$-pC_i^j = qC_{i+1}^{j+1} - (p + 2q + r)C_i^{j+1} + (q + r)C_{i-1}^{j+1} - s(C_{s,0}^j - C_{s,1}^j) \tag{C.37}$$

This allowed for the formation of a tridiagonal matrix assigned variable name B:

$$B = \begin{bmatrix} -(p+2q+r) & q & 0 & \dots & \dots & 0 \\ (q+r) & -(p+2q+r) & q & 0 & \dots & 0 \\ 0 & \ddots & \ddots & \ddots & \ddots & \vdots \\ \vdots & \ddots & \ddots & \ddots & \ddots & \vdots \\ 0 & \dots & \dots & 0 & (q+r) & -(p+2q+r) \end{bmatrix}$$

The boundary conditions were represented by column vectors identical to those used in the AD model's discretization (refer to Appendix C.1). The concentrations were also represented as vectors identical to those used in the PE model's discretization (refer to sub-section C.2). Writing Equation (C.37) in vector notation by substituting the relevant vectors and matrices produced Equation (C.38).

$$\vec{C}_{j+1} = \vec{B}^{-1} \left[-p\vec{C}_j - (q + r)\vec{b}_{j+1} - q\vec{d_{j+1}} + s(C_{s,0}^j - C_{s,1}^j) \right] \tag{C.38}$$

C.5.2 Stagnant Volume

In the discretization of the stagnant volume, the forward finite difference scheme was used for the temporal rate of change as shown in Equation (C.1). The implicit central difference was used for the discretization of the spatial pore dimension, as shown in Equation (C.22). Substituting the discretized elements into Equation (6.28) resulted in:

$$\frac{C_{s,i}^{j+1} - C_{s,i}^{j}}{\Delta t} = \frac{D_{df}}{\varepsilon(\beta_T - \beta_d)X^2}\left[\frac{C_{s,i-1}^{j+1} - 2C_{s,i}^{j+1} + C_{s,i+1}^{j+1}}{\Delta x^2}\right] \tag{C.39}$$

New simplification variables were defined:

$$\begin{aligned} v &= \varepsilon(\beta_T - \beta_d)X^2\Delta x^2 \\ w &= D\Delta t \end{aligned} \tag{C.40}$$

Rearranging and substituting the new variables into Equation (C.39) resulted in:

$$-vC_{s,i}^{j} = wC_{s,i-1}^{j+1} - (2w + v)C_{s,i}^{j+1} + wC_{s,i+1}^{j+1} \tag{C.41}$$

A tridiagonal matrix G was defined:

$$G = \begin{bmatrix} -(2w+v) & w & 0 & \dots & \dots & 0 \\ w & -(2w+v) & w & 0 & \dots & 0 \\ 0 & \ddots & \ddots & \ddots & \ddots & \vdots \\ \vdots & \ddots & \ddots & \ddots & \ddots & \vdots \\ 0 & \dots & \dots & 0 & w & -(2w+v) \end{bmatrix}$$

The boundary conditions and concentrations were represented by column vectors identical to those used in discretisation of the stagnant volume of the PE-D model (refer to sub-section C.2). Just as with the PE-D model, it should be noted that each pore will have different values for their boundary conditions based on the propagation of the solute molecules in the dynamic zone. Rearranging, substituting the G matrix and writing Equation (C.41) in vector notation resulted in:

$$\vec{C}_{s,j+1} = \vec{G}^{-1}\left[-v\vec{C}_{s,j} - w\vec{b}_{s,j+1} - w\vec{d}_{s,j+1}\right] \tag{C.42}$$

Appendix D

Model Stability Analysis

D.1 Stability Analysis: AD Model

A Von Neumann stability analysis was performed on the AD model. The Von Neumann method falls under the amplification category and makes use of the Fourier method for stability analysis. It looks at the propagation of system perturbations from one step to the next. A limitation of this analysis is its restriction to linear systems but it can still be applied to non-linear systems through linearization (Carlos, 2006; Trefethen, 1996).

The Von Neumann stability analysis breaks up the system equations into temporal and spatial dependence to enable the look at the growth of linear modes. It assumes an oscillatory dependence on space which allows for the synthesis of any initial condition. An example of this is shown in Equation (D.1), where A can be considered the amplification factor that is a function of the wave frequency k, n represents the imaginary number $\sqrt{-1}$, while j and i refer to the discretized nodes in the temporal and spatial domains respectively (Carlos, 2006; Trefethen, 1996).

$$u_i^j = A(k)^j e^{ink\Delta z} \tag{D.1}$$

For the AD equation, replacing the discretized elements of the expanded form of Equation (C.6) with the oscillatory dependence shown in Equation (D.1) results in Equation (D.2).

$$\begin{aligned} -2rA^j e^{ink\Delta z} &= 2pA^{j+1}e^{(i-1)nk\Delta z} - 4pA^{j+1}e^{ink\Delta z} + 2pA^{j+1}e^{(i+1)nk\Delta z} \\ -qA^{j+1}e^{(i+1)nk\Delta z} &+ qA^{j+1}e^{(i-1)nk\Delta z} - 2rA^{j+1}e^{ink\Delta z} \end{aligned} \tag{D.2}$$

Dividing by $A^j e^{ink\Delta z}$ and rearranging results in:

$$2r = A\left[4p + 2r - 2p\left(e^{-nk\Delta z} + e^{nk\Delta z}\right) + q\left(e^{nk\Delta z} - e^{-nk\Delta z}\right)\right] \tag{D.3}$$

Equation (D.3) can be further simplified to:

$$A = \frac{1}{2\frac{p}{r} + 1 + n\frac{q}{r}sin(k\Delta z) - 2\frac{p}{r}cos(k\Delta z)} \tag{D.4}$$

We can now multiply Equation (D.4), A, by its complex conjugate, A^*, in order to obtain, A^2, which possesses all real parts.

$$AA^* = A^2 = \left[\frac{1}{2\frac{p}{r} + 1 + n\frac{q}{r}sin(k\Delta z) - 2\frac{p}{r}cos(k\Delta z)}\right] \left[\frac{1}{2\frac{p}{r} + 1 - n\frac{q}{r}sin(k\Delta z) - 2\frac{p}{r}cos(k\Delta z)}\right] \tag{D.5}$$

Multiplying out Equation (D.5) and simplifying the results, produces:

$$A^2 = \frac{1}{1 + 4\frac{p^2}{r^2} + 4\frac{p}{r} + 4\frac{p^2}{r^2}cos^2(k\Delta z) - 8\frac{p^2}{r^2}cos(k\Delta z) - 4\frac{p}{r}cos(k\Delta z) + \frac{q^2}{r^2}sin(k\Delta z)} \tag{D.6}$$

When considering all the cases shown in Equation (D.7), the absolute value of the square of the amplification factor: $||AA^*|| = ||A||^2 \leq 1$. This means that the discretization scheme is unconditionally stable for a well posed problem.

$$\begin{aligned} &cos(k\Delta z) = 1 \quad \text{and } sin(k\Delta z) = 0 \\ &cos(k\Delta z) = -1 \quad \text{and } sin(k\Delta z) = 0 \\ &cos(k\Delta z) = 0 \quad \text{and } sin(k\Delta z) = 1 \\ &cos(k\Delta z) = 0 \quad \text{and } sin(k\Delta z) = -1 \end{aligned} \tag{D.7}$$

D.2 Stability Analysis: PE Model

The Von Neumann stability analysis was performed on the dynamic phase of the PE model by replacing the discretized elements in Equation (C.10) with the expanded form of the oscillatory dependence shown in Equation (D.1) which resulted in Equation (D.8).

$$-qA^j e^{ink\Delta z} = rA^{j+1}e^{(i-1)nk\Delta z} - (q+r)A^{j+1}e^{ink\Delta z} + S_{sink} \tag{D.8}$$

Since the Von Neumann stability analysis looks at the propagation of error, the source/sink term can be ignored. The justification for ignoring the source/sink term can be found below in sub-section D.2.1. Equation (D.8) can be rewritten as:

$$-qA^j e^{ink\Delta z} = rA^{j+1}e^{(i-1)nk\Delta z} - (q+r)A^{j+1}e^{ink\Delta z} \tag{D.9}$$

Cancelling similar terms on both sides of the equation and making A the subject of the formula results in:

$$A = \frac{-q}{re^{-nk\Delta z} - (q + r)} \tag{D.10}$$

Which can be rewritten as:

$$A = \frac{1}{-\frac{r}{q}(cos(k\Delta z) - nsin(k\Delta z)) + 1 + \frac{r}{q}} \tag{D.11}$$

Multiplying Equation (D.11) with its complex conjugate results in the following:

$$AA^* = A^2 = \left[\frac{1}{-\frac{r}{q}(cos(k\Delta z) - nsin(k\Delta z)) + 1 + \frac{r}{q}}\right] \left[\frac{1}{-\frac{r}{q}(cos(k\Delta z) + nsin(k\Delta z)) + 1 + \frac{r}{q}}\right] \tag{D.12}$$

Multiplying out Equation (D.12) and simplifying the results, produces:

$$A^2 = \frac{1}{1 + 2\frac{r}{q} + \frac{r^2}{q^2} + \frac{r^2}{q^2}(cos^2(k\Delta z) + sin^2(k\Delta z) - 2cos(k\Delta z)) - 2\frac{r}{q}cos(k\Delta z)} \tag{D.13}$$

When considering all the cases shown in Equation (D.7), the absolute value of the square of the amplification factor for Equation (D.13) is $||AA^*|| = ||A||^2 \leq 1$. This means that the discretization scheme is unconditionally stable for a well posed problem.

D.2.1 Justification for Elimination of Sink/Source Term

The Von Neumann analysis is based on the decomposition of errors into the Fourier series. The round-off error (Ξ_i^j) can be defined as:

$$\Xi_i^j = N_i^j - u_i^j \tag{D.14}$$

Where u_i^j is the true solution of the discretized equation and N_i^j is the numerical solution obtained from finite precision arithmetic leading to the round off error. Since u_i^j must satisfy

the discretized equation exactly, then Ξ_i^j must also satisfy the discretized equation. This is true if the partial differential equation is homogeneous and can be written in the form:

$$\mathcal{L}(u, u_t, u_x, u_x x, ...) = 0 \tag{D.15}$$

However, the PE and subsequent models all contain source/sink terms and therefore are heterogeneous in that:

$$\mathcal{L}(u, u_t, u_x, u_x x, ...) = S_{sink} \tag{D.16}$$

An important aspect of the $\mathcal{L}$ operator is that it is linear. Based on this attribute along with the rule that the true solution must satisfy the discretized equation represented by the linear operator $\mathcal{L}^*$, it can be argued that for a homogeneous system:

$$\mathcal{L}^*(\Xi) = \mathcal{L}^*(N) - \mathcal{L}^*(u) = 0 \tag{D.17}$$

While for a heterogeneous system:

$$\mathcal{L}^*(\Xi) = \mathcal{L}^*(N) - \mathcal{L}^*(u) = S_{sink} - S_{sink} = 0 \tag{D.18}$$

Therefore it can be seen from both Equations (D.17) and (D.18), that the linear operator on the error remains homogeneous regardless of whether or not the sink term is considered. Based on this, the stability analysis can be carried out without the inclusion of the sink/source term (Patankar, 1980; Weller, 2016).

D.3 Stability Analysis: PE-D Model

The Von Neumann stability analysis was performed on both the dynamic and stagnant volume of the PE-D model.

D.3.1 Dynamic Volume

Replacing the discretized elements in Equation (C.20) with the expanded form of the oscillatory dependence shown in Equation (D.1), resulted in Equation (D.19).

$$-pA^j e^{ink\Delta z} = -(q+p)A^{j+1}e^{(i-1)nk\Delta z} + qA^{j+1}e^{ink\Delta z} + S_{sink} \tag{D.19}$$

Ignoring the sink term (refer to sub-section D.2.1), dividing by $A^j e^{ink\Delta z}$ and rearranging to make A the subject of the formula resulted in:

$$A = \frac{-p}{-(q+p) + qe^{-nk\Delta z}} \tag{D.20}$$

Making use of Euler's trigonometric identities and dividing the top and bottom by $-p$, produced Equation (D.21).

$$A = \frac{1}{1 + \frac{q}{p} - \frac{q}{p}(cos(k\Delta z) - nsin(k\Delta z))} \tag{D.21}$$

Equation (D.21) is identical to Equation (D.11). In very much the same manner as that shown in sub-section D.2, multiplying it by its complex conjugate and testing the extreme cases shown in Equation (D.7) revealed that $||A||^2 \leq 1$ and the discretization scheme is unconditionally stable for a well posed problem.

D.3.2 Stagnant Volume

The discretized elements in Equation (C.25) were replaced by the oscillatory dependence shown in Equation (D.1). This resulted in Equation (D.22).

$$-vA^j e^{ink\Delta z} = wA^{j+1}e^{(i-1)nk\Delta z} - (2w+v)A^{j+1}e^{ink\Delta z} + wA^{j+1}e^{(i+1)nk\Delta z} \tag{D.22}$$

Dividing by $A^j e^{ink\Delta z}$ and rearranging to make A the subject of the formula resulted in:

$$A = \frac{-v}{(w(e^{-nk\Delta z} + e^{nk\Delta z}) - (2w+v)} \tag{D.23}$$

Making use of Eulers trigonometric identities and dividing the top and bottom by $-v$ resulted in:

$$A = \frac{1}{1 + 2\frac{w}{v} - \frac{w}{v}2cos(k\Delta z)} \tag{D.24}$$

Testing the extreme cases (relating to $cos(k\Delta z)$) shown in Equation (D.7) revealed that $||A||^2 \leq 1$ and the discretization scheme is unconditionally stable for a well posed problem.

D.4 Stability Analysis: PDE Model

The Von Neumann stability analysis was performed on the dynamic volume of the PDE model. Replacing the discretized elements in Equation (C.28) with the expanded form of the oscillatory dependence shown in Equation (D.1) resulted in Equation (D.25).

$$\begin{aligned} &-2pA^j e^{ink\Delta z} = (2q + r)A^{j+1}e^{(i-1)nk\Delta z} - (2p + 4q) \\ &A^{j+1}e^{ink\Delta z} + (2q - r)A^{j+1}e^{ink\Delta z} + S_{sink} \end{aligned} \tag{D.25}$$

Ignoring the source/sink term, dividing by $A^j e^{ink\Delta x}$ and rearranging to make A the subject of the formula resulted in:

$$A = \frac{-2p}{(-2p + 4q + (2q + r)e^{-nk\Delta z} + (2q - r)e^{-nk\Delta z}} \tag{D.26}$$

Making use of Eulers trigonometric identities and dividing the top and bottom by $-2p$ resulted in:

$$A = \frac{1}{1 + 2\frac{q}{p} - 2\frac{q}{p}cos(k\Delta z) + n\frac{r}{p}sin(k\Delta z))} \tag{D.27}$$

Equation (D.27) is identical to Equation (D.4) and multiplying it by its complex conjugate as shown in sub-section D.1, revealed that $||AA^*|| = ||A||^2 \leq 1$ and the discretization scheme is unconditionally stable for a well posed problem.

D.5 Stability Analysis: PDE-D Model

The Von Neumann stability analysis was performed on both the dynamic and stagnant phase of the PDE-D model.

D.5.1 Dynamic Volume

Replacing the discretized elements in Equation (C.37) with the expanded form of the oscillatory dependence shown in Equation (D.1), ignoring the sink term, results in Equation (D.28).

$$-pA^j e^{ink\Delta z} = q^{j+1}e^{(i+1)nk\Delta z} - (p+2q+r)A^{j+1}e^{ink\Delta z} + (q+r)A^{j+1}e^{(i-1)nk\Delta z} \tag{D.28}$$

Dividing by $A^j e^{ink\Delta z}$ and rearranging to make A the subject of the formula results in:

$$A = \frac{-p}{-q^{nk\Delta z} + (q+r)e^{-nk\Delta z} - (p+2q+r)} \tag{D.29}$$

Making use of Eulers trigonometric identities and dividing the top and bottom by $-p$ results in:

$$A = \frac{1}{1 + \left(\frac{2q}{p} + \frac{r}{p}\right) - \left(\frac{2q}{p} + \frac{r}{p}\right) cos(k\Delta z) + n\frac{r}{p} sin(k\Delta z)} \tag{D.30}$$

Equation (D.30) is very similar to Equation (D.4). Combining, $q + r$ into a single variable will make them identical. This means that multiplying Equation (D.30) with its complex conjugate and testing out the different cases shown in Equation (D.7) will result in $||A||^2 \leq 1$, proving and the discretization scheme is unconditionally stable for a well posed problem.

D.5.2 Stagnant Volume

As the stagnant volume for the PDE-D model was discretized in the same way as the PE-D model, it has already been shown to be unconditionally stable for a well posed problem.

Appendix E

Simplified Model Algorithms

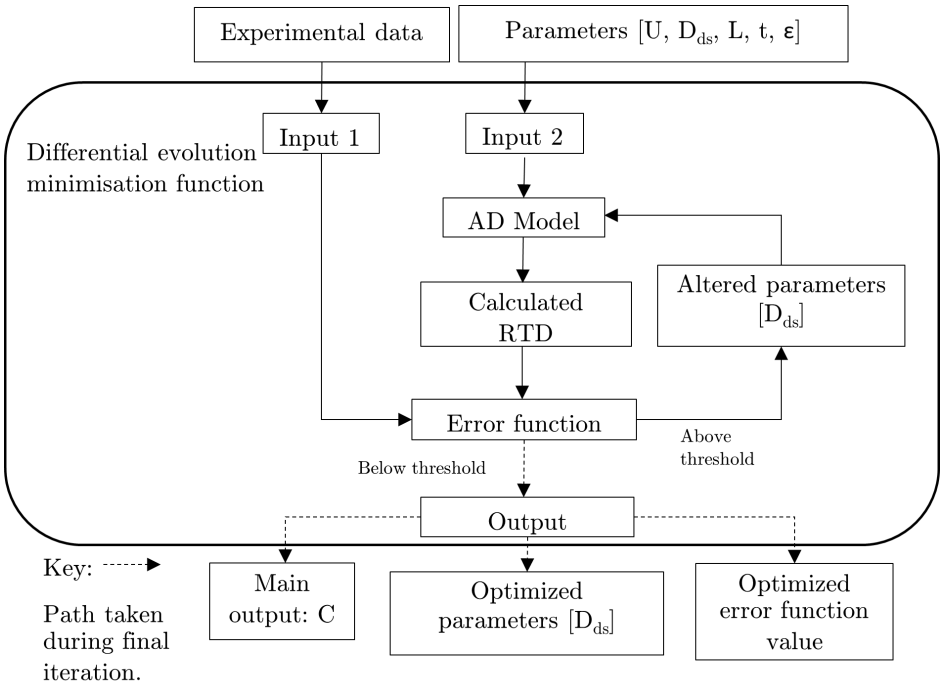

Figure E.1: Simplified model algorithm used in the optimisation of the AD model.

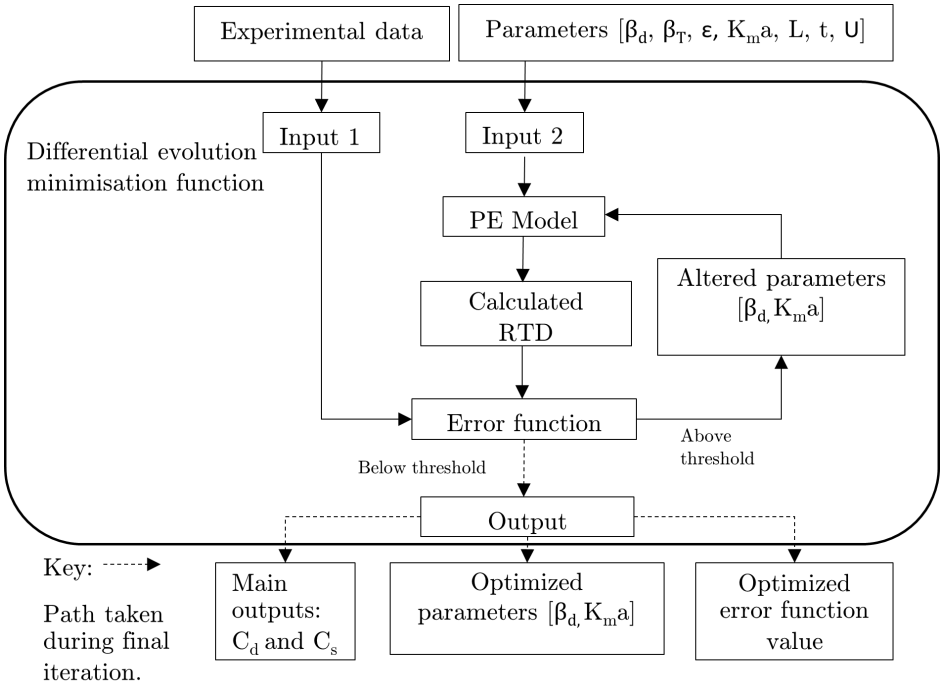

Figure E.2: Simplified model algorithm used in the optimisation of the PE model.

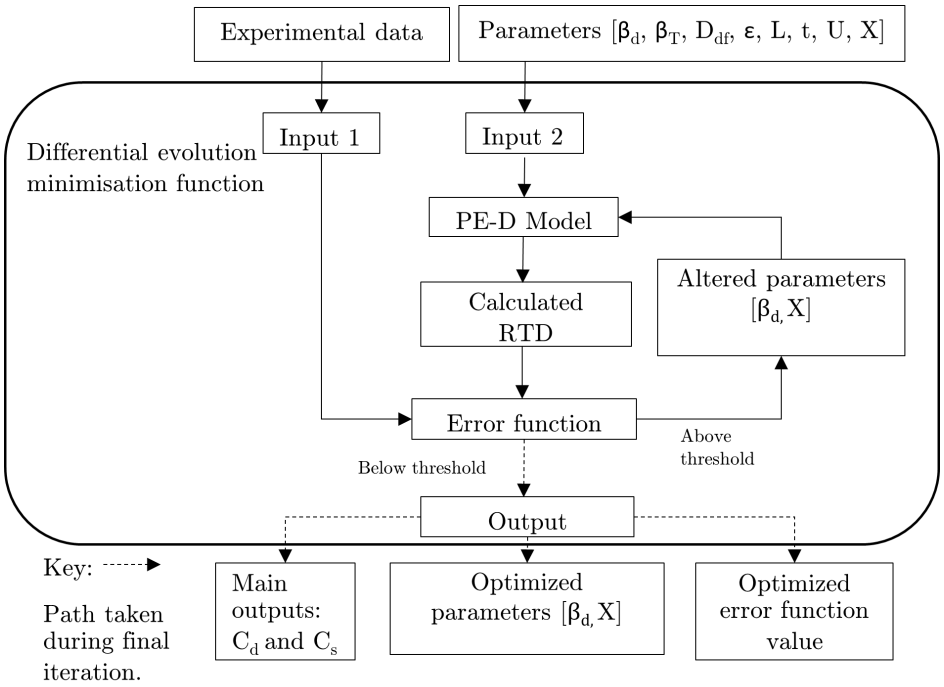

Figure E.3: Simplified model algorithm used in the optimisation of the PE-D model.

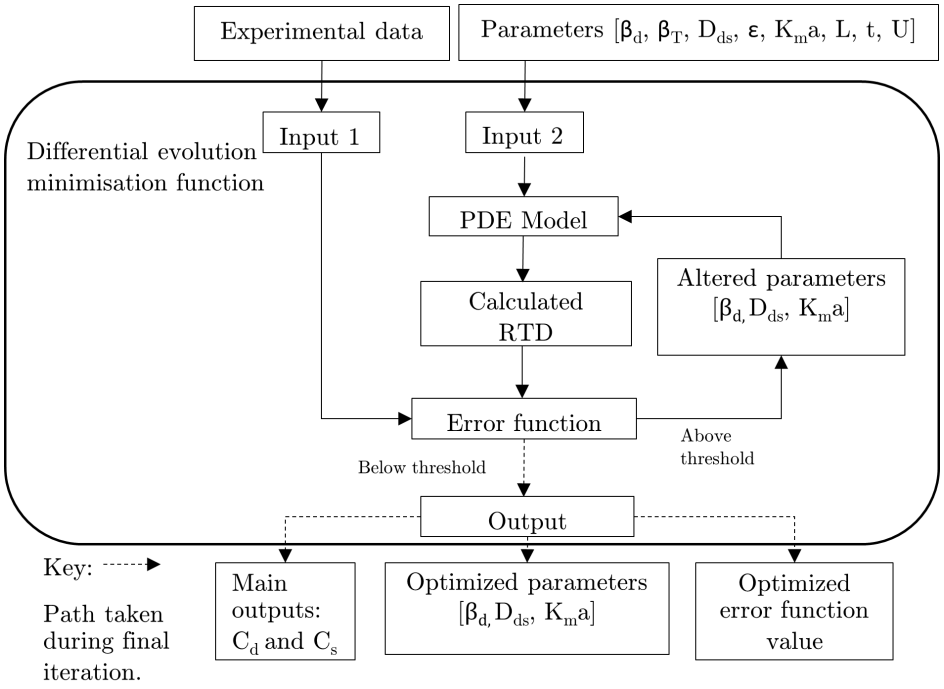

Figure E.4: Simplified model algorithm used in the optimisation of the PDE model.

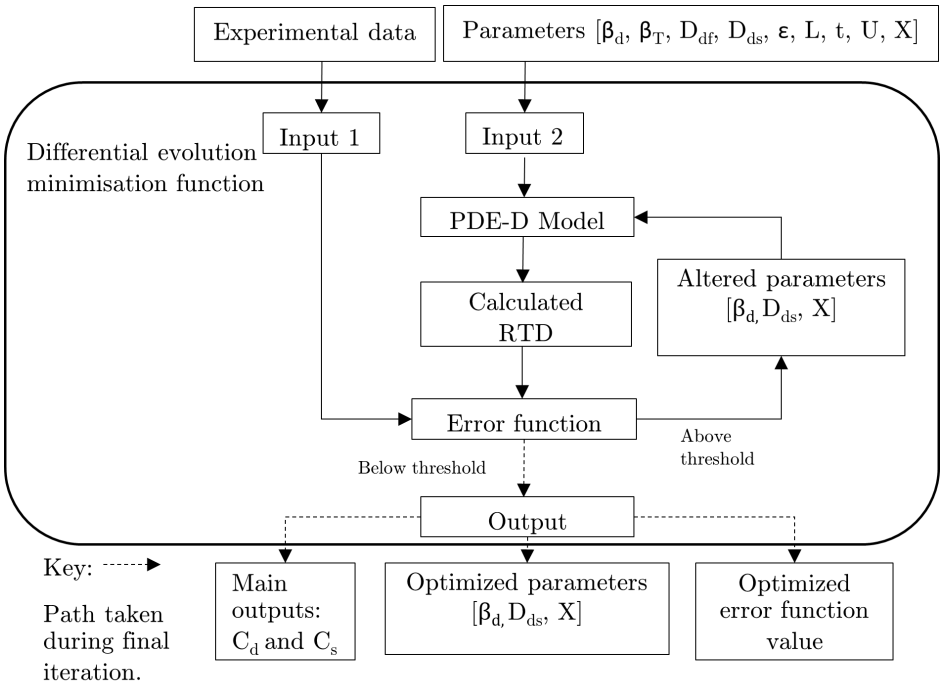

Figure E.5: Simplified model algorithm used in the optimisation of the PDE-D model.

Appendix F

Conductivity Theory and Measurement

The conductivity (υ) of a material is used to describe how much the material permits the flow of electricity. It is defined as the inverse of resistivity (ϵ) as can be seen from Equation (F.1). Electricity can be described as the movement of electrons through a solid material (Webster, 2004). When the medium is a solution, the current is carried by cations and anions. The ability of a solution to conduct electricity will depend on different factors including the temperature, concentration, mobility and the valence of ions. An example of a low conductivity solution is ultra pure water, while concentrated chemical samples can achieve high conductivity levels (Radiometer Analytical SAS, 2004).

$$\epsilon \equiv \frac{1}{\upsilon} \tag{F.1}$$

One of the ways conductivity can be measured is through the application of an alternating electrical current (I) to two electrodes immersed in a solution and the monitoring of the resulting potential difference between the electrodes (V)(refer to Figure F.1). Changes in the voltage are caused by the migration of ions which are typically produced by the dissolution of chemical compounds known as electrolytes. Depending on the degree to which these compounds ionise in solution, electrolytes can be classified as either strong or weak. Examples of strong electrolytes include strong acids and salts such as hydrochloric acid and potassium chloride, while weak electrolytes include weak acids such as acetic and nitrous acid.

The resistance (R) of the solution depicted in Figure F.1, can be calculated using Ohm's law:

$$R = \frac{V}{I} \tag{F.2}$$

The cell constant ($\bar{K}$) is defined as the ratio of the distance (d) between the electrodes, to the area (A) of each of the electrodes:

$$\bar{K} = \frac{d}{A} \tag{F.3}$$

The conductivity can then be calculated using Equation (F.4).

$$\upsilon = \frac{\bar{K}}{R} \tag{F.4}$$

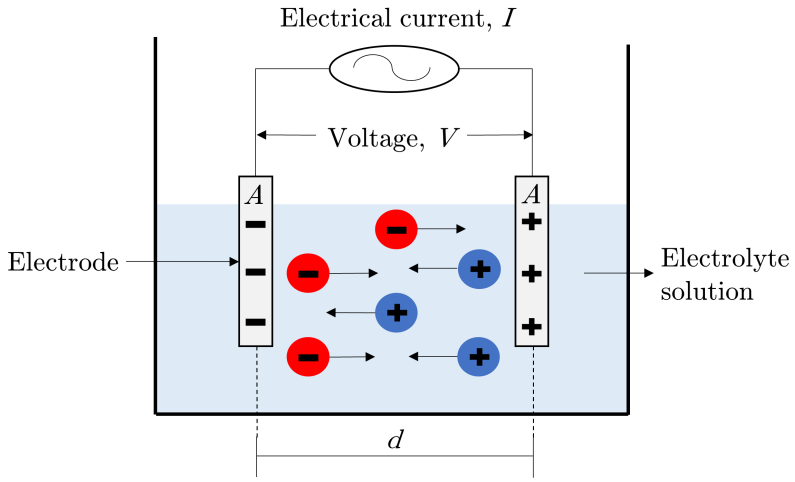

Figure F.1: Migration of ions caused by placements of charged electrodes, with areas equal to A and distance d apart, in an electrolytic solution. Based on Radiometer Analytical SAS (2004).

Equation (F.4) is the basic principle behind the operation of most conductivity probes used to measure the conductivity of electrolytic solutions.

It is important to note that temperature has an impact on conductivity readings. However, in recent years, it has been common practice to include an automatic temperature correction algorithm with a conductivity measurement set. The algorithm helps to convert a sample's conductivity at the measured temperature to that at a reference temperature, which is typically 25°C (Radiometer Analytical SAS, 2004).

Appendix G

Model Residual Analysis

G.1 GB Systems

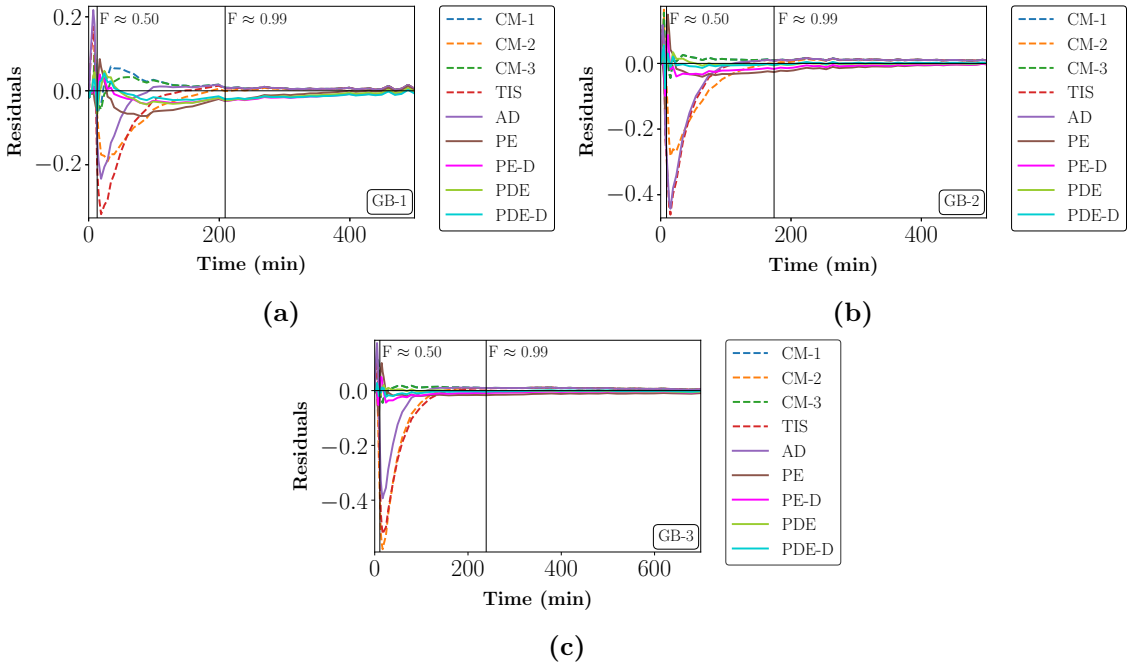

Figure G.1: Residual analysis of model fitted RTD data for GB beds: (a) GB-1 (2 mm), (b) GB-2 (5 mm), (c) GB-3 (15 mm).

G.2 GS Systems

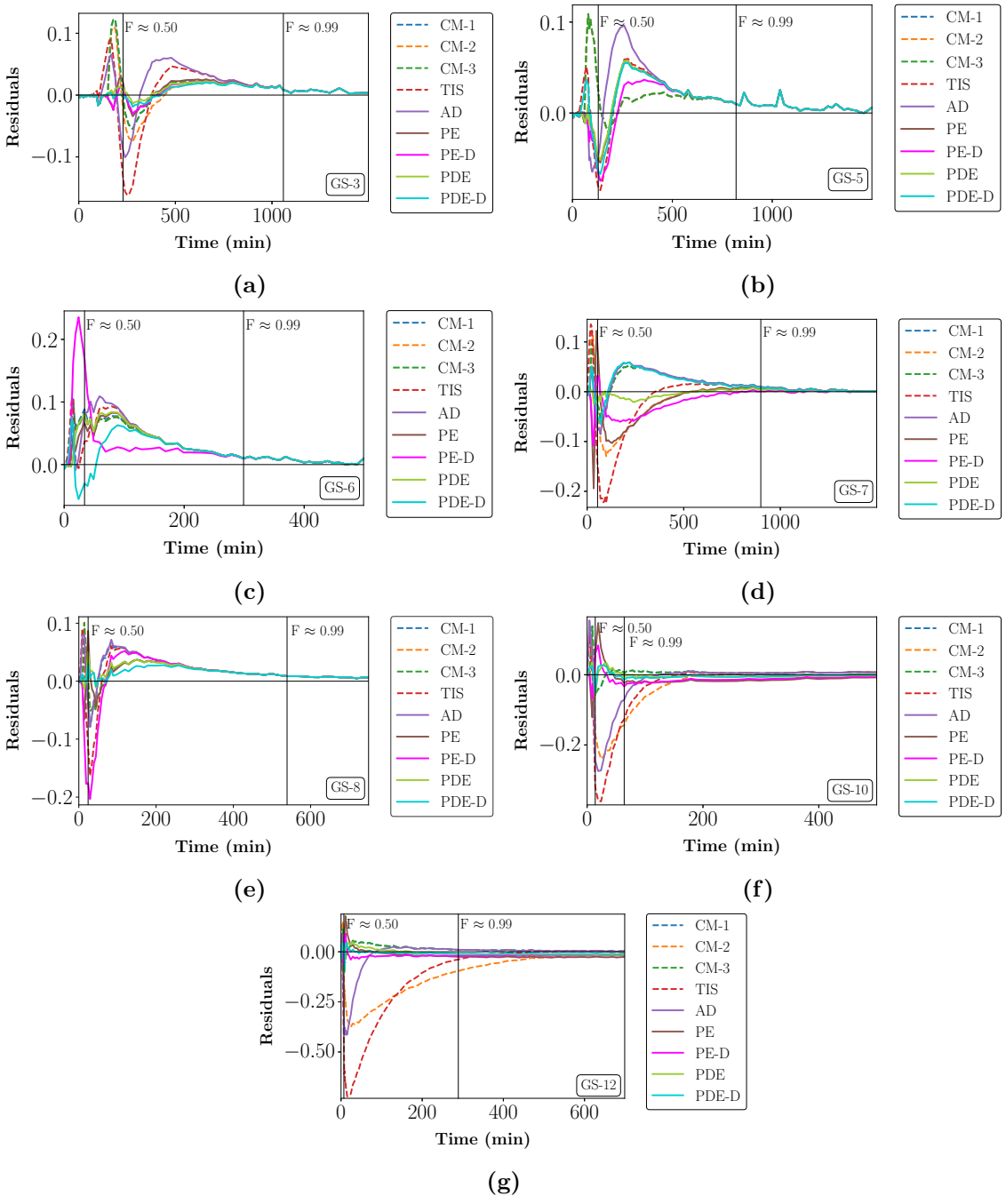

Figure G.2: Residual analysis of model fitted RTD data for GS beds: (a) 0.1 - 8 mm (GS-3), (b) GS-5 (0.5 - 8 mm) and (c) GS-6 (1 - 2 mm), (d) GS-7 (1 - 8 mm), (e) GS-8 (2.0 - 2.8 mm), (f) GS-10 (2.8 - 4.8 mm) and (g) GS-12 (4.8 - 5.6 mm).

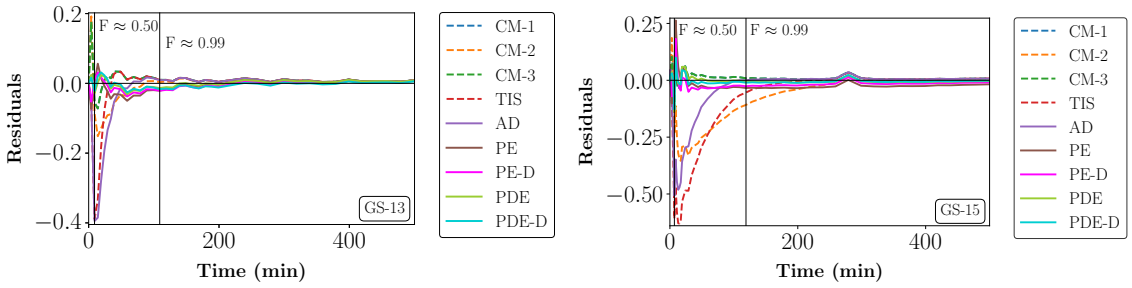

Figure G.3: Residual analysis of model fitted RTD data for GS beds: (a) GS-13 (4.8 - 6.7 mm) and (b) GS-15 (6.7 - 8 mm).

G.3 GW Systems

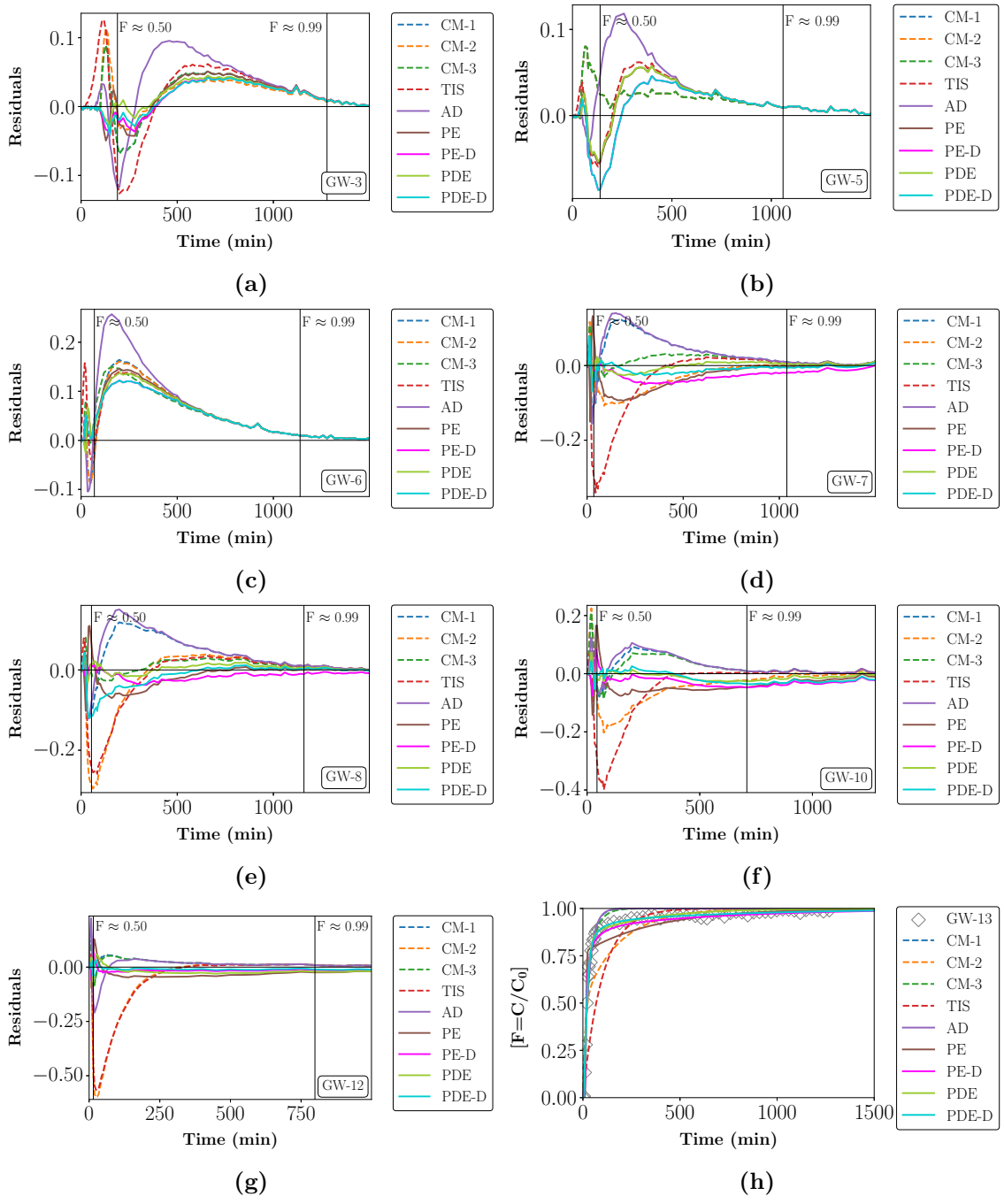

Figure G.4: Residual analysis of model fitted RTD data for GW beds: (a) GW-3 (0.1 - 8 mm), (b) GW-5 (0.5 - 8 mm), (c) GW-6 (1 - 2 mm), (d) GW-7 (1 - 8 mm), (e) GW-8 (2.0 - 2.8 mm), (f) GW-10 (2.8 - 4.8 mm), (g) GW-12 (4.8 - 5.6 mm) and (h) GW-13 (4.8 - 6.7 mm).

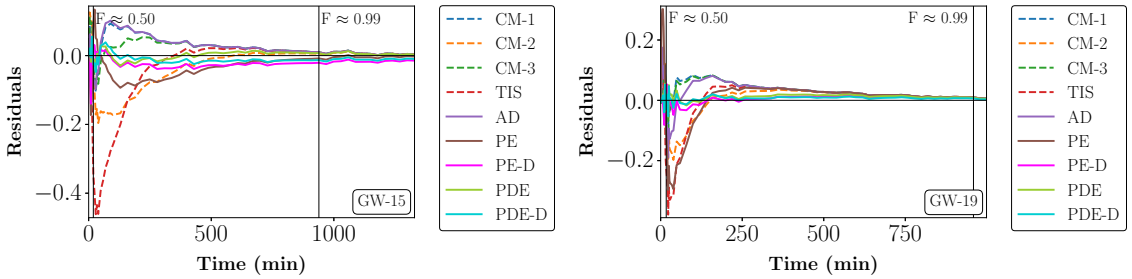

(a) **(b)**

Figure G.5: Residual analysis of model fitted RTD data for GW beds: (a) GW-15 (6.7 - 8 mm) and (b) GW-19 (13.2 - 16 mm).

G.4 MO Systems

G.4.1 Particle Size Fraction and Distribution

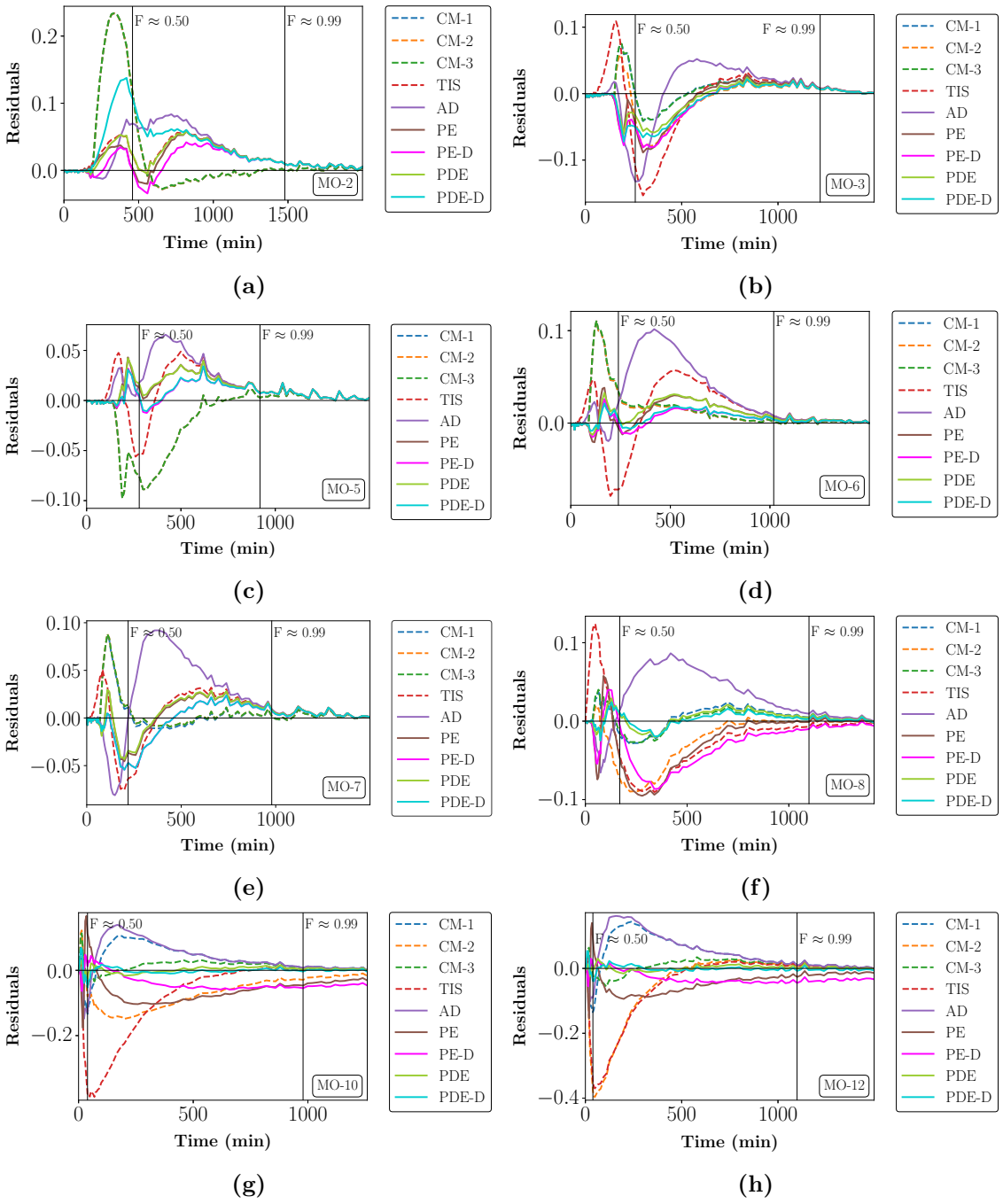

Figure G.6: Residual analysis of model fitted RTD data for MO beds: (a) MO-2 (0 - 8 mm), (b) MO-3 (0.1 - 8 mm), (c) MO-5 (0.5 - 8 mm), (d) MO-6 (1 - 2 mm), (e) MO-7 (1 - 8 mm), (f) MO-8 (2.0 - 2.8 mm), (g) MO-10 (2.8 - 4.8 mm) and (h) MO-12 (4.8 - 5.6 mm).

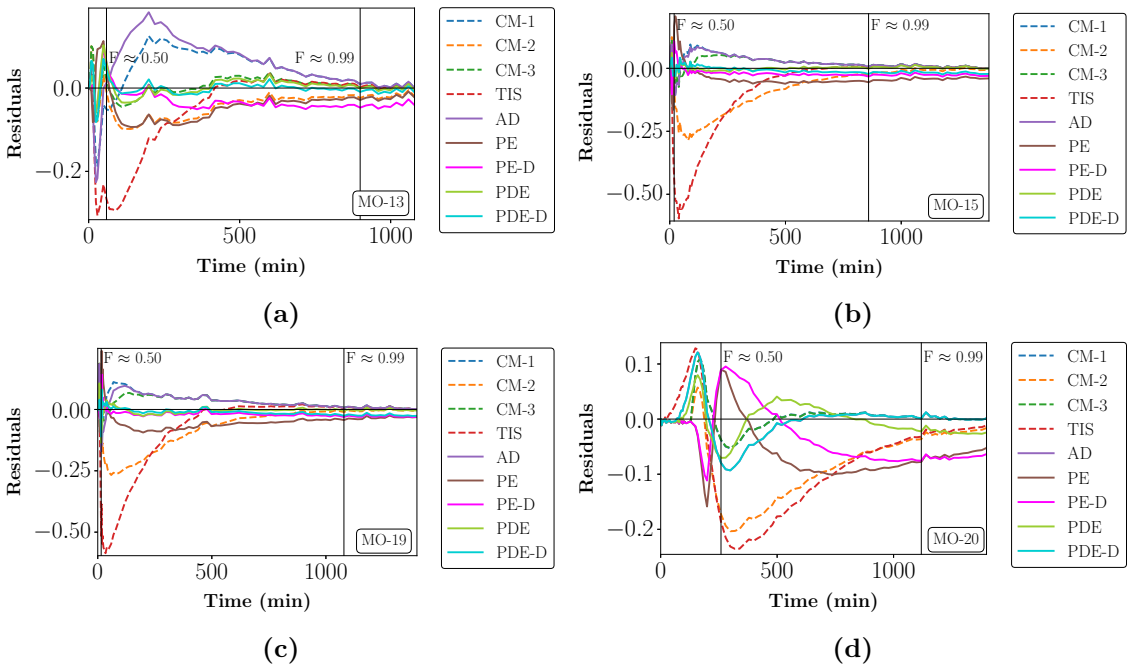

Figure G.7: Residual analysis of model fitted RTD data for MO beds: (a) MO-13 (4.8 - 6.7 mm), (b) MO-15 (6.7 - 8.0 mm), (c) MO-19 (13.2 - 16.0 mm) and (d) MO-20 (0 - 16.0 mm).

G.4.2 Packing Height

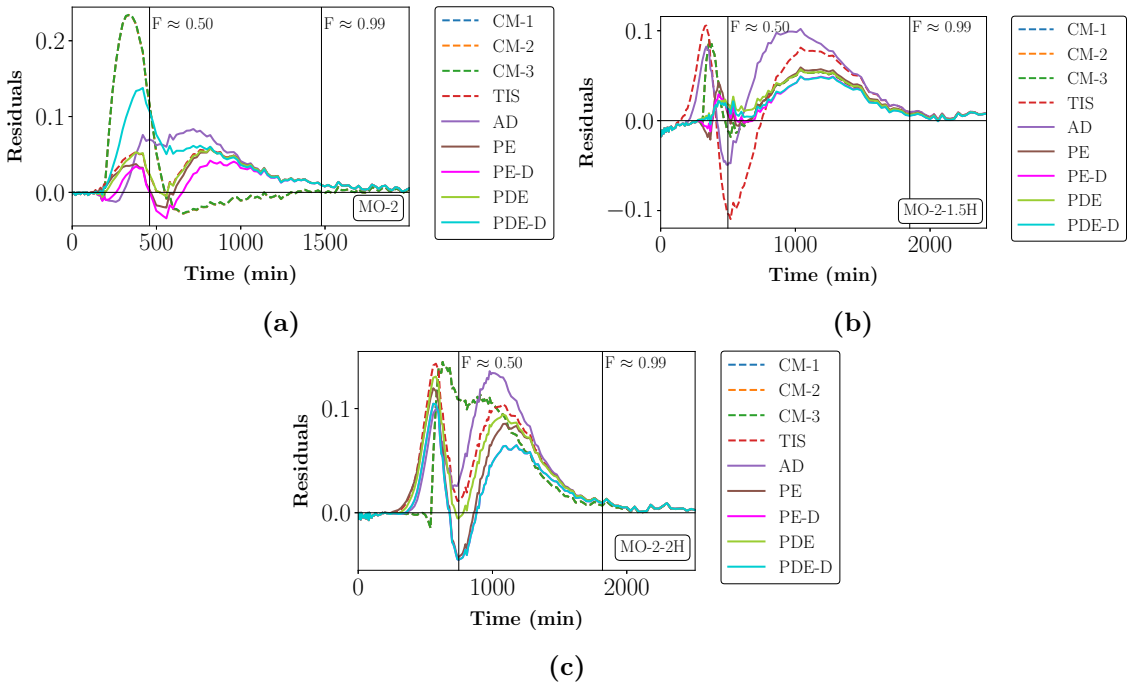

Figure G.8: Residual analysis of model fitted RTD data for MO beds of 0 - 8 mm particles: (a) MO-2 (normal bed heigth), (b) MO-2-1.5H (1.5 × normal bed height) and (c) MO-2-2H (2 × normal bed height).

G.4.3 State of Agglomeration

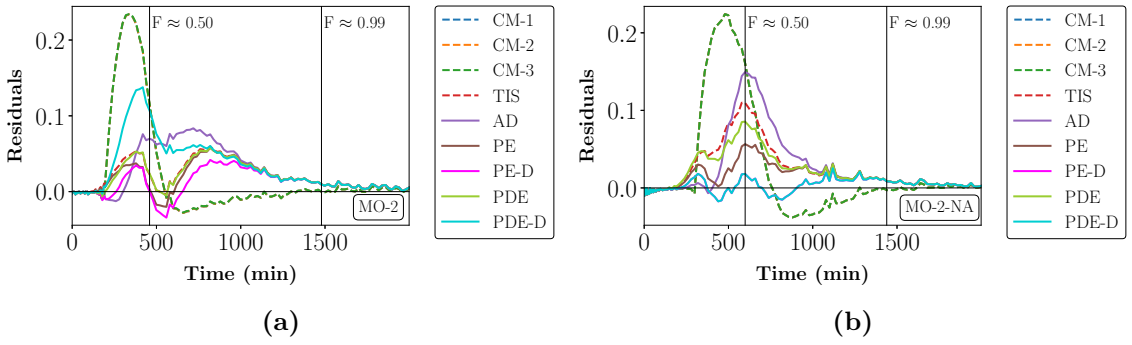

Figure G.9: Residual analysis of model fitted RTD data for MO beds of 0 - 8 mm particles: (a) agglomerated (MO-2) and (b) non-agglomerated (MO-2-NA).

G.4.4 Solution Viscosity

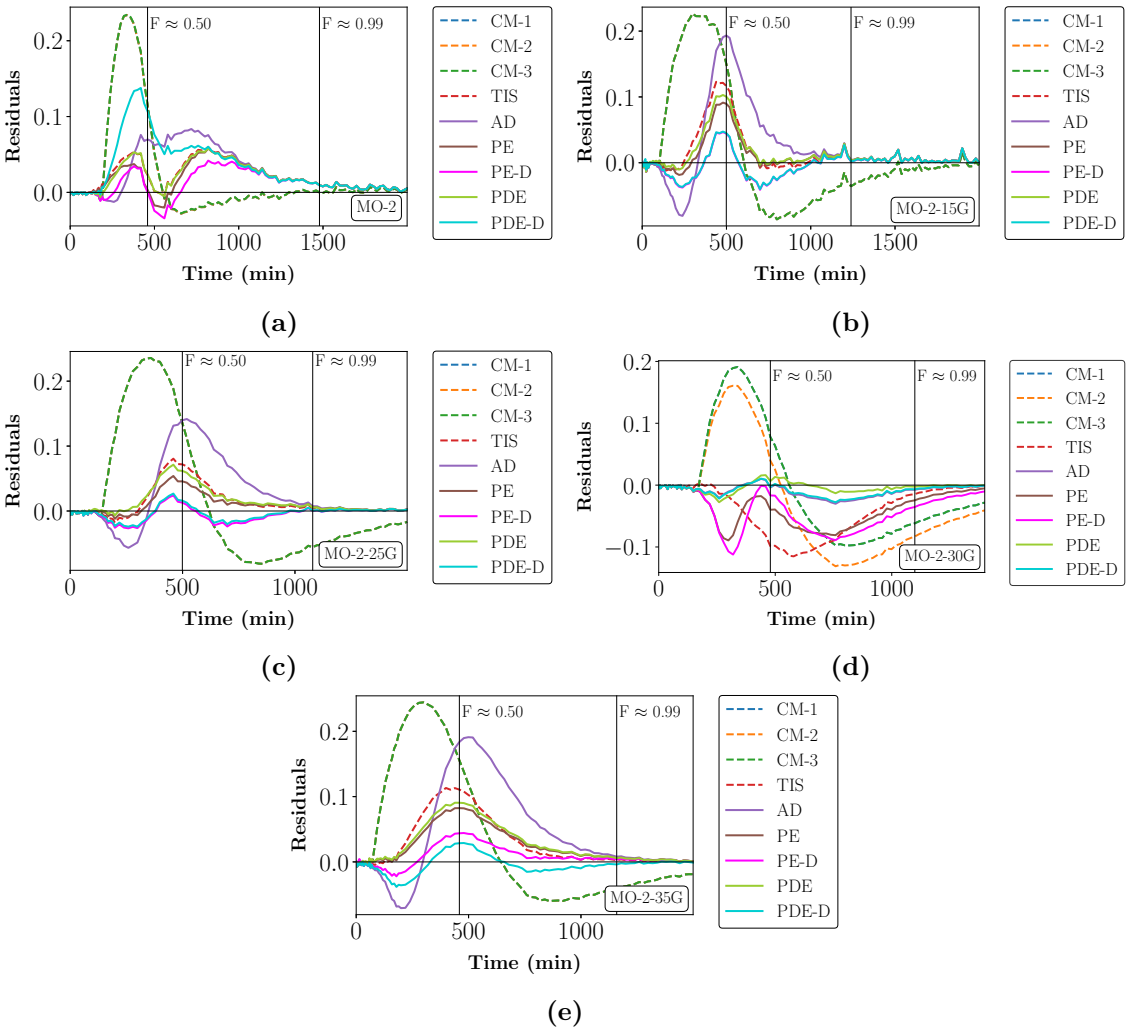

Figure G.10: Residual analysis of model fitted RTD data for MO beds of 0 - 8 mm particles and irrigated with solutions of different viscosities: (a) MO-2 (0.8 cP), (b) MO-2-15G (1.2 cP), (c) MO-2-25G (1.6 cP), (d) MO-2-30G (1.9 cP) and (e) MO-2-35G (2.2 cP).

Appendix H

Optimized Model Parameter and Goodness of Fit Data

Table H.1: Optimized parameters and goodness of fit data obtained for the four empirical models.[Key: size fraction (S.F.), Total PFR volume [V_P], Total volume [V_T], Total CSTR volume [V_C], Dead volume [V_D], Regression coefficient [R^2]]

E-tag	S.F. (mm)	$\frac{V_p}{V_T}$	CM-1				CM-2					CM-3						TIS		
			$\frac{V_C}{V_T}$	$\frac{V_D}{V_T}$	Error	R^2	$\frac{V_{C1}}{V_T}$	$\frac{V_{C2}}{V_T}$	$\frac{V_{Cmin}}{V_{Cmax}}$	Error	R^2	$\frac{V_{C1}}{V_T}$	$\frac{V_{C2}}{V_T}$	$\frac{V_D}{V_T}$	$\frac{V_{Cmin}}{V_{Cmax}}$	Error	R^2	N	Error	R^2
GB-1	2	0.21	0.27	0.52	0.207	0.992	0.74	0.05	0.07	0.529	0.948	0.23	0.08	0.48	0.25	0.187	0.994	1	0.863	0.862
GB-2	5	0.11	0.24	0.65	0.491	0.990	0.05	0.83	0.06	0.679	0.883	0.12	0.12	0.65	0.50	0.491	0.990	1	1.044	0.726
GB-3	15	0.13	0.17	0.69	0.204	0.993	0.43	0.43	0.50	1.475	0.508	0.09	0.09	0.69	0.50	0.204	0.993	1	1.347	0.590
GS-3	0.1 - 8.0	0.56	0.42	0.02	0.302	0.995	0.22	0.22	0.50	0.316	0.994	0.21	0.21	0.02	0.50	0.302	0.995	8	0.515	0.985
GS-5	0.5 - 8.0	0.40	0.60	0.00	0.286	0.994	0.30	0.30	0.50	0.289	0.994	0.30	0.30	0.00	0.50	0.289	0.994	5	0.291	0.994
GS-6	1.0 - 2.0	0.35	0.65	0.00	0.338	0.985	0.33	0.33	0.50	0.324	0.984	0.33	0.33	0.00	0.50	0.324	0.987	3	0.349	0.984
GS-7	1.0 - 8.0	0.12	0.51	0.36	0.296	0.988	0.12	0.76	0.14	0.521	0.963	0.26	0.26	0.36	0.50	0.296	0.988	1	0.843	0.902
GS-8	2.0-2.8	0.26	0.66	0.08	0.269	0.982	0.58	0.16	0.22	0.209	0.989	0.58	0.16	0.00	0.22	0.209	0.989	2	0.383	0.964
GS-10	2.8-4.8	0.13	0.33	0.55	0.169	0.989	0.09	0.79	0.10	0.705	0.804	0.16	0.16	0.55	0.50	0.169	0.989	1	0.899	0.682
GS-12	4.8-5.6	0.02	0.07	0.91	0.289	0.985	0.01	0.97	0.01	1.741	0.493	0.04	0.04	0.91	0.50	0.287	0.985	1	2.990	-0.494
GS-13	4.8-6.7	0.06	0.59	0.35	0.217	0.975	0.15	0.78	0.16	0.694	0.743	0.30	0.30	0.34	0.50	0.217	0.975	3	0.559	0.834
GS-15	6.7-8.0	0.02	0.15	0.83	0.231	0.982	0.02	0.96	0.02	1.155	0.549	0.07	0.07	0.83	0.50	0.231	0.982	1	1.907	-0.228
GW-3	0.1 - 8.0	0.39	0.61	0.00	0.327	0.993	0.42	0.19	0.31	0.327	0.995	0.30	0.30	0.00	0.50	0.327	0.993	3	0.527	0.983
GW-5	0.5 - 8.0	0.24	0.76	0.00	0.274	0.994	0.38	0.38	0.50	0.274	0.994	0.38	0.38	0.00	0.50	0.274	0.994	3	0.301	0.993
GW-6	1.0 - 2.0	0.14	0.86	0.00	0.671	0.937	0.43	0.43	0.50	0.665	0.938	0.67	0.19	0.00	0.22	0.611	0.948	1	0.649	0.941
GW-7	1.0 - 8.0	0.12	0.51	0.37	0.614	0.947	0.12	0.76	0.14	0.558	0.960	0.26	0.26	0.37	0.50	0.246	0.992	1	1.496	0.686
GW-8	2.0-2.8	0.09	0.45	0.46	0.600	0.944	0.46	0.46	0.50	1.180	0.785	0.06	0.64	0.21	0.09	0.195	0.994	1	1.049	0.830
GW-10	2.8-4.8	0.03	0.38	0.59	0.464	0.959	0.08	0.89	0.08	0.846	0.864	0.29	0.12	0.56	0.30	0.453	0.961	1	1.459	0.596
GW-12	4.8-5.6	0.06	0.15	0.79	0.278	0.981	0.47	0.47	0.50	1.910	0.250	0.06	0.10	0.78	0.39	0.301	0.981	1	1.818	0.320
GW-13	4.8-6.7	0.01	0.30	0.69	0.319	0.967	0.06	0.93	0.06	0.746	0.820	0.22	0.10	0.67	0.31	0.313	0.968	1	1.423	0.344
GW-15	6.7-8.0	0.01	0.29	0.70	0.345	0.961	0.05	0.94	0.05	0.632	0.400	0.30	0.07	0.62	0.19	0.294	0.981	1	1.279	0.468
GW-19	13.2-16.0	0.10	0.35	0.54	0.356	0.977	0.83	0.07	0.08	0.575	0.944	0.23	0.14	0.53	0.37	0.366	0.977	1	1.025	0.821
MO-2	0 - 8.0	0.40	0.60	0.00	0.695	0.979	0.30	0.30	0.50	0.695	0.979	0.30	0.30	0.00	0.50	0.695	0.979	8	0.283	0.997
MO-2-1.5H	0 - 8.0	0.53	0.47	0.00	0.343	0.995	0.23	0.23	0.50	0.343	0.995	0.23	0.23	0.00	0.50	0.343	0.995	6	0.565	0.986
MO-2-2H	0 - 8.0	0.71	0.29	0.00	0.821	0.975	0.14	0.14	0.50	0.821	0.975	0.14	0.14	0.00	0.50	0.821	0.975	13	0.646	0.984
MO-2-NA	0 - 8.0	0.54	0.46	0.00	0.762	0.976	0.23	0.23	0.50	0.762	0.976	0.23	0.23	0.00	0.50	0.762	0.976	11	0.385	0.994
MO-2-15G	0 - 8.0	0.22	0.78	0.00	0.954	0.959	0.39	0.39	0.50	0.954	0.959	0.39	0.39	0.00	0.50	0.954	0.959	5	0.357	0.994
MO-2-25G	0 - 8.0	0.29	0.71	0.00	0.904	0.956	0.36	0.36	0.50	0.904	0.956	0.36	0.36	0.00	0.50	0.904	0.956	7	0.239	0.997
MO-2-30G	0 - 8.0	0.30	0.63	0.07	0.734	0.969	0.35	0.35	0.50	0.773	0.966	0.31	0.31	0.07	0.50	0.734	0.969	6	0.473	0.987
MO-2-35G	0 - 8.0	0.16	0.84	0.00	1.003	0.942	0.42	0.42	0.50	1.003	0.942	0.42	0.42	0.00	0.50	1.003	0.942	4	0.418	0.986
MO-3	0.1 - 8.0	0.46	0.49	0.05	0.207	0.998	0.27	0.27	0.50	0.260	0.996	0.27	0.22	0.05	0.46	0.207	0.998	4	0.488	0.987
MO-5	0.5 - 8.0	0.58	0.42	0.00	0.317	0.995	0.21	0.21	0.50	0.317	0.995	0.21	0.21	0.00	0.50	0.317	0.995	9	0.218	0.998
MO-6	1.0 - 2.0	0.32	0.68	0.00	0.292	0.995	0.34	0.34	0.50	0.292	0.995	0.34	0.34	0.00	0.50	0.297	0.995	4	0.295	0.994
MO-7	1.0 - 8.0	0.27	0.73	0.00	0.217	0.997	0.36	0.36	0.50	0.222	0.997	0.36	0.36	0.00	0.50	0.222	0.997	3	0.273	0.995
MO-8	2.0-2.8	0.13	0.74	0.14	0.152	0.998	0.44	0.44	0.50	0.339	0.991	0.46	0.30	0.12	0.39	0.147	0.998	1	0.521	0.978
MO-10	2.8-4.8	0.02	0.32	0.66	0.530	0.942	0.04	0.94	0.05	0.795	0.869	0.40	0.05	0.53	0.12	0.240	0.996	1	1.746	0.370
MO-12	4.8-5.6	0.05	0.31	0.65	0.635	0.919	0.48	0.48	0.50	1.289	0.665	0.04	0.54	0.38	0.06	0.302	0.991	1	1.223	0.698
MO-13	4.8-6.7	0.02	0.45	0.53	0.553	0.929	0.06	0.92	0.06	0.421	0.959	0.61	0.06	0.30	0.10	0.228	0.988	1	1.039	0.751
MO-15	6.7-8.0	0.02	0.15	0.83	0.419	0.944	0.02	0.95	0.02	1.359	0.412	0.16	0.03	0.79	0.15	0.291	0.973	1	2.440	-0.896
MO-19	13.2-16.0	0.02	0.12	0.86	0.473	0.958	0.96	0.02	0.02	1.180	0.762	0.03	0.14	0.82	0.15	0.400	0.965	1	2.363	0.046
MO-20	0 - 16.0	0.29	0.46	0.26	0.252	0.996	0.36	0.36	0.50	0.833	0.958	0.21	0.25	0.25	0.46	0.252	0.996	2	1.016	0.938

Table H.2: Optimized parameters and goodness of fit data obtained for the five semi-phenomenological models. [Key: size fraction (S.F.), Dispersion coefficient [D_{ds}] (m^2/min), Dynamic saturation [β_d], Total saturation [β_T], Overall mass transfer coefficient [$K_m a$](min^{-1}), Maximum pore length [X](m), Regression coefficient [R^2].

E-tag	S.F. (mm)	AD			PE				PE-D				PDE					PDE-D				
		D_{ds}	Error	R^2	$\frac{\beta_d}{\beta_T}$	$K_m a$	Error	R^2	$\frac{\beta_D}{\beta_T}$	X	Error	R^2	$\frac{\beta_D}{\beta_T}$	D_{ds}	$K_m a$	Error	R^2	$\frac{\beta_D}{\beta_T}$	D_{ds}	X	Error	R^2
GB-1	2	1.12E-04	0.628	0.927	0.38	1.03E-04	0.254	0.988	0.36	0.07	0.157	0.995	0.43	1.07E-06	5.59E-05	0.180	0.994	0.37	2.36E-07	0.08	0.147	0.996
GB-2	5	2.16E+00	0.994	0.750	0.31	3.52E-05	0.284	0.980	0.29	0.10	0.186	0.991	0.36	1.98E-06	1.19E-05	0.106	0.997	0.29	8.13E-07	0.17	0.112	0.997
GB-3	15	5.95E+00	0.959	0.792	0.27	1.96E-05	0.212	0.990	0.27	0.14	0.143	0.995	0.31	1.06E-06	8.29E-06	0.044	1.000	0.27	4.17E-07	0.20	0.060	0.999
GS-3	0.1 - 8.0	6.29E-06	0.352	0.993	0.76	4.33E-04	0.150	0.999	0.73	0.02	0.132	0.999	0.78	1.25E-07	3.22E-04	0.112	0.999	0.75	2.76E-08	0.02	0.105	0.999
GS-5	0.5 - 8.0	8.84E-07	0.317	0.993	0.51	1.42E-03	0.220	0.997	0.48	0.01	0.239	0.996	0.51	7.40E-08	1.38E-03	0.217	0.997	0.67	7.51E-07	0.01	0.245	0.996
GS-6	1.0 - 2.0	2.24E-06	0.368	0.983	0.52	7.37E-04	0.293	0.989	0.46	0.02	0.201	0.970	0.52	8.78E-08	7.37E-03	0.310	0.988	0.99	2.90E-06	0.01	0.240	0.993
GS-7	1.0 - 8.0	6.91E-06	0.318	0.986	0.36	2.78E-04	0.490	0.967	0.32	0.03	0.304	0.987	0.57	1.96E-06	1.30E-04	0.082	0.999	0.94	6.69E-06	0.20	0.278	0.989
GS-8	2.0-2.8	6.10E-06	0.291	0.979	0.53	2.95E-04	0.191	0.991	0.48	0.03	0.146	0.944	0.60	6.96E-07	2.25E-04	0.161	0.994	0.54	4.70E-07	0.03	0.121	0.996
GS-10	2.8-4.8	4.06E+00	0.652	0.833	0.43	1.94E-05	0.245	0.976	0.39	0.12	0.170	0.989	0.52	1.98E-06	9.31E-06	0.095	0.997	0.42	1.00E-06	0.20	0.087	0.997
GS-12	4.8-5.6	9.10E+01	1.343	0.698	0.07	2.25E-05	0.439	0.968	0.07	0.10	0.352	0.979	0.10	3.08E-06	1.63E-05	0.206	0.993	0.07	1.01E-06	0.19	0.163	0.996
GS-13	4.8-6.7	5.38E-06	0.677	0.756	0.48	7.40E-05	0.148	0.989	0.42	0.07	0.109	0.994	0.55	2.46E-06	5.43E-05	0.083	0.996	0.41	7.52E-07	0.09	0.083	0.996
GS-15	6.7-8.0	3.74E+01	1.316	0.415	0.14	2.87E-05	0.378	0.952	0.12	0.12	0.264	0.977	0.20	6.62E-06	1.65E-05	0.197	0.987	0.10	1.55E-06	0.20	0.192	0.988
GW-3	0.1 - 8.0	1.28E-06	0.497	0.984	0.59	5.32E-04	0.271	0.995	0.55	0.02	0.230	0.997	0.64	1.89E-07	3.84E-04	0.224	0.997	0.56	4.20E-08	0.02	0.219	0.997
GW-5	0.5 - 8.0	2.08E-06	0.426	0.986	0.29	1.62E-03	0.271	0.994	0.19	0.01	0.316	0.992	0.30	6.85E-08	1.59E-03	0.267	0.994	0.19	1.00E-09	0.01	0.316	0.992
GW-6	1.0 - 2.0	4.45E-06	0.909	0.885	0.29	6.19E-04	0.617	0.947	0.19	0.02	0.545	0.959	0.29	1.24E-07	5.97E-04	0.593	0.951	0.19	1.00E-09	0.02	0.545	0.959
GW-1-8	1.0 - 8.0	6.91E-06	0.679	0.935	0.29	2.80E-04	0.535	0.960	0.25	0.03	0.257	0.991	0.44	1.96E-06	1.30E-04	0.148	0.997	0.74	6.69E-06	0.20	0.1941	0.9947
GW-8	2.0-2.8	1.32E-05	0.678	0.929	0.19	3.25E-04	0.366	0.979	0.14	0.03	0.158	0.996	0.31	2.39E-06	3.17E-04	0.115	0.998	0.34	4.76E-06	0.02	0.132	0.969
GW-10	2.8-4.8	2.12E-05	0.412	0.968	0.23	1.63E-04	0.485	0.955	0.19	0.05	0.262	0.987	0.39	3.54E-06	1.21E-04	0.154	0.996	0.25	1.28E-06	0.06	0.176	0.994
GW-12	4.8-5.6	1.45E+00	0.605	0.925	0.16	5.72E-05	0.303	0.981	0.15	0.10	0.138	0.996	0.16	9.82E-07	3.97E-05	0.179	0.993	0.15	3.82E-07	0.12	0.091	0.998
GW-13	4.8-6.7	8.03E-05	0.308	0.969	0.17	1.40E-04	0.394	0.950	0.14	0.06	0.209	0.986	0.35	5.58E-06	1.31E-04	0.150	0.993	0.18	2.83E-06	0.06	0.130	0.995
GW-15	6.7-8.0	8.66E-05	0.344	0.962	0.16	1.62E-04	0.384	0.952	0.13	0.05	0.224	0.984	0.32	6.68E-06	2.16E-04	0.111	0.996	0.15	3.11E-06	0.05	0.143	0.993
GW-19	13.2-16.0	6.42E-05	0.529	0.952	0.03	7.22E-04	1.017	0.824	0.27	0.05	0.171	0.995	0.41	1.81E-06	9.46E-05	0.151	0.996	0.29	5.63E-07	0.06	0.126	0.997
MO-2	0 - 8.0	6.02E-07	0.407	0.993	0.24	5.47E-03	0.256	0.997	0.44	0.01	0.205	0.998	0.38	6.67E-08	3.75E-03	0.274	0.997	1.00	9.01E-07	0.00	0.183	0.990
MO-2-1.5H	0 - 8.0	1.39E-06	0.527	0.988	0.68	4.00E-04	0.279	0.997	0.63	0.02	0.230	0.998	0.70	1.65E-07	3.29E-04	0.266	0.997	0.64	3.99E-08	0.02	0.227	0.998
MO-2-2H	0 - 8.0	7.35E-07	0.730	0.980	0.00	7.54E-03	0.507	0.990	0.41	0.01	0.414	0.994	0.35	6.50E-08	3.27E-03	0.566	0.988	0.41	1.00E-09	0.01	0.414	0.994
MO-2-NA	0 - 8.0	3.63E-07	0.494	0.990	0.00	1.71E-02	0.210	0.990	0.29	0.01	0.096	0.998	0.00	5.36E-08	1.58E-02	0.313	0.996	0.29	1.00E-09	0.01	0.096	1.000
MO-2-15G	0 - 8.0	7.70E-07	0.627	0.982	0.00	6.29E-03	0.257	0.997	0.03	0.01	0.188	0.998	0.00	6.34E-08	6.14E-03	0.294	0.996	0.03	1.77E-07	0.01	0.186	0.998
MO-2-25G	0 - 8.0	6.70E-07	0.501	0.986	0.00	8.34E-03	0.154	0.999	0.18	0.01	0.111	0.999	0.00	6.54E-08	8.16E-03	0.212	0.998	0.21	2.62E-07	0.01	0.101	0.999
MO-2-30G	0 - 8.0	1.20E-06	0.114	0.999	0.61	1.08E-03	0.397	0.991	0.61	0.02	0.447	0.989	0.98	1.07E-06	1.00E-09	0.077	1.000	1.00	1.10E-06	0.20	0.106	0.999
MO-2-35G	0 - 8.0	8.64E-07	0.725	0.970	0.01	4.99E-03	0.317	0.994	0.03	0.01	0.161	0.999	0.00	6.50E-08	5.07E-03	0.354	0.993	0.08	1.15E-06	0.00	0.129	0.999
MO-3	0.1 - 8.0	8.70E+00	0.375	0.992	0.62	7.00E-04	0.272	0.996	0.59	0.02	0.281	0.996	0.68	1.75E-07	4.84E-04	0.208	0.998	0.63	7.47E-08	0.02	0.242	0.997
MO-5	0.5 - 8.0	6.23E-07	0.240	0.997	0.66	1.10E-03	0.144	0.999	0.64	0.01	0.106	0.999	0.68	8.86E-08	9.96E-04	0.145	0.999	0.64	1.22E-08	0.01	0.106	0.999
MO-6	1.0 - 2.0	1.61E-06	0.385	0.991	0.50	8.79E-04	0.139	0.999	0.44	0.02	0.085	1.000	0.54	1.77E-07	7.96E-04	0.136	0.999	0.47	7.37E-08	0.02	0.081	1.000
MO-7	1.0 - 8.0	1.42E-06	0.403	0.990	0.39	1.20E-03	0.164	0.998	0.32	0.01	0.176	0.998	0.40	8.31E-08	1.16E-03	0.162	0.998	0.32	1.17E-09	0.01	0.176	0.998
MO-8	2.0-2.8	4.41E-06	0.402	0.987	0.28	7.37E-04	0.390	0.988	0.22	0.02	0.348	0.990	0.53	2.04E-06	5.68E-04	0.110	0.999	0.50	2.20E-06	0.02	0.086	0.999
MO-10	2.8-4.8	2.89E-05	0.642	0.915	0.12	2.30E-04	0.669	0.908	0.09	0.04	0.382	0.970	0.32	7.85E-06	4.44E-04	0.097	0.998	0.19	8.82E-06	0.02	0.141	0.996
MO-12	4.8-5.6	2.99E-05	0.675	0.908	0.14	2.78E-04	0.525	0.944	0.10	0.04	0.308	0.981	0.31	5.15E-06	3.50E-04	0.075	0.999	0.18	5.54E-06	0.03	0.120	0.997
MO-13	4.8-6.7	1.98E-05	0.707	0.885	0.11	3.33E-04	0.447	0.954	0.08	0.03	0.307	0.978	0.24	4.39E-06	4.73E-04	0.192	0.992	0.14	4.64E-06	0.02	0.179	0.993
MO-15	6.7-8.0	2.09E-04	0.410	0.946	0.10	7.26E-05	0.588	0.890	0.08	0.08	0.276	0.976	0.33	1.49E-05	2.34E-04	0.114	0.996	0.10	3.28E-06	0.08	0.154	0.993
MO-19	13.2-16.0	7.17E-04	0.552	0.948	0.08	1.22E-04	0.624	0.933	0.07	0.08	0.251	0.989	0.22	1.04E-05	1.80E-04	0.255	0.989	0.08	9.35E-07	0.08	0.222	0.992
MO-20	0 - 16.0	3.68E-06	0.356	0.992	0.50	2.56E-04	0.639	0.975	0.47	0.04	0.521	0.984	0.77	1.78E-06	3.03E-05	0.268	0.996	1.00	3.57E-06	0.2	0.355	0.992